Grant Agreement Number 608553

IMAGE
Integrated Methods for Advanced Geothermal Exploration

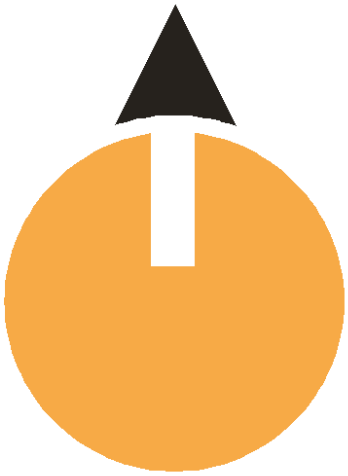

IMAGE-D3.1

Final report on:
understanding from deep drilling and exhumed systems

Responsible author	Domenico Liotta (UNIBARI)
Responsible WP-leader Responsible SP-leader	Domenico Liotta (UNIBARI) Gylfi Páll Hersir (ISOR)
Contributions by:	Domenico Liotta, Andrea Brogi, Martina Zucchi, Caterina Bianco, Massimiliano Ciacci, Rosa Anna Fregola, Alfredo Caggianelli (UNIBARI) Guðmundur Ómar Friðleifsson (HS Orka) Gylfi Páll Hersir, Helga Margrét Helgadóttir (ISOR) Giovanni Ruggieri, Valentina Rimondi, Andrea Dini, Andrea Orlando, Laura Chiarantini, Chiara Boschi (IGG-CNR)

Introduction & summary

This report summarizes the results of the studies carried out for the achievement of the objectives described at page 14 of 40 of the DoW, *i.e.:* the description of the geometric characteristics of the structural conduits and traps where geothermal fluids are channeled and stored, by studying exhumed geothermal systems to be compared to the active ones (Task 3.1). We studied also the geochemical features of the paleofluids (Task 3.1)

The main target of WP3 is to provide information on the geological processes and processes controlling the relationships between the geological structures and fluid flow. To follow this, we have applied the classical approach of structural geology and geochemistry of paleofluids and of hydrothermal minerals.

The field structural study produced new geological maps and highlighted the kinematics and geometry of the shear and extensional fractures, as later on described. The geochemical studies focused on the boundary conditions (P-T and geochemical properties) of reservoirs of high-temperature magmatic geothermal systems in both study areas, the exhumed Elba Island (Italy), for the continental crusta, and Geitafell (Iceland) for the oceanic crust. The geochemical study developed through: 1) rock sampling for laboratory analyses in key-areas comprising a selections of core-samples from bore-holes drilled in the Geitafell area and 2) mineralogical and petrographic studies and laboratory analyses of fluid inclusions, isotopes and mineral-chemistry on selected samples. Fluid inclusions, isotopes and minerals represent, in fact, unique geological archives to reconstruct the to derive the pressure-temperature and geochemistry-time evolution of luid circulations in fossil high-temperature magmatic-hydrothermal systems, to obtain information on water-rock interaction between host rock and fluids and to characterize the fluid source(s) that flowed in the fossil systems.

The study had benefitted of the scientific and fruitful integration between the Italian and Islandic teams both during the field and laboratory studies.

In this report therefore the results of the activities carried out during the first and second year of the IMAGE project. We have started the investigation of the exhumed and active geothermal systems in Italy and Iceland, as representative of continental and oceanic geothermal systems, respectively. As it concerns Italy, the eastern Elba Island is considered as the fossil exhumed analogue of the active Larderello geothermal field. As it concerns Iceland, Geitafell is the exhumed analogue of the Krafla active geothermal system.

Please note the Icelandic collection of samples and data was influenced by the date of beginning of the project (2 November 2013), in a period not favorable to fieldwork. Thus, the first collection of data was provided in the second half of May 2014, In Iceland.

The results here below summarized derive from the work of: Caterina Bianco, Massimiliano Ciacci, Martina Zucchi (PhD students, the latter two are IMAGE-funded scholarships), Alfredo Caggianelli, Rosa Anna Fregola, Domenico Liotta, Andrea Brogi (researchers) of Bari University, Guðmundur Omar Friðleifsson of HS-Orka, Helga Margrét Helgadóttir of ÍSOR, Giovanni Ruggieri, Andrea Dini, Andrea Orlando, Chiara Boschi (researchers, CNR-IGG), Valentina Rimondi and Laura Chiarantini (post-doc student, IMAGE funded scholarship, CNR-IGG).

In synthesis our studies allow us to state:

a) the analysis of exhumed geothermal systems give us fruitful information on what it is at depth in present geothermal fields whether the tectonic and stratigraphic context are strictly comparable;

b) the study of the relationships between fractures and mineralization indicate that transfer/transform faults and normal faults are the main structural conduits for channeling hydrothermal fluids;
c) the structural traps depends on the original permeable characteristics and geometry of the geological bodies that, in the continental crust, are affected by folds;
d) The analysis of the paleofluids by means of fluid inclusion studies indicated that supercritical conditions can be reached in the continental crust where T and P are sufficient;
e) The results from laboratory tests indicate that the composition of the palaeo-hydrothermal fluids can be reached simulating the leaching of wall-rock minerals by a saline fluid.

We believe that the collection and analysis of data was successful completed and it followed the schedule. We are confident to have reached our goals.

The text is followed by the annex containing the cited figures and tables. The two papers already published with some of the results hereafter summarized are also included at the end of this report.

TABLE OF CONTENT

CHAPTER 1 – exhumed geothermal systems in oceanic crust: Geitafell

In this chapter we report our studies on the exhumed geothermal system of Geitafell, as an example of geothermal systems located on oceanic crust. Geitafell (Fig.1.1) represents an analogue of the icelandic active geothermal systems. We have applied methodologies that follow the classical approach of field structural geology and geochemistry of fluids. We have also integrated these with studies carried out in boreholes.

1.1. Geological framework of Geitafell

The geological setting of the area has been intensively studied by Freidleifsson (1983a,b; 1984; 1986) and we follow his conclusions and geological map (Fig. 1.1.1). The study area is characterized by a Tertiary gabbro representing the inner part of the Geitafell Central volcano. This is a Miocene-Pliocene gabbro emplaced at shallow depth (2-4 km) and intruded in Late Miocene flood-basalts beds. The Geitafell Volcano is believed to be located in the rift valley during Miocene and, later on, in the framework of the crustal accretionary process affecting the divergent margins, has been migrating south-eastwards up to the present location, about 20km far from the Icelandic cost. Contact metamorphism of host-rocks is localized and reduced to few meters in the surroundings of the gabbro, and it is clearly marked by the occurrence of mm-size hornblende and augite in the rock-fabrics.
The structural and geochemical study was carried out close to the eastern side of the gabbro intrusion where seven boreholes were drilled into the contact aureole (Fig.1.1.2).
The distribution of extensional and shear veins and associated hydrothermal mineralization were analyzed in order to get information on the reservoirs and feeding channels. Data from fieldwork are integrated with the drillcores and geochemical data. Collection of data began in May 2014.

1.2. Field studies

The field mapping of the area was carried at 1:5000 scale and the result is presented in Fig. 1.1.2 where the location of the studied structural stations is also indicated. The survey was developed through field observations, also constrained by petrographic analyses conducted through optic and electronic microscope (SEM). The list of the collected samples is given in Table 1.2.1.
Gabbro is a hypidiomorphic granular texture, composed of bytownite labradorite, calcite, augite, and titanomagnetite. Olivine and orthopyroxene are most often completely pseudomorphed, mainly to talc, chlorite and magnetite. Host-rocks are made up of tholeiite, olivine tholeiite and feldspar porphyritic basalt flows, some of which also contain phenocrysts of pyroxene and olivine.
Gabbro and its hosting rocks (Fig.1.1.2) are affected by two significant sets of faults, SW-NE and NW-SE oriented. Fault slip surfaces and damage zones (up to 50m thick) of both systems are characterized by shear veins, filled with hydrothermal minerals, such andradite, epidote, quartz and calcite ($\pm$zeolith). Very often the damage zone and the cataclastic levels are affected by hydraulic breccias, now testified by regular and symmetric clasts embedded in hydrothermal minerals (Fig.1.2.1). Hydrothermal minerals such as those before listed have been also found in porous lava levels

hydraulically connected to main fault zones. In these more porous tholeitic levels, the hydrothermal minerals are recognizable in vesicles, up to 10cm in size (Fig.1.2.2).
Along the mineralized fault zones and their surroundings we have carried out a collection of structural and kinematic data in order to get information on their evolution and relation with the hydrothermal circulation (Table 1.2.2). The results from the database are reported in stereonets (Fig. 1.2.3) summarized in cumulative stereonets (Fig.1.2.4), clearly indicating two main structural trends in the area: the SW-NE system is mainly typified by a dominant normal component with a minor right-lateral component, whereas oblique-slip movements chiefly define the NW-SE system of faults. The throw of each structure appears in the order of some meters, as a maximum; the damage zone is defined by comminution of mafic rocks, resulting in breccias and matrix, often cemented by hydrothermal minerals such as epidote, although calcite, quartz, chlorite are diffuse. Rarely zeolite and andradite can locally occur. Mineralized faults and fractures affected the gabbro complex, as well as the hosting rocks. Usually, andradite is present in extensional and shear veins closer to the gabbro, whereas epidote, quartz, calcite and zeolite are found far from it, although the gabbro itself is affected by faults with hydrothermal fluids.

1.3. Boreholes

Core drilling operations commenced on May 10th, 2014, when the drill rig was transported from to the drill site at the Geitafell gabbro contact (Fig.1.1.2). The drill crew arrived on the 11th and started preparations for the first drillsite that evening and the following day. Drilling commenced May 12th with the drilling of an NQ size core at GG-1 (for Geitafell Gabbro-1) and ended May 20th when drilling of the seventh hole GG-7 was finished. The locations of the wells are shown in Fig. 1.1.2.

Conditions for drilling were good and in general it went very well. There were minor delays, mostly due to water circulation. Care was made to site the holes as close to the trail as possible (Fig.1.3.1). Drilling of the first three holes went well although there was only a small amount of host rock in GG-1. In GG-4 no host rock was found so the rig was moved to a new site nearby in an attempt to find more host rock. GG-5 and GG-6 soon reached into intrusive rocks and were abandoned after a short time of drilling. GG-7, however, showed good sections of host rock and the remaining meters of funded core drilling were used for that drillhole, down to 31.8 m. The casings in GG-6 and GG-7 needed to be somewhat deeper than in the earlier holes due to river gravel. Information on the drillholes, i.e. depth, coordinates, water table and depth of casings, is shown in Table 1.3.1. Core recovery was generally very good. GG-6 was the only hole where large parts seemed to be missing from some sections (Table 1.3.2). The holes were logged for temperature after drilling Results are presented in Table 1.3.3.

The cores were all taken from drill sites to the farm Hoffell where they were logged. As mentioned before cores from GG-1, GG-4, GG-5 and GG-6 all had substantial amount of intrusive rocks. The lithology logs of the cores are shown in Figure 1.3.2 along with markings of intrusions (red for mafic and green for intermediate or felsic rock). The rest of the holes had considerable amount of host rock with some excellent examples of contact metamorphism in vesicles and fractures (Figure 1.3.3).

All of the cores were scanned in detail with SmartCIS 1000E at Hoffell. After core logging and photo scanning were finished, the core was sampled for fluid inclusion analyses.

1.4. Geochemical studies

The extinct Geitafell central volcano, located in the east Iceland, provides a rare opportunity to study the evolution of volcano-hydrothermal systems that parallel those of the actively rifting neo-volcanic zone of Iceland, like the Krafla geothermal system.

Glacial erosion has exposed the gabbroic core and more than 2 km of volcanic strata in this 5–6Ma central volcano (Fridleifsson, 1983a). The exposures are particularly good in the northeastern part of the volcano. Extensive investigation of the stratigraphic, tectonic, intrusive and metamorphic evolution of this magma-hydrothermal system was undertaken by Fridleifsson (1983a,b, 1984, 1986), and summarized briefly below.

The Geitafell volcano formed in the active rift zone in central Iceland during the late Miocene to early Pliocene and was active for approximately 1m.y. It is predominantly composed of basaltic lavas and hyaloclastites, with lesser volumes of intermediate and felsic lavas (about 10% by volume). Intrusive units in the volcanic complex include radiating dikes, cone sheets and both gabbroic and granophyric large intrusive bodies.

Within the central volcano, evidence for up to seven periods of hydrothermal activity is preserved in the crosscutting relationships of alteration veins. The earliest veins predate metamorphic activity and are composed of limonite and clays. Upon the emplacement of a central gabbro, at paleo-depth of 1 to 1.5 km, a high-temperature system was active and produced a contact metamorphic aureole consisting of an inner aureole of sanidinite facies basaltic lava hornfels (formed by secondary augite-andesine-ore) enveloped by an outer aureole of skarn deposits (Fridleifsson, 1984). In the inner aureole, veins composed by andesine and pyroxene also occur; a change of secondary pyroxene is observed going from wall-rock that is characterized by salitic pyroxenes to the vein center characterized by hedenbergite.

The skarn is constituted by amygdales partly infilled by hedenbergite and garnet. The lava amygdales were earlier partly infilled by low-temperature minerals such as limonite, opaline silica, clays and possibly calcite, which reacted with metamorphic fluid to produce hedenbergite and garnet assemblages. Upon retrograde conditions hedenbergite was partly replaced by andradite containing inclusions of calcite. An actinolite-sphene vein mineral system occurring within the gabbro, partly replacing augite and ilmenite in the vein-wall-rock zones, was the first hydrothermal mineral assemblage to invade the gabbro heat source during cooling. Fridleifsson (1984) suggested that the skarn minerals were produced from supercritical fluid ($T \geq 400°C$, $P \leq 0.3$ kbar), whereas, the actinolite-sphene assemblage developed from super-heated steam (T $T \geq 300°C$, $P \leq 0.1$ kbar).

Later hydrothermal events superimposed the high-temperature assemblages, producing a widespread mineral alteration that includes: actinolite, epidote, chlorite, quartz, calcite and sulfides. Andradite garnet is also a common mineral in amygdale fillings, stratigraphically below the gabbro exposure at Geitafell. Mineralzones distinguished by their highest temperature index mineral are shown in Fig. 1.4.1.

Epidote is present in veins, amygdale fillings and as groundmass replacement in the actinolite, andradite and epidote zones. Finally, zeolite mineralization related to regional low-temperature hydrothermal system overprints the exposed high temperature mineralization of the central volcano, postdating the volcanic activity in the area.

1.4.1 Samples collection and location

Samples from Geitafell volcano were collected in May 2014. Some of these samples were core-samples coming from the boreholes drilled in the Geitafell gabbro contact aureole in cooperation with Iceland GeoSurvey (ÍSOR) and HS Orka within the IMAGE project (Fig. 2.2.2a).
Samples for mineralogical and fluid inclusions investigations were selected from drills GG1, GG2, GG7 (Fig. 1.4.2b) at variable depths, but always in correspondences of basaltic lava host rock. In addition, other two samples, GE19A and GE14, were selected. These samples are hydrothermal altered lava collected at surface, displaying different mineralogical assemblages located north and south of the Geitafell contact respectively (Fig. 2.2.2b),
Refer to Table 2.2.1 for a brief geological and mineralogical description of samples.
Moreover, samples were investigated for Sr, C and O isotopes (Table.1.4.2)

1.4.2 Mineralogy

Mineralogical assemblages of hydrothermal phases are schematically summarized in Table 1.4.3 compared with Geitafell alteration phases described by Fridleifsson (1983b).
EMPA analyses of selected mineralogical phases are reported in Table 1.4.4.
Primary mineralogical phases typical of the original basalt are hardly recognizable in the investigated samples. Only small elongated crystals of possible feldspar are observable in the wall rock in association with very abundant, iron oxides mostly ilmenite and magnetite. Sparse chalcopyrite grains are also observable. Some veins and masses of chlorite are also observed in the wall rocks, which abundance and extension increases in the proximity of hydrothermal veins.
Most of samples (GG1 17.60-17.70, GG2 3.41-3.48, GG2 16.66-16.76, GG7 13.00-13.10, GG19 A) are characterized by epidote – feldspar – chlorite hydrothermal phases. Samples are characterized by large irregular amygdales and numerous large veins generally filled by calcite and variable amount of quartz. Calcite occurs in few samples (GG2 16.66-16.76 and GG7 13.00-13.10), commonly in platy crystals (Fig. 1.4.3.).
Veins/amygdale margins are characterized by variable amounts of Fe-rich epidote crystals (Table 1.4.4) associated with calcite and K-feldspar (Fig. 1.4.4a; Table 1.4.4). Epidote occurs often as well developed crystals (Fig. 1.4.4b), generally zoned due to variable Fe content (sample GG19 A, Table 1.4.4).
Late chlorite (Table 1.4.4), with K-feldspar relicts, is also present at veins margins often infilling quartz and calcite voids occasionally in association with sphene, magnetite and rare apatite crystals. Iron oxides (magnetite?) occasionally occur also as big masses along the outer margins of amygdales in sample GG2 16.66-16.76.
Smaller veins (up to 100 μm) filled with quartz and epidote (Table 1.4.4) less Fe-rich compared to the previous one, are abundant in some samples, crosscutting the large hydrothermal veins.
Some large (up to some mm) late veins filled by calcite and quartz can occasionally cut the so far observed assemblages.
Two of the investigated samples (GG1 17.29-17.38 and GG1 21.33-21.43) are characterized by actinolite - epidote – feldspar – chlorite assemblage in hydrothermal veins. In the two samples large amygdales and veins up to some cm large occur. They are generally filled by abundant calcite and euhedral zoned epidote (Table 1.4.4) generally located along amygdale margins, in association with resorbed (?) albite crystals (Table 1.4.4) (Fig. 1.4.5a). Central part of veins is filled with calcite with dispersed abundant needle like amphibole crystals (from ferro-actinolite to ferro-tschermakitic hornblende: Table 1.4.4) crystals (Fig. 1.4.5b), which occurs also among albite crystals (Fig. 1.4.5c).

Several generation of veins filled by epidote and calcite-epidote-actinolite can be recognised in sample GG1 21.3-21.43.
One sample (GG7 28.1) is characterized by amygdales usually filled by actinolite, sphene and quartz, with actinolite partially replaced by late-stage chlorite (Fig. 1.4.6a, b) .
Three samples (GG7 23.93-24.04, GG7 29.23-29.39, GG7 29.43-29.61) coming from the medium-deeper portion of well GG7 and one sample from GG3 well (GG3 4.7) are characterized by garnet - actinolite - epidote – feldspar – chlorite assemblage in hydrothermal veins.
In all samples small globular amygdales (up to 1-2 mm large) filled by albite-epidote and chlorite are generally observable. Globular amygdales are commonly cut by small epidote veins.
Some big veins/amygdales (up to 1-2 cm large) are present in the samples showing garnets (0.1-1 mm size) generally occurring in central parts of veins. They range from anhedral, partially resorbed masses (Fig 1.4.7) to more rare euedral crystals (Fig. 1.4.8a) generally with andraditic composition (Table 1.4.4: GG7 23.93-24.04, GG7 29.23-29.39).
They display common inclusions of wollastonite, chalcopyrite and rare pyroxenes (possibly hedenbergite, see Table 1.4.4: GG7 23.93-24.04) (Fig. 1.4.7a); fractures filled by calcite and zeolites are also common in garnets (Fig. 1.4.7b). In sample GG7 29.43 abundant big zoned garnets occurs in the central part of amygdales (Fig. 1.4.8) that vary in composition between andradite in core (Fig. 1.4.8b: light grey portion) to andratite-grossular (Table 1.4.4) generally in rims (Fig. 1.4.8b: dark grey portions). Common inclusions of wollastonite are also present in garnets.
Abundant garnet are often present also along veins margins, displaying generally zoning and variable composition (Table 1.4.4, sample GG7 29.23-29.39) (Fig. 1.4.8a).
Big zoned garnets are particularly evident along sample GG7 29.43-29.61 amygdale margins, where moving from amygdale margins to the center, garnets range in composition from grossular-almandine, grossular-andradite, grossular-almandine (probably hydrogrossular; see Table 1.4.4, GG7 29.43-29.61 points 38, 42, 40) to andradite and andratite-grossular in the outer dark rims (Fig. 1.4.9).
Epidote (Table 1.4.4) is generally present at veins margins in association with needle like amphiboles (Fig. 1.4.9a and Fig. 1.4.9b).
Amphiboles range in composition from actinolite/ferro-actinolite to rare allumino ferro-tschermakitic hornblende (samples GG7 23.93-24.04 and GG7 29.23-29.39) and from ferro-horneblende to actinolitic horneblende in sample GG7 29.43-29.61 (Table 1.4.4).
Late chlorite (Table 1.4.4) often replaces epidote and amphiboles along the outer margin of veins (Fig. 1.4.8a). Some rare K-feldspar have been also observed in association with epidotes. The remnant part of veins in generally filled by calcite and minor quartz.
Common needle like actinolite crystals can be observed in some sample (GG7 29.43-29.61) also in the central portion of veins both in calcite and quartz (Fig. 1.4.8b).
Some late veins (up to few mm large) filled with calcite and zeolites (Heulandite-Laumontite like) crosscut the observed assemblage (Fig. 1.4.7b).

1.4.3 Fluid inclusions

Fluid inclusions were investigated in hydrothermal quartz, calcite and minor in garnet in doubly polished wafers (80 µm) in reflected light microscopy. These phases are considered as the hydrothermal mineralogical assemblage resulting of the intense hydrothermal circulation affecting the Geitafell area. No fluid inclusions were

observed in the other hydrothermal minerals identified at SEM or EMPA, such as actinolite, hedenbergite and wollastonite.
Notation of fluid inclusions is based on the phase assemblage occurring at room temperature, and on the homogenization mode. Fluid inclusions composed by a liquid and a vapor phase are noted V if they homogenize to the vapor phase (L+V→V), and L if the homogenization is to the liquid phase (L+V→L).

1.4.3.1 Petrography

In the following, the description of the fluid inclusions assemblage observed was distinguished for samples recovered from the boreholes and those located at surface.
Samples from boreholes
In quartz, fluid inclusions were not easily identified due to the strong hydrothermal alteration affecting the host rock and quartz itself. Moreover, fluid inclusions were generally small, rarely exceeding 10 μm of dimensions, further increasing the difficulty of their identification.
Fluid inclusions occur in small groups of 5-10 individuals in the center of quartz crystals. They often display an irregular shape and they are often affected by necking-down processes.
In calcite, fluid inclusions are not very abundant as for those in quartz. Dimensions ranges from 10 to 50 μm. Fluid inclusions often display a negative crystal shape, resembling the rombohedrical habitus of calcite.
In quartz and calcite, fluid inclusions were divided in four types (Fig. 1.4.10) on the base of the phase assemblage observed at room temperature:

i) Liquid-rich fluid inclusions (L+V), denoted as L1 (Fig. 1.4.10a), generally showing L/V ratio around 70-80%. L/V can be however very variable from 70% to 30% (Fig. 1.4.11).
ii) Liquid-only fluid inclusions (L), denoted as L2 (Fig. 1.4.9b). They present no vapour bubble at room temperature;
iii) Vapour-rich inclusions (V+L), denoted as V1. They present as dark inclusions, where the liquid is confined to small portions of the fluid inclusions volume (few percent of volume) (Fig. 1.4.10c);
iv) Vapour only fluid inclusions (V), denoted as V2 (Fig. 1.4.10d), where the liquid phase is absent to the resolution of the optical microscope.

In garnet, fluid inclusions were extremely rare, isolated inside the crystals, and often misinterpreted with solid phases, which are abundant inside the garnet. Fluid inclusions are generally liquid-rich (L+V), with relatively constant L/V ratio (~70%) (Fig. 1.4.12); some dark inclusions were found in association with L inclusions (Fig. 1.4.12). During heating, a vapour bubble may sometimes become recognizable in dark inclusions due to its quick movements prior of final homogenization; other times, no phase changes were observed during heating, and these inclusions may possibly represent vapour-only inclusions or opened inclusions.

Coexistence of L1, L2, V1 and V2 inclusions in the same quartz crystals and their location along the cleavage planes of calcites suggest that they are primary in origin (Roedder 1984), and they can also be considered Fluid Inclusion Assemblages (FIA) according to Goldstein and Reynolds (1994). Variable L/V ratios in L inclusions (Fig. 1.4.11), and their coexistence with liquid- and vapour-only inclusions indicate that they may be the result of an heterogenous trapping process (Shepherd et al., 1985), as that occurring during fluid immiscibility. Accordingly, L1 inclusions displaying L/V

~ 70-80% are those considered representative of the entrapment of a homogeneous fluid (liquid), and that could provide reliable P-T data about the Geitafell system.

Samples from altered lava at surface
In sample GE14, fluid inclusions were examined in calcite, garnet and quartz.
In calcite, fluid inclusions were around 50 µm in dimensions and display the typical negative habitus of the host phase. At room temperature, they present mostly as liquid-rich fluid inclusions (L1) with a very small vapour bubble and L/V ratio around 90%. In association to L1, high density liquid-only fluid inclusions (L2) were observed.
This fluid inclusions assemblage is typical of fluid inclusions formed at low temperature, around or less than 80 °C.
In quartz, fluid inclusions display the typical assemblage observed for core samples.
In garnet, fluid inclusions probably coexist with the abundant opaque mineral phases occurring in the centre of the crystals (Fig. 1.4.13). They occur as acicular-shaped inclusions, often being completely dark in color. Clear identification of the presence of a bubble vapour was not possible in any inclusions. Suspect liquid-rich fluid inclusions were however heated to detect any phase changes with increasing temperature.
In sample GE19A, fluid inclusions were extremely abundant in calcite. Fluid inclusions are generally around 50 µm in dimension and display the typical rombohedrical shape of the host phase (Fig. 1.4.14a). At room temperature, they present mostly as liquid-rich and vapour-rich fluid inclusions. A colorless mineral is sporadic found inside fluid inclusions (Fig. 1.4.14b), and was interpreted as a trapped phase during fluid inclusion formation. Raman analysis did not provide indication about the nature of this mineral phase.
They are mostly distributed along the planes of cleavage of calcite, suggesting they are primary in origin. Fluid inclusions assemblage at room temperature is similar as those described for core samples.

1.4.3.2 Microthermometry
Microthermometric data for fluid inclusions in core samples are summarized in Table 1.4.5.
L1 inclusions in quartz represent a relative homogenous group of Th with values being mostly comprised between 240° and 320 °C (Fig. 1.4.15). Lower and higher Th registered in some L1 inclusions are probably due to necking down, moreover heterogeneous trapping processes (i.e. liquid+vapour trapping during boiling) can also explain the anomalous highest Th of a L1 inclusion in quartz. These inclusions are not representative of trapping conditions; Th comprised in the 240-320 °C range is then considered representative of the temperature of fluids circulated in the Geitafell quartz. Frequency histograms for all samples are generally unimodal, with the mode located at 270°C or 290°C (Fig. 1.4.15). Whenever possible due to the morphology of fluid inclusions, Th was measured also for the associated V1 inclusions. Optical disappearance of the liquid phase was observed between 217°C and 313°C (Table 1.4.5), which is considered consistent with that observed for L1 inclusions, if we consider the difficult to accurately determine the final Th for these inclusions (Roedder 1984).
In quartz, initial melting of ice was observed around -20/-30 °C suggesting the fluid is generally poor saline. Tm_{ice} ranged -1.1° to 0.0°C for both L and V inclusions (Table 1.4.5), corresponding to salinity of 0 to 1.9 wt.% NaCl eq. (Fig. 1.4.16). Samples of GG7 drill core show small but remarkable higher salinity with respect to GG1 and GG2 samples, corresponding to 0.3-1.9 wt.% NaCl eq. and 0-0.8 wt.%

NaCl eq., respectively (Fig. 1.4.16). Accordingly, further lower Tm_{ice} of -3.4 °C was recovered in some sporadic inclusions in sample GG7 23.93-24.04, corresponding to a salinity of 5.5 wt.% NaCl eq.
In calcite, Th range is very wide, i.e. between 150°C (lower Th of 70°C measured in GG1 21.33-21.43 are considered as not representative and were excluded) and 280°C (Fig. 1.4.17). Particularly, modes for two core samples are located at 160°C and 250°C for samples GG1 21.33-21.43 and GG7 29.23-29.39, respectively (Fig. 1.4.17). Initial melting of ice was observed around -30°C suggesting the fluid is generally more saline than in quartz. In few inclusions, the formation of hydrates was observed due to the dark and grainy appearance of the inclusions before ice melting. However, it was not possible to measure this temperature with accuracy. Tm_{ice} ranged -6.9° to 0.0°C (Table 1.4.5), corresponding to salinities from 0 to 10.3 wt.% NaCl eq. (Fig. 1.4.18). Particularly, the highest salinities were associated to sample GG7 29.23-29.39, which reported mean values of 4.5 wt.% NaCl eq. against the 0.6 wt.% NaCl eq. value of GG1 21.33-21.43.
In garnet, data are few and rather inhomogeneous. Th spread the 213-357°C range (Table 1.4.5). Since fluid inclusion occurs as isolated individual inside the crystal, it is difficult to ascertain which temperature mostly represents garnet trapping condition of the fluid. Tm_{ice} is in the common low range reported for the associated quartz mineral.
Microthermometric data for fluid inclusions analyzed in samples recovered at surface are summarized in Table 1.4.5.
In sample GE14, careful observations were devoted to inclusions occurring in garnet suspected to be liquid- or vapour-rich. However, no phase transitions or L/V ratio modifications were observed up to 600 °C. We believe then that mostly of these inclusions did not actually represent fluid inclusions but they are rather trapped mineral phases inside the garnet.
Associated quartz and calcite display very different Th (Table 1.4.5), in the 230-280°C and 50-100°C range, respectively (Fig. 1.4.19). For calcite, metastable L2 inclusions were overcooled to -40°C to allow the nucleation of a vapour bubble, and then the measurement of Th. These Th are generally in the range of that measured in L1 inclusions, although sometimes higher. Higher Th in L2 is probably due to minor stretching of these inclusions during ice formation, which is common for fluid inclusions with very high L/V ratios (Shepherd et al., 1985). Data for L2 inclusions were included also in the histogram of Fig. 1.4.19, as suggested by the high temperature tail of Th distribution (>90°C).
Distribution modes are 70°C for calcite and 250 °C for quartz (Fig. 1.4.19).
Ice melting occurs at 0.0 °C in quartz, while common metastable phenomena were observed in calcite. During freezing of inclusions in calcite, the vapour bubble generally disappeared due to ice formation. Upon heating, vapour bubble nucleation is contemporaneous to ice formation, and occurred above 0°C and up to 4.8 °C (Table 1.4.5). In addition, most of fluid inclusions stretched after the first or the second cooling, and the vapour bubble expanded to occupy all the volume of the fluid inclusions. These behaviors are typical of high density fluid inclusions displaying very low salinity (Shepherd et al., 1985).
For sample GE19A, Th described a unimodal distribution with a clear mode at 260°C (Fig. 1.4.17). Salinities for these inclusions plot all homogeneously to 0 wt.% NaCl eq. (Table 1.4.5). CO_2 has not been detected in any inclusions, neither as a discrete liquid phase either as a minor component by clathrate formation or by phase changes around -56.6 °C.

1.4.3.3 SEM-EDS analysis

Evaporate mounds and patchy accumulations of salts were found on the surface of only two (GG7 23.93-24.04, GG7 29.23-29.39) of the four overheated samples selected for this type of analyses (Fig. 1.4.20). These two samples contain the FIs characterized by the lowest Tm_{ice} values (Table 1.4.5) and therefore contain FIs with the highest salinities (up 10.3 wt.% NaCl eq.). The lack of salts mounds on the surface of the other samples can be likely to the low-salinity of the trapped inclusions.

SEM-EDS analyses on salts from decrepitated FIs are qualitative or at the best semi-quantitative, because the non-ideal analytical setting and the non-homogeneous distribution of the salts (Roedder 1984). SEM-EDS analyses on the examined samples reveal significant amount of F in most of the precipitated salts. The accumulation of F can be probably related to the small solubility of fluorite (CaF_2): when the fluid come out from the decrepitated FIs, fluorite precipitated immediately around the escaping fractures. This imply that the analyses overestimated Ca and F of the mounds. Table 1.4.6 shows the results (in mol%) of SEM-EDS analyses on the precipitated, in this table F was not reported, whereas the concentration of Ca was reduced by an amount equal to half of the mol% of F. For the analyses on calcite Ca was not reported as most of the signal of this element come from this mineral. SO_4 was computed from the concentration of S.

Table 1.4.6 shows large concentration variation of the salts components likely because of the non-homogeneous precipitation of the different types salts. Although, the reported compositions doesn't represent the composition of the salts dissolved in fluid inclusions we can observe from Table 1.4.6 that most of the precipitated salts are characterized by high amount of Ca and SO_4.

1.4.4 Isotopic data

Selected samples were investigated for Sr, C and O isotopes in order to derive the source of the fluid and fluid/rock interaction mechanism. For Sr, the analyzed minerals were calcite, epidote, garnet and zeolite belonging to sample GE14, GE100 and GE101 (Table 1.4.2). For C and O analysis in calcite, both superficial and core-samples were investigated (Table 1.4.2). For core-samples, calcite powder was recovered from the white hydrothermal veins in the basalt host rock, and analyzed by XRD to ascertain for its composition.
Data for Sr, C and O isotopes accomplished in this work are reported in Table 1.4.7. An extensive review of stable isotopic composition of hydrothermal quartz and epidote in Geitafell has been recently published by Pope et al. (2014), and is reported in Table 1.4.8. $^{87}Sr/^{86}Sr$ range 0.703214 to 0.703889 (Table 1.4.7), and locate in the range described for Icelandic tholeiites (Hart et al., 1973).
$\delta^{13}C$ and $\delta^{18}O$ of hydrothermal calcites range -6.06‰ to -4.62‰ and -1.21‰ to 11.96‰, respectively (Table 1.4.7). In particular, $\delta^{18}O$ displays a very wide range of variation, which may indicate: i) multiple sources for the fluid; and/or ii) different temperature of formation (and hence different fractionation factors). Since the fractionation factor between the oxygen in calcite and the oxygen in the fluid is temperature-dependent, it was possible to derive the O isotopic composition of the fluid ($\delta^{18}O_{H2O}$) from the known $\delta^{18}O$ values in calcite and the temperature of calcite precipitation, obtained from fluid inclusions data. For this purpose, the equation of O'Neil et al. (1969) was employed; based on the mean Th measured in fluid

inclusions, the following temperature of precipitation of calcite were assumed: GE14 = 80°C, GE19A= 250°C, GG7 13.00-13.10, 23.93-24.04 and GG2 16.66-16.76 = 250 °C (corresponding to the mean Th of sample GG7 29.23-29.39). Recalculated $\delta^{18}O_{H2O}$ span from -8.4‰ to +4.6‰ (Table 1.4.7), with the lower values reported for superficial samples GE19A and GE14.
Similarly to O, measured $\delta^{13}C$ were employed to recover the isotopic composition of the CO_2 dissolved in the fluid ($\delta^{13}C_{CO2}$) by means of the equation of Bottinga (1968). Recalculated $\delta^{13}C_{CO2}$ are in Table 1.4.7 and range -4.8‰ to -0.3‰.

1.4.5 Mineralogy

As illustrated in paragraph 1.4.3 and table 1.4.3, mineralogy of all investigated samples is clearly comparable with Geitafell alteration phases described by Fridleifsson (1983b), which estimate that fluid pressure in the metasomatic contact aureole, approached the lithostatic pressure (≤ 0.3 Kbar).
Most of samples are characterized by epidote – feldspar – chlorite hydrothermal phases, in well developed amygdale halo zones and following Fridleifsson (1983b) classification, are ascribable to epidote alteration zone thus representing the late stage of intrusion cooling, and should have formed in hydrothermal system with temperature range around 230-280 °C.
Since the low temperature limit for actinolite formation in Iceland active high - temperature system is estimated above 280°C (Kristmannsdottir, 1979) all other samples actinolite bearing, should have formed during earlier cooling stages at higher temperature range. The upper temperature limit for the development of such phase is difficult to estimate (Fridleifsson & Bjornsson, 1986).
All samples characterized by actinolite - epidote – feldspar – chlorite hydrothermal phases (belonging to Fridleifsson (1983b) actinolite zone) should have formed above 280-300°C
Fridleifsson (1984) reported the presence at Geitafell of a contact metamorphic aureole consisting of an inner aureole of sanidinite facies basaltic lava hornfels (formed by secondary augite-andesine-ore) enveloped by an outer aureole of skarn deposits (hedenbergite and garnet). Whereas an actinolite-sphene assemblage occur within the gabbro and replace augite and ilmenite of the vein-wall-rock zones.
The presence of such high temperature hydrothermal phases typical of skarn assemblages like hedenbergitic pyroxenes, have been hardly detected among our samples. Only in the three samples with garnet - actinolite - epidote – feldspar – chlorite mineralogical assemblage (Fridleifsson, 1983b; andradite zone), hedenbergite and wollastonite inclusion have been commonly detected in andradite garnets. This could represent retrograde conditions in which the hedenbergite is replaced by andradite. Following Fridleifsson (1984), which report the temperature-oxygen fugacity diagram for such skarn minerals for 0.3 kbar and XCO_2= 0.1, the coexistence of andradite - hedenbergite phases may have a large range of temperature, from about 350°C up to over 500°C depending on oxygen fugacity. Since analysed garnets bears mostly wollastonite inclusions (instead of calcite) and assuming a value of XCO_2= 0.1, the lower temperature buffer for the previous retrograde condition (andradite - hedenbergite) can be estimated around 450°C (Fridleifsson,1984). These set of samples (garnet bearing) should therefore represent the highest temperature registered among the investigated drill holes.

1.4.6 Fluid inclusions: fluid composition and trapping conditions

The genetic coexistence of L1, L2, V1 and V2 in hydrothermal quartz and calcite of Geitafell system is likely related to fluid immiscibility processes such as boiling. The

variable L/V ratio showed by L1 inclusions is indeed a typical consequence of the contemporaneous trapping of liquid and vapour within a single inclusion (i.e., heterogeneous trapping) under immiscibility conditions (Roedder 1984). Under this assumption, there is no need for a pressure correction, and Th values for inclusions that trapped a homogenous phase correspond to the trapping temperature for the fluid (e.g. Shepherd et al., 1985). Accordingly, hydrothermal quartz indicates that fossil fluid circulated in a temperature range of 240°C and 320°C (Fig. 1.4.21) which is in rather good agrement with the temperature range suggested for the epidote and actinolite alteration zones by Fridleifsson (1983b). Calcite from borehole samples formed at lower temperature, in a large range comprised between 150°C and 270°C (Fig. 1.4.21) or even at lower temperature for calcite from surface sample (GE14).

Fluid inclusions in garnets are rare and they show a rather large Th range (Table 1.4.5), therefore, it was not possible to determine if FIs in garnets are representative of the original trapped fluid following the method of "Fluid Inclusion Assemblage" described by Goldstein and Reynolds (1994). Thus, the following discussion must be taken with caution. In addition, it is difficult to ascertain from petrographic data alone, if dark inclusions represent a vapor-phase trapped during immiscibility. However, as all dark inclusions in garnets didn't show liquid phase neither phase changes during microthermometric experiments, they would represent opened inclusions and not vapor-rich inclusions. Thus, boiling conditions probably didn't occurred during garnet precipitation. Considering that the inclusion with Th of 357°C (the maximum Th measured in fluid inclusions hosted in garnet) is representative of the original trapped fluid the isochore of this inclusion has been calculated following the work of Steele MacInnis et al. (2012) considering the salinity of the inclusion (1.1 wt. % NaCl). The isochore has been traced as a solid line departing from the L-V curve in Fig. 1.4.21 (the L-V curve at 1.1 wt. % NaCl eq. has not been traced since it overlaps with that of pure water). Critical points have been reported for pure water and a fluid with 1.1 wt. % NaCl, and corresponds to 374°C-218 bars and 384°C-243 bars, respectively (Knight and Bodnar, 1989). Pressures constrain must then be applied to derive P-T trapping conditions of the fluid. The paleo-depth of the Geitafell system is estimated to be 1600 m (Baumann, 2014; Fridleifsson, 1983a), corresponding to a hydrostatic pressure of ~160 bars. In addition, an ice cover of 500m or 1000m can be assumed; a density of 0.9 g/cm^3 was considered for ice in pressure estimates. For an ice cover of 500m (1000) m, the overpressure is ~ 45 bars (90 bars), corresponding to a total pressure of the system of ~200 or 250 bars (Fig. 1.4.21). Also considering an ice cover of 1000 m, a fluid trapping temperature of 370 °C was derived, which is lower than the critical temperature of a 1 wt. % NaCl eq., like that entrapped by garnet. We could calculate that in hydrostatic conditions, a minimum ice cover of ~2000 m should be hypothesized to reach the supercritical temperature of this fluid salinity, i.e. >384°C.

As an alternative hypothesis, based on the mineral assemblage hedenbergite-andradite, Fridleifsson (1984) considered that the gabbro contact aureole was characterized by a lithostatic load of about 1km, with an estimated fluid pressure around 300 bars. Under this hypothesis, an ice cover of only 500 m is enough to reach the supercritical conditions in the Geitafell hydrothermal system (Fig. 1.4.22).

Burchardt et al. (2011), on the basis of the measured orientations of inclined sheet intrusions, calculate the depth of the gabbros at Geitafell. These would represent the magma chamber feeding the inclined sheet intrusions. The calculated source depth of the sheets is 2 to 4 km below the paleo-land surface (Burchardt et al., 2011). This depth is significantly higher than that proposed by Fridleifsson (1986) for the gabbro intrusions (about 1 km below the ground surface). Fridleifsson (1983a, p. 58), however, also estimated the source depth (focal point) of the main cone sheet

systems (his intrusive phases 5 and 6) and concluded the source depth for the majority of cone sheets was at some 2.5 km below the center, i.e. above 1,5 km below the present exposure level.
In Figs. 1.4.21 and 1.4.22, the equilibrium line for the assemblage calcite+quartz ↔ wollastonite+CO_2 is also reported. Wollastonite was abundantly recovered inside garnet, but neither calcite or quartz are documented in equilibrium with this mineral (see section 1.4.3). To plot in the wollastonite-only field, a fluid inclusion trapped in garnet should then follow the isochore up to at least 500 bars (Figs. 1.4.21 and 1.4.22). From the above considerations, this pressure limit seems unrealistically high for the Geitafell system considering either hydrostatic pressure and lithostatic conditions (300 bars) proposed by Fridleifsson (1984) for the development the gabbro contact aureole.
The recent MSc work thesis of Baumann (2014) reported additional data on fluid inclusions in quartz and garnet of the Geitafell hydrothermal system. Similar to our work, fluid inclusions above the critical temperature of water were not observed in Baumann's work. In garnet, a maximum Th of 370°C was measured, and considering that inclusions a supercritical entrapment was possible assuming an ice cover of more than 500 m and a hydrostatic pressure regime. Results of our study and Baumann's work are moreover similar looking to the fluid composition, essentially low-saline (meteoric) fluid, although a boiling assemblage for fluid inclusions in quartz was not documented in that previous work.
Fluid inclusions study shows strong evidences that the fossil exhumed system of Geitafell was fed by a low-salinity fluid, suggesting a hydrothermal system mainly fed by meteoric water. In addition, CO_2 was present in the system as testified by hydrothermal calcite. The possible presence of dissolved CO_2 in fluid inclusions should be considered, as this may depress the Tm_{ice} and thus result in an overestimation of the real salinity (Hedenquist and Henley 1985). Since during freezing of fluid inclusions, clathrate formation was never observed, CO_2 in the Geitafell system may be estimated to be less than 0.85 m (~ 3.7 wt.%; Hedenquist and Henley 1985), corresponding to a depression of ice melting temperature of -1.48°C. Then, the presence of only CO_2 could not account for the lower Tm_{ice} reported for sample GG7 29.23-29.39 (and minor for GG1 21.33-21.43), where an increase trend of salinity of the fluid up to values ~10 wt. % NaCl eq. could be observed (Fig. 1.4.23). This trend is likely due to the precipitation of calcite at boiling. Such process, in fact, cause calcite precipitation and the preferential partitioning of the non-volatile solute to the liquid phase during the steam loss (and CO_2 loss). In general, geothermal systems are characterized by adiabatic boiling, in this case salinity increase is accompanied by a temperature decrease (Hedenquist and Henley, 1985). Adiabatic boiling process, however, cannot account to the significant salinity increase recorded by FIs of GG7 29.23-29.39. Large salinity increases without will only arise from open-system isothermal boiling, where the heat is supplied by the country rocks (cf. Simmons and Browne, 1997). In shallow, liquid-dominated system, isothermal boiling occurs rarely, and could explain only local, high salinity enrichment within fractures isolated from the rest of the system.
SEM-EDS analyses on salts mounds formed upon FIs decrepitation also suggest that the hydrothermal fluids contained dissolved Na, K, Mg, Ca, SO_4, Cl and F. In particular, these analyses evidenced the presence of significant concentration of Ca and SO_4. The occurrence of SO_4 suggest that significant amount of magmatic SO_2 was introduced in the Geitafell hydrothermal system. The acidity of the fluid related to SO_2 introduction would have favored cations (comprising Ca) mobilization from the dissolution of primary minerals.

1.4.7 Origin and evolution of hydrothermal circulation at Geitafell

Fluid inclusion and isotopic data indicate that the fossil hydrothermal system of Geitafell was fed by meteoric water. In particular, recalculated $\delta^{18}O_{H2O}$ range from -8.4‰ to +4.6‰ (Table 1.4.7), with the lower values reported for superficial samples GE19A and GE14. These lower values are consistent with a meteoric-derived fluid, which displays a $\delta^{18}O$ around -8‰ (Pope et al., 2014). However, samples from boreholes generally display more positive $\delta^{18}O_{H2O}$, particularly calcite in GG7 23.93-24.04, suggesting strong interactions with the Icelandic basalts, having $\delta^{18}O$ from +5.5‰ to about +3‰ (Faure 2001). Accordantly, similar positive ^{18}O shift of the fluid from a strictly meteoric composition, are reported in the analyzed quartz and epidote of Pope et al. (2014) (Table 1.4.8). Different water/rock ratios and/or the duration of this interaction may account for the variable $\delta^{18}O$ reported for the fluid.
$^{87}Sr/^{86}Sr$ of different hydrothermal minerals range between 0.703214 and 0.703889 (Table 1.4.7). These values are in the range described for Icelandic tholeiites (Hart et al., 1973) suggesting that Sr was incorporated in the hydrothermal fluid as a consequence of fluid/basalt interaction.
Similarly to O, measured $\delta^{13}C$ were employed to recover the isotopic composition of the CO_2 dissolved in the fluid ($\delta^{13}C_{CO2}$) by means of the equation of Bottinga (1968). Recalculated $\delta^{13}C_{CO2}$ are in Table 2.5.1 and range -4.8‰ to -0.3‰. Lower values are similar to those reported for Icelandic gases and believed to derive directly from the magma (Sano et al., 1985). For Krafla, for example, magmatic gas is considered to be present everywhere in the Krafla system (Ármannsson et al., 2014). However, a more positive value of $\delta^{13}C_{CO2}$ up -0.3‰ is reported in sample GE14 (Table 1.4.7), which is not surprising in the Icelandic systems. At the geothermal site of Geyser, extremely high $\delta^{13}C_{CO2}$ (+18‰) was indeed reported in geothermal gases (Sano et al., 1985) and attributed to multiple stage fractionation of CO_2 occurring at high temperature (>120°C). However, in our study, the more positive value is computed for calcite precipitating at ~80°C. Such enrichment in ^{13}C may be then the result of preferential partitioning of the light ^{12}C isotope in the steam phase during boiling of the fluid, that occurred at some depth in the Geitafell geothermal system and was documented in core-samples.
The petrographic assemblage and microthermometric data suggest that the system was at boiling during quartz and calcite precipitation, at temperatures not exceeding 300°C. Data indicate that quartz and calcite registered the highest temperature in correspondence to the bore-hole GG7 (Figs. 1.4.24, 1.4.22), probably suggesting the location of this area more proximal to the heat source and/or that it was an upflow zone.
Analysis of garnet does not provide much information about the system, although it highly represents the mineral phase with the highest temperature. Assuming that the fluid inclusion with highest Th was trapped at a fluid pressure of 300 bar conditions, an ice cover of 500 m should be supposed to reach the supercritical conditions documented by the mineral assemblage study of Friðleifsson (1984). Under this hypothesis, fluids with temperatures >380°C may have circulated in the Geitafell system.

1.4.8. Integration of the physical-chemical characteristics of the fossil fluids with those available from the Icelandic geothermal fields

The fossil hydrothermal system examined in this study shows major similarities with the Icelandic present-day systems, especially considering: i) fluid composition and sources; and ii) the temperature of the fluid. Similarly to the Geitafell system, present-day exploited high-temperature geothermal systems in Iceland are

characterized by meteoric-derived recharging reservoirs (Arnórsson, 1995), with the exception of Reykjanes and Svartsengi, where an important seawater component is supposed. Particularly, on the base of isotope data (δD, $\delta^{18}O$), the recharge was considered to be essentially local in origin for the subfields of Leirbotnar, Sudurhlídar and Leirhnúkur in Krafla, while the Suðurhlídar, Hvíthólar, Sandabotnar and sub-fields may be recharged from far south (Ármannsson et al., 2014). On the contrary, magmatic water is believed to contribute in very low amounts in modern systems (<0.6%) (Arnórsson, 1995).
Fluid temperature in Icelandic systems reach up to 380°C in deep boreholes (Arnórsson, 1995), and in most of the systems (Krafla, Námafjall, Nesjavellir, Reykjanes, Svartsengi and Eldvörp), temperature follows the boiling curve with depth (Arnórsson, 1995). In the high- temperature Leirbotnar sub-field, a lower geothermal zone ranging from 1000-1300 m down to the deepest well (2,200 m) is characterized by a fluid at boiling conditions at 300-350°C (Sveinbjornsdottir et al., 1996). In well KJ-38 in Krafla, temperature measurements with fluid inclusions indicate a formation temperature of quartz around 350°C at a depth of 1600 m (Mortensen, 2013). Concordantly, other sub-systems in Krafla, like Hvíthólar, Sandabotnar, Sudurhlídar and Vesturhlídar, are two-phase systems following the boiling curve up to 260-300°C. As reported by our study, fossil fluids circulated in Geitafell were characterized by similar comparable physical conditions, being characterized by fluid circulating at boiling and temperature mostly between 260 and 300 °C.
$^{87}Sr/^{86}Sr$ and stable isotopes in selected hydrothermal minerals concordantly point towards a meteoric origin of the fluid that circulated in the fossil system of Geitafell. Fluid/rock interactions are responsible for isotope shift of the fluid from the meteoric composition to more ^{18}O-enriched composition. Concordantly with the active geothermal systems of Iceland, and specifically with Krafla, CO_2 was mainly of magmatic-derivation.
The fossil hydrothermal system of Geitafell, therefore, can be considered truly representative of a paleo-geothermal analogue of Icelandic geothermal systems like Kafla.
The examined core-samples showed that very high-temperature mineral assemblages (i.e. hedenbergite and wollanstonite) are scarce as they were replaced by typical "geothermal" high-temperature mineral assemblages (i.e. garnets, actinolite, epidote). However, clear evidences of very high-temperature conditions at Geitafell are reported by Friðleifsson (1984) on the basis of the mineralogical assemblages. Considering the similarities between the Geitafell hydrothermal fossil system and the "Krafla like" Icelandic geothermal systems we can suppose on the basis of the mineralogical data of Geitafell that very high-temperature mineral assemblages occur below the presently exploited geothermal reservoirs. These assemblages can be used as pathfinders in the research of supercritical fluids during deep-drilling in super-hot zones. The only FIs that may record super-critical fluids at Geitafell are in garnet. However, FIs in this mineral are scarce and didn't show consistent microthermometric data this rises some doubt on their representativeness. However, if we assume that the inclusion with highest Th were trapped under supercritical conditions such conditions can occur at a pressure of at least 350 bars.

1.5. Final Remarks

Mineralogical, isotopic and fluid inclusion studies on core- and surface samples indicated that the Geitafell fossil hydrothermal system was characterized by a fluid circulation that caused the precipitation of typical secondary minerals (i.e. quartz, calcite, garnet, epidote, actinolite, albite, zeolites, etc.) found in many Icelandic geothermal systems. These phases replace previous high-

temperature skarn minerals (i.e. hedenbergite and wollanstonite) which occur as relict in the examined samples. However, widespread skarn minerals and contact-metamorphic phases were found in the surface samples at Geitafell (Friðleifsson, 1984).
The paleo-geothermal aqueous phase was usually low-salinity (0-1.5 wt.% NaCl equiv.), had meteoric origin and showed more or less intense interaction with the host magmatic rocks ($\delta^{18}O_{H2O}$ range from -8.4 to 4.6‰) . Whereas a magmatic origin was evidenced for CO_2 ($\delta^{13}C_{CO2}$ range from -4.8 to -0.3‰). The occurrence significant SO_4 in some fluid inclusion may be ascribed by magmatic input of S species in the fluid. The hydrothermal fluid circulated at boiling conditions, in some cases prolonged non-adiabatic boiling caused significant salinity increase (from 1.5 to 10 wt.% NaCl equiv.).
Temperature during quartz crystallization ranged from 240°C to 320°C; with the highest mean values in the area of the GG7 (Fig. 1.4.24) well which, therefore, might represent a paleo-upflow zone. During calcite deposition temperature was lower: mostly between 150°C and 270°C, in some cases down to about 80°C.
Supercritical conditions at Geitafell could be hypothesized for an inclusion in garnet if the fluid was trapped at a least 350 bars. However, this hypothesis must be taken with caution as the FIs in garnet might be not representative of the trapped fluid. Additional analyses should eventually confirm this hypothesis.
The hydrothermal alteration minerals and the characteristics of the paleo-geothermal fluids at Geitafell (i.e. fluid salinity and temperature) are comparable with those of the “Krafla-like” geothermal systems, supporting the hypothesis that this fossil system is a proxy of these systems. Thus, many information which can be obtained from the study of Geitafell samples can be extended to better understand the “Krafla-like” geothermal systems and in particular the physical-chemical conditions that occur below the exploited geothermal reservoirs.
Furthermore, the integration among field studies, borehole logs and fluid inclusion analyses brought to a conceptual model as sketched in Fig.1.5.1. This was based on the following points:

a) the fluid inclusions data indicate that the origin of the fluid is meteoric
b) the geological field study indicate that circulation of hydrothermal fluids was mostly controlled by the fault zones independently by their orientation.
c) The occurrence of the same hydrothermal mineralogical phases in SW-NE and NW-SE oriented fault systems indicate that the activity of both systems of faults is contemporaneous.
d) The permeable geological levels that are hydraulically connected with the main shear zones can represent reservoirs where hydrothermal fluids were stored.
e) The occurrence of fluid inclusions in andradite may suggest the possibility of supercritical conditions: if it were the case, we need a strong contribution by increasing pressure on fault zones. The only reasonable way to get it, it would be in terms of fault-valve behavior (Sibson, 1992), if other general conditions have been satisfied (e.g.: hydraulic head, Temperature, depth of the structural level).

Finally, we underline that the data deriving from the exhumed geothermal systems are in agreement with the present knowledge on the fluid circulation as it is defined in Krafla active geothermal field. This indicates that the study of fossil geothermal system in oceanic crust represents a powerful approach in order to get information about the properties of the fluids and on the relationships between geological structures and fluid flow. The information so far obtained, can effectively drive the exploration of the active geothermal systems.

Appendix 1

Analytical methods

Mineralogy was investigated using optical microscopy and EMPA (JEOL JXA-8600, 15 kV accelerating voltage, 10 nA beam current) at CNR-IGG of Firenze.
Microthermometric measurements were performed at Linkam THMSG600 heating-freezing stages coupled with ZEISS POL-BK at CNR-IGG of Firenze. The stages were calibrated by using pure H_2O with critical density, and mixed H_2O-CO_2 (CO_2 25% M) synthetic fluid inclusions. Accuracy was estimated to be ± 0.1 °C for final ice melting (Tm_{ice}), and ±1 °C for the vapour/liquid homogenization (Th). For samples where more than one host mineral was studied for fluid inclusions, different fragments were selected for analysis of each mineral.
Apparent salinity of fluid inclusions (Hedenquist and Henley, 1985) was expressed in weight percent equivalent NaCl (wt. % NaCl eq.), and calculated from Tmice following the equation of Bodnar and Vityk (1994). Generally, heating stages were accomplished after freezing, especially for analysis on quartz and garnet. However, this sequence was reversed for the study of fluid inclusions in calcite, due to the inelastic behavior reported for this mineral (Shepherd et al., 1985). Due to higher volume of ice with respect to liquid water, ice formation may be accompanied to stretching of fluid inclusions and consequently incorrect measurement of Th. In sample GE14, due to liquid/vapor metastability processes, monophase fluid inclusions could nucleate a vapor bubble only after overcooling up to -100°C. Erroneously high Th measured after overcooling was discarded.
Scanning electron microscopy-energy dispersive X-ray spectroscopy (SEM–EDS) were employed to characterize the dissolved salts present in fluid inclusions. SEM-EDS technique yields information on the morphology of daughter minerals, on their chemistry, and on fluid composition. The SEM study was conducted on a ZEISS EVO MA15 instrument, equipped with an OXFORD INCA 250 EDS detector, at the Centro di Microscopia Elettronica e Microanalisi of Firenze (M.E.M.A). Operating conditions were: 15 kV accelerating voltage, 150 mA emission current. Selected polished section of quartz and calcite were overheated at about 500°C producing fluid inclusion decrepitation and were then carbon-coated, and mounted for analysis. Fluid inclusion decrepitation allowed the trapped fluids to escape along newly formed fractures connecting the inclusions with the section surface. The aqueous solution quickly evaporated and precipitated the dissolved salts within the fractures and/or on the section surfaces. In some cases, salts mounds formed at the intersection of the fractures with the surface and they were analysed by SEM-EDS.
Raman analyses were carried out using a confocal Raman microprobe Horiba Jobin-Yvon LabRam-IR coupled with an optical microscope at Fondazione Prato Ricerche. The Raman device was equipped with a HeNe laser source (λ0 = 632.8 nm), a monochromator with holographic notch filter, a spectrometer with diffraction grating of 1800 g/mm, and a Peltier cooled CCD detector (1024 × 256pixels). The instrument was

calibrated against the Stokes Raman signal of pure Si at 520 cm−1 using a silicon wafer. Instrument control, data acquisition and elaboration were performed with the software LabSpec 5 (Horiba Jobin-Yvon). Raman spectroscopy was applied to identify some trapped minerals recovered in fluid inclusions and to detect the presence of CO_2 in the fluid.

Sr isotopes have been analyzed at the Dipartimento di Scienze della Terra Università di Firenze following the procedure described in Avanzinelli et al. (2005, and reference therein). Isotopic values have been obtained using a Thermal Ionisation Mass Spectrometer (TIMS) ThermoFinnigan Triton-Ti®. Mass fractionation of Sr isotopes has been exponentially corrected to $^{86}Sr/^{87}Sr=0.1194$.

Each powdered sample was analyzed for C and O isotopes (13/12C and 18/16O ratios) at the CNR-IGG of Pisa using a GasBench II (Finnigan) for automatic analysis of carbonate. Data are given following the standard δ-notation relative to Vienna Peedee Belemnite (PDB) and SMOW (Standard Mean Oceanic Water), respectively. Internal standard was regulatory inserted between the sample set and has an uncertainty <0.20 and <0.10 ‰ for $\delta^{13}C$ and $\delta^{18}O$, respectively.

Chapter 2 - exhumed geothermal systems in continental crust: eastern Elba Island

The study of exhumed geothermal systems in continental crust was carried out following the classical approach of structural geology and geochemistry of fluids and hydrothermal minerals. In general the continental crust evolution implies a greater complexity in the geometry of the geological bodies with respect to the oceanic settings. This implies an influence of the previous tectonic evolution on the reservoirs characteristics and geometry and a different fluid-rock interaction. We have studied The eastern Elba Island area, that is believed as a proxy of the active Larderello geothermal system (Fig.2.1).

2.1. Geological framework of Eastern Elba Island

The evolution of Elba Island is embedded in that one of the inner Northern Apennines, that is an Alpine collisional belt (Cretaceous – Early Miocene) later affected by extensional tectonics (middle Miocene-Present), coevally with the emplacement of crustal magmatic bodies (Fig. 2.1.1). The area under study is the eastern Elba Island where a complete fossil geothermal system crops out, from the heat source, represented by the Porto Azzurro monzogranite (about 5.9 Ma) to the main conduits and reservoirs, marked by the location of ore deposits.

2.2. Field studies

Since the fossil geothermal field insists on already deformed structure and we are interested to investigate the influence of the pre-existing geometries in determining reservoirs and structural conduits, we have realized a new geological map (scale 1:10000, Fig. 2.2.1) of the area, being the existing maps not prepared to highlight the relationship with ore deposits and structures.
The field map, integrated with analyses of rock samples (Table 2.2.1), produced the following results:

a) We have recognized seven tectonic units, five of them belonging to palaeogeographic continental domain (Fig. 2.2.2). This is a novelty in the present knowledge.
b) HP-LT metamorphic conditions were for the first time recognized in the Island; the study was based on thin sections (Fig. 2.2.3) and petrological and geochemical analyses (Table 2.2.2).
c) Hydrothermal circulation is associated to almost vertical oblique-slip brittle shear zones and to almost low-angle normal faults, recognized in key areas, such as the Capoliveri surroundings (Fig. 2.2.4), the Zuccale (Fig.2.2.5) and Barbarossa area (Fig.2.2.6). In all areas, shear veins with tourmaline, Fe-oxides and Fe-hydroxides and quartz (in order of decreasing temperature in the mineralizing fluids) characterize both structures, indicating their common activity during fluid circulation (Fig. 2.2.7).
d) The field survey indicated that the vertical structures are the most suitable for channeling hydrothermal fluids (Fig. 2.2.8) and that their activity postdated the one of the low-angle structures (Fig. 2.2.4 and 2.2.8).
e) Fluids within the vertical structures can laterally migrate, following pre-existing discontinuities and layer permeability differences (Fig.2.2.8), as well

as following pre-existing geometries developed during the collisional stage (Fig.2.2.9). This is the case that is illustrated in Fig. 2.2.10 where the field mapping highlighted that mineralization follows the orogenic fold geometries.

f) What it is reported in point (e), is what we have observed at the shallower structural levels; differently, at deeper structural levels, within the crystalline Paleozoic basement (micaschist), the mineralization is localized in shear fractures where also hydraulic breccias are present (Fig.2.2.11).

g) Using scan area (map at 1:100) of key areas in the basement, scan line and scan box methodology, we have collected useful data for defining the permeability determined by the fractures by measuring length and width of mineralized veins and applying the relation indicated in Fig. 2.2.12. The results are reported in table 2.2.3 and summarized in the diagrams given in fig. 2.2.13 for the different generations of recognized fractures. Similar results were recognized also in key areas at shallower levels (Fig. 2.2.14).

h) The occurrence of vertical structures controlling fluid flow seems to affect the Larderello geothermal field, too (fig. 2.2.15 and 2.2.16), as well as we have demonstrated in eastern Elba Island. Furthermore, kinematic indicators are consistent with those collected in the exhumed Elba Island geothermal system (Fig. 2.2.17).

2.3. Geochemical studies

The contact aureole of the buried Porto Azzurro pluton in the southeastern Elba Island is characterized by a widespread circulation of boron-rich saline fluids, issuing from felsic dykes, which led to the development of tourmaline-bearing metasomatic bodies and hydrothermal vein systems.

This system is evaluated as a possible exposed proxy of the deepest part of the Larderello-Travale geothermal field, where tourmaline veins, seismic reflectors bright-spots and anomalously conductive crust, have been detected in the contact aureoles of Plio-Pleistocene granites (Dini et al., 2005; Bertini et al., 2006). The study of the fossil hydrothermal systems exposed in eastern Elba Island can provide useful information about conditions attained in the contact zone of multiple acidic intrusions, with implications on the research of geothermal reservoirs (super-hot fluids) in the Larderello-Travale geothermal field.

The Calamita promontory is mainly made by low-medium to high metamorphic grade pelitic-psammitic hornfelses with levels of amphibolites (the Palaezoic Mt. Calamita Complex and the Late Triassic Verrucano Group), followed upward by medium grade carbonatic hornfels (Late Trias. - Lower Jura). The geometrically lower part of the Mt. Calamita Complex consists in garnet-bearing, two micas micaschists that Garfagnoli et al. (2005) correlated with ones present in the Paleozoic or pre-Paleozoic crystalline successions of Tuscany (e.g. subsurface of the Larderello geothermal field) (Fig.2.3.1). The widespread contact metamorphism, that affected the Calamita Schists (about 6-7 km in diameter) has been attributed to the emplacement of an intrusive body (Porto Azzurro pluton; 5.9-6.2 Ma), whose apophyses are represented by the monzogranite and tourmaline leucogranite dykes/sills cropping out in the area (Duranti et al. 1992; Dini et al., 2008; Maineri et al. 2003). The estimated P-T conditions during contact metamorphism of the Porto Azzurro pluton in eastern Elba ranges from 300°C (biotite zone) to 650 °C (andalusite-K-feldspar zone and wollastonite zone), with Pmax < 0.18-0.2 GPa (Duranti et al., 1992). Metamorphic grade increases eastward across the Calamita Promontory and the highest grade hornfelses crop out in the eastern part where the tourmaline leucogranite sills and dykes reach the maximum frequency (Garfagnoli et al. 2005 and references therein).

Iron deposits in Elba Island are all located along the eastern coast, describing a narrow N-S belt from Mt. Calendonzio (Rio Albano) to the Mt. Calamita mine. They occur at different structural levels of the complex tectonic pile (see this report), both above and below the Zuccale detachment fault. They have been interpreted as the expression of a paleo-geothermal reservoir comparable to the present-day main reservoirs at Larderello-Travale geothermal field.

2.3.1. Samples collection and location

Twenty-four samples belonging to five Elba Island key areas (Stagnone, Morcone, Ripalte, Valle Giove, Terra Nera, Bacino and Topinetti; Fig. 2.3.2) have been selected, and thereafter analyzed for fluid inclusions by the University of Bari and CNR-IGG (Table 2.3.1). Refer to Table 2.3.1 for a brief geological and mineralogical description of samples. Analytical methods are reported in Appendix 2.
The dyke-sill swarm, which is associated with abundant tourmaline-quartz hydrothermal veins and metasomatic masses in the Stagnone area, has been deeply investigated by Dini et al. (2008). Some chemical analyses on tourmaline have been done as well in this work. Moreover, tourmaline and quartz from the quartz-tourmaline veins of Stagnone have been analyzed for hydrogen, oxygen and boron isotopes. Moreover, O isotopes have been determined in hematite and quartz of Topinetti, Valle Giove and Terra Nera mineralized deposit.

2.3.2 Mineralogy

2.3.2.1 Calamita Peninsula

Chemical analyses of selected tourmalines from Porto Azzurro Pluton Stagnone area, felsic dykes and hydrothermal veins performed by Dini et al. (2008) are reported in Table 1.3.1.1. Main results are summarized in this paragraph.
Felsic dykes are characterized by quartz, K-feldspar, plagioclase and rare biotite or muscovite. Tourmaline is also present with euhedral shape reflecting the original high boron content of the magma (Fig. 2.3.3a). The analyzed tourmalines can be classified as schorl (low MgO content in the range 0.4–1.9 wt.%).
Metasomatic bodies have developed at the contact between leucogranites and the host hornfels over a distance of few centimetres up to 1 m, with preferential replacement of biotite rich layers by black microgranular tourmaline and quartz. They are made of fine-grained (100–500 μm) clusters of subhedral to euhedral tourmaline crystals with short prismatic habit (Fig. 2.3.3b). Crystals show zoning with progressive Mg enrichment towards the rim with schorl-dravite brown cores and dravitic dark-brown to green rims. The calcium content is higher (0.4–0.9 wt. %) than in magmatic tourmaline from felsic dykes (0.1–0.4 wt%) (Table 1.3.1.1).
Felsic dykes were sampled to analyze magmatic tourmaline for isotope composition and were denoted as F0 veins (Fig. 2.3.4a). Two sets of tourmaline-quartz veins (F1 and F2) characterize the hydrothermal system that crosscut felsic dykes, hornfels rock and metasomatic bodies (Fig. 2.3.4b,c). Another set of veins (F3) crosscut the previous F1 and F2 veins (Fig. 2.3.4d).
The F1 veins are low-angle veins with thicknesses range from 0.1 to 25 cm and are characterized by variable fabrics and infilling materials.
The F2 veins are high-angle veins moderately to steeply dipping to the W, with widths ranging from 0.2 to 8 cm. They are filled with fine-grained tourmaline and minor quartz with isotropic fabric.

The F3 veins, with widths ranging from few mm to 1-2 cm, are filled only with quartz and they perpendicular crosscut the other two vein systems.
Tourmalines have been analyzed in F1ST1A; F1ST4C; F2ST3A, F2ST1C, F1ST3A, samples, which are reported in Table 2.3.2 and Fig. 2.3.5.
Tourmalines in F2ST3A veins generally display a schorl – dravite composition with more variable calcium contents (0.1 – 0.9 wt. %) compared with those analyzed by Dini et al. (2008). Analyses of tourmalines from F1-veins show distinctly higher calcium and magnesium contents (1.1–3.2 and 7.1–11.3 wt.% respectively) and dravite-uvite composition.
Some feldspar and plagioclase and rare mica have been also found and analyzed with in veins (Table 2.3.2; Fig. 2.3.6). Common sphene and apatite crystals (white crystals in Fig. 2.3.6) have been found as accessory phases within quartz-tourmaline veins.
Some images of quartz-tourmaline veins sampled at Morcone and Ripalte areas are illustrated in Figs. 2.3.7 and 2.3.8.
At Morcone veins range in width from 2 to 12 cm and are filled with fine-grained dark tourmaline and abundant quartz. Most tourmalines are concentrated in polygonal aggregates with interstitial quartz, but some euhedral crystals commonly zoned are also common among quartz (Fig. 2.3.9).
Tourmaline composition is illustrated on Table 2.3.3 and range in composition from Mg-foitite to dravite with very lower contents in CaO (0.3-0.9 wt.%) and MgO (4.3 – 5.6 wt.%) compared to similar tourmalines from Stagnone.
Smaller quartz-tourmaline veins have been sampled at Ripalte where veins generally do not exceed 5-8 cm in width. Despite most of veins are filled by quartz, in some portions seb-euhedral tourmalines are associated with scarce quartz, mica (see Table 2.3.3) in a fine matrix of K-feldspars (Fig. 2.3.10).
Analyzed tourmalines show all dravitic composition (Table 2.3.3) with NaO, CaO and MgO contents similar of those analyzed at Morcone.

2.3.2.2 Iron mineralized areas

Iron deposits in Elba Island are all located along the eastern coast, describing a narrow N-S belt.
In the present report some samples from Rio Marina (Valle Giove, Bacino and Topinetti) and Terra Nera mines have been selected, and thereafter analyzed for fluid inclusions by the University of Bari and CNR-IGG.
From Rio Marina to Terra Nera the iron ore deposits are hosted in lenses and masses within formations of Monticiano-Roccastrada Unit (MU: Tuscan Unit largely consists of Upper Carboniferous-Triassic metasiliciclastic rocks and Jurassic to Oligocene epimetamorphic succession) or as veins, lenses and irregular masses associated to distal skarns mostly within marbles, calcschists and breccias.
Rio Marina and Terra Nera (shallow parts) mines are mostly characterized by: hematite (either with typical lamellar-micaceous habitus, or flattened rhombohedral crystals) ± pyrite and magnetite (with rare base metal sulfides) in veins; or euhedral pyrite ± hematite and base metal sulfides lenses/masses (usually strongly oxidized to goethite) (Dünkel 2002; Tanelli et al. 2001). Accessory mineral may include: calcite, quartz, chlorite, epidote, gypsum, adularia. Among sulphides the more common phases except pyrite are: sphalerite, chalcopyrite, galena, bismutinite and secondary phases like anglesite and cerussite.
Terra Nera (deep part) is characterized by distal skarn deposits with veins, lenses and irregular masses of: pyrhotite and pyrite with minor amount of magnetite, hematite and chalcopyrite, generally. Skarn minerals include hedenbergite, ilvaite, epidote (Tanelli et al., 2001).

The occurrence of numerous tiny (5–10 mm) crystals of cassiterite, scheelite (1–5 mm in size) and ferberite ($FeWO_4$) disseminated through the hematite-rich groundmasses are documented in both mines (Benvenuti et al., 2012).

2.3.3 Fluid inclusions

Results are thereafter subdivided for each areas of study, i.e. Stagnone, Ripalte, Morcone, Valle Giove, Terra Nera, Bacino and Topinetti. For each section, data are presented in the order of petrography of fluid inclusions, microthermometry, SEM-EDS, Raman and LA-ICPMS analysis.

2.3.3.1 Stagnone

Petrography of fluid inclusions

At Stagnone, quartz contains abundant fluid inclusions, particularly next to the host rock. In the analyzed samples, fluid inclusions were generally small, ranging 5-30 μm in dimensions. Phase assemblage is the same for both F1 and F2 veins (Table 2.3.1), then although differently specified, all the results refer to both type of veins.
Inclusions were divided in three types on the basis of the phases present at room temperature and on homogenization behavior:

v) S-type (L+V +S; ~ 30% of overall abundance), multiphase liquid-rich inclusions (L+V) and containing different minerals (S) at room temperature.

Based on petrographic observation, 7 different minerals (H, S1, S2, S3, S4, S5, S6) were distinguished in S inclusions. However, single inclusions may contain 4 solids at maximum. Such solids occupy from ~10% up to ~50% of the total inclusion volume. One of this mineral (H) is systematically present; thanks to its cubic habitus and isotropic behavior it was optically determined as halite (Fig. 2.3.11a,b,c). Associated to halite, one or two (S1 and S2) minerals are present in the majority of the multiphase inclusions; one of them (S1) is colorless to pale green, is rather large and shows relatively high relief (Fig. 2.3.11b). S2 solid is colorless, has low relief and occurs as platy crystals with elliptic shape (Fig. 2.3.11b,c). S3 is a red-brownish phase observed in about 20% of the inclusions (Fig. 2.3.11c); this phase is not associated to S1, being mutually exclusive. S4 and S5 are very small solids characterized by high relief (Fig. 2.3.11b), whereas S6 is an elongated solid (Fig. 2.3.11c). The systematic occurrence of H+S1+S2 solids or H+S1+S3±S6 solids within single fluid inclusion assemblage suggests that they are daughter minerals. S4 and S5 appear irregularly distributed, suggesting they are probably trapped minerals. However, due to the difficulty to observe such small solids in fluid inclusions, we cannot exclude that such solids are daughter minerals.
Within a number of multi-phase inclusions H, S1 and S3 solids show rather large volume compared to that occupied in other co-genetic inclusions. This phenomenon can be imputed to necking-down processes and/or to the occurrence of such phases in the fluid before its trapping within the inclusions (i.e., the fluid was oversaturated in one or more of such phases). In the latter case, the phase(s) already present in the fluid were trapped together with the fluid in the inclusion (heterogeneous trapping) as accidentally trapped minerals.
Except halite, the other daughter minerals occurring within multiphase inclusions that were recognized by SEM-EDS and Raman spectroscopy are Fe-bearing solids. Raman spectroscopy analyses, in fact, allowed the identification of S1, which resulted to be pyrosmalite [$(Fe^{2+},Mn)_8Si_6O_{15}(OH,Cl)_{10}$] (Fig. 2.3.12), and of S3 phase which resulted to be hematite (Fig. 2.3.13). Raman analysis did not allow the complete identification of the S2, although it indicated the presence of an OH band

(Fig. 2.3.13), which it was not detected for S6. Accordingly to SEM-EDS analysis, S2 and S6 minerals may be interpreted as hydrated Fe(Mn)-chlorides containing additional cations, such as K, Na, Ca (+Al). Because their small sizes S4 and S5 phases could not be analyzed by Raman spectroscopy, whereas during SEM-EDS inspections such phases were not found.
Based on the relation between halite and the vapour phase, S-type inclusions were further subdivided in S-a, if homogenization occurred by halite disappearance (L+V+H → L+H → L), or S-b if the homogenization temperature corresponds to vapour disappearance (L+V+H → L+V → L).

vi) L inclusions (~ 40% of overall abundance), liquid-rich (L+V). L inclusions were further distinguished on the base of the liquid/vapour (L/V) ratio in: a) L1, with L/V ratio ~ 70-80% (Fig. 2.3.11d), and b) L2, with L/V ratio ~ 60% (Fig. 2.3.11e). L1 inclusions may sometimes present a small dark daughter mineral often attached on the wall of the inclusion, identified as hematite by Raman analysis.

vii) V inclusions (30% of overall abundance), vapour-rich (V+L). L/V ratio is ~ 30-40% (Fig. 2.3.11f).

Groups of S and L inclusions often show a three dimensional random distribution suggesting that they are primary in origin (Roedder 1984), and they can also be considered Fluid Inclusion Assemblages (FIA) according to Goldstein and Reynolds (1994). Single large size (relative to host crystal) L1 inclusions were also considered primary in origin (Roedder 1984). L inclusions often show a negative-crystal shape, further corroborating their primary origin.
In F3 quartz veins, the rare fluid inclusions do not exceed 10 μm in dimensions. They are liquid-rich inclusions, similar to the L1 reported for F1 and F2 veins.
Because of its relatively poor optical features and fine-grained nature (100–500 μm), very few isolated inclusions could be observed within tourmaline veins. All these inclusions were found in larger crystals and they are two-phase similar to those found in quartz (Fig. 2.3.14). However, we cannot exclude the occurrence of very small multiphase inclusions not discernible at the optical microscope.

Microthermometry
Microthermometric data for all the types of fluid inclusions occurring at Stagnone are summarized in Table 2.3.4.
During heating, the homogenization sequence for solids other than halite was difficult to be observed due to the low dimensions of fluid inclusions, and to the lack of renucleation of such phases after first homogenization. Careful observations have then been limited to (relatively) big fluid inclusions, where mineral phase relations were clearly observable. Halite and complex Fe-chlorides usually dissolves below 400°C. Melting of S2 is generally the first phase change observed during heating above 25°C, particularly between 60°C and 90°C. Although they are similar in composition, S6 dissolved at much higher temperature, i.e., ~360°C. With continued heating, liquid-vapour homogenization by vapor-bubble disappearance (Th) is the next phase change in approximately 90% of S-type inclusions (S-a). Th varies widely from 192°C to 330°C with most inclusions homogenizing between 260°C and 280°C (Fig. 2.3.15a). Halite dissolution generally follows vapour by several tens of degrees (up to 150 °C), and locates in the 320-360°C range (Fig. 2.3.15b). Halite may sometimes persist above 420°C up to stretching of fluid inclusions which begin

around 450°C. The majority of fluid inclusions decrepitated or stretched prior to total homogenization, then temperature increase above 450°C was limited to specific sample fragments to avoid S inclusions disruption. In survived inclusions, pyrosmalite was nearly always the last phase to be left in the inclusions. With continuous heating, pyrosmalite displayed one of the four different behavior during heating: i) complete dissolution at relatively low temperature (350-390°C); ii) transition of the original crystals in small grains gradually disappearing up to 550-600°C, and eventually renucleating; or iii) reduction in dimensions without homogenization up final decrepitation; iv) stable and apparent no detectable decrease in size up to decrepitation.
Because the majority of inclusions homogenize by solids dissolution, Ts_{hal} was considered as the total homogenization temperature for multiphase S-a inclusions (Th(total)).
A small number of fluid inclusions (<10%) exhibits halite dissolution at temperatures below liquid-vapour homogenization (S-b). Halite dissolves at 141°C to 306°C and final homogenization to liquid occurs between 279°C to 315°C (Table 2.3.4).

Calculated salinities for S-a inclusions range from 37 wt.% to 49 wt.% NaCl eq., while lower values correspond to S-b inclusions (29 wt.% to 39 wt.% NaCl eq.) (Fig. 2.3.16).

Although differently specified, L1 and L2 inclusions were not further divided in microthermometric data presentation, as a clear distinction between these two typologies was difficult by optical inspection. Th displays a wide range, particularly for L inclusions (309-595°C) (Fig. 2.3.17), and much higher temperature for V-rich inclusions (520-596 °C), with only ~20% of inclusions homogenizing below 600 °C. Distribution frequency is multimodal for L inclusions, presenting a plateau at low temperature (350-400 °C), and two modes at higher temperature (450-475°C and 500-525°C). Initial melting of ice was observed around -50/-55 °C suggesting that salts like Fe- chlorides should be present in addition to the more common Ca and Mg ones. Dissolution of hydrates always occurred before ice, in the range of -33.1 to -23.2°C. Tm_{ice} ranged -31.3 to -12.3°C and -27.2 to -14.1°C for L and V inclusions, respectively (Table 2.3.4). For L inclusions, the distribution is characterized by several modes, i.e., -27.0, -22, -18.0, and -14 °C (Fig. 2.3.18); the mode of -18°C exactly coincides with that of V inclusions (Fig. 2.3.18). Calculated salinities are between 16 wt. to 30 wt.% NaCl eq. (Fig. 2.3.16).

For inclusions hosted in tourmaline, the few data spread a very wide range (178-413 °C), suggesting that they are probably affected by post trapping processes (like necking down and/or stretching). Tm_{ice} is in the range of that measured in quartz inclusions (Table 2.3.4).

SEM-EDS, Raman and LA-ICP-MS analysis
As expected by optical examination, halite was the main solid observed in S inclusions. The presence of major chloride salts is further confirmed by Raman spectroscopy, as most of daughter minerals did not yield any detectable Raman spectra. Commonly associated to halite, SEM-EDS analysis on platy crystals, presumably S2, indicates that this phase is essentially composed by Fe, Cl, Na and K, with lower amount of Ca and Al (Fig. 2.3.19a); however it cannot be excluded that some or all the detected Na actually come from the nearby halite crystal (Fig. 2.3.19a). S6 solid didn't produced any clear Raman signal, whereas SEM-EDS analyses on elongated solids found in multiphase inclusions indicate that also S6

solids are mainly composed by K, Fe, Cl, with minor Mn and Ca and Al. As indicated in the petrography section, these phases were interpreted as complex iron chlorides, although a clear identification of the mineral species was not possible. Low dimensions of these crystals (<1 μm), provided indeed a low signal and the impossibility to isolate radiation of the selected phase from the surrounding.
L inclusions were recognized at SEM by the remarkably absence of a cubic halite. Here, solids were interpreted as new formed phases, precipitated as a consequence of fluid evaporation during quartz crushing. These precipitates represent then the composition of the fluid contained in the inclusions. These phases are composed by a mixture of Fe, and mono/divalent ions such as K, Na, Ca, Mg, and Cl (Fig. 2.3.19b).
A summary of the fluid inclusions analyzed by LA-ICPMS is found in Table 2.3.5. As already pointed out by microthermometry and SEM-EDS analysis, in L-type fluid inclusions abundant cations other than Na are present in solution. LA-ICPMS indicated that these cations are essentially K and Fe (Fig. 2.3.20a), followed by Mg and minor contributions of Ba and Sr. In some cases, Na is not the most abundant cation, substituted by K and/or Fe (Table 2.3.5). Notably, Ca is generally absent in fluid inclusions. L inclusions are then particularly enriched in Fe (and Mn) (up to 90,000 mg/kg), though no daughter minerals containing this element were found in these inclusions (at least visible at microscope resolution). Base metals like Cu and Zn are associated minor elements, ranging hundreds to thousands mg/kg in concentration.
For multiphase inclusions, fluid composition is generally similar to that of L-inclusions; multiphase inclusions are then enriched in K and Fe (+Mn), although in this case also some Ca is reported (Fig. 2.3.20b).
Common to both the typologies of inclusions is the presence of B and Li, which were detected in almost all the analyzed samples. Li is present in almost all inclusions, in concentrations up to 9000 mg/kg (Table 2.3.5). Accordantly to LA-ICPMS data, B was detected in the liquid phase of L inclusions as the polyatomic BO_3^{3-} species by Raman spectroscopy (Fig. 2.3.21). Concentrations range from 170 to 29,000 mg/kg (Table 2.3.5), and seem to be randomly distributed among samples and fluid inclusions type.

CO_2 has not been detected in any inclusions, neither as a discrete liquid phase either by phase changes around -56.6 °C or from clathrate identification; therefore the concentration of CO_2 (if present) is ≤ 0.8 mol/kg (Hedenquist and Henley, 1985).

2.3.3.2 Ripalte

Petrography of fluid inclusions

At Ripalte, quartz contained abundant fluid inclusions, while no fluid inclusions were recovered in associated tourmaline. As observed for Stagnone, fluid inclusions were generally small, ranging 5-20 μm in dimensions. Phase assemblage is similar to that observed at Stagnone, with the presence of S-a type and associated L-type of inclusions. For S-type inclusions, optical identification and Raman analysis allows the identification of the same daughter minerals already observed at Stagnone: halite, pyrosmalite, complex Fe-chlorides, and hematite (Fig. 2.3.22a).
L-type inclusions are characterized by a constant L/V ratio, around 70% (Fig. 2.3.22b), corresponding to the L1 type observed at Stagnone. L2 type and V-rich inclusions were not observed at Ripalte.
In L-type fluid inclusions, we observed quite frequently the presence of a roundish and colorless minerals (S8; Fig. 2.3.22b), which has however not been identified by

Raman spectroscopy probably due to its low dimensions. This phase has been interpreted as a trapped mineral, although the common occurrence and relatively constant solid to liquid ratio may indicate it precipitated from the fluid during cooling to room temperature.

Microthermometry
A summary of the microthermometric data of Ripalte is presented in Table 2.3.4. S-type inclusions at Ripalte were all characterized by homogenization by halite dissolution (S-a). Vapour disappearance generally occurs in the 270-280°C temperature range, while halite dissolution generally follows vapour by several tens of degrees, and locates between 330° and 370°C, similar to the Stagnone area. At Ripalte, pyrosmalite generally dissolves below 390°C, although some crystals notably persist above 420°C.

Salinities for S-a inclusions range from 41 wt.% to 48 wt.% NaCl eq., with two clear modes at 41 and 44 wt.% NaCl eq.
Th for L inclusions is comprised between 284° and 406°C, with most of inclusions homogenizing in the 360-380°C range. Heating above Th resulted in decrepitation and/or stretching of most of fluid inclusions around 450 °C. Up to this temperature, no phase changes were observed in the S8 phase. A low number of fluid inclusions did not homogenize below 600°C, probably due to stretching processes occurring after fluid entrapment.
Initial melting of ice was observed around -50/-52 °C, while Tm_{ice} ranged -25.6° to -15.9°C (Table 2.3.4). Frequency distribution is polimodal, like the corresponding calculated salinities, which vary between 19 and 26 wt. % NaCl eq.

Raman and LA-ICP-MS analysis
Regarding the characterization of solid phases occurring in fluid inclusions by Raman analysis, the reader could refer to the description reported for the Stagnone area.
In L inclusions, CO_2 was commonly detected as a minor component in the vapour phase. Since dissolution of chlatrate was not observed during cooling stage, its concentration must be ≤ 0.8 mol/kg (Hedenquist and Henley, 1985).
A summary of the fluid inclusions analyzed by LA-ICPMS is found in Table 2.3.5. As already pointed for Stagnone, in L-type fluid inclusions cations other than Na are present in solution, and are mainly constituted by Fe, K, Mg (Fig. 12.3.22a), and minor Ba and Sr. As a mean value, Fe seems to be present in comparable concentrations to the Stagnone area (Fig. 2.3.22a). Multiphase inclusions are enriched in Fe>K>Mn≈Ca>Mg (Fig. 2.3.22b).
Common to both the typologies of fluid inclusions is the presence of B and Li that was detected in almost all the analyzed samples (Table 2.3.5). Accordantly, B was also detected in the liquid phase of L inclusions as the polyatomic BO_3^{3-} species by Raman spectroscopy. B and Li concentrations range from 53 to 1430 mg/kg and 53 to 499 mg/kg, respectively (Table 2.3.5), being remarkably lower than the contents detected at Stagnone.

2.3.3.3 Morcone

Petrography of fluid inclusions
At Morcone, quartz contained abundant fluid inclusions, while no fluid inclusions were recovered in associated tourmaline. Fluid inclusions are generally bigger than those observed in the previous locations, reaching 50 μm in dimensions.

Phase assemblage at room temperature allowed the distinction of three fluid inclusions types:

i) S-type inclusions, are liquid-rich with two up to three solids (L+V+S) (Fig. 2.3.24a). Solids do not occupy more than 30-40% of the total inclusions volume (S-b, see later). Based on optical observations and Raman analysis, these solids were identified as halite (H), pyrosmalite (S1) and hydrated complex Fe-chloride (S2).
ii) L-type inclusions (L+V) (Fig. 2.3.24b), are characterized by a constant L/V ratio, around 60%.
iii) V-type inclusions (V±L) (Fig. 2.3.24c), characterized by a narrow rim of liquid, which is often invisible under the microscope.

L- and V-type of fluid inclusions constitute the great part of the observed fluid inclusions (~90% of overall abundance), and they often show a three dimensional random distribution suggesting that they are primary in origin (Roedder 1984). Moreover, secondary trails in quartz are characterized by the presence of these inclusions. S-type inclusions are however very rare (~10% of overall abundance), and have been observed only in one of the two analyzed samples (F1MOR02). They are small (~10 μm) and they occur as small groups of 5-10 fluid inclusions mixed with liquid-rich inclusions.

Microthermometry
A summary of the microthermometric data of Morcone is presented in Table 2.3.4. S-type inclusions were all characterized by homogenization by vapor-bubble disappearance (S-b), which generally occurs in the 289-319°C range. Halite dissolution precedes vapour homogenization by 30-80°C, and locates around 230-240°C. At Morcone, pyrosmalite persists at temperatures above 370°C, and further heating was avoided to prevent decrepitation of the rare S fluid inclusions.

Calculated salinities for S inclusions range from 31 wt.% to 35 wt.% NaCl eq.
L inclusions constitute a very homogeneous group, showing minor variations in both Th and Tm_{ice}. Th is comprised between 323° and 378°C (average= 378°C), while Tm_{ice} varies between -5.1° to -3.9°C (Table 2.3.4), corresponding to a salinity between 5.3 and 8 wt. % NaCl eq.
V inclusions homogenized in the same temperature range reported for L inclusions (around 370°C). No phase variation was observed during freezing of V-rich inclusions, probably due to the small portion of the inclusion volume occupied by the liquid phase.

SEM-EDS, Raman and LA-ICP-MS analysis
Regarding the characterization of solid phases in fluid inclusions by Raman spectroscopy, the reader could refer to the description reported for the Stagnone area.
Due to the low salinity of fluid inclusions, no remarkable observations are reported about SEM-EDS analysis. Due to their scarcity, S-type fluid inclusions were not observed during analysis, while opening of the low salinity L or V inclusions did not result in the precipitation of significant amount of salts in the cavity of fluid inclusions.
Worth of mention is the Raman analysis on V inclusions, which indicated that CO_2, CH_4 and sometimes N_2 are presented as dissolved species in the vapour phase.

Quantification of each species was performed through comparison of the relative peaks height and internal laboratory standards. Abundances are in the order of CO_2 (~85-95%), followed by CH_4 (~5-11%), and N_2 (4-5%). Similarly to the Ripalte area, clathrate was not observed during freezing stage microthermometry indicating that CO2 in this inclusion is ≤ 0.8 mol/kg (Hedenquist and Henely, 1985).
LA-ICPMS was restricted to L inclusions, which are composed mainly by Na>K> Mg>Fe (Fig. 2.3.25) and sometimes Sr. Ba and Ca are absent from the fluid (Table 2.3.5). Concentrations of major cations are always lower than those detected at Stagnone and Ripalte areas, which is consistent with the lower salinities of this fluid. Common to the other localities, Fe (up to 2700 mg/kg), and Mn (up to 900 mg/kg) are common constituents of fluid composing quartz at Morcone. Similarly B (detected also by Raman spectroscopy) is present in concentrations up to 1000 mg/kg, while Li in concentrations up to 3000 mg/kg (Table 2.3.5)

2.3.3.4 Terra Nera

A total of nine fragments from seven samples coming from the Terra Nera area have been selected for fluid inclusion studies. All samples come from quartz-hematite veins hosted in rocks of the Rio Marina formation (Permian-Carboniferous) belonging to the Monticiano-Roccastrada Unit. Details on samples, including description of hosting rocks, mineralogical association and mineral host, are reported in Table 2.3.1.

Petrography of fluid inclusions

At Terra Nera, all the analyzed fluid inclusions are hosted by quartz crystals enclosed in a dominant hematite matrix from hematite-quartz veins. For this reason, these samples are generally very fragile, but for the case of the TN04-3 sample that is a large and well-formed quartz crystal.
Fluid inclusions in these samples are mainly primary (P) in origin, distributed in a three-dimensional random way within the crystal fragments; trails of pseudo-secondary (PS) and/or secondary (S) inclusions are also present. Sparse P inclusions are sometimes strictly mixed to S inclusions. The shape of the inclusions is almost regular (rounded to ovoidal and negative crystal forms) for S and PS inclusions, whereas the dominant P inclusions are frequently characterized by irregular forms. The whole size range of the FIs is 2 – 90 mm, with dominant dimensions 2 – 20 mm. Phase assemblage at room temperature allowed the identification of only L-type, (L+V) liquid-rich inclusions, characterized by a constant L/V ratio around 70% (Fig. 2.3.26). No solid (neither daughter minerals nor captive minerals) were observed at room temperature.

Microthermometry

Microthermometric data of FIs from Terra Nera samples are summarized in Table 2.3.4.
Homogenization by disappearance of the vapor bubble occurs in the whole Th range 211-403°C for a total of 271 analyzed FIs. Anyway, the dominant Th range for most of the inclusions (262 FIs) is 275-375°C.
In general, Tm_{ice} varies from -29.9° to -15.0°C, corresponding to a salinity between 18.6 and 28.6 wt. % NaCl eq, whereas Tm_{hy} varies from -33.0 to -14.1 °C (Table 2.3.4). Some of the Terra Nera fluid inclusions show a peculiar behavior during freezing-heating cycles, with the salt hydrates that melt after ice (i.e., at higher temperatures). In these samples, solids formed inside FIs during freezing experiments sometimes did not melt at room temperatures and persisted for several hours. They are possibly interpreted as metastable salt hydrates.

The graphical representations of the microthermometric data of Terra Nera are reported in Fig. 2.3.27 (Th frequency histogram, and salinity against Th plot, respectively).

Raman and LA-ICP-MS analysis
Results of LA-ICPMS analyses on fluid inclusions from Terra Nera are summarized in Table 2.3.5 They show that Na is the dominant cation in these fluids, with a mean content of 76812 mg/kg in solution. Other cations are also present in solution: mainly Mg (16009 mg/kg), followed by K (11510 mg/kg) and Fe (10096 mg/kg), with minor amounts of Mn (695 mg/kg), Sr (606 mg/kg), Ba (152 mg/kg), and Zn (107 mg/kg). Significant contents of Li (5358 mg/kg) and, subordinately, B (1482 mg/kg) are observed, whereas Ca is absent. The relative abundance of the main elements is Na>Mg>Fe>K (Fig. 2.3.28). Li and B are notably detected in all inclusions, in concentrations up to 7200 mg/kg and 2600 mg/kg, respectively (Table 2.3.5).
CO_2 was sporadically detected by Raman analysis. However, dissolution of clathrate was not observed during cooling indicating that CO_2 in this inclusion is ≤ 0.8 mol/kg (Hedenquist and Henely, 1985).

2.3.3.5 Bacino

Two small quartz crystals coming from the Bacino area have been selected for fluid inclusion studies. They come from extensional mineralized veins cutting rocks of the Verrucano group (Triassic) within the Monticiano-Roccastrada Unit. Details on samples are reported in Table 2.3.1.

Petrography of fluid inclusions
At Bacino, all the analyzed fluid inclusions are hosted by well-formed small single-crystals of quartz. These quartz crystals also contained abundant solid inclusions of chlorite in their typical "rosette" aggregate-form (Fig. 2.3.29a,b). Notably, FIs are always well separated and far-away from the groups of chlorite solid inclusions.
Fluid inclusions in these samples are mostly primary (P) in origin, distributed in a random way within the crystal fragments; a few pseudo-secondary (PS) fluid inclusions are also present along trails. The shape of the inclusions is almost regular, with some more irregular and elongated forms for the biggest inclusions. Their dimensions are larger than those of FIs from Terra Nera, with size range 10 – 170 mm.
Phase assemblage at room temperature allowed the identification of only L-type, (L+V) liquid-rich inclusions, characterized by a constant L/V ratio around 80% (Fig. 2.3.29c). In a few cases, solids identified as captive minerals (possibly, chlorite) were also observed at room temperature (Fig. 2.3.29d).

Microthermometry
Microthermometric data of FIs studied in the quartz samples from Bacino are summarized in Table 2.3.4. A total number of 60 FIs have been analyzed.
Homogenization by disappearance of the vapor bubble occurs in two main separate Th ranges: 199-234°C (for 15 FIs), and 258-297°C (for 42 FIs). The approximate bimodal distribution of Th values for these samples is shown by the frequency histogram in Fig. 2.3.33a. Those solids observed at room temperature and identified as captive minerals (Fig. 2.3.29d) did not melt upon heating.

Fluids entrapped in Bacino samples have lower salinities compared to those of Terra Nera. In general, an unimodal distribution of salinity is presented by FIs from Bacino, with a very narrow salinity range. In fact, Tm_{ice} varies from -12.9° to -9.0°C, corresponding to a salinity between 12.8 and 16.8 wt.% NaCl eq, whereas Tm_{hy} varies from -24.1 to -22.5 °C (Table 2.3.4). Salt hydrates always melt before ice crystals (i.e., at lower temperatures).
The salinity against Th plot of Bacino (Fig. 2.3.30) indicates a general vertical trend with a small gap of measures in the Th range 234-258°C. This could approximately correspond to cooling of a single fluid.

SEM-EDS, Raman and LA-ICP-MS analysis

Neither SEM-EDS nor Raman spectroscopy analyses were performed on the Bacino samples.
Results of LA-ICPMS analyses on fluid inclusions from Bacino are summarized in Table 2.3.5. Also in this case Na is the dominant cation, with a mean content of 50537 mg/kg in solution. Other cations are also present in solution: mainly Mg (5675 mg/kg), followed by K (4053 mg/kg) and Fe (1565 mg/kg), with minor amounts of Zn (643 mg/kg), Cu (595 mg/kg), Sr (189 mg/kg), and Mn (103 mg/kg). Significant contents of Li (3465 mg/kg) and, subordinately, B (568 mg/kg) are observed, whereas Ca is absent. These LA-ICPMS data are consistent with the lower salinities (as compared to those of Terra Nera fluids) measured by microthermometric analyses for the Bacino fluids. Anyway, as to the relative abundances of the main elements, these are similar as in the case of Terra Nera: Na>Mg>K>Fe (Fig. 2.3.31).
Small amount of CO_2 was detected by Raman analyses in the vapour phase of an inclusion from Bacino. However, dissolution of clathrate was not observed during cooling indicating that CO2 in this inclusion is ≤ 0.8 mol/kg (Hedenquist and Henley, 1985).

2.3.3.6 Topinetti

The analyzed fluid inclusions from Topinetti area are all enclosed within quartz crystals found in hematite-bearing hydrothermal veins crossing the Rio Marina formation (Permian-Carboniferous) within the Monticiano-Roccastrada Unit. Details on samples are reported in Table 2.3.1.

Petrography of fluid inclusions
Fluid inclusions entrapped within quartz crystals from Topinetti mainly show a three-dimensional random distribution, and are interpreted as primary (P) in origin. Also pseudo-secondary (PS) inclusions, aligned along trails that stop within single crystal grains, have been observed. The shape of the inclusions is mostly regular up to negative-crystal forms, with a few irregular forms especially for the biggest inclusions (Fig. 2.3.32a). Their dimensions range between 2 – 57 mm.
Phase assemblage at room temperature allowed the identification of only L-type, (L+V) liquid-rich inclusions, characterized by constant L/V ratios around 70-80% (Fig. 2.3.32b).

Microthermometry
Microthermometric data of FIs studied in Topinetti quartz crystals are summarized in Table 2.3.4. A total number of 128 FIs have been analyzed.
Homogenization by disappearance of the vapor bubble occurs in tho whole Th range 172-326°C for a total of 123 FIs. An approximate trimodal distribution of Th values for these samples is shown by the frequency histogram in Fig. 2.3.33a.

As concerns salinities of fluids from Topinetti, Tm_{ice} varies from -19.0° to -0.5°C, corresponding to a fairly wide salinity range between 0.9 and 21.7 wt.% NaCl eq, whereas Tm_{hy} varies from -29.1 to -22.1 °C (Table 2.3.4). Salt hydrates always melt before ice crystals (i.e., at lower temperatures).
The salinity against Th plot of Topinetti (Fig. 2.3.33b) indicates a general inclined trend, corresponding to mixing of different fluids. A vertical trend indicating cooling for the highest salinity fluids is also visible from the same plot (Fig. 2.3.33b).

Raman and LA-ICP-MS analysis
Results of LA-ICPMS analyses on fluid inclusions from Topinetti are summarized in Table 2.3.5. Also in this case Na is the dominant cation, with a mean content of 84871 mg/kg in solution. This result indicates that Topinetti fluids are characterized by the highest Na content as compared to those from Terra Nera, Bacino and Valle Giove. Other cations are also present in solution: in this case mainly Fe (11186 mg/kg) and K (11752 mg/kg), followed by Mg (5077 mg/kg) and Ca (1771 mg/kg), with minor amounts of Mn (825 mg/kg), Sr (538 mg/kg), Zn (121 mg/kg), and Ba (81 mg/kg). Significant contents of Li (6300 mg/kg) and, subordinately, B (1499 mg/kg) are also observed. Hence, LA-ICPMS data show that, as compared to Terra Nera and Bacino, FIs from Topinetti are characterized by a peculiar composition because of the presence of Ca, and in terms of the relative abundance of the components: for Topinetti Na>Fe>K > Mg>Ca (Fig. 2.3.34). Similar to the other localities, Li and B are always detected in remarkable amounts in the fluid (Table 2.3.5).

No CO_2 was detected by Raman analyses in that vapor phase of FIs from Topinetti.

2.3.3.7 Valle Giove
A total of twelve fragments from six samples coming from the Valle Giove area have been selected for fluid inclusion studies. The samples come from hematite-pyrite-quartz-adularia veins and from calcite-pyrite mineralizations hosted in rocks of either the Verrucano group (Triassic) or the Rio Marina formation (Permian-Carboniferous), all belonging to the Monticiano-Roccastrada Unit. Details on samples, including description of hosting rocks, mineralogical association and mineral host, are reported in Table 2.3.1.

Petrography of fluid inclusions
At Valle Giove, the analyzed fluid inclusions are hosted by quartz and calcite crystals. Quartz crystals present abundant FIs, sometimes with a banded appearance with a separation between parallel crystal-zones that alternatively are more transparent (characterized by a lower density of FIs), and more "milky" and/or "smoky" (with a higher density of FIs). Most of the calcite crystals show a sharp separation into two growth zones: an inner zone that is darker and richer of FIs, and an outer zone, close and parallel to the rims of the crystal, that is more transparent and with a lower density of FIs (sometimes secondary in origin). Also a few completely transparent calcite crystals, containing a small number of FIs distributed in isolated and sparse groups, are present.
Fluid inclusions in Valle Giove samples are mostly primary (P) in origin, distributed in a three-dimensional random way within the crystal fragments; a few trails of pseudo-secondary (PS) and secondary (S) inclusions are also present. The shape of the inclusions is almost regular, with rounded up to negative-crystal forms (Fig. 2.3.35a). A few elongated and more irregular forms have also been observed for the biggest primary inclusions. The whole size range of the FIs is 3 – 380 mm.

Phase assemblage at room temperature within quartz crystals allowed the identification of L-type, (L+V) liquid-rich inclusions, characterized by a constant L/V ratio around 70%. In some cases, birefringent captive-minerals (Fig. 2.3.35b) have been observed within FIs hosted in quartz. At room temperature, calcite crystals are mainly characterized by L-type, (L+V) liquid-rich inclusions with constant L/V ratio around 70% (Fig. 2.3.35c), whereas a few S-type FIs, (L+V+S) with S = halite (Fig. 2.3.35d), are present in the outer growth-zones corresponding to the last crystallization stages. Dark monorefringent captive minerals (possibly pyrite) have been sporadically observed within FIs hosted in calcite.

Microthermometry
Microthermometric data of the FIs analyzed in quartz and calcite crystals from Valle Giove are summarized in Table 2.3.4. A total number of 211 FIs in quartz and 103 FIs in calcite have been analyzed.
Homogenization by disappearance of the vapor bubble occurs in tho whole Th range 178-353°C for a total of 295 FIs. An approximate trimodal distribution of Th values for these samples is shown by the frequency histogram in Fig. 2.3.36a.
In detail, L-type FIs in quartz crystals from Valle Giove are characterized by a Th range 210 – 311°C, whereas Tm_{ice} varies from -28.0° to -0.3°C, corresponding to a fairly wide salinity range between 0.5 and 27.4 wt.% NaCl eq.. Salt hydrates always melt before ice crystals (i.e., at lower temperatures), with Tm_{hy} values ranging from -26.6 to -21.0 °C (Table 2.3.4).
Calcite crystals contain both L-type and S-type FIs, with an overall Th range between 178 and 353°C for a total of 87 inclusions. The more abundant L-type inclusions are characterized by Th values ranging from 247 to 353 °C, whereas Tm_{ice} varies from -22.4° to -13.5°C, corresponding to a salinity range between 17.4 and 24.0 wt.% NaCl eq.. Salt hydrates always melt before ice crystals (i.e., at lower temperatures), with Tm_{hy} values ranging from -28.0 to -24.8 °C (Table 2.3.4). Calcite S-type inclusions are less abundant (a total of 15 FIs) and located near the rims of the calcite crystals corresponding to the last crystallization stages. They are characterized by lower Th values (178-292°C). The solid S is represented by halite daughter minerals that always melt before disappearance of the vapour bubble in the $T_{S_{NaCl}}$ range 194-235 °C, the latter corresponding to salinities ranging between 31.6 and 33.8 wt% NaCl eq..
The salinity against Th plot of Valle Giove (Fig. 2.3.36b) indicates a general inclined trend (corresponding to mixing of different fluids) superimposed over several vertical trends (each corresponding to cooling of a single fluid). Hence mixing of several cooling fluids is registered by FIs from the Valle Giove area. Among the analyzed samples, a single and large quartz crystal registers almost all the above mentioned fluids (but those hypersaline, that are registered by the S-type inclusions near the rims of calcite crystals). Such fluids are entrapped by a large number of FIs distributed in a random way, all merged and mixed each other, with no apparent chronologically distinction among different fluids. Hence, in general, Valle Giove records the mixing of several coeval fluids of low to medium salinity (those corresponding to the L-type inclusions). The cooler hypersaline fluid registered by S-type inclusions in the rims of calcite crystals could possibly correspond to a late sealing of the system with a consequent increase of the salinity of the fluid.

SEM-EDS, Raman and LA-ICP-MS analysis
SEM-EDS analyses were performed on crushed quartz crystal-fragments from the Valle Giove area. In the exposed open cavities some precipitated solids representing the composition of the fluids, namely NaCl (Fig. 2.3.37a) and mixed (Na,K,Ca,Cl)-

salts (Fig. 2.3.37b), were detected. Captive minerals enclosed in the cavities, mainly phyllosilicates as biotite (Fig. 2.3.37c) and chlorite (Fig. 2.3.37d), were also detected. Results of LA-ICPMS analyses on L-type and S-type fluid inclusions from Valle Giove are summarized in Table 2.3.5. L-type fluid inclusions in quartz contain approximately equal amounts of Na (38606 mg/kg) and K (38314 mg/kg). Other cations are also present in solution: mainly Fe (13976 mg/kg), followed by Mg (7712 mg/kg) and Cu (1176 mg/kg), with minor amounts of Mn (356 mg/kg), Sn (233 mg/kg), Zn (115 mg/kg), and Sr (112 mg/kg). No Ca was detected by LA-ICPMS within quartz FIs. Significant contents of Li (1280 mg/kg) were also detected. Hence, the relative abundance of the main components for the fluids entrapped within quartz crystals from Valle Giove is Na≈K>Fe>Mg (Fig. 2.3.38). For S-type FIs within calcite crystals from Valle Giove, the relative abundance of the main components is Na>Mg>Mn>Fe≈K>Sr. As to both L-type and S-type fluid inclusions within calcite crystals, it is possible that some Ca is present among the fluid constituents in this case, even though the high amounts detected by LA-ICPMS are surely affected by the Ca content of the calcite matrix.

2.3.4 Isotope analysis

2.3.4.1. Hydrogen and oxygen isotope in tourmaline, quartz and hematite

A summary of the H isotope composition of tourmaline of the quartz-tourmaline veins occurring at Stagnone and Morcone is reported in Table 2.3.6. Additional analyses were conducted in: i) a biotite separated from the Mt. Calamita Schists (sample GN1B); ii) two epidotes recovered at Terra Nera (TN3 EP) and Ginevro (Ginevro); and iii) an ilvaite recovered in the skarn deposits at Torre di Rio.
δD range -154‰ to -49‰ (Table 2.3.6), with the samples TR01A and F2MOR01 displaying the more negative and positive values, respectively.
The composition of H in the original fluid (δD_{H2O}) was computed with the temperature data derived from fluid inclusions microthermometry performed on the associated quartz, and using the equation of Kotzer et al. (1993). The employed temperatures were then: T = 550°C for Stagnone, and T = 443°C for Morcone. For epidote, the temperature of 440°C was assumed, corresponding the highest temperature value of the Terra Nera deposit. For ilvaite and biotite, T = 550°C was employed since these minerals are associated to a skarn deposit (ilvaite at Torre di Rio) or to a high temperature metamorphosed rock (biotite of Mt. Calamita Schists).
δD_{H2O} range between -64.2‰ and -17.1.9‰, with the highest value reported for the epidotes of the area of Terra Nera and Ginevro (Table 2.3.6).
A summary of the O isotope composition of quartz and hematite sampled in different mineralized areas is reported in Table 2.3.6. A further analysis was conducted on a quartz sample (TR02) obtained from the skarn of Torre di Rio.
For the areas of Terra Nera and Valle Giove, assuming isotope equilibrium between the pair mineral quartz-hematite, it was possible to derive their temperature of formation since their fractionation factors is known from the equation of Zheng (1991). For Valle Giove, we obtained two consistent values around 350°C (351.4°C and 348.6°C) for the samples 14VG02 and 14VG04, while a value of 386.7°C was obtained for 14VG03. In accordance, a temperature of 352.09°C was obtained considering the adularia-hematite pair (Zhen, 1991) for the sample 14VG03. The temperature of 350°C was then assumed as representative of the quartz formation for the mineralized deposit of Valle Giove.

For Terra Nera, only sample TN2 gave some realistic O isotope data for hematite. By applying the equation of Zheng (1991), a temperature of formation of 365 °C was obtained for hydrothermal quartz precipitated in this area.

Finally, δO composition of the fluid (δO_{H2O}) was recalculated from δO_{QZ} and the equation of Zheng (1993) (Table 2.3.6) at the temperatures suggested by the quartz-hematite geothermometry when available. For the area of Topinetti and Torre di Rio, temperatures of 300°C and 550°C were assumed. δO_{H2O} are all extremely positive, ranging from 3.6‰ to 10.6 ‰

2.3.4.2. Boron, strontium and neodymium isotopes in tourmaline

Tourmaline is stable over a wide range of pressures (P), temperatures (T) and fluid compositions (X), and possesses a crystal structure that may accommodate a large variety of trace elements. Due to the low diffusion rates of elements in the tourmaline structure and along with this mineral's general chemical and mechanical robustness once crystallized, tourmaline may record information on a multitude of geological events. Consequently, tourmaline can be a valuable petrogenetic tracer of the igneous environment and may record unique information about fluid-rock and fluid-fluid interactions in hydrothermal system. Recent advances in microanalytical methods have produced an increasing number of trace element data for tourmaline (see Drivenes et al., 2015 and references therein). However, most studies have focused on hydrothermal veins associated to various ore deposits, and isotopic data on tourmaline-bearing, granite-related magmatic-hydrothermal systems are still relatively scarce.

This part of the Task 3.1 aims to evaluate the differences in boron, strontium and neodymium isotopic ratios between varying textural occurrences of tourmaline in the Calamita magmatic-hydrothermal system and characterizes any systematic differences between magmatic and hydrothermal tourmaline as well as between different generations of hydrothermal tourmaline. As already stressed before, the Calamita magmatic-hydrothermal system can be envisaged as an exposed proxy of the high temperature hydrothermal system presently active in the deepest part of the Larderello-Travale geothermal field (Tuscany). Dini et al. (2008) described the strict relationship between the emplacement/crystallizzation of tourmaline bearing leucogranites in the biotite-rich pelitic hornfels of Calamita peninsula and the development of a hydrothermal system made up by metasomatic tourmalinite masses and a complex network of sub-horizontal and sub-vertical tourmaline-quartz (±feldspar and micas) veins/breccias. Tourmaline-rich hydrothermal rocks overprint metamorphic host rocks as well as locally crosscut the leucogranite bodies. Monzogranite intrusions in Calamita contain late-magmatic tourmaline spots but they never produce the extensive tourmalinization/tourmaline veining associated with the leucogranite bodies. Just in cases where leucogranites emplaced together with monzogranites, tourmalinization/tourmaline veining occurs through both magmatic and metamorphic rocks. Tourmalines in leucogranite dykes/sills are schorl (Na- Fe-rich end member), whereas in veins/breccias and metasomatic masses, tourmaline composition ranges from schorl-dravite (intermediate content of Fe and Mg) through dravite (Na- Mg-rich end member) to uvite (Ca- Mg-rich end member). This compositional shift is evidence for an increasing contribution to the magmatic boron-rich fluids by Mg-Ca-Ti-rich external component represented by biotite-rich and amphibolite host rocks.

Emplacement of tourmaline bearing leucogranites and circulation of B-rich hydrothermal fluids extensively affected the eastern coast of the Calamita Peninsula while the central part (higher elevation) and the western coast show minor magmatic intrusions and hydrothermal effects. The differential distribution of magmatic and hydrothermal rocks suggests an asymmetry of the magmatic-hydrothermal system that was eccentrically centered along the eastern coast. Following this hypothesis, outcrops along the east coast represent a proximal zone of the magmatic-hydrothermal, close to its apical part, while the central-western zone of Calamita Peninsula represents a distal, and relatively shallower zone rarely reached by B-rich magmas and hydrothermal fluids. Samples of monzogranite, leucogranite, tourmaline-rich veins/breccias and pelitic hornfels were sampled from the proximal zone, in Barbarossa, Stagnone and Ginevro beach areas. In Barbarossa area, monzogranite-hosted tourmaline-rich veins/breccias were collected, while in Stagnone and Ginevro beach areas hornfels-hosted veins/breccias were selected.

This part of the Task 3.1 was focused on outcrops placed along the east coast in order to work on the proximal high-temperature zone and avoid any possible effects of fluids coming from shallow crustal levels (e.g. meteoric). Isotopic variation detected in these samples should be, as much as possible, related to the evolution of fluids at the magmatic-hydrothermal transition and their potential variation through water-rock interactions. Thus the isotopic reservoirs that are relevant for this system should be: 1) the crustal-derived magmatic rocks (monzogranites, leucogranites); 2) the pelitic hornfels host (biotite-plagioclase-andalusite micaschist). From previous studies on Tuscan Magmatic Province (e.g. Dini et al., 2005) we already know that there is a significant difference in isotopic composition between crustal magmas and Palaeozoic basement cropping out in Tuscany: crustal magmatic rocks show highly variable 87Sr/86Sr ratios (from 0.713 to 0.724) and a minor variability in 143Nd/144Nd ratios (from 0.51211 to 0.51223) that are significantly different from the Palaeozoic basement (87Sr/86Sr ≈ 0.724-0.731; 143Nd/144Nd ≈ 0.51197-0.51205). Boron isotopic compositions are also different (Dini, unpublished data; Dini et al., 2001; Tonarini et al., 1998): crustal magmatic rocks show higher d11B ratios (between -6 and -10 ‰) than Palaeozoic micaschists (between -9 and -13 ‰). Strontium and Nd contents of our magmatic and metamorphic rocks are in the same range (tens-hundreds µg/g), while the boron content can be significantly higher in magmatic rocks (B = up to thousands µg/g) than in metamorphic rocks (tens-hundred µg/g). Considering the normal behavior of these elements in magmatic systems (Sr and Nd are compatible while B is incompatible) the fluids released by these magmas were strongly enriched in boron and significantly depleted in Sr and Nd. As soon as they were issued from the magmatic rocks, fluids became in contact with a rock reservoir (pelitic hornfels) that had a higher Sr and Nd content but a significantly lower B content. Therefore, tourmaline crystallized at different stages of fluid-rock interaction could have recorded an important shift in the isotopic composition of Sr and Nd but a negligible variation in B isotope ratios. However, boron isotopes can fractionate and possible deviation between magmatic and hydrothermal values must be discussed in terms of temperature- and coordination-dependent effects.
Results are reported in Table 2.3.7 and in Figures 2.3.38/1 and 2.3.38/2. Whole rocks (monzogranite, leucogranite and pelitic hornfels) show distinct isotopic compositions that are consistent with data already available for Tuscany. Monzogranite and leucogranite have distinct higher 143Nd/144Nd and lower 87Sr/86Sr isotope ratios with respect to the pelitic hornfels (Fig. 2.3.38/1 and 2.3.38/2). In spite of similar 143Nd/144Nd ratios, the significantly higher 87Sr/86Sr

ratios distinguish leucogranites from monzogranites (Fig. 2.3.38/1). Tourmaline spots separated from monzogranites and tourmaline micro-phenocrysts separated from leucogranites display 143Nd/144Nd and 87Sr/86Sr isotope ratios in equilibrium with their own magmatic host rock (Fig. 2.3.38/1). Hydrothermal tourmalines from metasomatic masses and veins/breccias hosted in pelitic hornfels (Stagnone and Ginevro beach) show Sr and Nd isotope compositions that are intermediate between leucogranites and pelitic hornfels. On the contrary, the hydrothermal tourmaline from veins hosted in monzogranite (Barbarossa) provided 87Sr/86Sr and 143Nd/144Nd ratios that are intermediate between leucogranites and the monzogranites.
Boron isotope compositions of monzogranites, leucogranites and pelitic hornfels are also different. Magmatic tourmaline from leucogranites shows the highest values (d11B between -6.3 and -6.6 ‰), while slightly lower ratios (-7.3 and -7.4 ‰) were detected in late-magmatic tourmaline spots from the monzogranite. Finally, boron isotope analyses of politic hornfelses (whole rocks) provided significantly lower values (from -10 to -11.2 ‰).
d11B values of metasomatic and hydrothermal tourmalines from all the localities (from -6.5 to -6.7 ‰) are similar to those measured in magmatic tourmaline from the leucogranites.
The discussion of isotopic data for the metasomatic-hydrothermal tourmalines must be developed in comparison with data obtained on magmatic and metamorphic rocks. Sr and Nd isotopic systematics clearly indicate that the fluids responsible for the formation of tourmaline hydrothermal rocks at Calamita Peninsula were issued by the leucogranite magmas and then they extensively interacted with the pelitic hornfels host. The distinctly less radiogenic Sr isotope composition of Monzogranites locally controls the isotopic signature of some small tourmaline veins (at Barbarossa) that are shifted from the composition of leucogranites towards the monzogranite field.
The same consideration can be desumed by d11B values of metasomatic and hydrothermal tourmalines: they exactly match the boron isotopic composition of leucogranites. In this case d11B of fluids seems to be not affected by either the interaction with the pelitic hornfels, nor the isotopic fractionation during fluid exholution and temperature decrease.
The lack of effects related to the fluid-rock interaction is coherent with the large difference in content between the extremely B-rich fluid exholved by leucogranite magmas and the politic hornfels. More intriguing is the lack of any significant isotopic fractionation between the magmatic tourmaline in the leucogranite and the hydrothermal tourmalines in the veins/breccias. As already stressed by Tonarini et al. (1998), in peraluminous high temperature systems the fractionation of boron isotopes between tourmaline and its growing medium (melt, fluid) is negligible and the boron isotopic signature of the magma is maintained through the entire magmatic-hydrothermal evolution.

In conclusion, the application of Sr, Nd and B isotope systematics to the Calamita boron rich magmatic-hydrothermal system provides the following important informations:
the fluids responsible for the pervasive tourmalinization and tourmaline veining were provided by the B-rich leucogranite magmas.
The fluid-rock interaction in the pelitic hornfels slightly modified Sr and Nd isotope composition of fluids but the magmatic signature of B isotopes was not modified.
In proximal zones of peraluminous, B-rich magmatic systems hosted by metamorphic formations, boron isotope ratios recorded in tourmalines are a good

monitor of the magmatic source while tourmaline chemistry and Sr-Nd isotopes provide information on the degree of fluid interaction with host rocks.
Multiple isotopes study of tourmaline (including also O and H isotopes) is a useful exploration tool for defining proximal zones of paleo-geothermal systems dominated by high temperature magmatic fluids and for predicting the type of fluid expected in active geothermal systems associated with peraluminous granite intrusions (e.g. Larderello).

2.3.4.3 Mineralogy

The development of quartz-tourmaline veins and tourmaline-rich metasomatic masses in the Calamita promontory is related to a hydrothermal system, affecting an area exceeding 20 km^2, and representing a major hydrothermal event characterized by boron-rich saline fluids. Such fluids circulated close to their magmatic source, as indicated by the spatial distribution of tourmaline veins and felsic dykes clearly exposed in the Stagnone area.
The variable tourmaline compositions observed in Stagnone area can provide some information on the fluids involved. The tourmaline hosted in felsic dykes has typical schorl composition reflecting the very low Mg content of the acidic magma (Dini et al., 2008). In contrast, the schorl-dravite composition typical of metasomatic tourmaline, hydrothermal veins indicate chemical interaction with biotite-rich layers in hornfels rocks. This suggests a direct link between the metasomatic fluids, equilibrated with hornfels and fluids involved in the early stage of metasomatic process.
The significant change in composition especially in tourmaline from F1 veins, shifting towards uvite composition, indicates Ca-rich fluid circulation, suggesting a different fluid source distinct from the magmatic one. A possible contribution from the interaction of boron-rich fluids with mafic rocks, as the amphibolite bodies interbedded within the hornfels (CaO _9.2 wt%; TiO2 _2.3 wt%; Puxeddu et al., 1984), can be suggested (Dini et al., 2008).
Generally speaking, the metasomatic B-rich fluids which selectively replaced the biotite-rich layers of the Calamita Schists produce tourmalines with a dominantly dravitic composition. The low Fe and negligible Mg contents of the felsic magma that fed the leucogranites is, in fact, a limiting factor in the precipitation of magmatic tourmaline (schorl), leading to a massive exsolution of boron-rich fluid from the magma that can be buffered by the reaction with biotite-rich host rocks to produce metasomatic and hydrothermal tourmaline (London 1999).

2.3.4.4 Fluid inclusions: fluid composition and trapping conditions

Calamita Peninsula

Fluid inclusions occurring at Stagnone and Ripalte (and partially Morcone) indicate that at least two different fluids circulated in these areas, which are represented by the two major types of fluid inclusions recovered in quartz, i.e. multiphase and liquid-rich (and vapour-rich).
The fluid trapped by S inclusions was very saline fluid (40-48 wt. % NaCl eq.), becoming saturated in mineral phases during its cooling from trapping conditions to room temperature. However, the fluid was locally oversaturated prior of trapping, as denoted by the entrapment of halite and Fe-bearing phases as captive minerals (heterogeneous trapping). These inclusions were therefore excluded from further considerations.

Abundance of Fe-bearing phases in S inclusions, such as pyrosmalite, Fe-chlorides and hematite, suggests elevated Fe concentrations for this fluid. Accordingly, $FeCl_2$ is among the most abundant components in magmatic-hydrothermal systems (Bodnar et al., 2014), particularly in porphyry Cu deposits (Roedder 1984). Fe-pyrosmalite in fluid inclusions is generally observed in fluids with strong evidence of magmatic derivation, as documented by its common occurrence in Cu-Au-Co and Pb-Zn-Ag deposits in NW Queensland (Australia) (Li and Naldrett, 1993; Dong and Pollard, 1997; Fu et al., 2003), and in skarn deposits of Thailandia (Zaw et al., 2007) and Slovakia (Koděra et al., 1998). In addition, Koděra et al. (2003) show evidences that pyrosmalite in fluid inclusions may result from retrograde reactions of clinopyroxene (hedenbergite) during post-entrapment cooling below 450°C. This hypothesis seems however improbable for our study since no stable transition of pyrosmalite to a new mineral phase were generally observed in our inclusions.
Fe-chlorides and hematite are listed between the ten most common mineral phases reported in fluid inclusions (Shepherd 1985), and the early findings of hydrated Fe chlorides are from Bolivian porphyry Sn deposits (Grant et al., 1977).
Besides the employment of different techniques, we did not succeed to determine the chemical formula of the $FeCl_2$-hydrates occurring at Stagnone, Ripalte or Morcone. Based on the recent experimental work of Lecumberri-Sanchez et al. (2015) on the H_2O-NaCl-$FeCl_2$ system, $FeCl_2$-hydrates present a decreasing hydratation number with increasing salinity. Loosing water molecules by $FeCl_2$-hydrates corresponds to peritectic reactions moving from the $FeCl_2{\cdot}6H_2O$ hydrate to the anhydrous $FeCl_2$ (lawrencite); temperatures from ~70 to 77 °C correspond to the transition from $FeCl_2{\cdot}4H_2O$ to $FeCl_2{\cdot}2H_2O$. Dissolution temperature for the solid phase S2 at Stagnone, starting as low as 62-90°C, may then correspond to hydrates composition ranging from $FeCl_2{\cdot}4H_2O$ to $FeCl_2{\cdot}2H_2O$. However, based on thermodynamic calculations, Lecumberri-Sanchez et al. (2015) predicted that inclusions consisting of solid $FeCl_2{\cdot}4H_2O$ (~63 wt.% $FeCl_2$) would be in equilibrium with almost no liquid at room temperature. On the contrary, our samples at Stagnone (Ripalte and Morcone) reported abundant liquid+vapour+solids, suggesting that our phases are probably composed by additional cations in their crystalline structures (K, Na etc.), as indicated by SEM-EDS analysis, and they cannot be modeled as simply $FeCl_2$-hydrates.
Quantitative analysis by LA-ICPMS indicated than Fe concentrations in the fluid was comparable to or greater than the concentrations of other major cations (Na and K) (Table 2.3.5). In the Calamita Peninsula, NaCl, $FeCl_2$ and KCl dominate then the fluid chemistry and only minor $CaCl_2$ is present. Ratios of $FeCl_2/(NaCl+ FeCl_2)$ (mass weight) in the fluid fall between 0.20 to 0.59 (LA-ICPMS), corresponding to a calculated *real* salinity (Lecumberri-Sanchez et al., 2015), expressed in terms of $wNaCl + wFeCl_2$ wt.%, between 43 and 59 wt.%.
These salinities differences are responsible for fluid-density variations and therefore to the relatively wide range of homogenization temperatures (either to liquid or to halite) observed for S inclusions. These temperatures define the minimum temperature estimate for the fluid (Roedder 1984; Shepherd et al., 1985), i.e. fluid in S inclusions was trapped at *least* at 280-400 °C (whole range for S inclusions). Isochores construction and pressure correction estimates will then be necessary to obtain the real T, P trapping conditions for the fluid (Roedder, 1984).
Figure 2.3.39 illustrates the relationship between Ts_{NaCl} and Th for Stagnone, Ripalte and Morcone. As noted before, most of fluid inclusions at Stagnone and Ripalte homogenize by halite dissolution (S-a type). These inclusions provide most of information, since they are constrained by phase-equilibria thermodynamics to have been trapped in the one phase field, i.e., liquid-stable field (Bodnar et al., 1985).

Coexisting with a low-density and low saline vapour phase for these inclusions is therefore excluded (Cline and Vanko, 1995). Accordingly, a vapour-rich population of fluid inclusions displaying low salinities and similar homogenization temperature, indicative of fluid immiscibility, has not been reported in our study.
Although S-a population of fluid inclusions exhibits a wide range of homogenization and salinities, the bulk of data of Stagnone and Ripalte are grouped in the center of a Ts_{hal} vs Th diagram (Fig. 2.3.39), reporting homogenization to liquid at 260-300°C, halite dissolution at 315-370°C, and a salinity range of 40-45 wt.% NaCl eq.. These data were then employed to derive trapping conditions for these inclusions.
As experimental data describing fluid density for H_2O-NaCl-$FeCl_2$ system are nonexistent, data for the H_2O-NaCl system were used instead. In Fig. 2.3.40, the two liquidi surfaces (LIQ) for salinities of 40 and 45 wt.% NaCl eq. (LIQ(40) and LIQ(45)), the corresponding liquid-vapour curves and the three phase curve (L+H+V) have been reported. The liquidus separates the fields in which liquid + halite (L+H) and liquid (L) are stable, while the liquid-vapour curve separates the L field from the L+V field. Under the L+H+V curve, a vapour phase is oversaturated in halite. The point in which the LIQ meets the corresponding L+V and L+V+H curve corresponds to the temperature at which an inclusion will exhibit halite dissolution occurring together with vapour disappearance. A hypothetical isochore originating from this point divides then fluid inclusions homogenizing by halite dissolution (low temperature, left side of the diagram) from those homogenizing to liquid (high temperature, right side of the diagram).
The position of the isochores for S-a has been calculated following the work of Steele-MacInnis et al. (2012), while the work of Bodnar (1994) was employed to trace liquidi surfaces. In Fig. 2.3.40, isochores for S-a multiphase inclusions (thick black lines) originate at temperature of halite dissolution on the corresponding liquidi surface, i.e. 315°C and 370°C for LIQ(40) and LIQ(45), respectively. For each liquidus surface two isochores are reported, considering the temperature range for liquid-vapour homogenization in our dataset (260°C and 300°C) (isochores in the L+H field starting from Th =260°C and Th =300 °C from the L+V curve have not been reported to avoid confusion). Trapping conditions for each salinity value is comprised between the corresponding isochores. The gray shaded area in Fig. 2.3.40 represents the smallest P-T-X region that could have produced the dataset described by S-a at Stagnone and Ripalte, i.e. fluids with salinities between 40 and 45 wt.% NaCl eq., liquid homogenization temperature of 260-300°C, and halite dissolution between 315 and 370°C. Small fluctuations in both the three variables may account for the data variability observed in these areas.
From this reconstruction, it results a minimum trapping pressure for S-a inclusions of ~1100 bar (Fig. 2.3.40). Maximum pressure estimates are based on the P-T during contact metamorphism due to the intrusion of the Porto Azzurro pluton in in the Mt. Calamita Peninsula, which reached a Tmax of 650 °C (andalusite-K-feldspar zone and wollastonite zone), with Pmax < 0.18-0.2 GPa (Duranti et al., 1992). A pressure of 2000 bars defines then the upper limit of trapping conditions for most of S-a inclusions, whose trapping temperatures vary between 370°C and 420°C.
Trapping conditions for other S inclusions can then now be evaluated. S-a inclusions where halite dissolves at very higher temperature than vapour (e.g. 150 °C of difference between Th and Ts_{NaCl}) or where Th is very low (~225 °C) could have been trapped at even greater pressure (>2500 bars), and might reflect periods of time where the system was overpressured, like before fracturing events. Multiphase inclusions of S-b type (Ts_{hal}<Th) may have followed an isochore path like those indicated by dashed line in Fig. 2.3.40. This isochore has been calculated considering the lowest salinity reported for S-b inclusions at Stagnone (29 wt. % NaCl eq.,

corresponding to TsNaCl = 141°C and Th= 301.5°C), since other isochores for S-b inclusions will plot between this one and LIQ40. Similar to S-b at Stagnone, the isochore for an S-b inclusion at Morcone (mean salinity of 34 wt.% NaCl eq.) will plot on the right with respect of the S-a multiphase curves (dotted blue line; Fig. 2.3.40). The position of these isochores indicated that these inclusions may have been trapped at lower pressure and similar temperatures than more saline fluids, or at higher temperatures and similar pressures (Fig. 2.3.40). In our opinion, the first hypothesis seems to be the most favorable since geological reconstructions indicates that the area of Morcone should be characterized by lower pressures than Stagnone and Ripalte. System depressurization may then explain the shift of the fluid from the S-a field of fluid inclusion to the S-b one.

The fluid trapped by L and V inclusions at Stagnone and Ripalte is moderately saline (16 to 30 wt. NaCl eq.). Common to S inclusions, LA-ICPMS analysis indicated that the fluid composition is dominated by NaCl, KCl and $FeCl_2$, which accounts for the low freezing point depression observed during freezing running stages. Particularly, first-melting temperatures as low as -52/-50°C reflect then the presence of $FeCl_2$ in the fluid. As a consequence the solubility of NaCl was probably reduced due to salting out effects, particularly enhanced in the presence of divalent cations (Roedder 1984). The abundance of Na is then lower than that indicated by microthermetry, which is based on the simple H_2O-NaCl system. Calculated $FeCl_2/(NaCl+FeCl_2)$ based on LA-ICPMS analysis is between 0.10 and 0.60, corresponding to a calculated salinity (wNaCl +w$FeCl_2$ wt. %) between 17 and 23 wt.% (Lecumberri-Sanchez et al., 2015).

To elucidate any difference in fluid chemistry between the sites of Stagnone and Ripalte, fluid composition was described by a ternary diagram Fe-K-Mg, representing the major constituents of the fluids besides Na (Fig. 2.3.41). Fluid inclusions recovered in quartz-torumaline veins at Stagnone display variable Fe/Mg ratios (Fe/Mg= 0 to 5 molar ratios; LA-ICPMS analysis), while these values are generically lower (Fe/Mg=0-1 molar ratios; LA-ICPMS analysis) for inclusions associated Ripalte (Fig. 2.3.41). Mg enrichment for these veins is in accordance with the generic fluid evolution model proposed for tourmaline at Stagnone, which denotes chemical interaction of the fluid with biotite-rich layers in the rock (Dini et al., 2008)

L inclusions displayed a rather variable range of Th which is not correlated to salinity (Fig. 2.3.42); we supposed then the presence of two different populations of fluid inclusions at Stagnone, presenting similar salinities (salinity range of 20-25 wt. % NaCl eq.) but different temperatures. We distinguished then a high temperature population with a Th comprised in the 500-540°C range, corresponding to L2 inclusions, and a low temperature population represented by L1 with a mean Th of 370°C. This last population almost exactly overlaps with that observed at Ripalte (Fig. 2.3.42), suggesting that these two areas trapped similar fluids. Petrographic association of L1 and L2 inclusions, similar salinities and composition indicate that L1 inclusions likely represent an evolution from the first, high temperature L2 population.

Similarly to multiphase inclusions, we referred to the simple H_2O-NaCl system to reconstruct the P-T trapping condition for L inclusions (Steele-MacInnis et al., 2012). Six isochores (thick line, pink colour; Fig.2.3.42) have then been calculated considering Th=500-540°C for L2 inclusions, and Th=370°C for L1 inclusions, and a salinity range of 20-25 wt. % NaCl eq.. Since the isochores Th= 540°C-25 wt. % NaCl eq. and Th= 500°C-20 wt. % NaCl are comprised in the field described by the other two isochores of L2 inclusions, they have not been traced in Fig.2.3.40 to avoid confusion. In addition, isochores for L inclusions at Ripalte are depicted in green

color (Fig. 2.3.40) for the Th and salinity ranges observed for these inclusions (350-400°C; 20-25 wt.% NaCl eq.; Fig. 2.3.42).
Considering the stability field of andalusite as a limiting factor, trapping pressures for L2 inclusions at Stagnone could not have exceeded 1300-1600 bars in lithostatic regime, corresponding to a trapping temperature around 650-660°C. In accordance, trapping temperatures are in the range of those hypothesized by Duranti et al. (1992), during the thermal peak of metamorphism (T_{max} ≤650°C). Small pressure variations inside this range may explain the shift of fluid inclusions inside the field of L2 inclusions; alternatively, a a isobaric cooling from 650°C to 610°C at 1300 bars could be hypothesized. This pressure estimate implicitly assumes that the depth of formation of quartz-tourmaline veins equals the depth of contact metamorphism in the host rocks of Eastern Elba (5-6 km; Mazzarini et al., 2011). However, leucogranitic sills of the Calamita Peninsula, genetically linked to quartz-tourmaline veins, were located at only 3 km depth in the crust (Mazzarini and Musumeci, 2008). Following the work of Mazzarini et al. (2011), the depth of tourmaline veins is assumed to be closer to 3 km, i.e., shallower than that corresponding to the metamorphic aureole. At this depth, trapping pressure would be reduced to ~ 800 bars, which is consistent with the critical pressure of 739 bars for a 20 wt.% NaCl eq. saline fluid. Considering the near critical assemblage observed for L and inclusions at Stagnone (see later in this paragraph), the *minimum* pressure estimate for this system could not located far away from this pressure limit, deriving then a *minimum* trapping temperature for L2 inclusions of ~540-570°C. The pressure P-T range for L2 inclusions can be then confined to 740 bar<Pmax<1600 bars and 540°C<Tmax<650 °C. A simple isobaric cooling for 100-150°C may explain the trapping of this fluid on the L1 isochores at temperatures around 420° and 510°C.
Data for V inclusions occurring at Stagnone are scant, randomly distributed, and difficult to be modeled. In particular, we considered only the very few cases where Th<600°C (Table 1.5.1.1). It is important to note that Th determination for vapour-rich inclusions is rarely accurate. Studies on synthetic fluid inclusions have then demonstrated that a rim of liquid is still present on the wall of inclusions at a temperature at which the fluid inclusion appears to have homogenized (Roedder 1984). Similarly, a small amount of liquid is always entrapped together with the vapour phase (Roedder 1984), generating a range of Th which is higher than that predictable by a pure homogenous trapping.
The behavior of V inclusions during microthermometry supports the possibility that these inclusions trapped a fluid approaching critical densities. Vapour inclusions in fact presented almost no change in vapour dimensions up to few tens of degrees of the suspected final homogenization. Rapidly expansion of the vapour to fill the inclusion volume is then typical of inclusions with almost critical densities (Roedder 1984). Due to this peculiar behavior, final homogenization of V inclusions that still present a vapour bubble at 600°C probably occurs not far away from this temperature limit.
In Fig. 2.3.40, the critical isochore has been calculated for a composition of 20 wt.% NaCl eq. (dotted black line). Depending on its density (ρ_F) with respect to the critical value (ρ_C), a fluid near the critical point will display homogenization on the right or on the left of the critical isochore. Fluid inclusions with $\rho_F>\rho_C$ will homogenize to liquid on the left of the critical isochore (liquid stable field) at a temperature which is below the critical value; fluid inclusions with $\rho_F<\rho_C$ will homogenize to vapour on the right of the critical isochore (vapour stable field) at temperatures higher than critical temperature. The isochore for a V inclusion with a salinity of 20 wt.% NaCl eq. has been calculated using the software packages ISOC and BULK (Bakker 2003), and is delineated as a short pink dotted line in Fig. 2.3.40. Temperature limitations of the

available models did not allow a further extension of the isochore in the P-T space. However, as it is clear from Fig. 2.3.40, pressure and temperature fluctuations may have been responsible for fluid density to vary above and below the critical isochore, forming the corresponding L2 and V assemblage observed in the Stagnone area. Theoretically, for any value of salinity, V should display Th higher than the corresponding L inclusions. Due to the low number of V inclusions homogenizing <600°C, this condition was not verifiable in our system. In addition, it should be observed that increases in fluid salinity will shift the critical point to higher temperatures and pressure (e.g., see the critical point for a solution with a salinity of 25 wt.% NaCl eq.; Fig. 2.3.40), resulting in L inclusions that homogenize at higher temperature than the V inclusions with lower salinity.
Finally, quartz at Morcone registered the presence of an additional fluid, showing lower Th and salinity with respect to those observed at Stagnone and Ripalte. Compositionally, this fluid shares some similarities with the other two, being enriched in Fe(Mn), B and Li (Table 2.3.5). Moreover, the fluid circulated at Morcone follows the trend of Mg-enrichment (Fe/Mg= 0-0.2 molar ratio) observed for inclusions in F2 at Stagnone and Ripalte (Fig. 2.3.41), denoting high chemical interaction between the fluid and Mg-rich host rock. Based on the above considerations, the fluid trapped at Morcone can be genetically linked to that observed at Stagnone and Ripalte. Isochore for L inclusions were calculated at Th= 368°C and salinity = 7.5 wt.% NaCl eq. (mean values for the fluid inclusions dataset). Similarly to Stagnone, the association of L- and V-type at Morcone indicates pressure fluctuation above critical temperature, although they occur at lower temperature than at Stagnone. Considering the critical temperature of 443°C for a 7.5 wt.% NaCl eq. fluid, trapping temperature was near that value, corresponding to a trapping pressure of ~760 bars (Fig2.3.40).

Iron mineralized areas
Considering the H_2O-NaCl system, isochores have been calculated to reconstruct the P-T trapping conditions.
For Terra Nera and Valle Giove, three isochores have been calculated corresponding to the maximum, minimum and mean Th registered for the fluid inclusions datasets. Mean values for Th and salinity were extrapolated from the samples analyzed for quartz-hematite geothermometry (TN2 for Terra Nera and VG02 for Valle Giove, section 1.5.), which offer the opportunity to derive a pressure corrections for these systems.
For Terra Nera, the mean isochore was calculated at Th = 290°C and salinity = 20 wt. % NaCl eq., whereas for Valle Giove a Th = 275°C and a salinity = 17 wt.% were assumed. Mean isochores are plotted as dash-dot red and blue lines for Terra Nera and Valle Giove respectively (Fig. 2.3.43). A pressure correction was then applied considering the temperature estimates obtained from the quartz-hematite geothermometry, which indicated a quartz forming temperature of 365°C and 350 °C for Terra Nera and Valle Giove, respectively (see paragraph 1.5). In these conditions, trapping pressure was derived to be equal to 1100 bars for both systems, corresponding to a depth of formation of ~ 4 km under a lithostatic pressure regime. Consequently, the maximum and minimum trapping temperatures under this lithostatic pressure for each deposit have been derived (i.e., maximum and minimum isochore), considering the realistic maximum and minimum Th reported each dataset, where salinity was maintained as fix variable. Input data were as follows: for Terra Nera, Th_{max} = 350°C, Th_{min} = 275 °C; for Valle Giove, Th_{max} = 300°C, Th_{min} = 240 °C (Fig. 2.3.44). These isochores were delineated as solid red and blue lines in Fig.

2.3.44. Assuming 1100 bars as the pressure correction for these systems, trapping temperatures are then comprised in the intervals 350-440°C and 310-380°C for Terra Nera and Valle Giove, respectively. For Valle Giove, the isochore referred to halite-saturated inclusions in calcite (Th = 276.9 °C, Ts_{NaCl} = 221.1; salinity = 33 wt. % NaCl eq.) was moreover reported (dotted blue line; Fig. 2.3.44)
Since the frequency distributions of Th are polimodal, and the average means could not adequately represent the distribution of data, mean isochores were not calculated for the deposits of Topinetti and Bacino. Instead, only two isochores, corresponding to the maximum and minimum Th value observed for each dataset are reported in Fig. 2.3.44. Input data were: for Topinetti, Th_{max} = 320°C, Th_{min} = 185 °C, salinity = 20 wt. % NaCl eq.; for Bacino, Th_{max} = 280°C, Th_{min} = 205 °C, salinity = 15 wt. % NaCl eq. These isochores were delineated as solid pink (Topinetti) and green (Bacino) lines in Fig. 2.3.44. Similarly to Valle Giove and Terra Nera, we assumed that the deposits of Topinetti and Bacino formed under a lithostatic pressure regime at 1100 bars. Under this condition, trapping temperature for the fluid are comprised in the intervals 240-400°C and 265-360°C for Topinetti and Bacino, respectively.
As it is clear from Fig. 2.3.44, thermal fluctuations inside the deposits were responsible for the formation of fluid inclusions plotting on different isochores and displaying different Th during homogenization. Moreover, a simple isobaric cooling may explain the transition from the highest trapping temperature of Terra Nera to the lower temperature for the deposits of Topinetti and Bacino. For Topinetti and Valle Giove, the occurrence of low-salinity fluid inclusions correlated with low Th (Figs. 2.3.33 and 2.3.36) may suggest mixing with another low-salinity fluid (meteoric-derived?), and hence that the hydrothermal system was open to the surface under the last stages of its formation. For this reason, the lower limit of pressure stability for all the mineralized areas is fixed at 400 bars (Fig. 2.3.43), corresponding to the fluid pressure occurring at 4 km depth in hydrostatic conditions.

2.3.4.5. Origin and evolution of hydrothermal circulation in eastern Elba Island

During the late Miocene, the emplacement of the Porto Azzurro (5.2-6.9 Ma; Maineri et al., 2003) at shallow levels in the crust led to the development of a wide contact aureole of 6-7 km of diameter affecting the entire Calamita Peninsula. Late magmatic fluids released in the hornfelsic aureole are highly saline and B enriched (Dini et al., 2008), resulting in the development of hydrothermal systems and associated extensive boron metasomatism in the areas of Stagnone, Ripalte and Morcone. Progressive accumulation of B-rich fluids in the system highly caused overpressure conditions and eventually hydrofracturing. To these events, it is associated the formation of the quartz-tourmaline veins studied in this work (Dini et al., 2008). Thanks to structural reconstructions, fluid inclusions study and isotopic analysis of fluid characteristics, a model for the ancient hydrothermal systems of Stagnone, Ripalte and Morcone and the associated mineralized areas of Rio Marina and Terra Nera can be proposed. These mineralized areas were believed to represent the superficial part of the fossil complex geothermal system of Eastern Elba.
Petrographic observations of fluid inclusions at Stagnone did not allow to characterize the timing of the different population of fluid inclusions, particularly S and L (and V) types. In our opinion, L inclusions likely predates multiphasic ones, and can be related to tourmaline deposition as suggested by the occurrence of L inclusions in tourmaline. However, we cannot exclude that also the fluid trapped in S inclusions significantly contributed to B-metasomatism. In accordance, Raman and LA-ICPMS analysis indicates the presence of B in both types of fluid inclusions.

Fluid inclusions observations and microthermometric data suggest that high temperature L inclusions may have exsolved directly from the crystallizing melt (Cline and Vanko, 1994) at lithostatic pressure comprised between ~800 and 1600 bars (Fig. 2.3.45). Mild fluctuations in pressure resulted in conditions which shifted fluid density below and above critical conditions, producing the typical assemblage of V and L2 inclusions observed at Stagnone. If a mean pressure value of 1300 bars is assumed, progressive cooling of the system resulted in the formation of lower temperature L1 inclusions and S inclusions occupying the lower pressure portion of the trapping field (Fig. 2.3.45). Progressively sealing of the system resulted in increasing salinity of fluid inclusions (Shinohara et al., 1989), corresponding to the stage when S-b type fluid inclusions were formed. Higher salinity and associated higher pressure conditions are depicted by inclusions homogenizing by halite dissolution (S-a) with Ts_{NaCl} between 315 and 400°C. For these inclusions, increasing pressure above 1300 bars to more than 2000 bars (Fig. 2.3.45) corresponds to the transition from lithostatic to supra-lithostatic conditions, like those that predate hydrofracturing events. Particularly, this phase is testified by S-a inclusions that exhibit high Ts_{NaCl} (>400°C) and low Th (~220°C). After hydrofracturing, pressure collapse may have resulted in the formation of L1 inclusions trapped around 800 bars. The variability of fluid inclusions assemblage between the sites of Stagnone, Ripalte and Morcone may provide further information on the geometry of the hydrothermal system. The area of Ripalte did not register the temperature peak related to the first exsolution of fluid from the crystallizing magma (it lacks of L2 and V inclusions), indicating it probably represents a cooler (and depressurized?) part of the reservoir. Morcone represents an area where P-T conditions where additionally reduced with respect to Ripalte. Here, the rare occurrence of S-b and the concomitant lacking of S-a inclusions suggests that Morcone was only partly influenced by the overpressure conditions experienced by Stagnone and Ripalte.

Progressively cooling and depressurization of the hydrothermal system moving east to west in the Calamita Peninsula (from Stagnone to Morcone sites) is consistent with the compositional changes observed in the fluid, particularly for K concentrations. LA-ICPMS analysis on the three type of L inclusions encountered at Stagnone, Ripalte and Morcone denotes in fact a low but remarkable increase in Na/K (molar ratio) as the fluid is evolved from Stagnone to Morcone area (Fig. 2.3.46) in accordance with common use of this ratio for geothermometry (Giggenbach, 1988).

Based on fluid inclusions study on Rio Marina and Terra Nera, these areas registered the presence of a fluid that show some major chemical analogies with those circulated in the Calamita Peninsula. Particularly, as indicated by LA-ICPMS analysis, fluids circulating in both areas show comparable concentrations of B, Li and Fe (Table 2.3.5), while the highest salinity values (~25 wt. % NaCl eq.) reported in L-type fluid inclusions at Terra Nera and Valle Giove are comparable with that of L-type inclusions at Stagnone (Fig. 2.3.47). Similarly, hypersaline S-type inclusions observed in the Calamita Peninsula also occur at Valle Giove. These observations highly indicate a common source for the fluid circulated in the deeper and surficial reservoirs of Elba Island, with the main difference represented by the remarkably lower temperature reported for the superficial reservoir (Fig. 2.3.48). In accordance, fluid circulated in the mineralized areas generally display higher Na/K molar ratios with respect to the fluid recovered in the Calamita Peninsula (Fig. 2.3.47). Following our model, B-rich magmatic fluids precipitating tourmaline in the Calamita Peninsula were passively enriched in Fe by reaction with the biotite in the Mt. Calamita Schists (see report Task 3.2), and transferred to the more superficial reservoirs, where it cooled and gave rise to the widespread Fe mineralizations characterizing east Elba

Island. However, lower salinity and associated lower temperature in fluid inclusions of some of these deposits, particularly at Valle Giove and Topinetti (Fig. 2.3.48), highly indicate a mixing trend of these deep-derived magmatic fluids with a low-saline, with a possible meteoric derivation.
Higher salinity fluids (S inclusions) in the Calamita Peninsula are interpreted to be exsolved from the magma at increasing pressure (Shinohara et al., 1989). The occurrence of some hypersaline fluid inclusions at Valle Giove indicate that such fluids sporadically reached shallower levels. Temperature of the hypersaline fluids at Valle Giove and in the Calamita Peninsula is comparable (Fig. 2.3.49). As the fluids didn't cooled during its infiltration at shallower level the rise of the fluid from deeper levels was relatively fast.
This study show evidences of a very high temperature fossil fluid circulation at Stagnone, which may have locally approached supercritical conditions. For example, a fluid with a salinity of 20 wt.% NaCl eq. has been trapped by L inclusions at P-T conditions higher than the corresponding critical point for the H_2O-NaCl system (Fig. 2.3.40). This conclusion is moreover valid if we consider the high contents of $FeCl_2$ reported for this fluid. Differently from the behavior of other divalent chlorides, critical points in the H_2O-$FeCl_2$ system are indeed shifted to lower pressures than those in the H_2O-NaCl one (Steele-MacInnis et al., 2015), expanding the field of supercritical conditions to lower pressures. Critical conditions seem however not to be extended in space but limited to sporadic areas inside the system. Furthermore, supercritical conditions seem to have existed in the Morcone area with a circulation of fluids at 440°C and 800 bars (Fig. 2.3.45).

2.3.4.6. Integration of the physical-chemical characteristics of the fossil fluids with those available from the Larderello geothermal field

In this paragraph we integrate and compare the information obtained on the fossil reservoirs of Elba Island exhumed hydrothermal system, with those available from the active geothermal system of Larderello in order to better understand the characteristics of high-temperature geothermal reservoirs and in particular to get insight on the super-hot geothermal reservoir that presumably occur below the presently exploited reservoirs at Larderello. The exhumed Elba Island hydrothermal system shares significant common features with the active geothermal system of Larderello. At Larderello, multiple plutonic acidic complexes with distinct ages and isotopic characters were identified by Dini at al. (2005). Multiple intrusive emplacements are, in fact, essential to maintain a long-lived, relatively large thermal anomaly such as those occurring in the Larerello area. In the eastern part of Elba Island we can observe just the top of an acidic intrusive complex (Porto Azzurro pluton), however by comparison with the western Elba (Dini et al., 2002), the presence of several stacked intrusions at depth is realistic and also a necessary requisite to explain the widespread contact metamorphism and the occurrence of skarn bodies also north of Mt. Calamita peninsula. Either at Larderello and in eastern part Elba Island, the intrusive bodies were emplaced at relatively shallow depth (3-8 km) within Paleozoic metamorphic rocks.
At Larderello, two geothermal reservoirs are recognised and industrially exploited: 1) a shallow steam-dominated reservoir is hosted at 500-1500 m depth in the Mesozoic carbonate formations of the Tuscan nappe units and in the Late Triassic evaporitic levels of a tectonic wedges complex, and is characterized by medium-high permeability, present-day temperatures of about 220-250°C and a pressure of about 20 bar at 1000 m depth; 2) a deep superheated steam reservoir, in vaporstatic equilibrium with the shallow one, is hosted in fractured metamorphic basement and

thermo-metamorphic rocks at depths ranging between 2000 and 4500 m, and is characterized by a high anisotropic permeability distribution, temperatures ranging between 300-350°C and a reservoir pressure of 70 bar at 3000 m depth (Batini et al., 2003). Present-day reservoir fluids at Larderello are steam dominated, largely composed by H_2O (up to 95%) with CO_2, CH_4, H_2S and N_2 as major components, and noble gases present in ppm (Scandiffio et al., 1995). Stable isotope data on H_2O (before re-injection) indicate meteoric water as the main source of the vapor (Craig,1963; Ferrara et al., 1965). A simple mixing between two end-members could explain the isotopic composition of the steam produced in the field (Panichi et al., 1995; Scandiffio et al., 1995).The former end-member is a primary deep steam having typical values of $\delta D = 40\pm2‰$ and $\delta^{18}O = 0\pm2‰$, resulting from extensive water-rock interactions, which shifted the original meteoric $\delta^{18}O$ value towards more positive values. An alternative explanation of the steam's origin has been proposed by D'Amore and Bolognesi (1994), who hypothesized the mixing of two end-members, meteoric waters, and magmatic fluids produced by the crystallization of a deep-seated magma body. In Elba Island the hydrothermal systems related to Fe-deposits of Valle Giove, Bacino and Topinetti within the Triassic Verrucano formation probably represented the shallower reservoir. Whereas, the Terra Nera hydrothermal system occurs within Paleozoic Rio Marina formation and it likely represents a deeper reservoir. The nature of the fluid that circulated in these systems significantly differ from those presently occurring in the Larderello geothermal field, in fact, FIs data showed that the fossil hydrothermal system was characterized by: 1) reservoir fluids with variable salinities (1-33 wt.% NaCl eq.) and unusual composition (i.e. significant presence of Li, B, Fe, K etc.), 2) temperature between 200 and 440°C, and 3) reservoir pressure comprised between lithostatic and hydrostatic values (Fig. 2.3.44). These fluids were interpreted to be same saline fluids of magmatic derivation that circulated within the Mt. Calamita schists found in the FIs in quartz-tourmaline veins of Calamita Peninsula (see paragraph). Such fluids got enriched in Fe as a consequence biotite-fluid interaction and tourmaline deposition (see report of task 3.2 for details) within Mt. Calamita schists, after that they raised towards shallower structural depositing the Fe mineralization and they eventually mixed with meteoric fluids as evidenced by salinity variation at Topinetti, Valle Giove and Bacino (Figs. 2.3.30, 2.3.33, 2.3.36).

The steam-dominated nature of the Larderello field, however, arises from the natural evolution of the system. Hydrothermal mineralization and FIs, in fact, document that a liquid phase was present in the past in the Laredello geothermal system (Gianelli and Ruggieri, 2002). Thermal and structural context, likely, allowed the geothermal system to pass from an initial water phase to the current steam condition. Studies on FIs within igneous quartz, contact-metamorphic and hydrothermal minerals showed that the past fluid circulation in the Larderello fields was characterized by several types of fluids and a complex sequence of fluid trapping during evolving pressure-temperature conditions (Cathelineau et al., 1994; Boiron et al., 2007, and references therein). In particular, FIs studies showed the occurrence of early fluids, dominated by magmatic derived and contact-metamorphic fluids, followed by a more recent fluid circulation. This latter stage is characterized by fluids comparable with those of FIs associated to the iron deposits of Elba Island. Specifically, trapping temperature (between 150 and 400°C) and salinities (from around 0 wt.% NaCl to halite saturated liquid) reported for these late FIs (Valori et al., 1992; Ruggieri et al., 1999; Boiron et al., 2007; Boyce et al., 2003) support the analogy between the fossil (Elba Island) and the active (Larderello) hydrothermal systems.

Another similarity between the active and the fossil systems is documented by the tourmaline veins. As shown by FIs the formation of tourmaline-rich metasomatic

bodies and veins of Mt. Calamita were related to the circulation of B-bearing saline or hypersaline brines of magmatic origin. These fluids were likely issued from the Porto Azzurro granitic intrusion and/or from other buried intrusions. B-metasomatism affected both the Calamita schist host rock and granites, in particular, metasomatic fluids selectively replaced the biotite-rich layers of the Calamita Schists producing tourmalines as demonstrated by the experimental data (see report of Task 3.2). Analogously, tourmaline veins occur in the deepest part of the Larderello geothermal field whereas quartz-tourmaline fragments were erupted by the San Pompeo 2 well geothermal well that probably reached the so-called K-horizon seismic in the reflector (Dini et al., 2008). This horizon is an intense and continuous seismic reflector exhibiting local "bright spot" features inside the Palaeozoic crystalline basement (Batini et al., 1983; Gianelli et al., 1997; Brogi et al., 2005). Its depth varies between 3-4 km in the western zone and 8-10 km in the Travale geothermal area (Bertini et al., 2006). This seismic facies is characterized by a lozenge-shape geometry whose thickness is estimated in about 2 km. The nature of the K-horizon is still a subject of debate. However, regardless of the interpretation of the K-horizon, the only phenomenon that is able to account for this seismic "bright spots" is the presence of micro-cracks and micro-fractures filled locally by fluids (Marini and Manzella, 2005). The K- horizon was never reached during deep drilling, except, in the San Pompeo 2 well. This well blew out on reaching fracture zone at depth (about 2900 m below the surface level). Temperature exceeding 400°C and pressure far above 240 bars was estimated for the fluid produced from fracture zone (Batini et al., 1983). During the blow-out abundant fragments of quartz–tourmaline veins and tourmaline breccias erupted by the geothermal well as consequence of the presence of pressurized fluid. The K-horizon, therefore, likely represent a super-hot pressurized geothermal reservoir characterized by boron metasomatic processes. Because to the difficulty of fluid sampling only some information on the fluid discharged during the blow-out were obtained, specifically the gas phase reported in Marini and Manzella (2005) (X_{CO2}=0.6140, X_{H2}=0.2760, X_{CH4}=0.1157, X_{CO}=0.0012) was characterized by high amount of H_2 and CH_4. However, the nature of the fluid stored in this reservoir is still not clear. FIs in Larderello deep core-samples of granites or in high-temperature assemblage (comprising tourmaline) recorded the circulation of: 1) Li-Na-rich saline fluids and compositionally complex brines (exsolved from granites), and 2) aqueous-carbonic fluids (produced by heating of Paleozoic rocks during contact-metamorphism). These fluids probably circulated at depth >2500 m below the ground level, usually at temperatures of 425–690°C and under lithostatic pressures of approximately 900-1300 bars or at pressures below lithostatic values (only the aqueous-carbonic fluids) during system decompression (Cathelineau et al., 1994). These, super-hot fluids were probably trapped within a paleo K-horizon, and occur at present in a zone characterized by lower T and P because of rock uplift and/or cooling of the system (Boiron et al., 2007).Temperature and pressure of this fluid circulation are rather similar to those estimated for the super-hot fossil hydrothermal circulation in the Mt. Calamita from FIs of quartz-tourmaline veins. In addition, both fluid circulation were characterized by the occurrence of magmatic derived fluid. At Larderello previous studies didn't reported the occurrence of Fe, B in trapped fluid as in quartz-tourmaline veins, but only of Li, K and Na (Cathelineau et al., 1994). However, the information on the composition of these FIs are partial as they were not analysed by LA-ICP-MS. The main difference between the two super-hot systemss is the of occurrence aqueous-carbonic FIs at Larderello and the lack of them at Elba Island. A thermal metamorphic origin from the reaction between water and the graphite present in the metamorphic basement, was suggested for the aqueous-carbonic fluids at Larderello, especially the volatiles

(CO_2–CH_4), trapped within FIs (Boiron et al., 2007). Thus, the lack of these fluids in quartz-tourmaline veins may simply reflect the absence of graphite in the Mt. Calamita schist. In conclusion, the integration FIs obtained in this study on quartz-tourmaline with those of previous study on Larderello geothermal field evidenced that both systems were characterized by super-hot reservoirs (400-650°C) storing saline or hypersaline fluids of magmatic derivation, with exotic composition, under lithostatic pressure values. At Larderello, the super-hot reservoir can be still present within the K-horizon. As suggested by the blow-out of the San Pompeo 2 well and also by the "magmatic-contribution" evidenced by $^3He/^4He$ data (R/Ra reach maximum values of 2.7-3.2) and high N_2/He and N_2/Ar ratios, in present-day fluids (Magro et al., 2003, and references therein). By the analogy between the present-day and the fossil reservoirs we can predict the physical-chemical characteristics of the magmatic fluid that should occur with the reservoir.

2.4. Final Remarks

The integration among the geological survey, the structural and kinematic study in eastern Elba Island and the results of geochemical analyses, suggest the following main points:

a) the geothermal fluids circulation occurred with fluids having high temperature (650°C) down to lower temperatures (about 200-300°C); this circulation was coeval with the brittle deformation, represented by the activity of the low-angle normal faults and almost vertical oblique-slip fault systems.
b) Circulation of fluids is mostly controlled by the almost vertical structures from which fluids laterally migrated into the hydraulically connected structural traps.
c) At shallower levels, the geometry of the structural traps is defined by the interplay between lithology (impervious vs. permeable) and previous deformational events.
d) At deeper levels the circulation of fluids is controlled by fractures, mostly.
e) Supercritical conditions can be reached where fluid temperature is very high (above 600°C) and Pressure is significant (>0.4 kbar).
f) Fluids are of magmatic origin progressively mixed with meteoric water, from deeper to shallower levels
g) Tectonic evolution and structural setting of the eastern Elba Island appears to be comparable with that of the Larderello geothermal field.

Furthermore, Mineralogical, isotopic and fluid inclusion studies indicated the occurrence of a super-hot reservoir filled by B-bearing saline/hypersaline fluids of magmatic derivation. Water-rock interaction in the reservoir caused the biotite destruction, tourmaline precipitation and Fe-enrichment in the fluids. The pressure-temperature-salinity-chemical and isotopic characteristics of these fluids are:
Saline fluids: 420<T<650 °C; 740<P<1600 bars; salinity: 16-30 wt. % NaCl eq.; composition: Na= 54,902; Mg= 8,601; K= 29,663 Fe= 28,892 mg/kg
Hypersaline fluids: 370<T<420 °C; 1100<P<2000 bars; salinity: 29-49 wt. % NaCl eq.; composition: Na=173,945 Mg=18,448 K= 57,949 Fe= 105,783 mg/kg
δD_{H2O} = -64.2‰ to -24.9 ‰; $\delta^{18}O_{H2O}$ = 11.2 to 11.3 ‰
These Fe-rich fluid were transferred at higher structural level within lower temperature reservoirs and precipitated Fe-mineralization. Within the reservoir the deep fluid mixed with fluid of meteoric origin. The pressure-temperature-salinity-chemical and isotopic characteristics of the fluids within the shallower reservoirs are:

Saline fluids: 200<T<440 °C; 400<P<1100 bars; salinity: 0-29 wt. % NaCl eq.; composition Na = 62,706 Mg = 8,618 K= 16,407 Fe=13,460;
Hypersaline fluids: 300<T<330 °C; 400<P<1100 bars; salinity: 31-34 wt. % NaCl eq.; composition Na=130,000 Mg=109,580K= 36,212 Fe= 37,261
$\delta^{18}O_{H2O}$ = 3.6 - 10.6 ‰.
The fossil super-hot reservoir of Elba Island is a proxy of the super-hot reservoir which is presumably present within the seismic K-horizon of the Larderello geothermal field. This analogy can be applied in order to predict the physical-chemical features of the fluids that should be stored within present-day super-hot reservoir. In particular, assuming that L FIs are representative of the fluid occurring at the level of the K-horizon at Larderello, we can estimate from the minimum P-T values of such inclusions that the P-T that should occur at the top of the K-horizon are: T~420°C, P~740 bars.
Finally, we underline that the data deriving from the exhumed geothermal system continental crust represents a powerful approach in order to get information about the properties of the fluids and on the relationships between geological structures and fluid flow. The information so far obtained, can effectively drive the exploration of the analogue active geothermal systems.

Appendix 2

Analytical methods

Chemical analyses of tourmalines were performed using a JEOL-FXA-8600 electron microprobe (CNR–IGG, Firenze) in wavelength-dispersive mode with acceleration voltage = 15 kV, sample current = 10 nA and 4 μm beam size. WDS element peaks were measured with counting time of 10 s (Na), 15 s (Si, K), 30 s (Fe) and 40 s (Al, Cr, Mg, Mn, Ca, F); background was counted for 10 s. Albite was used as reference standard for Si and Na (TAP); plagioclase for Al (TAP); olivine for Mg (TAP); sanidine for K (PET); diopside for Ca (PET); ilmenite for Ti (PET) and Fe (LIF); chromite for Cr (LIF); bustamite for Mn (LIF) and apatite for F (TAP). The detection limit under the specified conditions was approximately 0.05 wt%.
Most of the fluid inclusions were studied in quartz (Stagnone, Morcone, Valle Giove, Terra Nera, Topinetti), and, when present, in calcite (Valle Giove). Rarely fluid inclusions were studied in tourmaline (Stagnone). Fluid inclusions were investigated in doubly polished wafers (80 μm) in reflected light microscopy.
Several types of fluid inclusions were distinguished, and their notation is based on the phase assemblage occurring at room temperature, and on the homogenization mode. Fluid inclusions composed by a liquid and a vapor phase are noted V if they homogenize to the vapor phase (L+V→V), and L if the homogenization is to the liquid phase (L+V→L). Fluid inclusions which present a liquid, a vapor and solids are multiphase inclusions, denoted as S.
Microthermometric measurements were performed at Linkam THMSG600 heating-freezing stages coupled with ZEISS POL-BK, and Olympus BX53P microscopes for CNR-IGG, and University of Bari, respectively. The stages were calibrated by using pure H_2O with critical density, and mixed H_2O-CO_2 (CO_2 25% M) synthetic fluid inclusions. Accuracy was estimated to be ± 0.1 °C for final ice melting (Tm_{ice}) and hydrate melting temperature (Tm_{hy}), and ±1 °C for the vapour/liquid homogenization (Th), and halite dissolution temperature (Ts_{NaCl}). In order to avoid overheating phenomena to S inclusions, which commonly decrepitate above Ts_{NaCl}, S and L inclusions were studied in different fragments for each sample. Due to

metastability, S inclusions were highly reluctant to freeze during low temperature measurements. Therefore, Tm_{ice} were determined only in L and V inclusions.
Scanning electron microscopy-energy dispersive X-ray spectroscopy (SEM–EDS), and Raman spectroscopy were employed as complementary techniques to characterize solids, fluids and eventually gaseous components in fluid inclusions. SEM-EDS technique yields information on the morphology of daughter minerals, on their chemistry, and on fluid composition. It is however destructive and poor selective. On the contrary, Raman spectroscopy has the advantage to be non-destructive, and more specific. Unfortunately, major chloride species (es. NaCl, KCl, and $CaCl_2$) are very weak Raman scatters, preventing their analysis by Raman spectroscopy, although their common presence in fluid inclusions. In this study, besides solids, Raman spectroscopy was applied to detect any polyatomic ions and/or gaseous components in the fluid.
The SEM study was conducted on a ZEISS EVO MA15 instrument, equipped with an OXFORD INCA 250 EDS detector, at the Centro di Microscopia Elettronica e Microanalisi of Firenze (M.E.M.A). Operating conditions were: 15 kV accelerating voltage, 150 mA emission current. Fragments of quartz known to contain fluid inclusions were broken, allowing daughter minerals and newly formed salts to be directly exposed to surface. Quartz fresh surfaces were then carbon-coated, and mounted for analysis.
Raman analyses were performed with a LabRAM microspectrometer (Horiba Jobin Yvon, at GeoRessources, Vandœuvre-lès-Nancy, France) equipped with a 1800 g mm−1 grating and a × 80 Olympus objective. The exciting radiation was provided by the 514.5 nm line of an Ar+ laser (Stabilite 2017, Newport Corp., Spectra Physics) at a power of 400 mW.
Laser ablation - inductively coupled plasma mass spectrometry (LA-ICPMS) has become one of the most sensitive and accurate technique for the determination of the concentration of major and trace elements in individual fluid inclusions. Selected samples and fluid inclusions were then analyzed for LA-ICPMS at the G2R laboratory of Nancy (France). The LA-ICPMS instrument comprises a GeoLas excimer laser (ArF, 193 nm, Microlas, Göttingen Germany) and an Agilent 7500c quadrupole ICP-MS equipped with an octopole reaction-cell using H_2 gas, and a collision-cell using He gas. The laser beam is focused onto the sample within an ablation cell with a Schwarzschild objective (magnification x25) linked with a CCD camera. Synthetic glass from the National Institute of Standard and Technology (NIST) are used for calibration of the different analysed elements and respective masses (200 pulses at 5Hz). The design as an optical imaging system permits the use of different crater diameters (24, 32 or 60 µm) at a constant energy density on the sample, by adjusting an aperture in the laser beam path. Li, B, Na, K, Mg, Ca, Ba, Sr, Mn, Fe, Cu, Zn, Sn and W were analysed. Concentrations were calculated according to Leisen et al. (2012). Analytes were considered as detected only when the magnitude of the shift of the LA-ICPMS signal relative to background was higher than three times the standard deviation of the background (Longerich et al., 1996). Particularly, data for multiphase inclusions should be taken with caution; due to the low dimensions of Elba fluid inclusions compared to the laser beam diameter, LA-ICPMS gave information of the inclusions as a bulk and not specifically on the fluid. For example, concentrations of Fe and Mn at Stagnone, Ripalte and Morcone were easily overestimated due to the presence of Fe-bearing daughter minerals in fluid inclusions, which were ablated during analysis. Accordingly, unrealistic results for some elements may be found also for L inclusions analyses probably due to the presence of trapped minerals invisible at microscope resolution. Finally, incomplete removal of matrix interference additionally contributed to erroneous quantification of

some elements in both S- and L-type of inclusions. Misleading results are then identified in red color in Table 1.3.1 (reporting the results of LA-ICPMS analysis) and not further considered in the discussion sections.
Salinity of fluid inclusions was expressed in weight percent equivalent NaCl (wt. % NaCl eq.). For L and V inclusions salinity was calculated from Tm_{ice} following the equation of Bodnar and Vityk (1994), which assumes that the composition of the fluid may be described by the binary H_2O-NaCl system. It should be noted that this salinity represents only an approximation of the real value for the systems under study, because other divalent cations (Ca^{2+}, Mg^{2+}, Fe^{2+} etc.) in addition to Na^{+} are present in many of the examined inclusions. This hypothesis is corroborated by: ii) the low eutectic temperature observed during freezing analysis (T_e ~-50/-55 °C); ii) Tm_{ice} lower than the eutectic H_2O-NaCl value (-21.2 °C), and iii) SEM-EDS and LA-ICPMS analysis of the fluid.
For NaCl-saturated inclusions, S-type salinity was calculated following the methods of Lecumberri-Sanchez et al. (2012) and Steele-MacInnis et al. (2012) for Sa and Sb inclusions (see later), respectively.
The hydrogen isotope compositions were made at the IGG-CNR (Pisa, Italy) using high-temperature (1400°C) reduction methods with He-carrier gas and a TC-EA (Flash1112HT, Thermo Fisher) interfaced to a Delta Plus XP mass spectrometer. The results are given in the standard δ-notation, expressed relative to VSMOW in permil (‰). Replicate hydrogen isotope analyses of internal standards had an average precision better than ± 5‰.
Oxygen isotopic composition was obtained by laser fluorination. Analyses for standards were obtained on grain separates at the Institute of Earth Sciences at the University of Lausanne (Switzerland). Grains of quartz, hematite and adularia have been carefully picked under the stereomicroscope to avoid inclusions and loaded into the chamber (between 1 and 2 mg of material for each analyses), together with quartz standard.
Following a routine procedure, the chamber was evacuated for a minimum of 1 h and pre-fluorinated between 10 and 12 h (overnight) followed by a 10 min pre-fluorination. Samples were heated by a CO2 laser in a F2 atmosphere (~ 100 mbar of F2) to yield O2 that was purified and analyzed as O2 in a dual-inlet gas-source mass-spectrometer (Thermo Finnigan RMS 253). Analyses were standardized by replicate analyses (2 or more) on the same day of LS-1 (in house standard Lausanne quartz 18.1‰) or NBS-28 quartz (9.64‰, Coplen et al., 1983) and reported in standard per mil notation relative to Vienna Standard Mean Ocean Water (VSMOW). Typical precision for the standard analyses is ± 0.1‰ (1 standard deviation, SD) and accuracy relative to the accepted value is ± 0.2‰.

Sr Nd and B isotopic compositions were measured (at IGGI, CNR Pisa) on different aliquotes of the same batch of tourmaline powder (about 150 mg for each tourmaline sample). 20 mg of powder was used for determination of Sr, Rb, Nd and Sm by ICP-MS (acid total digestion); 120 mg for Sr and Nd isotopes and 5 mg for B isotopes. Sr and Nd isotopic compositions were determined using a Finnigan MAT 262V multicollector mass-spectrometer after conventional ion-exchange procedures for Sr and Nd separation from the matrix. Sr total blank was better than 2 ng while Nd total blank was less than 1 ng during the period of measurement. Measured 87Sr/86Sr ratios have been normalized to 86Sr/88Sr= 0.1194; 143Nd/144Nd ratios to 146Nd/144Nd=0.7219. During collection of the isotopic data, 15 replicate analyses of SRM 987 (SrCO3) standard gave an average value of 0.710200±8 (2σ mean) and 14 measurements of La Jolla standard gave an average 143Nd/144Nd of 0.511851 ± 3 (2σ mean). All 87Sr/86Sr data were normalized to a value of 0.71025 for the SRM 987 standard. Boron isotope compositions were determined at IGG-CNR

Pisa, Italy using a VG Isomass 54E positive thermal ionization mass spectrometer. Measurements followed separation of B by ion-exchange procedures. Procedure accuracy was evaluated by replicate measurements of the standard NIST SRM 951 and yielded a standard deviation of 0.5‰.

References

Ármannsson, H., Fridriksson, T., Benjamínsson, J., & Hauksson, T. (2015). History of Chemical Composition of Geothermal Fluids in Krafla, Northeast Iceland, with Special Emphasis on the Liquid Phase. Proceedings World Geothermal Congress 2015 Melbourne, Australia, 19-25 April 2015, 1-7.

Ármannsson, H., Fridriksson, T., Gudfinnsson, G. H., Ólafsson, M., Óskarsson, F., & Thorbjörnsson, D. (2014). IDDP—The chemistry of the IDDP-01 well fluids in relation to the geochemistry of the Krafla geothermal system. Geothermics 49, 66-75.

Arnórsson S. (1995). Geothermal systems in Iceland: structure and conceptual models-I High-temperature areas. Geothermics 24, 561-602.

Avanzinelli R., Boari E., Conticelli S., Francalanci L., Guarnieri L., Perini G., Petrone C.M., Tommasini S,. Ulivi M. (2005). High precision Sr, Nd, and Pb isotopic analyses and reproducibility using new generation thermal ionisation mass spectrometer: aims and perspective for isotope geology applications. Period. Mineral. 74,147–166.

Bakker, R.J. (1999). Adaptation of the Bowers and Helgeson (1983) equation of state to the H2O-CO2-CH4-N2-NaCl system. Chem. Geol. 154, 225–36.

Bakker, R.J. (2003). Package FLUIDS 1. Computer programs for analysis of fluid inclusion data and for modelling bulk fluid properties. Chem. Geol. 194, 3-23.

Batini F., Bertini G., Gianelli G., Pandeli E., Puxeddu M. (1983) – Deep structure of the Larderello field: contribution from recent geophysical and geological data. Mem. Soc. Geol. Ital., 25, 219–235.

Batini F., Brogi A., Lazzarotto A., Lotta D., Pandeli E. (2003) Geological features of the Larderello-Travale and Mt. Amiata geothermal areas (southern Tuscany, Italy). Episodes, 26, 239–244.

Baumann D. (2014). Alteration and petrology in a fossil hydrothermal system at Geitafell central volcano, Iceland. Master Thesis, Department of Earth Science, ETH Zurich, Switzerland, pp. 51.

Benvenuti, M., Dini, A., D'orazio, M., Chiarantini, L., Corretti, A., Costagliola, P. (2012) The tungsten and tin signature of iron ores from Elba island (taly): a tool for provenance studies of iron production in the mediterranean region, Archaeometry 55, 3 (2013) 479–506.

Bertini, G., Casini, M., Gianelli, G., Pandeli, E. (2006). Geological structure of a long-living geothermal system, Larderello, Italy. Terra Nova 18, 163–169.

Bodnar, R. J. (1994). Synthetic fluid inclusions: XII. The system H2O-NaCl. Experimental determination of the halite liquidus and isochores for a 40 wt% NaCl solution. Geochim. Cosmochim. Acta 58, 1053-1063.

Bodnar, R. J., Burnham, C. W., Sterner, S. M. (1985). Synthetic fluid inclusions in natural quartz. III. Determination of phase equilibrium properties in the system H2O-NaCl to 1000 C and 1500 bars. Geochim. Cosmochim. Acta 49, 1861-1873.

Bodnar, R. J., Lecumberri-Sanchez, P., Moncada, D., Steele-MacInnis, M. (2014). Fluid inclusions in hydrothermal ore deposits. In: Holland H. D. and Turekian K. K. (Eds.) Treatise on Geochemistry, 13. Elsevier, Oxford, 119–142 (second ed.).

Bodnar, R.J., and Vytik, M.O. (1994). Interpretation of microthermometric data for H2O–NaCl fluid inclusions. In: Vivo, B.D., Frezotti, M.L. (Eds.) Fluid Inclusions

in Minerals: Methods and Applications. Virginia Polytechnic Institute, Blacksburg, 117–130.

Boiron M.C., Cathelineau M., Ruggieri G., Jeanningros A., Gianelli G., Banks D.A. (2007) Active contact metamorphism and CO2–CH4 fluid production in the Larderello geothermal field (Italy) at depths between 2.3 and 4 km. Chem. Geol., 237, 303–328.

Bottinga, Y. (1968). Calculation of fractionation factors for carbon and oxygen isotopic exchange in the system calcite-carbon dioxide-water. J. Phys. Chem., 72, 800-808.

Bowers, T.S., and Helgeson, H.C. (1983). Calculation of the thermodynamic and geochemical consequences of nonideal mixing in the system H2O-CO2-NaCl on phase relations in geologic systems: equation of state for H2O-CO2-NaCl fluids at high pressures and temperatures. Geochim. Cosmochim. Acta 47, 1247–1275.

Boyce A.J., Fulignati P., Sbrana A. (2003) Deep hydrothermal circulation in the granite intrusion beneath Larderello geothermal area (Italy): constraints from mineralogy, fluid inclusions and stable isotopes. J. Volcan. Geotherm. Res. 126, 243–262.

Brogi A., Lazzarotto A., Liotta D., Ranalli G. (2005) Crustal structures in the geothermal areas of Southern Tuscany (Italy): insights from the CROP 18 deep seismic reflection lines. J. Volcan. Geotherm. Res., 148, 60-80.

Burchardt, S., D. C. Tanner, V. R. Troll, M. Krumbholz, and L. E. Gustafsson (2011), Three-dimensional geometry of concentric intrusive sheet swarms in the Geitafell and the Dyrfjöll volcanoes, eastern Iceland, Geochem. Geophys. Geosyst., 12, Q0AB09.

Cathelineau M., Marignac C., Boiron M.C., Gianelli G., Puxeddu M. (1994) Evidence for Li-rich brines and early magmatic fluid rock interaction in the Larderello geothermal system. Geochim. Cosmochim. Acta, 58, 1083–1099.

Cline, J.S., and Vanko, D.A. (1995). Magmatically generated saline brines related to molybdenum at Questa, New Mexico, USA, in, Thompson, J.F.H., ed., Magmas, Fluids, and Ore Deposits: Mineralogical Association of Canada Short Course Series, Victoria, B.C., Canada, 23, 153-174.

Craig H. (1963) The isotope geochemistry of water and carbon in geothermal areas. In: Nuclear Geology on Geothermal Areas, E. Tongiorgi (Ed.), Pisa, Lab. di Geol. Nucl., CNR, Pisa.

D'Amore F., Bolognesi L. (1994) Isotopic evidence for a magmatic contribution to fluids of the geothermal systems of Larderello, Italy, and The Geysers, California. Geothermics, 23, 21–32.

Dini A., Gianelli G. , Puxeddu M., Ruggieri G. (2005a) Origin and evolution of Pliocene– Pleistocene granites from the Larderello geothermal field (Tuscan Magmatic Province, Italy). Lithos, 81, 1-31.

Dini A., Innocenti F., Rocchi S., Tonarini S., Westerman D.S. (2002) The magmatic evolution of the late Miocene laccolith-pluton-dyke granitic complex of Elba Island, Italy. Geol Mag 139: 257-279

Dini A., Mazzarini F., Musumeci G., Rocchi S. (2008). Multiple hydro-fracturing by boron-rich fluids in the Late Miocene contact aureole of eastern Elba Island (Tuscany, Italy) Source. Terra Nova, 20, 318-326.

Dini A., Tonarini S., Leeman W.P., Ertan I.E. and Pezzotta F. (2001) – Geochemical behavior of boron at the magmatic-hydrothermal transition: insights from d11B of tourmaline in peraluminous granites (Elba Island, Italy). In: Cidu R. (Ed.), Water-Rock Interaction. Proceedings of the 10th International Symposium on Water-Rock Interaction (WRI10). Balkema. Vol. 2, 1513-1516.

Dini, A., Gianelli, G., Puxeddu, M. and Ruggieri, G. (2005). Origin and evolution of Pliocene–Pleistocene granites from the Larderello geothermal field (Tuscan Magmatic Province, Italy). Lithos 81, 1–31.

Dini, A., Mazzarini, F., Musumeci, G., Rocchi, S. (2008). Multiple hydro-fracturing by boron-rich fluids in the Late Miocene contact aureole of eastern Elba Island (Tuscany, Italy). Terra Nova 20, 318-326.

Dong, G., and Pollard, P. J. (1997). Identification of ferropyrosmalite by Laser Raman microprobe in fluid inclusions from metalliferous deposits in the Cloncurry District, NW Queensland, Australia. Mineral. Mag. 61, 291-294.

Driesner, T., and Heinrich, C. A. (2007). The system H2O–NaCl. Part I: Correlation formulae for phase relations in temperature–pressure–composition space from 0 to 1000° C, 0 to 5000bar, and 0 to 1 X NaCl. Geochim. Cosmochim. Acta 71, 4880-4901.

Drivenes K., Larsen R.B., Müller A., Sørensen B.E., Wiedenbeck M., Raanes M.P. (2015) Late-magmatic immiscibility during batholith formation: assessment of B isotopes and trace elements in tourmaline from the Land's End granite, SW England. Contributions to Mineralogy and Petrology, 169, 1-27.

Dünkel, I. (2002) The genesis of East Elba iron ore deposits and their interrelation with Messinian tectonics, Tübinger Geowissenschaftliche Arbeiten, Reihe A: Geologie, Paläontologie, Stratigraphie, 65, 1–143.

Duranti, S., Palmeri, R., Pertusati, P.C., Ricci, C.A. (1992). Geological evolution and metamorphic petrology of the basal sequence of eastern Elba (complex II). Acta Vulcanol. 2, 213-229.

Faure G. (2001). The origin of volcanic rocks in the oceans. In: Origin of igneous rocks: the isotopic evidence. Springer-Verlag Berlin-Heidelberg, Chapter 2, 31-101.

Ferrara G.C., Gonfiantini R., Panichi C. (1965) La composizione isotopica del vapore di alcuni soffioni di Larderello e dell'acqua di alcune sorgenti e mofete della Toscana, Atti Soc. Tosc. Sc. Nat., 72, 3–21.

Fridleifsson, G,O. (1984). Mineralogical evolution of hydrothermal system II: Heat sources - Fluid interactions, Geothermal Resources Council Transactions, 8, 119-123.

Fridleifsson, G,O. and Björnsson, S., (1986). Geothermal Activity in the Geitafell Central Volcano. Fifth International Symposium on Water-Rock Interactions, Reykjavik, Iceland. Extended Abstracts, p 214-217.

Fridleifsson, G. Ó. (1983a). The geology and alteration history of the Geitafell central volcano, southeast Iceland. PhD Thesis, Faculty of Science, University of Edinburgh, pp. 371.

Fridleifsson, G. Ó. (1983b). Mineralogical evolution of a hydrothermal system. Geothermal Resources Council, Transactions 7, 147-152.

Fridleifsson, G.O., 1983a. The geology and the alteration history of the Geitafell central volcano, southeast Iceland. In: Doctoral Dissertation. Grant Institute of Geology, University of Edinburgh, United Kingdom.

Fridleifsson, G.O., 1983b. Mineralogical evolution of a hydrothermal system. Geothermal Resources Council. Transactions 7, 147–152.

Fridleifsson, G.O., 1984. Mineralogical evolution of a hydrothermal system II. Heat sources – fluid interactions. Geothermal Resources Council Transactions 8, 119–123.

Fridleifsson, G.O., 1986. Geothermal activity in the Geitafell central volcano. In: Fifth International Symposium on Water-Rock Interaction, Reykjavik Iceland, extended abstracts, pp. 214–217.

Fu, B., Williams, P. J., Oliver, N. H., Dong, G., Pollard, P. J., Mark, G. M. (2003). Fluid mixing versus unmixing as an ore-forming process in theCloncurry Fe-oxide-Cu Au District, NW Queensland, Australia: evidence from fluid inclusions. J. Geochem. Expl. 78, 617-622.

Garfagnoli, F., Menna, F., Pandeli, E. Principi, G. (2005). The Porto Azzurro Unit (Mt. Calamita Promontory, southeastern Elba Island, Tuscany): stratigraphic, tectonic and metamorphic evolution. Boll. Soc. Geol. It., Vol. Spec. 3, 119-138.

Gianelli G., Manzella A., Puxeddu M. (1997) - Crustal models of the geothermal areas of southern Tuscany (Italy). Tectonophysics, 281, 221–239.

Gianelli G., Ruggieri G. (2002) Evidence of a contact metamorphic aureole with high-temperature metasomatism in the deepest part of the active geothermal field of Larderello, Italy. Geothermics, 31, 443– 474.

Goldstein, R. H., and Reynolds, T. J. (1994). Systematics of fluid inclusions in diagenetic minerals: SEPM Short Course 31. Society for Sedimentary Geology, 199.

Grant, J. N., Halls, C., Avila, W., Avila G. (1977). Igneous geology and the evolution of hydrothermal systems in some sub-volcanic tin deposits of Bolivia. Geol. Soc. London Special Publ. 7, 117–126.

Harker, R. I., and Tuttle, O. F. (1956). Experimental data on the PCO2-T curve for the reaction; calcite-quartz<--> wollastonite-carbon dioxide. Am. J. Sci. 254, 239-256.

Hart, S. R., J-G. Schilling, and J. L. Powell. (1973). Basalts from Iceland and along the Reykjanes Ridge: Sr isotope geochemistry. Nature 246, 104-107.

Hedenquist J.W., Henley R.W. (1985).The importance of CO2 on freezing point measurements of fluid inclusions; evidence from active geothermal systems and implications for epithermal ore deposition. Econ. Geol. 80,1379-1406.

Hedenquist, J.W., Henley, R.W. (1985). The importance of CO2 on freezing point measurements of fluid inclusions: evidence from active geothermal systems and implication for epithermal ore deposition. Econ. Geol. 80, 1379–1406.

Knight, C. L., and Bodnar, R. J. (1989). Synthetic fluid inclusions: IX. Critical PVTX properties of NaCl-H 2 O solutions. Geochim. Cosmochim. Acta 53, 3-8.

Koděra, P., Murphy, P. J., Rankin, A. H. (2003). Retrograde mineral reactions in saline fluid inclusions: The transformation ferropyrosmalite↔ clinopyroxene. Am. Mineral. 88, 151-158.

Koděra, P., Rankin, A. H., Lexa, J. (1998). Evolution of fluids responsible for iron skarn mineralisation: An example from the Vyhne-Klokoc deposit, Western Carpathians, Slovakia. Mineral. Petrol. 64, 119-147.

Kotzer, T. G., Kyser, T. K., King, R. W., Kerrich, R. (1993). An empirical oxygen-and hydrogen-isotope geothermometer for quartz-tourmaline and tourmaline-water. Geochim. Cosmochim. Acta 57, 3421-3426.

Kristmannsdottir, H. (1979). Alteration of basaltic rocks by hydrothermal activity at 100-300°C. In Mortland and Farmer (eds.), International Clay Conference 1978, Elsevier, Amsterdam, pp. 359-367.

Lecumberri-Sanchez, P., Steele-MacInnis, M., Bodnar, R. J. (2012). A numerical model to estimate trapping conditions of fluid inclusions that homogenize by halite disappearance. Geochim. Cosmochim. Acta 92, 14-22.

Lecumberri-Sanchez, P., Steele-MacInnis, M., Bodnar, R. J. (2015). Synthetic fluid inclusions XIX. Experimental determination of the vapor-saturated liquidus of the system H_2O–NaCl–$FeCl_2$. Geochim. Cosmochim. Acta 148, 34-49.

Leisen, M., Dubessy, J., Boiron, M.-C., Lach, P. (2012). Improvement of the determination of element concentrations in quartz-hosted fluid inclusions by

LA-ICP-MS and Pitzer thermodynamic modeling of ice melting temperature. Geochim. Cosmochim. Acta 90, 110–125.

Li, C., and Naldrett, A. J. (1993). High chlorine alteration minerals and calcium-rich brines in fluid inclusions from the Strathcona deep copper zone, Sudbury, Ontario. Econ. Geol. 88, 1780-1796.

Longerich, H.P., Jackson S.E., Günther D. (1996). Laser ablation inductively coupled plasma mass spectrometric transient signal data acquisition and analyte concentration calculation. J. Anal. At. Spectrometry 11, 899-904.

Magro G., Ruggieri G., Gianelli G., Bellani S. and Scandiffio G. (2003) - Helium isotopes in paleofluids and present day fluids in the Larderello geothermal field: constraints on the heat source. J. Geophys. Res., 108, 1–12.

Maineri, C., Benvenuti. M., Costagliola, P., Dini, A., Lattanzi, P., Ruggieri, G. and Villa, I.M. (2003). Sericitic alteration at the La Crocetta deposits (Elba Island, Italy): interplay between magmatism, tectonic and hydrothermal activity. Mineral Deposita 38, 67-86.

Marini L., Manzella A. (2005) Possible seismic signature of the α–β quartz transition in the lithosphere of Southern Tuscany (Italy). J. Volcanol. Geotherm. Res., 148, 81–97.

Mazzarini, F., and Musumeci, G. (2008). Hydrofracturing-related sill and dyke emplacement at shallow crustal levels: the Eastern Elba Dyke Complex, Italy. Geol. Soc. London Special Publ. 302, 121-129.

Mazzarini, F., Musumeci, G., Cruden, A. R. (2011). Vein development during folding in the upper brittle crust: The case of tourmaline-rich veins of eastern Elba Island, northern Tyrrhenian Sea, Italy. J. Struct. Geol. 33, 1509-1522.

Mortensen, A.K. (2013). Stratigraphic, tectonic and temperature mapping through geological well logging: Icelandic experience. Short Course on Conceptual Modelling of Geothermal Systems. 24 February - 2 March 2013, Santa Tecla, El Salvador.

O'Neil, J. R., R. N. Clayton and T. K. Mayeda (1969). Oxygen isotope fractionation in divalent metal carbonates. J. Chem. Phys. 51, 5547-555.

Panichi C., Scandiffio G., Baccarin F. (1995) Variation of geochemical parameters induced by reinjection in the Larderello area. In: Proceedings of the Geothermal Congress 1995, 18–31 May, Florence, Italy (E. Barbier et al. eds.), 1845–1849.

Pope, E. C., Bird, D. K., & Arnórsson, S. (2014). Stable isotopes of hydrothermal minerals as tracers for geothermal fluids in Iceland. Geothermics 49, 99-110.

Puxeddu, M., Saupe´, F., Déchomets, R., Gianelli, G. and Moine, B. (1984). Geochemistry and stratigraphic correlations – application to the investigation of geothermal and mineral resources of Tuscany, Italy. Chem. Geol. 43, 77–113.

Roedder E. (1984). Fluid Inclusions. Reviews in Mineralogy. Vol. 12, pp. 644.

Roedder, E. (1984). Fluid Inclusions. Rev. Mineral., Vol. 12, pp. 644.

Ruggieri G., Cathelineau M., Boiron M.C., Marignac C. (1999) Boiling and fluid mixing in the chlorite zone of the Larderello geothermal field. Chem. Geol., 154, 237–256.

Sano, Y., Urabe, A., Wakita, H., Chiba, H., & Sakai, H. (1985). Chemical and isotopic compositions of gases in geothermal fluids in Iceland. Geochem. J. 19, 135-148.

Scandiffio G., Panichi C., M. Valenti (1995) Geochemical evolution of fluids in the Larderello geothermal field. In: Proceedings of the Geothermal Congress 1995, 18–31 May, Florence, Italy (E. Barbier et al. eds.), 1839–1843.

Shepherd, T. J., Rankin, A. H., & Alderton, D. H. M. (1985). A practical guide to fluid inclusion studies. Blackie, pp. 239.

Shepherd, T. J., Rankin, A. H., Alderton, D. H. M. (1985). A practical guide to fluid inclusion studies. Blackie, pp. 239.

Shimizu, M., Hyama, J.T. (1982), Zink-lead skarn deposits of the Nakatatsu mine, central Japan. Econ. Geol. 77, 1000-1012.

Shinohara, H., Iiyama, J. T., Matsuo, S. (1989). Partition of chlorine compounds between silicate melt and hydrothermal solutions: I. Partition of NaCl-KCl. Geochim. Cosmochim. Acta 53, 2617-2630.

Simmons S.F., Browne P.R.L. (1997) Saline fluid inclusions in sphalerite from the Broadlands Ohaaki geothermal system: a coincidental trapping of fluids being boiled toward dryness. Econ. Geol. 92, 485–489.

Steele-MacInnis, M., Lecumberri-Sanchez, P., & Bodnar, R. J. (2012). HokieFlincs_H2O-NaCl: A Microsoft Excel spreadsheet for interpreting microthermometric data from fluid inclusions based on the PVTX properties of H2O–NaCl. Computers & Geosciences 49, 334-337.

Steele-MacInnis, M., Lecumberri-Sanchez, P., Bodnar, R. J. (2012). HokieFlincs_H_2O-NaCl: A Microsoft Excel spreadsheet for interpreting microthermometric data from fluid inclusions based on the PVTX properties of H_2O–NaCl. Computers & Geosciences, 49, 334-337.

Steele-MacInnis, M., Lecumberri-Sanchez, P., Bodnar, R. J. (2015). Synthetic fluid inclusions XX. Critical PTX properties of H_2O –$FeCl_2$ fluids. Geochim. Cosmochim. Acta 148, 50-61.

Sveinbjornsdottir, A. E., Coleman, M. L., & Yardley, B. W. D. (1986). Origin and history of hydrothermal fluids of the Reykjanes and Krafla geothermal fields, Iceland. Contributions to Mineralogy and Petrology 94, 99-109.

Tanelli, G., Benvenuti, M., Costagliola, P., Dini, A., Lattanzi, P., Manieri, C., Mascaro, I., Ruggieri, G. (2001) The iron mineral deposits of Elba Island: state of the art, Ofioliti, 26, 239–48.

Tonarini S., Dini A., Pezzotta F. & Leemann W. (1998) – Boron isotopic composition of zoned (schorl-elbaite) tourmalines, Mt. Capanne Li-Cs pegmatites, Elba (Italy). European Journal of Mineralogy , 10, 941-951.

Valori, A., Cathelineau, M., Marignac, C., (1992) Early fluid migration in a deep part of the Larderello geothermal field: a fluid inclusion study of the granite sill from well Monteverdi. J. Volcanol. Geotherm. Res. 51, 115–131.

Zaw, K., Rodmanee, T., Khositanont, S., Thanasuthipitak, T., Ruamkid, S. (2007). Geology and genesis of Phu Thap Fah gold skarn deposit, northeastern Thailand: implications for reduced gold skarn formation and mineral exploration. In: Tantiwanit , W. (Ed.) Proceedings of International Conference on Geology of Thailand: Towards Sustainable Development and Sufficiency Economy (GEOTHAI'07). Bangkok (Thailand), November 2007, pp. 93-95.

Zheng, Y. F. (1991). Calculation of oxygen isotope fractionation in metal oxides. Geochim. Cosmochim. Acta 55, 2299-2307.

Zheng, Y. F. (1993). Calculation of oxygen isotope fractionation in anhydrous silicate minerals. Geochim. Cosmochim. Acta 57, 1079-1079.

ANNEX

Fig.1.1 – Location of the area (red square) where the Geitafell exhumed geothermal field is exposed.

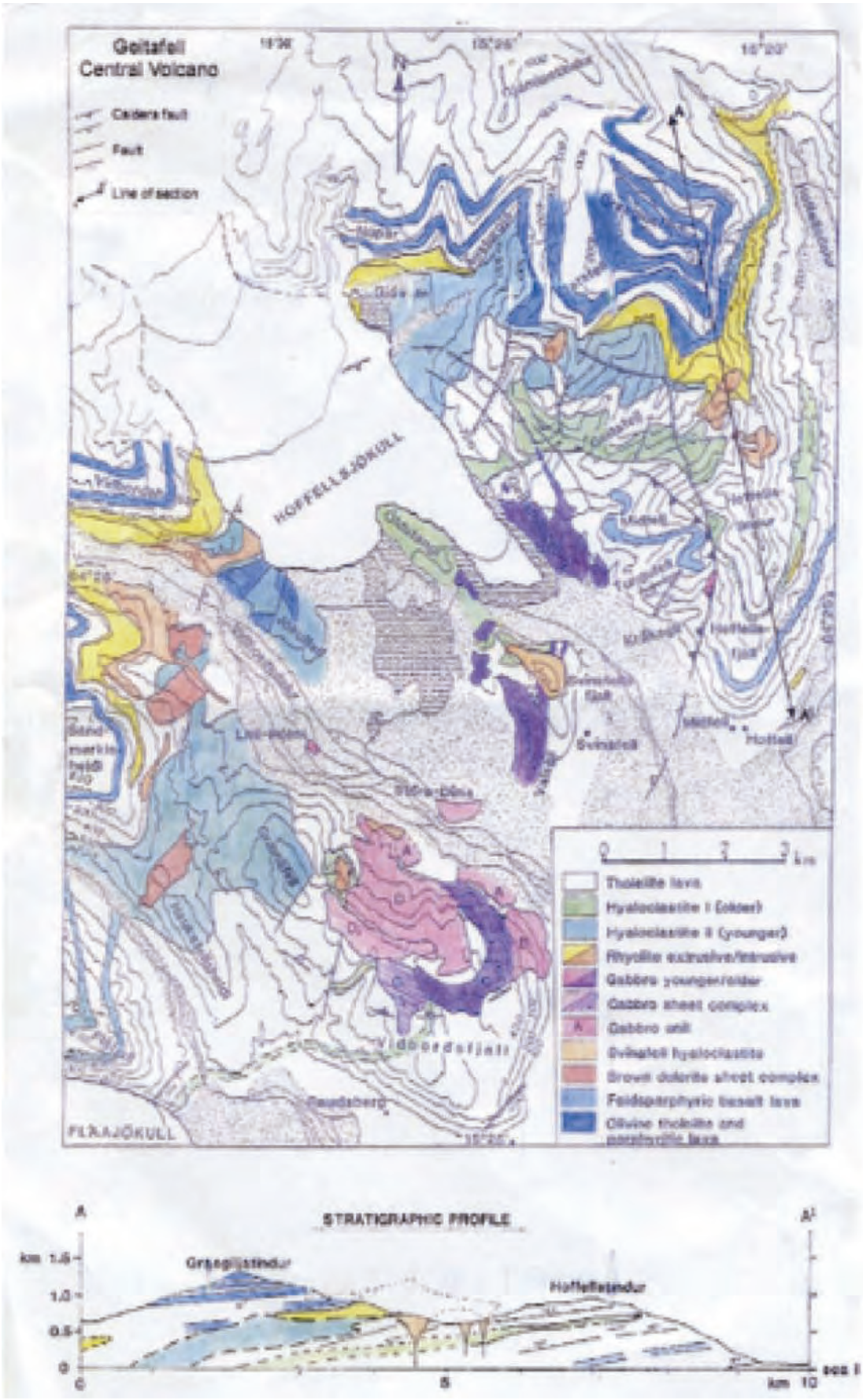

Fig. 1.1.1 – Geological map of the Geitafell area (from Freidleifsson, 1983). The area studied in detail is located in the easterna flank of the Hoffell glacier.

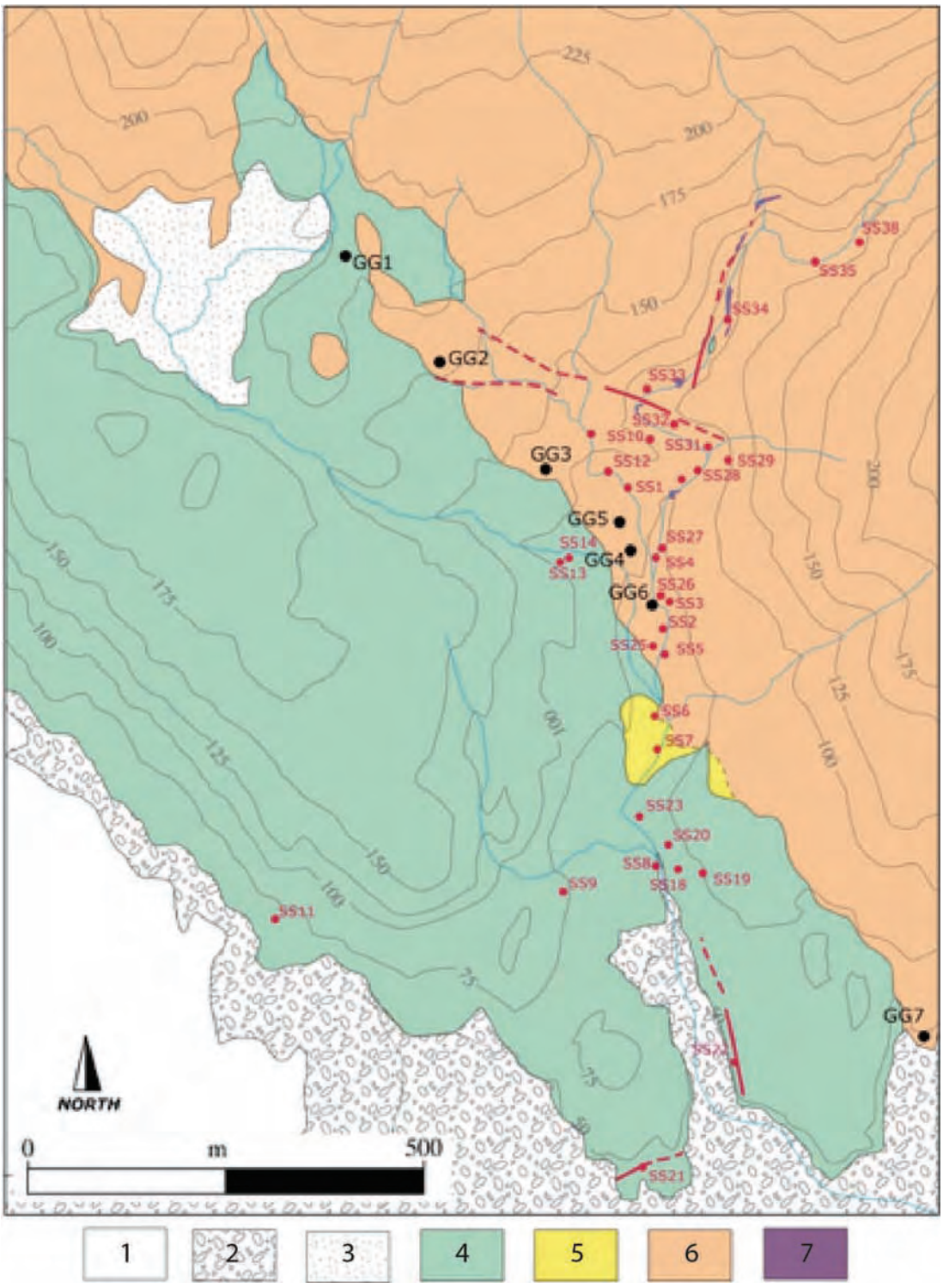

Fig.1.1.2 – geological map of the area under study with location of the boreholes (GG1-GG7) and structural stations (SSG1-SSG38). Symbols: 1 – Glacier; 2 – alluvial plane; 3 – detritum; 4 – Miocene-Pliocene gabbro; 5) horneblende-bearing host-rock; 6 – Miocene tholeitic lavas; 7 – epidote-bearing shear zone

Table 1.2.3 - list of the collected samples in Geitafell

GG-1	N 64°25'40.62" W 15°23'54.78"	190 m	14/05/2014	First drillhole along the Geitafell Gabbro contact aureole. Core depth 21.74 m. Samples from the drill are numbered in the following.		petrographic & fluid inclusions analysis
GG-1 16.16-16.22		-16.16 to -16.22		Brecciated sample taken at the contact between the porphyritic gabbro/dolerite and the host basalt. Infilling of secondary hydrothermal minerals of greenish colour.	No hydrothermal minerals are recognized by visual inspection	
GG-1 17.29-17.36		-17.28 to -17.36		Host rock: brecciated fine grained basalt; central nucleus with hydrothermal quartz and epidote.	Quartz, epidote	
GG-1 17.60-17.70		-17.60 to -17.70		Host rock: fine grained basalt; hydrothermal circulation with quartz/calcite (epidote?) forming a small vein and infilling cavities.	Quartz (calcite?), epidote?	
GG-1 21.33-21.43		-21.33 to -21.43		Host rock: brecciated fine grained basalt sampled very close to the contact with the gabbro. Strongly alterated. Hydrothermal vein withy epidote and quartz (calcite).	Epidote, quartz (calcite?)	
GG-2	N 64°25'36.66" W 15°23'46.62"	174 m	14/05/2014	Second drillhole along the Geitafell Gabbro contact aureole. Core depth 30.1 m. Samples from the drill are numbered in the following.		petrographic & fluid inclusions analysis
GG-2 3.41-3.48		-3.41 to - 3.48		Breccia/fault. White hydrothermal minerals (quartz/calcite?), mixed with epidote and chlorite.	quartz?, calcite?, epidote, chlorite?	
GG-2 3.66-3.76		-3.66 to -3.76		Host rock: basalt lava highly fractured and vesciculated. Hydrothermal veins and amigdales filled with quartz and green minerals (epidote?).	Quartz, epidote?	
GG-2 4.66-4.81		-4.66 to -4.81		Host rock: basalt lava; amigdales filled with hydrothermal epidote (chlorite?), quartz (calcite?) and black roundish minerals.	epidote, chlorite?, quartz, calcite?	
GG-2 6.77-6.86		-6.77 to -6.86		Host rock: basalt lava highly fractured and vesciculated. Veins and amigdales filled with quartz (calcite?) and epidote (chlorite?).		
GG-2 10.14-10.28		-10.14 to -10.28		Host rock: basalt lava. Amigdales filled with quartz (calcite?) and epidote.	quartz, calcite?, epidote	

GG-2 16.66-16.76		-16.66 to -16.76		Hydrothermal breccia filled up with hydrothermal minerals: quartz (calcite?) and epidote.	quartz, calcite?, epidote	
GG-2 19.07-19.17		-19.07 to -19.17		Host rock: basalt lava cut by a later basalt vein. Amigdales filled with black roundish minerals.		
GG-2 25.57-25.69		-25.57 to -25.69		Host rock: basalt lava. Well-developed hydrothermal quartz (calcite?) vein.	quartz, calcite?	
GG-2 26.91-26.99		-26.91 to -26.99		Felsite intrusion with hydrothermal veinlets.	epidote	
GG-2 28.46		-28.46		Quartz and possibly minor calcite crystals of hydrothermal origin.	quartz, calcite?	
GG-4	N 64°25'28.26" W 15°23'29.28"	93 m	19/05/2014	Fourth drillhole along the Geitafell Gabbro contact aureole. Core depth 17.83 m. Samples recovered at different depth are numbered in the following.		petrographic & fluid inclusions analysis
GG-4 6.60-6.73		-6.60 to -6.73		Granophiric intrusion; it shows similar macroscopic characteristics to the breccia-filling materials observed at surface and containing fluid inclusions in quartz.		
GG-5	N 64°25'29.34" W 15°23'29.70"	97 m	19/05/2014	Fifth drillhole along the Geitafell Gabbro contact aureole. Core depth 6.6 m. Samples recovered at different depth are numbered in the following.		petrographic & fluid inclusions analysis
GG-5 3.00-3.10		-3.0 to -3.10		Basalt dike. Small cavities and veins filled with epidote.	epidote	
GG-3.83-3.98		-3.83 to -3.98		Host rock: basalt lava. Small cavities filled with white minerals (quartz?).	quartz?, calcite?	
GG-6	N 64°25'25.92" W 15°23'26.76"	92 m	19/05/2014	Sixth drillhole along the Geitafell Gabbro contact aureole. Core depth 10.7 m. Samples recovered at different depth are numbered in the following.		petrographic & fluid inclusions analysis
GG-6 4.08-4.16		-4.08 to -4.16		Host rock: basalt lava: hydrothermal vein and cavities filled with black roundish minerals.	quartz, calcite?	
GG-6 6.16-6.26		-6.16 to -6.26		Host rock: basalt lava. Hydrothermal vein with quartz (calcite?) and alteration with green minerals.	quartz, calcite?, epidote?	

GG-7	N 64°25'7.74" W 15°23'2.82"	57 m	19/05/2014	Seventh drillhole along the Geitafell Gabbro contact aureole. Core depth 31.8 m. Samples recovered at different depth are numbered in the following.		petrographic & fluid inclusions analysis
GG-7 9.21-9.33		-9.21 to -9.33		Host rock: basalt lava. Amigdales filled with black roundish minerals.		
GG7 11.40-11.57		-11.40 to -11.57		Host rock: basalt lava.		
GG-7 13.00-13.10		-13.0 to -13.10		Host rock: basalt lava vesciculated. Hydrothermal vein and amigdales filled with quartz (and epidote?)	quartz, epidote?	
GG-7 23.93-24.04		-23.93 to -24.04		Host rock: basalt lava. Hydrothermal vein filled with quartz and epidote, and black roundish minerals.	quartz, epidote	
GG-7 29.23-29.39		-29.23 to -29.39		Host rock: basalt lava. Hydrothermal vein filled with quartz and epidote, and amigdales with black roundish minerals.	quartz, epidote	
GG-7 29.43-29.61		-29.43 to -29.61		Host rock: basalt lava. Hydrothermal vein with albite and quartz. Hydrothermal diffusion halo surrounding amigdales.	quartz, albite	
GE 100	N 64°24'51.81" W 15°23'58.45"		20/05/2014	Basalt lava with amigdales partially filled by zeolites	zeolite	Isotope analysis (Si
GE101	N 64°24'51.81" W 15°23'58.45"		20/05/2014	Basalt lava with amigdales partially filled by zeolites	zeolite	Isotope analysis (Si
DIJ	N 64°39'48.30" W 14°27'15.89"		20/05/2014	Basalt lava with amigdales partially filled by zeolites	zeolite	Isotope analysis (Si

GE 19 A,B,C,D	N 64°26' 0,9" W 15° 24' 8,1"		20/06/2014	Mineralized basalt		mineralogical & petrographic analysis
GE 20 A,B	N 64°25' 13,9" W 15° 24' 3,3"		24/06/2014	Gabbro and basalt		petrographic analysis
GE 20 C,D	N 64°25' 13,9" W 15° 24' 3,3"		24/06/2014	Mineralized shear veins		Mineralogical and petrographic analyses
GE 21 A,B	N 64°25' 13,9" W 15° 24' 3,3"		24/06/2014	Gabbro with mineralized veins		mineralogical & petrographic analysis
GE 21 C	N 64°25' 13,9" W 15° 24' 3,3"		24/06/2014	Basalt		petrographic analysis
GE 22 A,B,C,D,E	N 64°25' 23,5" W 15° 24' 12,6"		24/06/2014	Basalt with mineralized veins		mineralogical & petrographic analysis
GE 23 A,B	N 64°25' 28,1" W 15° 23' 34,6"		26/06/2014	Gabbro and basalt		petrographic analysis
GE 24 A,B,C,D	N 64°25' 27,9" W 15° 23' 35,6"		26/06/2014	Mineralized shear vein		mineralogical & petrographic analysis
GE 25 A,BI,BII	N 64°25' 31,8" W 15° 23' 30,8"		28/06/2014	Mineralized fault plane in basalt		mineralogical & petrographic analysis
GE 26	N 64°25' 31,6" W 15° 23' 22,4"		29/06/2014	Basalt and mineralized veins		mineralogical & petrographic analysis
GE 27	N 64°25' 31,8" W 15° 23' 30,8"		19/07/2014	Mineralized veins hosted in basalt		mineralogical & petrographic analysis
GE 28	N 64°25' 31,8" W 15° 23' 30,8"		19/07/2014	Mineralized veins hosted in basalt		mineralogical & petrographic analysis
GE 29	N 64°25' 31,8" W 15° 23' 30,8"		19/7/2014	Shear veins hosted in basalt		mineralogical & petrographic analysis
GE 30	N 64°25' 24,7" W 15° 23' 25,3"		19/7/2014	Tensional and shear veins hosted in mineralized basalt		mineralogical & petrographic analysis
GE 31	N 64°25' 24,7" W 15° 23' 25,3"		19/7/2014	Mineralized porphyric basalt		mineralogical & petrographic analysis
GE 32	N 64°25' 24,7" W 15° 23' 25,3"		19/7/2014	Porphyric basalt		mineralogical & petrographic analysis
GE 33	N 64°25' 24,7" W 15° 23' 25,3"		19/7/2014	Mineralized porphyric basalt		mineralogical & petrographic analysis
GE 34	N 64°25' 24,7" W 15° 23' 25,3"		19/7/2014	Tensional vein hosted in mineralized basalt		mineralogical & petrographic analysis
GE 35	N 64°25' 24,7" W 15° 23' 25,3"		19/7/2014	Mineralized basalt		mineralogical & petrographic analysis
GE 35 B	N 64°25' 24,7" W 15° 23' 25,3"		19/7/2014	Mineralized basalt		mineralogical & petrographic analysis

GE 55	N 64°24' 38,4" W 15° 21' 55,8"		21/7/2014	Mineralized veins		mineralogical & petrographic analysis
GE 56	N 64°25' 15,2" W 15° 23' 25,6"		21/8/2014	Gabbro with mineralized veins		mineralogical & petrographic analysis
GE 57	N 64°25' 15,2" W 15° 23' 25,6"		21/8/2014	Gabbro with slikenside		mineralogical & petrographic analysis
GE 58	N 64°25' 15,2" W 15° 23' 25,6"		21/8/2014	Gabbro		mineralogical & petrographic analysis
GE 59	N 64°25' 15,2" W 15° 23' 25,6"		21/8/2014	Basaltic sheet		mineralogical & petrographic analysis
GE 60	N 64°25' 07,2" W 15° 23' 21,4"		22/8/2014	Basaltic sheet with slikenside		mineralogical & petrographic analysis
GE 61	N 64°25' 16,2" W 15° 23' 26,4"		22/8/2014	Gabbro with mineralized veins		mineralogical & petrographic analysis
GE 62	N 64°24' 38,4" W 15° 21' 55,8"		22/8/2014	Mineralized veins		mineralogical & petrographic analysis
GE 63	N 64°25' 17,4" W 15° 23' 29,1"		23/8/2014	Porphyritic basalt		mineralogical & petrographic analysis
GE 64	N 64°25' 19" W 15° 23' 27,6"		23/8/2014	Basaltic sheet		mineralogical & petrographic analysis
GE 65	N 64°25' 31,8" W 15° 23' 19,4"		23/8/2014	Basalt		mineralogical & petrographic analysis
GE 66	N 64°25' 32,4" W 15° 23' 21,1"		25/8/2014	Altered basalt with mineralized veins		mineralogical & petrographic analysis
GE 67A,B,C	N 64°25' 32,4" W 15° 23' 21,1"		25/8/2014	Porphyritic basalt		mineralogical & petrographic analysis
GE 68	N 64°25' 33,5" W 15° 23' 27,1"		25/8/2014	Altered basalt		mineralogical & petrographic analysis
GE 69	N 64°25' 33,5" W 15° 23' 27,1"		25/8/2014	Basalt		mineralogical & petrographic analysis
GE 70	N 64°25' 32,8" W 15° 23' 26,6"		26/8/2014	Altered Basalt		mineralogical & petrographic analysis
GE 71	N 64°25' 34,9" W 15° 23' 26,6"		26/8/2014	Porphyritic basalt		mineralogical & petrographic analysis
GE 72	N 64°25' 34,9" W 15° 23' 26,6"		26/8/2014	Basalt		mineralogical & petrographic analysis
GE 73	N 64°25' 34,9" W 15° 23' 26,6"		26/8/2014	Altered Basalt		mineralogical & petrographic analysis
GE 74	N 64°25' 37,5" W 15° 23' 18,9"		26/8/2014	Basalt breccia (cataclasite) with mineralization		mineralogical & petrographic analysis

GE 36	N 64°25' 24,7" W 15° 23' 25,3"		19/7/2014	Shear calcite vein		mineralogical & petrographic analysis
GE 37			20/7/2014	Samples collected in alluvial sediments		mineralogical & petrographic analysis
GE 38	N 64°25' 15,4" W 15° 23' 27,6"		20/7/2014	Mineralized tensional and shear veins		mineralogical & petrographic analysis
GE 39	N 64°25' 15,4" W 15° 23' 27,6"		20/7/2014	Mineralized tensional and shear veins		mineralogical & petrographic analysis
GE 40	N 64°25' 15,4" W 15° 23' 27,6"		20/7/2014	Gabbro		petrographic analysis
GE 41	N 64°25' 33,9" W 15° 23' 32,2"		20/7/2014	Mineralized veins		mineralogical & petrographic analysis
GE 41	N 64°25' 33,9" W 15° 23' 32,2"		20/7/2014	Mineralized veins		mineralogical & petrographic analysis
GE 42	N 64°25' 31,8" W 15° 23' 30,8"		20/7/2014	Mineralized porphyric basalts		mineralogical & petrographic analysis
GE 43	N 64°25' 31,8" W 15° 23' 30,8"		20/7/2014	Mineralized fault breccia		mineralogical & petrographic analysis
GE 44	N 64°25' 31,8" W 15° 23' 30,8"		20/7/2014	Porphyric basalt		petrographic analysis
GE 45	N 64°25' 13,9" W 15° 24' 3,3"		20/7/2014	Mineralized veins		mineralogical & petrographic analysis
GE 46	N 64°25' 28,1" W 15° 23' 34,6"		21/7/2014	Gabbro and basalt		petrographic analysis
GE 47	N 64°25' 27,9" W 15° 23' 35,6"		21/7/2014	Mineralized shear vein		mineralogical & petrographic analysis
GE 48	N 64°25' 58,4" W 15° 24' 6,1"		21/7/2014	Mineralized basalt		mineralogical & petrographic analysis
GE 49	N 64°26' 0,9" W 15° 24' 8,1"		21/7/2014	Mineralized basalt		mineralogical & petrographic analysis
GE 50	N 64°26' 0,9" W 15° 24' 8,1"		21/7/2014	Vacuolar basalt		petrographic analysis
GE 51	N 64°24' 38,4" W 15° 21' 55,8"		21/7/2014	Mineralized basalt		mineralogical & petrographic analysis
GE 52	N 64°24' 38,4" W 15° 21' 55,8"		21/7/2014	Vacuolar basalt		petrographic analysis
GE 53	N 64°24' 38,4" W 15° 21' 55,8"		21/7/2014	Mineralized basalt		mineralogical & petrographic analysis
GE 54	N 64°24' 38,4" W 15° 21' 55,8"		21/7/2014	Mineralized basalt		mineralogical & petrographic analysis

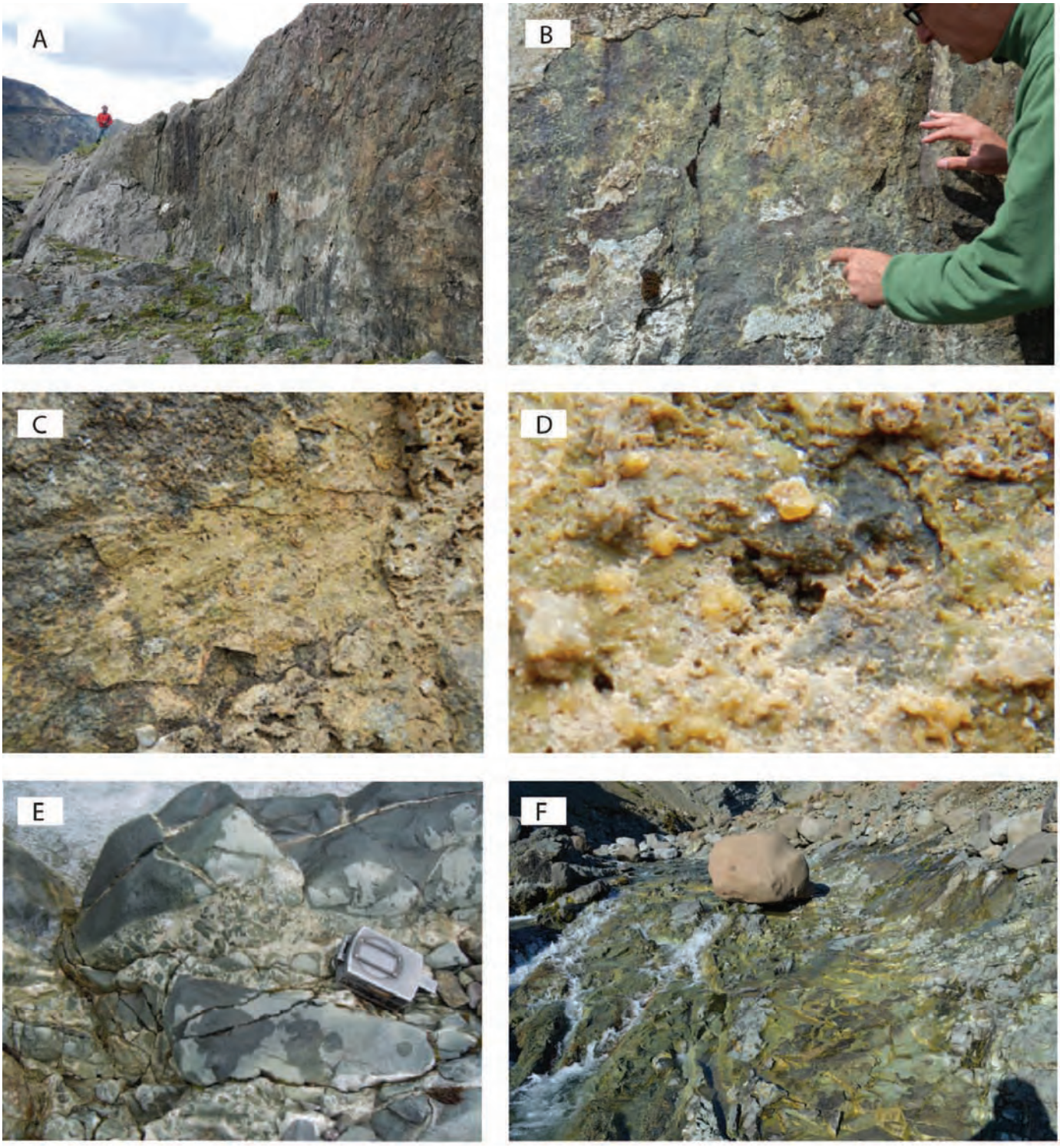

Fig. 1.2.1 – (A) SW-NE trending fault in gabbro. (B) epidote and andradite shear vein on the fault-slip surface of (A); (C) and (D) details from (B); (E) – cataclasite with calcite; (F) cataclasite with epidote.

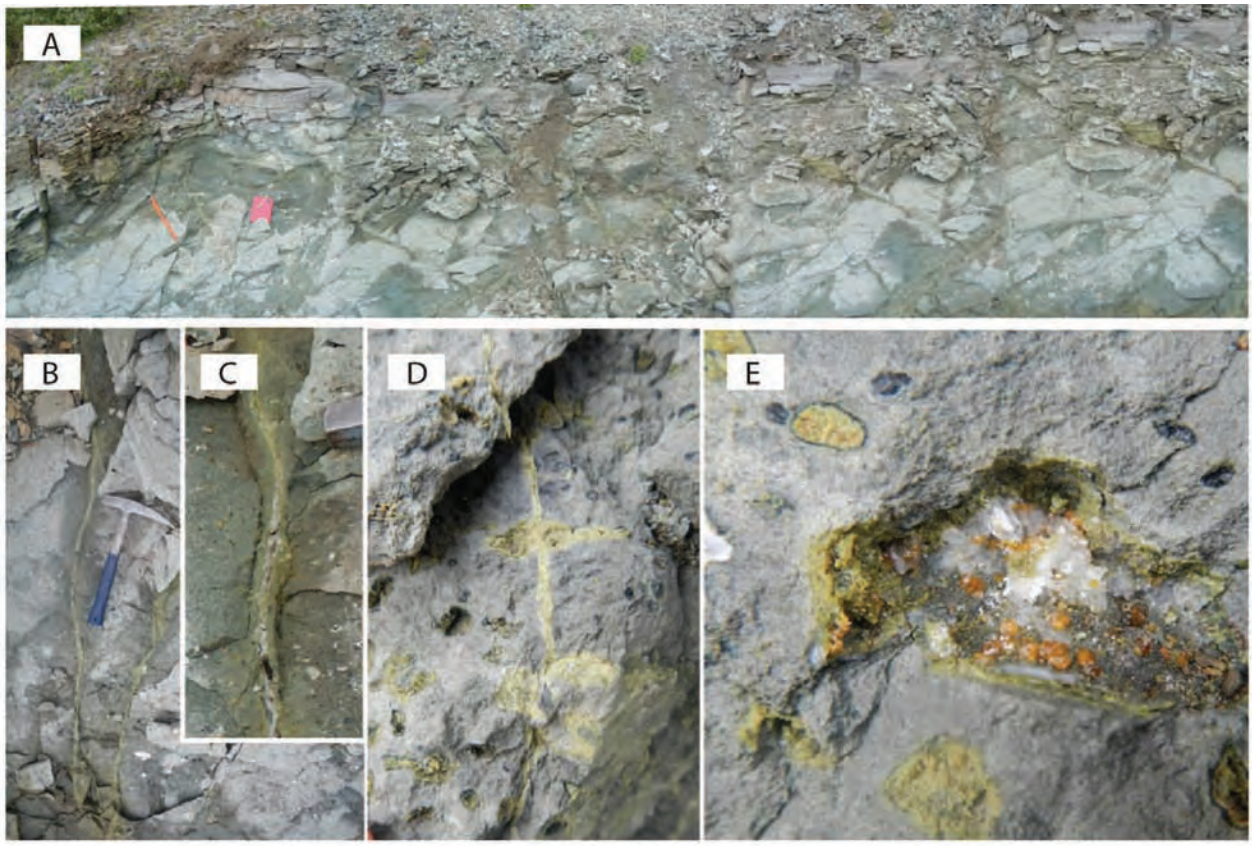

Fig.1.2.2. – (A) porous tholeitic mineralized lava level; (B) and (C) epidote bearing fractures (D) fractures connecting vesicles with hydrothermal mineralization; (E) detail of a vesicle.

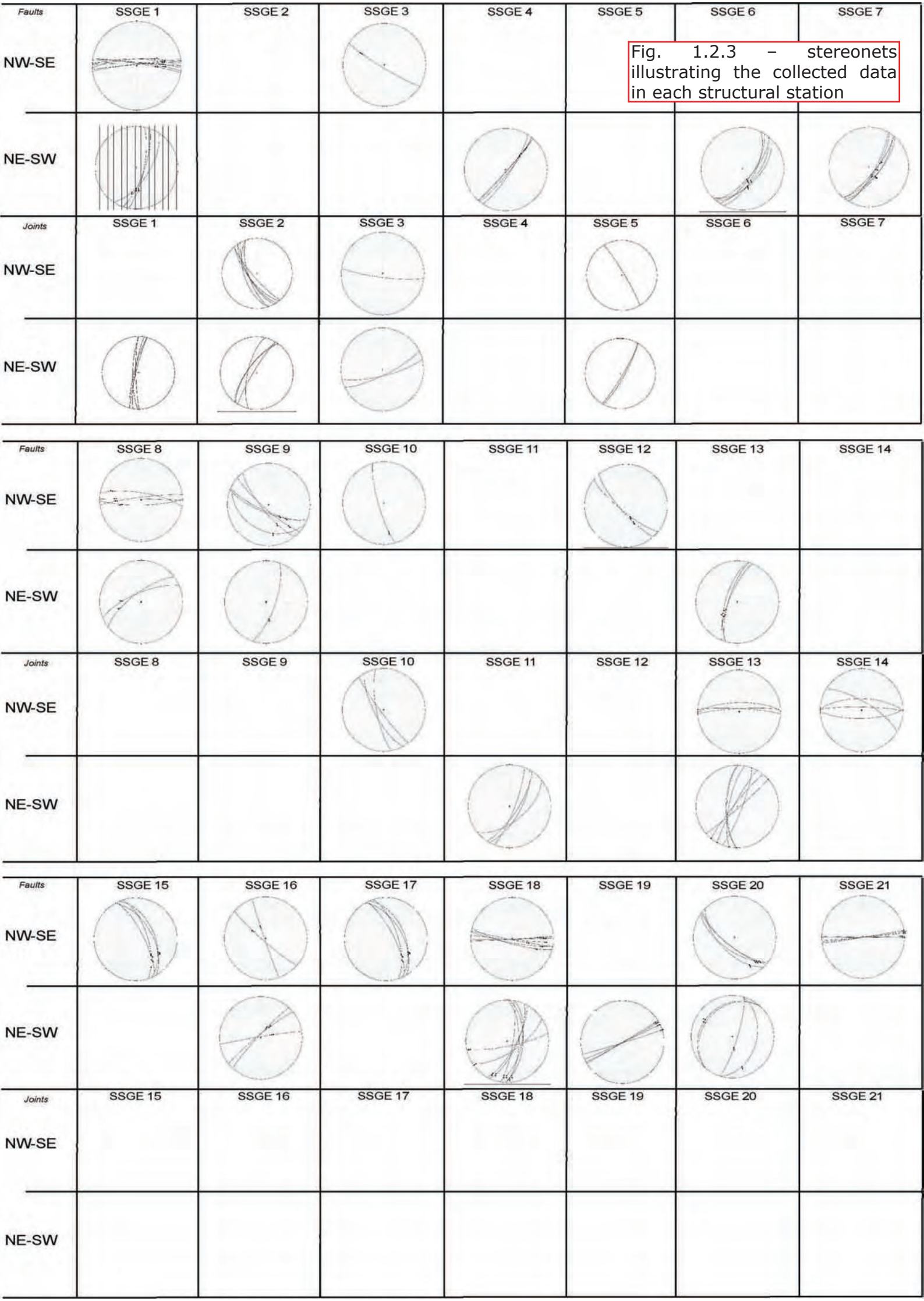

Fig. 1.2.3 – stereonets illustrating the collected data in each structural station

Faults	SSGE 1	SSGE 2	SSGE 3	SSGE 4	SSGE 5	SSGE 6	SSGE 7
NW-SE							
NE-SW							
Joints	SSGE 1	SSGE 2	SSGE 3	SSGE 4	SSGE 5	SSGE 6	SSGE 7
NW-SE							
NE-SW							

Faults	SSGE 8	SSGE 9	SSGE 10	SSGE 11	SSGE 12	SSGE 13	SSGE 14
NW-SE							
NE-SW							
Joints	SSGE 8	SSGE 9	SSGE 10	SSGE 11	SSGE 12	SSGE 13	SSGE 14
NW-SE							
NE-SW							

Faults	SSGE 15	SSGE 16	SSGE 17	SSGE 18	SSGE 19	SSGE 20	SSGE 21
NW-SE							
NE-SW							
Joints	SSGE 15	SSGE 16	SSGE 17	SSGE 18	SSGE 19	SSGE 20	SSGE 21
NW-SE							
NE-SW							

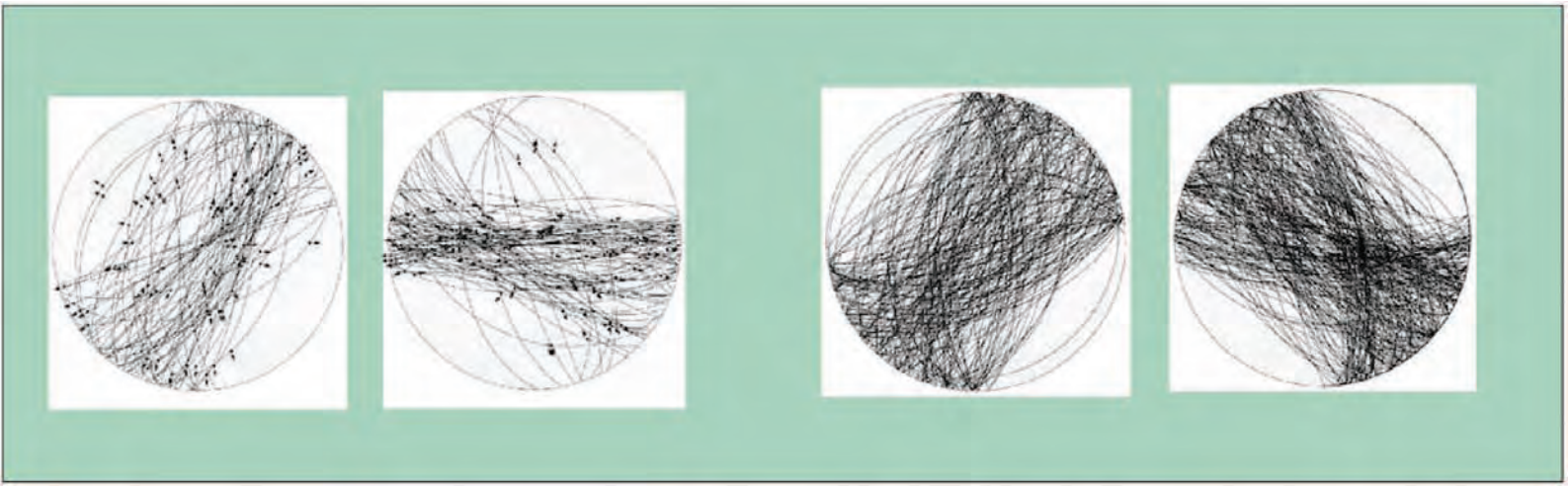

Fig. 1.2.4 – four stereonets (lower emisphere) indicating the distribution of faults (the first two from the right) and fracture attitudes in the Geitafell area.

Fig. 1.3.1 – (A) the small drill rig at site GG-2; B) the first core from GG-1.

Well	ID number	Depth (m)	Coordinates	m a. s. l.	Water table (m)	3.5" casing (m)
GG-1	72771	2.174	N64 25.677 W15 23.913	190	0	282
GG-2	72772	301	N64 25.611 W15 23.777	174	2	30
GG-3	72773	1.583	N64 25.527 W15 23.608	124	2	~2.8
GG-4	72774	1.783	N64 25.471 W15 23.488	93	5	30
GG-5	72775	66	N64 25.489 W15 23.495	97	not measured	30
GG-6	72776	107	N64 25.432 W15 23.446	92	not measured	40
GG-7	72777	318	N64 25.129 W15 23.047	57	5	465

Table 1.3.1 - Information on drillholes at the Geitafell gabbro contact aureole

Core	Section	Top depth	Bottom depth	Drilled length	Core recovery (m)	Core recovery (%)
GG-1	1	2.82	5.19	0.57	0.25	67.6
GG-1	2	3.19	6.32	3.13	3.00	98.4
GG-1	3	6.32	9.34	3.02	3.02	100.0
GG-1	4	9.34	12.37	3.03	3	99.0
GG-1	5	12.37	15.35	2.98	3.08	103.4
GG-1	6	15.35	18.44	3.09	2.83	91.6
GG-1	7	18.44	21.42	2.98	3.04	102.7
GG-2	1	3.21	6.41	3.2	2.66	83.1
GG-2	2	6.41	7.14	0.73	0.99	135.5
GG-2	3	7.14	9.74	2.6	2.58	99.2
GG-2	4	9.74	12.74	3	2.98	99.3
GG-2	5	12.74	15.65	2.91	2.92	100.3
GG-2	6	15.65	16.85	1.2	1.15	95.8
GG-2	7	16.85	18.75	1.9	1.93	101.1
GG-2	8	18.75	21.74	2.99	2.68	89.6
GG-2	9	21.74	24.54	2.8	2.87	102.5
GG-2	10	24.54	27.03	2.49	2.62	105.6
GG-2	11	27.03	30.1	3.08	3.06	99.4
GG-3	1	2.97	5.68	0.71	0.61	85.9
GG-3	2	3.68	5.01	1.33	1.34	100.8
GG-3	3	5.01	6.58	1.57	1.56	99.4
GG-3	4	6.58	9.68	3.1	3.07	99.0
GG-3	5	9.68	10.5	0.82	0.86	104.9
GG-3	6	10.5	12.75	2.25	2.25	100.0
GG-3	7	12.75	14.12	1.37	1.46	106.6
GG-3	8	14.12	15.83	1.71	1.29	75.7
GG-4	1	3.08	3.6	0.52	0.45	86.5
GG-4	2	3.6	6.3	2.7	2.75	101.9
GG-4	3	6.3	8.58	2.28	2.5	109.6
GG-4	4	8.58	9.6	1.02	0.86	84.3
GG-4	5	9.6	11.98	2.38	2.45	102.1
GG-4	6	11.98	15.07	3.09	3.04	98.4
GG-4	7	15.07	17.87	2.8	2.2	78.6
GG-5	1	1	3.45	0.45	0.45	100.0
GG-5	2	3.45	3.83	0.38	0.26	68.4
GG-5	3	3.83	5.29	1.46	1.16	79.5
GG-5	4	3.29	6.6	1.31	1.31	100.0
GG-6	1	4.03	4.64	0.61	0.57	93.4
GG-6	2	4.64	5.37	0.73	0.43	58.9
GG-6	3	5.37	6.06	0.69	0.1	14.5
GG-6	4	6.06	6.76	0.7	0.7	100.0
GG-6	5	6.76	8.9	2.14	2.08	97.2
GG-6	6	8.9	10.08	1.18	0.97	82.2
GG-6	7	10.08	10.66	0.58	0.24	41.4
GG-6	8	10.86	10.96	0.28	0.105	37.5
GG-7	1	4.8	5.12	0.32	0.20	62.0
GG-7	2	5.12	6.54	1.42	1.42	100.0
GG-7	3	6.54	9.56	3.02	3.08	102.3
GG-7	4	9.56	11.2	1.64	1.30	79.0
GG-7	5	11.2	12.68	1.48	1.40	94.6
GG-7	6	12.68	13.63	0.95	1.07	112.6
GG-7	7	13.63	15.68	2.05	2.01	98.0
GG-7	8	15.68	17.07	1.39	1.39	100.0
GG-7	9	17.07	18.68	1.61	1.71	106.2
GG-7	10	18.68	20.37	1.69	1.67	99.0
GG-7	11	20.37	20.67	0.3	0.30	100.0
GG-7	12	20.67	21.68	1.01	1.01	100.0
GG-7	13	21.68	22.01	0.33	0.33	100.0
GG-7	14	22.01	24.6	2.59	2.55	98.5
GG-7	15	24.6	26.19	1.59	1.52	95.6
GG-7	16	26.19	26.88	0.69	0.79	114.5
GG-7	17	28.88	27.65	0.77	0.77	100.0
GG-7	18	27.65	28.49	0.84	0.51	61.0
GG-7	19	28.49	28.6	0.11	0.11	100.0
GG-7	20	28.6	29.12	0.52	0.36	70.0
GG-7	21	29.12	30.24	1.12	1.06	95.0
GG-7	22	30.24	31.8	1.56	1.42	91.0

Table 1.3.2 - Core recovery in the Geitafell drillholes

Well	Temperature (°C)					
	5 m	10 m	15 m	20 m	25 m	30 m
GG-1	4,2	4,9	5,1	5,2		
GG-2	4,5	5,2	5,6	5,9	6,1	6,2
GG-3	3,6	4,9	5,4			
GG-4	4,7	5,6	6,1			
GG-7	4,7	5	5,4	5,7	6,1	6,4

Table 1.3.3. - Temperature measurements in the Geitafell wells

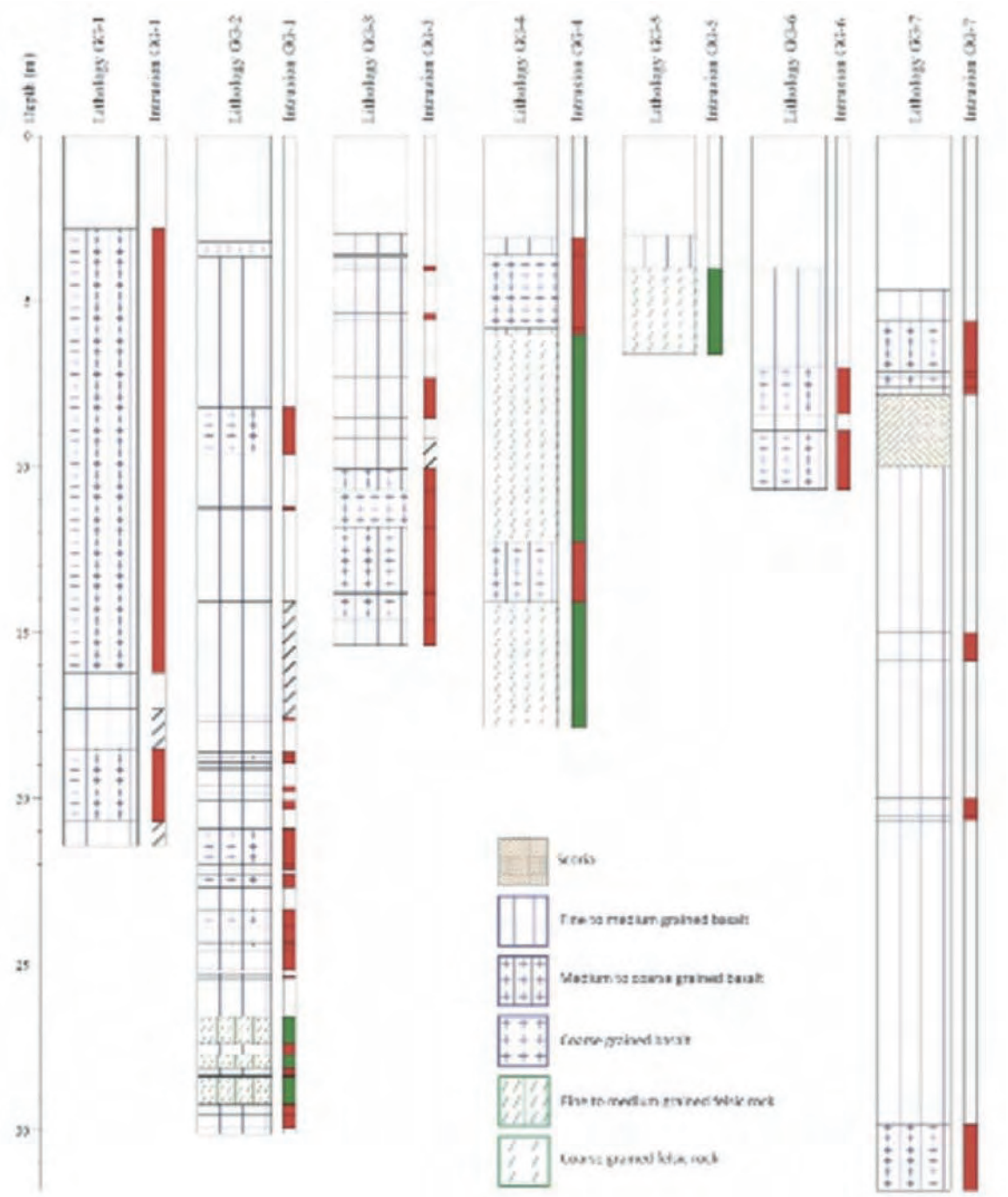

Fig. 1.3.2 – Logging of the lithology of cores from GG-1 to GG-7. The uppermost part of the lithology column shows the depth of casing in each well (white part). Intrusion column shows the location of intrusions, red being mafic and green felsic.

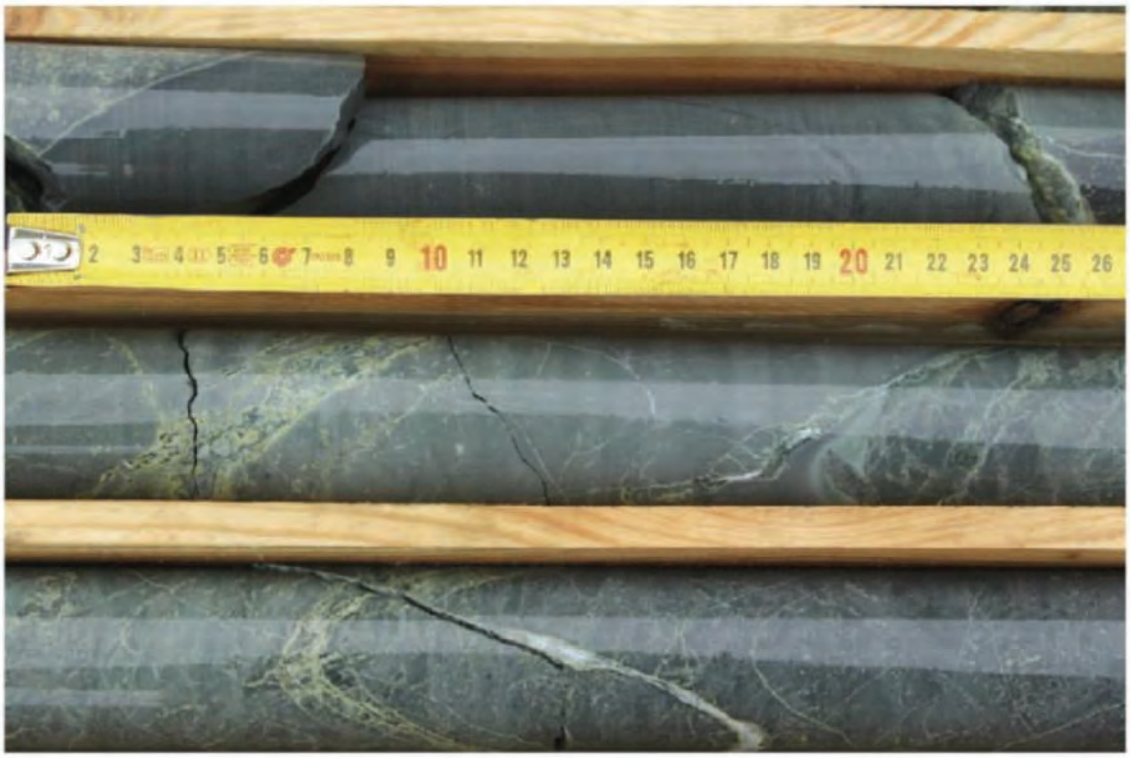

Fig. 1.3.3. – Fracture fillings in host rock from GG-2, between 26 and 28 m.

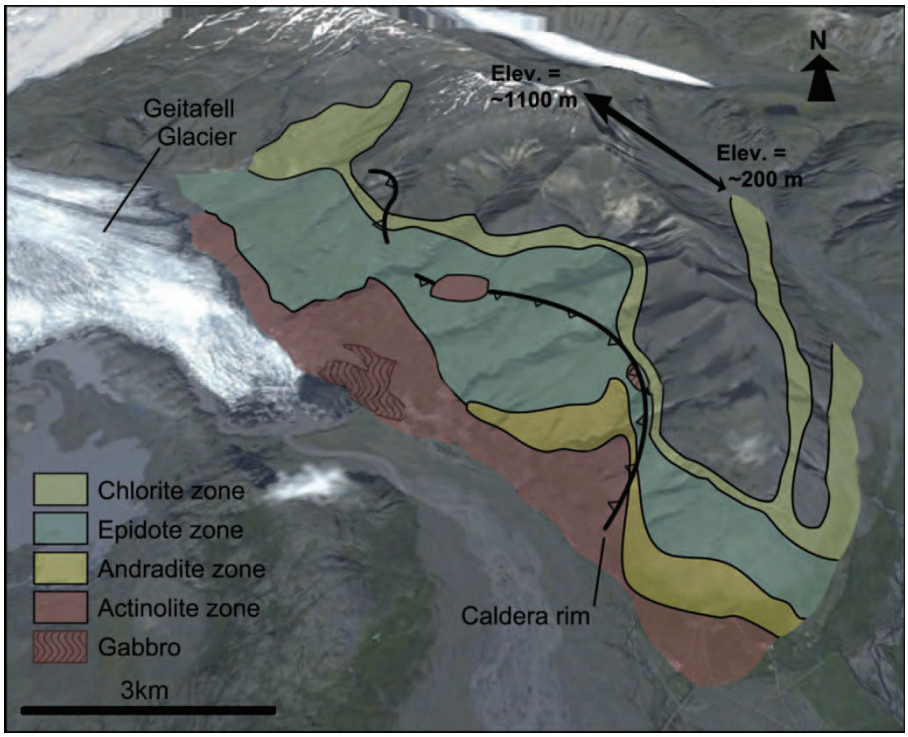

Fig. 1.4.1 - Overlaid on a digital elevation map (courtesy of Google Earth) is the range of occurrence for the index minerals chlorite, epidote, andradite garnet and actinolite (after Fridleifsson 1983b).

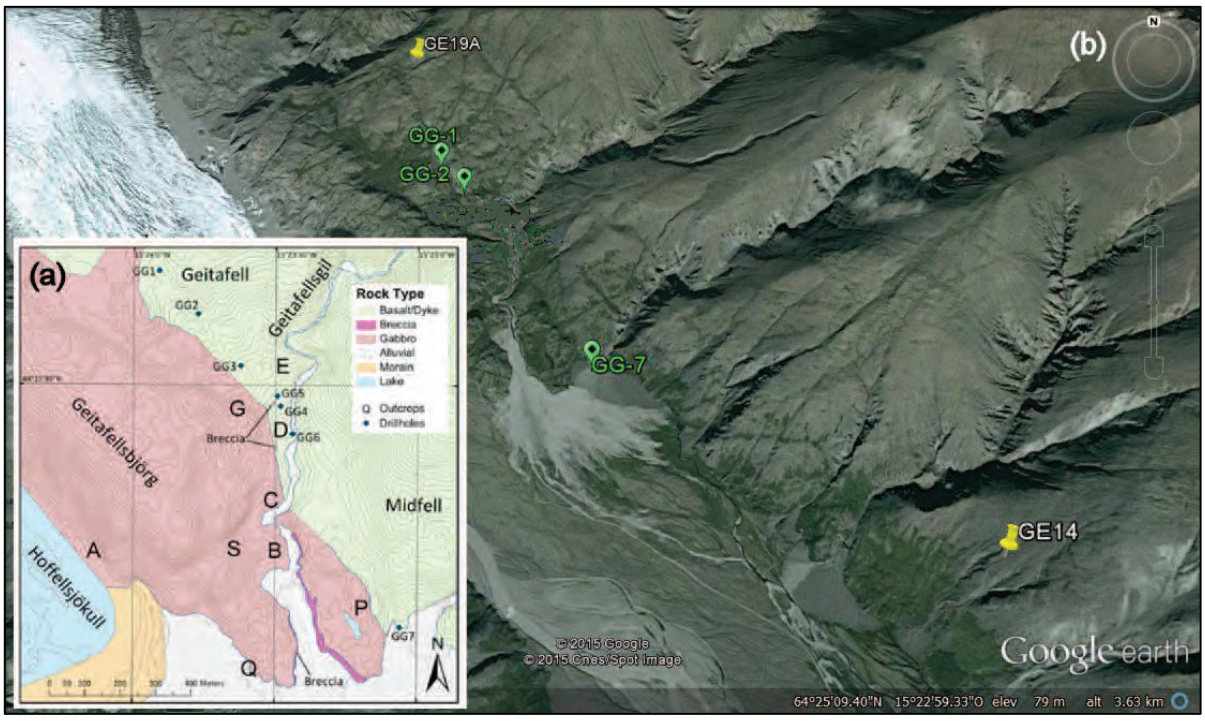

Fig. 1.4.2. a) localization of the boreholes drilled in May 2014 in the Geitafell contact metamorphic aureole (modified after Baumann, 2014); b) localization of the selected samples analyzed for petrography and fluid inclusions.

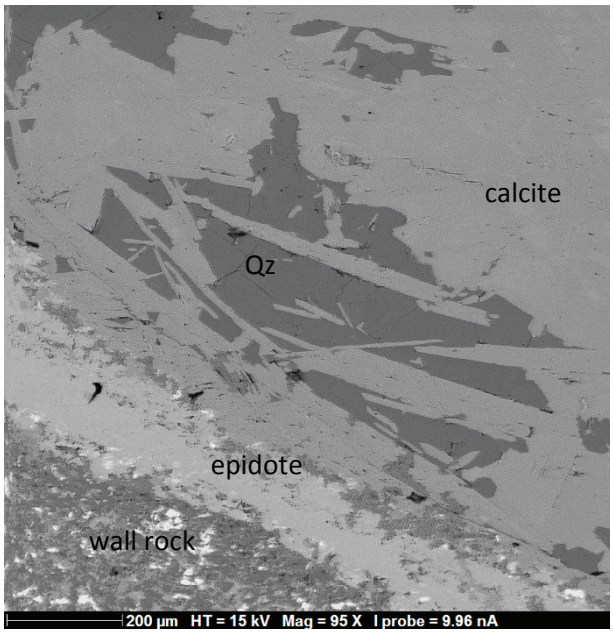

Fig. 1.4.3. Sample GG7 13.00-13.10: hydrothermal vein filled by epidote, quartz (Qz) and platy calcite (electron backscattered image).

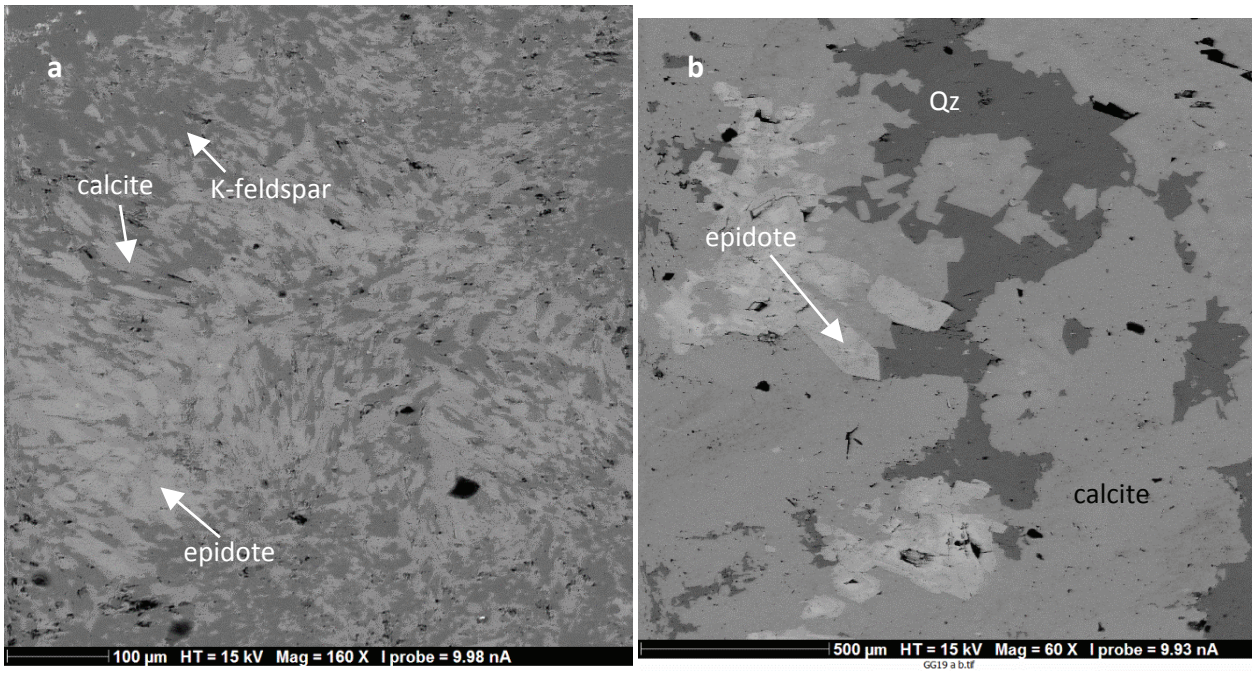

Fig. 1.4.4. (a) Sample GG7 13.00-13.10: masses in the amygdale filled by epidote (light grey) calcite (medium gray) and k-feldspar (dark grey) (EBS image); (b) Sample GG19 A: zoned epidote among quartz and calcite.

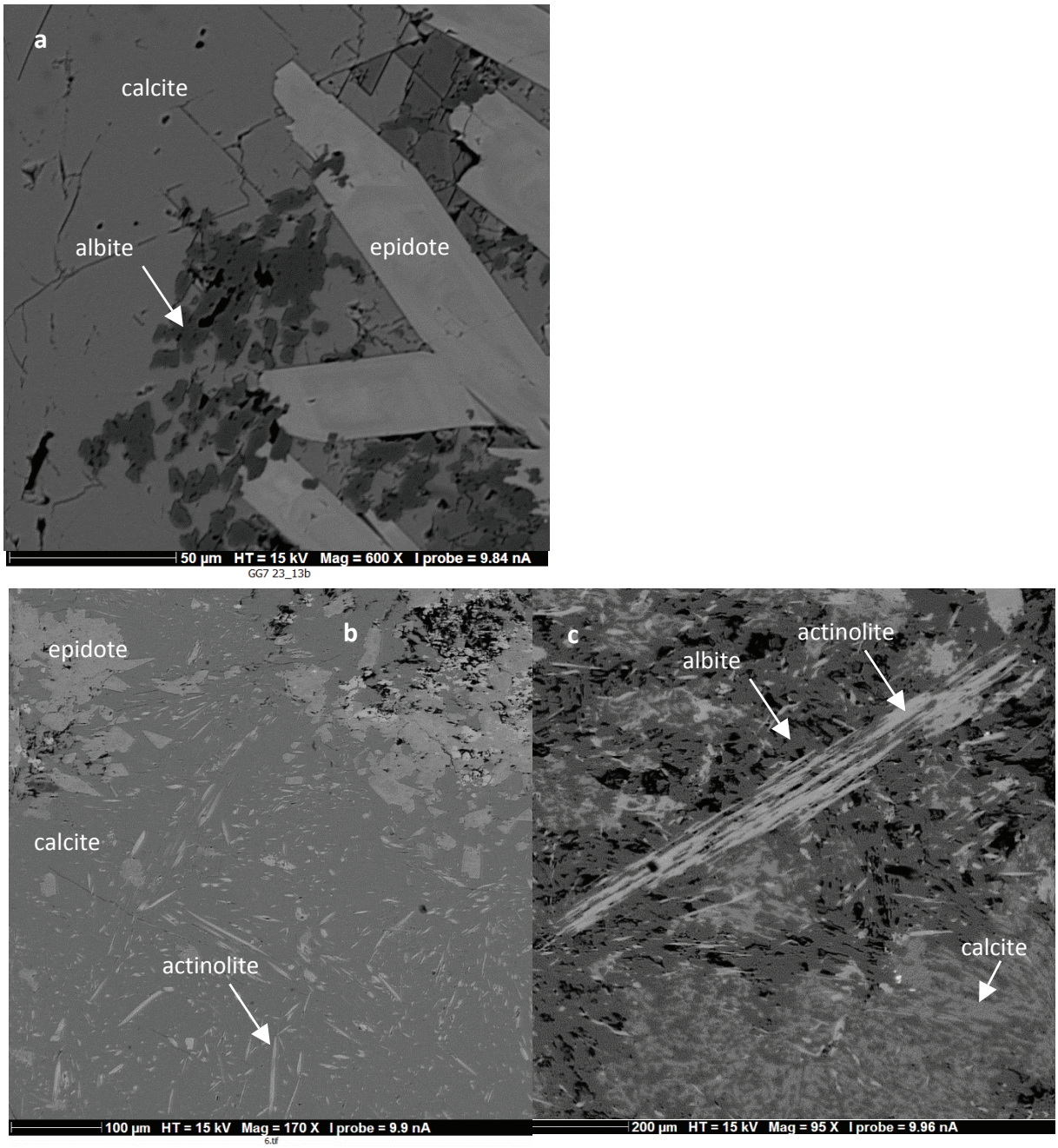

Fig. 1.4.5. (a) Sample GG1 17.29 with zoned epidote and albite relicts in calcite (EBS image); (b) Sample GG1 21.33-21.43: central portion of amygdale filled by calcite and actinolite crystals (EBS image); (b) Sample GG1 17.29-17.38: actinolite crystals among albite and calcite (EBS image).

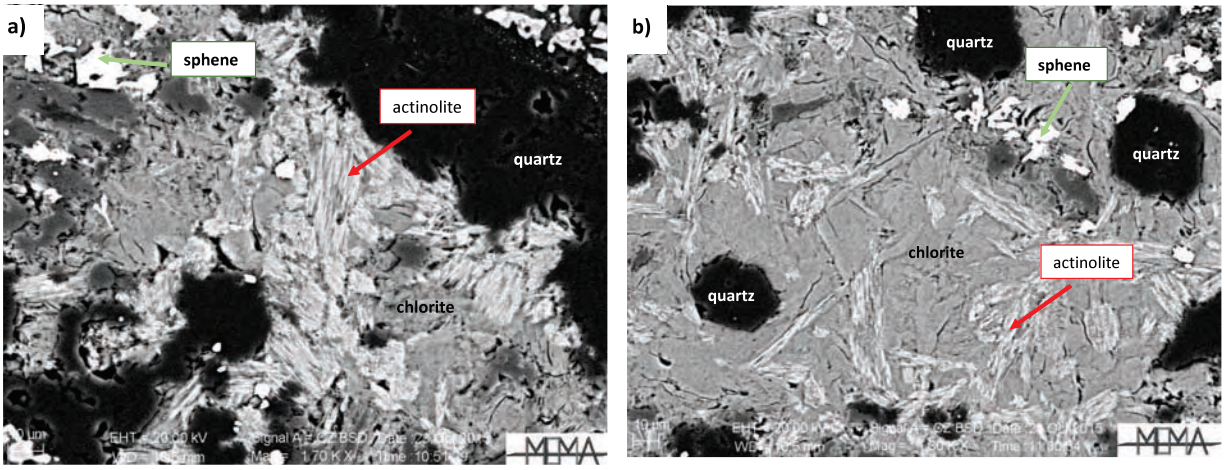

Fig. 1.4.6. (a and b) Image of sample GG7 characterized by abundant actinolite (partially replaced by chlorite) in association with quartz and sphene crystals (backscattered electron image).

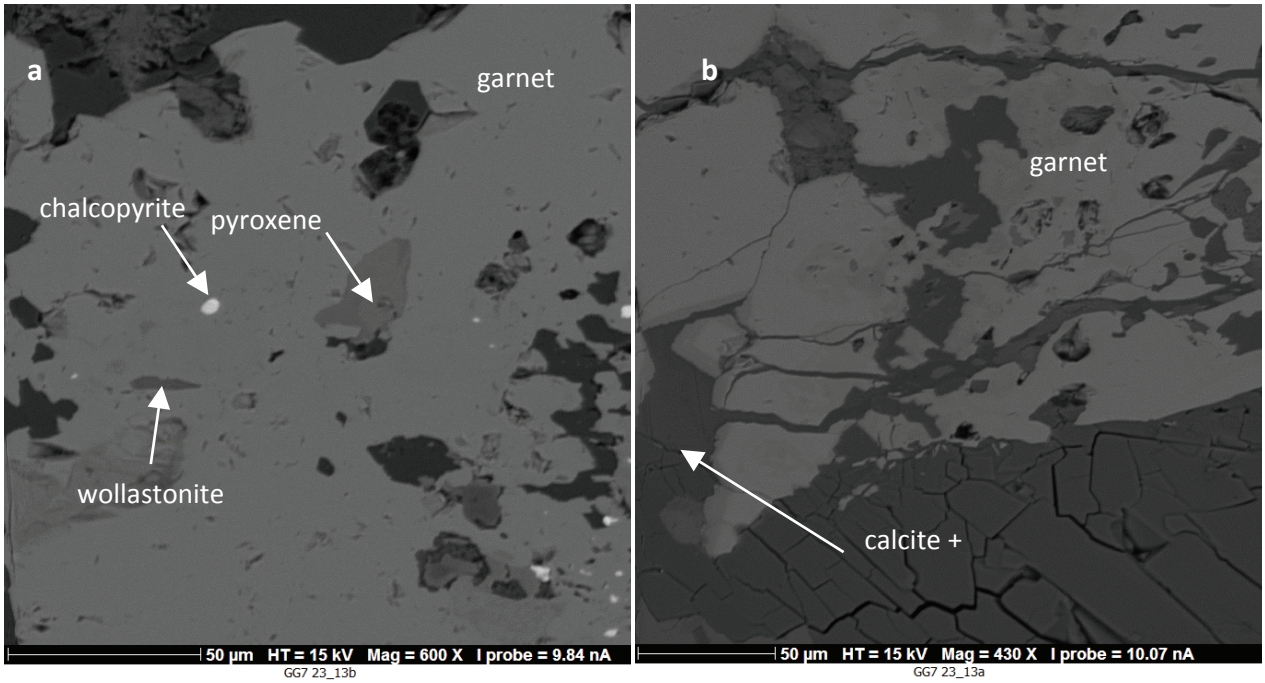

Fig. 1.4.7. (a) Sample GG7 23.93-24.04: Garnet with wollastonite, pyroxene and chalcopyrite inclusions (EBS image); (b) Sample GG7 23.93-24.04: calcite plus zeolite veins cutting garnets (EBS image).

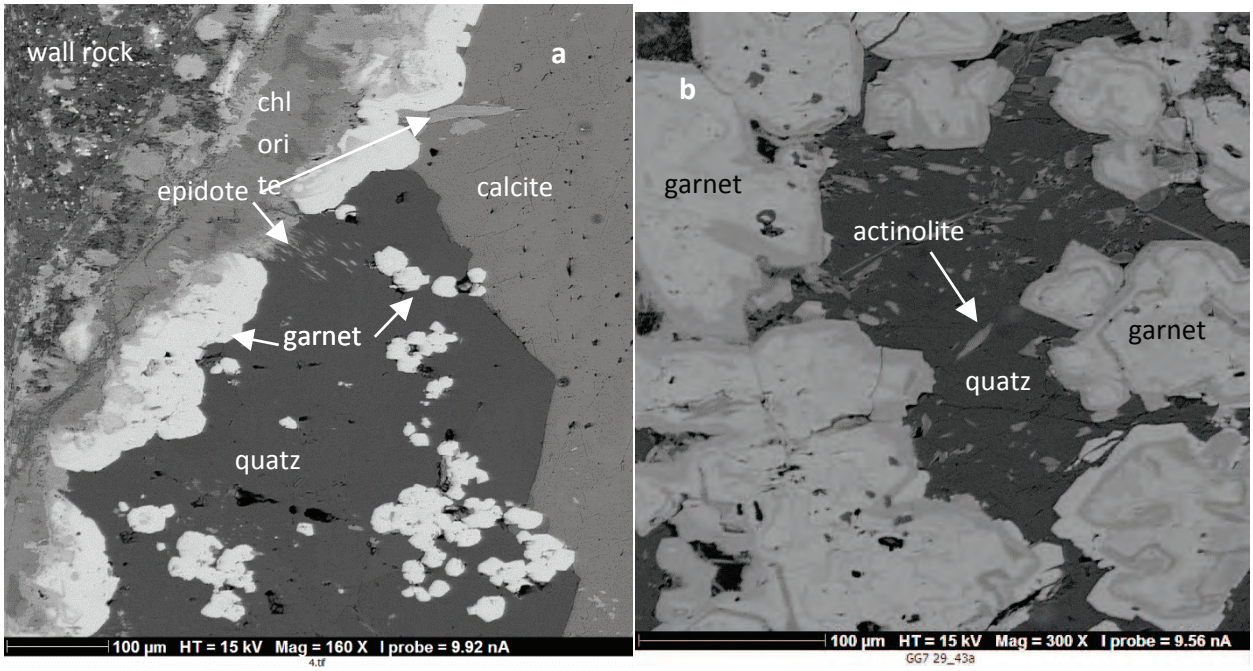

Fig 1.4.8. (a) Samples GG7 29.23-29.39: caltite and quartz veins with garnets (EBS image); (b) Sample GG7 29.43-29.61: zoned garnets in central parts of amygdale (EBS image).

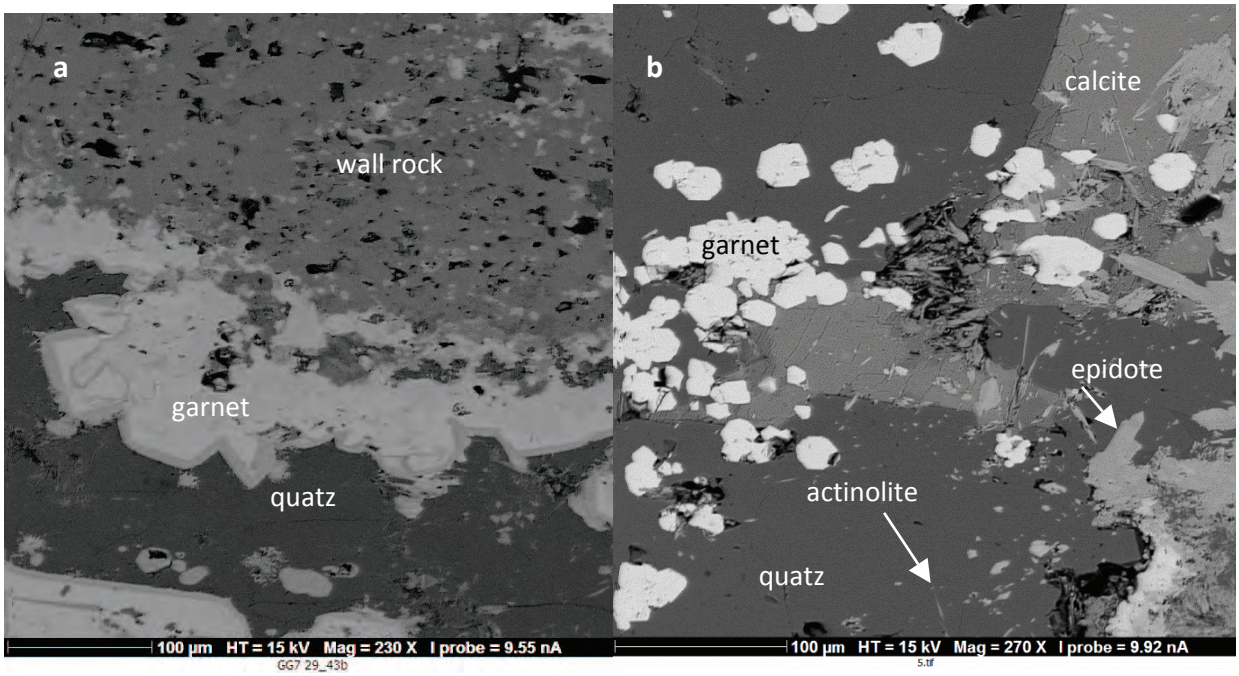

Fig. 1.4.9. (a) Sample GG7 29.43-29.61: zoned crystals along amygdale margins (EBS image); (b) Sample GG7 19.23: vein margins with epidote (EBS image).

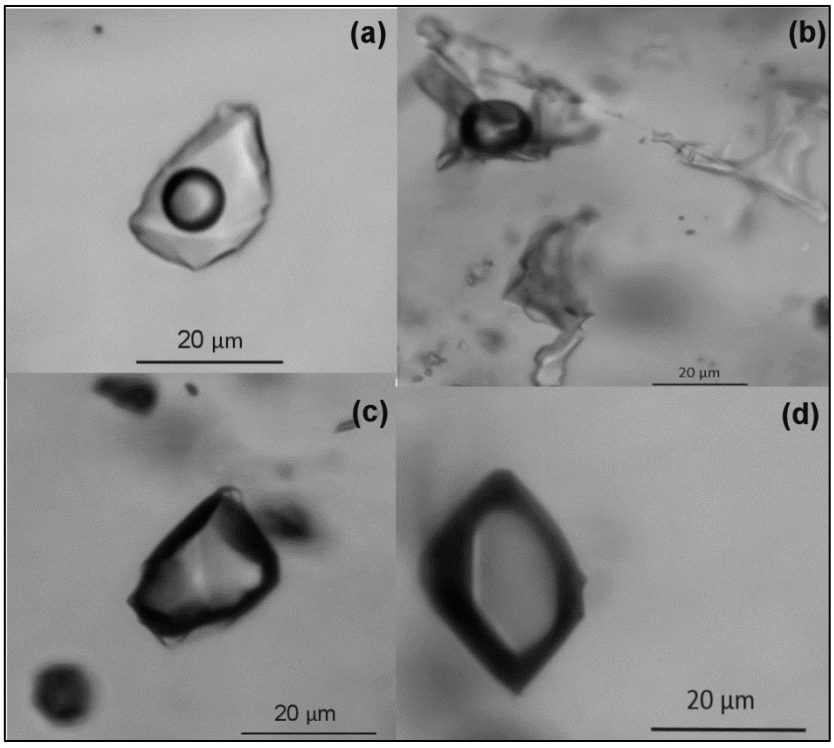

Fig. 1.4.10. Typical fluid inclusions type occurring in hydrothermal quartz and calcite observed in core samples of Table 1 at Geitafell ; a) liquid-rich (L+V) inclusions, L1; b) liquid-only fluid

inclusions, L2; c) vapour-rich (V+L) inclusion, V1; d) only-vapour (V) inclusion, V2. All photographs are for fluid inclusions hosted in quartz (sample GG1 3.41-3.48).

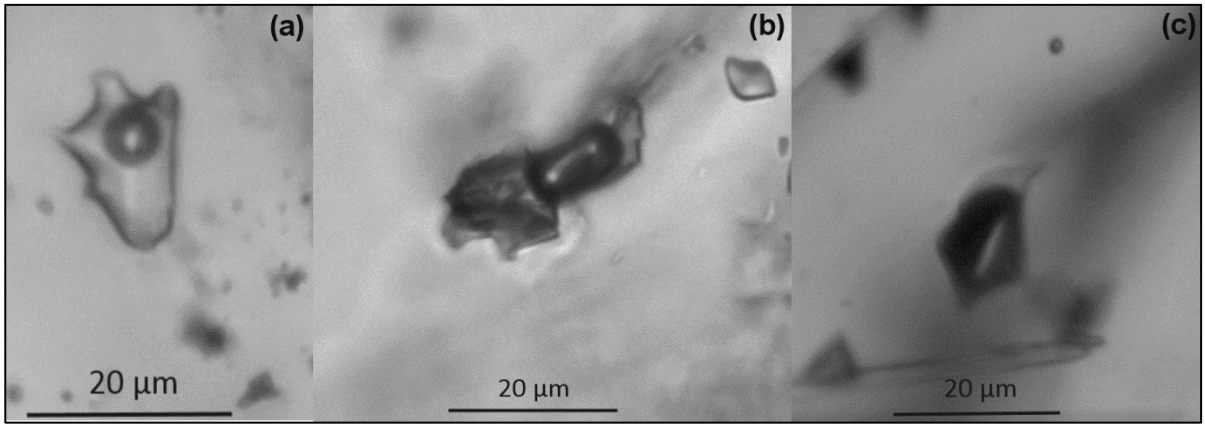

Fig. 1.4.11. L1 inclusions in quartz and calcite with variable L/V ratio; a) L/V ~70%; b) L/V ~50%; c) L/V ~30%. All photographs are for fluid inclusions hosted in quartz (sample GG1 17.29-17.38).

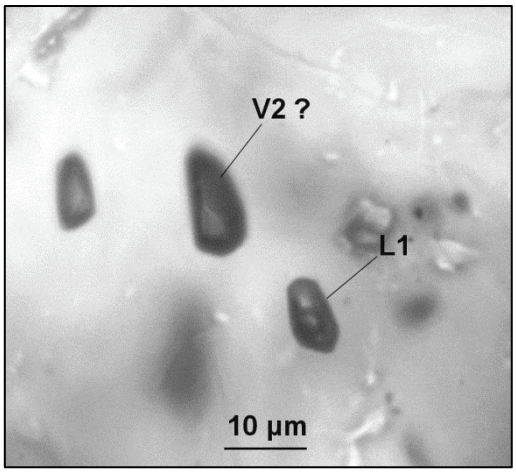

Fig. 1.4.12 Fluid inclusion in garnet of L1 and probably V2 type (sample GG7 23.93-24.04).

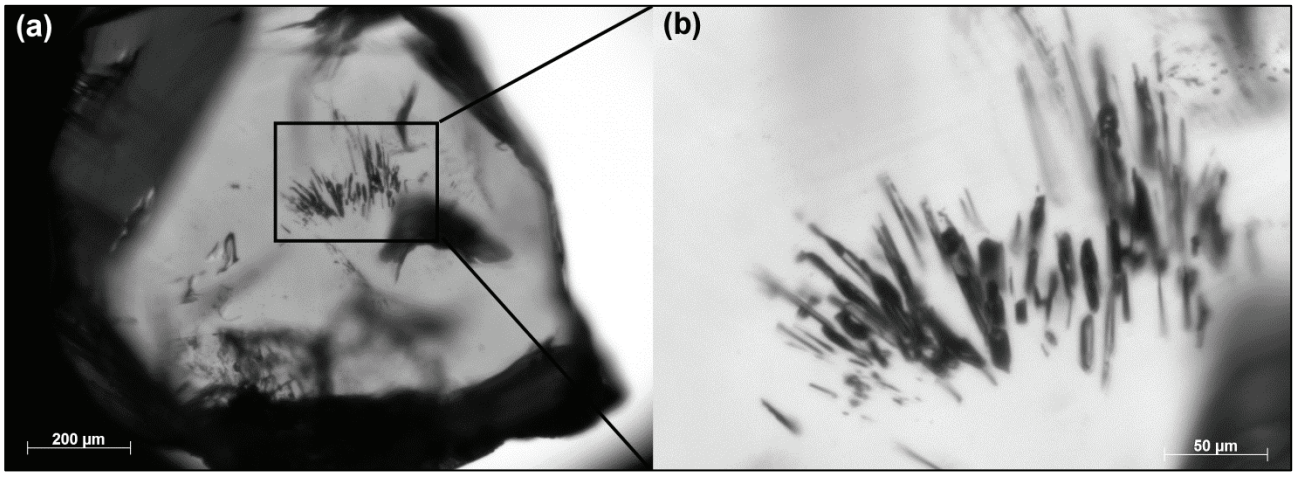

Fig. 1.4.13. Fluid inclusion in garnet of sample GE14; b) zoom of fluid inclusions and mineral phases trapped in the centre of the garnet crystal and highlighted by the black square in a).

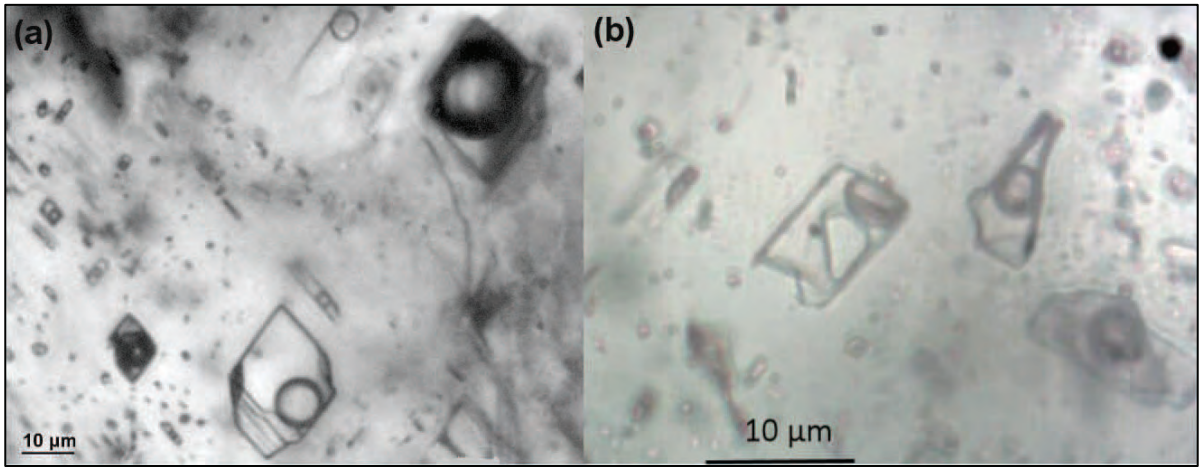

Fig. 1.4.14. Fluid inclusion in calcite (sample GE19A); a,b) liquid-rich fluid inclusions (L1), with a captive mineral (b) not identified by Raman spectroscopy.

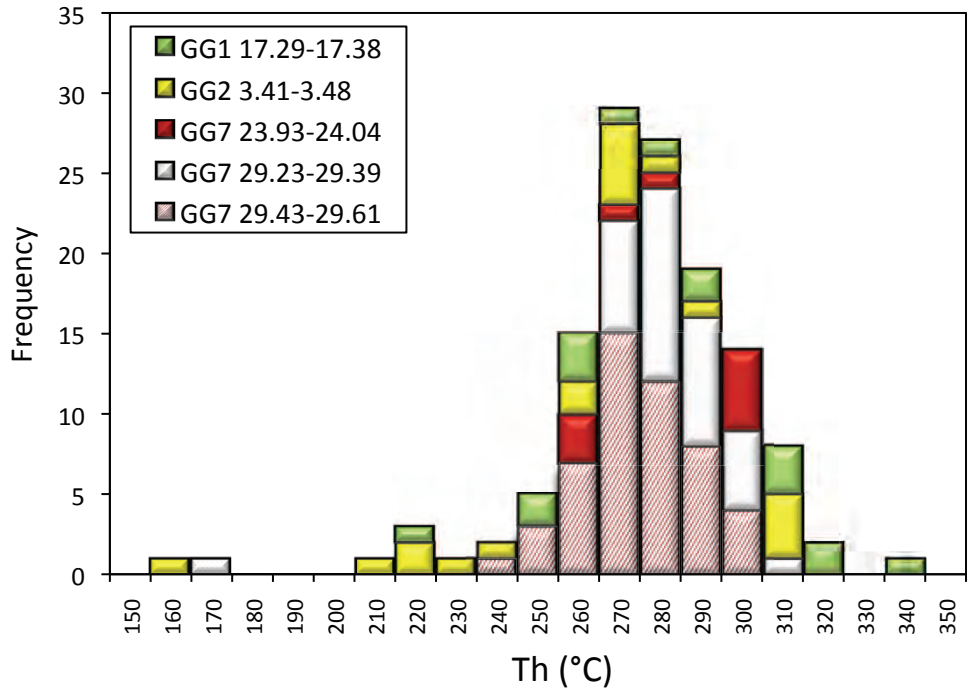

Fig. 1.4.15. Th for L1 inclusions in quartz from boreholes samples.

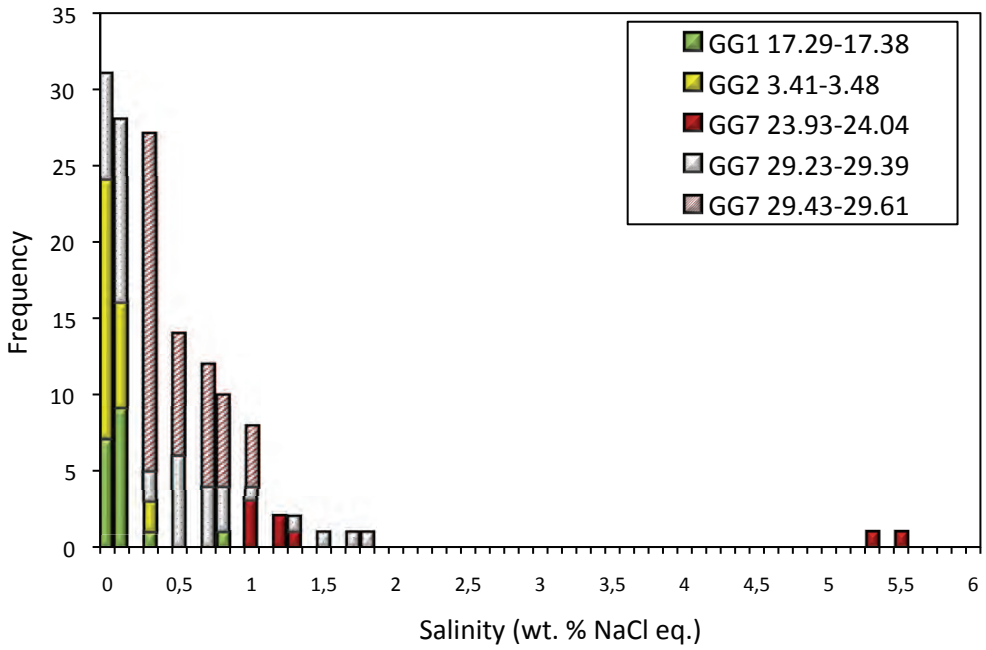

Fig. 1.4.16 Calculated salinity for L1 inclusions in quartz from boreholes samples.

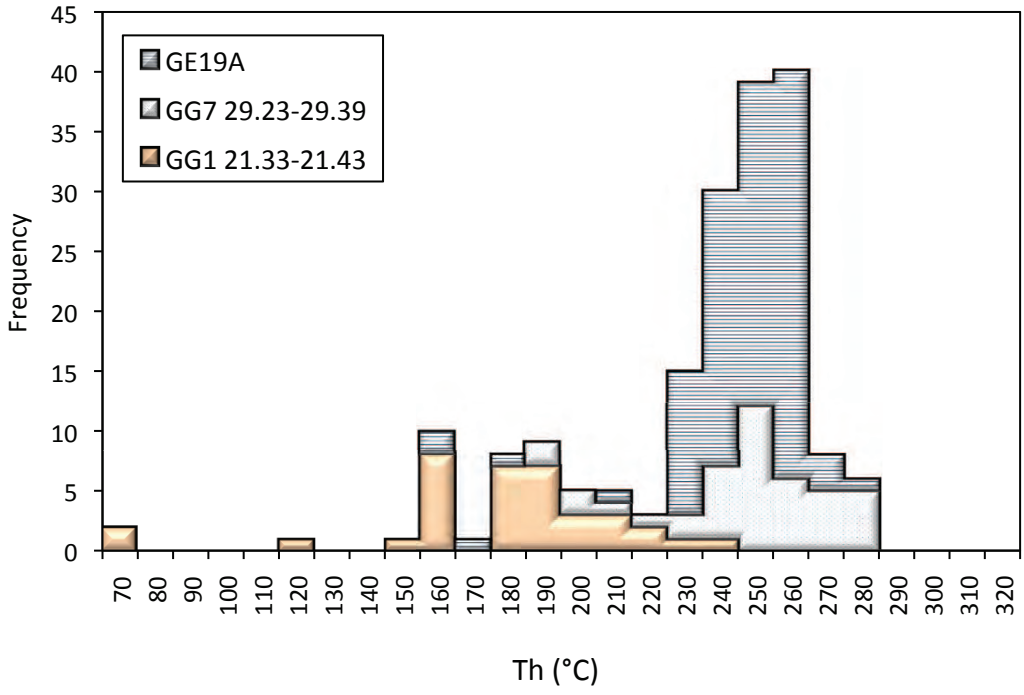

Fig. 1.4.17. Th for L1 inclusions in calcite.

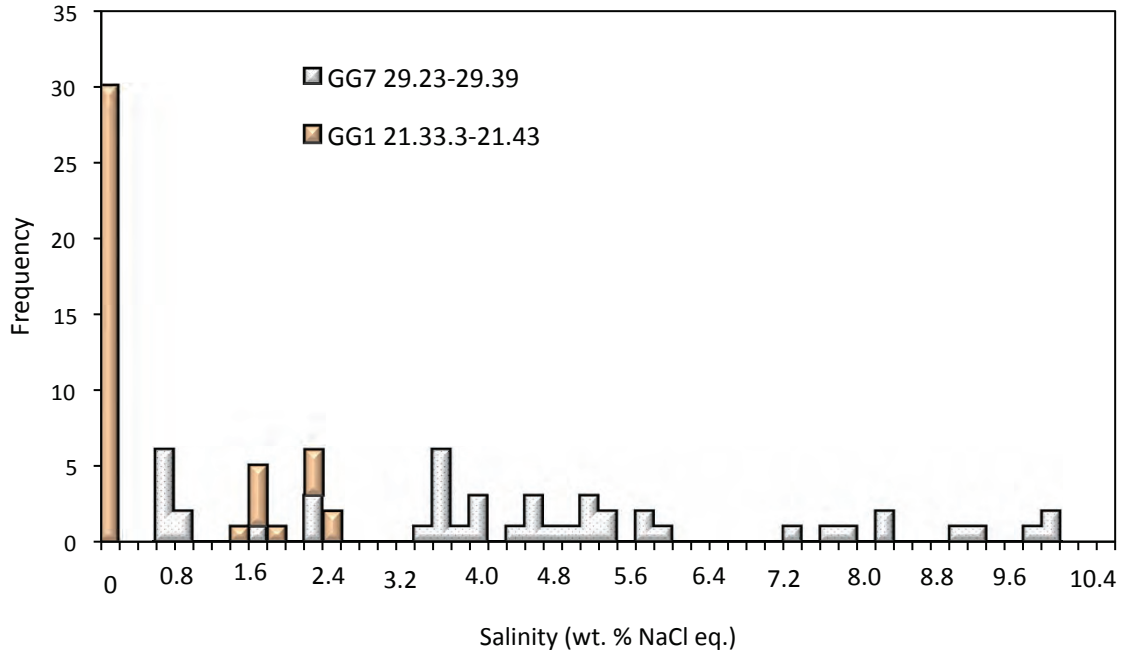

Fig. 1.4.18. Calculated salinity for L1 inclusions in calcite from boreholes.

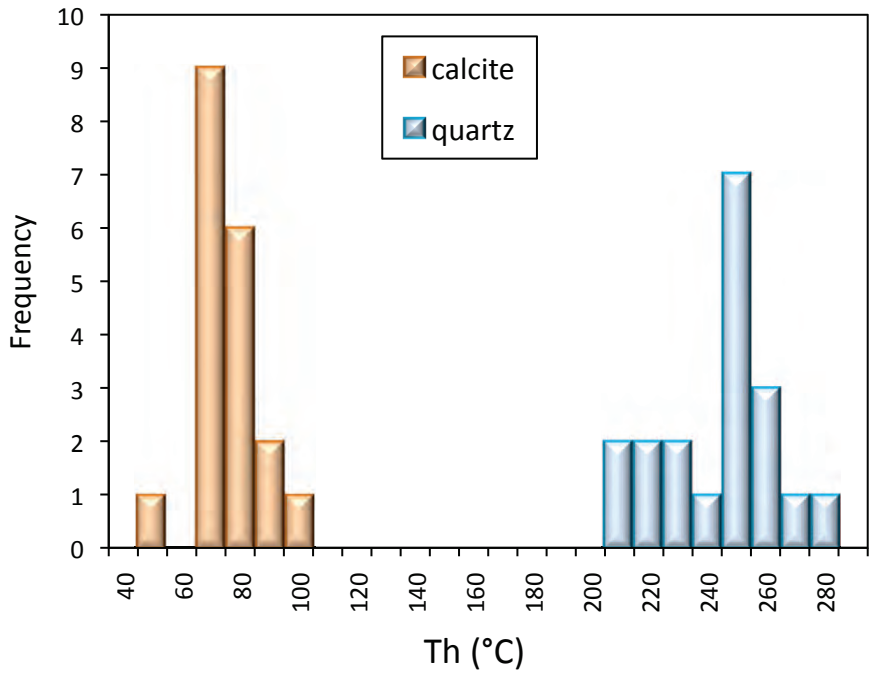

Fig. 1.4.19. Th data for fluid inclusions in calcite (L1+L2) and quartz (L1) of sample GE14.

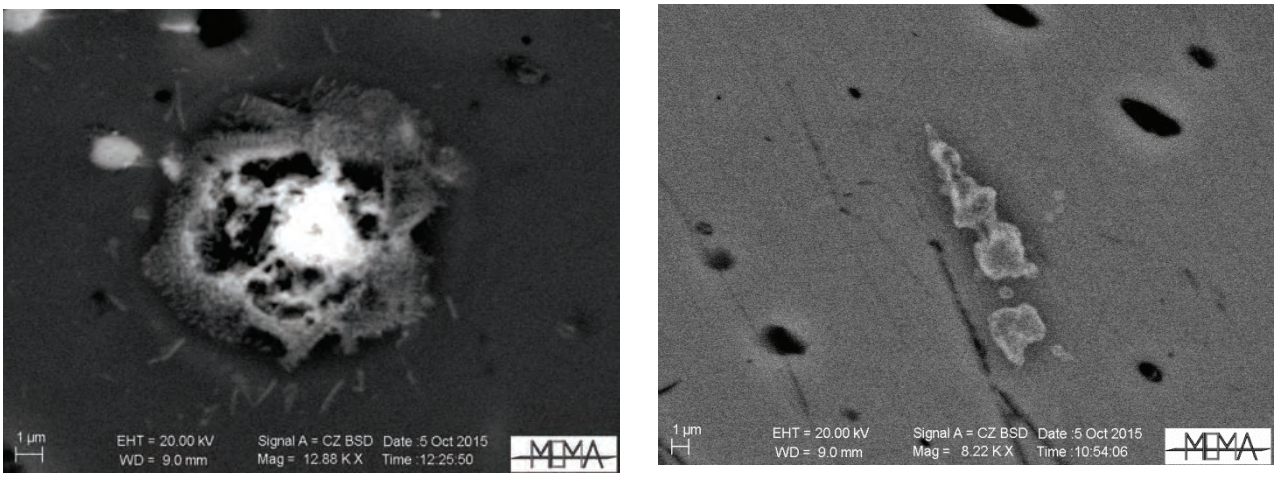

Fig. 1.4.20. a) Salts mound formed on quartz after fluid leaking from an underlying decrepitated fluid inclusion (sample GG7 23.93-24.04); b) accumulation of salts precipitated on calcite after fluid inclusion decrepitation (sample GG7 29.23-29.39)

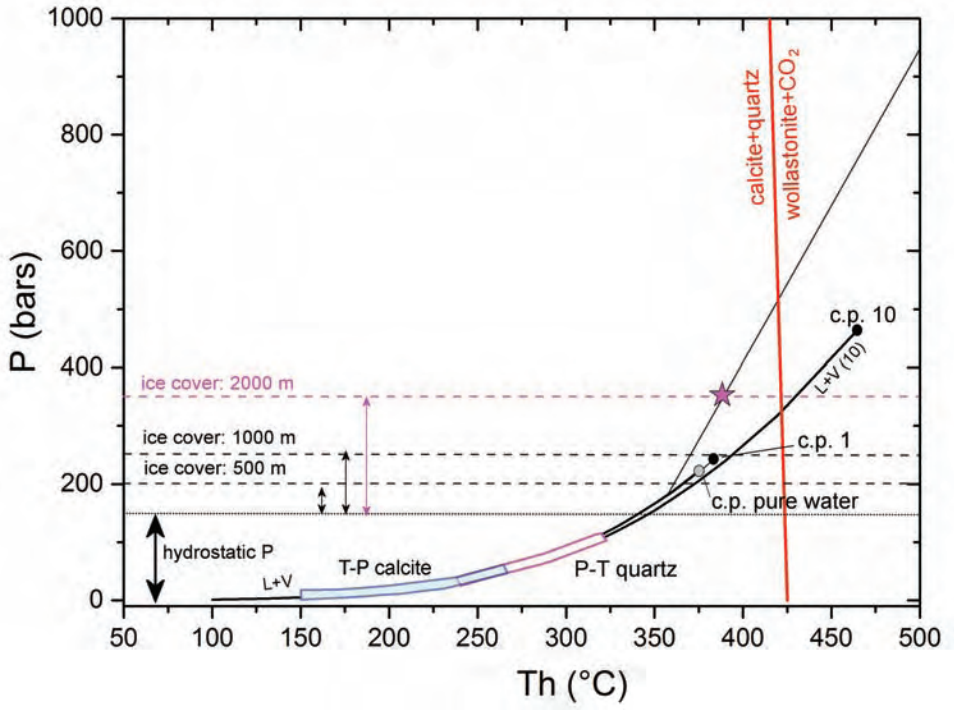

Fig. 1.4.21. P-T trapping conditions for fluid inclusions in quartz (green field) and garnet (pink star) from the Geitafell system. The different pressures hypothesized for inclusion trapping in garnet assume an hydrostatic pressure regime corresponding to a paleodepth of the Geitafell system of 1600 m and three different ice covers. The calcite+quartz↔wollastonite+CO_2 equilibrium line is from Harker and Tuttle (1956).

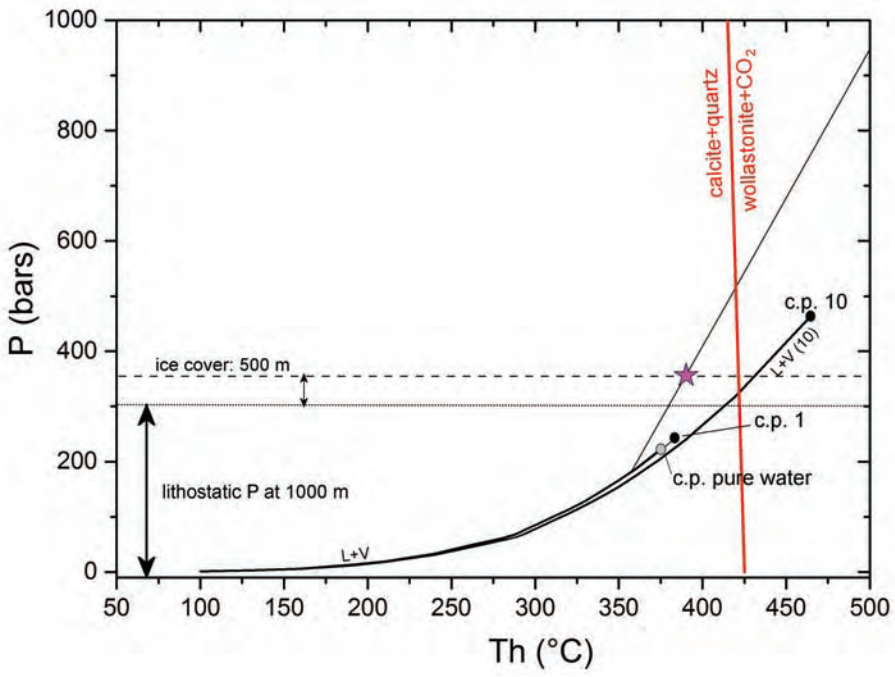

Fig. 1.4.22. P-T trapping conditions for fluid inclusion in garnet from the Geitafell system assuming a trapping pressure of 350 bars corresponding to a lithostatic load of about 1km (300 bars) as hypothesized by Fridleifsson (1984) plus an ice cover of 500 m. The calcite+quartz↔wollastonite+CO_2 equilibrium line is from Harker and Tuttle (1956).

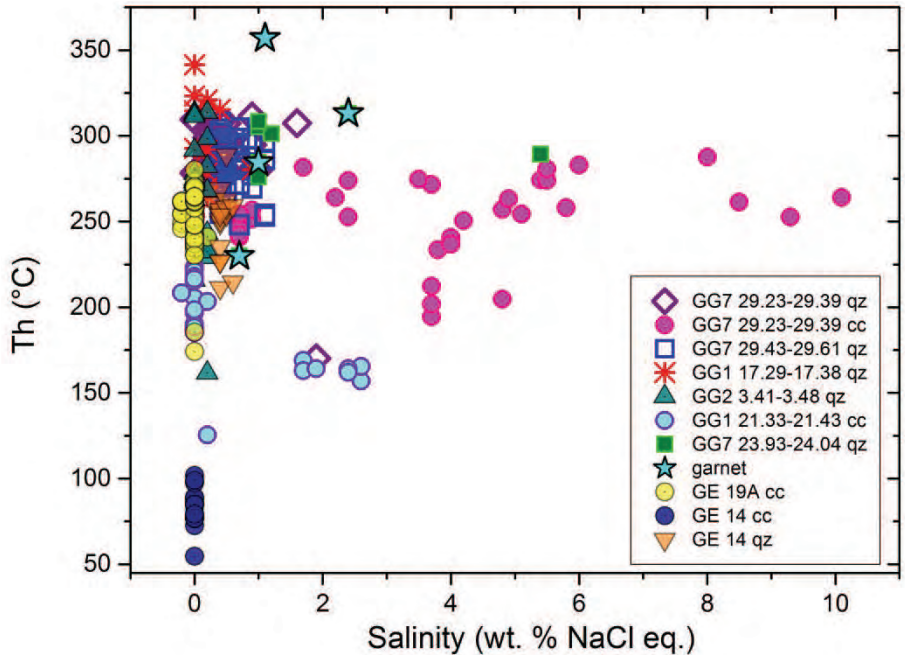

Fig. 1.4.23. Th vs salinity data for all the dataset.

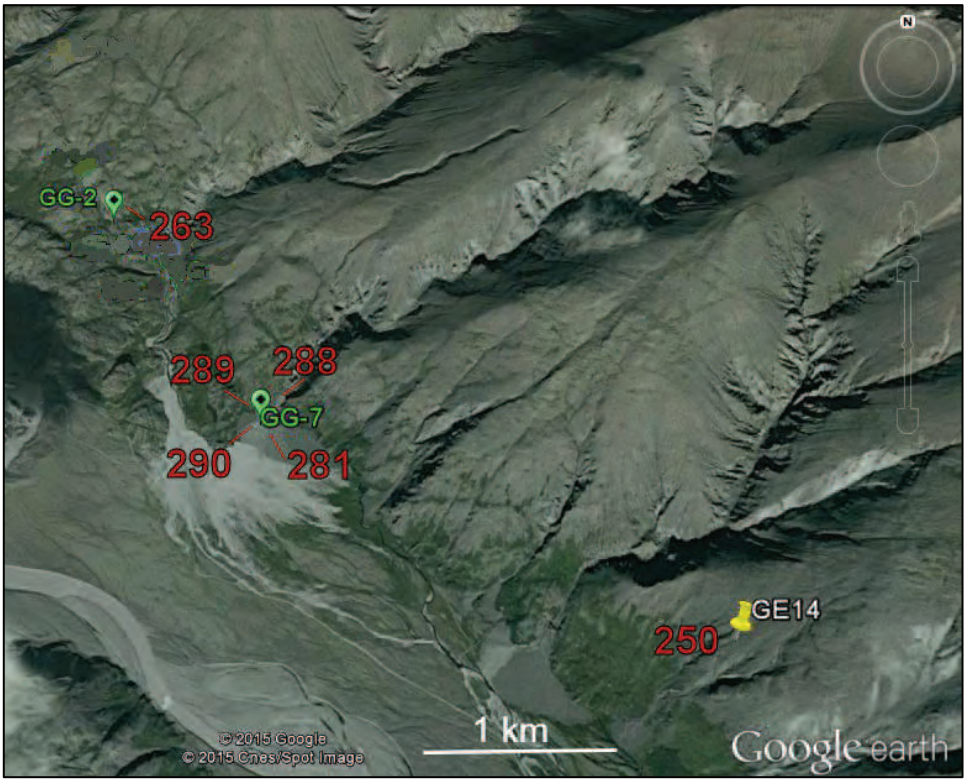

Fig. 1.4.24. Map of distribution of the Th measured in fluid inclusions in quartz.

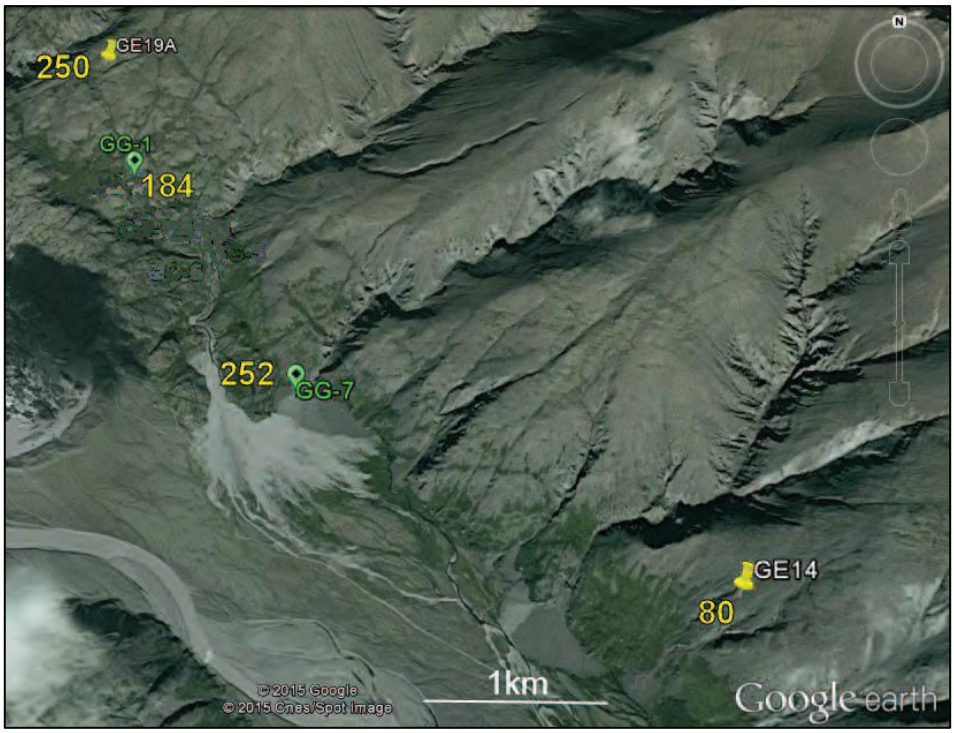

Fig. 1.4.25. Map of distribution of the Th measured in fluid inclusions in calcite.

SAMPLE ID	LOCATION	MACROSCOPIC SAMPLE DESCRIPTION	HOST MINERAL
GG1 17.29-17.38	Drillcores samples recovered from boreholes made in the metamorphic aureole of the Geitafell gabbro, Fig. 1	Host rock: brecciated fine grained basalt; central nucleus with hydrothermal quartz and epidote	quartz
GG1 17.60-17.70		Host rock: fine grained basalt; hydrothermal circulation with quartz/calcite (epidote?) forming a small vein and infilling cavities	no fluid inclusions observed
GG1 21.33-21.43		Host rock: brecciated fine grained basalt sampled very close to the contact with the gabbro. Strongly alterated. Hydrothermal vein withy epidote and quartz (calcite).	calcite
GG2 3.41-3.48		Breccia/fault. White hydrothermal minerals (quartz/calcite?), mixed with epidote and chlorite.	quartz
GG2 16.66-16.76		Hydrothermal breccia filled up with hydrothermal minerals: quartz (calcite?) and epidote.	no fluid inclusions observed
GG3 4.7		Host rock: basalt lava vesciculated. Hydrothermal vein and amigdales filled with quartz, garnet, epidote, chlorite	fluid inclusions not studied
GG7 13.00-13.10		Host rock: basalt lava vesciculated. Hydrothermal vein and amigdales filled with quartz (and epidote?)	no fluid inclusions observed
GG7 28.1		Host rock: basalt lava. Hydrothermal vein and amygdales filled by actinolite, quartz, sphene, chlorite .	fluid inclusions not studied
GG7 23.93-24.04		Host rock: basalt lava. Hydrothermal vein filled with quartz (calcite) and epidote.	quartz, garnet
GG7 29.23-29.39		Host rock: basalt lava. Hydrothermal vein filled with quartz and epidote, and amigdales with black roundish minerals.	quartz, calcite
GG7 29.43-29.61		Host rock: basalt lava. Hydrothermal vein with albite and quartz. Hydrothermal diffusion halo surrounding amigdales.	quartz, garnet
GE14	Superficial samples; Fig. 2	Hydrothermal altered lava. Amigdales filled with hydrothermal minerals: quartz, calcite, garnet and zeolite.	quartz, calcite, garnet
GE19A		Hydrotheraml altered basalt with a compact vein mineralized with calcite and epidote	calcite

Table 1.4.1: Summary of samples analyzed for mineralogy and fluid inclusions

Sample ID	analyzed mineral	$^{87}Sr/^{86}Sr$	$^{13}C/^{12}C$	$^{18}O/^{16}O$
GE14	garnet, calcite, epidote, zeolite	x	x (calcite)	x (calcite)
GE100	zeolite	x		
GE101	zeolite	x		
GE19A	calcite			x
GG7 13.00-13.10	calcite			x
GG7 23.93-24.04	calcite			x
GG2 16.66-16.76	calcite			x

Table 1.4.2: Samples selected for isotopic analyses of Sr, C, O

Geltafell secondary alteration phases																					
	Chlorite zone	Epidote zone	Andradite zone	Actinolite zone	GG1_17.6	GG2_3.41	GG2_16.66	GG19_A	GG7_13	GG7_23.13	GG7_29.23	GG7_29.43	GG1_17.29	GG1_21.33
Quartz	x	X	X	X	X	x	x	x	X	x	X	x		
Calcite	x	X	X	X	X	X	X	X	x	X	X	X	X	X
Smectite	x	x												
Talc	x													
Chlorite	X	X	X	X	x	X	X	x	X	X	X	X		x
Albite/K feld	X	X	X	X		x			X	x			X	X
Epidoto		X	X	X	X	x	x	X	X	X	X	X	X	X
Garnet			X	X						X	X	X		
Actinolite			X	X						X	X	X	X	X
Hedenbergite			x	x										
Limonite	x	X	x	x										
Fe-oxides		x	X	X					x					
Sphene	x	x	X	X					x					
Pyrite	x	X	X	X										
Zeolites*	X	X	X	X						X		x		
X = index mineral														
X = abundant														
X = scarce														
* related to regional low-temperature hydrothermal alteration overprinting														

Table 1.4.3: Summary of the skarn and hydrothermal minerals in the main alteration zones at Getafell as reported by Fridleifsson (1983b) and within the examined core samples.

Table 1.4.4: Electron microprobe analyses and calculated structural formulae (apfu) of selected skarn and hydrothermal minerals found in the examined core samples (cont.).

	chlorite	chlorite	chlorite	chlorite	chlorite		epidote	epidote	epidote	epidote	epidote	epidote_core	epidote_rim	epidote	epidote	epidote	epidote	
sample	**GG2 3.41**	**GG2 3.41**	**GG7 13**	**GG7 23.13**	**GG7_29.23**		**GG2 3.41**	**GG7 13**	**GG7 13**	**GG19 A**	**GG19 A**	**GG1 17.29**	**GG1 17.29**	**GG7 23.13**	**GG7 23.13**	**GG7_29.23**	**GG7_29.43**	
zone			big veins	vein margins	vein margins			big veins	small veins					vein margins	vein margins	vein margins	amigd. margin	
analyses	2	3	8	24	24		7	3	4	12	13	22	21	20	22	19	6	
SiO_2	29.571	29.482	27.851	28.207	28.751		37.931	37.909	38.802	38.381	37.723	38.629	38.618	37.604	38.455	38.369	37.779	
TiO_2	0.000	0.011	0.154	0.020	0.000		0.000	0.289	0.000	0.000	0.000	0.000	0.000	0.089	0.158	0.068	0.000	
Al_2O_3	16.431	15.355	17.452	16.820	16.909		22.836	21.612	24.057	25.294	22.617	27.173	24.711	19.792	24.308	20.478	22.809	
FeO	25.318	29.206	26.833	24.689	26.170		12.877	14.334	10.945	8.926	12.263	8.769	12.263	17.209	12.194	14.894	13.399	
MnO	0.231	0.363	0.276	0.596	0.346		0.115	0.297	0.364	0.054	0.009	0.189	0.007	0.055	0.422	0.108	0.272	
MgO	16.489	14.074	13.091	15.354	16.919		0.137	0.142	0.221	0.215	0.146	0.099	0.134	0.150	0.061	0.127	0.091	
CaO	0.000	0.240	0.109	0.022	0.000		23.144	22.736	22.787	23.475	23.107	23.441	22.982	22.385	22.031	23.035	22.746	
Na_2O	0.162	0.122	0.106	0.059	0.042		0.000	0.000	0.000	0.000	0.000			0.000	0.000	0.000	0.000	
K_2O	0.181	0.000	0.252	0.173	0.312		0.000	0.000	0.000	0.000	0.000			0.000	0.000	0.000	0.000	
Cr_2O_3	0.058	0.000	0.000	0.013	0.000		0.000	0.016	0.028	0.000	0.000	0.000	0.050			0.000	0.009	
Sum	88.442	88.850	86.083	85.951	89.4477		97.041	97.335	97.204	96.345	95.864	98.299	98.763	97.282	97.629	97.079	97.106	
	Numbers of ions on the basis of 28 oxygens:						*Numbers of ions on the basis of 25 oxygens; all Fe as Fe3+*											*Num*
Si	6.16	6.24	5.82	6.06	5.94	Si	6.02	6.03	6.10	6.07	6.05	5.97	5.99	6.02	6.06	6.12	6.00	Si
Al IV	1.84	1.76	2.18	1.94	2.06	Al VI	-0.02	-0.03	-0.10	-0.07	-0.05	0.03	0.01	-0.02	-0.06	-0.12	0.00	Al
sum Z	8.00	8.00	8.00	8.00	8.00	sum z	6.00	6.00	6.00	6.00	6.00	6.00	6.00	6.00	6.00	6.00	6.00	Fe
																		sur
Al VI	2.19	2.07	2.13	2.31	2.03	Al IV	4.29	4.07	4.56	4.78	4.33	4.92	4.51	3.75	4.41	3.97	4.27	
Ti	0.00	0.00	0.00	0.00	0.00	Fe3+	1.71	1.93	1.44	1.22	1.67	1.08	1.49	2.25	1.59	2.03	1.73	Ca
Mg	5.12	4.44	5.01	4.92	5.39	sum	6.00	6.00	6.00	6.00	6.00	6.00	6.00	6.00	6.00	6.00	6.00	Na
Fe2+	4.41	5.18	4.79	4.44	4.48													K
Mn	0.04	0.07	0.05	0.11	0.03	Ti	0.00	0.03	0.00	0.00	0.00	0.00	0.00	0.01	0.00	0.01	0.00	Sr
Ca	0.00	0.05	0.02	0.01	0.09	Fe3+	0.00	-0.02	0.00	-0.04	-0.02	0.06	0.10	0.06	0.08	-0.04	0.05	Ba
Na	0.07	0.05	0.04	0.02	0.00	Mn	0.02	0.04	0.05	0.01	0.00	0.02	0.00	0.01	0.00	0.01	0.04	sur
K	0.05	0.00	0.07	0.05	0.00	Mg	0.03	0.03	0.05	0.05	0.03	0.02	0.03	0.04	0.06	0.03	0.02	
sum	11.88	11.87	12.06	11.85	12.02	Ca	3.94	3.87	3.84	3.98	3.97	3.88	3.82	3.84	3.80	3.94	3.87	**sum**
						K	0.00	0.00	0.00	0.00	0.00	0.00	0.00	0.00	0.00	0.00	0.00	
Mg #	53.71	46.19	51.61	52.56	54.60	sum Y	3.99	3.96	3.95	3.99	3.99	3.99	3.95	3.95	3.93	3.95	3.98	An
																		Ab
						Tot.	15.99	15.96	15.95	15.99	15.99	15.99	15.95	15.95	15.93	15.95	15.98	Or
						Mg #	1.86	1.74	3.48	4.11	2.08	1.96	1.91	1.53	3.46	1.50	1.19	
						Fe2O3*	14.31	15.93	12.16	9.92	13.63	9.74	13.63	19.12	14.10	16.55	14.89	

Table 1.4.4: Electron microprobe analyses and calculated structural formulae (a.p.f.u) of selected skarn and hydrothermal minerals found in the examined core samples.

Sample ID	Mineral host	Fluid inclusion	Homogenization	Th range (°C)	Tm_{ice} range (°C)
GG1 17.29-17.38	quartz	L1	L+V→ L	230-341 (15)	-0.5/0.0 (17)
		V1	V+L→ V	230 (1)	-0.1 (1)
GG1 21.33-21.43	calcite	L1	L+V→ L	126-247 (36)	-1.5/0.0 (41)
GG2 3.41-3.48	quartz	L2	L+V→ L* (after cooling)	214-276 (3)	0.0 (1)
		L1	L+V→ L	162-314 (19)	-0.2/0.0 (24)
		V2	/	/	-0.2 (1)
		V1	V+L→ V	217-313 (6)	-0.1 (1)
GG7 23.93-24.04	quartz	L1	L+V→ L	267-308 (10)	-3.4/-0.6 (8)
	garnet	L1	L+V→ L	230-313 (4)	-1.4/-0.4 (3)
GG7 29.23-29.39	quartz	L1	L+V→ L	170-311 (34)	-1.1/0.0 (40)
	calcite	L1	L+V→ L	190-288 (42)	-6.9/-0.4 (47)
GG7 29.43-29.61	quartz	L1	L+V→ L	248-308 (50)	-0.6/-0.2 (49)
	garnet	L1	L+V→ L	277/357 (2)	-0.6 (1)
GE14	calcite	L2	L+V→ L* (after cooling)	79-102 (5)	metastable: above 0°C
		L1	L+V→ L	55-89 (13)	metastable: above 0.0°C
	quartz	L1	L+V→ L	211-289 (19)	-0.1/0.0 (20)
GE19A	calcite	L1	L+V→ L	162-280 (105)	-0.1/0.0 (100)

Table 1.4.5: Summary of the microthermometric data of the fluid inclusions analyzed in the Getafell samples

Sample	Fis host mineral	Ca (mol%)	Na (mol%)	K (mol%)	Mg (mol%)	Cl (mol%)	SO4 (mol%)
GG7 23.93-24.04	quartz	22.24	13.50	0.69	0.00	17.36	46.21
GG7 23.93-24.04	quartz	12.46	39.12	0.42	1.87	31.79	14.34
GG7 23.93-24.04	quartz	29.30	27.80	0.86	0.50	23.58	17.96
GG7 23.93-24.04	quartz	27.02	28.21	0.58	1.03	41.17	1.98
GG7 29.23-29.39	calcite		66.78	0.00		11.85	21.37
GG7 29.23-29.39	calcite		63.71	0.07		33.64	2.57

Table 1.4.6: SEM-EDS analyses of the salts precipitated from decrepitated inclusions

Sample ID	analyzed mineral	$^{87}Sr/^{86}Sr$	$\delta^{13}C$	$\delta^{18}O$	$\delta^{13}C_{CO2}$	$\delta^{18}O_{H2O}$
GE14	garnet	0.703889				
	epidote	0.703243				
	calcite	0.703247	-4.97	11.87	-0.3	-7.6
	zeolite	0.703221				
GE100	zeolite	0.703214				
GE101	zeolite	0.703223				
GE19A	calcite		-6.06	-1.21	-4.8	-8.4
GG7 13.00-13.10a	calcite		-5.10	5.24	-3.8	-2.0
GG7 23.93-24.04	calcite		-4.62	11.96	-3.4	4.6
GG2 16.66-16.76	calcite		-4.77	-0.02	-3.5	-7.3

Table 1.4.7: Summary of the isotope composition (‰) of Sr, C and O and recalculated isotope composition of the fluid

Sample	Mineral	δD_{SMOW} (‰)	$\delta^{18}O_{SMOW}$ (‰)
005	quartz		7.6
006	epidote	-95	-5.6
007	quartz		3.4
008	quartz		1.2
010	epidote	-93	-6.1
012	epidote	-90	-6.2
016	epidote	-91	0.4
017	epidote	-99	-1.4
018	epidote		-4.3
019	epidote	-84	-4.6
001	epidote	-86	-5.1
001	quartz		1
025	epidote	-94	-5.3
029	epidote	-84	-5.7
029	quartz		3.4
030	epidote	-95	-5.3
033	epidote		-4.8
034	epidote	-84	-1.5
036a	epidote	-84	-6.2
036a	quartz		2.2
036c	epidote	-84	-5.7
036d	epidote	-93	-5.5
037	epidote	-81	-5.1
038	epidote	-98	
039	epidote	-108	-3.3
Table 2.5.2	Summary of stable isotope composition of Geitafell hydrothermal mineral of Pope et al. (2014)		

Table 1.4.8: Summary of stable isotope composition of different hydrothermal minerals reported by Pope at al. (2014)

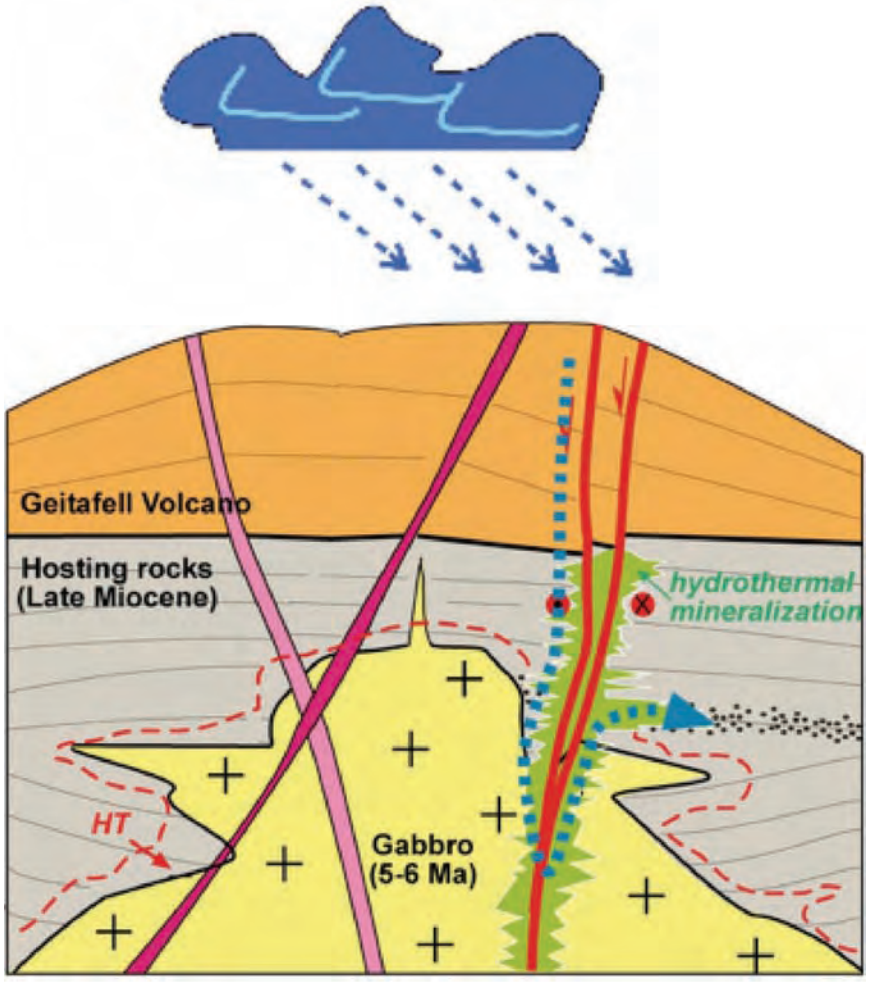

Fig. 1.5.1. – conceptual model of the hydrothermal circulation in Geitafell exhumed geothermal system.

Fig. 2.1 – Location map of the exhumed geothermal system of Elba Island and of the active Larderello one.

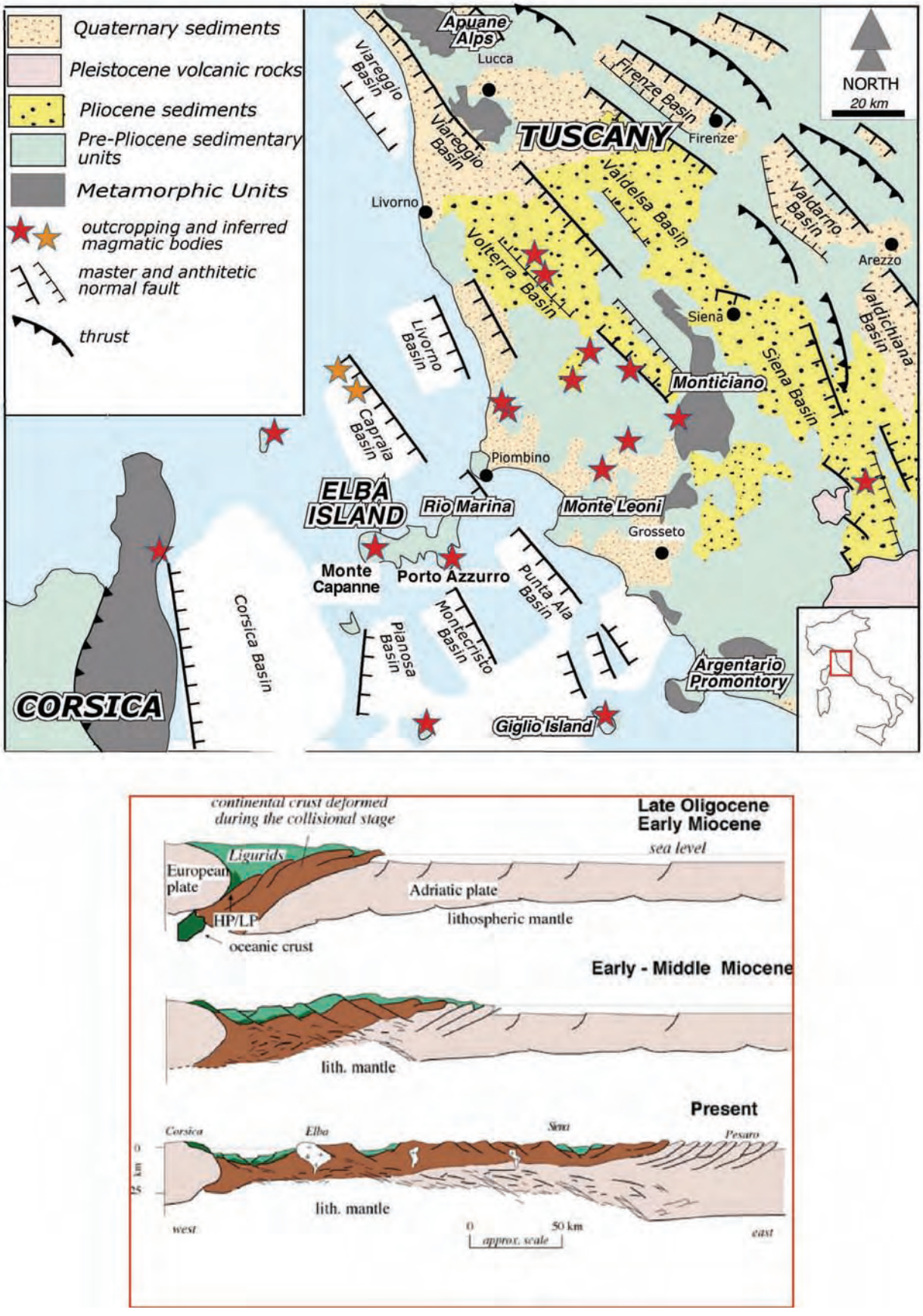

Fig. 2.1.1 – Top: schematic geological map of the inner northern Apennines; bottom: schematic geological cross sections illustrating the collisional and extensional post-collisional evolution of the inner northern Apennines.

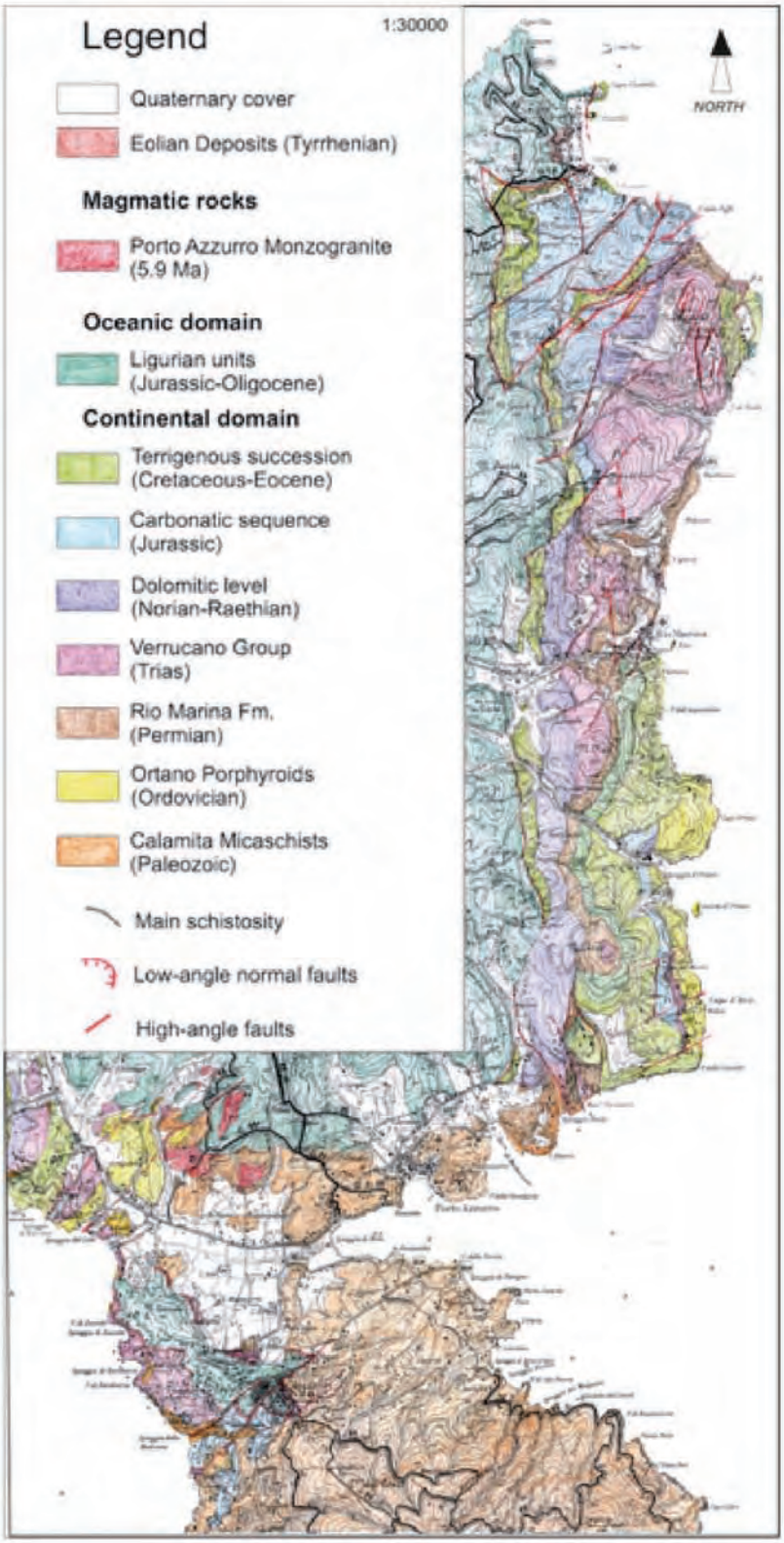

Fig. 2.2 – Geological map of the eastern Elba island

Table 2.2.1 - samples collected during this study

Sample	Location	Rock Type	Cause	Sampling date
C1	Cavo area	Limestone	Mineralogy	27/06/2013
C2	Cavo area	Limestone	Mineralogy	27/06/2013
C3	Cavo area	Limestone	Mineralogy	27/06/2013
C4	Cavo area	Limestone	Mineralogy	27/06/2013
C5	Cavo area	Limestone	Mineralogy	27/06/2013
C6	Cavo area	Limestone	Mineralogy	27/06/2013
C7	Cavo area	Limestone	Mineralogy	27/06/2013
C8	Cavo area	Limestone	Mineralogy	27/06/2013
C9	Cavo area	Limestone	Mineralogy	27/06/2013
C10	Cavo area	Metamorphic Siltstone	Mineralogy	28/06/2013
C11	Cavo area	Metamorphic Siltstone	Mineralogy	28/06/2013
C12	Cavo area	Marble	Mineralogy	28/06/2013
C13	Cavo area	Marble	Mineralogy	28/06/2013
C14A	Cavo area	Serpentinite	Mineralogy	28/06/2013
C14B	Cavo area	Serpentinite	Mineralogy	28/06/2013
C15	Cavo area	Phyllite	Mineralogy	28/06/2013
C16	Rio Marina harbour	Calcschist	Mineralogy	28/06/2013
C17	Rio Marina harbour	Calcschist	Mineralogy	28/06/2013
C18	Rio Marina harbour	Calcschist	Mineralogy	28/06/2013
C19	Rio Marina harbour	Metabasite	Mineralogy	28/06/2013
C20	Mt. Calamita area	Phyllite	Mineralogy	29/06/2013
FCA	Capoliveri area	Marble	Mineralogy	01/07/2013
FCD	Capoliveri area	Marble	Mineralogy	04/07/2013
FCE	Capoliveri area	Marble	Mineralogy	04/07/2013
CO1A	Ortano area	Calcschist	Mineralogy	01/10/2013
CO1B	Ortano area	Marble	Mineralogy	01/10/2013
CO1C	Ortano area	Marble	Mineralogy	01/10/2013
CO2	Ortano area	Calcschist	Mineralogy	01/10/2013
CO3U	Ortano area	Serpentinite	Mineralogy/Microstructure	02/10/2013
CO3D	Ortano area	Serpentinite	Mineralogy/Microstructure	02/10/2013
CO4A	Ortano area	Phyllite	Mineralogy/Microstructure	02/10/2013
CO4B	Ortano area	Phyllite	Mineralogy/Microstructure	02/10/2013
CO5A	Ortano area	Phyllite	Mineralogy/Microstructure	02/10/2013
CO5B	Ortano area	Phyllite	Mineralogy/Microstructure	02/10/2013
CO6	Ortano area	Phyllite	Mineralogy	02/10/2013
CO7	Ortano area	Marble	Mineralogy	02/10/2013
CO8A	Ortano area	Phyllite	Mineralogy	02/10/2013
CO8B	Ortano area	Phyllite	Mineralogy	02/10/2013
CO8BIS	Ortano area	Phyllite	Mineralogy	02/10/2013
CO9	Ortano area	Phyllite	Mineralogy/Microstructure	03/10/2013
CO10	Ortano area	Phyllite	Mineralogy	03/10/2013
CO12	Ortano area	Phyllite	Mineralogy	03/10/2013
K1	Cavo area	Limestone	Mineralogy	25/11/2013
K2	Cavo area	Limestone	Mineralogy	27/11/2013
K3	Cavo area	Limestone	Mineralogy	28/11/2013
K4	Cavo area	Limestone	Mineralogy	28/11/2013
K5	Cavo area	Limestone	Mineralogy	28/11/2013
K6	Cavo area	Limestone	Mineralogy	28/11/2013
K7	Cavo area	Limestone	Mineralogy	01/12/2013
K9	Cavo area	Limestone	Mineralogy	01/12/2013
K10	Cavo area	Limestone	Mineralogy	01/12/2013
K11	Cavo area	Limestone	Mineralogy	01/12/2013
K12	Cavo area	Limestone	Mineralogy	01/12/2013

Sample	Location	Rock Type	Cause	Sampling date
K100	Cavo area	Limestone	Mineralogy	13/01/2014
K101	Cavo area	Limestone	Mineralogy	14/01/2014
K102	Cavo area	Limestone	Mineralogy	14/01/2014
K103	Cavo area	Limestone	Mineralogy	14/01/2014
K104	Cavo area	Limestone	Mineralogy	14/01/2014
K105	Cavo area	Limestone	Mineralogy	14/01/2014
K106	Cavo area	Limestone	Mineralogy	22/01/2014
K107	Cavo area	Limestone	Mineralogy	22/01/2014
K108	Cavo area	Limestone	Mineralogy	23/01/2014
K109	Cavo area	Limestone	Mineralogy	23/01/2014
K110	Cavo area	Limestone	Mineralogy	26/01/2014
K200	Cavo area	Limestone	Mineralogy	17/02/2014
K201	Cavo area	Limestone	Mineralogy	18/02/2014
K202	Cavo area	Limestone	Mineralogy	21/02/2014
K203	Cavo area	Limestone	Mineralogy	21/02/2014
K204	Cavo area	Limestone	Mineralogy	22/02/2014
K302	Capo d'Arco area		Mineralogy	18/03/2014
K303	Capo d'Arco area		Mineralogy	18/03/2014
K304	Capo d'Arco area		Mineralogy	18/03/2014
K305	Capo d'Arco area		Mineralogy	19/03/2014
K306	Capo d'Arco area		Mineralogy	19/03/2014
K307	Capo d'Arco area		Mineralogy	20/03/2014
RMT1A	Rio Marina Harbour	Metabasite	Mineralogy	10/07/2014
RMT2A	Rio Marina Harbour	Metabasite	Mineralogy	10/07/2014
RMT2B	Rio Marina Harbour	Metabasite	Mineralogy	10/07/2014
RMT2C	Rio Marina Harbour	Metabasite	Mineralogy	10/07/2014
RMT3A	Rio Marina Harbour	Metabasite	Mineralogy	10/07/2014
RMT3B	Rio Marina Harbour	Metabasite	Mineralogy	10/07/2014
RMT4A	Rio Marina Harbour	Metabasite	Mineralogy	10/07/2014
RMT4B	Rio Marina Harbour	Metabasite	Mineralogy	10/07/2014
RMT5A	Rio Marina Harbour	Metabasite	Mineralogy	10/07/2014
RMT5B	Rio Marina Harbour	Metabasite	Mineralogy	10/07/2014
RMT6A	Rio Marina Harbour	Metabasite	Mineralogy	10/07/2014
RMT6B	Rio Marina Harbour	Metabasite	Mineralogy	10/07/2014
RMT7A	Rio Marina Harbour	Metabasite	Mineralogy	10/07/2014
RMT7B	Rio Marina Harbour	Metabasite	Mineralogy	10/07/2014
V6A	Cala delle Alghe	Metamorphic siltstone	Mineralogy/Microstructure	04/09/2014
V6B	Cala delle Alghe	Metamorphic siltstone	Mineralogy/Microstructure	04/09/2014
V7	Cala delle Alghe	Serpentinite	Mineralogy/Microstructure	04/09/2014
V8	Cala delle Alghe	Serpentinite	Mineralogy/Microstructure	04/09/2014
V9	Cala delle Alghe	Serpentinite	Mineralogy/Microstructure	04/09/2014
V12A	Cala delle Alghe	Serpentinite	Mineralogy/Microstructure	04/09/2014
V12B	Cala delle Alghe	Serpentinite	Mineralogy/Microstructure	04/09/2014
V13	Cala delle Alghe	Serpentinite	Mineralogy/Microstructure	04/09/2014
V14	Cala delle Alghe	Serpentinite	Mineralogy/Microstructure	04/09/2014
VK	Cala delle Alghe	Serpentinite	Mineralogy/Microstructure	04/09/2014
V15	Cala delle Alghe	Serpentinite	Mineralogy/Microstructure	04/09/2014
V16	Cala delle Alghe	Serpentinite	Mineralogy/Microstructure	04/09/2014

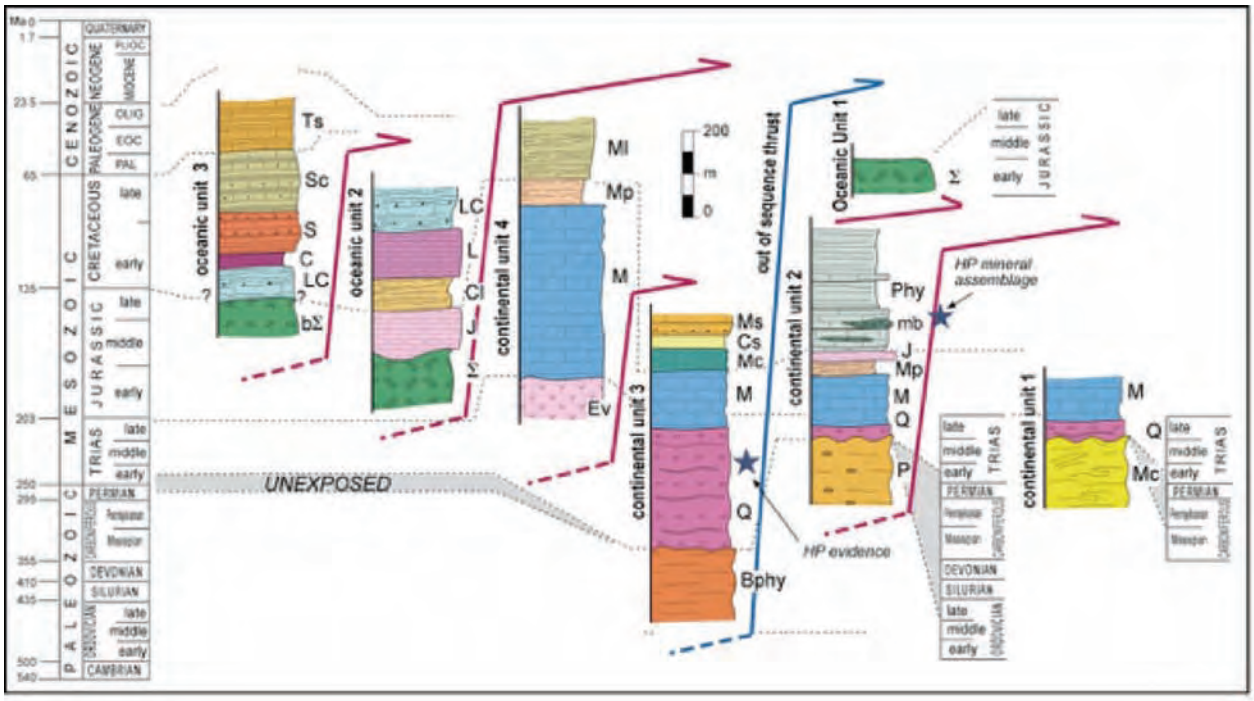

Figure 2.2.2 - Tectono-stratigraphic columns of the seven tectonic units belonging to continental and oceanic environments, and forming the tectonic pile of Elba Island. From left to right, and from the bottom in each column: oceanic unit 3: bΣ = Breccia of ophiolitic rocks; LC = limestone and shale (Palombini Shales Fm); C = shale (Varicoluored Shales Fm); S = sandstone and shale (Ghiaieto Sandstones Fm); Sc = sandstone and marlstone (Marina di Campo Fm); Ts = shale with limestone and marlstone (Colle Reciso Fm). Oceanic unit 2: Σ = ophiolite; J = radiolarite (Mt. Alpe Cherts Fm); Cl = calcilutite and cherty limestone (Nisportino Fm); L = cherty limestone (Calpionella Limestones Fm); LC = limestone and shale (Palombini Shales Fm). Continental unit 4: Ev = evaporite (Calcare Cavernoso Fm); M = massive and cherty limestone a nd dolostone (Pania di Corfino Fm, Mt. Cetona Fm, Calcare Massiccio Fm, Grotta Giusti Limestones, Rosso Ammonitico Fm, Limano cherty Limestones Fm); Mp= marls (Posidonia Marlstones Fm); Ml = Varicolored Shales (Cavo Fm). Continental unit 3: Bphy = black phyllite (Rio Marina Fm); Q = quartzite and phyllite (Verruca Fm, Mt. Serra quartzite Fm); M = marble (Valle Giove Limestones Fm; Capo Pero Limestone Fm; Capo Castello Calcschists Fm); Mc = cherty marble; Cs = calcschist and phyllite (Varicoloured Sericitic Schist Fm); Ms = metasandstone and phyllite (Pseudomacigno Fm). Continental unit 2: P = porphyroids, quartzite and phyllite (Ortano Unit); Q = quartzite; M = massive and cherty limestone and dolostone (Valdana marble Fm); Mp = marls (Posidonia Marlstones Fm); J = radiolarite; Phy = calcschist with interbedded metabasite (Mb) and phyllite (Acquadolce Unit). Oceanic unit 1: Σ = ophiolite. Continental unit 1: Mc = micaschist (Mt. Calamita Fm); Q = quartzite and phyllite (Quarziti di Barabarca Fm); M = dolostone (Crystalline dolostone and dolomitic limestone Fm).

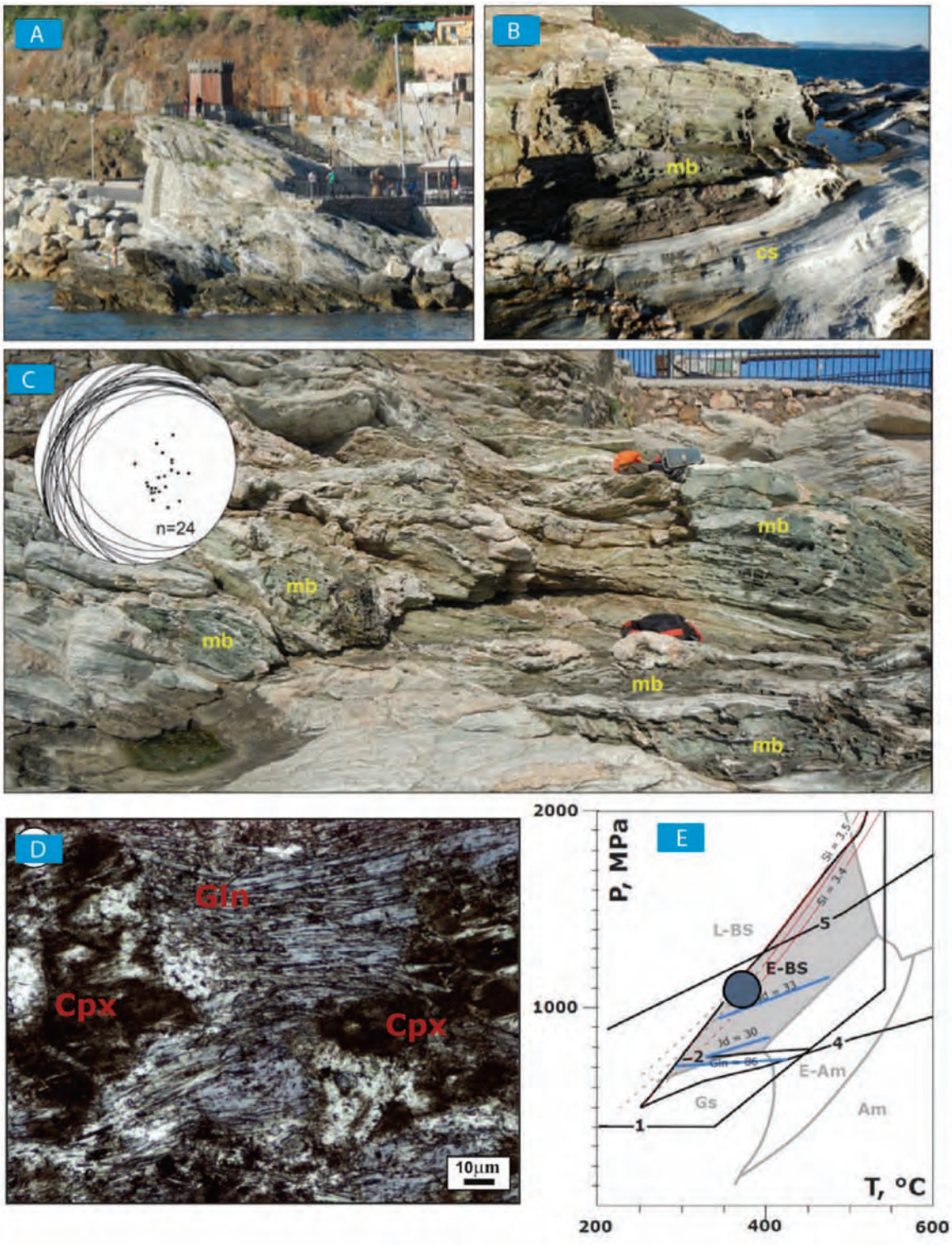

Figure 2.2.3 - (A) and (B) panoramic view of the sampling area where (C) lenses of metabasite embedded in calcshist; (D) rock fabric characterized by the presence of porphyroclasts of clinopyroxene and glaucophane (E) P-T diagram where the thermobaric conditions are highlighted.

	Amphiboles		Clinopyroxenes				Feldspars		Epidotes		Chlorite
	Gln	Act	Omph	Agt	Di	Aug	Ab	An	Czo	Ps	
wt.%											
SiO_2	58.08	57.28	55.20	54.00	51.63	52.13	68.36	42.51	39.27	37.87	30.03
TiO_2	0.22	0.03	0.10	0.01	1.00	0.03	0.01	0.01	0.12	0.06	0.02
Al_2O_3	9.63	1.06	7.20	3.26	2.15	4.44	19.50	36.79	32.55	22.28	20.74
Cr_2O_3		0.04	0.28	0.19	0.02				0.02	0.09	0.03
FeO_t	9.76	6.89	9.36	9.86	6.71	13.69	0.07	0.17	1.4	12.55	14.26
MnO	0.17	0.30	0.13	0.23	0.19	0.22			0.03	0.11	0.38
MgO	10.56	18.47	7.44	9.90	15.04	14.23	0.01	0.01	0.06	0.03	20.97
CaO	1.09	11.20	11.65	15.19	21.64	13.22	0.03	19.80	23.55	22.18	0.06
Na_2O	6.16	0.86	7.34	5.33	0.36	0.35	11.68	0.05	0.01	0.03	0.01
K_2O	0.02	0.03	0.04	0.04	0.03	0.11		0.03	0.01	0.02	0.08
Tot	95.69	96.16	98.74	98.01	98.77	98.42	99.66	99.37	97.02	95.22	86.58
ΣO	23	23	6	6	6	6.066	8	8	25	25	28
Si	8.063	8.087	2.011	2.003	1.929	1.982	2.994	1.982	6.027	6.320	5.986
Al^{IV}					0.071	0.018	1.008	2.024			2.014
Al^{VI}	1.576	0.176	0.309	0.143	0.024	0.181			5.895	4.387	2.864
Ti	0.022	0.004	0.003		0.028	0.001			0.014	0.008	0.003
Cr		0.004	0.008	0.006	0.001				0.002	0.012	0.005
Fe	1.133	0.813	0.285	0.306	0.210	0.435	0.003	0.007	0.180	1.751	2.377
Mn	0.020	0.036	0.004	0.007	0.006	0.007			0.004	0.016	0.064
Mg	2.190	3.885	0.404	0.547	0.838	0.806	0.001	0.001	0.014	0.007	6.231
Ca	0.163	1.693	0.455	0.604	0.866	0.538	0.001	0.989	3.872	3.966	0.013
Na	1.658	0.234	0.519	0.383	0.026	0.026	0.992	0.005	0.003	0.010	0.004
K	0.003	0.005	0.002	0.002	0.001	0.005		0.002	0.002	0.004	0.020
Fe^{3+}	0.266	0.024	0.175	0.227	0.017						
Fe^{2+}	0.867	0.789	0.110	0.079	0.193	0.435					
ΣCat	14.828	14.937	4.000	4.000	4.000	4.000	4.998	5.009	16.013	16.480	19.581
X_{Gln}	0.86										
X_{Jd}			0.33	0.15							
X_{Wo}					0.46	0.30					
X_{En}					0.44	0.45					
X_{Fs}					0.10	0.25					
X_{Q}			0.48	0.62							
X_{Ae}			0.19	0.24							
X_{Ps}									0.09	0.82	
X_{An}							0.00	1.00			
X_{Ab}							1.00	0.00			
X_{Mg}	0.72	0.83	0.78	0.87	0.81	0.65					

Table 2.2.2 chemical analyses of the samples with HP-LT paragenesis

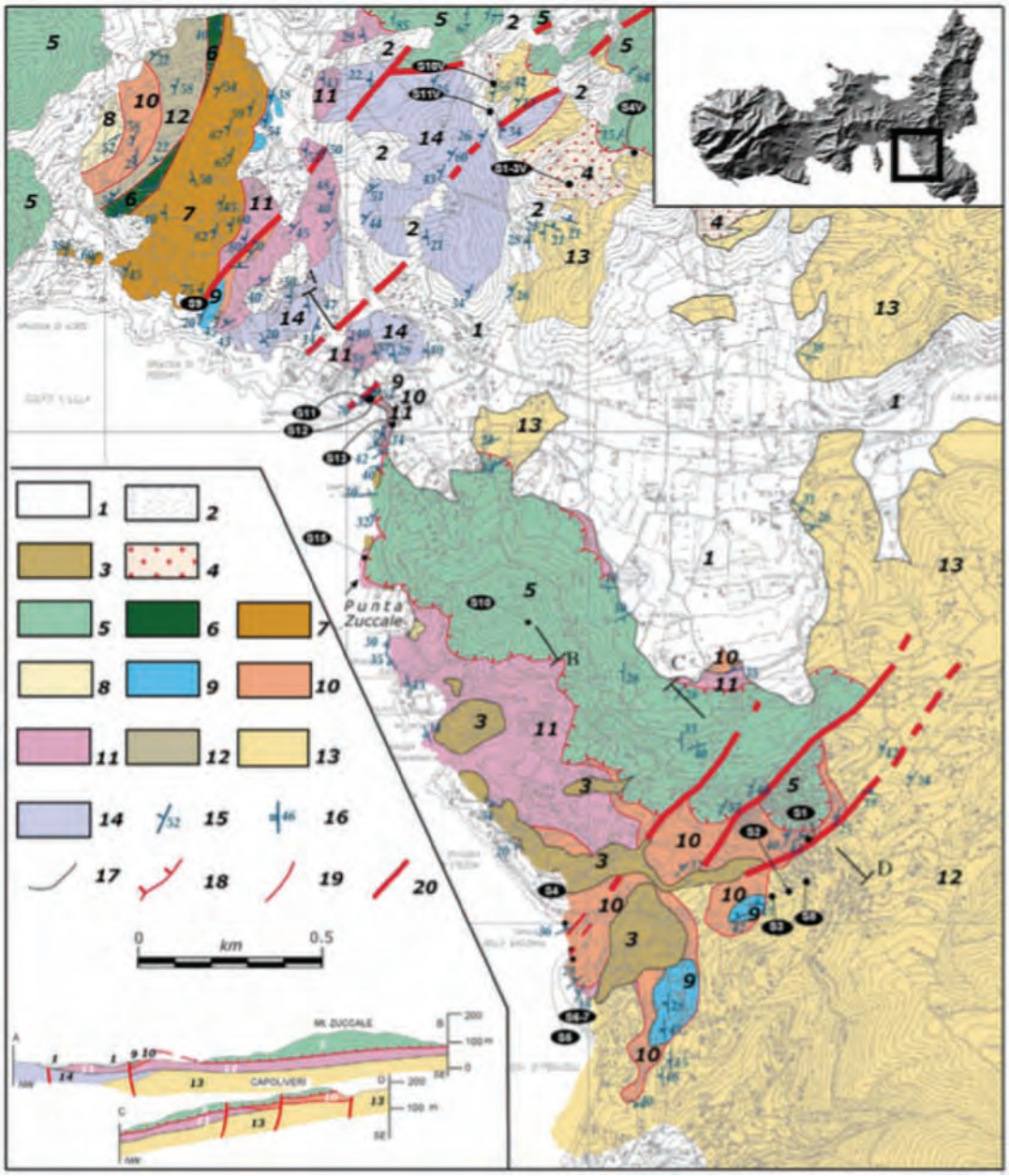

Figure 2.2.4 – Geological map and cross sections of the Capoliveri area and surroundings. 1. Alluvial and beach deposits (Holocene); 2. Debris (Holocene); 3. Eolian sandstone (Pleistocene); 4. Porto Azzurro monzogranite; Ligurian Units: 5. terrigeneous and calcareous sediments (late Cretaceous); 6 and 7. Acquadolce Unit: ophiolite and serpentine (Jurassic) and metasiltite and phyllite with quartz vein (Cretaceous), respectively; 8. Grassera Fm: marly limestone and claystone (Cretaceous); TuscanMetamorphic Complex: 9. Valdana Fm.: whitish massivemarble (early Jurassic); 10. Tocchi Fm. yellowish dolostone; 11. Barabarca Fm: quartz metaconglomerate and interlayered phyllite (early–middle Triassic); 12. Rio Marina Fm. graphitic phyllite and metaconglomerate (late Carboniferous - early Permian); 13.Mt. Calamita Fm: Qtz+Mu+Bt+And+K-feldsparmicaschist (early Carboniferous); 14.Ortano Fm: porphyroid and porphyric schist (middle Ordovician); 15. bedding attitude; 16. main schistosity attitude; 17. stratigraphic contact; 18. Zuccale normal fault; 19. low angle fault; 20. high angle fault.

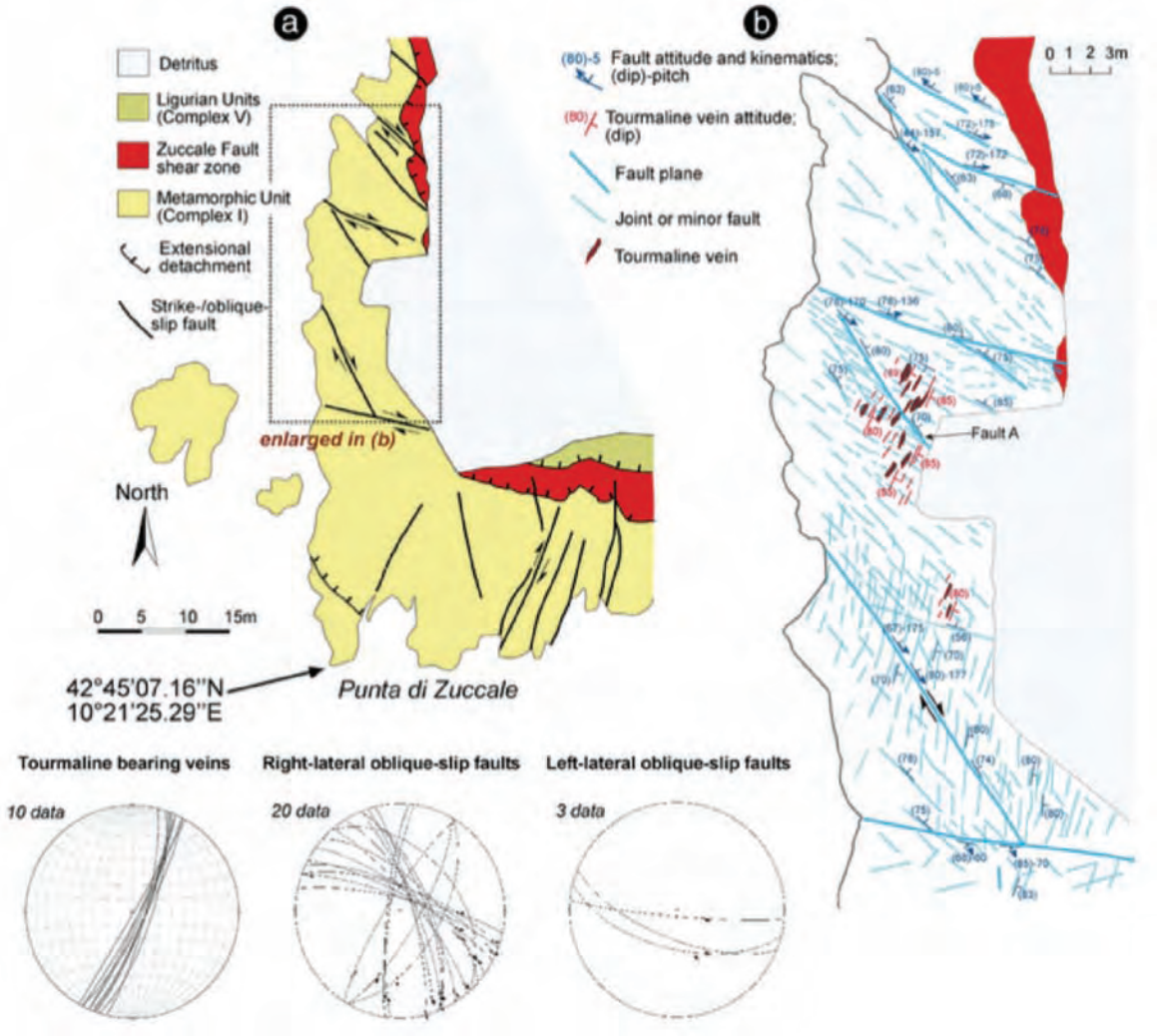

Fig. 2.2.5 – Structural sketch of the Punta Zuccale area (location in Fig. 3): (a) main brittle structures affecting the footwall and the shear zone of the Zuccale fault; (b) relationships among tourmaline bearing veins, transtensional faults and their associated minor fractures. Structural and kinematic data are plotted in stereographic diagrams, lower emisphere, equiareal projection.

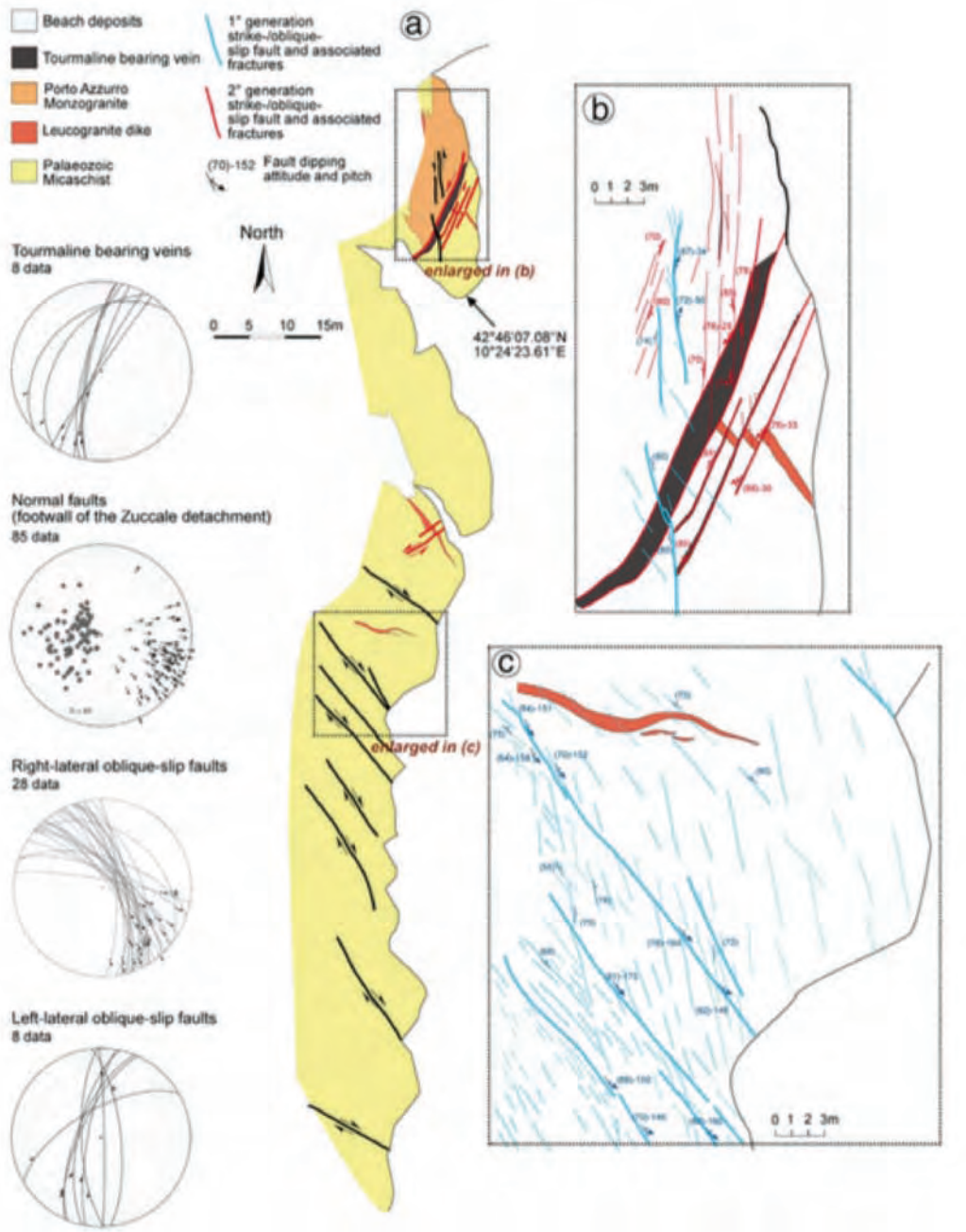

Fig. 2.2.6 – Structural sketch of the Barbarossa western coast (location in Fig. 2). (a) Main brittle structures affecting the footwall of the Zuccale fault. (b) Relationships between tourmaline bearing faults with their associated minor structures and leucogranite dike. (c) Detailed sketch illustrating the geometric and kinematic features of the transtensional faults. Structural and kinematic data are plotted in stereographic diagrams, lower emisphere.

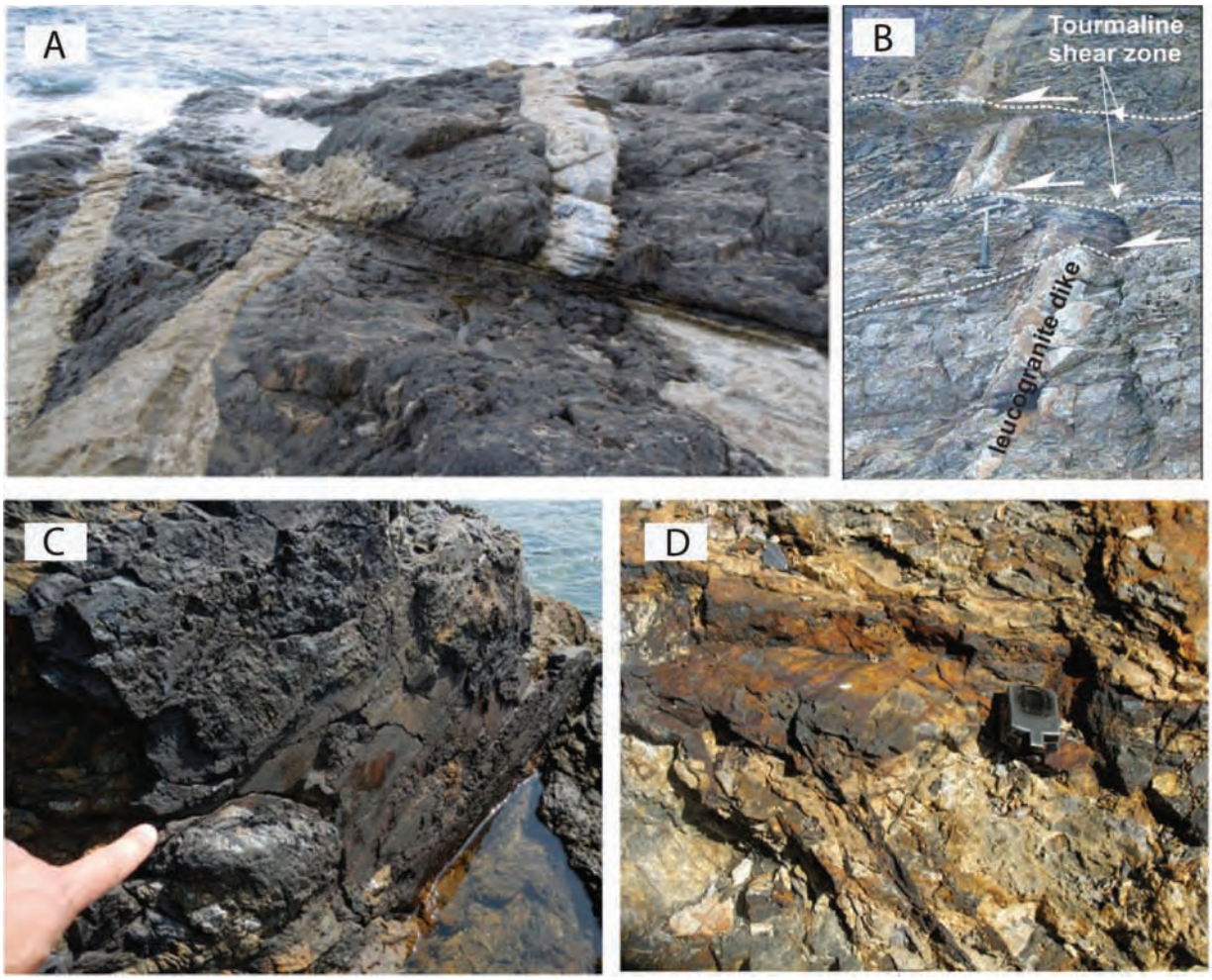

Fig. 2.2.7 – (A) low-angle fault with tourmaline and quartz shear vein; (B) vertical shear zone with quartz and tourmaline shear veins; (C) vertical fault-slip surface with hematite shear vein; (D) low-angle fault slip plane with hematite shear vein.

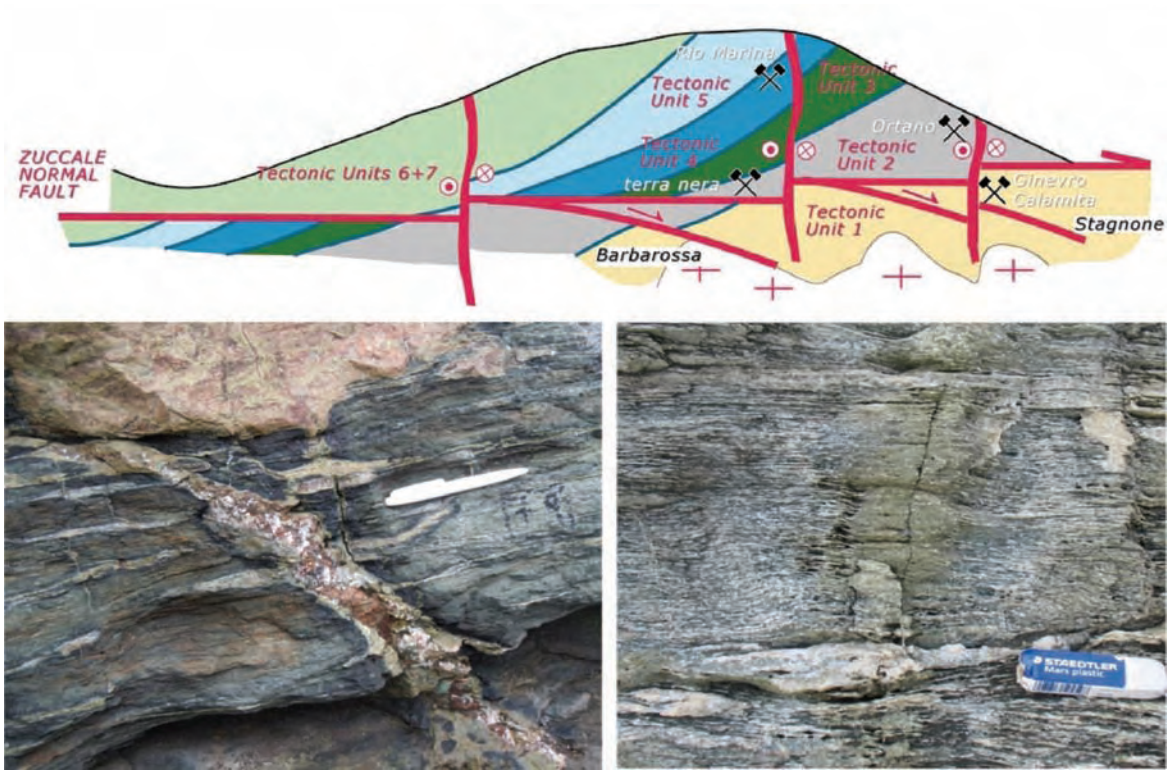

Fig. 2.2.8 – top: conceptual model of the relationships between vertical and low-anlge faults in the eastern Elba Island; bottom left: extensional veind filled up with hydrothermal quartz and relationships with pre-existing foliation; bottom right: vertical vein filled up of epidote and relationships with pre-existing foliation.

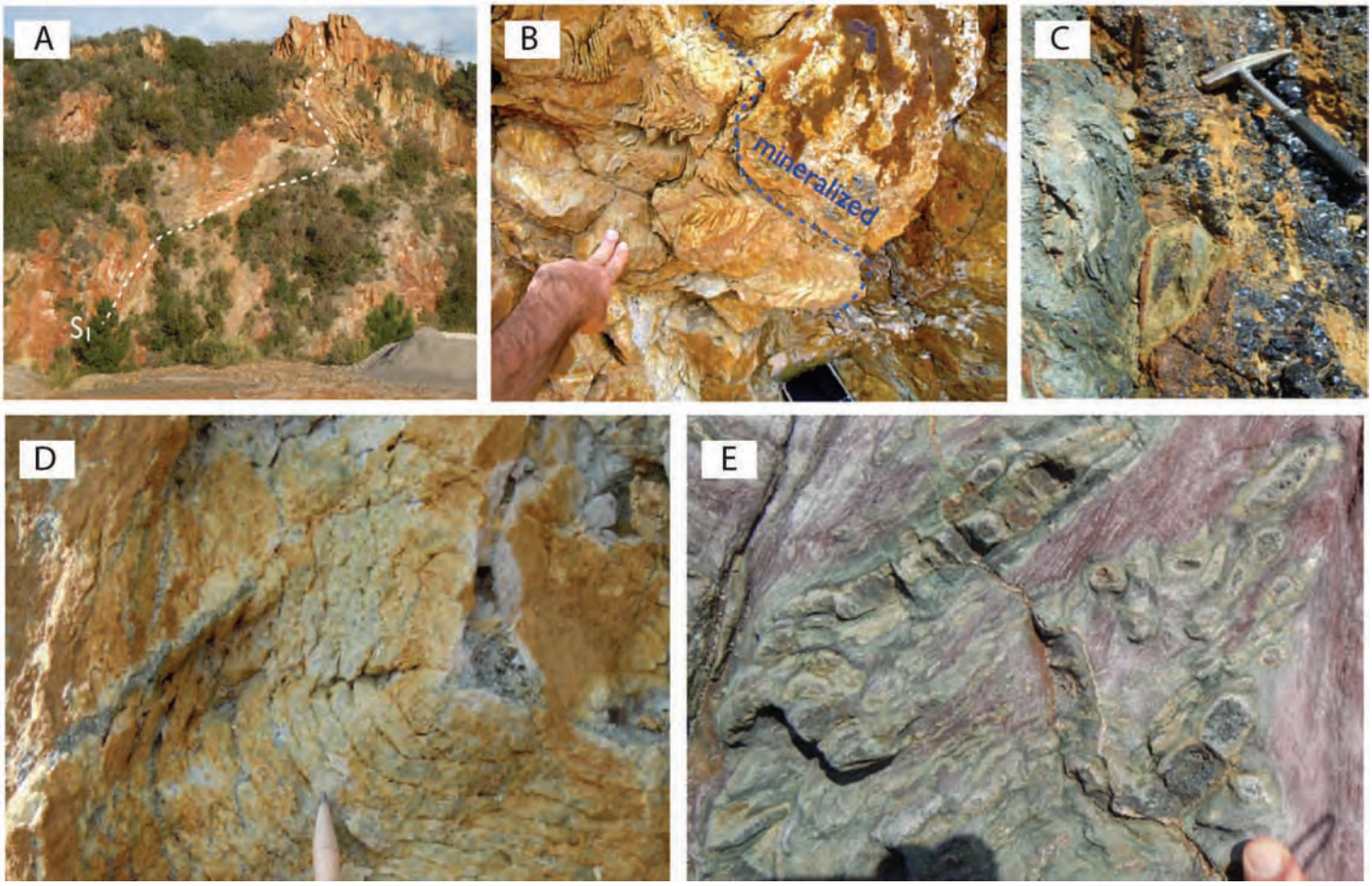

Fig. 2.2.9 – (A) folds developed during the collisional event of the inner northern Apennines; S1 indicates the main schistosity.(B) deformation controls the geometry of the geological bodies and of ore-deposits. (D) pre-existing foliation controls the fluid flow; (E) contrast of permeability is a major factor for fluid flow in the Elba Island exhumed geothermal system.

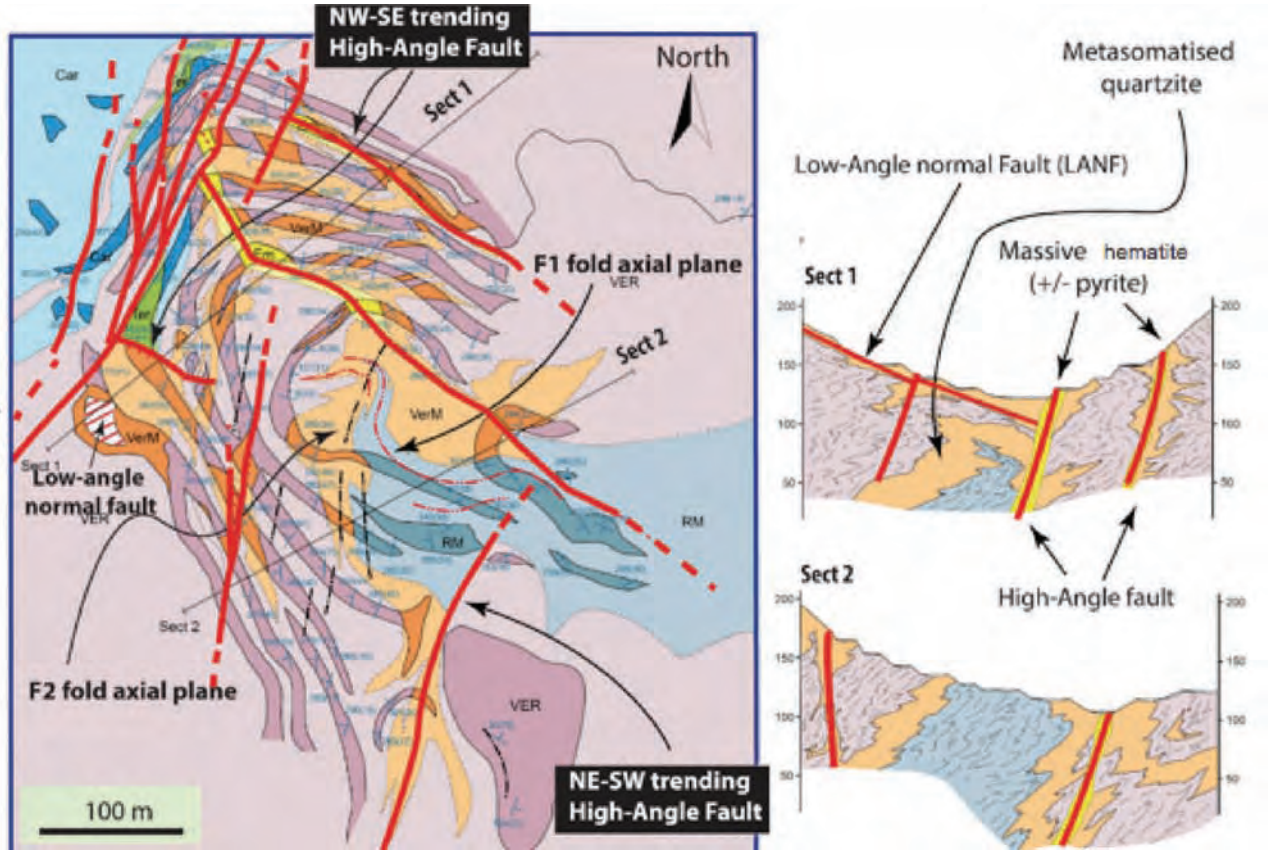

Fig. 2.2.10 – geological map and cross section of the ore-deposits in Valle Giove area. It is illustrated how the geometry of the mineralized bodies is controlled by the orogenetic folds.

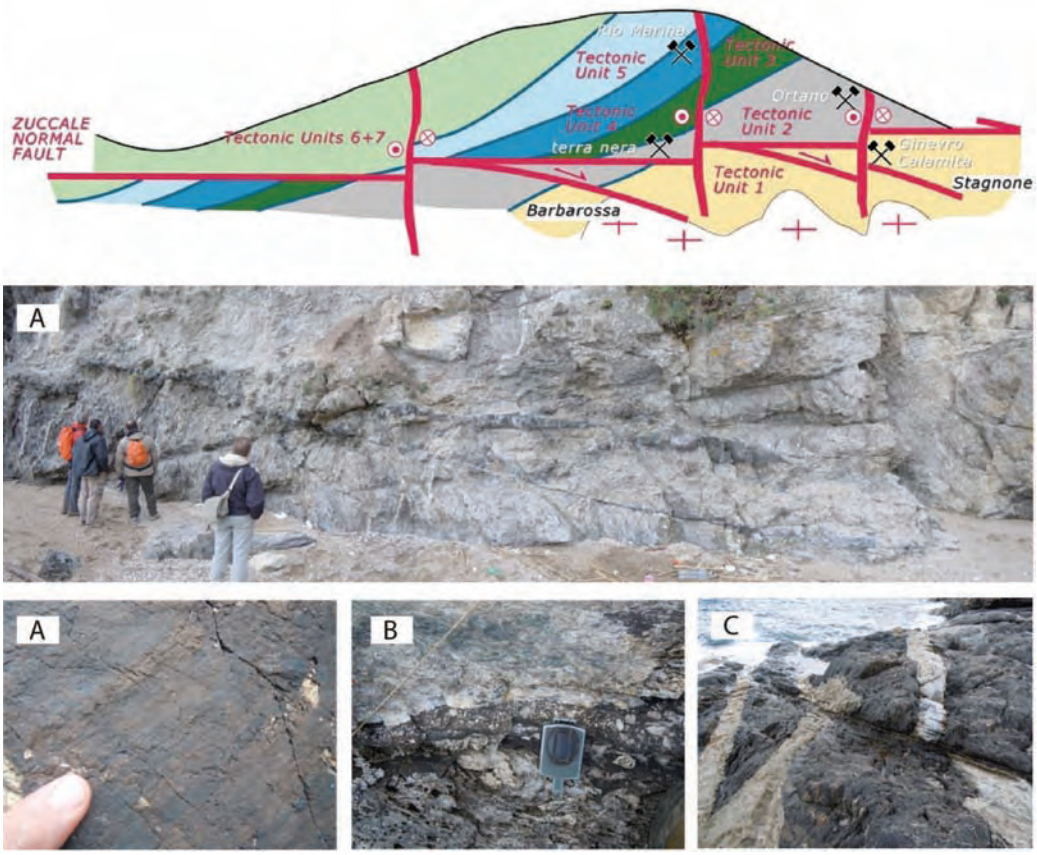

Fig. 2.2.11 – Top: conceptual model of the eastern Elba Island where the Stagnone area is indicated. This is the structural location of the deeper study structural level, within the paleozoic micaschist. Here the permeability is controlled by shear fractures with lozenge shape geometry (A), only. The fault zone shows hydraulic breccias (B) and low-angle attitudes (C)

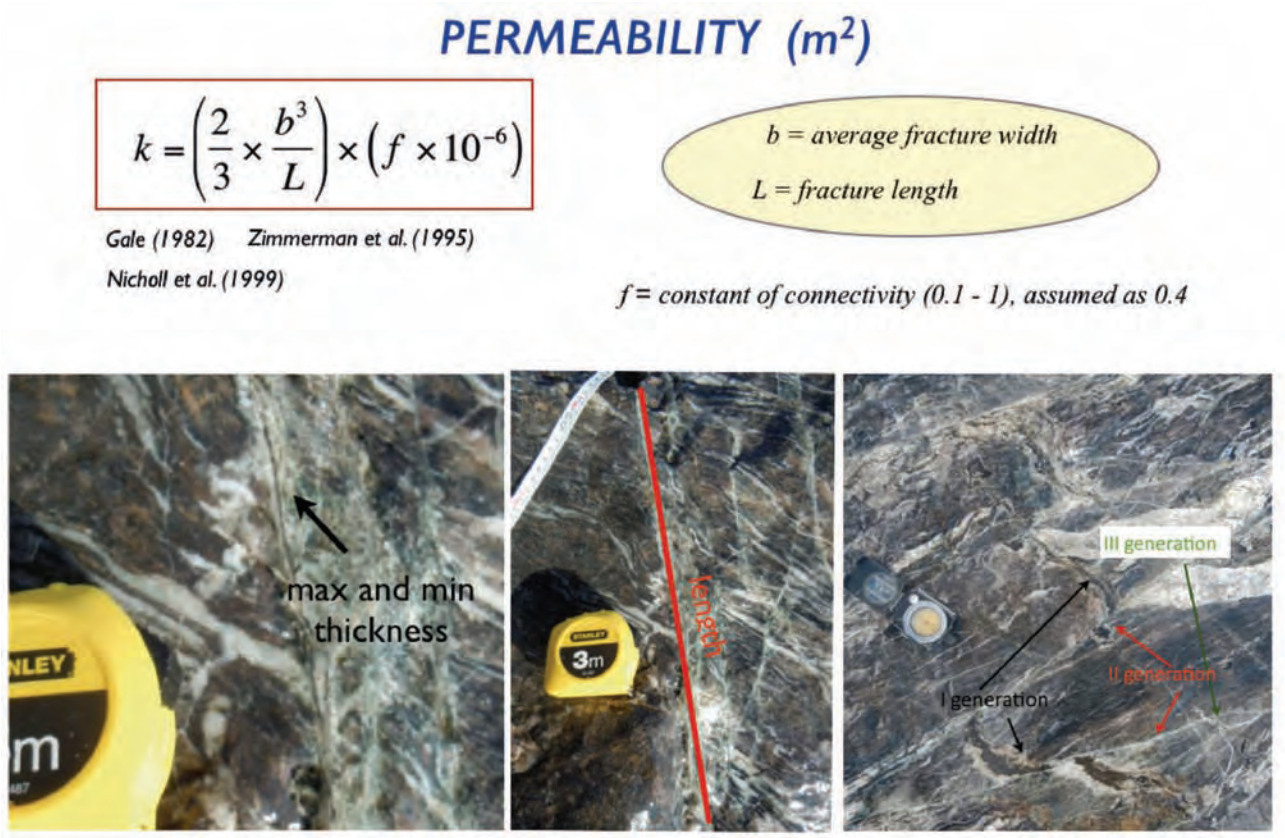

Fig. 2.2.12 – the computation of permeability is based on the equation here reported. The photos illustrate the parameters that have boeen collected in the field for the recognized different generation of fractures.

Table 2.2.3 – data collected for the computation of the permeability value

CROSS-SECTION	n. SCAN BOX	FAULT GENERATION	n. FRACTURES	DISTANCE m		average DISTANCE m	min WIDTH m	max WIDTH m	average WIDTH m (b)	LENGTH m (L)	tot. LENGTH m	SCAN BOX AREA m^2	b/L	F	K	1/K	ARITHMETIC AVERAGE	HARMONIC AVERAGE
A	1	III	1	0.5	0.9		0.0001	0.0015	0.0008	0.105			0,007619048	0,4	1,30032E-15	7,69043E+14		
			2	0.5	0.9		0.0005	0.001	0.00075	0.035			0,021428571	0,4	3,21429E-15	3,11111E+14		
			3	0.5	0.9		0.0005	0.001	0.00075	0.048			0,015625	0,4	2,34375E-15	4,26667E+14		
			4	0.5	0.9		0.0001	0.002	0.00105	0.065			0,016153846	0,4	4,74923E-15	2,1056E+14		
			5	0.5	0.9	**0.7**	0.0001	0.0002	0.00015	0.112	0.365	0.16	0,001339286	0,4	8,03571E-18	1,24444E+17		
																2,52324E+16	2,32312E-15	**3,96316E-17**
	2	III	1	1.5	1.9		0.0002	0.0005	0.00035	0.022			0,015909091	0,4	5,19697E-16	1,9242E+15		
			2	1.5	1.9		0.0005	0.002	0.00125	0.06			0,020833333	0,4	8,68056E-15	1,152E+14		
			3	1.5	1.9		0.0001	0.0005	0.0003	0.048			0,00625	0,4	1,5E-16	6,66667E+15		
			4	1.5	1.9		0.0002	0.001	0.0006	0.05			0,012	0,4	1,152E-15	8,68056E+14		
			5	1.5	1.9		0.0003	0.002	0.00115	0.082			0,01402439	0,4	4,94593E-15	2,02186E+14		
			6	1.5	1.9		0.0002	0.0008	0.0005	0.042			0,011904762	0,4	7,93651E-16	1,26E+15		
			7	1.5	1.9		0.0002	0.0005	0.00035	0.077			0,004545455	0,4	1,48485E-16	6,73469E+15		
			8	1.5	1.9		0.0001	0.0005	0.0003	0.07			0,004285714	0,4	1,02857E-16	9,72222E+15		
			9	1.5	1.9		0.0001	0.0002	0.00015	0.175			0,000857143	0,4	5,14286E-18	1,94444E+17		
			10	1.5	1.9		0.0005	0.001	0.00075	0.038			0,019736842	0,4	2,96053E-15	3,37778E+14		
			11	1.5	1.9		0.0001	0.0002	0.00015	0.024			0,00625	0,4	3,75E-17	2,66667E+16		
			12	1.5	1.9		0.0001	0.0002	0.00015	0.045			0,003333333	0,4	2E-17	5E+16		
			13	1.5	1.9		0.0001	0.0002	0.00015	0.038			0,003947368	0,4	2,36842E-17	4,22222E+16		
			14	1.5	1.9		0.0001	0.0002	0.00015	0.085			0,001764706	0,4	1,05882E-17	9,44444E+16		
			15	1.5	1.9	**1.7**	0.0001	0.0002	0.00015	0.12	0.976	0.16	0,00125	0,4	7,5E-18	1,33333E+17		
																3,79295E+16	1,30387E-15	**2,63647E-17**
	3	I	1	2.5	2.9		0.0003	0.0015	0.0009	0.058			0,015517241	0,4	3,35172E-15	2,98354E+14		
			2	2.5	2.9		0.0003	0.002	0.00115	0.028			0,041071429	0,4	1,44845E-14	6,90392E+13		
			3	2.5	2.9		0.0005	0.002	0.00125	0.234			0,00534188	0,4	2,22578E-15	4,4928E+14		
			4	2.5	2.9	**2.7**	0.0005	0.0045	0.0025	0.188	0.508	0.16	0,013297872	0,4	2,21631E-14	4,512E+13		
																2,15448E+14	1,05563E-14	**4,64149E-15**
		III	1	2.5	2.9		0.0001	0.002	0.00105	0.065			0,016153846	0,4	4,74923E-15	2,1056E+14		
			2	2.5	2.9	**2.7**	0.0002	0.002	0.0011	0.038	0.103	0.16	0,028947368	0,4	9,34035E-15	1,07062E+14		
																1,58811E+14	7,04479E-15	**6,29678E-15**
	4	III	1	3.5	3.9	**3.7**	0.0001	0.0002	0.00015	0.232	0.232	0.16	0,000646552	0,4	3,87931E-18	2,57778E+17		
																2,57778E+17	3,87931E-18	**3,87931E-18**
																		3,87931E-18
	5	I	1	4.5	4.9		0.0003	0.003	0.00165	0.04			0,04125	0,4	2,99475E-14	3,33918E+13		
			2	4.5	4.9		0.0005	0.003	0.00175	0.08			0,021875	0,4	1,78646E-14	5,59767E+13		
			3	4.5	4.9		0.0003	0.002	0.00115	0.07			0,016428571	0,4	5,79381E-15	1,72598E+14		
			4	4.5	4.9		0.0003	0.004	0.00215	0.185			0,011621622	0,4	1,43256E-14	6,98052E+13		
			5	4.5	4.9		0.0002	0.002	0.0011	0.073			0,015068493	0,4	4,8621E-15	2,05672E+14		
			6	4.5	4.9	**4.7**	0.0005	0.0025	0.0015	0.075	0.523	0.16	0,02	0,4	1,2E-14	8,33333E+13		
				4.5	4.9											1,03463E+14	1,41323E-14	**9,6653E-15**
		II	1	4.5	4.9	**4.7**	0.0002	0.002	0.0011	0.205	0.205	0.16	0,005365854	0,4	1,73138E-15	5,77573E+14		
														0,4		5,77573E+14	1,73138E-15	**1,73138E-15**
		III	1	4.5	4.9		0.0005	0.002	0.00125	0.215			0,005813953	0,4	2,42248E-15	4,128E+14		
			2	4.5	4.9		0.0002	0.005	0.0026	0.14			0,018571429	0,4	3,34781E-14	2,98703E+13		
			3	4.5	4.9	**4.7**	0.0005	0.004	0.00225	0.268	0.623	0.16	0,008395522	0,4	1,1334E-14	8,82305E+13		
																1,76967E+14	1,57448E-14	**5,65077E-15**
	6	I	1	5.5	5.9	**5.7**	0.0015	0.004	0.00275	0.192	0.192	0.16	0,014322917	0,4	2,88845E-14	3,46206E+13		
																3,46206E+13	2,88845E-14	**2,88845E-14**
		III	1	5.5	5.9		0.0001	0.0002	0.00015	0.046			0,00326087	0,4	1,95652E-17	5,11111E+16		
			2	5.5	5.9		0.0001	0.0015	0.0008	0.026			0,030769231	0,4	5,25128E-15	1,9043E+14		
			3	5.5	5.9	**5.7**	0.0005	0.002	0.00125	0.13	0.202	0.16	0,009615385	0,4	4,00641E-15	2,496E+14		
																1,71837E+16	3,09242E-15	**5,81946E-17**
	7	III	1	6.5	6.9		0.0002	0.005	0.0026	0.065			0,04	0,4	7,21067E-14	1,38683E+13		
			2	6.5	6.9		0.0005	0.003	0.00175	0.35			0,005	0,4	4,08333E-15	2,44898E+14		
			3	6.5	6.9		0.0002	0.003	0.0016	0.22			0,007272727	0,4	4,96485E-15	2,01416E+14		
			4	6.5	6.9		0.0001	0.001	0.00055	0.05			0,011	0,4	8,87333E-16	1,12697E+15		
			5	6.5	6.9	**6.7**	0.0002	0.001	0.0006	0.035	0.72	0.16	0,017142857	0,4	1,64571E-15	6,07639E+14		
																4,38959E+14	1,67376E-14	**2,27812E-15**

	8	I	1	7.5	7.9		0.001	0.004	0.0025	0.038			0,065789474	0,4	1,09649E-13	9,12E+12		
			2	7.5	7.9		0.0002	0.0065	0.00335	0.14			0,023928571	0,4	7,16102E-14	1,39645E+13		
			3	7.5	7.9		0.0005	0.0025	0.0015	0.08			0,01875	0,4	1,125E-14	8,88889E+13		
			4	7.5	7.9		0.0001	0.0055	0.0028	0.184			0,015217391	0,4	3,18145E-14	3,14322E+13		
			5	7.5	7.9	**7.7**	0.0002	0.0065	0.00335	0.16	0.602	0.16	0,0209375	0,4	6,2659E-14	1,59594E+13		
																3,1873E+13	5,73966E-14	**3,13745E-14**
		III	1	7.5	7.9		0.0005	0.0015	0.001	0.078			0,012820513	0,4	3,4188E-15	2,925E+14		
			2	7.5	7.9	**7.7**	0.0001	0.002	0.00105	0.27	0.348	0.16	0,003888889	0,4	1,14333E-15	8,74636E+14		
																5,83568E+14	2,28107E-15	**1,7136E-15**
	9	I	1	8.5	8.9		0.0002	0.0035	0.00185	0.138			0,013405797	0,4	1,2235E-14	8,17326E+13		
			2	8.5	8.9		0.001	0.004	0.0025	0.28			0,008928571	0,4	1,4881E-14	6,72E+13		
			3	8.5	8.9		0.001	0.0035	0.00225	0.084			0,026785714	0,4	3,61607E-14	2,76543E+13		
			4	8.5	8.9	**8.7**	0.001	0.0045	0.00275	0.08	0.582	0.16	0,034375	0,4	6,93229E-14	1,44252E+13		
																4,7753E+13	3,31499E-14	**2,09411E-14**
		III	1	8.5	8.9	**8.7**	0.0001	0.0005	0.0003	0.038	0.038	0.16	0,007894737	0,4	1,89474E-16	5,27778E+15		
																5,27778E+15	1,89474E-16	**1,89474E-16**
	10	I	1	9.5	9.9		0.0005	0.005	0.00275	0.2			0,01375	0,4	2,77292E-14	3,60631E+13		
			2	9.5	9.9		0.002	0.012	0.007	0.125			0,056	0,4	7,31733E-13	1,36662E+12		
			3	9.5	9.9		0.0005	0.014	0.00725	0.041			0,176829268	0,4	2,47856E-12	4,03461E+11		
			4	9.5	9.9		0.002	0.0075	0.00475	0.405			0,011728395	0,4	7,05658E-14	1,41712E+13		
			5	9.5	9.9		0.0015	0.015	0.00825	0.11			0,075	0,4	1,36125E-12	7,34619E+11		
			6	9.5	9.9		0.005	0.016	0.0105	0.165			0,063636364	0,4	1,87091E-12	5,345E+11		
			7	9.5	9.9		0.003	0.018	0.0105	0.04			0,2625	0,4	7,7175E-12	1,29576E+11		
			8	9.5	9.9		0.002	0.0055	0.00375	0.09			0,041666667	0,4	1,5625E-13	6,4E+12		
			9	9.5	9.9		0.003	0.004	0.0035	0.045			0,077777778	0,4	2,54074E-13	3,93586E+12		
			10	9.5	9.9		0.002	0.015	0.0085	0.108			0,078703704	0,4	1,51636E-12	6,59475E+11		
			11	9.5	9.9		0.0015	0.003	0.00225	0.068			0,033088235	0,4	4,46691E-14	2,23868E+13		
			12	9.5	9.9		0.001	0.0025	0.00175	0.12			0,014583333	0,4	1,19097E-14	8,3965E+13		
			13	9.5	9.9	**9.7**	0.004	0.037	0.0205	0.4	1.917	0.16	0,05125	0,4	5,74342E-12	1,74112E+11		
																1,3148E+13	1,69115E-12	**7,6057E-14**
		III	1	9.5	9.9		0.0002	0.001	0.0006	0.152			0,003947368	0,4	3,78947E-16	2,63889E+15		
			2	9.5	9.9	**9.7**	0.0001	0.0002	0.00015	0.094	0.246	0.16	0,001595745	0,4	9,57447E-18	1,04444E+17		
																5,35417E+16	1,94261E-16	**1,8677E-17**
	11	I	1	10.5	10.9		0.002	0.015	0.0085	0.148			0,057432432	0,4	1,10653E-12	9,03725E+11		
			2	10.5	10.9		0.002	0.012	0.007	0.11			0,063636364	0,4	8,31515E-13	1,20262E+12		
			3	10.5	10.9		0.002	0.0055	0.00375	0.175			0,021428571	0,4	8,03571E-14	1,24444E+13		
			4	10.5	10.9		0.0005	0.007	0.00375	0.14			0,026785714	0,4	1,00446E-13	9,95556E+12		
			5	10.5	10.9	**10.7**	0.001	0.005	0.003	0.052	0.625	0.16	0,057692308	0,4	1,38462E-13	7,22222E+12		
																6,34571E+12	4,51462E-13	**1,57587E-13**
		III	1	10.5	10.9		0.0005	0.003	0.00175	0.41			0,004268293	0,4	3,48577E-15	2,8688E+14		
			2	10.5	10.9		0.0003	0.002	0.00115	0.07			0,016428571	0,4	5,79381E-15	1,72598E+14		
			3	10.5	10.9		0.0002	0.001	0.0006	0.152			0,003947368	0,4	3,78947E-16	2,63889E+15		
			4	10.5	10.9		0.0001	0.0002	0.00015	0.038			0,003947368	0,4	2,36842E-17	4,22222E+16		
			5	10.5	10.9		0.0001	0.0002	0.00015	0.078			0,001923077	0,4	1,15385E-17	8,66667E+16		
			6	10.5	10.9		0.0001	0.0002	0.00015	0.02			0,0075	0,4	4,5E-17	2,22222E+16		
			7	10.5	10.9		0.0003	0.0015	0.0009	0.045			0,02	0,4	4,32E-15	2,31481E+14		
			8	10.5	10.9		0.0002	0.0035	0.00185	0.215			0,008604651	0,4	7,85318E-15	1,27337E+14		
			9	10.5	10.9		0.0005	0.0023	0.0014	0.248			0,005645161	0,4	2,95054E-15	3,38921E+14		
			10	10.5	10.9		0.0001	0.0002	0.00015	0.091			0,001648352	0,4	9,89011E-18	1,01111E+17		
			11	10.5	10.9		0.0001	0.0002	0.00015	0.057			0,002631579	0,4	1,57895E-17	6,33333E+16		
			12	10.5	10.9	**10.7**	0.0005	0.0023	0.0014	0.115	1.539	0.16	0,012173913	0,4	6,3629E-15	1,57161E+14		
																2,66257E+16	2,60425E-15	**3,75576E-17**
B	1	I	1	0.8	1.2	1	0.017	0.032	0.0245	0.396	0.396	0.16						
													0,061868687	0,4	9,90311E-12	1,00978E+11		
		III	1	0.8	1.2		0.0001	0.0005	0.0003	0.085						1,00978E+11	9,90311E-12	**9,90311E-12**
			2	0.8	1.2		0.0001	0.0002	0.00015	0.048			0,003529412	0,4	8,47059E-17	1,18056E+16		
			3	0.8	1.2		0.0001	0.0005	0.0003	0.081			0,003125	0,4	1,875E-17	5,33333E+16		
			4	0.8	1.2	1	0.0001	0.0002	0.00015	0.028	0.242	0.16	0,003703704	0,4	8,88889E-17	1,125E+16		
													0,005357143	0,4	3,21429E-17	3,11111E+16		
																2,6875E+16	5,61219E-17	**3,72093E-17**

	2	III	1	1.8	2.2		0.0002	0.0005	0.00035	0.135								
			2	1.8	2.2		0.0001	0.0002	0.00015	0.04			0,002592593	0,4	8,46914E-17	1,18076E+16		
			3	1.8	2.2		0.0001	0.0005	0.0003	0.062			0,00375	0,4	2,25E-17	4,44444E+16		
			4	1.8	2.2	2	0.0001	0.0002	0.00015	0.07	0.307	0.16	0,00483871	0,4	1,16129E-16	8,61111E+15		
													0,002142857	0,4	1,28571E-17	7,77778E+16		
																3,56602E+16	5,90444E-17	**2,80424E-17**
	4	I	1	3.8	4.2		0.002	0.004	0.003	0.034								
			2	3.8	4.2		0.005	0.023	0.014	0.078			0,088235294	0,4	2,11765E-13	4,72222E+12		
			3	3.8	4.2		0.002	0.012	0.007	0.075			0,179487179	0,4	9,3812E-12	1,06596E+11		
			4	3.8	4.2		0.005	0.009	0.007	0.088			0,093333333	0,4	1,21956E-12	8,19971E+11		
			5	3.8	4.2		0.004	0.04	0.022	0.34			0,079545455	0,4	1,03939E-12	9,62099E+11		
			6	3.8	4.2		0.001	0.005	0.003	0.184			0,064705882	0,4	8,35137E-12	1,19741E+11		
			7	3.8	4.2		0.0015	0.005	0.00325	0.074			0,016304348	0,4	3,91304E-14	2,55556E+13		
			8	3.8	4.2	4	0.0015	0.01	0.00575	0.205	1.078	0.16	0,043918919	0	1,23705E-13	8,08375E+12		
													0,02804878	0,4	2,47297E-13	4,04372E+12		
																5,55171E+12	2,57668E-12	**1,80125E-13**
	5	I	1	4.8	5.2		0.0002	0.001	0.0006	0.115								
			2	4.8	5.2		0.002	0.007	0.0045	0.07			0,005217391	0,4	5,0087E-16	1,99653E+15		
			3	4.8	5.2		0.002	0.01	0.006	0.18			0,064285714	0,4	3,47143E-13	2,88066E+12		
			4	4.8	5.2		0.0002	0.005	0.0026	0.088			0,033333333	0,4	3,2E-13	3,125E+12		
			5	4.8	5.2		0.003	0.01	0.0065	0.08			0,029545455	0,4	5,32606E-14	1,87756E+13		
			6	4.8	5.2	5	0.003	0.011	0.007	0.105	0.638	0.16	0,08125	0,4	9,15417E-13	1,0924E+12		
													0,066666667	0,4	8,71111E-13	1,14796E+12		
																3,37258E+14	4,17905E-13	**2,96509E-15**
	8	I	1	7.8	8.2		0.0002	0.0003	0.00025	0.074								
			2	7.8	8.2		0.0004	0.0008	0.0006	0.05			0,003378378	0,4	5,63063E-17	1,776E+16		
			3	7.8	8.2		0.0002	0.0003	0.00025	0.052			0,012	0,4	1,152E-15	8,68056E+14		
			4	7.8	8.2		0.0002	0.0035	0.00185	0.14			0,004807692	0,4	8,01282E-17	1,248E+16		
			5	7.8	8.2		0.0002	0.001	0.0006	0.32			0,013214286	0,4	1,20602E-14	8,29171E+13		
			6	7.8	8.2		0.0005	0.001	0.00075	0.065			0,001875	0,4	1,8E-16	5,55556E+15		
			7	7.8	8.2		0.0002	0.0015	0.00085	0.18			0,011538462	0,4	1,73077E-15	5,77778E+14		
			8	7.8	8.2		0.001	0.005	0.003	0.355			0,004722222	0,4	9,09815E-16	1,09912E+15		
			9	7.8	8.2		0.0002	0.0003	0.00025	0.125			0,008450704	0,4	2,02817E-14	4,93056E+13		
			10	7.8	8.2		0.0005	0.003	0.00175	0.11			0,002	0,4	3,33333E-17	3E+16		
			11	7.8	8.2		0.001	0.008	0.0045	0.11			0,015909091	0,4	1,29924E-14	7,69679E+13		
			12	7.8	8.2	8	0.0002	0.017	0.0086	0.28	1.861	0.16	0,040909091	0	2,20909E-13	4,52675E+12		
													0,030714286	0,4	6,05768E-13	1,6508E+12		
		III	1	7.8	8.2		0.0002	0.001	0.0006	0.063						5,71299E+15	7,30128E-14	**1,7504E-16**
			2	7.8	8.2		0.0001	0.0005	0.0003	0.045			0,00952381	0,4	9,14286E-16	1,09375E+15		
			3	7.8	8.2		0.0002	0.001	0.0006	0.075			0,006666667	0,4	1,6E-16	6,25E+15		
			4	7.8	8.2		0.0003	0.0015	0.0009	0.194			0,008	0,4	7,68E-16	1,30208E+15		
			5	7.8	8.2	8	0.0002	0.0008	0.0005	0.058	0.435	0.16	0,004639175	0,4	1,00206E-15	9,97942E+14		
													0,00862069	0,4	5,74713E-16	1,74E+15		
																2,27676E+15	6,83812E-16	**4,39222E-16**

	9	I	1	8.8	9.2	9	0.0005	0.002	0.00125	0.274	0.274	0.16	0,004562044	0,4	1,90085E-15	5,2608E+14		
																5,2608E+14	1,90085E-15	**1,90085E-15**
		III	1	8.8	9.2		0.0008	0.002	0.0014	0.065			0,021538462	0,4	1,12574E-14	8,88302E+13		
			2	8.8	9.2		0.0002	0.002	0.0011	0.178			0,006179775	0,4	1,99401E-15	5,01503E+14		
			3	8.8	9.2		0.0002	0.0015	0.00085	0.105			0,008095238	0,4	1,55968E-15	6,41156E+14		
			4	8.8	9.2	9	0.0005	0.001	0.00075	0.084	0.432	0.16	0,008928571	0,4	1,33929E-15	7,46667E+14		
																4,94539E+14	4,0376E-15	**2,02209E-15**
	10	III	1	9.8	10.2		0.0001	0.0002	0.00015	0.12			0,00125	0,4	7,5E-18	1,33333E+17		
			2	9.8	10.2	10	0.0001	0.001	0.00055	0.14	0.26	0.16	0,003928571	0,4	3,16905E-16	3,15552E+15		
																6,82444E+16	1,62202E-16	**1,46532E-17**
	11	III	1	10.8	11.2		0.0002	0.0015	0.00085	0.145			0,005862069	0,4	1,12943E-15	8,85406E+14		
			2	10.8	11.2		0.0002	0.0008	0.0005	0.07			0,007142857	0,4	4,7619E-16	2,1E+15		
			3	10.8	11.2		0.0005	0.0015	0.001	0.052			0,019230769	0,4	5,12821E-15	1,95E+14		
			4	10.8	11.2		0.0002	0.0008	0.0005	0.045			0,011111111	0,4	7,40741E-16	1,35E+15		
			5	10.8	11.2		0.0005	0.002	0.00125	0.098			0,012755102	0,4	5,31463E-15	1,8816E+14		
			6	10.8	11.2		0.0001	0.0002	0.00015	0.035			0,004285714	0,4	2,57143E-17	3,88889E+16		
			7	10.8	11.2	11	0.0001	0.0002	0.00015	0.115	0.56	0.16	0,001304348	0,4	7,82609E-18	1,27778E+17		
																2,44836E+16	1,83182E-15	**4,08437E-17**
C	1	I	1	0.5	0.9	0,7	0.0005	0.0055	0.003	0.378	0.378	0.16	0,007936508	0,4	1,90476E-14	5,25E+13		
																5,25E+13	1,90476E-14	**1,90476E-14**
	2	I	1	1.5	1.9		0.0015	0.0045	0.003	0.145			0,020689655	0,4	4,96552E-14	2,01389E+13		
			2	1.5	1.9		0.001	0.002	0.0015	0.115			0,013043478	0,4	7,82609E-15	1,27778E+14		
			3	1.5	1.9		0.0005	0.0023	0.0014	0.402			0,003482587	0,4	1,82023E-15	5,4938E+14		
			4	1.5	1.9		0.0005	0.0045	0.0025	0.372			0,00672043	0,4	1,12007E-14	8,928E+13		
			5	1.5	1.9		0.0008	0.005	0.0029	0.4			0,00725	0	1,62593E-14	6,15031E+13		
			6	1.5	1.9	1,7	0.0005	0.0023	0.0014	0.25	1.684	0.16	0,0056	0,4	2,92693E-15	3,41655E+14		
																1,98289E+14	1,49481E-14	**5,04314E-15**
		III	1	1.5	1.9		0.0002	0.001	0.0006	0.085			0,007058824	0,4	6,77647E-16	1,47569E+15		
			2	1.5	1.9		0.0001	0.0002	0.00015	0.068			0,002205882	0,4	1,32353E-17	7,55556E+16		
			3	1.5	1.9	1,7	0.0001	0.0002	0.00015	0.053	0.206	0.16	0,002830189	0,4	1,69811E-17	5,88889E+16		
																4,53067E+16	2,35954E-16	**2,20718E-17**
	3	I	1	2.5	2.9		0.0002	0.001	0.0006	0.05			0,012	0,4	1,152E-15	8,68056E+14		
			2	2.5	2.9		0.0001	0.0035	0.0018	0.225			0,008	0,4	6,912E-15	1,44676E+14		
			3	2.5	2.9		0.0002	0.001	0.0006	0.072			0,008333333	0,4	8E-16	1,25E+15		
			4	2.5	2.9		0.0002	0.0005	0.00035	0.042			0,008333333	0,4	2,72222E-16	3,67347E+15		
			5	2.5	2.9	2,7	0.0001	0.0018	0.00095	0.265	0.654	0.16	0,003584906	0,4	8,62767E-16	1,15906E+15		
																1,41905E+15	1,9998E-15	**7,04696E-16**

		III	1	2.5	2.9		0.0001	0.0002	0.00015	0.12			0,00125	0,4	7,5E-18	1,33333E+17		
			2	2.5	2.9		0.0002	0.0004	0.0003	0.035			0,008571429	0,4	2,05714E-16	4,86111E+15		
			3	2.5	2.9		0.0001	0.0002	0.00015	0.024			0,00625	0,4	3,75E-17	2,66667E+16		
			4	2.5	2.9		0.0001	0.0005	0.0003	0.03			0,01	0,4	2,4E-16	4,16667E+15		
			5	2.5	2.9		0.0002	0.0015	0.00085	0.123			0,006910569	0,4	1,33144E-15	7,51069E+14		
			6	2.5	2.9		0.0001	0.0002	0.00015	0.028			0,005357143	0,4	3,21429E-17	3,11111E+16		
			7	2.5	2.9		0.0001	0.001	0.00055	0.038			0,014473684	0,4	1,16754E-15	8,56499E+14		
			8	2.5	2.9		0.0001	0.001	0.00055	0.02			0,0275	0,4	2,21833E-15	4,50789E+14		
			9	2.5	2.9		0.0001	0.001	0.00055	0.015			0,036666667	0,4	2,95778E-15	3,38092E+14		
			10	2.5	2.9		0.0005	0.001	0.00075	0.04			0,01875	0,4	2,8125E-15	3,55556E+14		
			11	2.5	2.9		0.0005	0.0008	0.00065	0.027			0,024074074	0,4	2,71235E-15	3,68685E+14		
			12	2.5	2.9		0.0005	0.001	0.00075	0.058			0,012931034	0,4	1,93966E-15	5,15556E+14		
			13	2.5	2.9		0.0001	0.0002	0.00015	0.063			0,002380952	0,4	1,42857E-17	7E+16		
			14	2.5	2.9		0.0002	0.001	0.0006	0.052			0,011538462	0,4	1,10769E-15	9,02778E+14		
			15	2.5	2.9		0.0005	0.002	0.00125	0.11			0,011363636	0,4	4,73485E-15	2,112E+14		
			16	2.5	2.9		0.0003	0.002	0.00115	0.06			0,019166667	0,4	6,75944E-15	1,47941E+14		
			17	2.5	2.9		0.0003	0.002	0.00115	0.17			0,006764706	0,4	2,38569E-15	4,19167E+14		
			18	2.5	2.9		0.0005	0.0025	0.0015	0.21			0,007142857	0,4	4,28571E-15	2,33333E+14		
			19	2.5	2.9		0.0005	0.0008	0.00065	0.06			0,010833333	0,4	1,22056E-15	8,19299E+14		
			20	2.5	2.9		0.0002	0.002	0.0011	0.171			0,006432749	0,4	2,07563E-15	4,81781E+14		
			21	2.5	2.9		0.0001	0.0002	0.00015	0.068			0,002205882	0,4	1,32353E-17	7,55556E+16		
			22	2.5	2.9		0.0001	0.0002	0.00015	0.054			0,002777778	0	1,66667E-17	6E+16		
			23	2.5	2.9	2,7	0.0002	0.0015	0.00085	0.183	1.759	0.16	0,004644809	0,4	8,949E-16	1,11744E+15		
																1,79854E+16	1,70309E-15	**5,56007E-17**
	6	III	1	5.5	5.9		0.0002	0.0015	0.00085	0.33			0,002575758	0,4	4,96263E-16	2,01506E+15		
			2	5.5	5.9		0.0001	0.0005	0.0003	0.045			0,006666667	0,4	1,6E-16	6,25E+15		
			3	5.5	5.9		0.0003	0.001	0.00065	0.065			0,01	0,4	1,12667E-15	8,87574E+14		
			4	5.5	5.9	5,7	0.0002	0.003	0.0016	0.255	0.695	0.16	0,00627451	0,4	4,2834E-15	2,33459E+14		
																2,34652E+15	1,51658E-15	**4,26162E-16**
	7	II	1	6.5	6.9	6,7	0.008	0.012	0.01	0.386	0.386	0.16	0,025906736	0,4	6,90846E-13	1,4475E+12		
																1,4475E+12	6,90846E-13	**6,90846E-13**
		III	1	6.5	6.9		0.0001	0.0002	0.00015	0.02			0,0075	0,4	4,5E-17	2,22222E+16		
			2	6.5	6.9		0.0001	0.0002	0.00015	0.065			0,002307692	0,4	1,38462E-17	7,22222E+16		
			3	6.5	6.9		0.0001	0.0002	0.00015	0.04			0,00375	0,4	2,25E-17	4,44444E+16		
			4	6.5	6.9		0.0002	0.0005	0.00035	0.03			0,011666667	0,4	3,81111E-16	2,62391E+15		
			5	6.5	6.9		0.0004	0.002	0.0012	0.21			0,005714286	0,4	2,19429E-15	4,55729E+14		
			6	6.5	6.9		0.0001	0.0002	0.00015	0.064			0,00234375	0,4	1,40625E-17	7,11111E+16		
			7	6.5	6.9		0.0004	0.0015	0.00095	0.135			0,007037037	0,4	1,69358E-15	5,90465E+14		
			8	6.5	6.9		0.0002	0.001	0.0006	0.055			0,010909091	0,4	1,04727E-15	9,54861E+14		
			9	6.5	6.9	6,7	0.0005	0.002	0.00125	0.115	0.734	0.16	0,010869565	0,4	4,52899E-15	2,208E+14		
																2,38718E+16	1,10452E-15	**4,18905E-17**

	8	III	1	7.5	7.9		0.002	0.007	0.0045	0.142			0,031690141	0,4	1,71127E-13	5,84362E+12		
			2	7.5	7.9		0.0005	0.0022	0.00135	0.138			0,009782609	0,4	4,75435E-15	2,10334E+14		
			3	7.5	7.9		0.0005	0.004	0.00225	0.305			0,007377049	0,4	9,95902E-15	1,00412E+14		
			4	7.5	7.9	7,7	0.0001	0.0002	0.00015	0.241	0.826	0.16	0,000622407	0,4	3,73444E-18	2,67778E+17		
																6,70236E+16	4,6461E-14	**1,49201E-17**
	9	III	1	8.5	8.9		0.0005	0.001	0.00075	0.248			0,003024194	0,4	4,53629E-16	2,20444E+15		
			2	8.5	8.9		0.001	0.002	0.0015	0.115			0,013043478	0,4	7,82609E-15	1,27778E+14		
			3	8.5	8.9		0.0005	0.001	0.00075	0.035			0,021428571	0,4	3,21429E-15	3,11111E+14		
			4	8.5	8.9		0.0005	0.0015	0.001	0.156			0,006410256	0,4	1,7094E-15	5,85E+14		
			5	8.5	8.9	8,7	0.001	0.0025	0.00175	0.185	0.739	0.16	0,009459459	0,4	7,72523E-15	1,29446E+14		
																6,71556E+14	4,18573E-15	**1,48908E-15**
	10	III	1	9.5	9.9		0.001	0.002	0.0015	0.235			0,006382979	0,4	3,82979E-15	2,61111E+14		
			2	9.5	9.9	9,7	0.001	0.0065	0.00375	0.385	0.62	0.16	0,00974026	0,4	3,6526E-14	2,73778E+13		
														0,4		1,44244E+14	2,01779E-14	**6,93268E-15**
	11	III	1	10.5	10.9		0.0002	0.0004	0.0003	0.28			0,001071429	0,4	2,57143E-17	3,88889E+16		
			2	10.5	10.9	10,7	0.0003	0.001	0.00065	0.12	0.4	0.16	0,005416667	0,4	6,10278E-16	1,6388E+15		
																2,02637E+16	3,17996E-16	**4,93492E-17**
D	1	I	1	0.5	0.9		0.0002	0.0015	0.00085	0.285			0,002982456	0,4	5,7462E-16	1,74028E+15		
			2	0.5	0.9		0.0005	0.001	0.00075	0.04			0,01875	0,4	2,8125E-15	3,55556E+14		
			3	0.5	0.9		0.0002	0.001	0.0006	0.08			0,0075	0,4	7,2E-16	1,38889E+15		
			4	0.5	0.9	0,7	0.0002	0.0005	0.00035	0.06	0.465	0.16	0,005833333	0,4	1,90556E-16	5,24781E+15		
																2,18313E+15	1,07442E-15	**4,58057E-16**
		III	1	0.5	0.9		0.0001	0.001	0.00055	0.288			0,001909722	0,4	1,54051E-16	6,49136E+15		
			2	0.5	0.9		0.0001	0.0002	0.00015	0.084			0,001785714	0,4	1,07143E-17	9,33333E+16		
			3	0.5	0.9		0.0001	0.001	0.00055	0.16			0,0034375	0,4	2,77292E-16	3,60631E+15		
			4	0.5	0.9	0,7	0.0001	0.0002	0.00015	0.17	0.702	0.16	0,000882353	0,4	5,29412E-18	1,88889E+17		
																7,308E+16	1,11838E-16	**1,36836E-17**
	2	I	1	1.5	1.9		0.0001	0.0003	0.0002	0.064			0,003125	0,4	3,33333E-17	3E+16		
			2	1.5	1.9		0.0001	0.001	0.00055	0.15			0,003666667	0,4	2,95778E-16	3,38092E+15		
			3	1.5	1.9		0.0001	0.0003	0.0002	0.03			0,006666667	0,4	7,11111E-17	1,40625E+16		
			4	1.5	1.9		0.0001	0.0003	0.0002	0.13			0,001538462	0,4	1,64103E-17	6,09375E+16		
			5	1.5	1.9	1,7	0.0002	0.001	0.0006	0.17	0.544	0.16	0,003529412	0,4	3,38824E-16	2,95139E+15		
																2,22665E+16	1,51091E-16	**4,49106E-17**

		III	1	1.5	1.9		0.0001	0.0002	0.00015	0.09			0,001666667	0,4	1E-17	1E+17		
			2	1.5	1.9		0.0001	0.0002	0.00015	0.025			0,006	0,4	3,6E-17	2,77778E+16		
			3	1.5	1.9		0.0001	0.0002	0.00015	0.058			0,002586207	0,4	1,55172E-17	6,44444E+16		
			4	1.5	1.9		0.0005	0.001	0.00075	0.025			0,03	0,4	4,5E-15	2,22222E+14		
			5	1.5	1.9		0.0001	0.0002	0.00015	0.03			0,005	0,4	3E-17	3,33333E+16		
			6	1.5	1.9		0.0001	0.0002	0.00015	0.025			0,006	0,4	3,6E-17	2,77778E+16		
			7	1.5	1.9		0.0005	0.001	0.00075	0.035			0,021428571	0,4	3,21429E-15	3,11111E+14		
			8	1.5	1.9		0.0002	0.001	0.0006	0.075			0,008	0,4	7,68E-16	1,30208E+15		
			9	1.5	1.9		0.0002	0.0015	0.00085	0.152			0,005592105	0,4	1,07741E-15	9,2815E+14		
			10	1.5	1.9		0.0001	0.0002	0.00015	0.105			0,001428571	0,4	8,57143E-18	1,16667E+17		
			11	1.5	1.9		0.0001	0.0002	0.00015	0.06			0,0025	0,4	1,5E-17	6,66667E+16		
			12	1.5	1.9		0.0002	0.001	0.0006	0.108			0,005555556	0,4	5,33333E-16	1,875E+15		
			13	1.5	1.9		0.0001	0.0002	0.00015	0.085			0,001764706	0,4	1,05882E-17	9,44444E+16		
			14	1.5	1.9		0.0001	0.0015	0.0008	0.255			0,003137255	0,4	5,35425E-16	1,86768E+15		
			15	1.5	1.9		0.0001	0.0005	0.0003	0.055			0,005454545	0,4	1,30909E-16	7,63889E+15		
			16	1.5	1.9		0.0001	0.0002	0.00015	0.054			0,002777778	0,4	1,66667E-17	6E+16		
			17	1.5	1.9		0.0001	0.0002	0.00015	0.075			0,002	0	1,2E-17	8,33333E+16		
			18	1.5	1.9	1,7	0.0002	0.0008	0.0005	0.105	1.417	0.16	0,004761905	0,4	3,1746E-16	3,15E+15		
																3,843E+16	6,25954E-16	**2,60214E-17**
	4	I	1	3.5	3.9		0.001	0.0055	0.00325	0.378			0,008597884	0,4	2,42174E-14	4,12927E+13		
			2	3.5	3.9	3,7	0.0005	0.006	0.00325	0.228	0.606	0.16	0,014254386	0,4	4,01499E-14	2,49067E+13		
																3,30997E+13	3,21836E-14	**3,02118E-14**
		III	1	3.5	3.9		0.0005	0.001	0.00075	0.04			0,01875	0,4	2,8125E-15	3,55556E+14		
			2	3.5	3.9		0.0001	0.0002	0.00015	0.092			0,001630435	0,4	9,78261E-18	1,02222E+17		
			3	3.5	3.9		0.0002	0.0015	0.00085	0.32			0,00265625	0,4	5,11771E-16	1,954E+15		
			4	3.5	3.9		0.0002	0.001	0.0006	0.07			0,008571429	0,4	8,22857E-16	1,21528E+15		
			5	3.5	3.9		0.0001	0.0002	0.00015	0.023			0,006521739	0,4	3,91304E-17	2,55556E+16		
			6	3.5	3.9		0.0001	0.0002	0.00015	0.035			0,004285714	0,4	2,57143E-17	3,88889E+16		
			7	3.5	3.9	3,7	0.0005	0.001	0.00075	0.13	0.71	0.16	0,005769231	0,4	8,65385E-16	1,15556E+15		
																2,44782E+16	7,26734E-16	**4,08528E-17**
	5	III	1	4.5	4.9		0.0002	0.0015	0.00085	0.104			0,008173077	0,4	1,57468E-15	6,3505E+14		
			2	4.5	4.9	4,7	0.0005	0.001	0.00075	0.15	0.254	0.16	0,005	0,4	7,5E-16	1,33333E+15		
																9,84192E+14	1,16234E-15	**1,01606E-15**
	7	I	1	6.5	6.9		0.0015	0.021	0.01125	0.265			0,04245283	0,4	1,43278E-12	6,97942E+11		
			2	6.5	6.9		0.001	0.02	0.0105	0.33			0,031818182	0,4	9,35455E-13	1,069E+12		
			3	6.5	6.9	6,7	0.0015	0.0215	0.0115	0.155	0.75	0.16	0,074193548	0,4	2,61656E-12	3,82181E+11		
																7,16374E+11	1,6616E-12	**1,39592E-12**
		III	1	6.5	6.9		0.0001	0.0025	0.0013	0.235			0,005531915	0,4	2,49305E-15	4,01115E+14		
			2	6.5	6.9		0.0005	0.001	0.00075	0.04			0,01875	0,4	2,8125E-15	3,55556E+14		
			3	6.5	6.9	6,7	0.0005	0.001	0.00075	0.028	0.303	0.16	0,026785714	0,4	4,01786E-15	2,48889E+14		
																3,35187E+14	3,1078E-15	**2,98341E-15**
	8	III	1	7.5	7.9		0.0001	0.0002	0.00015	0.11			0,001363636	0,4	8,18182E-18	1,22222E+17		
			2	7.5	7.9		0.001	0.002	0.0015	0.15			0,01	0,4	6E-15	1,66667E+14		
			3	7.5	7.9		0.0003	0.0007	0.0005	0.072			0,006944444	0,4	4,62963E-16	2,16E+15		
			4	7.5	7.9		0.0001	0.0005	0.0003	0.075			0,004	0,4	9,6E-17	1,04167E+16		
			5	7.5	7.9		0.0002	0.001	0.0006	0.135			0,004444444	0,4	4,26667E-16	2,34375E+15		
			6	7.5	7.9	7,7	0.0002	0.0005	0.00035	0.08	0.622	0.16	0,004375	0,4	1,42917E-16	6,99708E+15		
																2,40511E+16	1,18945E-15	**4,15782E-17**

	9	III	1	8.5	8.9		0.0005	0.001	0.00075	0.13			0,005769231	0,4	8,65385E-16	1,15556E+15		
			2	8.5	8.9		0.0002	0.001	0.0006	0.17			0,003529412	0,4	3,38824E-16	2,95139E+15		
			3	8.5	8.9		0.0001	0.0008	0.00045	0.198			0,002272727	0,4	1,22727E-16	8,14815E+15		
			4	8.5	8.9		0.0001	0.0002	0.00015	0.085			0,001764706	0,4	1,05882E-17	9,44444E+16		
			5	8.5	8.9		0.0003	0.0015	0.0009	0.09			0,01	0,4	2,16E-15	4,62963E+14		
			6	8.5	8.9		0.0003	0.001	0.00065	0.075			0,008666667	0,4	9,76444E-16	1,02412E+15		
			7	8.5	8.9	8,7	0.0001	0.0002	0.00015	0.11	0.858	0.16	0,001363636	0,4	8,18182E-18	1,22222E+17		
																3,29155E+16	6,40307E-16	**3,03808E-17**
	10	III	1	9.5	9.9		0.0001	0.0005	0.0003	0.382			0,00078534	0,4	1,88482E-17	5,30556E+16		
			2	9.5	9.9	9,7	0.0001	0.0013	0.0007	0.378	0.76	0.16	0,001851852	0,4	2,41975E-16	4,13265E+15		
																2,85941E+16	1,30412E-16	**3,49722E-17**
	11	III	1	10.5	10.9		0.0001	0.0002	0.00015	0.205			0,000731707	0,4	4,39024E-18	2,27778E+17		
			2	10.5	10.9		0.0001	0.0002	0.00015	0.058			0,002586207	0,4	1,55172E-17	6,44444E+16		
			3	10.5	10.9		0.0001	0.0002	0.00015	0.055			0,002727273	0,4	1,63636E-17	6,11111E+16		
			4	10.5	10.9		0.0001	0.0002	0.00015	0.15			0,001	0,4	6E-18	1,66667E+17		
			5	10.5	10.9		0.0001	0.0004	0.00025	0.06			0,004166667	0,4	6,94444E-17	1,44E+16		
			6	10.5	10.9	10,7	0.0001	0.0004	0.00025	0.065	0.593	0.16	0,003846154	0,4	6,41026E-17	1,56E+16		
														0,4		9,16667E+16	2,9303E-17	**1,09091E-17**
														0,4				
E	1	I	1	1.5	1.9		0.0005	0.003	0.00175	0.15			0,011666667	0,4	9,52778E-15	1,04956E+14		
			2	1.5	1.9		0.0003	0.0025	0.0014	0.12			0,011666667	0,4	6,09778E-15	1,63994E+14		
			3	1.5	1.9	1,7	0.0005	0.004	0.00225	0.21	0.48	0.16	0,010714286	0,4	1,44643E-14	6,91358E+13		
																1,12695E+14	1,00299E-14	**8,87348E-15**
		III	1	1.5	1.9		0.0005	0.002	0.00125	0.04			0,03125	0,4	1,30208E-14	7,68E+13		
			2	1.5	1.9		0.0005	0.002	0.00125	0.072			0,017361111	0,4	7,2338E-15	1,3824E+14		
			3	1.5	1.9		0.0002	0.0015	0.00085	0.14			0,006071429	0,4	1,16976E-15	8,54875E+14		
			4	1.5	1.9		0.0001	0.003	0.00155	0.25			0,0062	0,4	3,97213E-15	2,51754E+14		
			5	1.5	1.9		0.0001	0.0002	0.00015	0.085			0,001764706	0,4	1,05882E-17	9,44444E+16		
			6	1.5	1.9		0.0001	0.0002	0.00015	0.24			0,000625	0,4	3,75E-18	2,66667E+17		
			7	1.5	1.9		0.0001	0.0002	0.00015	0.025			0,006	0,4	3,6E-17	2,77778E+16		
			8	1.5	1.9		0.0001	0.0002	0.00015	0.12			0,00125	0,4	7,5E-18	1,33333E+17		
			9	1.5	1.9		0.0001	0.0002	0.00015	0.08			0,001875	0,4	1,125E-17	8,88889E+16		
			10	1.5	1.9		0.0001	0.0002	0.00015	0.03			0,005	0,4	3E-17	3,33333E+16		
			11	1.5	1.9		0.0001	0.0002	0.00015	0.08			0,001875	0	1,125E-17	8,88889E+16		
			12	1.5	1.9	1,7	0.0005	0.001	0.00075	0.085	1.247	0.16	0,008823529	0,4	1,32353E-15	7,55556E+14		
																6,12842E+16	2,23587E-15	**1,63174E-17**
	2	I	1	2.5	2.9		0.02	0.035	0.0275	0.225			0,122222222	0,4	2,46481E-11	40570999249		
			2	2.5	2.9	2,7	0.0005	0.003	0.00175	0.28	0.505	0.16	0,00625	0,4	5,10417E-15	1,95918E+14		
																9,79795E+13	1,23266E-11	**1,02062E-14**
		III	1	2.5	2.9		0.0001	0.0002	0.00015	0.072			0,002083333	0,4	1,25E-17	8E+16		
			2	2.5	2.9		0.0001	0.0002	0.00015	0.075			0,002	0,4	1,2E-17	8,33333E+16		
			3	2.5	2.9	2,7	0.0002	0.001	0.0006	0.055	0.202	0.16	0,010909091	0,4	1,04727E-15	9,54861E+14		
																5,47627E+16	3,57258E-16	**1,82606E-17**
	3	III	1	3.5	3.9		0.0002	0.001	0.0006	0.112			0,005357143	0,4	5,14286E-16	1,94444E+15		
			2	3.5	3.9		0.0002	0.0005	0.00035	0.15			0,002333333	0,4	7,62222E-17	1,31195E+16		
			3	3.5	3.9		0.0002	0.0005	0.00035	0.2			0,00175	0,4	5,71667E-17	1,74927E+16		
			4	3.5	3.9	3,7	0.0001	0.0002	0.00015	0.105	0.567	0.16	0,001428571	0,4	8,57143E-18	1,16667E+17		
																3,73058E+16	1,64062E-16	**2,68055E-17**

	4	III	1	4.5	4.9		0.0001	0.0002	0.00015	0.152			0,000986842	0,4	5,92105E-18	1,68889E+17		
			2	4.5	4.9		0.0001	0.0005	0.0003	0.13			0,002307692	0,4	5,53846E-17	1,80556E+16		
			3	4.5	4.9		0.0002	0.001	0.0006	0.11			0,005454545	0,4	5,23636E-16	1,90972E+15		
			4	4.5	4.9		0.0001	0.0015	0.0008	0.312			0,002564103	0,4	4,37607E-16	2,28516E+15		
			5	4.5	4.9		0.0002	0.001	0.0006	0.15			0,004	0,4	3,84E-16	2,60417E+15		
			6	4.5	4.9		0.0005	0.002	0.00125	0.195			0,006410256	0,4	2,67094E-15	3,744E+14		
			7	4.5	4.9		0.0002	0.0015	0.00085	0.275			0,003090909	0,4	5,95515E-16	1,67922E+15		
			8	4.5	4.9		0.0001	0.0002	0.00015	0.115			0,001304348	0	7,82609E-18	1,27778E+17		
			9	4.5	4.9	4,7	0.0002	0.002	0.0011	0.17	1.609	0.16	0,006470588	0,4	2,08784E-15	4,78963E+14		
																3,6006E+16	7,52075E-16	**2,77732E-17**
	5	I	1	5.5	5.9		0.0005	0.007	0.00375	0.056			0,066964286	0,4	2,51116E-13	3,98222E+12		
			2	5.5	5.9		0.001	0.01	0.0055	0.134			0,041044776	0,4	3,31095E-13	3,02029E+12		
			3	5.5	5.9	5,7	0.0015	0.0035	0.0025	0.023	0.213	0.16	0,108695652	0,4	1,81159E-13	5,52E+12		
																4,17417E+12	2,54457E-13	**2,39569E-13**
		II	1	5.5	5.9		0.001	0.025	0.013	0.23			0,056521739	0,4	2,54725E-12	3,92581E+11		
			2	5.5	5.9		0.0005	0.03	0.01525	0.24			0,063541667	0,4	3,94064E-12	2,53766E+11		
			3	5.5	5.9		0.0002	0.016	0.0081	0.34			0,023823529	0,4	4,16816E-13	2,39914E+12		
			4	5.5	5.9		0.001	0.005	0.003	0.08			0,0375	0,4	9E-14	1,11111E+13		
			5	5.5	5.9		0.001	0.015	0.008	0.18			0,044444444	0,4	7,58519E-13	1,31836E+12		
			6	5.5	5.9		0.003	0.009	0.006	0.045			0,133333333	0,4	1,28E-12	7,8125E+11		
			7	5.5	5.9		0.001	0.01	0.0055	0.03			0,183333333	0	1,47889E-12	6,76183E+11		
			8	5.5	5.9	5,7	0.001	0.005	0.003	0.19	1.335	0.16	0,015789474	0,4	3,78947E-14	2,63889E+13		
																5,41516E+12	1,31875E-12	**1,84667E-13**
	6	II	1	6.5	6.9		0.001	0.007	0.004	0.412			0,009708738	0,4	4,14239E-14	2,41406E+13		
			2	6.5	6.9		0.001	0.01	0.0055	0.22			0,025	0	2,01667E-13	4,95868E+12		
			3	6.5	6.9	6,7	0.002	0.015	0.0085	0.385	1.017	0.16	0,022077922	0,4	4,25368E-13	2,35091E+12		
																1,04834E+13	2,2282E-13	**9,53889E-14**
		III	1	6.5	6.9		0.0001	0.0002	0.00015	0.26			0,000576923	0,4	3,46154E-18	2,88889E+17		
			2	6.5	6.9		0.0001	0.0002	0.00015	0.05			0,003	0,4	1,8E-17	5,55556E+16		
			3	6.5	6.9		0.0001	0.0002	0.00015	0.048			0,003125	0,4	1,875E-17	5,33333E+16		
			4	6.5	6.9		0.0005	0.0015	0.001	0.072			0,013888889	0,4	3,7037E-15	2,7E+14		
			5	6.5	6.9	6,7	0.0001	0.0002	0.00015	0.08	0.51	0.16	0,001875	0,4	1,125E-17	8,88889E+16		
																9,73873E+16	7,51033E-16	**1,02683E-17**
	7	II	1	7.5	7.9	7,7	0.001	0.005	0.003	0.432	0.432	0.16	0,006944444	0,4	1,66667E-14	6E+13		
																6E+13	1,66667E-14	**1,66667E-14**
		III	1	7.5	7.9		0.0001	0.0002	0.00015	0.07			0,002142857	0,4	1,28571E-17	7,77778E+16		
			2	7.5	7.9		0.0001	0.0002	0.00015	0.06			0,0025	0,4	1,5E-17	6,66667E+16		
			3	7.5	7.9		0.0001	0.0002	0.00015	0.025			0,006	0,4	3,6E-17	2,77778E+16		
			4	7.5	7.9		0.0002	0.001	0.0006	0.04			0,015	0,4	1,44E-15	6,94444E+14		
			5	7.5	7.9		0.0002	0.0015	0.00085	0.125			0,0068	0,4	1,31013E-15	7,63281E+14		
			6	7.5	7.9		0.0001	0.0002	0.00015	0.085			0,001764706	0,4	1,05882E-17	9,44444E+16		
			7	7.5	7.9		0.0002	0.001	0.0006	0.11			0,005454545	0,4	5,23636E-16	1,90972E+15		
			8	7.5	7.9		0.0001	0.0002	0.00015	0.08			0,001875	0,4	1,125E-17	8,88889E+16		
			9	7.5	7.9	7,7	0.0001	0.0002	0.00015	0.03	0.625	0.16	0,005	0,4	3E-17	3,33333E+16		
																4,3584E+16	3,76607E-16	**2,29442E-17**

F	1	I	1	1.2	1.6		0.0005	0.003	0.00175	0.3			0,005833333	0,4	4,76389E-15	2,09913E+14		
			2	1.2	1.6		0.0001	0.0002	0.00015	0.045			0,003333333	0,4	2E-17	5E+16		
			3	1.2	1.6		0.0002	0.0024	0.0013	0.106			0,012264151	0,4	5,52704E-15	1,80929E+14		
			4	1.2	1.6		0.0002	0.0024	0.0013	0.115			0,011304348	0,4	5,09449E-15	1,9629E+14		
			5	1.2	1.6		0.0005	0.0043	0.0024	0.4			0,006	0,4	9,216E-15	1,08507E+14		
			6	1.2	1.6		0.0001	0.011	0.00555	0.352			0,015767045	0,4	1,29511E-13	7,72138E+12		
			7	1.2	1.6		0.0001	0.0005	0.0003	0.05			0,006	0,4	1,44E-16	6,94444E+15		
			8	1.2	1.6		0.0001	0.0005	0.0003	0.055			0,005454545	0,4	1,30909E-16	7,63889E+15		
			9	1.2	1.6		0.0001	0.0005	0.0003	0.035			0,008571429	0,4	2,05714E-16	4,86111E+15		
			10	1.2	1.6		0.0002	0.001	0.0006	0.06			0,01	0,4	9,6E-16	1,04167E+15		
			11	1.2	1.6		0.0005	0.0015	0.001	0.05			0,02	0,4	5,33333E-15	1,875E+14		
			12	1.2	1.6		0.0002	0.0015	0.00085	0.078			0,010897436	0,4	2,09957E-15	4,76287E+14		
			13	1.2	1.6		0.0001	0.0002	0.00015	0.062			0,002419355	0,4	1,45161E-17	6,88889E+16		
			14	1.2	1.6		0.0003	0.001	0.00065	0.038			0,017105263	0	1,92719E-15	5,18889E+14		
			15	1.2	1.6	1,4	0.0003	0.001	0.00065	0.04	1.786	0.16	0,01625	0,4	1,83083E-15	5,46199E+14		
																9,45382E+15	1,11185E-14	**1,05777E-16**
	2	I	1	2.2	2.6		0.0002	0.002	0.0011	0.215			0,005116279	0,4	1,65085E-15	6,05748E+14		
			2	2.2	2.6	2,4	0.0005	0.0025	0.0015	0.115	0.33	0.16	0,013043478	0,4	7,82609E-15	1,27778E+14		
																3,66763E+14	4,73847E-15	**2,72656E-15**
		III	1	2.2	2.6		0.0001	0.0005	0.0003	0.07			0,004285714	0,4	1,02857E-16	9,72222E+15		
			2	2.2	2.6	2,4	0.0001	0.0007	0.0004	0.052	0.122	0.16	0,007692308	0,4	3,28205E-16	3,04688E+15		
																6,38455E+15	2,15531E-16	**1,56628E-16**
	3	III	1	3.2	3.6		0.0002	0.0045	0.00235	0.315			0,007460317	0,4	1,09866E-14	9,10203E+13		
			2	3.2	3.6		0.0002	0.003	0.0016	0.275			0,005818182	0,4	3,97188E-15	2,5177E+14		
			3	3.2	3.6		0.0005	0.004	0.00225	0.105			0,021428571	0,4	2,89285E-14	3,45679E+13		
			4	3.2	3.6		0.0002	0.0015	0.00085	0.052			0,016346154	0,4	3,14936E-15	3,17525E+14		
			5	3.2	3.6		0.0001	0.0005	0.0003	0.053			0,005660377	0,4	1,35849E-16	7,36111E+15		
			6	3.2	3.6		0.0001	0.0025	0.0013	0.088			0,014772727	0,4	6,65758E-15	1,50205E+14		
			7	3.2	3.6	3,4	0.0001	0.0002	0.00015	0.079	0.967	0.16	0,001898734	0,4	1,13924E-17	8,77778E+16		
																1,3712E+16	7,6916E-15	**7,29288E-17**
G	1	III	1	0.6	1		0.001	0.0025	0.00175	0.145			0,012068966	0,4	9,85632E-15	1,01458E+14		
			2	0.6	1		0.001	0.0015	0.00125	0.05			0,025	0,4	1,04167E-14	9,6E+13		
			3	0.6	1		0.001	0.003	0.002	0.295			0,006779661	0,4	7,23164E-15	1,38281E+14		
			4	0.6	1		0.001	0.002	0.0015	0.023			0,065217391	0,4	3,91304E-14	2,55556E+13		
			5	0.6	1		0.0001	0.0002	0.00015	0.062			0,002419355	0,4	1,45161E-17	6,88889E+16		
			6	0.6	1		0.001	0.0025	0.00175	0.2			0,00875	0,4	7,14583E-15	1,39942E+14		
			7	0.6	1	0,8	0.0001	0.0002	0.00015	0.052	0.827	0.16	0,002884615	0,4	1,73077E-17	5,77778E+16		
																1,81668E+16	1,05447E-14	**5,50453E-17**

	2	II	1	1.6	2		0.0005	0.0015	0.001	0.135			0,007407407	0,4	1,97531E-15	5,0625E+14		
			2	1.6	2		0.001	0.0025	0.00175	0.14			0,0125	0,4	1,02083E-14	9,79592E+13		
			3	1.6	2	1,8	0.0005	0.002	0.00125	0.075	0.35	0.16	0,016666667	0,4	6,94444E-15	1,44E+14		
																2,49403E+14	6,37603E-15	**4,00957E-15**
		III	1	1.6	2		0.0001	0.0002	0.00015	0.24			0,000625	0,4	3,75E-18	2,66667E+17		
			2	1.6	2	1,8	0.0001	0.0002	0.00015	0.115	0.355	0.16	0,001304348	0,4	7,82609E-18	1,27778E+17		
																1,97222E+17	5,78804E-18	**5,07042E-18**
	3	II	1	2.6	3		0.002	0.004	0.003	0.097			0,030927835	0,4	7,42268E-14	1,34722E+13		
			2	2.6	3		0.001	0.003	0.002	0.192			0,010416667	0,4	1,11111E-14	9E+13		
			3	2.6	3		0.001	0.005	0.003	0.128			0,0234375	0,4	5,625E-14	1,77778E+13		
			4	2.6	3		0.0005	0.0025	0.0015	0.117			0,012820513	0,4	7,69231E-15	1,3E+14		
			5	2.6	3		0.001	0.003	0.002	0.048			0,041666667	0,4	4,44444E-14	2,25E+13		
			6	2.6	3		0.0005	0.0015	0.001	0.04			0,025	0,4	6,66667E-15	1,5E+14		
			7	2.6	3		0.0005	0.004	0.00225	0.082			0,027439024	0,4	3,70427E-14	2,69959E+13		
			8	2.6	3		0.0005	0.0015	0.001	0.021			0,047619048	0,4	1,26984E-14	7,875E+13		
			9	2.6	3		0.0015	0.005	0.00325	0.228			0,014254386	0,4	4,01499E-14	2,49067E+13		
			10	2.6	3		0.0002	0.002	0.0011	0.04			0,0275	0,4	8,87333E-15	1,12697E+14		
			11	2.6	3		0.001	0.006	0.0035	0.087			0,040229885	0,4	1,31418E-13	7,60933E+12		
			12	2.6	3		0.001	0.002	0.0015	0.045			0,033333333	0,4	2E-14	5E+13		
			13	2.6	3		0.0015	0.006	0.00375	0.14			0,026785714	0,4	1,00446E-13	9,95556E+12		
			14	2.6	3	2,8	0.0005	0.0025	0.0015	0.145	1.41	0.16	0,010344828	0,4	6,2069E-15	1,61111E+14		
																6,3984E+13	3,98019E-14	**1,56289E-14**
	4	I	1	3.6	4		0.001	0.006	0.0035	0.185			0,018918919	0,4	6,18018E-14	1,61808E+13		
			2	3.6	4		0.0015	0.0055	0.0035	0.305			0,01147541	0,4	3,74863E-14	2,66764E+13		
			3	3.6	4	3,8	0.002	0.01	0.006	0.158	0.648	0.16	0,037974684	0,4	3,64557E-13	2,74306E+12		
																1,52001E+13	1,54615E-13	**6,57892E-14**
		II	1	3.6	4		0.0002	0.0015	0.00085	0.11			0,007727273	0,4	1,48879E-15	6,71687E+14		
			2	3.6	4		0.0025	0.005	0.00375	0.15			0,025	0,4	9,375E-14	1,06667E+13		
			3	3.6	4		0.0025	0.0055	0.004	0.405			0,009876543	0,4	4,21399E-14	2,37305E+13		
			4	3.6	4		0.0002	0.0015	0.00085	0.102			0,008333333	0,4	1,60556E-15	6,22837E+14		
			5	3.6	4		0.0001	0.0005	0.0003	0.26			0,001153846	0	2,76923E-17	3,61111E+16		
			6	3.6	4	3,8	0.0005	0.002	0.00125	0.041	1.068	0.16	0,030487805	0,4	1,27033E-14	7,872E+13		
																6,25313E+15	2,52859E-14	**1,5992E-16**
		III	1	3.6	4		0.0001	0.0002	0.00015	0.078			0,001923077	0,4	1,15385E-17	8,66667E+16		
			2	3.6	4		0.00002	0.0015	0.00076	0.055			0,013818182	0,4	2,12837E-15	4,69843E+14		
			3	3.6	4	3,8	0.0004	0.002	0.0012	0.102	0.235	0.16	0,011764706	0,4	4,51765E-15	2,21354E+14		
																2,91193E+16	2,21918E-15	**3,43415E-17**

H	1	I	1	0.6	1		0.0005	0.003	0.00175	0.19			0,009210526	0,4	7,52193E-15	1,32945E+14		
			2	0.6	1	0,8	0.0005	0.002	0.00125	0.392	0.582	0.16	0,003188776	0,4	1,32866E-15	7,5264E+14		
																4,42792E+14		
	2	II	1	1.6	2	1,8	0.0005	0.015	0.00775	0.205	0.205	0.16	0,037804878	0,4	6,05508E-13	1,65151E+12		
																1,65151E+12	6,05508E-13	**6,05508E-13**
		III	1	1.6	2		0.0005	0.001	0.00075	0.048			0,015625	0,4	2,34375E-15	4,26667E+14		
			2	1.6	2		0.0001	0.0002	0.00015	0.05			0,003	0,4	1,8E-17	5,55556E+16		
			3	1.6	2		0.0001	0.0002	0.00015	0.05			0,003	0,4	1,8E-17	5,55556E+16		
			4	1.6	2		0.0001	0.0002	0.00015	0.025			0,006	0,4	3,6E-17	2,77778E+16		
			5	1.6	2		0.0001	0.0002	0.00015	0.02			0,0075	0,4	4,5E-17	2,22222E+16		
			6	1.6	2		0.0005	0.001	0.00075	0.055			0,013636364	0,4	2,04545E-15	4,88889E+14		
			7	1.6	2		0.0001	0.0005	0.0003	0.07			0,004285714	0,4	1,02857E-16	9,72222E+15		
			8	1.6	2		0.0001	0.0002	0.00015	0.075			0,002	0,4	1,2E-17	8,33333E+16		
			9	1.6	2		0.0001	0.0002	0.00015	0.065			0,002307692	0,4	1,38462E-17	7,22222E+16		
			10	1.6	2	1,8	0.0005	0.001	0.00075	0.075	0.533	0.16	0,01	0,4	1,5E-15	6,66667E+14		
																3,27971E+16	6,13491E-16	**3,04905E-17**
	3	II	1	2.6	3	2,8	0.0001	0.0025	0.0013	0.28	0.28	0.16	0,004642857	0,4	2,09238E-15	4,77924E+14		
																4,77924E+14	2,09238E-15	**2,09238E-15**
		III	1	2.6	3		0.001	0.003	0.002	0.04			0,05	0,4	5,33333E-14	1,875E+13		
			2	2.6	3		0.0001	0.001	0.00055	0.05			0,011	0,4	8,87333E-16	1,12697E+15		
			3	2.6	3		0.0002	0.002	0.0011	0.34			0,003235294	0,4	1,04392E-15	9,57926E+14		
			4	2.6	3		0.0001	0.0002	0.00015	0.052			0,002884615	0,4	1,73077E-17	5,77778E+16		
			5	2.6	3		0.0001	0.001	0.00055	0.09			0,006111111	0,4	4,92963E-16	2,02855E+15		
			6	2.6	3		0.0001	0.0002	0.00015	0.07			0,002142857	0,4	1,28571E-17	7,77778E+16		
			7	2.6	3		0.0001	0.0002	0.00015	0.045			0,003333333	0,4	2E-17	5E+16		
			8	2.6	3		0.001	0.002	0.0015	0.04			0,0375	0,4	2,25E-14	4,44444E+13		
			9	2.6	3		0.0001	0.0002	0.00015	0.065			0,002307692	0,4	1,38462E-17	7,22222E+16		
			10	2.6	3		0.0002	0.0015	0.00085	0.155			0,005483871	0,4	1,05656E-15	9,46469E+14		
			11	2.6	3		0.0001	0.0002	0.00015	0.03			0,005	0,4	3E-17	3,33333E+16		
			12	2.6	3		0.0001	0.0002	0.00015	0.028			0,005357143	0,4	3,21429E-17	3,11111E+16		
			13	2.6	3	2,8	0.0002	0.001	0.0006	0.165	1.17	0.16	0,003636364	0,4	3,49091E-16	2,86458E+15		
																2,54008E+16	6,13764E-15	**3,93689E-17**

A vertical	1	I	1	0.2	0.6		0.0003	0.004	0.00215	0.166			0,012951807	0,4	1,59653E-14	6,2636E+13		
			2	0.2	0.6		0.00001	0.0025	0.001255	0.2			0,006275	0,4	2,63554E-15	3,79429E+14		
			3	0.2	0.6		0.0005	0.006	0.00325	0.268			0,012126866	0	3,41573E-14	2,92763E+13		
			4	0.2	0.6	0,4	0.002	0.008	0.005	0.45	1.084	0.16	0,011111111	0,4	7,40741E-14	1,35E+13		
																1,2121E+14	3,17081E-14	**8,25013E-15**
	2	I	1	1.2	1.6	1,4	0.085	0.18	0.1325	0.4	0.4	0.16	0,33125	0,4	1,5508E-09	644827609,4		
																644827609,4	1,5508E-09	**1,5508E-09**
	3	I	1	2.2	2.6		0.0007	0.003	0.00185	0.364			0,005082418	0,4	4,63855E-15	2,15584E+14		
			2	2.2	2.6		0.001	0.0035	0.00225	0.124			0,018145161	0,4	2,4496E-14	4,0823E+13		
			3	2.2	2.6		0.002	0.115	0.0585	0.376			0,155585106	0	1,41987E-10	7042899877		
			4	2.2	2.6	2,4	0.018	0.075	0.0465	0.368	1.232	0.16	0,126358696	0,4	7,28584E-11	13725248863		
																6,41071E+13	5,37186E-11	**1,55989E-14**
	4	I	1	3.2	3.6		0.001	0.009	0.005	0.46			0,010869565	0,4	7,24638E-14	1,38E+13		
			2	3.2	3.6		0.0015	0.0064	0.00395	0.25			0,0158	0,4	6,57385E-14	1,52118E+13		
			3	3.2	3.6		0.001	0.004	0.0025	0.15			0,016666667	0	2,77778E-14	3,6E+13		
			4	3.2	3.6	3,4	0.0005	0.0065	0.0035	0.145	1.005	0.16	0,024137931	0,4	7,88506E-14	1,26822E+13		
														0,4		1,94235E+13	8,12077E-14	**5,1484E-14**
		II	1	3.2	3.6	3,4	0.001	0.007	0.004	0.205			0,019512195	0,4	8,3252E-14	1,20117E+13		
			2				0.0005	0.0105	0.0055	0.134	0.339	0.16	0,041044776	0,4	3,31095E-13	3,02029E+12		
																7,516E+12	2,07173E-13	**1,33049E-13**
B vertical	2	I	1	1.4	1.8		0.0015	0.042	0.02175	0.28			0,077678571	0,4	9,79915E-12	1,0205E+11		
			2	1.4	1.8		0.001	0.017	0.009	0.35			0,025714286	0,4	5,55429E-13	1,80041E+12		
			3	1.4	1.8	1,6	0.003	0.04	0.0215	0.22	0.85	0.16	0,097727273	0,4	1,20465E-11	83011558731		
																6,61824E+11	7,46703E-12	**1,51098E-12**
	3	I	1	2.4	2.8		0.0001	0.0002	0.00015	0.078			0,001923077	0,4	1,15385E-17	8,66667E+16		
			2	2.4	2.8		0.0001	0.0002	0.00015	0.03			0,005	0,4	3E-17	3,33333E+16		
			3	2.4	2.8		0.0001	0.005	0.00255	0.4			0,006375	0,4	1,10543E-14	9,04629E+13		
			4	2.4	2.8		0.0001	0.0002	0.00015	0.045			0,003333333	0,4	2E-17	5E+16		
			5	2.4	2.8		0.0001	0.0002	0.00015	0.23			0,000652174	0,4	3,91304E-18	2,55556E+17		
			6	2.4	2.8		0.0001	0.0002	0.00015	0.105			0,001428571	0,4	8,57143E-18	1,16667E+17		
			7	2.4	2.8		0.0001	0.0035	0.0018	0.12			0,015	0,4	1,296E-14	7,71605E+13		
			8	2.4	2.8		0.0001	0.0002	0.00015	0.055			0,002727273	0,4	1,63636E-17	6,11111E+16		
			9	2.4	2.8		0.0001	0.0002	0.00015	0.038			0,003947368	0,4	2,36842E-17	4,22222E+16		
			10	2.4	2.8		0.0001	0.0002	0.00015	0.04			0,00375	0,4	2,25E-17	4,44444E+16		
			11	2.4	2.8		0.0001	0.001	0.00055	0.372			0,001478495	0	1,19265E-16	8,38467E+15		
			12	2.4	2.8	2,6	0.0001	0.002	0.00105	0.23	1.743	0.16	0,004565217	0,4	1,34217E-15	7,4506E+14		
																5,82748E+16	2,13435E-15	**1,71601E-17**
	4	I	1	3.4	3.8		0.0001	0.0005	0.0003	0.08			0,00375	0,4	9E-17	1,11111E+16		
			2	3.4	3.8		0.0005	0.002	0.00125	0.175			0,007142857	0,4	2,97619E-15	3,36E+14		
			3	3.4	3.8		0.001	0.002	0.0015	0.1			0,015	0,4	9E-15	1,11111E+14		
			4	3.4	3.8	3,6	0.0001	0.0005	0.0003	0.14	0.495	0.16	0,002142857	0,4	5,14286E-17	1,94444E+16		
																7,75067E+15	3,0294E-15	**1,29021E-16**
C vertical	1	I	1	0.15	0.55	0,35	0.06	0.22	0.14	0.4	0.4	0.16	0,35	0,4	1,82933E-09	546647230,3		
																546647230,3	1,82933E-09	**1,82933E-09**
	3	I	1	2.15	2.55	2,35	0.0002	0.002	0.0011	0.28	0.28	0.16	0,003928571	0,4	1,26762E-15	7,88881E+14		
																7,88881E+14	1,26762E-15	**1,26762E-15**

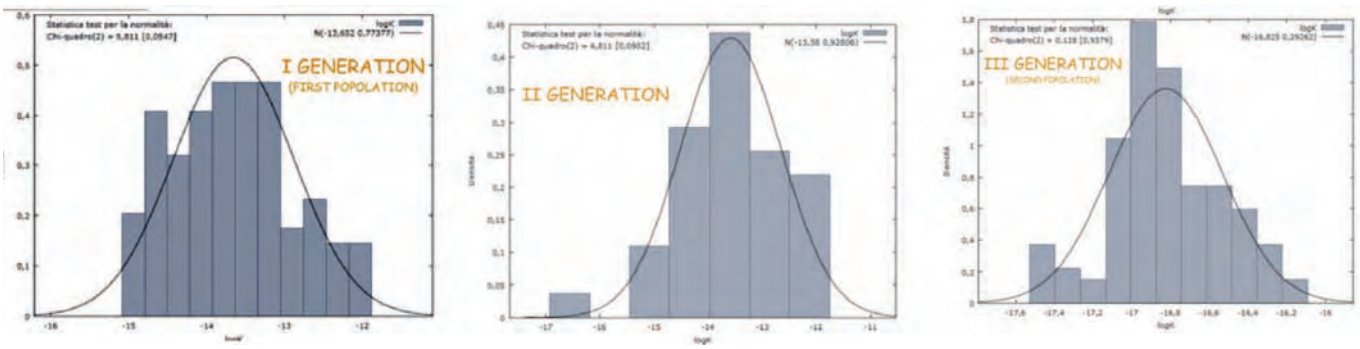

Fig. 2.2.13 – histogram illustrating the relationships between permeability and density of fractures fro the different generation of fractures recognized in the deeper studied structural level.

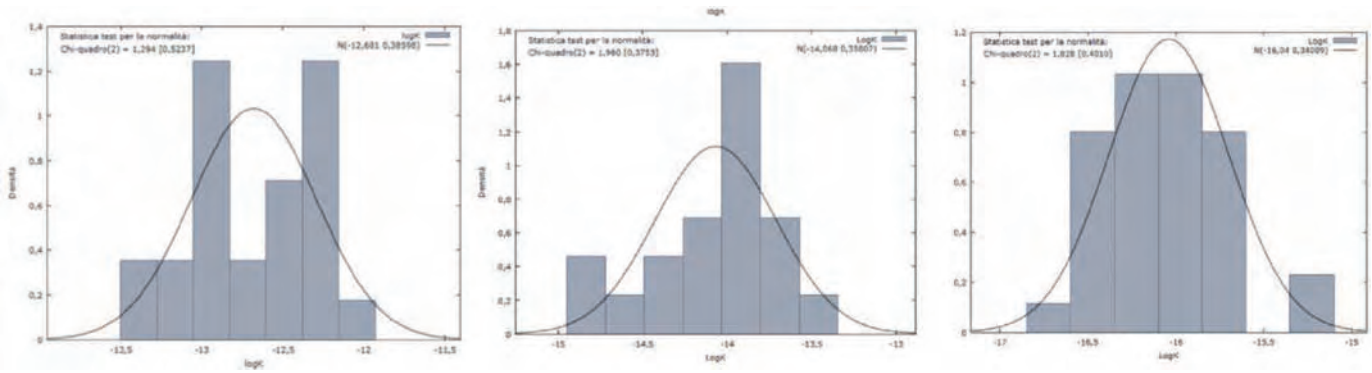

Fig. 2.2.14 - histogram illustrating the relationships between permeability and density of fractures fro the different generation of fractures recognized in the shallower studied structural level.

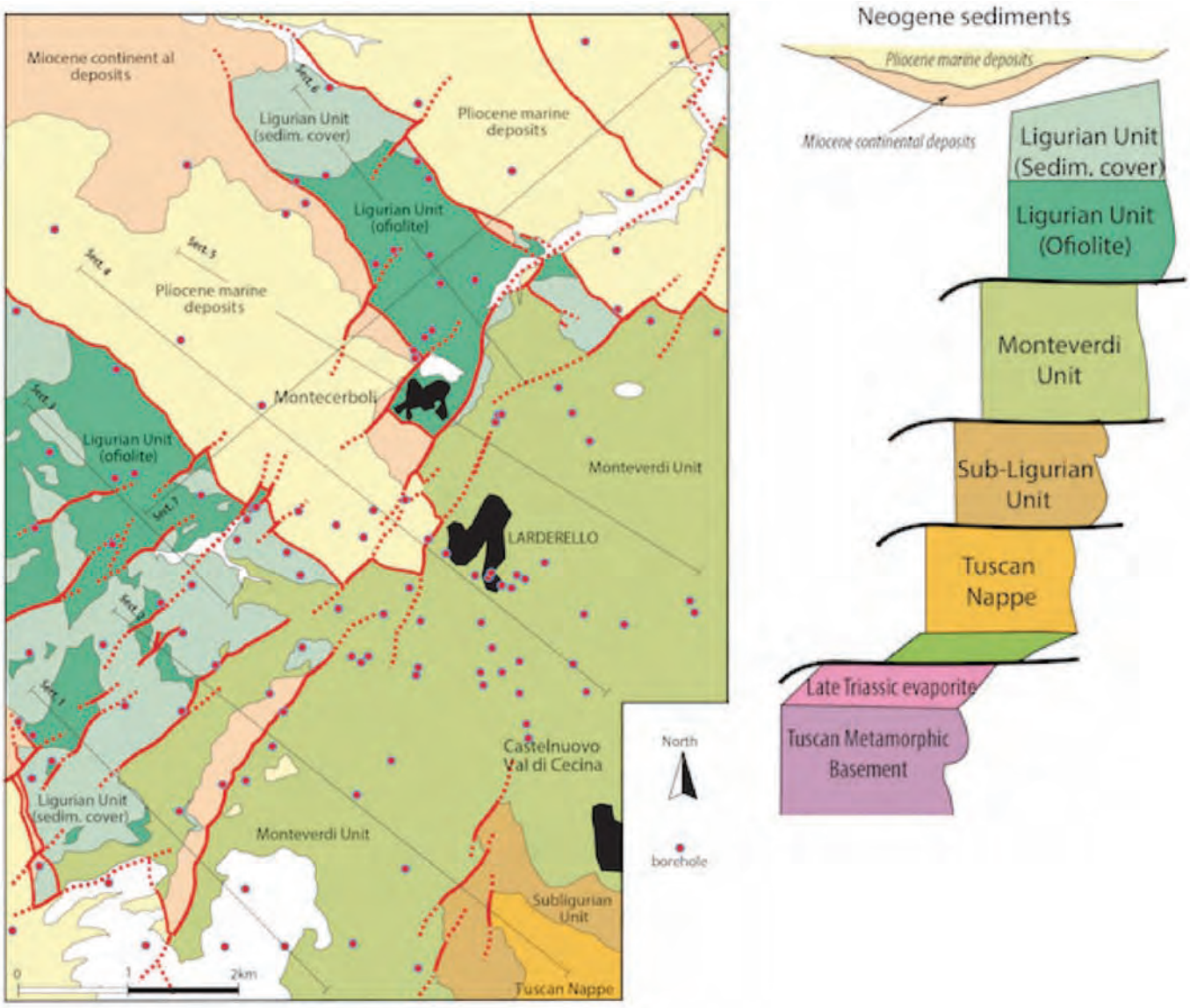

Fig. 2.2.15 – geological map and tectono-stratigraphic column of the surroundings of the Larderello area.

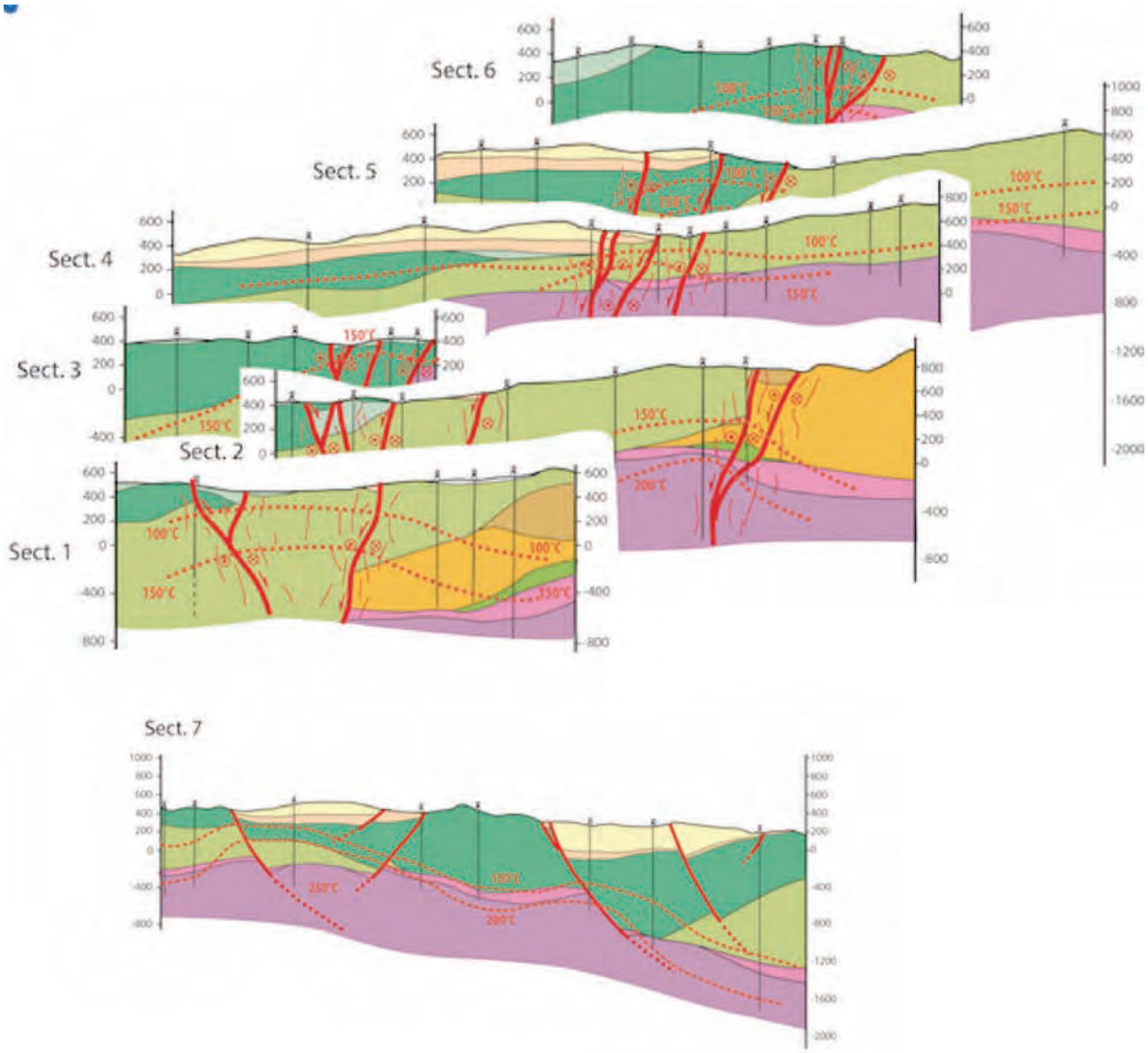

Fig. 2.2.16 – Geological cross section through the Larderello area witrh indication of the deep temperatures as measured from boreholes. Traces in fig. 2.2.15

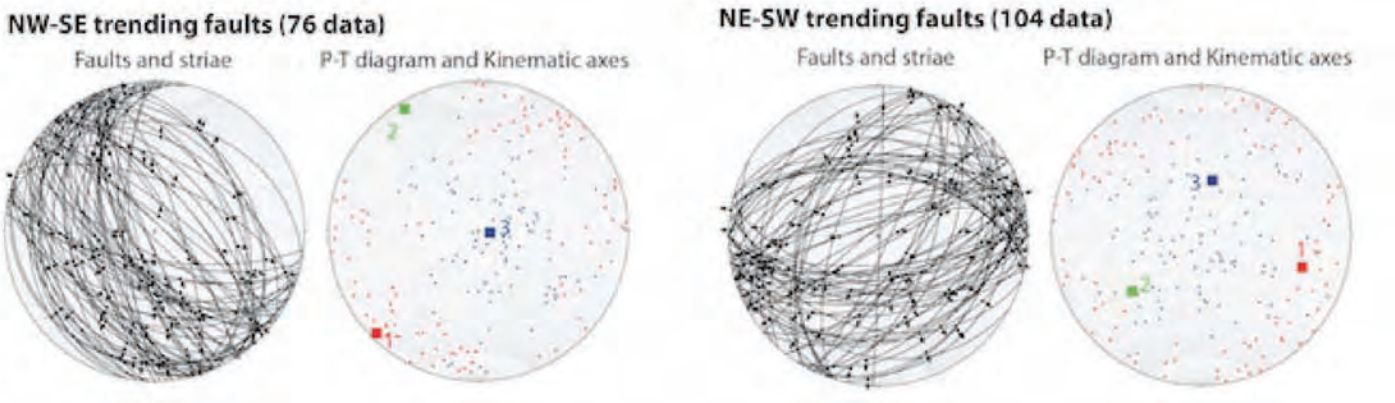

Fig. 2.2.17 – cumulative stereonets of the Larderello area from the data collected in this study.

Tectonophysics xxx (2015) xxx–xxx

Contents lists available at ScienceDirect

Tectonophysics

journal homepage: www.elsevier.com/locate/tecto

Coexistence of low-angle normal and high-angle strike- to oblique-slip faults during Late Miocene mineralization in eastern Elba Island (Italy)

Domenico Liotta [a,*], Andrea Brogi [a], Marco Meccheri [b], Andrea Dini [c], Caterina Bianco [a], Giovanni Ruggieri [d]

[a] Department of Earth and Geoenvironmental Sciences, University of Bari "Aldo Moro", Via Orabona 4, Bari, Italy
[b] Department of Physics, Earth and Environmental Sciences, University of Siena, Via Laterina 8, Siena, Italy
[c] CNR-IGG National Council of Research, Geosciences and Georesources Institute, Pisa, Italy
[d] CNR-IGG National Council of Research, Geosciences and Georesources Institute, Florence, Italy

ARTICLE INFO

Article history:
Received 2 April 2014
Received in revised form 26 May 2015
Accepted 24 June 2015
Available online xxxx

Keywords:
Extensional tectonics
Fractures
Mineralization
Northern Apennines

ABSTRACT

In this paper we deal with the kinematic and chronological relationships among low angle normal faults and high angle strike- to oblique-slip faults in an exhumed mineralized area, where shear veins and minor associated structures filled with the same mineral assemblage has been interpreted as indicators of coeval fault activities. The study area is located in the eastern Elba Island, where a mineralized late Miocene-early Pliocene low-angle normal fault (Zuccale fault) and high-angle strike- to oblique-slip faults extensively crop out, the latter giving rise to the Capoliveri-Porto Azzurro shear zone. The field study highlighted that: (a) the damage zones of both fault sets are mineralized by syn-kinematic tourmaline, graphite, Fe-oxides and/or Fe-oxyhydroxides shear veins, thus indicating their coeval activity during the hydrothermal event (5.9–5.4 Ma); (b) the Capoliveri-Porto Azzurro shear zone is constituted by a network of fractures, whose geometry and kinematics display the evolution of a NE-trending left-lateral oblique-slip transtensional shear zone; (c) its internal architecture is defined by tourmaline and Fe-oxides and/or Fe-oxyhydroxides mineralized veins, framed in the same kinematic field characterizing the Zuccale fault evolution; for this reason, the Capoliveri–Porto Azzurro shear zone is interpreted as a transfer zone active during the low-angle fault activity; (d) the Capoliveri–Porto Azzurro shear zone played the role of a significant normal fault during the Late Pliocene–Pleistocene, therefore favouring the deepening of the Tyrrhenian Basin with respect to the uplift and exhumation of the mid-crustal rocks of the Elba Island. It is finally argued that the interaction between the low-angle normal fault and the almost vertical shear zone determined an increase of permeability, favouring the mineralizing fluid flow during the hydrothermal stage and, reasonably, the previous emplacement of the Porto Azzurro magmatic body.

1. Introduction

In rifting environments, extension is often accommodated by coexisting normal faults and nearly orthogonal strike- to oblique-slip faults (Bally et al., 1981; Ebinger, 1989; Gibbs, 1989; Lister et al., 1986), the latter playing the role of transfer zones. By this way, the contemporaneous extension of adjacent crustal sectors is permitted, overstepping the mechanical differences that properly characterize the brittle crust (Peacock, 2003). Transfer zones are therefore significant regional structures accompanying thinning of the crust, such as the case of divergent margins (Ben-Avraham, 1992; Bosworth, 1985; Fantozzi, 1996) and/or intraplate rifting environments (Duebendorfer and Black, 1992; Larsen, 1988; Milani and Davison, 1988; Nelson et al., 1992). This framework is largely documented for those areas where extension is characterized by high-angle normal faults and nearly orthogonal strike- to oblique-slip faults (Gibbs, 1984, 1989, 1990).

Differently, studies on the relationships between low-angle normal faults and contemporaneous high-angle strike- to oblique-slip faults are scarce, since only those areas where uplift is accompanied by exhumation can offer the possibility to investigate their relations. A further complication derives from the fact that the vertical structures are good candidates to be reactivated (*e.g.:* Sibson, 1990; Collettini et al., 2005; Nortiel et al., 2011; Alçiçek et al., 2013; Ghalayini et al., 2014) during the latest stage of deformation, thus resulting the youngest structures. This implies that the vertical structures mainly show the effects of the youngest deformation, often hiding the evidences of their original contemporaneity with the low-angle normal fault activity.

In such a context, syn-kinematic hydrothermal mineralization in fault zones can contribute to define the chronological relationships among faults with different spatial and kinematic features, since the hydrothermal mineralization is a transient geological event, at local scale (Pirajno, 2009).

For this reason, the Eastern Elba Island is an ideal region to address this topic (Fig. 1). In fact it represents an exhumed sector of the inner Northern Apennines where coexisting of low-angle normal faults

* Corresponding author. Tel.: +39 0805442573.
E-mail address: domenico.liotta@uniba.it (D. Liotta).

http://dx.doi.org/10.1016/j.tecto.2015.06.025
0040-1951/

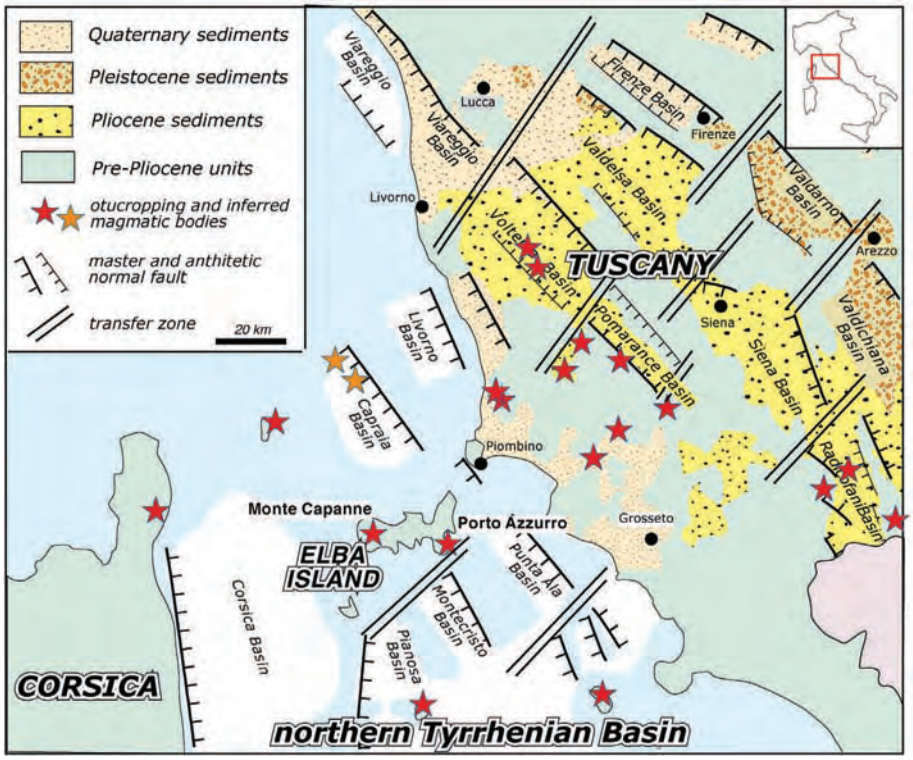

Fig. 1. Structural sketch map of the Northern Tyrrhenian Basin and Tuscany. The main Pliocene–Quaternary basins, transfer zones and magmatic bodies are indicated (after Bartole, 1995; Pascucci et al., 2007; Dini et al., 2008).

(Pertusati et al., 1993; Smith et al., 2007) and ore deposits (Dini, 2003; Tanelli et al., 2001) are well documented. Using mineralizations as time-tracers, we document the coeval activity of low-angle normal faults and high-angle strike- to oblique-slip faults and the reactivation of these latter as normal faults during subsequent tectonic evolution. The results have fallouts on the understanding of the relationships between geological structures and mineralizing fluid path.

2. Geological framework

The inner Northern Apennines originated from the convergence and collision (late Cretaceous–early Miocene) between the Adria promontory and the European plate, represented by the Sardinia–Corsica massif (Molli, 2008 with references therein). This process resulted in the stacking of tectonic units deriving from the paleogeographic domains of the inner Northern Apennines. These are as follows, from the top (Carmignani et al., 1994): (*a*) the Ligurian Units, derived from the Ligurian-Piedmont Domain, and consisting of remnants of Jurassic oceanic crust and its late Jurassic-Cretaceous, mainly clayey, sedimentary cover; (*b*) the Sub-Ligurian Units (Sub-Ligurian Domain), made up of Cretaceous-Oligocene turbidites. Ligurian and Sub-Ligurian units were thrust eastward over the Tuscan Nappe during late Oligocene–early Miocene; (*c*) the Tuscan Nappe, belonging to the internal Tuscan Domain, made up of a late Triassic–early Miocene sedimentary succession developed in evaporitic, platform, pelagic and foredeep environments. During late Oligocene–early Miocene times, the Tuscan Nappe detached from its substratum along the late Triassic evaporite level and was thrust onto the Tuscan Metamorphic Complex (external Tuscan Domain), that is composed of Palaeozoic–early Miocene metamorphic rocks (Carmignani et al., 1994; Vai and Martini, 2001).

After nappe stacking, eastward migrating extension (e.g. Barchi, 2010; Boccaletti et al, 1971; Carmignani et al., 1995; Doglioni, 1991; Lavecchia, 1988; Liotta et al., 1998; Molli, 2008; Patacca et al., 1990; Rossetti et al., 2015) affected the inner Northern Apennines (i.e., northern Tyrrhenian Basin and Tuscany), from early–middle Miocene to the Present (Brunet et al., 2000; Carmignani et al., 1995; Jolivet et al., 1990; Storti, 1995). Extension was a continuous process through time (Brogi et al., 2005a, 2005b), although, for sake of clarity, two main stages can be defined. The oldest extensional event occurred during Miocene (Brogi and Liotta, 2008; Brogi, 2011 with references therein) and determined the development of mainly eastward dipping normal faults, which produced: (a) the lateral segmentation of the more competent levels within the previously stacked tectonic units; (b) the consequent westward rotation of their hangingwalls; (c) the direct superimposition of the Ligurian Units on the late Triassic evaporite and/or on the Palaeozoic phyllite, both representing regional detachment levels; and (d) an extension of at least 120% (Carmignani et al., 1994). The youngest extensional event (Barchi, 2010; Dallmeyer and Liotta, 1998), active since the Pliocene (Fig. 1), is characterized by NW-trending normal faults crosscutting the previously developed structures (Calamai et al., 1970; Lazzarotto and Mazzanti, 1978; Mazzanti, 1966), and defining tectonic depressions where Pliocene to Quaternary marine to continental sediments were deposited (Bossio et al., 1993; Brogi et al., 2013; Liotta, 1996; Martini and Sagri, 1993). These depressions were coeval with NE-trending transfer zones (Liotta, 1991), along which the magmatic activity was concentrated (Acocella and Funiciello, 2002, 2006; Brogi et al., 2010; Dini et al., 2008). The amount of extension associated to this event is about 6–7% (Carmignani et al., 1994).

At regional scale, the clearest evidence of extensional tectonics is the opening of the Tyrrhenian Basin (Fig. 1), initiated in the Corsica Basin during the earliest Miocene (Moeller et al., 2013; Rossetti et al., 2015; Zitellini et al., 1986). Interpretations of seismic reflection lines through the Tyrrhenian Basin reveal extensional crustal structures similar to those characterizing Tuscany (Contrucci et al., 2005; Mauffret et al., 1999); in particular, NW-trending structural depressions delimited by almost orthogonal transfer zones have been largely documented in

Please cite this article as: Liotta, D., et al., Coexistence of low-angle normal and high-angle strike- to oblique-slip faults during Late Miocene mineralization in eastern Elba I..., Tectonophysics (2015), http://dx.doi.org/10.1016/j.tecto.2015.06.025

the surroundings of the Elba Island (e.g.: Bartole, 1995; Pascucci et al., 1999; Pascucci et al., 2007).

In this framework, the Elba Island (Fig. 2) is an exhumed sector of the Northern Apennines chain (Jolivet et al., 1994) where the above-mentioned stacked units are traditionally grouped and described as five "complexes" (Fig. 2; Trevisan, 1950; Keller and Pialli, 1990; Pertusati et al., 1993; Dini et al., 2008; Smith et al., 2010). This structural setting is well exposed in eastern Elba Island where oceanic and continental units are doubled and involved in out-of-sequence thrusts (Keller and Pialli, 1990) dated at early Miocene (19.68 ± 0.15 Ma, Deino et al., 1992) by $^{39}Ar/^{40}Ar$ geochronology.

As a consequence of the uplift and exhumation of the Elba mid-crustal rocks, the Palaeozoic micaschist (Complex I), representing the deepest unit exposed in the inner Northern Apennines (Musumeci et al., 2011), widely crops out in the Monte Calamita promontory (Fig. 2). Exhumation also involved the mid-crustal magmatic intrusions of the Monte Capanne and Porto Azzurro monzogranite complexes, respectively located to the western and eastern sides of the Elba Island (Fig. 2). The main body of the well-exposed Monte Capanne complex results from multiple magmatic injections (Farina et al., 2011), whose emplacement is estimated at about 7 Ma (Westerman et al., 2004). The Porto Azzurro monzogranite is younger and dated at 5.9 ± 0.2 Ma ($^{39}Ar/^{40}Ar$ method) by Maineri et al. (2003), although a maximum age of 6.23 ± 0.06 Ma (^{39}Ar /^{40}Ar method) is envisaged by Musumeci et al. (2011).

In eastern Elba Island, an important hydrothermal fluid circulation during magma cooling controlled the occurrence of tourmaline mineralization and Fe-oxides ore deposits, among many other minor hydrothermal mineral associations (Dini, 2003; Tanelli et al., 2001).

The relationships between extension and magmatism involve the evolution of the low-angle Zuccale normal fault, representing one of the main unroofing structures of the Elba Island magmatic complexes (Fig. 2). On the basis of cartographic evidence, its horizontal throw is estimated in about 6 km (Fig. 2), a part of which was gained after the emplacement of the Porto Azzurro monzogranite (Pertusati et al., 1993). The activity of the Zuccale fault is encompassed between late Miocene, as derived from the age of the associated magmatic bodies, and early Pliocene (Westerman et al., 2004). This structure, described by several authors (Pertusati et al., 1993; Collettini and Holdsworth, 2004; Smith et al., 2007), crops out in the surroundings of Capoliveri and Porto Azzurro localities (Figs. 1 and 2).

3. The Capoliveri–Porto Azzurro area

The Zuccale normal fault is crosscut by faults (Geological Map of Italy, 2013) defining a NE-trending shear zone (the Capoliveri–Porto Azzurro shear zone, Fig. 2), about 2 km wide and 7 km long, at least, composed of aligned and parallel fault segments. The relationships between the Zuccale normal fault and the NE-trending fault system are exposed in the Capoliveri surroundings where we carried out a detailed field mapping (Fig. 3). Then, in order to better define kinematics and structural features of the fault segments, we studied outcrops along the Capoliveri coast (Fig. 3) and we enlarged our analysis along their NE-trend, in the Barbarossa area (Fig. 2).

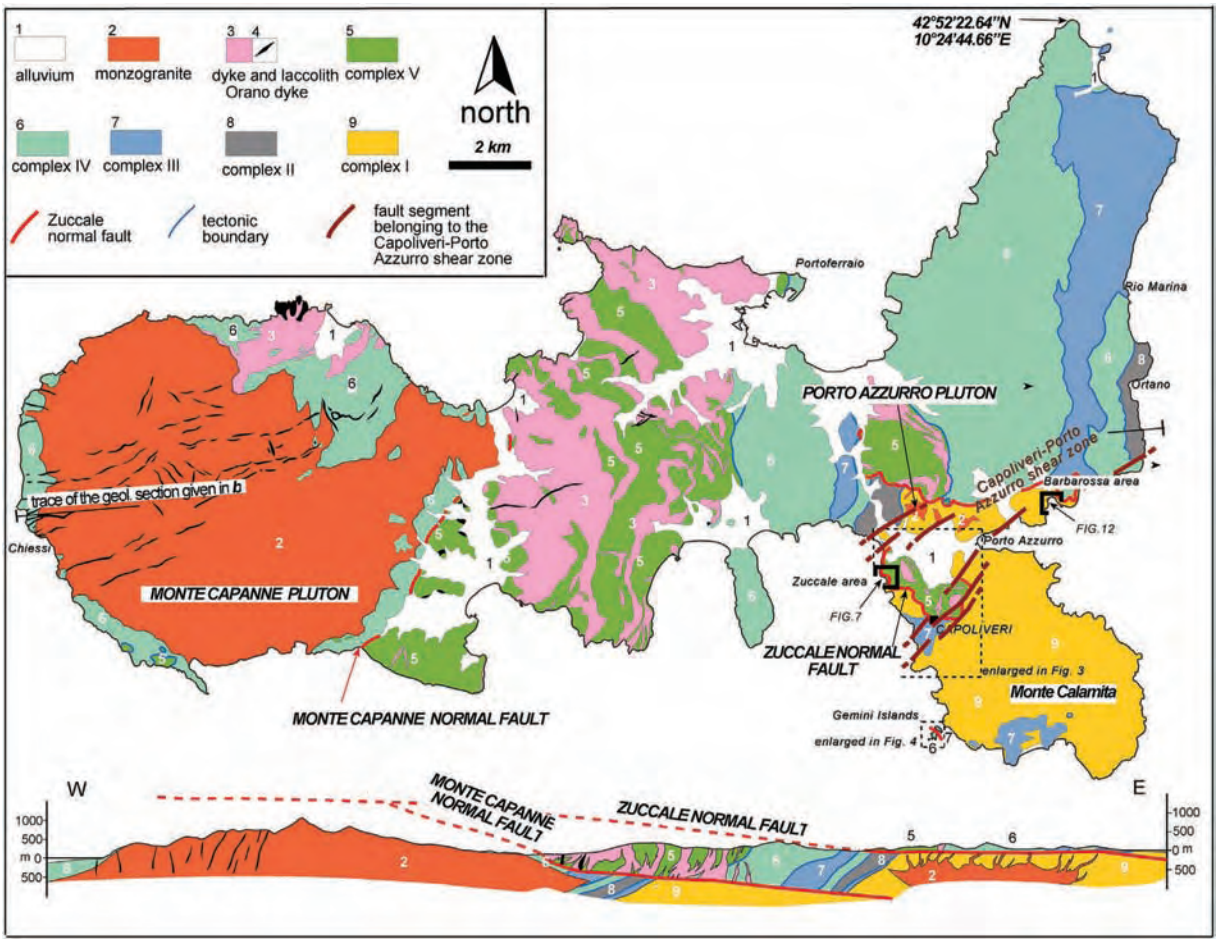

Fig. 2. Schematic geological map of the Elba Island and related geological cross section. The study areas are squared.

Please cite this article as: Liotta, D., et al., Coexistence of low-angle normal and high-angle strike- to oblique-slip faults during Late Miocene mineralization in eastern Elba I..., Tectonophysics (2015), http://dx.doi.org/10.1016/j.tecto.2015.06.025

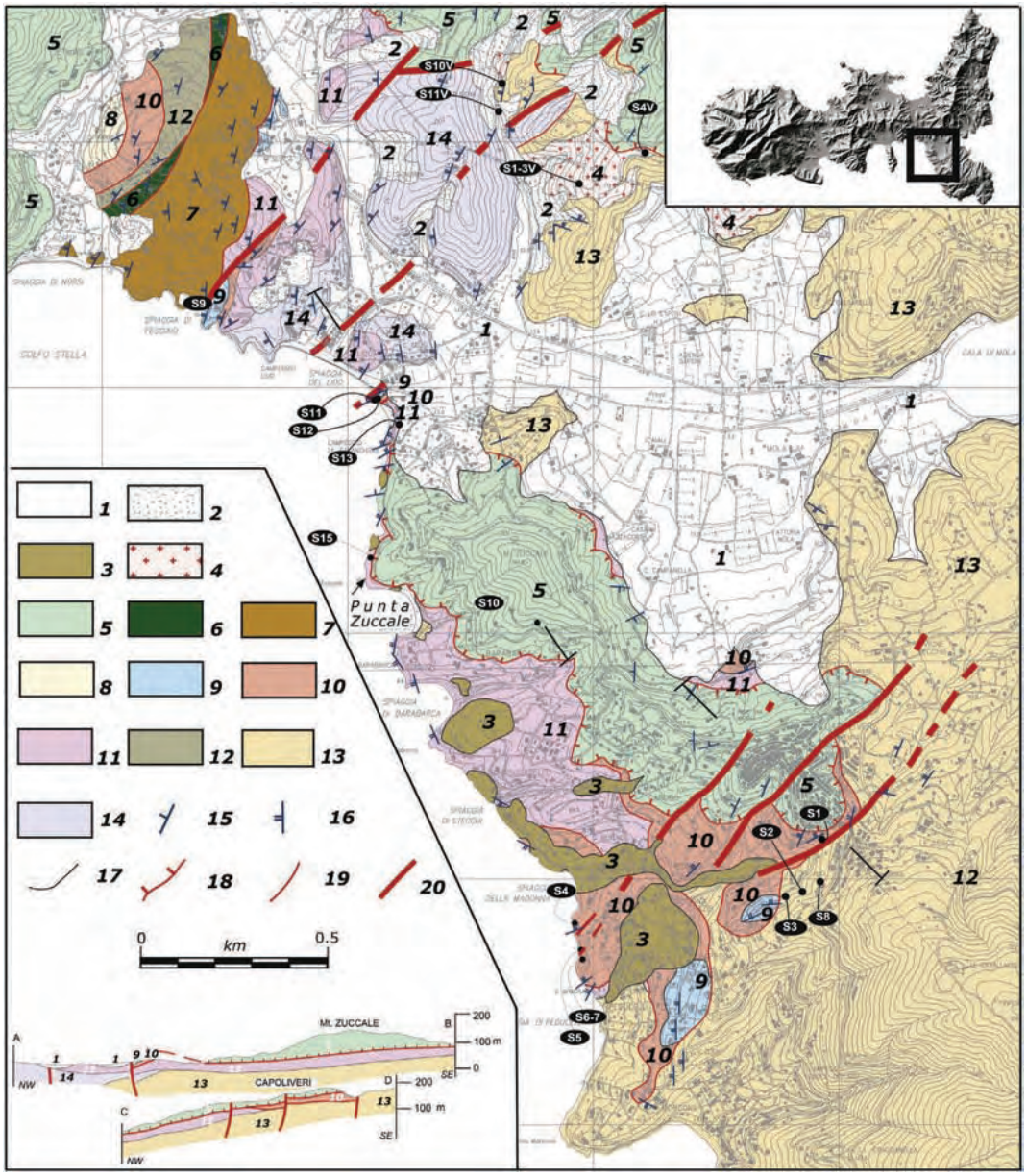

Fig. 3. Geological map and cross sections of the Capoliveri area and surroundings. 1. Alluvial and beach deposits (Holocene); 2. Debris (Holocene); 3. Eolian sandstone (Pleistocene); 4. Porto Azzurro monzogranite; Ligurian Units: 5. terrigeneous and calcareous sediments (late Cretaceous); 6 and 7. Acquadolce Unit: ophiolite and serpentine (Jurassic) and metasiltite and phyllite with quartz vein (Cretaceous), respectively; 8. Grassera Fm: marly limestone and claystone (Cretaceous); Tuscan Metamorphic Complex: 9. Valdana Fm.: whitish massive marble (early Jurassic); 10. Tocchi Fm. yellowish dolostone; 11. Barabarca Fm: quartz metaconglomerate and interlayered phyllite (early–middle Triassic); 12. Rio Marina Fm. graphitic phyllite and metaconglomerate (late Carboniferous - early Permian); 13. Mt. Calamita Fm: Qtz + Mu + Bt ± And ± K-feldspar micaschist (early Carboniferous); 14. Ortano Fm: porphyroid and porphyric schist (middle Ordovician); 15. bedding attitude; 16. main schistosity attitude; 17. stratigraphic contact; 18. Zuccale normal fault; 19. low angle fault; 20. high angle fault.

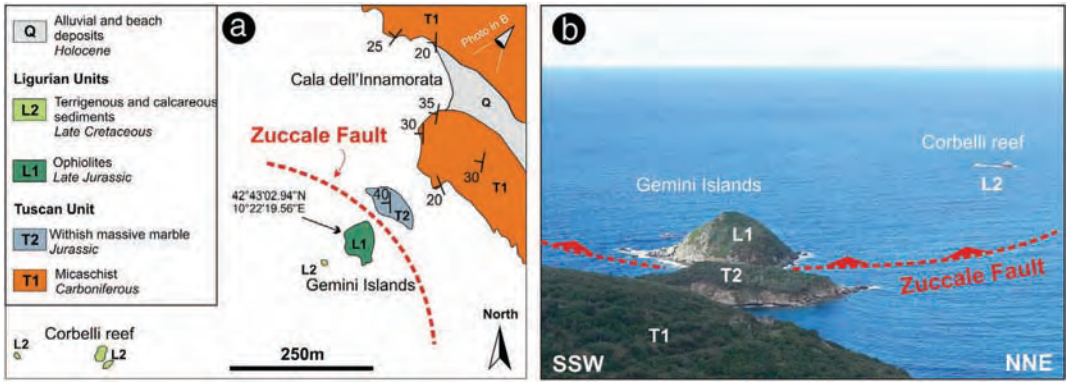

Fig. 4. (A and B) Geological sketch map and panoramic view of the Gemini Islands, respectively; in A, the trace of the Zuccale Fault is highlighted. Location in Fig. 2.

Please cite this article as: Liotta, D., et al., Coexistence of low-angle normal and high-angle strike- to oblique-slip faults during Late Miocene mineralization in eastern Elba I..., Tectonophysics (2015), http://dx.doi.org/10.1016/j.tecto.2015.06.025

3.1. Capoliveri area

At map scale (Fig. 3), the main important structures are as follows: (a) the almost vertical, aligned and parallel NE-trending fault segments, crosscutting the Zuccale fault, and here referred to as the Capoliveri–Porto Azzurro shear zone (Fig. 2 and 3); (b) the Zuccale normal fault, displaying a NW-gently dipping attitude in the surroundings of the Capoliveri village. Differently, more to the south, it dips to the

Fig. 5. Structures associated to the NE-trending fault system in the Capoliveri area. (a) Panoramic view of a fault zone (Station 7, in Figs. 3 and 6) with a meter-thick damage zone characterized by different slip-surfaces. (b) Particular of the carbonate mineralization in the cataclasite. (c) Different generations of slip surfaces with their own slickenlines, affecting the damage zone. (d) NE-trending mineralized fault zone at Lido di Capoliveri area (Station 11, Fig. 3 and 6). (e) Detail of the mineralized vein and its host-rock. (f) Slickelines indicating the dominant normal component characterizing the younger event.

Please cite this article as: Liotta, D., et al., Coexistence of low-angle normal and high-angle strike- to oblique-slip faults during Late Miocene mineralization in eastern Elba I..., Tectonophysics (2015), http://dx.doi.org/10.1016/j.tecto.2015.06.025

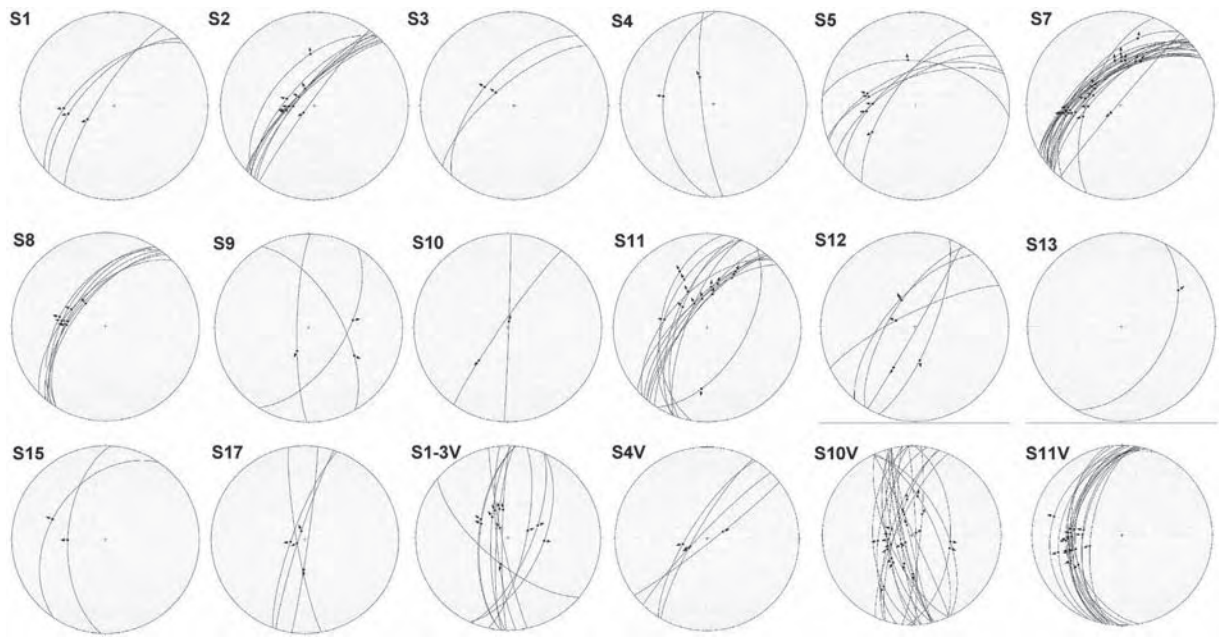

Fig. 6. Stereographic diagrams lower emisphere, equiareal projection, of the structural and kinematic data, collected in the Capoliveri area. Location of the structural stations in Fig. 3. Stereograms were performed with "FaultKin" 5.2.6, by R.W. Allmendinger, http://www.geo.cornell.edu/geology/faculty/RWA/RWA.html.

SW, as constrained by the Gemini Islands structural setting (Figs. 2 and 4).

As it regards the NE-trending faults, the length of each fault segment ranges between 1 and 5 km with a maximum vertical throw of about 30–40 m, while the total vertical displacement of the shear zone exceeds at least 100 m (Fig. 3). The best exposures are close to the Spiaggia della Madonna (stations 6 and 7, Fig. 3) and Lido di Capoliveri (stations 11 and 12, Fig. 3) where a system of parallel faults affects middle–late Triassic and Jurassic marble (Fig. 5). The damage zones are commonly characterized by joints and minor fault planes whose density increases approaching the respective main slip surfaces, as testified by the fracture spacing, from 1 m to 2–3 cm close to the related fault plane. The cataclasite bands, up to 1 m thick, are commonly localized in the hangingwall of the main fault (Fig. 5a); these consist of a lithological homogeneous carbonate breccia, with elements ranging between 5 cm and few millimeters, and deriving from the comminution of the marble.

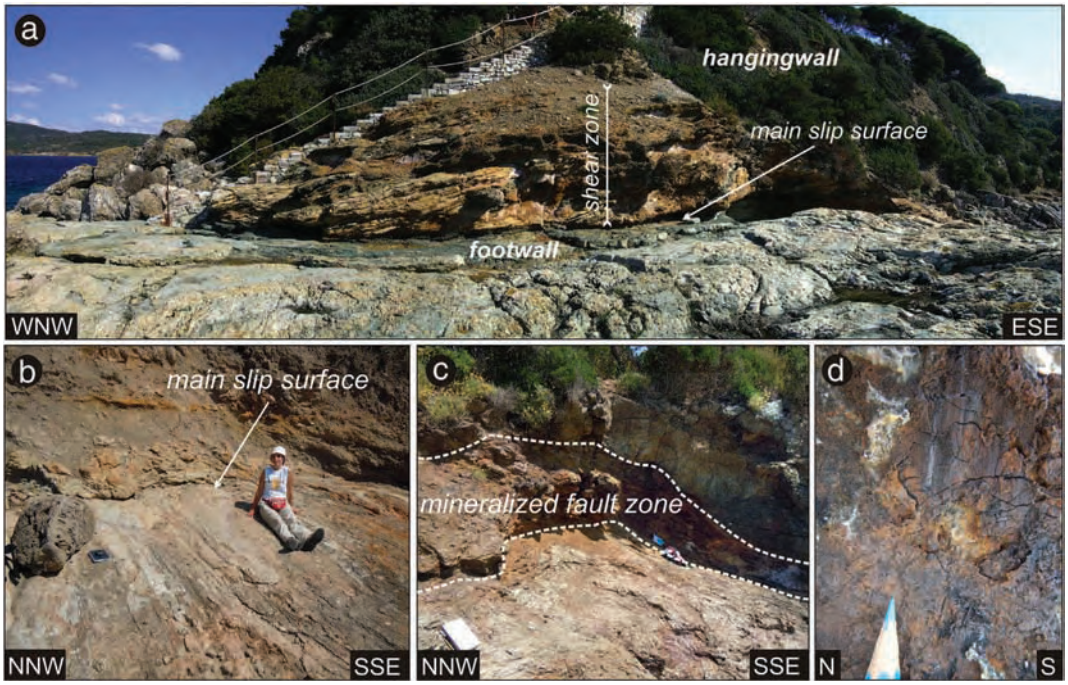

Fig. 7. Geometric and kinematic features of the Zuccale fault zone. (a) Panoramic view of the Zuccale fault zone exposed at Punta Zuccale (location in Fig. 3). (b) Slickenlines on the main slip surface. (c) Fe-oxides and/or Fe-oxyhydroxides mineralized Zuccale fault zone. (d) Fe-oxides and/or Fe-oxyhydroxides shear vein on the main slip surface.

Please cite this article as: Liotta, D., et al., Coexistence of low-angle normal and high-angle strike- to oblique-slip faults during Late Miocene mineralization in eastern Elba I..., Tectonophysics (2015), http://dx.doi.org/10.1016/j.tecto.2015.06.025

The matrix and cement are calcitic, although the latter can be locally scarce. Cataclasite often channeled fluids, which deposited calcite within pockets (Fig. 5b). Kinematic indicators on polished fault planes consist of slickenlines and calcite fibers, indicating at least three main superimposed oblique movements, from dextral to sinistral shear components (Fig. 5c), although the younger event is with a dominant normal component (Fig. 5f). Fe-oxides and/or Fe-oxyhydroxides extensional large veins, 1 to 2 m thick, are often associated to these brittle shear zones (station 12 in Figs. 3, 5d), testifying their close relationships with the mineralizing fluid flow. Similar structural and kinematic data are observed from the other investigated structural sites in the Capoliveri area (Figs. 3 and 6) where slickenlines were detected along fault surfaces affecting the micaschist.

The best exposure of the Zuccale normal fault (Fig. 7a) is at Punta Zuccale (Fig. 3), where the Ligurian Units directly rest on the early–middle Triassic quartzite (Quarziti di Barabarca Fm, in Garfagnoli et al., 2005). The boundary is marked by a flat-lying shear zone, gently dipping to the East (<15°), characterized by a cataclasite up to 5 m thick. A description of its internal stratigraphy and texture is reported in Collettini and Holdsworth (2004). In agreement with Pertusati et al. (1993) and Collettini and Barchi (2004), the shear zone shows S/C and C/C′ structures clearly indicating a top-to-the-east sense of shear. The main slip surface, localized at the top of the early–middle Triassic quartzite (Barabarca Fm), is characterized by grooves and mechanical striations with Fe-oxides and/or Fe-oxyhydroxides (Fig. 7b–d). These evidences indicate that the Zuccale low-angle normal fault evolved from ductile to brittle deformation (Pertusati et al., 1993; Collettini and Holdsworth, 2004; Collettini and Barchi, 2004).

At Punta Zuccale brittle structures affect the footwall of the Zuccale fault (Fig. 8) and are here described considering their mineralization features and cross-cutting relationships. Some of them clearly dissect the flat-lying Zuccale shear zone (see also: Smith et al., 2007). The oldest brittle structures in the footwall are tourmaline veins, mainly composed of dravite (Fig. 9a); these are mm-thick and up to 15 cm long extensional veins (Fig. 9b) with dip direction attitude of about 120/80 (Fig. 8), and at high angle (about 70°) to the main quartzite foliation. Tourmaline veins characterize a small area in the footwall (Fig. 8). The dravite event is followed by NW–SE, SW–NE and WNW–ESE trending fault systems (Fig. 8) with cm to dm offsets (Fig. 9c–e). The NW–SE and SW–NE trending fault systems are sub-vertical, undulated, irregular and characterized by opposite dip-directions (Fig. 10a). These form 1 m thick damage zones, on average, with associated shear fractures and minor faults (Fig. 10b–c). The damage zones are defined by spaced shear fractures, determining isolated lithons, progressively larger getting away from

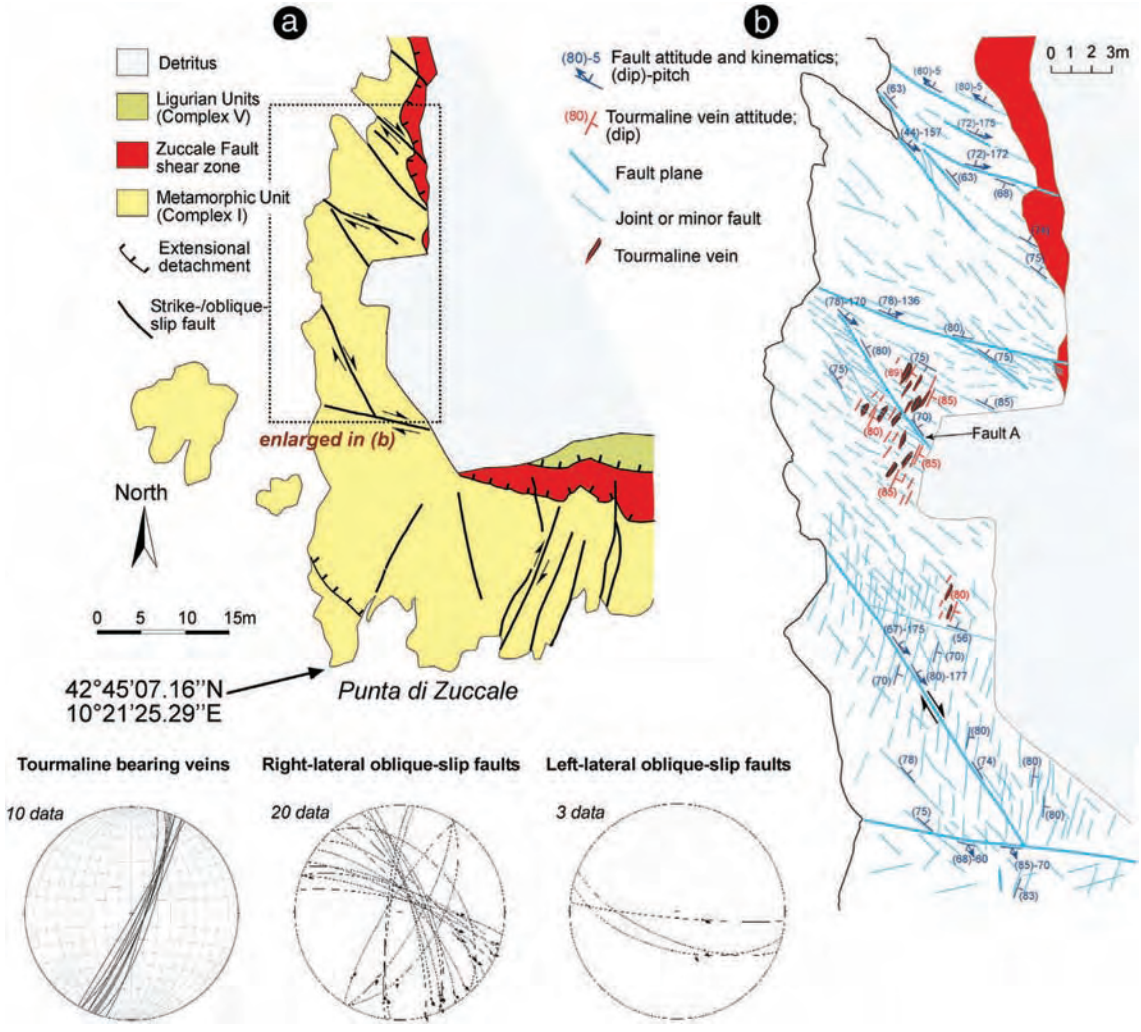

Fig. 8. Structural sketch of the Punta Zuccale area (location in Fig. 3): (a) main brittle structures affecting the footwall and the shear zone of the Zuccale fault; (b) relationships among tourmaline bearing veins, transtensional faults and their associated minor fractures. Structural and kinematic data are plotted in stereographic diagrams, lower emisphere, equiareal projection, performed with OSXStereonet 1.0, by Cardozo and Allmendinger, and "FaultKin" 5.2.6, by R.W. Allmendinger, both from http://www.geo.cornell.edu/geology/faculty/RWA/RWA.html.

Please cite this article as: Liotta, D., et al., Coexistence of low-angle normal and high-angle strike- to oblique-slip faults during Late Miocene mineralization in eastern Elba I..., Tectonophysics (2015), http://dx.doi.org/10.1016/j.tecto.2015.06.025

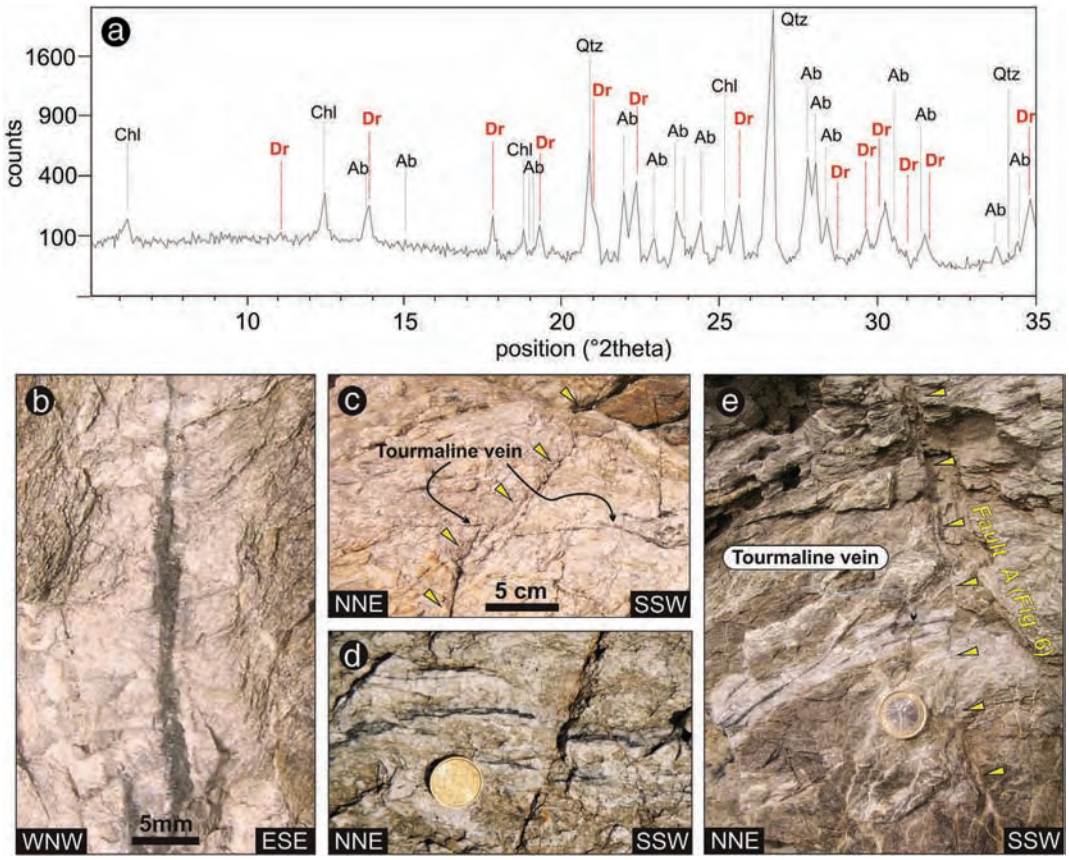

Fig. 9. Tourmaline bearing veins exposed at Punta Zuccale. Location in Fig. 8. (a) X-ray diffractogram, indicating the occurrence of quartz (Qtz), albite (Ab), chlorite (Chl) and tourmaline in its dravite (Dr) variety. (b) Typical outcropping features of the tourmaline vein. (c–d) Relationships between tourmaline vein and subsequent brittle structures. (e) Tourmaline vein dissected by a transtensional fault, referred to as "fault A" in Fig. 8.

their slip surfaces (Fig. 10a–b). The cataclasite of these structures is composed of comminuted quartzite elements, ranging in size from 0.1 to 2 cm. The core zone is typified by the smallest elements, located along the slip zone, few mm thick. The cataclasite is cemented by Fe-oxides and/or Fe-oxyhydroxides, quartz and/or calcite, derived from fluids circulating through the permeable rock volumes; the mineralization can partially or totally fill the voids along the main fault and its associated fractures (Fig. 10d–e). The angular relationships between minor fractures and the main slip surfaces indicate a dominant right-lateral shear component (Fig. 11a–b), as it is also suggested by the occurrence of clear extensional jogs (Fig. 11c) along shear planes.

Slickenlines and aligned quartz/calcite fibers on fault planes (Figs. 10a–b and 11d) are oblique, with pitches from 140° to 170° (Fig. 8). Thus, joining information from angular relationships, extensional jogs and slickelines pitches, we interpret the dominant kinematics as transtensional with dextral component.

Some of these faults dissect the cataclasite of the Zuccale normal fault, producing centimeter to decimeter offsets (Fig. 11e–j), often channeling carbonate-rich fluids which permeate the slip surface, its associated fractures (Fig. 10e–f) and the pre-existing foliations within the Zuccale shear zone.

The few WNW-ESE oriented faults (Fig. 8) display kinematic indicators suggesting a dominant normal movement with a minor sinistral component. No clear field data are available to define the chronological relationships with the previously described right-lateral oblique slip faults. However, the fact that these appear to interrupt the other fault systems, and the lack of mineralization in their fault zones, suggest that these postdate the mineralizing event.

3.2. Barbarossa area

Following toward NE the trend of the faults mapped in the Capoliveri surroundings (Fig. 3), the most suitable area for the goals of this work is the Barbarossa area (Figs. 2 and 12). The Porto Azzurro monzogranite and the Palaeozoic micaschist host-rocks are well exposed in the eastern (Capobianco promontory; see also: Smith et al., 2010) and northwestern parts of the Barbarossa gulf. Here, we describe low-angle and sub-vertical brittle structures, their cross-cutting relationships and associated mineralization.

Concerning the low-angle structures, a slip zone affecting the micaschist belonging to the Mt. Calamita Fm crops out extensively in the footwall of the Zuccale normal fault (Fig. 13a). Such a slip zone consists of graphite-rich low-angle fault plane (Fig. 13b), developed within a cataclasite level deriving from the comminution of graphite and quartz crystals (Fig. 13c). Extensional and shear veins with Fe-oxides and/or Fe-oxyhydroxides characterize the damage zone of this structure (Fig. 13e).

Kinematic indicators are given by the relationships between the main graphite-bearing fault zone and associated minor faults and fractures (Fig. 13d) and by the mesostructures on the fault-slip plane. These are lunate structures, grooves, mega-grooves (Fig. 13d) and quartz shear veins (Fig. 13f), with a top-to-the-east sense of shear, defining a clear normal movement (Fig. 12), consistent with the kinematics of the Zuccale normal fault (Collettini and Barchi, 2004; Pertusati et al., 1993). Thus, the graphite-bearing low angle normal fault is interpreted as a structurally deeper subsidiary structure of the Zuccale main normal fault, being located in its footwall, few tens meters below the main detachment.

Please cite this article as: Liotta, D., et al., Coexistence of low-angle normal and high-angle strike- to oblique-slip faults during Late Miocene mineralization in eastern Elba I..., Tectonophysics (2015), http://dx.doi.org/10.1016/j.tecto.2015.06.025

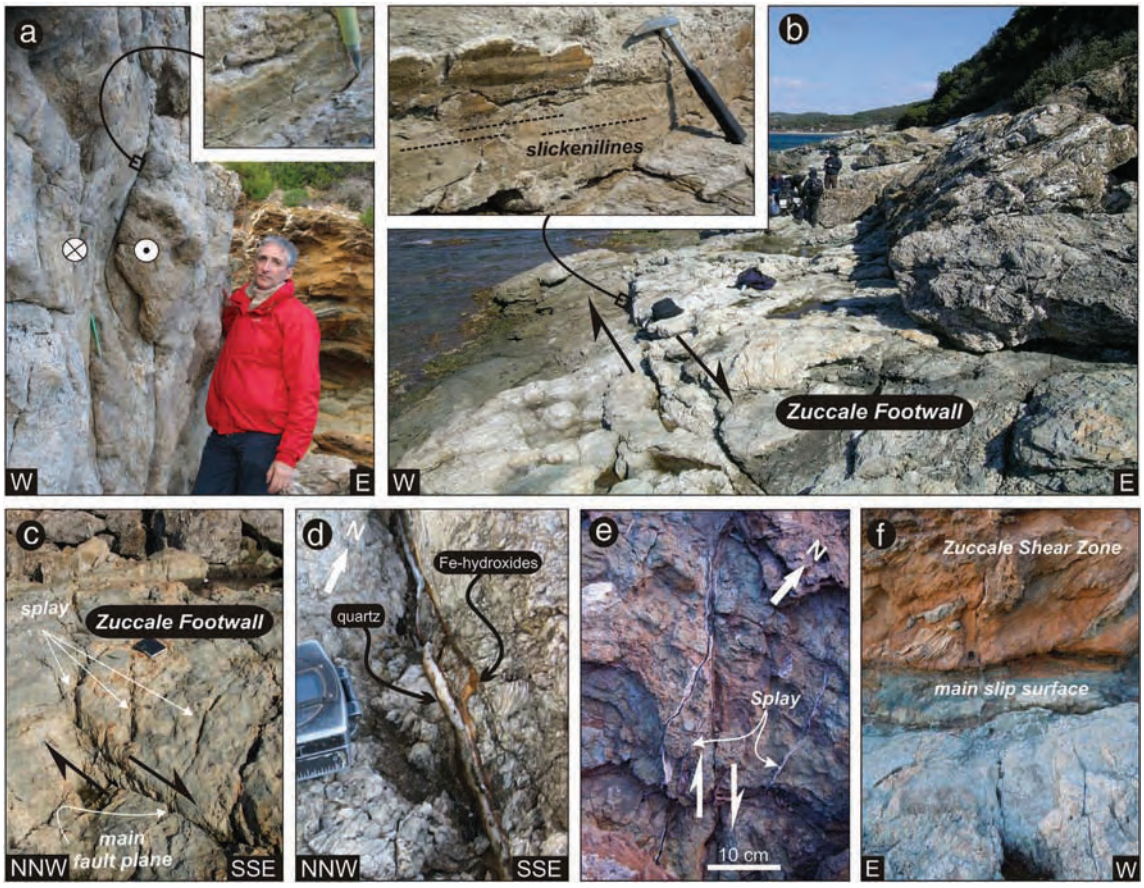

Fig. 10. Structures affecting the footwall and shear zone of the Zuccale normal fault, at Punta Zuccale: (a) Right lateral strike-slip fault damage zone displaying anostomosed fault segments determining lozange-shaped lithons. Location in Fig. 7. (b) En-echelon right-lateral strike-slip fault segment linked by highly damaged rock volume. (c) Right-lateral strike-slip fault tip zone characterized by horse tail-wing structures. (d) Plane view of a fault slip surface with Fe-oxides and/or Fe-oxyhydroxides shear vein. (e) Plane view of a carbonate mineralization in a right-lateral strike-slip fault and in its associated fractures. (f) Carbonate vein affecting the footwall and the Zuccale shear zone.

Another significant low-angle normal fault in the Zuccale footwall is recognizable in the Capobianco promontory (Fig. 14); it affects the roof of the 5.9 Ma Porto Azzurro monzogranite (Fig. 14a–c) with K-feldspar megacrystals (Dini et al., 2008). The outcrop is characterized by a fault gauge about 3 m thick (Fig. 14c), mostly made up of comminuted quartz and biotite (Fig. 14d) from the monzogranite, that is located in the footwall of the structure (Fig. 14e).

In the late cooling stage, the monzogranite and surrounding host-rocks were injected by hydrothermal fluids which deposited tourmaline ± quartz (Fig. 15a–b). This hydrothermal circulation continued through time, mainly channeled in the damage zone of nearly SW–NE vertical faults, dissecting the monzogranite and its host rocks, as it is suggested by the evolution of the deformation from ductile (Fig. 15e–f) to brittle (Fig. 15c–d) shear zones, with tourmaline-bearing veins.

As it regards the sub-vertical faults, the most prominent feature of the 1–2 m thick damage zone, is given by splays having low-angle relationships with the main slip surface (Fig. 15g). Often, these structures consist of tourmaline shear veins, few mm to cm thick (Fig. 15g). In the veins, the crystal mass is composed of comminuted tourmaline and rare quartz, thus suggesting that the shear activity was coeval and postdated the mineral deposition (Fig. 15h–i). Nevertheless, nearly euhedral tourmaline crystals (Fig. 15h–i), suggest that crystallization sealed voids when the shear activity ceased.

The kinematic indicators of the sub-vertical faults are shear veins, slickensides (Fig. 15j) and the relationships between fractures and main fault surfaces (Fig. 15k–l); all of them are consistent in indicating a dominant sinistral transtensional component (Fig. 12) in their slip movement.

Finally, as already observed at Punta Zuccale, tourmaline-bearing fault planes are crosscut by NW–SE trending faults with local Fe-oxides and/or Fe-oxyhydroxides shear veins (Fig. 16a–b). Kinematic indicators are provided by the relationships between the main and minor fractures (Fig. 16c–g) and by slickenlines on the fault planes (Fig. 16h–i), suggesting a dominant dextral transtensional movement (Fig. 12). The NW–SE and SW–NE trending faults are characterized by mutual cross-cutting relationships attesting their affinity to a common strain field whose activity persisted through time (Fig. 16j).

4. Discussion

The study areas (Figs. 8 and 12), located within the Capoliveri–Porto Azzurro shear zone, reveal mineralized faults and shear veins with different kinematics and trends. However, these can be related to a common framework, with W–E stretching direction (Fig. 17a), consistent with the kinematics of the Zuccale normal fault (Smith et al., 2007) and subsidiary low-angle structures (Fig. 12).

4.1. Structural synthesis

The cross-cutting relationships among mineralized structures show that the Fe-oxides and/or Fe-oxyhydroxides-bearing faults developed after the tourmaline-bearing faults. Therefore, we interpret these latter as the first deformational features formed during the magma cooling, as also indicated by the ductile to brittle tourmaline-bearing shear structures affecting the monzogranite (Fig. 15e–f). Furthermore, as the tourmaline-bearing structures trend parallel to the map-scale faults

Please cite this article as: Liotta, D., et al., Coexistence of low-angle normal and high-angle strike- to oblique-slip faults during Late Miocene mineralization in eastern Elba I..., Tectonophysics (2015), http://dx.doi.org/10.1016/j.tecto.2015.06.025

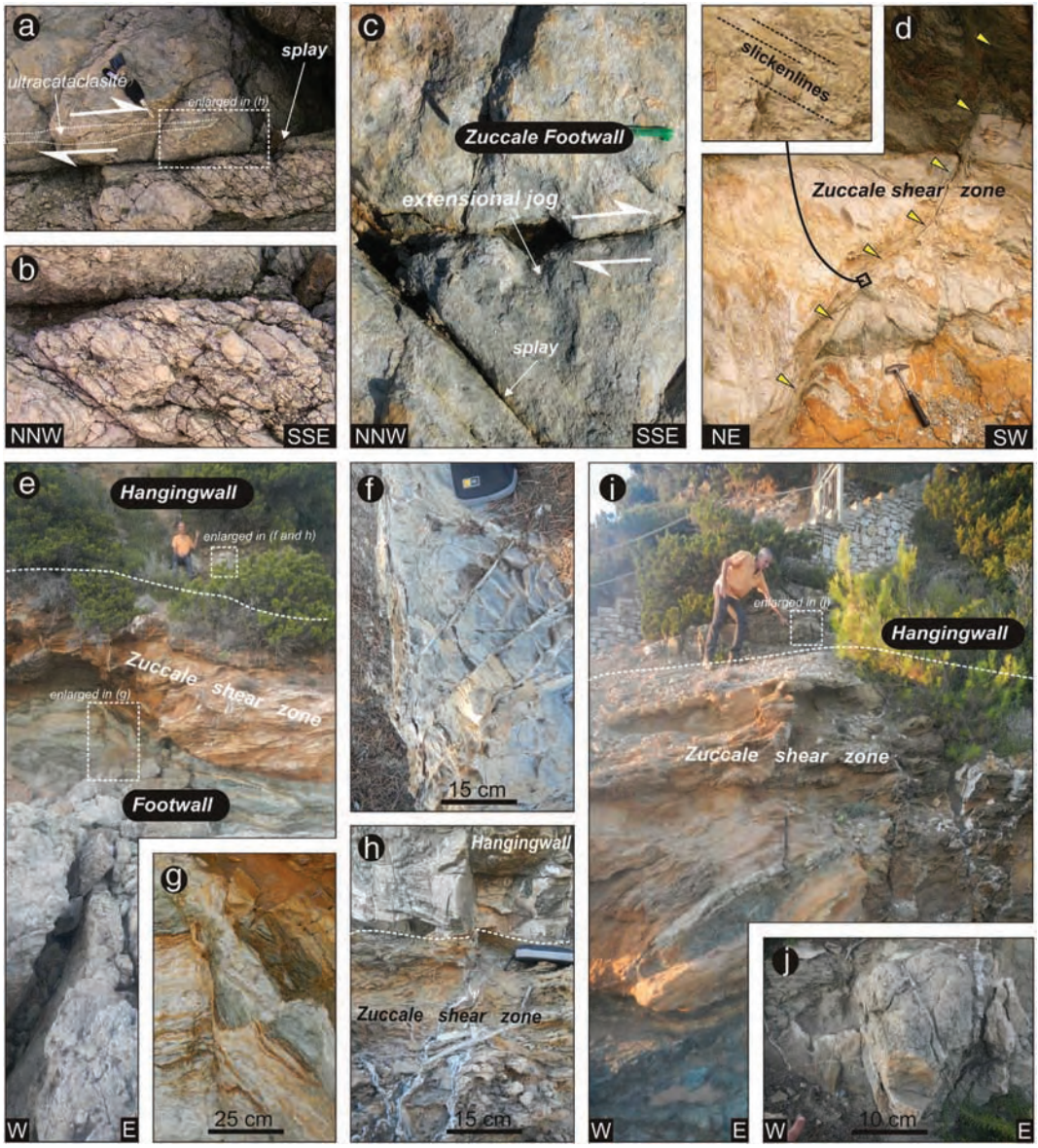

Fig. 11. Relationships between mineralization and transcurrent faults affecting the Zuccale footwall and shear zone at Punta Zuccale. Location in Fig. 8. (a and b) The transtensional faults are often characterized by minor fractures determining a damage zone of about 1 m thick. (c) Extensional jog associated to a right-lateral strike-slip fault. (d) Examples of fault dissecting the Zuccale shear zone. (e–j) Panoramic views, with details, showing the continuity of the brittle structures through the entire fault zone; in the hangingwall (Ligurian Units), the deformation is expressed by localized calcite/quartz veins.

(Fig. 3), we argue that the NE-trending direction remained dominant through time favoring the development of new brittle structures after the magma cooling stage.

On the basis of the relationships between brittle structures and mineralization, it results that the late (brittle) activity of the Zuccale normal fault is surely coeval with the hydrothermal stage. In fact: (a) the low-angle normal faults (Fig. 13) affecting the Zuccale footwall are characterized by cataclasite with syn-kinematic graphite deposition (reasonably related to geothermal fluid circulation along the fault zone), later dissected by almost vertical Fe-oxides and/or Fe-oxyhydroxides-bearing structures; (b) the Zuccale cataclasite is permeated by Fe-oxides and/or Fe-oxyhydroxides mineralizing fluids during its activity (Fig. 7). A similar process has been envisaged to the late stage of hydrothermal circulation determining oxidation of Fe-rich brines exsolved from the Monte Capanne pluton (cf. Rossetti and Tecce, 2008; Rossetti et al., 2007).

Furthermore, it results that the Fe-oxides and/or Fe-oxyhydroxides-bearing structures are subsequent to the graphite and tourmaline mineralization (Fig. 17b), although in the frame of the same kinematics explaining both the Capoliveri–Porto Azzurro shear zone and Zuccale structures (Fig. 17a). Moreover, taking into account the depth at which the Zuccale fault acted (about 4–5 km: Westerman et al., 2004), a significant role of the mineralizing fluid pressure in enhancing fractures is reasonable, as it is presented and argued in Smith et al. (2007).

The concomitant circulation of the same mineralizing fluids in both low-angle normal and high-angle faults, indicates that fault interaction increased the secondary permeability, addressing the fluid path.

The time interval in which fluid circulation occurred, should be <1 Ma, considering that: (a) the hydrothermal fluids are associated to the Porto Azzurro cooling monzogranite; (b) the latter is compositionally similar to the Monte Capanne monzogranite (Fig. 2), that cooled down in < 1 Ma (Caggianelli et al., 2014); (c) the hydrothermal

Please cite this article as: Liotta, D., et al., Coexistence of low-angle normal and high-angle strike- to oblique-slip faults during Late Miocene mineralization in eastern Elba I..., Tectonophysics (2015), http://dx.doi.org/10.1016/j.tecto.2015.06.025

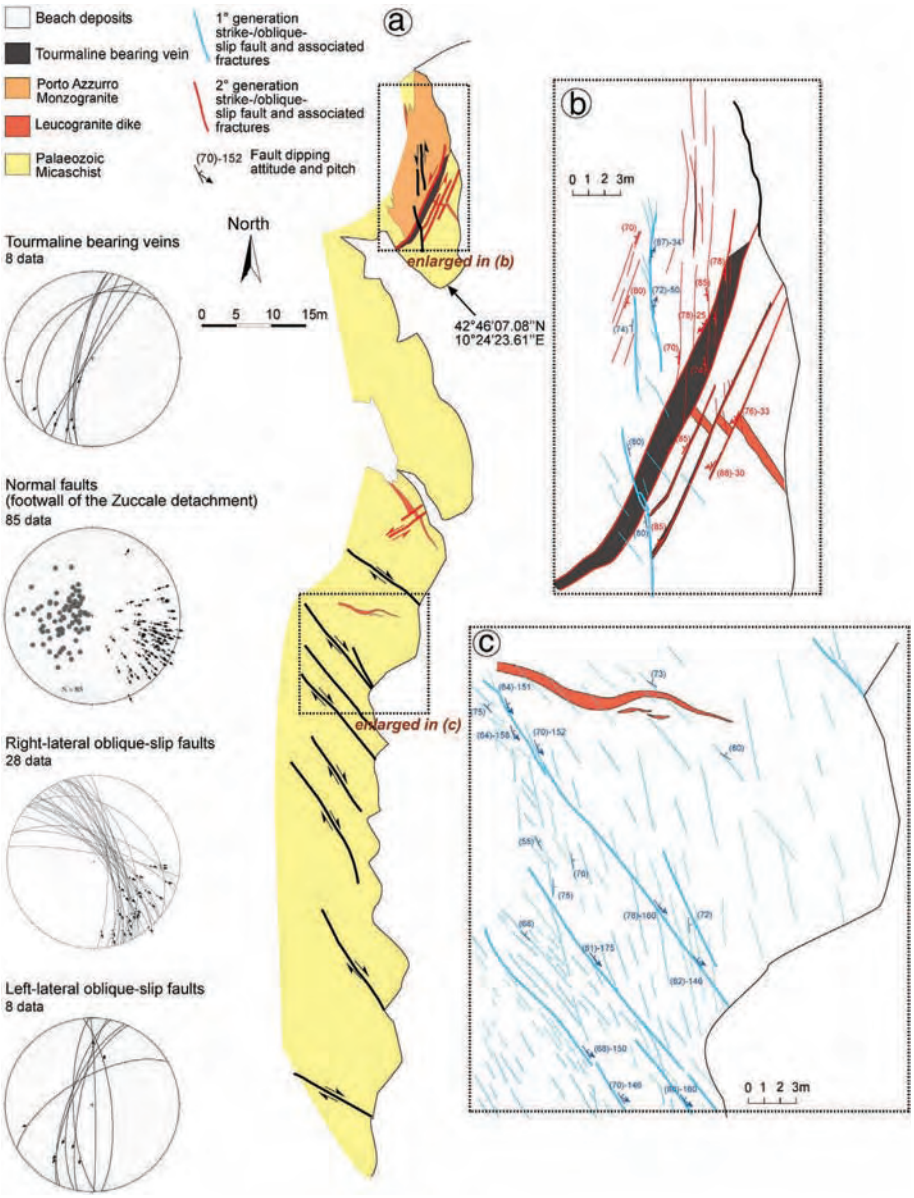

Fig. 12. Structural sketch of the Barbarossa western coast (location in Fig. 2). (a) Main brittle structures affecting the footwall of the Zuccale fault. (b) Relationships between tourmaline-bearing faults with their associated minor structures and leucogranite dike. (c) Detailed sketch illustrating the geometric and kinematic features of the transtensional faults. More information in the text. Structural and kinematic data are plotted in stereographic diagrams, lower emisphere, equiareal projection, with "FaultKin" 5.2.6, by R.W. Allmendinger, http://www.geo.cornell.edu/geology/faculty/RWA/RWA.html.

stage should be concluded when the opening of the Pliocene Punta Ala Basin (Bartole, 1995) began (Fig. 17b), in the frame of the Miocene-Pliocene extensional evolution of the inner Northern Apennines (Fig. 1).

In summary, the coeval activity between the final stage of the low-angle Zuccale normal fault and the Capoliveri–Porto Azzurro shear zone and their kinematic compatibility, point to a common strain field, at least active from the cooling of the monzogranite to the opening of the Punta Ala Basin. In this scenario, we explain the role of the Capoliveri–Porto Azzurro structure as a transfer zone, active at least during the final brittle behavior of the Zuccale fault.

The different offsets between the low-angle Zuccale fault (6 km at least) and the Capoliveri–Porto Azzurro transfer zone (tens of meters for each segment) is explained as deriving from a small shift of the shear plane of the Zuccale fault, along the Capoliveri–Porto Azzurro structure. In fact, transfer zones accommodate different steps between normal fault segments (Peacock, 2003), thus their offset is not directly linked to the throw of the associated normal fault segments.

4.2. Relative chronology of strike-slip shearing and magma emplacement

Two more questions are still open about the Capoliveri–Porto Azzurro transfer zone: was it active during the earlier (ductile) stage of the Zuccale normal fault? And, did it play a role during the emplacement of the Porto Azzurro magmatic body? Considering that the deformation was active from the initial period of magma cooling, insisting in the same volume of rocks where magma emplaced, it is suggested that the Capoliveri–Porto Azzurro transfer zone also influenced the location of the magma flow and of the subsequent hydrothermal circulation. This is in agreement with Dini et al. (2008) who proposed that the NE-trending transfer zones of the inner Northern Apennines controlled the emplacement of the Miocene–Pliocene magmatic complexes.

Please cite this article as: Liotta, D., et al., Coexistence of low-angle normal and high-angle strike- to oblique-slip faults during Late Miocene mineralization in eastern Elba I..., Tectonophysics (2015), http://dx.doi.org/10.1016/j.tecto.2015.06.025

Fig. 13. Main features of the graphite-bearing fault zone in Barbarossa western coast. (a) Panoramic view. (b) Graphite-bearing fault slip surface. (c) Graphite-rich cataclasite. (d) Panoramic view of the extensional fault zone affecting the footwall of the Zuccale fault and detail of the shear surface. (e) Fe-oxides and/or Fe-oxyhydroxides shear vein in the graphite-rich cataclasite. (f) Quartz fibers characterizing minor shear veins associated to the fault zone.

However, several authors in the Elba Island claimed a connection between the evolution of the low angle normal faults and magma emplacement. Daniel and Jolivet (1995) suggested that the emplacement of the Monte Capanne pluton was accompanied and accommodated by the coeval activity of east-dipping extensional shear zones. In contrast, Farina et al. (2011) envisaged that the internal dynamics of the Monte Capanne magma chamber played a dominant role for the space accommodation of the pluton, and extensional tectonics was mostly induced by isostatic effects, favoring the unroofing of the Monte Capanne magma body (Boullin et al., 1993: Westerman et al., 2004; Cifelli et al., 2012). Similarly, and concerning the Porto Azzurro granodiorite, Duranti et al. (1992) and Pertusati et al. (1993) explained the Zuccale normal fault as gravitational and developed after the doming effect due to the emplacement of the Porto Azzurro pluton (Trevisan, 1950). Smith et al. (2010), on the basis of structural observations, suggest a contemporaneity between fault activity and magma emplacement, without ruling out possible isostatic effects, the latter being responsible for the dome-shape of the Zuccale fault in the Monte Calamita area where micaschist with HT-mineralogical assemblage widely crops out (Garfagnoli et al., 2005). In this view, the dome shape of the Zuccale fault in the Calamita area, as it has been reconstructed considering southwestern and northeastern fault plane dipping attitudes in the Gemini Islands (Fig. 5) and Porto Azzurro areas (Fig. 3b) respectively, is interpreted as a consequence of the isostasy due to the magma emplacement (Pertusati et al., 1993; Smith et al., 2010; Westerman et al., 2004) and/or to the pluton exhumation, occurred at the end of magmatism (Cifelli et al., 2012).

Concerning the geometry of the Zuccale fault, as already indicated by Jolivet et al. (1998), we underline that, to the south of the Capoliveri area, the map-trace of this structure is constrained by the Gemini Islands (Fig. 4). We therefore dissent from Smith et al. (2010) who indicate that, in the Calamita area, the Zuccale fault is located between the micaschist and its cover and, from Mazzarini et al. (2012) who suggest that the Zuccale fault is limited to the Capoliveri area, only.

Summarizing, it is a fact that the Porto Azzurro monzogranite is affected by the Zuccale low-angle normal fault and, at the same time, it is reasonable to assume that the final geometry of the fault plane was influenced by isostatic processes deriving from the magma emplacement and pluton exhumation. Furthermore, it is evident that the deformation associated to the Capoliveri–Porto Azzurro transfer zone is active during the cooling stage of Porto Azzurro monzogranite (Fig. 15e–f). It is therefore proposed that the emplacement of the Porto Azzurro monzogranite was controlled by the interplay between the Zuccale low-angle normal fault and the Capoliveri–Porto

Please cite this article as: Liotta, D., et al., Coexistence of low-angle normal and high-angle strike- to oblique-slip faults during Late Miocene mineralization in eastern Elba I..., Tectonophysics (2015), http://dx.doi.org/10.1016/j.tecto.2015.06.025

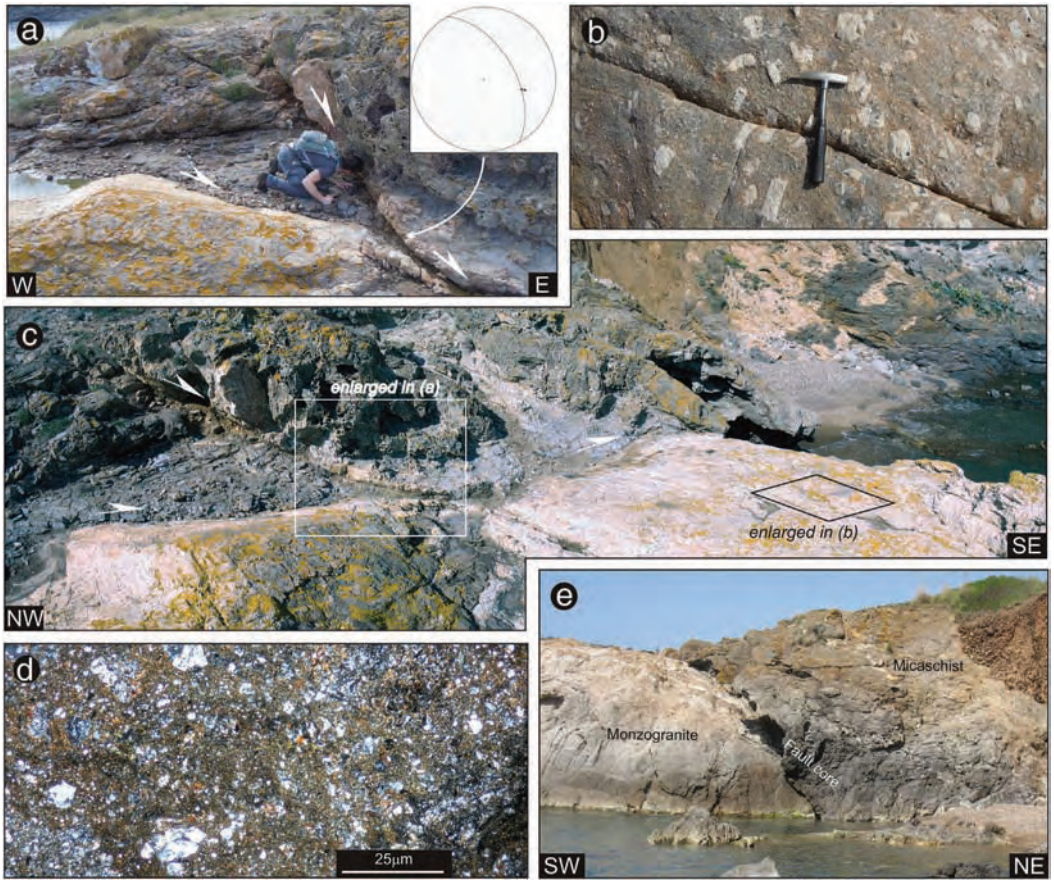

Fig. 14. Features of the low-angle normal fault in the Porto Azzurro monzogranite at Capobianco locality. (a–c) Panoramic view, details on the kinematics and lithological features of the igneous rock, with the typical K-feldspar megacrystals (plane view). (d) Thin section from the cataclasite, illustrating the comminution of quartz, biotite and K-feldspars from the monzogranite involved in the shear deformation. (e) Panoramic view of the fault core zone.

Azzurro transfer zone, following a process similar to that one described for the hydrothermal stage.

4.3. Significance on the Pliocene regional tectonic evolution

Since Miocene–Pliocene, the paleogeographic reconstructions account for a significant regional uplift and exhumation of the Elba Island (*e.g.*: Lazzarotto and Mazzanti, 1965). Evidences of vertical movements are given by the kinematic analysis carried out in structural stations S2, S3, S9, S11, S12 (Figs. 3 and 6); this analysis indicates that the NE-trending faults display slickenlines showing a dominant normal movement, although right- or left-lateral minor components were also recognized (Figs. 5 and 6).

Consequently, a different time evolution of the Zuccale normal fault with respect to the NE-trending shear zone is envisaged: we suggest in fact that the Capoliveri–Porto Azzurro transfer zone, representing a crustal weakness rock-volume, might play a role even after the mineralizing events, continuing its activity with a different kinematics, and favoring regional uplift. In this latter time evolution, the calcite veins (Smith et al., 2007) crosscutting the Zuccale detachment (Figs. 10e–f and 11d–g) can be also framed.

A further issue emerging from our study is that the kinematic and structural data of the tourmaline-bearing structures cannot be reconciled in the same tectonic framework as proposed by Mazzarini et al. (2011). These authors explain the dome-shape of the Monte Calamita area as a consequence of an antiform with tourmaline veins controlled by the fold evolution, thus assuming a compressional tectonics for the Northern Apennines up to Pliocene, at least. Musumeci and Vaselli (2012) proposed a similar view by studying an area to the NW of Capoliveri village (corresponding to the NW sector of the Fig. 3 map). They describe west-dipping rock-units affected by top-to-the-east shear deformation (in the Present coordinates), developed during the contact metamorphism induced by the Porto Azzurro monzogranite. Furthermore, they proposed that the occurrence of mid-temperature (MT) contact metamorphic rocks, sandwiched between levels with HT-LP metamorphic conditions is an evidence of a compressional event affecting the late Messinian aureole. Compression occurred by means of an out-of-sequence thrust developed at mid-crustal depth, carrying up, in its hangingwall, the Porto Azzurro monzogranite, the host-Palaeozoic micaschist, and the stacked tectonic pile above it.

In order to evaluate the compressional interpretation for the Porto Azzurro pluton, we argue that: (a) in the Elba Island, radiometric data of the main schistosity dated at about 20 Ma the stacking of nappes (Deino et al., 1992); noteworthy, similar radiometric ages (25–22 Ma) for HP/LT conditions (about 350 °C and 1.2 GPa, in rocks of continental origin) have been recognized in the surrounding islands and on-shore (Brunet et al., 2000); (b) radiometric and petrological data indicating HP-conditions were never documented in the inner Northern Apennines and Tuscan archipelago during Pliocene; (c) even assuming the same lithology in the metamorphic aureole (but this is not the case described by Musumeci and Vaselli, 2012), the occurrence of MT mineral assemblages sandwiched between HT-parageneses is a weak argument, being this distribution mainly controlled by fluid migration in pre-existing mechanical discontinuities; (d) our geological map is different

Please cite this article as: Liotta, D., et al., Coexistence of low-angle normal and high-angle strike- to oblique-slip faults during Late Miocene mineralization in eastern Elba I..., Tectonophysics (2015), http://dx.doi.org/10.1016/j.tecto.2015.06.025

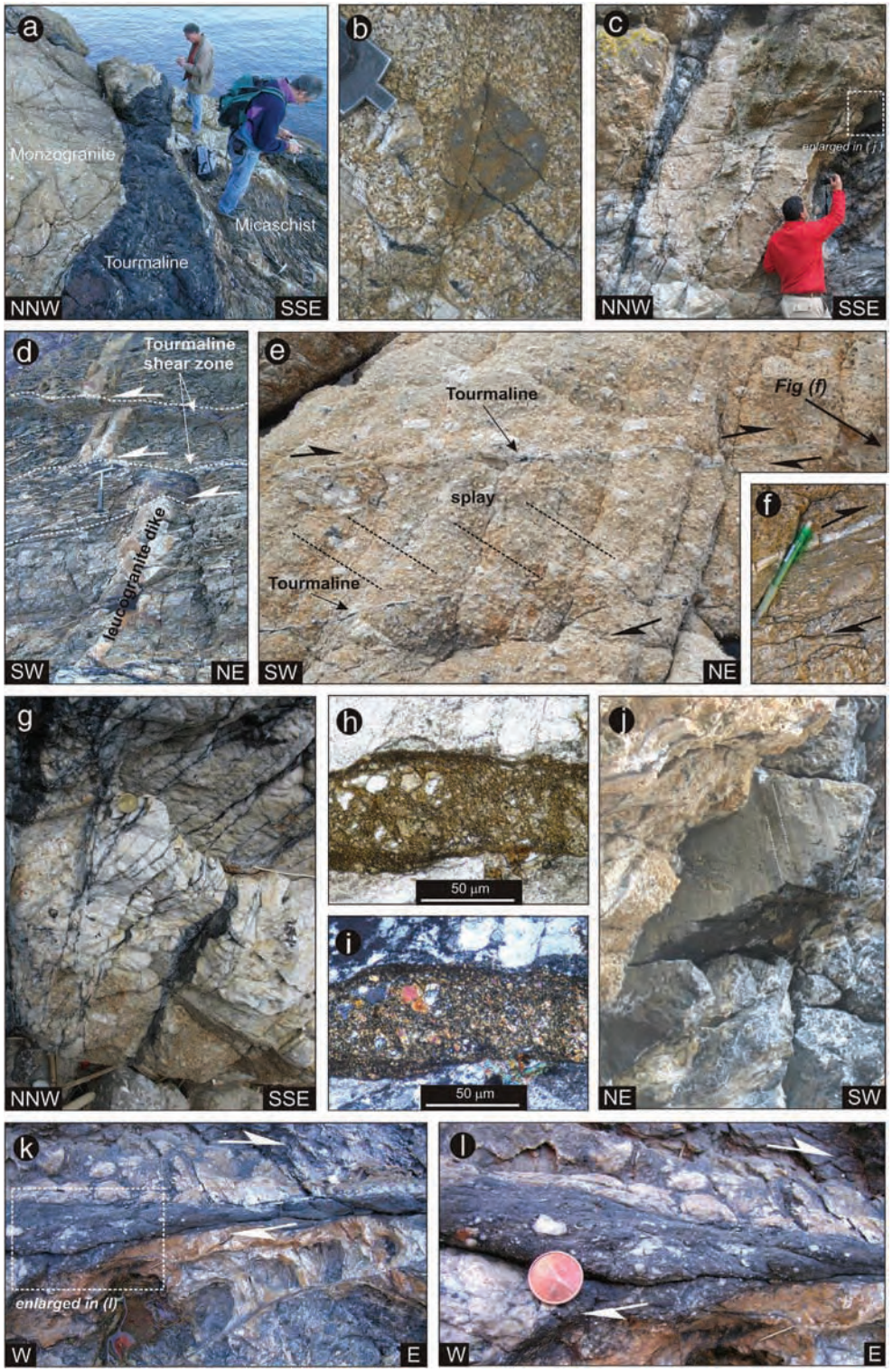

Fig. 15. Tourmaline-bearing shear zone features in the Barbarossa area. (a) Tourmaline at the boundary between the Porto Azzurro monzogranite and the Palaeozoic micaschist. (b) The tourmaline crystallization occurred after magma cooling, as indicated by the tourmaline-bearing veins dissecting both K-feldspar megacrystals and enclaves. (c) Fault zone with tourmaline shear veins. (d) Left-lateral strike-slip tourmaline-bearing shear zones dissecting micaschist and leucogranite dike. (e–f) Ductile-brittle shear zone affecting the monzogranite and quartz-tourmaline mineralized vein. (g) Relationships between main fault and associated fractures in a volume rock affected by tourmaline-rich fluid circulation. (h–i) Plane and cross-polarized light thin sections of tourmaline shear vein illustrating the comminution of tourmaline and quartz. (j) Slickenlines affecting tourmaline-bearing fault slip surface. (k–l) Shear zone with associated tourmaline-rich shear vein and detail.

from that one published by Musumeci and Vaselli (2012), in terms of distribution of the geological units, structures and mapped lithotypes. Finally, we sustain that the Zuccale fault can be better explained as an extensional detachment rather than a regional Messinian-Pliocene (or younger) out-of-sequence thrust. Hence, the present attitude of the HT-shear zones described by Musumeci and Vaselli (2012) needs a

Please cite this article as: Liotta, D., et al., Coexistence of low-angle normal and high-angle strike- to oblique-slip faults during Late Miocene mineralization in eastern Elba I..., Tectonophysics (2015), http://dx.doi.org/10.1016/j.tecto.2015.06.025

Fig. 16. Main features of the brittle structures dissecting the tourmaline-bearing veins and shear zones in the Barbarossa area. (a–b) Two examples of right- and left-lateral faults with Fe-oxides and/or Fe-oxyhydroxides crust on their fault slip surfaces affecting tourmaline veins. (c) Plane view of a tip zone of a left-lateral fault dissecting tourmaline veins. (d) Plane view of an extensional jog in a right-lateral fault. (e) Plane view of a tip zone with extensional jogs in a left-lateral fault. (f–g) Leucogranite dike affected by dm-thick fault zone defined by interconnected fractures. (h–i) Kinematic indicators on oblique-slip fault surface affecting micaschist. (j) Cross-cutting relationships between faults: arrows indicate the movement of the younger fault.

different explanation, that can be found in the rotations associated to the lateral segmentation affecting the crust of the inner Northern Apennines since the Miocene, as explained in Brogi et al. (2005a) and Barchi (2010, with references therein).

5. Conclusions

This study underlines the fundamental role of hydrothermal mineralization in reconstructing the activity of articulated fault systems in terms of chronological and cross-cutting relationships among faults, as it is the case of low-angle normal faults and their associated transfer zones.

As it regards the study area, we conclude that the Capoliveri–Porto Azzurro shear zone was active during the hydrothermal stage, in a time span encompassed between the cooling of the Porto Azzurro monzogranite and the opening of the Punta Ala Basin, and contemporaneously with the Zuccale normal fault activity. It is therefore suggested that the Capoliveri–Porto Azzurro shear zone played the role of a transfer zone during the extensional process determining the Zuccale normal fault. In this framework, a role of the mineralizing fluid pressure in enhancing fractures cannot be excluded. We argue that the interplay

Please cite this article as: Liotta, D., et al., Coexistence of low-angle normal and high-angle strike- to oblique-slip faults during Late Miocene mineralization in eastern Elba I..., Tectonophysics (2015), http://dx.doi.org/10.1016/j.tecto.2015.06.025

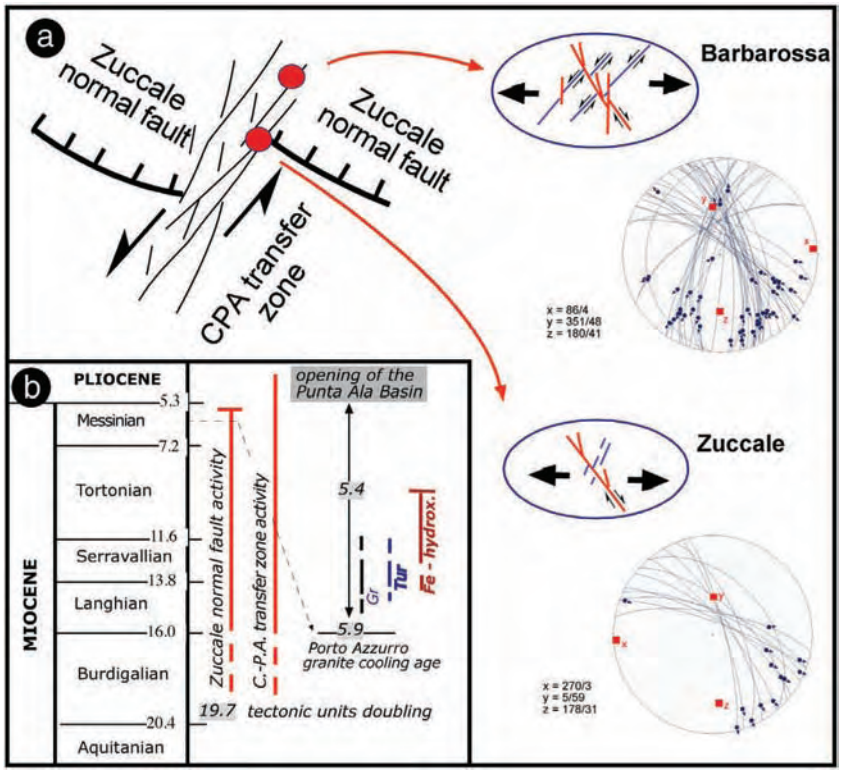

Fig. 17. (a) Structural sketch illustrating the relationships between tourmaline-bearing (blue lines) and Fe-oxides and/or Fe-oxyhydroxides-bearing (red lines) fractures in the study areas. The stereonets (lower hemisphere) display the direction of the main kinematic axes during hydrothermal circulation ("FaultKin" 5.2.6, by R.W. Allmendinger, http://www.geo.cornell.edu/geology/faculty/RWA/RWA.html). (b) Time relationships among tectonic, magmatic and hydrothermal events, summarized on the basis of available age determinations and crosscutting relationships between mineralized shear veins. It is assumed that the estimated radiometric age of 5.39 ± 0.46 Ma, obtained through (U + Th)–He and K–Ar geochronology, for the formation of the Fe-oxide ore deposits (Lippolt et al., 1995) is indicative for the whole Fe-hydrothermal mineralizations recognized in our study areas.

between the Zuccale detachment and the Capoliveri–Porto Azzurro transfer zone (Fig. 18a) caused a localized increase of the permeability, thus favoring magma emplacement and doming effect on the local surface (Fig. 18b), in a time-span encompassed between middle Miocene and early Pliocene. Later, during the cooling stage (Fig. 18c), the structures associated to the transfer zone channeled the hydrothermal fluids that permeated the cataclastic levels associated to the Zuccale fault during the stage of its brittle behavior. Finally, the Capoliveri–Porto Azzurro transfer zone protracted its activity, cross-cutting the Zuccale normal fault and giving rise to vertical displacements during the Pliocene-Quaternary, and thus contributing to the uplift and exhumation of the Elba Island.

Concluding, the study of the deformation associated to the Capoliveri–Porto Azzurro transfer zone indicates that: (a) the internal structure of this transfer zone is composed of small segments of subvertical, dominantly left-lateral oblique slip transtensional faults, defining a continuous weak crustal sector; (b) the study areas are examples of exhumed hydrothermal systems which can represent field analogues of active geothermal systems characterized by a similar geological context.

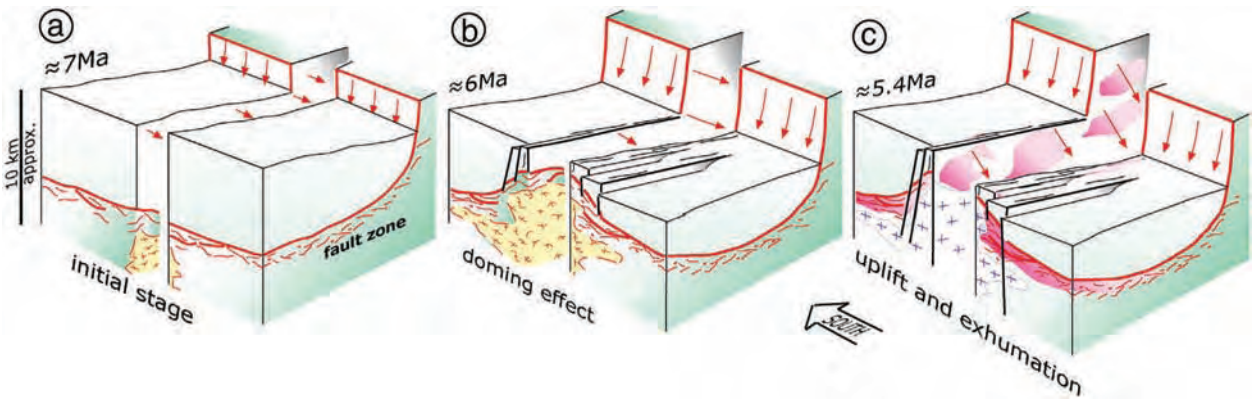

Fig. 18. Conceptual model illustrating the relationships among Zuccale normal fault, Capoliveri–Porto Azzurro transfer zone, magmatism and hydrothermalism during late Miocene–early Pliocene time span. (a) During the Messinian, the Porto Azzurro monzogranite emplaced, at mid crustal level, at the intersection between normal and transfer fault, where permeability increased. (b) During the Late Messinian, as a consequence of isostasy, a doming effect on the geological bodies and structures above the roof of the magmatic body was induced. (c) Cooling of the Porto Azzurro monzogranite and hydrothermal stage, during which the damage zones associated to the transfer fault provided the main upflow channels for fluids, permeating the cataclasite of the Zuccale normal fault during its activity.

Please cite this article as: Liotta, D., et al., Coexistence of low-angle normal and high-angle strike- to oblique-slip faults during Late Miocene mineralization in eastern Elba I..., Tectonophysics (2015), http://dx.doi.org/10.1016/j.tecto.2015.06.025

Acknowledgments

The research leading to these results has received funding from the European Community's Seventh Framework Programme under grant agreement no. 608553 (Project IMAGE). M.M. was funded by University of Siena grants. We are grateful to the Editors L. Joilvet and H. Thybo for their comments. Criticisms from C.Collettini, F. Rossetti and two other anonymous referees helped us to improve the original version of this manuscript.

References

Acocella, V., Funiciello, R., 2002. Transverse structures and volcanic activity along the Tyrrhenian margin of central Italy. Boll. Soc. Geol. Ital. 1, 739–747.
Acocella, V., Funiciello, R., 2006. Transverse systems along the extensional Tyrrhenian margin of central Italy and their influence on volcanism. Tectonics 25. http://dx.doi.org/10.1029/2005TC001845.
Alçiçek, M.C., Brogi, A., Capezzuoli, C., Liotta, D., Meccheri, M., 2013. Superimposed basin formation during Neogene–Quaternary extensional tectonics in SW-Anatolia (Turkey): Insights from the kinematics of the Dinar Fault Zone. Tectonophysics 608, 713–727.
Bally, A.W., Bernoulli, D., Davis, G.A., Montadert, L., 1981. Listric normal faults. Ocean. Acta. Proceedings of the 26th international geological congress, Geology of continental margins symposium, Paris, July 7-17 1980, pp. 87–101.
Barchi, M.R., 2010. The Neogene-Quaternary evolution of the Northern Apennines: crustal structure, style of deformation and seismicity. In: Beltrando, M., Peccerillo, A., Mattei, M., Conticelli, S., Doglioni, C. (Eds.), The Geology of Italy. Journ. of the Virtual Explorer 36, p. 10 (http://virtualexplorer.com.au/).
Bartole, R., 1995. The North Tyrrhenian–Northern Apennines post-collisional system: constraints for a geodynamic model. Terra Nova 7, 7–30.
Ben-Avraham, Z., 1992. Development of asymmetric basins along continental trasform faults. Tectonophysics 215, 209–220.
Boccaletti, M., Elter, P., Guazzone, G.J.P., 1971. Plate tectonic models for the development of the western Alps and Northern Apennines. Nature 234, 108–111.
Bossio, A., Costantini, A., Lazzarotto, A., Liotta, D., Mazzanti, R., Mazzei, R., Salvatorini, G., Sandrelli, F., 1993. Rassegna delle conoscenze sulla stratigrafia del Neoautoctono Toscano. Mem. Soc. Geol. Ital. 49, 17–98.
Bosworth, W., 1985. Geometry of propagating continental rifts. Nature 316, 625–627.
Boullin, J.P., Bouchez, J.L., Lespinasse, P., Pecher, A., 1993. Granite emplacement in an extensional setting: an AMS study of the magmatic structures of Monte Capanne (Elba, Italy). Earth Planet. Sci. Lett. 118, 263–279.
Brogi, A., 2011. Bowl-shaped basin related to low-angle detachment during continental extension: the case of the controversial Neogene Siena Basin (central Italy, Northern Apennines). Tectonophysics 499, 54–76.
Brogi, A., Liotta, D., 2008. Highly extended terrains, lateral segmentation of the substratum, and basin development: the middle–late Miocene Radicondoli Basin (inner northern Apennines, Italy). Tectonics 27. http://dx.doi.org/10.1029/2007TC002188.
Brogi, A., Lazzarotto, A., Liotta, D., CROP18 Working Group, 2005a. Structural features of southern Tuscany and geological interpretation of the CROP18 seismic reflection survey (Italy. Boll. Soc. Geol. Ital. 3, 13–236.
Brogi, A., Lazzarotto, A., Liotta, D., Ranalli, G., 2005b. Crustal structures in the geothermal areas of southern Tuscany (Italy): insights from the CROP 18 deep seismic reflection lines. J. Volcanol. Geotherm. Res. 148, 60–80.
Brogi, A., Liotta, D., Meccheri, M., Fabbrini, L., 2010. Transtensional shear zones controlling volcanic eruptions: the Middle Pleistocene Monte Amiata volcano (inner Northern Apennines, Italy). Terra Nova 22, 137–146.
Brogi, A., Fidolini, F., Liotta, D., 2013. Tectonic and sedimentary evolution of the Upper Valdarno Basin: new insights from the lacustrine Santa Barbara Basin. Ital. J. Geosci. 132, 81–97.
Brunet, C., Monié, P., Jolivet, L., Cadet, J.P., 2000. Migration of compression and extension in the Tyrrhenian Sea, insights from $^{40}Ar/^{39}Ar$ ages on micas along a transect from Corsica to Tuscany. Tectonophysics 321, 127–155.
Caggianelli, A., Ranalli, G., Lavecchia, A., Liotta, D., Dini, A., 2014. Post-emplacement thermo-rheological history of a granite intrusion and surrounding rocks: the Monte Capanne pluton, Elba Island, Italy. In: Llana-Fúnez, S., Marcos, A., Bastida, F. (Eds.), Deformation Structures and Processes within the Continental Crust. Geological Society, London, Special Publications 394, pp. 129–143.
Calamai, A., Cataldi, R., Squarci, R., Taffi, L., 1970. Geology, geophysics and hydrogeology of the Monte Amiata geothermal fields: I. Maps and comments. Geothermics. Spec. Issue 1, 1–9.
Carmignani, L., Decandia, F.A., Fantozzi, P.L., Lazzarotto, A., Liotta, D., Meccheri, M., 1994. Tertiary extensional tectonics in Tuscany (northern Apennines, Italy). Tectonophysics 238, 295–315.
Carmignani, L., Decandia, F.A., Disperati, L., Fantozzi, P.L., Lazzarotto, A., Liotta, D., Oggiano, G., 1995. Relationships between the Sardinia–Corsica–Provencal Domain and the Northern Apennines. Terra Nova 7, 128–137.
Cifelli, F., Minelli, L., Rossetti, F., Urru, G., Mattei, M., 2012. The emplacement of the Late Miocene Monte Capanne intrusion (Elba Island, Central Italy): constraints from magnetic fabric analyses. Int. J. Earth Sci. 101, 787–802.
Collettini, C., Barchi, M.R., 2004. A comparison of structural data and seismic images for low-angle normal faults in the Northern Apennines (Central Italy): constraints on activity. Geol. Soc. Lond., Spec. Publ. 224, 95–112.
Collettini, C., Holdsworth, R.E., 2004. Fault zone weakening and character of slip along low-angle normal faults: insights from the Zuccale fault, Elba, Italy. J. Geol. Soc. Lond. 161, 1039–1051.
Collettini, C., Chiaraluce, L., Pucci, S., Barchi, M.R., Cocco, M., 2005. Looking at fault reactivation matching structural geology and seismological data. J. Struct. Geol. 27, 937–942.
Contrucci, I., Mauffret, A., Brunet, C., Nercessian, A., Bethoux, N., Ferrandini, J., 2005. Deep structure of the North Tyrrhenian Sea from multi-channel seismic profiles and on land wide angle reflection/refraction seismic recording (LISA cruise): geodynamical implications. Tectonophysics 406, 141–163.
Dallmeyer, R.D., Liotta, D., 1998. Extension, uplift of rocks and cooling ages in thinned crustal provinces: the Larderello geothermal area (inner northern Apennines, Italy). Geol. Mag. 135, 193–202.
Daniel, J.M., Jolivet, J., 1995. Interaction of detachments and granitic plutons during extension in the Tyrrhenian Sea (Elba Island). Bull. Soc. Geol. Fr. 166, 341–354.
Deino, A., Keller, J.V.A., Minelli, G., Pialli, G., 1992. Datazioni $^{39}Ar/^{40}Ar$ del metamorfismo dell'Unita` di Ortano-Rio Marina (Isola d'Elba): risultati preliminari. Studi Geol. Camerti 1, 187–192.
Dini, A., 2003. Ore deposits, industrial minerals and geothermal resources. Per. Mineral. 72, 41–52.
Dini, A., Westerman, D.S., Innocenti, F., Rocchi, S., 2008. Magma emplacement in a transfer zone: the Miocene mafic Orano dyke swarm of Elba Island, Tuscany, Italy. Geol. Soc. Lond. Spec. Publ. 302, 131–148.
Doglioni, C., 1991. A proposal of kinematic modeling for W-dipping subductions. Possible applications to the Tyrrhenian-Apennines system. Terra Nova 3 (423), 434.
Duebendorfer, E.M., Black, R.A., 1992. Kinematic role of transverse structures in continental extension: an example from the Las Vegas Valley shear zone, Nevada. Geology 20, 1107–1110.
Duranti, S., Palmeri, R., Pertusati, P.C., Ricci, C.A., 1992. Geological evolution and metamorphic petrology of the basal sequence of eastern Elba (complex II). Acta Vulcanol. 2, 213–229.
Ebinger, C.J., 1989. Geometric and kinematic development of border faults and accommodation zones, Kivu-Rusizi rift, Africa. Tectonics 8, 117–133.
Fantozzi, P.L., 1996. Transition from continental to oceanic rifting in the Gulf of Aden:structural evidence from field mapping in Somalia and Yemen. Tectonophysics 259, 285–311.
Farina, F., Dini, A., Innocenti, F., Rocchi, S., Westerman, D.S., 2011. Rapid incremental assembly of the Monte Capanne pluton (Elba Island, Tuscany) by downward stacking of magma sheets. GSA Bull. 122, 1463–1479.
Garfagnoli, F., Menna, F., Pandeli, E., Principi, G., 2005. The Porto Azzurro Unit (Mt. Calamita promontory, south-eastern Elba Island, Tuscany): stratigraphic, tectonic and metamorphic evolution. Boll. Soc. Geol. Ital. 3, 119–138.
Geological map of Italy (2013) - 1:50000 scale. Fogli 316, 328, 329. http://www.isprambiente.gov.it/Media/carg/toscana.html.
Ghalayini, R., Daniel, J.M., Homberg, C., Nader, F.H., Comstock, J.E., 2014. Impact of Cenozoic strike-slip tectonics on the evolution of the northern Levant Basin (offshore Lebanon). Tectonics 33, 2121–2142.
Gibbs, A.D., 1984. Structural evolution of extensional basin margins. J. Geol. Soc. Lond. 141, 609–620.
Gibbs, A.D., 1989. Structural styles in Basin formation. In: Taukard, A.J., Balkwill, H.R. (Eds.), Extensional tectonics and stratigraphy of the North Atlantic Margins. AAPG Memoir 46, pp. 81–93.
Gibbs, A.D., 1990. Linked faults in basin formation. J. Struct. Geol. 12, 795–803.
Jolivet, L., Dubois, R., Fournier, R., Goffe', B., Michard, A., Jourdan, C., 1990. Ductile extension in alpine Corsica. Geology 18, 1007–1010.
Jolivet, L., Daniel, J.M., Truffert, C., Goffé, B., 1994. Exhumation of deep crustal metamorphic rocks and crustal extension in back-arc regions. Lithos 33, 3–30.
Jolivet, L., Faccenna, C., Goffe, B., Mattei, M., Rossetti, M., Brunet, C., Storti, F., Funiciello, R., Cadet, J.P., Nicola d'Agostino, N., Parra, T., 1998. Midcrustal shear zones in postorogenic extension: example from the northern Tyrrhenian Sea Journ. Geophys. Res. 103, 12,123–12,160.
Keller, J.V.A., Pialli, G., 1990. Tectonics of the Island of Elba: a reappraisal. Boll. Soc. Geol. Ital. 109, 413–425.
Larsen, P.H., 1988. Relay structures in the Lower Permian basement-involved extension system, Early Greenland. J. Struct. Geol. 10, 3–8.
Lavecchia, G., 1988. The Tyrrhenian-Apennines system: structural setting and seismotectogenesis. Tectonophysics 147, 263–296.
Lazzarotto, A., Mazzanti, R., 1965. Stratigrafia neogenica toscana: studio geologico di tre sezioni del complesso neoautoctono di Pomarance e Castelnuovo Val di Cecina (Provincia di Pisa). Boll. Soc. Geol. Ital. 84, 291–302.
Lazzarotto, A., Mazzanti, R., 1978. Geologia dell'Alta Val di Cecina. Boll. Soc. Geol. Ital. 95, 1365–1487.
Liotta, D., 1991. The Arbia-Val Marecchia line, Northern Apennines. Eclogae Geol. Helv. 84, 413–430.
Liotta, D., 1996. Analisi del settore centro-meridionale del Bacino pliocenico di Radicofani, Toscana meridionale. Boll. Soc. Geol. Ital. 115, 115–143.
Liotta, D., Cernobori, L., Nicolich, R., 1998. Restricted rifting and its coexistence with compressional structures: results from CROP 3 traverse (Northern Apennines, Italy). Terra Nova 10, 16–20.
Lippolt, H., Wernicke, R., Bahr, R., 1995. Paragenetic specularite and adularia (Elba, Italy) - Concordant (U + Th)-He and K-Ar ages. Earth Planet. Sci. Lett. 132, 43–51.
Lister, G.S., Etheridge, M.A., Symonds, P.A., 1986. Detachment faulting and the evolution of passive continental margins. Geology 14, 246–250.
Maineri, C., Benvenuti, M., Costagliola, P., Dini, A., Lattanzi, P., Ruggieri, G., Villa, I.M., 2003. Sericitic alteration at the La Crocetta deposit (Elba Island, Italy): interplay between magmatism, tectonics and hydrothermal activity. Mineral. Deposita 38, 67–86.
Martini, I.P., Sagri, M., 1993. Tectono-sedimentary characteristics of late Miocene-Quaternary extensional basins of Northern Apennines, Italy. Earth Sci. Rev. 34, 197–233.

Please cite this article as: Liotta, D., et al., Coexistence of low-angle normal and high-angle strike- to oblique-slip faults during Late Miocene mineralization in eastern Elba I..., Tectonophysics (2015), http://dx.doi.org/10.1016/j.tecto.2015.06.025

Mauffret, A., Contrucci, I., Brunet, C., 1999. Structural evolution of the Northern Tyrrhenian Sea from new seismic data. Mar. Pet. Geol. 16, 381–407.
Mazzanti, R., 1966. Geologia della zona di Pomarance-Larderello (Prov. di Pisa). Mem. Soc. Geol. Ital. 5, 105–138.
Mazzarini, F., Musumeci, G., Cruden, A.R., 2011. Vein development during folding in the upper brittle crust: the case of tourmaline-rich veins of eastern Elba Island, northern Tyrrhenian Sea, Italy. J. Struct. Geol. 33, 1509–1522.
Mazzarini, F., Musumeci, G., Cruden, A.R., 2012. Interactions between low-angle normal faults and plutonism in the upper crust: insights from the island of Elba, Italy: comment. Geol. Soc. Am. Bull. 124, 1917–1919.
Milani, E.J., Davison, I., 1988. Basement control and transfer tectonics in the Recôncavo-Tucano-Jatobá rift, Northeast Brazil. Tectonophysics 154, 41–70.
Moeller, S., Grevemeyer, I., Ranero, C.R., Berndt, C., Klaeschen, D., Sallares, V., Zitellini, N., De Franco, R., 2013. Early-stage rifting of the northern Tyrrhenian Sea Basin: results from a combined wide-angle and multichannel seismic study. Geochem. Geophys. Geosyst. 14, 3032–3052.
Molli, G., 2008. Northern Apennines-Corsica orogenic system: an updated overview. In: Siegesmund, S., Fügenschuh, B., Froitzheim, N. (Eds.), Tectonic aspects of the Alpine–Dinaride–Carpathian system. Geol. Soc., London, Spec. Publ. 298, pp. 413–442.
Musumeci, G., Vaselli, L., 2012. Neogene deformation and granite emplacement in the metamorphic units of northern Apennines (Italy): insights from mylonitic marbles in the Porto Azzurro pluton contact aureole (Elba Island). Geosphere 8 (2), 470–490.
Musumeci, G., Mazzarini, F., Tiepolo, M., Di Vincenzo, G., 2011. U-Pb and ^{40}Ar-^{39}Ar geochronology of Palaeozoic units in the northern Apennines: determining protolith age and alpine evolution using the Calamita Schist and Ortano Porphyroid. Geol. J. 46, 288–310.
Nelson, R.A., Patton, T.L., Morley, C.K., 1992. Rift-segment interaction and its relation to hydrocarbon exploration in rift systems. AAPG Bull. 74, 1153–1169.
Nortiel, G.S., Oliver, N.H.S., Blenkinsop, T.G., Keys, D.L., McLellan, J.G., Oxenburgh, S., 2011. New faults v. fault reactivation: implications for fault cohesion, fluid flow and copper mineralization, Mount Gordon Fault Zone, Mount Isa District, Australia. Geol. Soc. Lond. Spec. Publ. 359, 287–311.
Pascucci, V., Merlini, S., Martini, I.P., 1999. Seismic stratigraphy of the Miocene–Pleistocene sedimentary basins of the Northern Tyrrhenian Sea and western Tuscany (Italy). Basic Res. 11, 337–356.
Pascucci, V., Martini, I.P., Sagri, M., Sandrelli, F., 2007. Effects of transverse structural lineaments on the Neogene–quaternary basins of Tuscany (inner Northern Apennines, Italy). In: Nichols, G., Williams, E., Paola, C. (Eds.), Sedimentary processes, environments and basins: a tribute to Peter Friend. Intern. Ass. Sediment., Spec. Publ. 38, pp. 155–182.
Patacca, E., Sartori, R., Scandone, P., 1990. Tyrrhenian basin and Apenninic arcs: kinematic relations since Late Tortonian times. Mem. Soc. Geol. Ital. 45, 425–451.
Peacock, D.C.P., 2003. Scaling of transfer zones in the British Isles. J. Struct. Geol. 25, 1561–1567.
Pertusati, P.C., Raggi, G., Ricci, C.A., Duranti, S., Palmeri, R., 1993. Evoluzione post-collisionale dell'Elba centro-orientale. Mem. Soc. Geol. Ital. 49, 297–312.
Pirajno, F., 2009. Hydrothermal Process and Mineral System. Springer (1250 pp.).
Rossetti, R., Tecce, F., 2008. Composition and evolution of fluids during skarn development in the Monte Capanne thermal aureole, Elba Island, central Italy. Geofluids 8, 167–180.
Rossetti, R., Tecce, F., Billi, A., Brilli, M., 2007. Patterns of fluid flow in the contact aureole of the Late Miocene Monte Capanne pluton (Elba Island, Italy): the role of structures and rheology. Contrib. Mineral. Petrol. 153, 743–760.
Rossetti, F., Glodny, J., Theye, T., Maggi, M., 2015. Pressure–temperature–deformation–time of the ductile Alpine shearing in Corsica: from orogenic construction to collapse. Lithos 218–219, 99–116.
Sibson, R.H., 1990. Rupture nucleation on unfavourably oriented faults. Bull. Seismol. Soc. Am. 80, 1580–1604.
Smith, S., Holdsworth, R.E., Collettini, C., Imber, J., 2007. Using footwall structures to constrain the evolution of low-angle normal faults. J. Geol. Soc. Lond. 164, 1187–1191.
Smith, S.A.F., Holdsworth, R.E., Collettini, R.E., 2010. Interactions between plutonism and low-angle normal faults in the upper crust: insights from the Island of Elba, Italy. Geol. Soc. Am. Bull. 123, 329–346.
Storti, F., 1995. Tectonics of the Punta Bianca promontory: insights for the evolution of the northern Apennines-northern Tyrrheman Sea basin. Tectonics 14, 832–847.
Tanelli, G., Benvenuti, M., Costagliola, P., Dini, A., Lattanzi, P., Manieri, C., Mascaro, I., Ruggieri, G., 2001. The iron mineral deposits of Elba Island: state of the art. Ofioliti 26, 239–248.
Trevisan, L., 1950. L'Elba orientale e la sua tettonica di scivolamento per gravità. Mem. Ist. Geol. Univ. Padova 16, 1–30.
Vai, G.B., Martini, I.P., 2001. Anatomy of an Orogen: the Apennines and Adjacent Mediterranean Basins. Kluwer Academic Publishers, p. 631.
Westerman, D.S., Dini, A., Innocenti, F., Rocchi, S., 2004. Rise and fall of a nested Christmas- tree laccolith complex, Elba Island, Italy. In: Breitkreuz, C., Petford, N. (Eds.), Physical geology of high-level magmatic systems. Geol. Soc., London, Spec. Publ. 234, pp. 195–213.
Zitellini, N., Trincardi, F., Marani, M., Fabbri, A., 1986. Neogene tectonics of the northern Tyrrhenian Sea. Giorn. Geol. 48, 25–40.

Please cite this article as: Liotta, D., et al., Coexistence of low-angle normal and high-angle strike- to oblique-slip faults during Late Miocene mineralization in eastern Elba I..., Tectonophysics (2015), http://dx.doi.org/10.1016/j.tecto.2015.06.025

Journal of Geodynamics 91 (2015) 13–25

Contents lists available at ScienceDirect

Journal of Geodynamics

journal homepage: http://www.elsevier.com/locate/jog

HP-LT metamorphism in Elba Island: Implications for the geodynamic evolution of the inner Northern Apennines (Italy)

Caterina Bianco[a,*], Andrea Brogi[a], Alfredo Caggianelli[a], Giovanna Giorgetti[b], Domenico Liotta[a], Marco Meccheri[b]

[a] Dipartimento di Scienze della Terra e Geoambientali, Via Orabona 4, Bari, Italy
[b] Dipartimento di Scienze Fisiche, della Terra ed Ambientali, Via Laterina 4, Siena, Italy

ARTICLE INFO

Article history:
Received 20 February 2015
Received in revised form 11 August 2015
Accepted 12 August 2015
Available online 14 August 2015

Keywords:
HP-LT metamorphism
Metabasite
Northern Apennines
Tuscan Archipelago
Late Oligocene-Early Miocene

ABSTRACT

The inner Northern Apennines belt (*i.e.*, northern Tyrrhenian Sea and Tuscany) is an Alpine chain affected by high-*P* metamorphic conditions during its evolution. Although Elba Island is structurally located close to the Adria-Europe suture zone, for several authors it represents a sector of the orogen affected by low-*P* metamorphism. The involvement of Elba Island tectonic units in high-*P* metamorphism was only suspected for the sparse presence of phengitic white mica in the metasedimentary rocks. This paper presents the first clear evidence of high-*P* and low-*T* metamorphism found in metabasite rocks embedded in the Cretaceous calcschist of eastern Elba Island. Mineral composition of metabasite includes Gln + Cpx + Ep + Ab + Act + Qtz + Ilm ± Ti-oxide ± Spn and is indicative of a former equilibration in the epidote blueschist subfacies and subsequent retrogression in the greenschist facies. Recorded metamorphic conditions are $P = 0.9–1.0$ GPa and $T = 330–350$ °C. Tectonic discrimination using immobile elements in the metabasite does not point to an oceanic setting. As a consequence, the metasedimentary succession containing metabasite is explained as belonging to the Tuscan continental domain and not to the Ligurian-Piedmont Ocean, as previously interpreted. Our results have two significant implications: (i) it is confirmed and strengthened that the tectonic stacking of the Elba Island units did not occur in a low-pressure context; (ii) Elba Island is now completely reconciled in the tectonic and metamorphic evolution of the inner Northern Apennines.

1. Introduction

The Northern Apennines belt is an eastward verging alpine chain deriving from the convergence and subsequent collision between Corsica-Sardinia massif and Adria microplate, believed of European and African pertinence, respectively (Molli, 2008 with references therein).

High-*P* metamorphic conditions have been recognized in metasiliciclastic and metabasite rocks, along a roughly W-E transect, from the Tuscan Archipelago up to the exhumed Metamorphic Complex, cropping out in Tuscany (Fig. 1).

Thermobarometry applied on metasediments indicates *P*–*T* values (Fig. 1) of 1.0–1.5 GPa and ≤350 °C, in the Tuscan Archipelago (Rossetti et al., 1999, 2001). Differently, inland, the *P*-values are slightly lower, between 0.6 and 1.2 GPa, and *T* is in the range 350–450 °C (Kligfield et al., 1986; Theye et al., 1997; Giorgetti et al., 1998; Elter and Pandeli, 2002; Brogi and Giorgetti, 2012). High-*P* metamorphism is dated at Late Oligocene-Early Miocene, on the basis of $^{40}Ar/^{39}Ar$ radiometric method (Brunet et al., 2000). Higher and older thermobaric conditions are recorded in north-eastern Corsica. Here, estimated *P*–*T* values reach 2 GPa and 380 °C and are referred to Eocene (Jolivet et al., 1998; Brunet et al., 2000) and Oligocene (Rossetti et al., 2015). The metamorphic event is related to westward verging thrusts (Fig. 1) involving the oceanic rocks presently exposed in the Alpine Corsica.

Thus, along the Corsica-Tuscany W-E transect (Fig. 1), Elba Island represents the westernmost outcropping evidence of tectonic units verging to the east (Trevisan, 1950), as it is the case of the Northern Apennines belt. In addition, as further on described, the structure of Elba Island is characterized by the superimposition of continental units over the oceanic ones, the latter already stacked on the continental successions (Pertusati et al., 1993 with references therein). This fact enforced the interpretation that the collisional suture between the European and African plates passes close to Elba Island (Keller and Pialli, 1990; Pandeli et al., 2001; Balestrieri et al., 2011).

* Corresponding author.
E-mail address: caterina.bianco@uniba.it (C. Bianco).

http://dx.doi.org/10.1016/j.jog.2015.08.001
0264-3707/

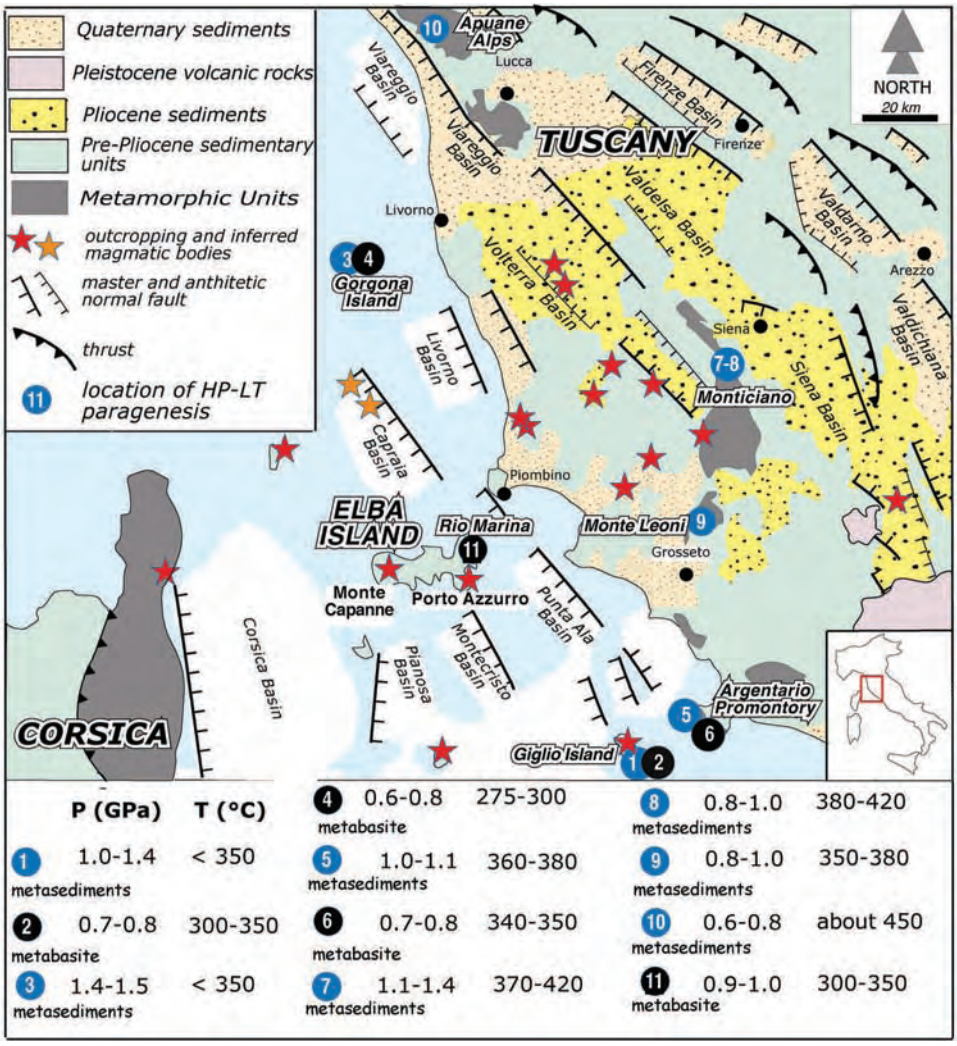

Fig. 1. Structural sketch map of Tuscany (inner Northern Apennines) with location of the HP-LT mineralogical assemblages in metabasites (black circle) and other rock types (metasediments). The *P*–*T* values from Rio Marina (no. 11) are provided in this paper. Other data are from: Kligfield et al. (1986), Theye et al. (1997), Giorgetti et al. (1998), Rossetti et al. (1999), Brunet et al. (2000), Rossetti et al. (2001), Elter and Pandeli (2002), Brogi and Giorgetti (2012).

Although phengite composition in metasedimentary rocks suggested occurrence of high-*P* metamorphism (Pandeli et al., 2001), the lack of a limiting mineral assemblage made this indication questionable. Thus, it is generally believed that orogenic deformation (Late Oligocene-Early Miocene) took place under low-*P* metamorphic conditions (Keller and Coward, 1996; Garfagnoli et al., 2005; Musumeci and Vaselli, 2012).

For this reason, Elba Island resulted a distinctive case with respect to the surrounding areas, with fallouts on the supposed evolution of the Northern Tyrrhenian Basin (Bonini et al., 2014).

In this paper we document, for the first time, the occurrence of a high-*P* mineral assemblage in metabasite interlayered with Cretaceous calcschist (Acquadolce Unit *Auctt.*). We conclude that high-*P* and low-*T* metamorphism affected the whole tectonic pile of Elba Island, at least up to the Early Burdigalian, as suggested by Deino et al. (1992) age measurements, thus reconciling Elba Island with the evolution of the Northern Apennines belt.

2. Northern Apennines geological framework

The geodynamic process leading to the Northern Apennines orogenesis determined the eastward stacking of several tectonic units belonging to oceanic, transitional and continental paleogeographic domains. These are, respectively: (a) the Ligurian Units, consisting of remnants of Jurassic oceanic crust, with the Jurassic-Cretaceous cover (Ligurian Domain); (b) the Sub-Ligurian Units, represented by Cretaceous-Oligocene turbidites; (c) the inner Tuscan Domain, made up of a complete sedimentary succession of evaporitic, platform, pelagic and foredeep environments, ranging in age from Late Trias to Early Miocene. During Late Oligocene-Early Miocene, the Tuscan succession (with the already stacked Ligurian and Subligurian Units above it) was internally deformed and detached from its substratum along the late Triassic evaporite level, giving rise to the Tuscan Nappe. This latter stacked over the external Tuscan domain, that was deformed in isoclinal folds and duplex structures, under metamorphic conditions from the blueschist to the greenschist facies (Carmignani and Kligfield, 1990; Carmignani et al., 1994; Jolivet et al., 1998; Brunet et al., 2000; Rossetti et al., 2002; Molli, 2008; Brogi and Giorgetti, 2012). In early-middle Miocene (Jolivet et al., 1990; Carmignani et al., 1995; Brunet et al., 2000; Bonini et al., 2014) the tectonic regime changed and an eastward migrating extension affected the inner Northern Apennines up to Present.

Extension in the inner Northern Apennines is believed to have been active since middle Miocene (Carmignani and Kligfield, 1990; Jolivet et al., 1994; Pauselli et al., 2006, Barchi, 2010 with references therein). Differently, Bonini et al. (1994), Bonini and Moratti (1995), Moratti and Bonini (1998), Sani et al. (2009), Musumeci

and Vaselli (2012) and Bonini et al. (2013) account for a contractional tectonic regime. This view led some authors to reconsider the Neogene-Quaternary evolution of the inner northern Apennines and to suggest a basically continuous (Bonini et al., 1999; Finetti et al., 2001; Finetti, 2006) or pulsing (Bonini and Sani, 2002; Bonini et al., 2014; Musumeci et al., 2015) collisional process, active from the Cretaceous to Pliocene-Pleistocene times. A deep discussion on the reasons why a continuous extensional framework better explains the regional geological features of the inner Northern Apennines is given in Brogi et al. (2005a,b), Brogi and Liotta (2008), Barchi (2010), Brogi et al. (2013) and Liotta et al. (2015) and to these papers we address the reader.

Extension, therefore, continuously developed through time, although two main events can be distinguished (Barchi, 2010 with references therein). The first one, during Miocene, determined the lateral segmentation of the more competent levels within the previously stacked tectonic units and the consequent superimposition of the Ligurian Units (at the top of the tectonic pile) on the deeper basal detachment levels. These are localized within the late Triassic evaporite and the Palaeozoic phyllite (Bertini et al., 1991; Baldi et al., 1994). The stair-case geometry of the faults gave rise to bowl-shaped structural depressions where Langhian-Messinian marine to evaporitic and continental sediments deposited (Brogi and Liotta, 2008). During Pliocene-Quaternary, the second extensional event determined normal faults crosscutting the previously developed compressional and extensional structures, thus defining new tectonic depressions filled up by Pliocene to Quaternary marine and continental sediments (Bossio et al., 1993). Since late Miocene, extension is accompanied by crustal anatectic magmatism with minor contribution of mantle melts (Peccerillo, 2003).

2.1. Elba Island geological framework

Integrating previous papers (Trevisan, 1950; Keller and Pialli, 1990; Pertusati et al., 1993; Bortolotti et al., 2001 with references therein) with the data here further on illustrated, we distinguish seven main tectonic units, belonging both to continental and oceanic environments and forming the tectonic pile of Elba Island (Fig. 2). The deeper outcropping continental unit (continental unit 1, Fig. 3) is made up of early Carboniferous micaschist (Musumeci et al., 2011) and its Triassic-Jurassic siliciclastic and carbonatic cover (Porto Azzurro Unit, in Garfagnoli et al., 2005).

The 2nd continental unit (Fig. 3) is made up of metamorphic rocks consisting of middle Ordovician porphyroid (Ortano porphyroids, Musumeci et al., 2011) covered by Mesozoic continental to marine metasediments (Duranti et al., 1992). The latter are late Triassic to Jurassic metacarbonate, calcschist and metaradiolarite passing to a Cretaceous succession made up of calcschist and phyllite with levels of metasiltstone and metasandstone. Calcschist contains discontinuous lenses of metabasite (Fig. 3), the main focus of this paper. The third continental unit (Fig. 3) consists of low-grade metamorphic rocks including late Carboniferous phyllite, overlain by Triassic continental quartzite and phyllite, Triassic-?Jurassic marble and by Cretaceous-Oligocene carbonatic and terrigenous metasedimentary succession (Bortolotti et al., 2001). The forth continental unit (Fig. 3) is related to the Tuscan Nappe, composed of late Triassic, locally vacuolar and fragmented calcareous dolostone, overlain by Jurassic marine carbonate and Cretaceous-Oligocene calcareous and marly pelagic sediments. The oceanic unit 1 (Fig. 3) is interposed between the second and the third continental units by means of out-of-sequence thrust (Keller and Pialli, 1990; Pertusati et al., 1993; Keller and Coward, 1996) referred to early Burdigalian (Deino et al., 1992; Pertusati et al., 1993). This unit is a tectonic slice made up of Jurassic ophiolite. Finally, the oceanic units 2 and 3 (Fig. 3) consist of remnants of Jurassic ophiolite, Jurassic radiolarite and Cretaceous-Eocene calcareous and terrigenous sediments, with levels of ophiolitic breccia. After the stacking of the tectonic pile, Elba Island was affected by Miocene extensional structures and magmatism (Fig. 2), giving rise to the emplacement of the Monte Capanne (about 7.0 Ma, Westerman et al., 2004), and Porto Azzurro (about 6 Ma, Maineri et al., 2003; Musumeci et al., 2011) laccolith-pluton-dyke granitic complexes (Dini et al., 2002), respectively located to the western and eastern sides of Elba Island (Fig. 2). Regionally, magma emplacement and cooling (Caggianelli et al., 2014) determined the origin of thermo-metamorphic aureoles (Barberi and Innocenti, 1965; Duranti et al., 1992; Rossetti et al., 2007) with a low-*P* mineral assemblage overprinting the older metamorphic paragenesis related to the collisional event (Duranti et al., 1992; Pertusati et al., 1993). Moreover, a diffuse hydrothermalism determined Fe-ore deposits (Tanelli, 1983; Tanelli et al., 2001), particularly in the eastern Elba Island. After these later events, it was surprising to find relics of high-pressure metamorphic paragenesis still preserved in metabasite lithons, embedded in the calcshist of the continental unit 2 (Fig. 3).

3. Rock fabric

The sampling area (Figs. 4 and 5A) is structurally located in the lower part of the Cretaceous succession of the continental unit 2 (Fig. 3). Here, lenses of metabasite, from few cm to about 2 m thick (Fig. 5B), are embedded in calcschist, mainly along the main schistosity, gently NW-dipping (Fig. 5C and D). The metabasite is laterally segmented at different scales (Fig. 5E–H), indicating a pervasive deformation. The rock fabric is characterized by porphyroclasts of mafic minerals within a chloritic matrix (Fig. 5I) and by S/C structures.

In calcschist, the main foliation, generally parallel to the lithological layering (Fig. 5), is locally deformed by tight and isoclinal folds with ≈304°/30° plunging hinge lines (Fig. 6A and B). These folds, characterized by the lack of an axial plane foliation, account for thermal conditions typical of the ductile domain. The stretching lineation, NW-SE trending, is well defined by elongated calcite crystals (Fig. 6C). The mineral association (Fig. 6D) on the main schistosity is made up of $Cal + Dol + Qtz + Bt + Ms + Chl \pm Ti\text{-}FeOxides \pm Ab \pm Ap \pm Ep$ (mineral abbreviations after Kretz (1983) and Bucher and Frey (1994). Close to this outcrop (Fig. 4), few tens of meters southwards, white mica on the main foliation has been dated through $^{40}Ar/^{39}Ar$ method at 19.68 ± 0.15 Ma (Deino et al., 1992). A new deformation episode affected the previous structures, locally determining SE-verging open folds.

4. Evidence of HP metamorphism

Main evidence of high-*P* and low-*T* metamorphic conditions is from the metabasite embedded in the calcschist. The nature of the parental material of the metabasite was ascertained by XRF analyses for three rock samples. Results in Table 1 indicate low contents in SiO_2 (down to 43.60 wt.%) and K_2O (down to 0.58 wt.%) and high contents in MgO (up to 9.92 wt.%) and Na_2O (up to 3.49 wt.%). Finally, a wide variation in CaO (from 6.28 to 12.36 wt.%) and elevated values of L.O.I. (up to 9.25 wt.%) can be noted. Classification of these rocks was performed by Winchester and Floyd (1977) diagram based on immobile elements, as modified by Pearce (1996, 2014). In Fig. 7 the analyzed rocks are in the field of basalt, near the boundaries with the andesite/basaltic andesite and alkali basalt fields, resulting different from N-MORB, the well known ophiolitic lavas of Troodos and Semail (Pearce, 2014) and from the ophiolitic rocks belonging to the Ligurian oceanic crust (Ricci and Serri, 1975; Brunacci et al., 1982). In addition, the analyzed metabasite differs from the other mafic rocks (Fig. 7) of the Tuscan Domain

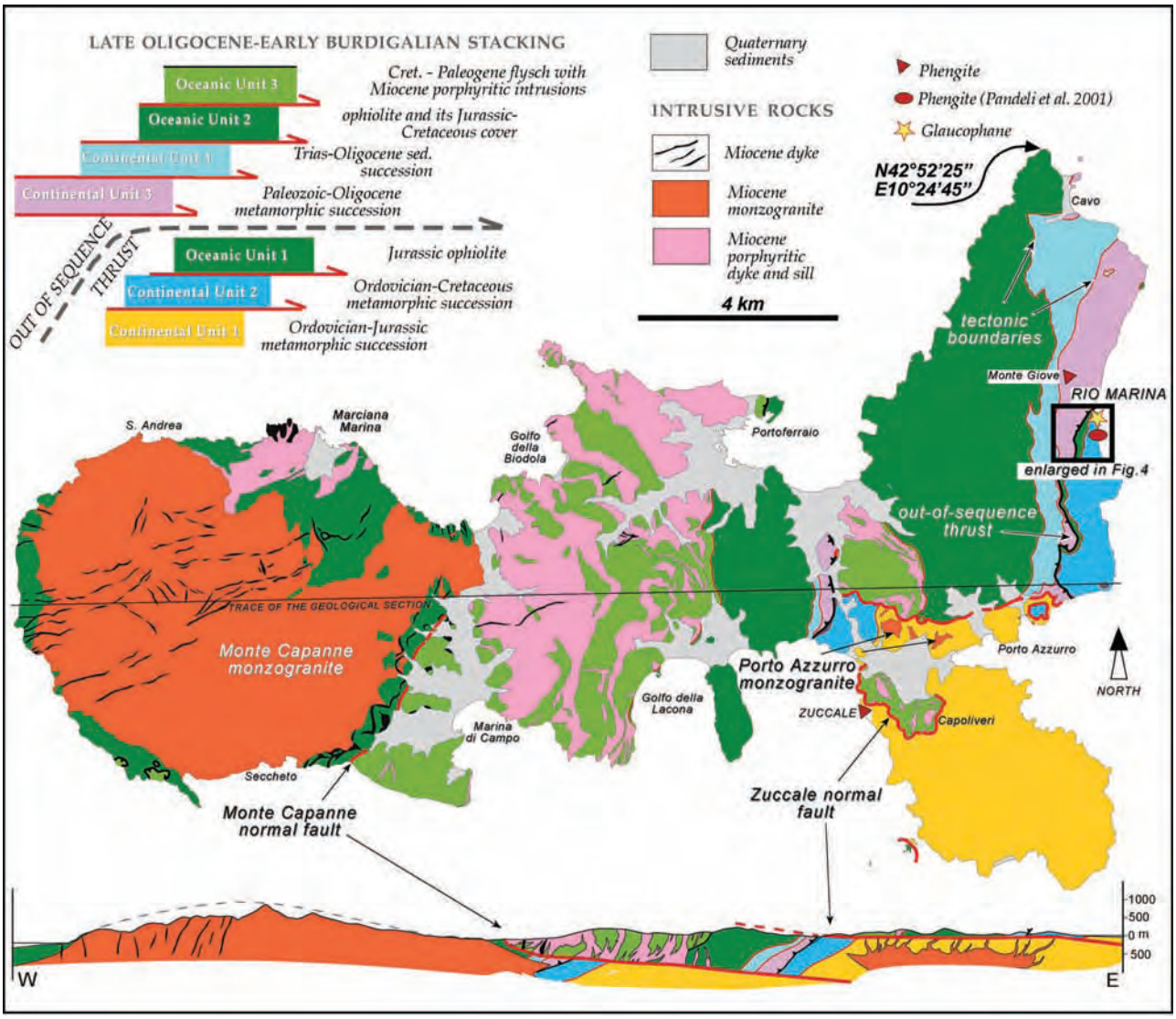

Fig. 2. Geological sketch map of Elba Island. The relationships between the tectonic units, as described in the text, are highlighted. The location of the phengite- and glaucophane-bearing rocks is also indicated.

(Ricci and Serri, 1975; Brogi et al., 2000) and, obviously, from those intruded in the Ligurian Domain (Stoppa et al., 2014). It can be also observed that the Elba Island metabasite shows a transitional character between tholeiite and alkali basalt types.

The mineralogical composition of the metabasite includes *Gln + Cpx + Ep + Ab + Act + Qtz + Ilm ± Ti-oxide ± Spn*. It is indicative of former equilibration in the epidote blueschist subfacies (Evans, 1990) and later retrogression in the greenschist facies. Metabasite has fine grain size and, sometimes, mylonitic fabric characterized by clinopyroxene porphyroclasts in a matrix mainly made up of glaucophane and epidote + chlorite. Clinopyroxene porphyroclasts are typically rounded and fragmented (Fig. 8A–C), probably representing relics of former magmatic diopside and augite. They usually appear brownish with rare portions, apparently unaffected by alteration, preserving bright interference colors. Elongated glaucophane crystals, recognizable for the pale lavender color shades, are preferentially oriented along the main foliation (Fig. 8C) and wrap around clinopyroxene porphyroclasts (Fig. 8D). Glaucophane is present also in the strain shadows and in the fractures of the stretched porphyroclasts (Fig. 8A and B). Epidote occurs in minor amounts with respect to glaucophane and it is represented by small grains of both clinozoisite and pistacite. Epidote is occasionally zoned with clinozoisite cores and pistacite rims, a feature reflecting the transition to lower pressure conditions. Ilmenite and rutile, if present, are scattered throughout the rock, showing a variable grain size. Sometimes, ilmenite can be surrounded by sphene (Fig. 8E). Rock portions characterized by the abundance of chlorite, epidote and sphene, when glaucophane and clinopyroxene relics are scarce (Fig. 8E), indicate that later retrogression was non-pervasive and took place in the greenschist facies. Another common textural evidence of retrogression is represented by albite blasts enclosing glaucophane and by the presence of calcite ± actinolite veins cross-cutting the main foliation (Fig. 8F).

In Table 2 microprobe analyses and structural formulae of selected minerals, representative of the metabasite assemblage in sample C19, are provided. We focus hereafter on those mineral phases (*i.e.*, glaucophane, clinopyroxene, epidote) used to constrain the *P–T* conditions of the epidote blueschist subfacies metamorphism.

Blue-amphibole nomenclature was defined according to Leake et al. (1997) by using the software Probe-Amph (Tindle and Webb, 1994). It was established that all Na-amphibole analyses are related

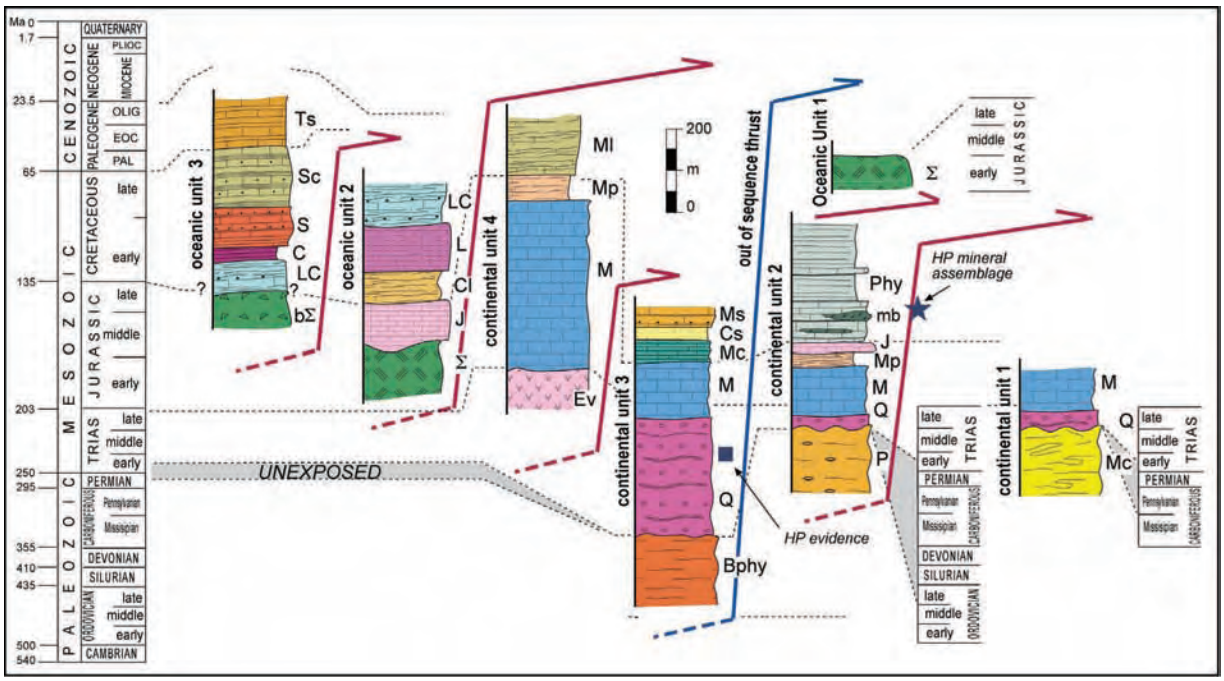

Fig. 3. Tectono-stratigraphic columns of the seven tectonic units belonging to continental and oceanic environments, and forming the tectonic pile of Elba Island. From left to right, and from the bottom in each column: oceanic unit 3: bΣ = Breccia of ophiolitic rocks; LC = limestone and shale (Palombini Shales Fm); C = shale (Varicoluored Shales Fm); S = sandstone and shale (Ghiaieto Sandstones Fm); Sc = sandstone and marlstone (Marina di Campo Fm); Ts = shale with limestone and marlstone (Colle Reciso Fm). Oceanic unit 2: Σ = ophiolite; J = radiolarite (Mt. Alpe Cherts Fm); Cl = calcilutite and cherty limestone (Nisportino Fm); L = cherty limestone (Calpionella Limestones Fm); LC = limestone and shale (Palombini Shales Fm). Continental unit 4: Ev = evaporite (Calcare Cavernoso Fm); M = massive and cherty limestone and dolostone (Pania di Corfino Fm, Mt. Cetona Fm, Calcare Massiccio Fm, Grotta Giusti Limestones, Rosso Ammonitico Fm, Limano cherty Limestones Fm); Mp = marls (Posidonia Marlstones Fm); Ml = Varicolored Shales (Cavo Fm). Continental unit 3: Bphy = black phyllite (Rio Marina Fm); Q = quartzite and phyllite (Verruca Fm, Mt. Serra quartzite Fm); M = marble (Valle Giove Limestones Fm; Capo Pero Limestone Fm; Capo Castello Calcschists Fm); Mc = cherty marble; Cs = calcschist and phyllite (Varicoloured Sericitic Schist Fm); Ms = metasandstone and phyllite (Pseudomacigno Fm). Continental unit 2: P = porphyroids, quartzite and phyllite (Ortano Unit); Q = quartzite; M = massive and cherty limestone and dolostone (Valdana marble Fm); Mp = marls (Posidonia Marlstones Fm); J = radiolarite; Phy = calcschist with interbedded metabasite (Mb) and phyllite (Acquadolce Unit). Oceanic unit 1: Σ = ophiolite. Continental unit 1: Mc = micaschist (Mt. Calamita Fm); Q = quartzite and phyllite (Quarziti di Barabarca Fm); M = dolostone (Crystalline dolostone and dolomitic limestone Fm). Formational names after Bortolotti et al. (2001) and Garfagnoli et al. (2005). The star and the square indicate the structural levels of the analyzed metabasite and of the rock where phengite was found, respectively. See the main text for more details.

Table 1
XRF analyses of three metabasite samples. Analyses were performed by Philips Magix Pro (Dipartimento di Scienze Fisiche, della Terra, ed Ambientali University of Siena).

	C19	RMT2	RMT3
wt.%			
SiO_2	44.84	43.60	44.15
TiO_2	1.15	0.84	1.03
Al_2O_3	17.04	13.72	15.23
FeO_t	10.52	7.96	9.45
MnO	0.16	0.09	0.12
MgO	9.92	7.29	9.55
CaO	6.28	12.36	9.80
Na_2O	2.10	3.49	3.11
K_2O	0.58	1.04	0.59
P_2O_5	0.14	0.13	0.14
L.O.I.	6.86	9.25	6.68
Tot	99.59	99.77	99.85
ppm			
Ni	139	91	133
Cr	287	199	265
V	193	111	157
Rb	40	46	26
Sr	234	483	445
Ba	21	104	46
Y	24	17	22
Zr	106	91	105
Nb	8	7	7
La	23	7	10
Ce	70	27	38

to glaucophane (Fig. 9A). Content in glaucophane molecula X_{Gln}, calculated as $Al^{VI}/[Fe^{3+} + Al^{VI}]$ ranges from 0.65 to 0.86. Ca-amphibole analyses are related to Fe-actinolite with average X_{Mg} of 0.83.

Clinopyroxene nomenclature was defined following Morimoto et al. (1988) and using the PX-NOM software (Sturm, 2002). Clinopyroxene porphyroclasts surrounded by glaucophane fibers are classified in most cases as omphacite and, secondly, as aegirine-augite (Fig. 9B). For these sodic types, proportion of jadeite molecula ranges from 0.24 to 0.33, indicating their involvement in the high-pressure metamorphic event. However, a smaller number of analyses, generally pertaining to isolated porphyroclasts (Fig. 9C) without external glaucophane fibers, can be classified as diopside (X_{Mg} = 0.81) and, in one case, as augite (X_{Mg} = 0.65). Therefore, these can be ascribed to magmatic clinopyroxene relics.

Epidote is represented by both clinozoisite- and pistacite-rich terms. The content in pistacite molecula (X_{Ps}) has been calculated by Fe/[(Al-4) + Fe] on the basis of ΣO = 25. It results that clinozoisite is characterized by a minimum value of X_{Ps} = 0.09 and pistacite by a maximum value of X_{Ps} = 0.82.

Interestingly, in the matrix of two samples of metabasite, microanalyses allowed to recognize the presence of anorthite with composition very close to pure calcic plagioclase end-member (Table 2). Anorthite was probably generated from a former lawsonite in response to the later heating produced at low-*P* conditions by the emplacement of the Porto Azzurro monzogranite pluton, as an effect of the reaction lawsonite = anorthite + H_2O (Fig. 10).

The mineral compositional data from metabasite were used for a preliminary estimation of the *P*–*T* conditions in the epidote-blueschist metamorphic subfacies. To this end, we

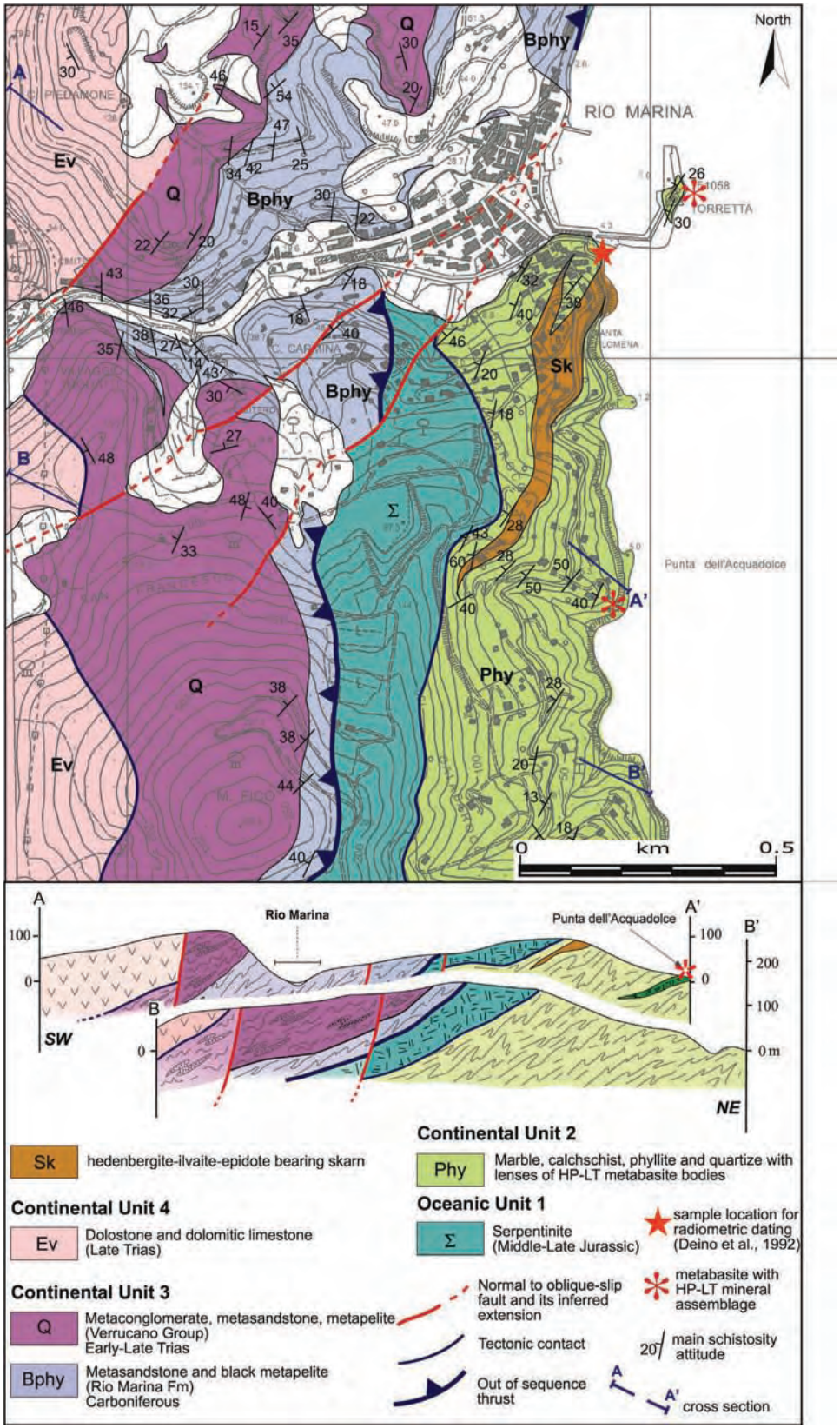

Fig. 4. Geological map and cross-sections of the Rio Marina area.

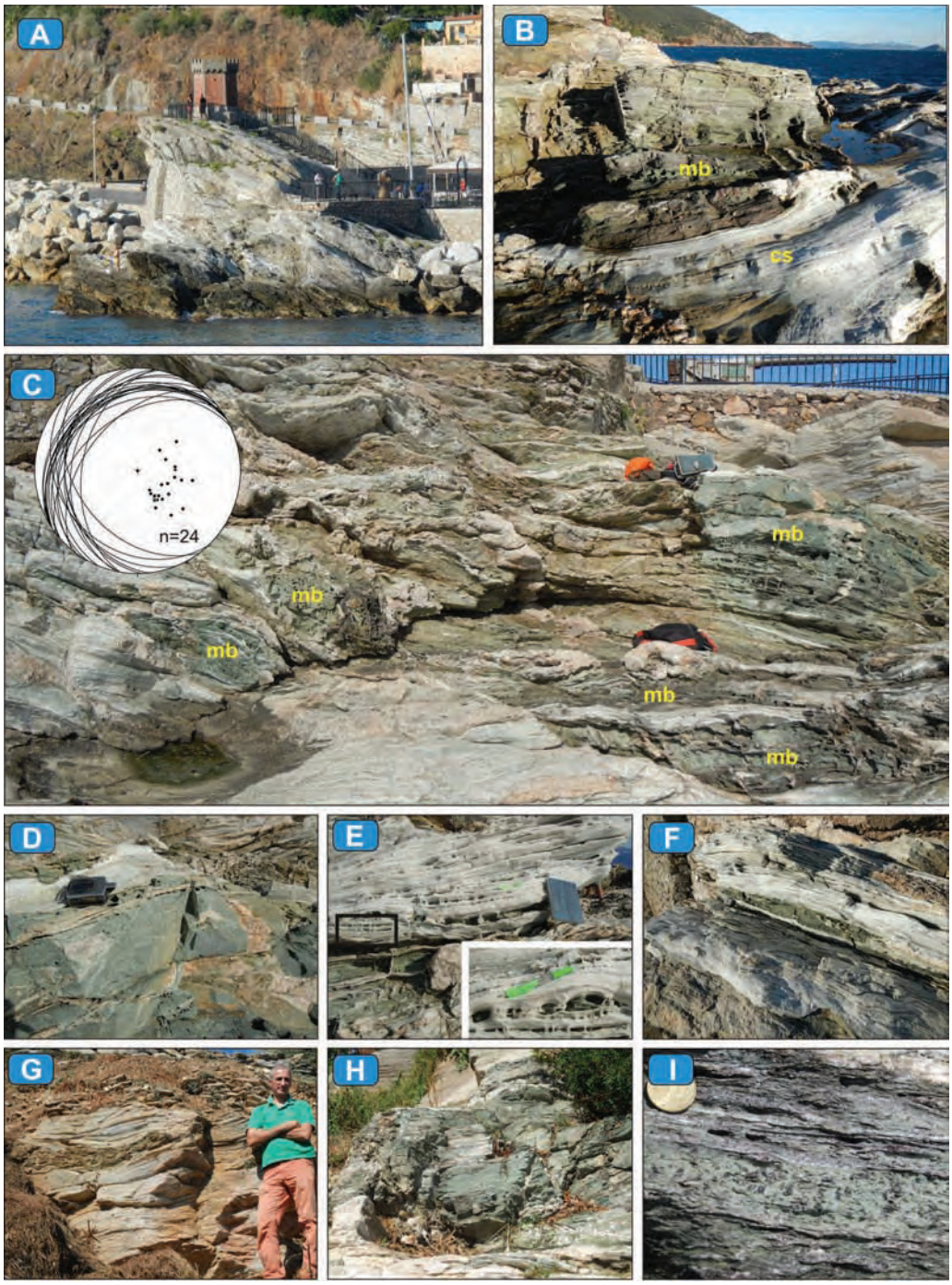

Fig. 5. (A) panoramic view of the sampling area (N42°48′54.9″ E10°25′53.3″); (B) lenses of metabasite embedded in calcshist; (C) metabasite lenses located mainly along the main schistosity, gently NW-dipping; (D) detail of metabasite lens; (E–H) metabasite laterally segmented at different scales indicating the pervasiveness of the deformation; (I) rock fabric characterized by the presence of porphyroclasts of mafic minerals within a chloritic matrix.

considered the pyroxene porphyroclasts with omphacite composition (max X_{Jd} = 0.33) and glaucophane (max X_{Gln} = 0.86). We firstly used the approach described by Sturm (2002) based on the albite = jadeite + quartz equilibrium, experimentally determined by Holland (1980). This calibration was obtained for temperatures higher than those typical of the blueschist facies but, according to Sturm (2002), extrapolation to lower temperatures produces small uncertainties in *P* values and can provide acceptable preliminary estimates. Therefore, considering the maximum content of jadeite molecula (X_{Jd} = 0.33) in omphacite, pressure values ranging from 0.95 to 1.10 GPa are obtained, if the field of the epidote blueschists subfacies by Tsujimori and Ernst (2013) is considered (Fig. 10). Indeed, the relatively low content of epidote in the metabasite and the suspected former presence of lawsonite, now replaced by anorthite, point to a peak *P*–*T* condition in the neighborhood of the transition from lawsonite- to epidote-blueschist subfacies, characterized by low contents in both lawsonite and epidote (Zhang et al., 2009).

In Fig. 10 the isopleth related to the observed maximum content in jadeite molecula meets the transition line between the two subfacies at a *T* of *c*. 330 °C, corresponding to a pressure of *c*. 0.95 GPa. Lower *P* estimates (Fig. 10) are obtained on the basis of the Na-amphibole composition. By following the calibration of Maruyama et al. (1986) and by plotting the isopleth related to the maximum

Table 2
Representative mineral analyses in metabasite (sample C19). Beam width was approximately of 1 μm. Mineral abbreviations according to Kretz (1983) and Bucher and Frey (1994): Gln = glaucophane; Act = actionolite; Omph = omphacite; Agt = aegirine-augite; Di = diopside; Aug = augite; Czo = clinozoisite; Ps = pistacite. Analyses were performed on the JEOL 8200 microprobe, at the University of Milan, operating in WDS/EDS with an accelerating voltage of 15 kV and 5 nA current. Beam width was approximately of 1 μm.

	Amphiboles		Clinopyroxenes				Feldspars		Epidotes		Chlorite
	Gln	Act	Omph	Agt	Di	Aug	Ab	An	Czo	Ps	
wt.%											
SiO_2	58.08	57.28	55.20	54.00	51.63	52.13	68.36	42.51	39.27	37.87	30.03
TiO_2	0.22	0.03	0.10	0.01	1.00	0.03	0.01	0.01	0.12	0.06	0.02
Al_2O_3	9.63	1.06	7.20	3.26	2.15	4.44	19.50	36.79	32.55	22.28	20.74
Cr_2O_3		0.04	0.28	0.19	0.02				0.02	0.09	0.03
FeO_t	9.76	6.89	9.36	9.86	6.71	13.69	0.07	0.17	1.4	12.55	14.26
MnO	0.17	0.30	0.13	0.23	0.19	0.22			0.03	0.11	0.38
MgO	10.56	18.47	7.44	9.90	15.04	14.23	0.01	0.01	0.06	0.03	20.97
CaO	1.09	11.20	11.65	15.19	21.64	13.22	0.03	19.80	23.55	22.18	0.06
Na_2O	6.16	0.86	7.34	5.33	0.36	0.35	11.68	0.05	0.01	0.03	0.01
K_2O	0.02	0.03	0.04	0.04	0.03	0.11		0.03	0.01	0.02	0.08
Tot	95.69	96.16	98.74	98.01	98.77	98.42	99.66	99.37	97.02	95.22	86.58
ΣO	23	23	6	6	6	6.066	8	8	25	25	28
Si	8.063	8.087	2.011	2.003	1.929	1.982	2.994	1.982	6.027	6.320	5.986
Al^{IV}					0.071	0.018	1.008	2.024			2.014
Al^{VI}	1.576	0.176	0.309	0.143	0.024	0.181			5.895	4.387	2.864
Ti	0.022	0.004	0.003		0.028	0.001			0.014	0.008	0.003
Cr		0.004	0.008	0.006	0.001				0.002	0.012	0.005
Fe	1.133	0.813	0.285	0.306	0.210	0.435	0.003	0.007	0.180	1.751	2.377
Mn	0.020	0.036	0.004	0.007	0.006	0.007			0.004	0.016	0.064
Mg	2.190	3.885	0.404	0.547	0.838	0.806	0.001	0.001	0.014	0.007	6.231
Ca	0.163	1.693	0.455	0.604	0.866	0.538	0.001	0.989	3.872	3.966	0.013
Na	1.658	0.234	0.519	0.383	0.026	0.026	0.992	0.005	0.003	0.010	0.004
K	0.003	0.005	0.002	0.002	0.001	0.005		0.002	0.002	0.004	0.020
Fe^{3+}	0.266	0.024	0.175	0.227	0.017						
Fe^{2+}	0.867	0.789	0.110	0.079	0.193	0.435					
ΣCat	14.828	14.937	4.000	4.000	4.000	4.000	4.998	5.009	16.013	16.480	19.581
X_{Gln}	0.86										
X_{Jd}			0.33	0.15							
X_{Wo}					0.46	0.30					
X_{En}					0.44	0.45					
X_{Fs}					0.10	0.25					
X_Q			0.48	0.62							
X_{Ae}			0.19	0.24							
X_{Ps}									0.09	0.82	
X_{An}							0.00	1.00			
X_{Ab}							1.00	0.00			
X_{Mg}	0.72	0.83	0.78	0.87	0.81	0.65					

content in glaucophane molecula in the field of epidote blueschist subfacies, a pressure value slightly above 0.7 GPa is estimated. This result might indicate that, after the peak pressure condition, glaucophane re-equilibrated in a later stage during exhumation.

A confirmation of the high-pressure metamorphic event was obtained from SEM-EDS analyses revealing the presence of white mica (Fig. 11A) with an elevated content in celadonite molecula (X_{Cel} = 0.5 and Si = 3.5 a.p.f.u.) in metabasite sample RMT3 (Table 3). However, although it qualitatively suggests high-*P* conditions, the lack of a limiting mineral assemblage in equilibrium with phengite (*i.e.*, K-feldspar, quartz, Mg/Fe silicates) precludes quantifying pressure by a geobarometric approach.

Another indication in favor of the high-pressure metamorphism comes from a phengite-bearing quartzite (sample RIO6A) in the Torre Giove locality (Figs. 2 and 11B and Table 3). The main schistosity is defined by Qtz + Ms + Kln ± Cal ± Fe–Ti oxide. In some cases, detrital grains of white mica are surrounded by aggregates of newly-formed flakes of phengite (Fig. 11B) with Si content of about 3.5 a.p.f.u. (Table 3).

5. Discussion and conclusions

The metasedimentary succession where we have found metabasite, has been differently interpreted through time. According to Trevisan (1950), Barberi et al. (1969), Perrin (1975) and Keller and Pialli (1990), it is considered as a part of the sedimentary succession belonging to the Tuscan Domain. Differently, Duranti et al. (1992) interpreted the ophiolite slice (*i.e.*, the oceanic unit 1 in Fig. 3) and the underlying metasedimentary succession, including the study metabasite, as belonging to the same overturned Jurassic-Cretaceous oceanic succession of the inner Ligurian Domain (Pertusati et al., 1993). This unit was later affected by contact metamorphism during the emplacement of the Porto Azzurro monzogranite (Duranti et al., 1992). Pandeli et al. (2001) followed this interpretation and suggested that the succession can be related to the sedimentary evolution of the Piedmont Ocean.

In order to contribute to this issue, chemical composition of the Elba Island metabasite has been compared with the available analyses of the Tuscany mafic rocks (Ricci and Serri, 1975; Brunacci et al., 1982; Brogi et al., 2000; Stoppa et al., 2014). The results are illustrated in the immobile element TAS proxy diagram (Fig. 7). These indicate that the study metabasite displays compositional features, which are distinct from MORB, alkali basalts and lamprophyres of Tuscany. This transitional signature leads us to rule out the attribution of the Elba Island metabasite to an oceanic setting, and specifically to the Ligurian-Piedmont Ocean. Therefore, the metabasite should be considered as emplaced in a sedimentary succession belonging to a transitional (Sub-Ligurian Domain)

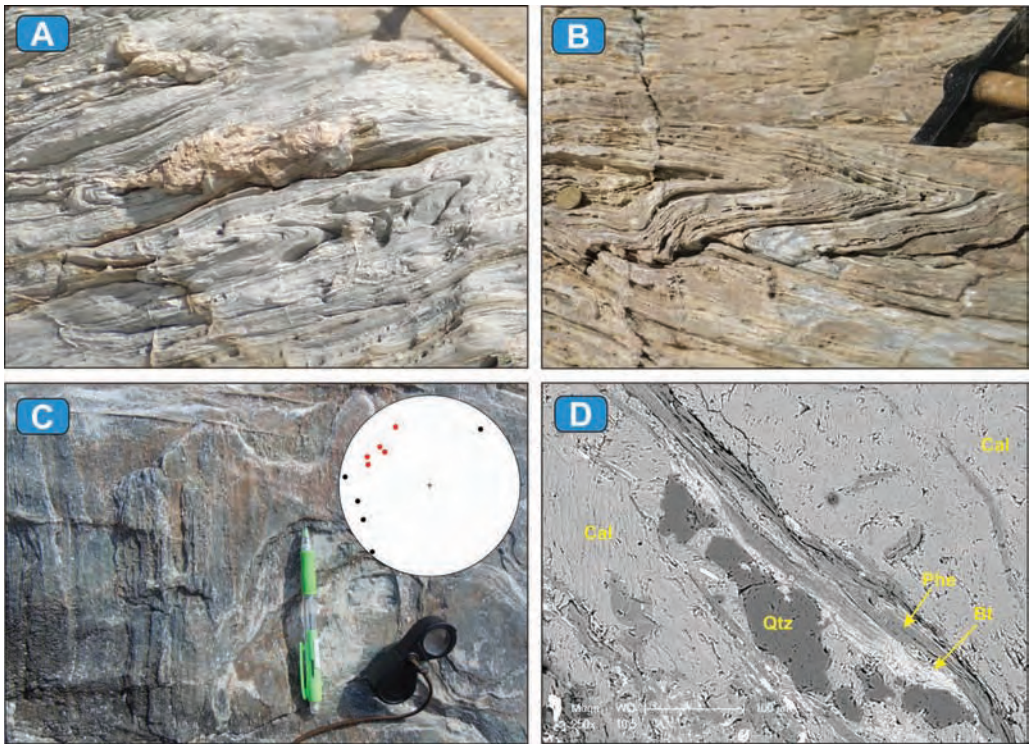

Fig. 6. (A, B) tight and isoclinal folds with ≈304°/30° plunging hinge lines deforming the main foliation in calcschist; (C) stretching lineation well defined by elongated calcite crystals, NW-SE trending; (D) SEM-BSE (scanning electron microscopy-back scattered electron) image showing the textural characteristics and paragenesis of micaschists. Mineral abbreviations after Kretz (1983) and Bucher and Frey (1994).

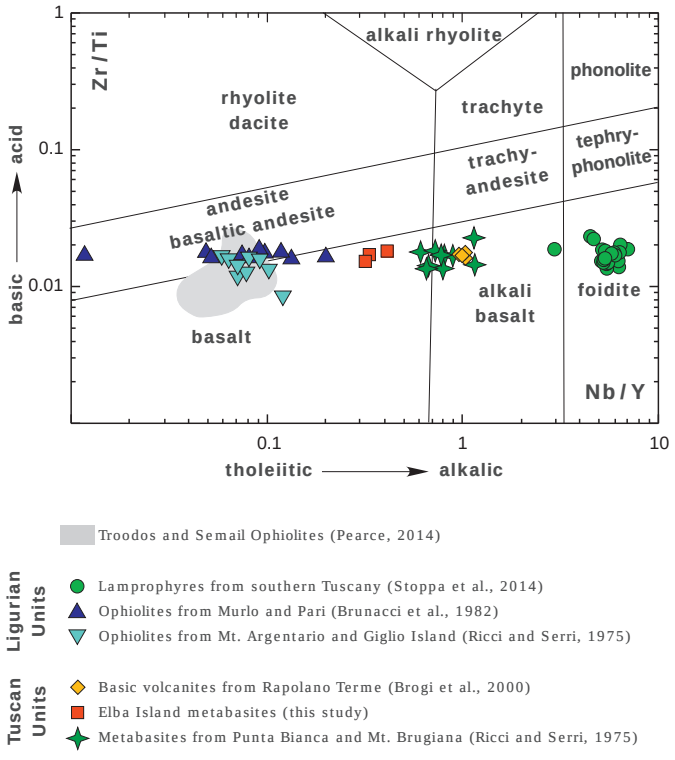

Fig. 7. Immobile element-based TAS proxy diagram (Pearce, 2014). Samples of the metabasite under study (red squares) are compared with the ophiolitic lavas from Troodos and Semail (Pearce, 2014) and with the mafic rocks from the Ligurian and Tuscan Units. (For interpretation of the references to color in this figure legend, the reader is referred to the web version of this article.)

Table 3
Selected SEM/EDS analyses of phengite in metabasite (sample RMT3) and quartzite (RIO6B). Analyses were performed on the Philips XL30 SEM at the University of Siena, operating in EDS/EDAX with an accelerating voltage of 20 kV.

	Metabasite RMT3	Quartzite RIO6A
wt.%		
SiO_2	52.69	51.65
TiO_2	0.15	0.19
Al_2O_3	24.61	23.77
FeO_t	3.34	5.93
MnO	0.12	0.11
MgO	4.97	2.98
CaO	0.18	0.11
Na_2O	0.12	0.08
K_2O	9.66	10.96
Tot	95.84	95.77
ΣO	11	11
Si	3.49	3.50
Al^{IV}	0.51	0.50
Al^{VI}	1.41	1.40
Ti	0.01	0.01
Fe	0.19	0.34
Mn	0.00	0.01
Mg	0.49	0.30
Ca	0.01	0.01
Na	0.01	0.01
K	0.82	0.95
ΣCat	6.94	7.02
X_{Cel}	0.49	0.50

or continental crust environment (Tuscan Domain). In relation to this latter point, it is worth to note that, on the basis of lithological and structural features, there is a general agreement to interpret the continental rock succession of Elba Island as a part of the Tuscan Domain (Trevisan, 1950; Barberi et al., 1969; Perrin, 1975; Keller and Pialli, 1990; Pertusati et al., 1993; Bortolotti et al., 2001). In

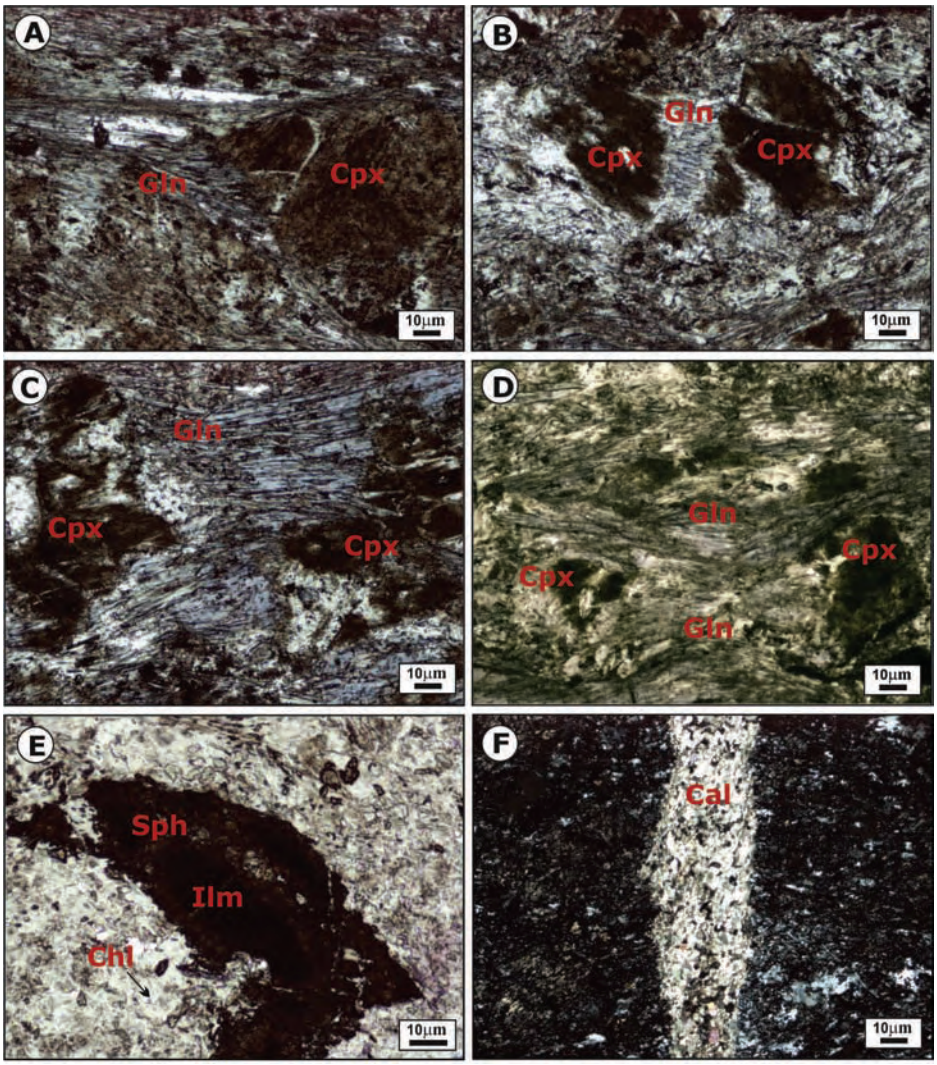

Fig. 8. Micrographs of a metabasite sample (plane polarized light in A–E and crossed polars in F). (A) Rounded porphyroclast of clinopyroxene with strain shadow filled by glaucophane. (B) Stretched and fractured porphyroclast of clinopyroxene. Fracture is filled by glaucophane fibers grown parallel to the stretching direction. (C) Elongated well-developed glaucophane crystals, mostly oriented along the main foliation between clinopyroxene porphyroclasts. (D) Glaucophane fibers wrapping around porfiroclasts of clinopyroxene. (E) Rock portion affected by retrogression in greenschist facies, as shown by the widespread chlorite and by the corona of sphene around ilmenite. (F) Late calcite vein cross-cutting at high angle the main foliation. Mineral symbols from Kretz (1983).

this reasonable picture, considering that Elba Island is presently located in the innermost part of the Northern Apennines, we relate the metabasite-bearing calcschist to the inner Tuscan Domain. Consequently, we sustain that the calcschist cannot be referred to the sedimentary succession of the ophiolite slice (oceanic unit 1 in Fig. 3), as explained by Duranti et al. (1992), Pertusati et al. (1993) and Pandeli et al. (2001). In this view, such ophiolite slice, overlying the calcschist, is interpreted as a different tectonic unit (Fig. 2).

Mineral association and *P*–*T* conditions point to an equilibration of the metabasite in the epidote blueschist subfacies with a pressure value of 0.9–1.0 GPa. Studies on metamorphic rocks of the inner Northern Apennines (Fig. 1) indicate an eastward decrease of pressure (Rossetti et al., 2002, with references therein), from 1.3–1.6 GPa (Gorgona and Giglio Islands, Fig. 1) to 0.8–1.0 GPa (southern Tuscany), as obtained on metasediments with Fe–Mg silicates (Giorgetti et al., 1998; Rossetti et al., 1999, 2001; Agard et al., 2000).

A comparative analysis of thermobarometric estimates obtained for metamorphic rocks of the inner Northern Apennines (Fig. 1), shows that the *P*–*T* conditions in metabasites are encompassed between 0.6 and 0.8 GPa (T = 275–350 °C). Instead, *P*-values obtained from metasediments range from 0.8 to 1.5 GPa (T = 350–450 °C) in six out of seven localities. Thus, it can be inferred that metabasites usually provide pressure estimates lower than metasediments.

Although pressure in Elba Island is slightly higher (P = 0.9–1.0 GPa; T = 330–350 °C) than that obtained for the other metabasites, we consider all the barometric values consistent with the same tectono-metamorphic framework of the inner Northern Apennines. On this basis, the result provided by the Elba Island metabasite has two significant implications: (i) the tectonic stacking of the Elba Island units did not occur in a low-*P* context, as sustained by Pertusati et al. (1993) and, more recently, by Musumeci and Vaselli (2012); (ii) Elba Island is now reconciled in the tectonic and metamorphic evolution of the Northern Apennines. Furthermore, it results that its stratigraphic and metamorphic evolution is significantly similar to the one described for Gorgona Island, suggesting that the interpretation of the Gorgona calcschist as a part of the Piedmont Ocean (Capponi et al., 1990; Pandeli et al., 2001; Rossetti et al., 2001) should be revised. Furthermore, the Gorgona-Elba Islands alignment is believed to comprehend the suture zone of the Northern Apennines (Nardi,

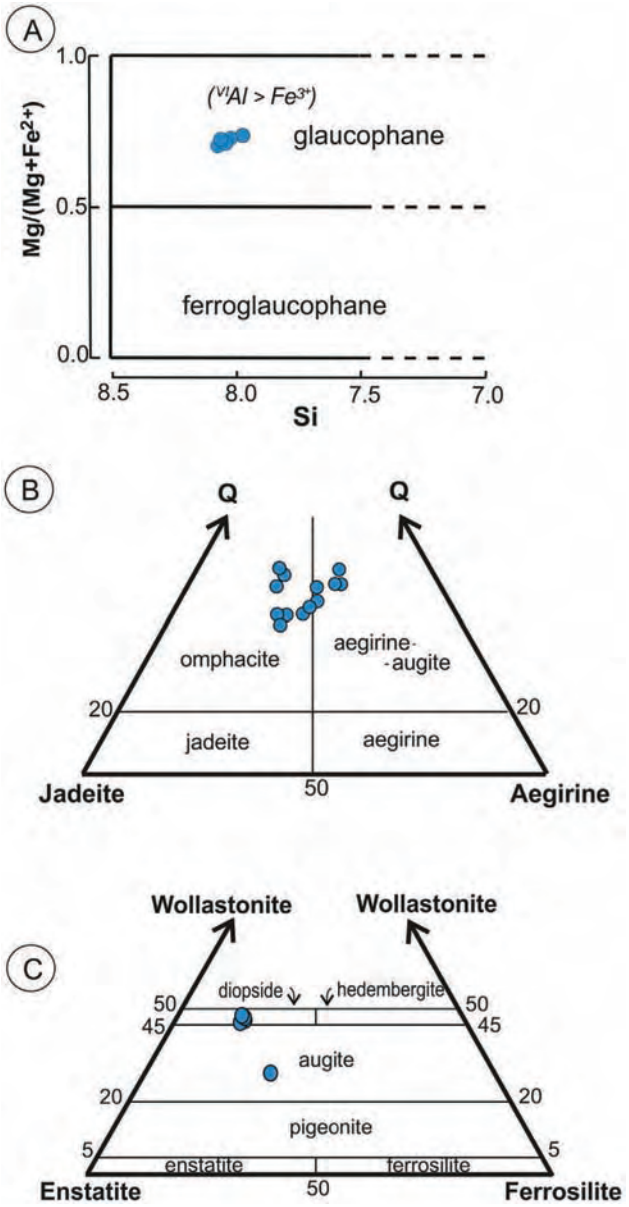

Fig. 9. (A) Classification diagram of Na-Amphiboles in metabasite (after Leake et al., 1997). (B) Classification diagram of Morimoto et al. (1988) for Ca–Na pyroxenes in the metabasite; Q = wollastonite + enstatite + Ferrosilite. (C) Classification diagram of Morimoto et al. (1988) for Ca–Fe–Mg pyroxenes in the metabasite.

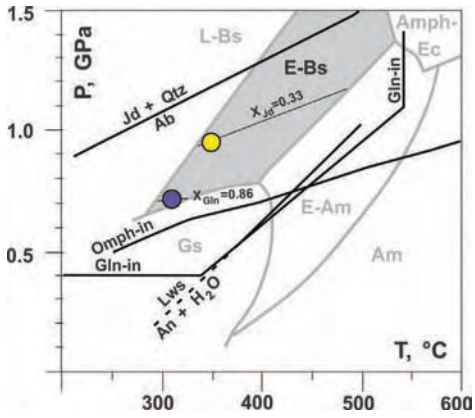

Fig. 10. *P–T* diagram showing approximate metamorphic conditions (circles) for the Elba Island metabasite constrained by mineral assemblage and composition of omphacite (yellow) and glaucophane (lilac). X_{Jd} isopleth calculated with the aid of the Sturm (2002) software on the basis of Ab = Jd + Qtz equilibrium calibrated by Holland (1980). X_{Gln} isopleth from calibration by Maruyama et al. (1986). Subfacies boundaries by Tsujimori and Ernst (2013) and some relevant equilibria are reported. Metamorphic facies and sub-facies abbreviations: L-Bs = lawsonite blueschist; E-Bs = epidote blueschist; Gs = greenschist; E-Am = epidote – amphibolite; Am = amphibolite; Amph-Ec = amphibole eclogite. Mineral stability boundary and equilibria: Gln-in = stability boundary of glaucophane by Maresch (1977); Omph-in = stability boundary of omphacite-in a jadeite-enriched MORB (MORB+ in Tsujimori and Ernst, 2013); Ab = Jd + Qtz by Tsujimori and Ernst (2013); Lws = An + H_2O by Crawford and Fyfe (1965). Mineral abbreviations according to Kretz (1983). (For interpretation of the references to color in this figure legend, the reader is referred to the web version of this article.)

1968; Elter and Pertusati, 1973; Pandeli et al., 2001); nevertheless, although the location of the suture zone is out of the goals of this study, it can be argued that this suture zone should be located to the West, between Corse and the Elba-Gorgona Islands alignment.

Finally, considering the presence of phengite with elevated Si content in rock from the Monte Giove area, it is reasonable to hypothesize that continental units 2 and 3 (Fig. 3) have been affected by high *P*-metamorphism. Consequently, it can be inferred that also the oceanic unit 1, interposed between the continental units 2 and 3 (Figs. 3 and 4), underwent the same type of metamorphism. The absence of a corresponding paragenesis, is probably an effect of re-equilibration after the thermal perturbation produced by the emplacement of the Porto Azzurro monzogranite (Pertusati et al., 1993; Bortolotti et al., 1994).

As it regards the timing of metamorphism, we have in the area two different radiometric ages: Brunet et al. (2000) dated white mica on the main schistosity of calcschist cropping out in Gorgona Island (Fig. 1), obtaining 25.5 ± 0.3 Ma by $^{40}Ar/^{39}Ar$ geochronology; by the same method, Deino et al. (1992) dated the white mica,

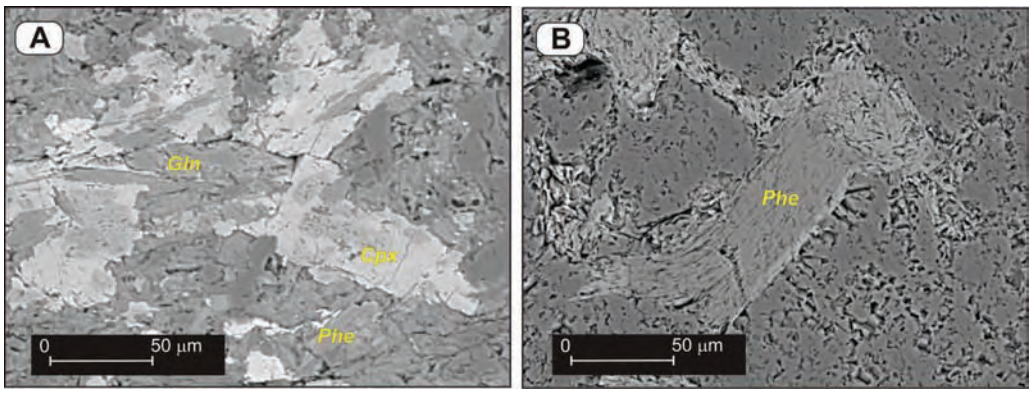

Fig. 11. SEM-BSE (scanning electron microscopy-back scattered electron) images: (A) RMT3 metabasite sample with glaucophane (Gln), clinopyroxene (Cpx) and phengite (Phe). (B) Phengite from Torre Giove quartzite, with a higher content in celadonite in the rim (lighter color).

grown on the main schistosity of the Elba Island calcschist (Fig. 4), providing a radiometric age of 19.68 ± 0.15 Ma. Furthermore, comparable ages of 27 Ma, in southern Tuscany, and of about 30 Ma, in the Tuscan Archipelago, were also estimated by fission track method on zircon (Balestrieri et al., 2011).

Assuming that the study metabasite and hosting calcschist record the same deformational event and considering that both glaucophane in metabasite, and white mica in calcschist, are syn-kynematic, we suggest that the radiometric ages are indicative for the high-*P* metamorphic event during late Oligocene-early Burdigalian.

Acknowledgments

The research leading to these results has received funding from the European Community's Seventh Framework Programme under grant agreement No. 608553 (Project IMAGE). The Editor W.P. Schellart, and the Reviewers M.L. Balestrieri and M. Bonini are deeply thanked for their fruitful comments and suggestions.

References

Agard, P., Goffé, B., Touret, J.L.R., Vidal, O., 2000. Retrograde fluid evolution in blueschist-facies metapelites (Schistes lustrés unit Western Alps). Contrib. Mineral. Petrol. 140, 296–315.

Baldi, P., Bertini, G., Cameli, G.M., Decandia, F.A., Dini, I., Lazzarotto, A., Liotta, D., 1994. Tettonica distensiva post-collisionale nell'area geotermica di Larderello (Toscana meridionale). Stud. Geol. Camerti Spec 1, 183–193.

Balestrieri, M.L., Pandeli, E., Bigazzi, G., Carosi, R., Montomoli, C., 2011. Age and temperature constraints on metamorphism and exhumation of the syn-orogenic metamorphic complexes of Northern Apennines, Italy. Tectonophysics 509, 254–271.

Barberi, F., Dallan, L., Franzini, M., Giglia, G., Innocenti, F., Marinelli, G., Raggi, R., Ricci, C.A., Squarci, P., Taffi, L., Trevisan, L., 1969. Note illustrative della Carta Geologica d' Italia alla scala1 100 000 Foglio 126 (Isola d'Elba). Serv. Geol. d'Ital., 32.

Barberi, F., Innocenti, F., 1965. Le rocce cornubianitico-calcaree dell'anello termometamorfico del Monte Capanne (Isola d'Elba). Atti Soc. Toscana Sci. Nat. Mem. Ser. A 72, 306–398.

Barchi, M.R., 2010. The Neogene-Quaternary evolution of the Northern Apennines: crustal structure, style of deformation and seismicity. In: Beltrando, M., Peccerillo, A., Mattei, M., Conticelli, S., Doglioni, C. (Eds.), The Neogene-Quaternary Evolution of the Northern Apennines: Crustal Structure, Style of Deformation, Seismicity, vol. 36. Journ. Virt. Explorer, http://dx.doi.org/10.3809/jvirtex.2009.00220.

Bertini, G., Cameli, G.M., Costantini, A., Decandia, F.A., Di Filippo, M., Dini, I., Elter, F.M., Lazzarotto, A., Liotta, D., Pandeli, E., Sandrelli, F., Toro, B., 1991. Struttura geologica fra i monti di Campiglia e Rapolano Terme (Toscana meridionale): stato attuale delle conoscenze e problematiche. Stud. Geol. Camerti 1, 155–178.

Bonini, M., Moratti, G., 1995. Evoluzione tettonica del bacino neogenico di Radicondoli-Volterra (Toscana meridionale). Boll. Soc. Geol. Ital. 114, 549–573.

Bonini, M., Moratti, G., Sani, F., 1999. Evolution and depocentre migration in thrust-top basins: inferences from the Messinian Velona Basin (northern Apennines, Italy). Tectonophysics 304, 95–108.

Bonini, M., Moratti, G., Sani, F., Balestrieri, M.L., 2013. Compression-to-extension record in the Late Pliocene-Pleistocene Upper Valdarno Basin (Northern Apennines Italy): structural and thermochronological constraints. Ital. J. Geosci. 132, 54–80.

Bonini, M., Sani, F., 2002. Extension and compression in the northern Apennines (Italy) hinterland: evidence from the late Miocene-Pliocene Siena-Radicofani Basin and relations with basement structures. Tectonics 22, 1–35.

Bonini, M., Cerrina Feroni, A., Martinelli, P., Moratti, G., Valleri, G., Cerini, L., 1994. Intramessinian angular unconformity within the Radicondoli syncline (Siena, Tuscany, Italy): structural and biostratigraphical preliminary data. Me. Soc. Geol. Ital. 48, 501–507.

Bonini, M., Sani, F., Stucchi, E.M., Moratti, G., Benvenuti, M., Menanno, G., Tanini, C., 2014. Late Miocene shortening of the Northern Apennines back-arc. J. Geodyn. 74, 1–31.

Bortolotti, V., Cellai, D., Martin, S., Principi, G., Tartarotti, P., Vaggelli, G., 1994. Ultramafic rocks from the eastern Elba island ophiolites (Tyrrhenian Sea Italy). Mem. Soc. Geol. Ital. 48, 195–202.

Bortolotti, V., Fazzuoli, M., Pandeli, F., Principi, G., Babbini, A., Corti, S., 2001. Geology of Central and Eastern Elba Island Italy. Ofioliti 26, 97–150.

Bossio, A., Costantini, A., Lazzarotto, A., Liotta, D., Mazzanti, R., Mazzei, R., Salvatorini, G.F., Sandrelli, F., 1993. Rassegna delle conoscenze sulla stratigrafia del Neoautoctono toscano. Mem. Soc. Geol. Ital. 49, 17–98.

Brogi, A., Fidolini, F., Liotta, D., 2013. Tectonic and sedimentary evolution of the Upper Valdarno Basin: new insights from the lacustrine S. Barbara Basin. Ital. J. Geosci. 132, 81–97.

Brogi, A., Giorgetti, G., 2012. Tectono-metamorphic evolution of the siliciclastic units in the Middle Tuscan Range (inner Northern Apennines): Mg–carpholite bearing quartz veins related to syn-metamorphic syn-orogenic foliation. Tectonophysics 526–529 (2012), 167–184.

Brogi, A., Lazzarotto, A., Liotta, D., CROP 18 Working Group, 2005a. Structural features of southern Tuscany and geological interpretation of the CROP 18 Seismic Reflection Survey (Italy). Boll. Soc. Geol. Ital. 3, 213–236.

Brogi, A., Lazzarotto, A., Liotta, D., Ranalli, G., 2005b. Crustal structures in the geothermal areas of southern Tuscany (Italy): insights from the CROP 18 deep seismic reflection lines. J. Volcanol. Geotherm. Res. 148, 60–80.

Brogi, A., Liotta, D., 2008. Highly extended terrains, lateral segmentation of the substratum, and basin development: the Middle-Late Miocene Radicondoli Basin (inner northern Apennines, Italy). Tectonics 27, http://dx.doi.org/10.1029/2007TC002188 TC 5002.

Brogi, A., Cornamusini, G., Costantini, A., Di Vincenzo, G., Lazzarotto, A., 2000. Cretaceous volcanism of the southern Tuscany: record of volcanic bodies from Tuscan succession of Rapolano Terme. Mem. Soc. Geol. Ital. 55, 329–337.

Brunacci, S., Donati, C., Faraone, D., 1982. Indagini petrografiche e chimiche su ofioliti della Toscana Affioramenti nell'area compresa tra Murlo e Pari (provv. di Siena e Grosseto). Ofioliti 7, 41–78.

Brunet, C., Monie, P., Jolivet, L., Cadet, J.P., 2000. Migration of compression and extension in the Tyrrhenian sea, insights from $^{40}Ar/^{39}Ar$ ages on micas along a transect from Corsica to Tuscany. Tectonophysics 321, 127–155.

Bucher, K., Frey, M., 1994. Petrogenesis of Metamorphic Rocks. Springer-Verlag, Berlin, pp. 318.

Caggianelli, A., Ranalli, G., La Vecchia, A., Liotta, D., Dini, A., 2014. Post-emplacement thermo-rheological history of a granite intrusion and surrounding rocks: the Monte Capanne pluton, Elba Island, Italy. In: Llana-Fúnez, S., Marcos, A., Bastida, F. (Eds.), Deformation Structures and Processes Within the Continental Crust, vol. 394. Geological Society, London, Special Publications, pp. 129–143.

Capponi, G., Giammarino, S., Mazzanti, R., 1990. Geologia e morfologia dell'Isola di Gorgona. Quad. Mus. Stor. Nat. Livorno 11, 115–137.

Carmignani, L., Decandia, F.A., Disperati, L., Fantozzi, P.L., Lazzarotto, A., Liotta, D., Meccheri, M., 1994. Tertiary extensional tectonics in Tuscany (Northern Apenines, Italy). Tectonophysics 238, 295–315.

Carmignani, L., Decandia, F.A., Disperati, L., Fantozzi, P.L., Lazzarotto, A., Liotta, D., Oggiano, G., 1995. Relationships between the Sardinia-Corsica-Provencal Domainand the Northern Apennines. Terranova 7, 128–137.

Carmignani, L., Kligfield, R., 1990. Crustal extension in the Northern Apennines: the transition from compression to extension in the Alpi Apuane core complex. Tectonics 9, 1275–1303.

Crawford, W.A., Fyfe, W.S., 1965. Lawsonite equilibria. Am. J. Sci. 263, 262–270.

Deino, A., Keller, J.V.A., Minelli, G., Pialli, G., 1992. Datazioni $^{39}Ar/^{40}Ar$ del metamorfismo dell'Unità di Ortano-Rio Marina (Isola d'Elba): risultati preliminari. Stud. Geol. Camerti 1, 187–192.

Dini, A., Innocenti, F., Rocchi, S., Tonarini, S., Westerman, D.S., 2002. The magmatic evolution of the Late Miocene laccolith–pluton–dyke granitic complex of Elba Island Italy. Geol. Mag. 139, 257–279.

Duranti, S., Palmieri, R., Pertusati, P.C., Ricci, C.A., 1992. Geological evolution and metamorphic petrology of the basal sequences of eastern Elba (Complex II). Acta Vulcanol. 2, 213–229.

Elter, F.M., Pandeli, E., 2002. The HP-LP meta-ophiolitic unit and Verrucano of the Cala Grande Area in the Argentario Promontory (southern Tuscany Italy): structural metamorphic evolution and regional considerations. Ofioliti 27 (2), 91–102.

Elter, P., Pertusati, P.C., 1973. Considerazioni sul limite Alpi-Appennino e sulle sue relazioni con l'arco delle Alpi occidentali. Mem. Soc. Geol. Ital. 12, 359–375.

Evans, B.W., 1990. Phase relations of epidote-blueschists. Lithos 25, 3–23.

Finetti, I.R., 2006. Basic regional crustal setting and superimposed local pluton-intrusion related tectonics in the Larderello-Monte Amiata geothermal province, from integrated CROP seismic data. Boll. Soc. Geol. Ital. 125, 117–146.

Finetti, I., Boccaletti, M., Bonini, M., Del Ben, A., Geletti, R., Pipan, M., Sani, F., 2001. Crustal section based on CROP seismic data across the North Tyrrhenian-northern Apennines-Adriatic Sea. Tectonophysics 343, 135–163.

Garfagnoli, F., Menna, F., Pandeli, E., Principi, G., 2005. The Porto Azzurro Unit (Mt. Calamita promontory, south-eastern Elba Island, Tuscany): stratigraphic, tectonic and metamorphic evolution. Boll. Soc. Geol. Ital. 3, 119–138.

Giorgetti, G., Goffé, B., Memmi, I., Nieto, F., 1998. Metamorphic evolution of Verrucano metasediments in northern Apennines: new petrological constraints. Eur. J. Miner. 10, 1295–1308.

Holland, T.J.B., 1980. The reaction albite=jadeite + quartz determined experimentally in the range 600°–1200 °C. Am. Miner. 65, 129–134.

Jolivet, L., Daniel, J.M., Truffert, C., Goffé, B., 1994. Exhumation of deep crustal metamorphic rocks and crustal extension in arc and back-arc regions. Lithos 33, 3–30.

Jolivet, L., Dubois, R., Fournier, R., Goffé, B., Michard, A., Jourdan, C., 1990. Ductile extension in alpine Corsica. Geology 18, 1007–1010.

Jolivet, L., Faccenna, C., Goffé, B., Mattei, M., Rossetti, F., Brunet, C., Storti, F., Funiciello, R., Cadet, J.P., D'Agostino, N., Parra, T., 1998. Midcrustal shear zones in postorogenic extension: example from the northern Tyrrhenian Sea. J. Geophys. Res. 103 (B6), 12123–12160.

Keller, J.V.A., Pialli, G., 1990. Tectonics of the island of Elba: a reappraisal. Boll. Soc. Geol. Ital. 109, 413–425.

Keller, J.V.A., Coward, M.P., 1996. The structure and evolution of the Northern Tyrrhenian Sea. Geol. Mag. 133, 1–16.

Kligfield, R., Hunziker, J., Dallmayer, R.D., Schamel, S., 1986. Dating of deformation phases using K–Ar and $^{40}Ar/^{39}Ar$ techniques: results from the Northern Apennines. J. Struct. Geol. 8, 781–798.
Kretz, R., 1983. Symbols for rock-forming minerals. Am. Mineral. 68, 277–279.
Leake, B.E., Woolley, A.R., Arps, C.E.S., Birch, W.D., Gilbert, M.C., Grice, J.D., Hawthorne, F.C., Kato, A., Kisch, H.J., Krivovichev, V.G., Linthout, K., Laird, J., Mandarino, J.A., Maresch, W.V., Nickel, E.H., Rock, N.M.S., Schumacher, J.C., Smith, D.C., Stephenson, N.C.N., Ungaretti, L., Whittaker, E.J.W., Guo, Y.Z., 1997. Nomenclature of amphiboles: report of the subcommittee on amphiboles of the International Mineralogical Association, commission on new minerals and mineral names. Am. Miner. 82, 1019–1037.
Liotta, D., Brogi, A., Meccheri, M., Dini, A., Bianco, C., Ruggieri, G., 2015. Coexistence of low-angle normal and high-angle strike-to oblique-slip faults during Late Miocene mineralization in eastern Elba Island (Italy). Tectonophysics.
Maresch, W.V., 1977. Experimental studies on glaucophane: an analysis of present knowledge. Tectonophysics 43, 109–125.
Maruyama, S., Cho, M., Liou, J.G., 1986. Experimental investigations of blueschist-greenschist transition equilibria: pressure dependence of Al_2O_3 contents in sodic amphiboles – a new geobarometer. Geol. Soc. Am. Mem. 164, 1–16.
Maineri, C., Benvenuti, M., Costagliola, P., Dini, A., Lattanzi, P., Ruggieri, G., Villa, I.M., 2003. Sericitic alteration at the La Crocetta deposit (Elba Island Italy): interplay between magmatism, tectonics and hydrothermal activity. Miner. Depos. 38, 67–86.
Molli, G., 2008. Northern Apennine–Corsica orogenic system: an updated overview. Geological Society, London, Special Publications 298, 413–442.
Moratti, G., Bonini, M., 1998. Structural development of the Neogene Radicondoli-Volterrra and adjoining hinterland basins in western Tuscany (northern Apennines, Italy). Geol. J. 33, 223–241.
Morimoto, N., Fabries, J., Ferguson, A.K., Ginzburg, R.M., Seifert, F., Zussman, J., Aoki, K., Gottardi, G., 1988. Nomenclature of pyroxenes. Am. Miner. 73, 1123–1133.
Musumeci, G., Mazzarini, F., Cruden, A.R., 2015. The Zuccale Fault, Elba Island Italy: a new perspective from fault architecture. Tectonics, http://dx.doi.org/10.1002/2014TC003809.
Musumeci, G., Mazzarini, F., Tiepolo, M., Di Vincenzo, G., 2011. U–Pb and $^{40}Ar–^{39}Ar$ geochronology of Palaeozoic units in the Northern Apennines: determining protolith age and alpine evolution using the Calamita Schist and Ortano Porphyroids. Geol. J. 46, 288–310.
Musumeci, G., Vaselli, L., 2012. Neogene deformation and granite emplacement in the metamorphic units of northern Apennines (Italy): insights from mylonitic marbles in the Porto Azzurro pluton contact aureole (Elba Island). Geosphere 8, 470–490.
Nardi, R., 1968. Le unità alloctone della Corsica e la loro correlazione con le unità delle Alpi e dell'Appennino. Mem. Soc. Geol. Ital. 7, 328–344.
Pandeli, E., Puxeddu, M., Ruggieri, G., 2001. The metasiliciclastic-carbonate sequence of the Acquadolce Unit (eastern Elba Island): new petrographic data and palaeogeographic interpretation. Ofioliti 26, 207–218.
Pauselli, C., Barchi, M.R., Federico, C., Magnani, M.B., Minelli, G., 2006. The crustal structure of the northern Apennines (central Italy): an insight by the CROP03 seismic line. Am. J. Sci. 306, 428–450.
Pearce, J.A., 1996. A user's guide to basalt discrimination diagrams. In: Wyman, D.A. (Ed.), Trace Element Geochemistry of Volcanic Rocks: Applications for Massive Sulphide Exploration, Short Course Notes, vol. 12. Geol. Ass. Canada, pp. 79–113.
Pearce, J.A., 2014. Immobile elements finger printing of ophiolite. Elements 10, 101–108.
Peccerillo, A., 2003. Plio-quaternary magmatism in Italy. Episodes 26, 222–226.
Perrin, M., 1975. L'ile d'Elbe et la limite Alpes-Apennin: données sur la structure géologique et l'évolution tectogenétique de l'Elbe Alpine et de l'Elbe Apennine. Boll. Soc. Geol. Ital. 94, 1929–1955.
Pertusati, P., Raggi, G., Ricci, C.A., Duranti, S., Palmeri, R., 1993. Evoluzione post-collisionale dell'Elba centro-orientale. Mem. Soc. Geol. Ital. 49, 297–312.
Ricci, C.A., Serri, G., 1975. Evidenze geochimiche sulla diversa affinità petrogenetica delle rocce basiche comprese nelle serie a facies Toscana. Boll. Soc. Geol. Ital. 94, 1187–1198.
Rossetti, F., Faccenna, C., Jolivet, L., Funiciello, R., Tecce, F., Brunet, C., 1999. Syn-versus post-orogenic extension: the case study of Giglio Island (Northern Tyrrenian Sea, Italy). Tectonophysics 304, 73–92.
Rossetti, F., Faccenna, C., Jolivet, L., Funiciello, R., Goffè, B., Tecce, F., Brunet, C., Monié, P., Vidal, O., 2001. Structural signature and exhumation P–T–t path of the Gorgona blueschist sequence (Tuscan Archipelago, Italy). Ofioliti 26, 175–186.
Rossetti, F., Faccenna, C., Jolivet, L., Goffé, B., Funiciello, R., 2002. Structural signature and exhumation P–T–t paths of the blueschist units exposed in the interior of the Northern Apennine chain, tectonic implications. Boll. Soc. Geol. Ital. 1, 829–842.
Rossetti, F., Glodny, J., Theye, T., Maggi, M., 2015. Pressure–temperature–deformation–time of the ductile Alpine shearing in Corsica: from orogenic construction to collapse. Lithos, http://dx.doi.org/10.1016/j.lithos.2015.01.011.
Rossetti, F., Tecce, F., Billi, A., Brilli, M., 2007. Patterns of fluid flow in the contact aureole of the Late Miocene Monte Capanne pluton (Elba Island Italy): the role of structures and rheology. Contrib. Mineral. Petrol. 153, 743–760.
Sani, F., Bonini, M., Piccardi, L., Vannucci, G., Delle Donne, G., Benvenuti, M., Moratti, G., Corti, G., Montanari, D., Sedda, L., 2009. Late Pliocene-Quaternary evolution of outermost hinterland basins of the Northern Apennines (Italy), and their relevance to active tectonics. Tectonophysics 476, 336–356.
Stoppa, F., Rukhlov, A.S., Bell, K., Schiazza, M., Vichi, G., 2014. Lamprophyres of Italy: early Cretaceous alkaline lamprophyres of Southern Tuscany, Italy. Lithos 188, 97–112.
Sturm, R., 2002. PX-NOM-an interactive spreadsheet program for the computation of pyroxene analyses derived from the electron microprobe. Comput. Geosci. 28, 473–483.
Tanelli, G., 1983. Mineralizzazioni metallifere e minerogenesi della Toscana. Mem. Soc. Geol. Ital. 25, 91–109.
Tanelli, G., Benvenuti, M., Costagliola, P., Dini, A., Lattanzi, P., Manieri, C., Mascaro, I., Ruggieri, G., 2001. The iron mineral deposits of Elba Island: state of the art. Ofioliti 26, 239–248.
Theye, T., Reinhardt, J., Goffè, B., Jolivet, L., Brunet, C., 1997. Fe- and Mg-carpholite from the Monte Argentario (Italy): first evidence for high-pressure metamorphism of the metasedimentary Verrucano sequence, and significance for P–T path reconstruction. Eur. J. Miner. 9, 859–873.
Tindle, A.G., Webb, P.C., 1994. Probe-AMPH-A spreadsheet program to classify microprobe-derived amphibole analyses. Comput. Geosci. 20, 1201–1228.
Tsujimori, T., Ernst, W.G., 2013. Lawsonite blueschists and lawsonite eclogites as proxies for palaeo-subduction zone processes: a review. J. Metamorph. Geol., http://dx.doi.org/10.1111/jmg.12057.
Trevisan, L., 1950. L'Elba orientale e la sua tettonica di scivolamento per gravità. Mem. Inst. Geol. Univ. Padova 16, 1–30.
Westerman, D.S., Dini, A., Innocenti, F., Rocchi, S., 2004. Rise and fall of a nested Christmas-tree laccolith complex, Elba Island, Italy. In: Breitkreuz, C., Petford, N. (Eds.), Physical Geology of High-Level Magmatic Systems, 234. Geological Society, London, Special Publications, pp. 195–213.
Winchester, J.A., Floyd, P.A., 1977. Geochemical discrimination if different magma series and their differentiation products using immobile elements. Chem. Geol. 20, 325–343.
Zhang, Z.C., Mao, J.W., Saunders, A.D., Ai, Y., Li, Y., Zhao, L., 2009. Petrogenetic modeling of three mafic-ultramafic layered intrusions in the Emeishan large igneous province, SW China, based on isotopic and bulk chemical constraints. Lithos 113, 369–392.

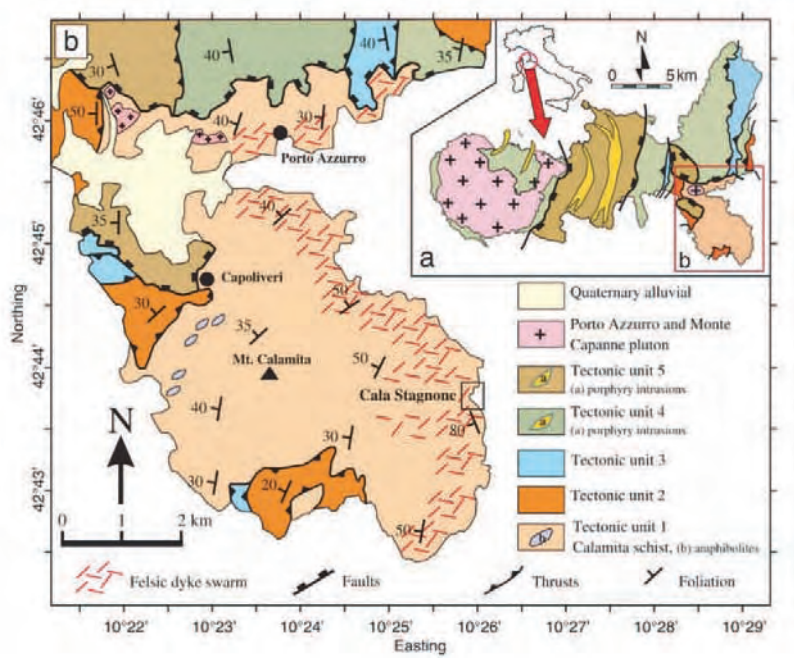

Fig. 2.3.1 - (a) Geological sketch of the Elba Island; (b) Geological map of south-eastern Elba Island (Calamita Peninsula and Porto Azzurro; modified after Dini et al., 2008). The tectonic units derive from both Tethyan Ocean (Ligurian units; Complex IV and V) and Adria continental margin (Tuscan units; Complex I, II and III). Late Miocene intrusive rocks in central-western Elba Island consist of a laccolithic porphyry complex, the Monte Capanne pluton and a mafic dyke swarm, while in eastern Elba Island, they consist of the Porto Azzurro pluton, a felsic dyke-sill system and a mafic dyke swarm.

Fig. 2.3.2 - Localization of investigated areas and samples analyzed for fluid inclusions.

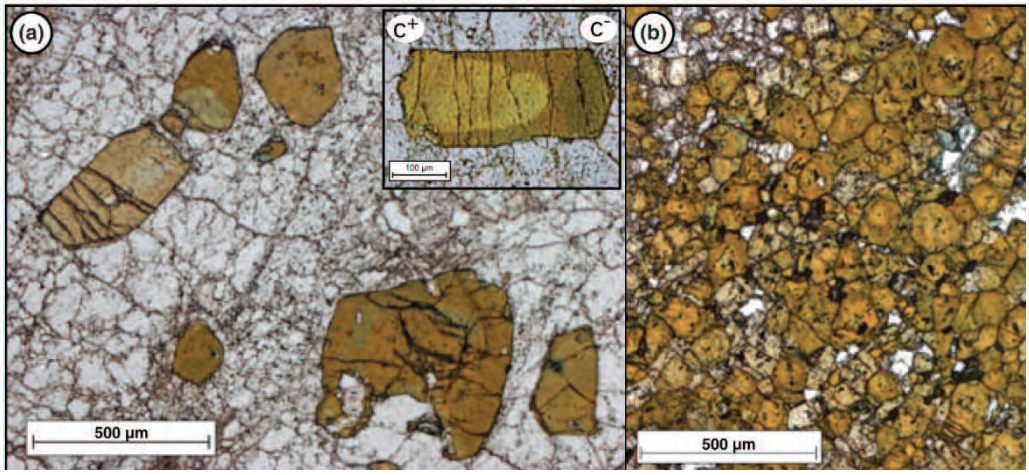

Fig. 2.3.3 (a) Euhedral crystals of schorl in felsic dyke. All crystals are distinctly zoned; (b) Polygonal aggregate of metasomatic tourmaline with interstitial quartz. The crystals show a concentric zoning (after Dini et al., 2008).

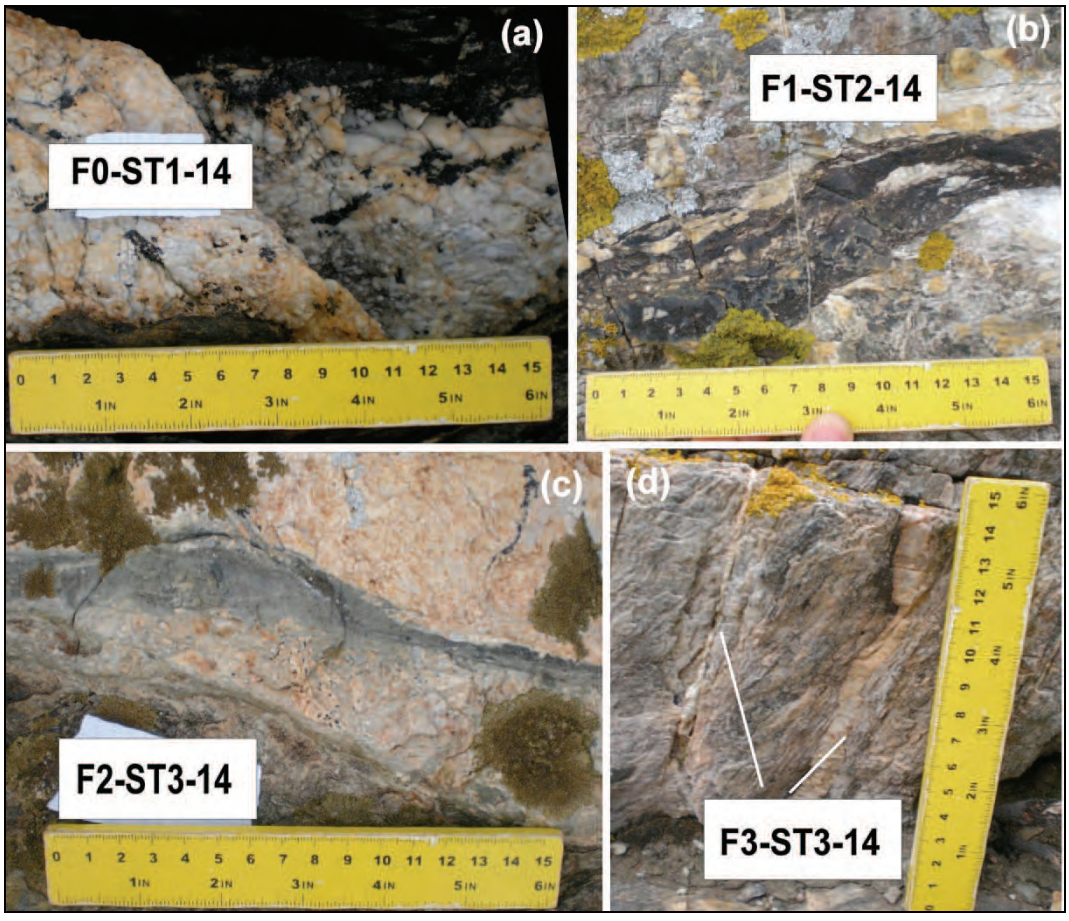

Fig. 2.3.4. (a) Felsic dyke with black crystals of magmatic tourmaline (F0) (sample F0-ST1-14); (b) low-angle quartz-tourmaline hydrothermal veins (F1) (sample F1-ST2-14); (c) high-angle quartz-tourmaline hydrothermal veins (F2) (sample F2-ST3-14); (d) high-angle quartz hydrothermal veins (F3) (sample F3-ST3-14).

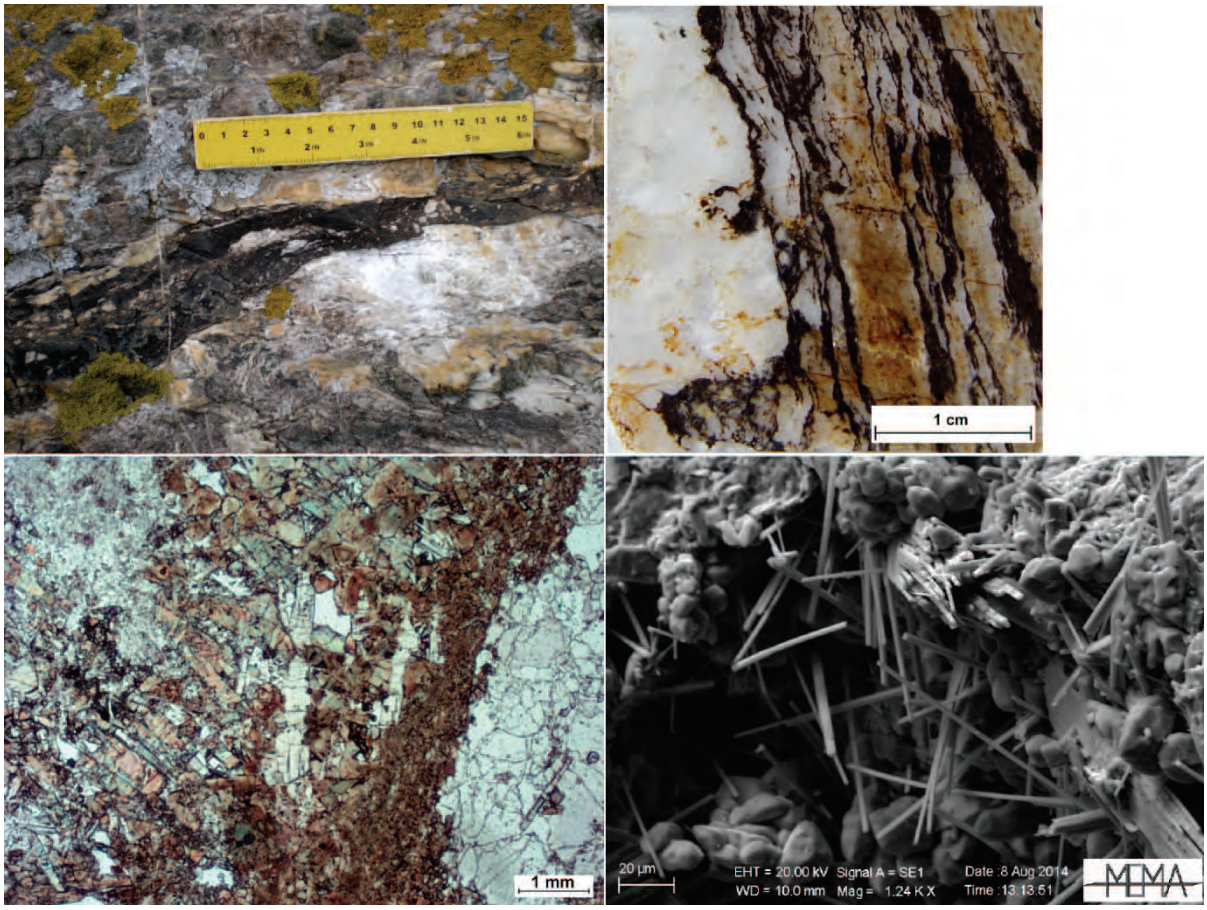

Fig. 2.3.5.Tourmaline veins at Sagnone area (a) macroscopic image of black tourmaline in F1 veins within Mt. Calamita Schists; (b), black tourmaline veins and associated quartz along long schistosity; (c) optical microscope image (transmitted light) of sample F1-ST6-14 with both polygonal aggregates of tourmaline (brown) and elongated euhedral crystals (pink colour) associated with quartz (white); (d) electron microscope image (secondary electron) of sample F1-ST3-14 with elongated tourmaline crystals and quartz.

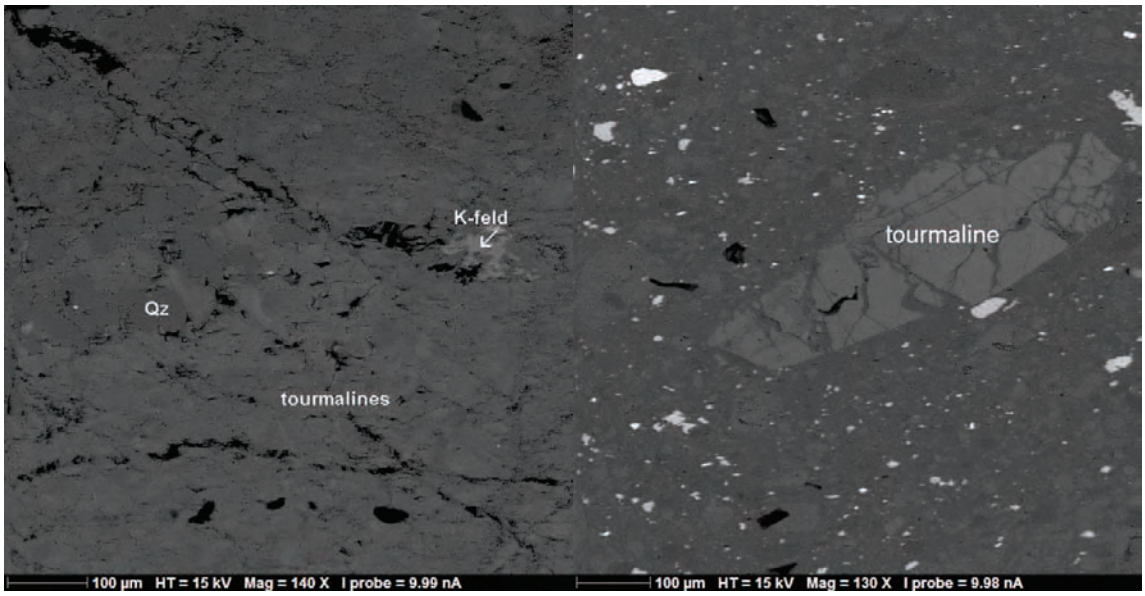

Fig. 2.3.6. Tourmaline veins at Stagnone area (electron backscattered image): (a) polygonal aggregates of zoned tourmaline (medium grey) among quartz (dark grey) and k-feldspar (light grey); (b) big tourmaline elongated crystal surrounded by quartz and small tourmaline crystals, abundant sphene and apatite crystals (white) occur in the vein.

Fig. 2.3.7 . Quartz-tourmaline veins at Morcone: (a) some meters long veins filled by dark tourmalines; (b) close-up view of vein during the sampling.

Fig. 2.3.8 . Small quartz-tourmaline vein at Ripalte.

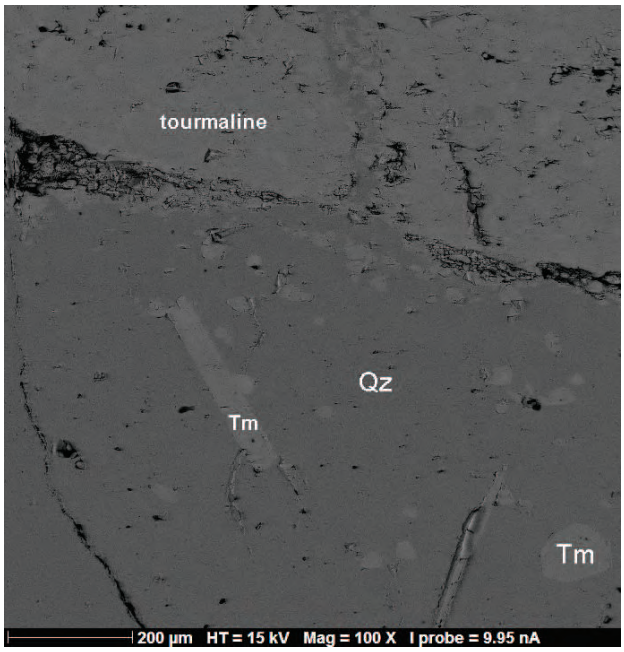

Fig. 2.3.9. Tourmaline veins from Morcone characterized by polygonal aggregates of tourmaline (medium grey, up in the image) and quartz (dark grey), a big tourmaline elongated crystal of tourmaline is observable in quartz (electron backscattered image).

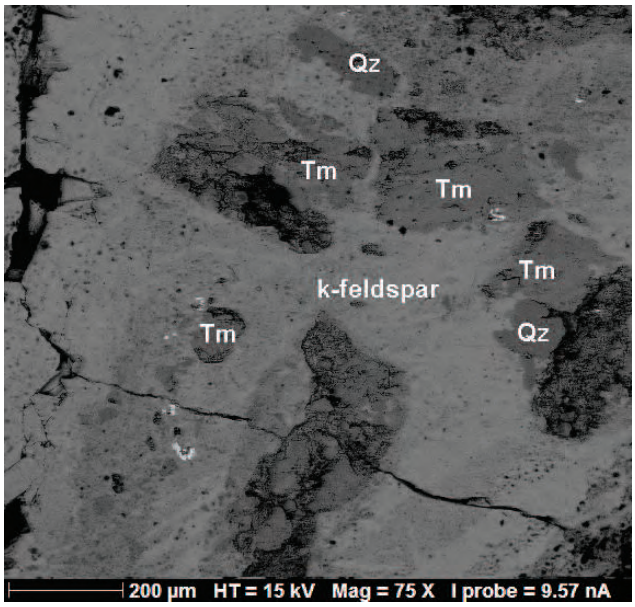

Fig. 2.3.10. Tourmaline vein sample from Ripalte with sub-euhedral tourmalines (medium grey), scarce quartz (dark grey) and abundant K-feldspar (light grey).

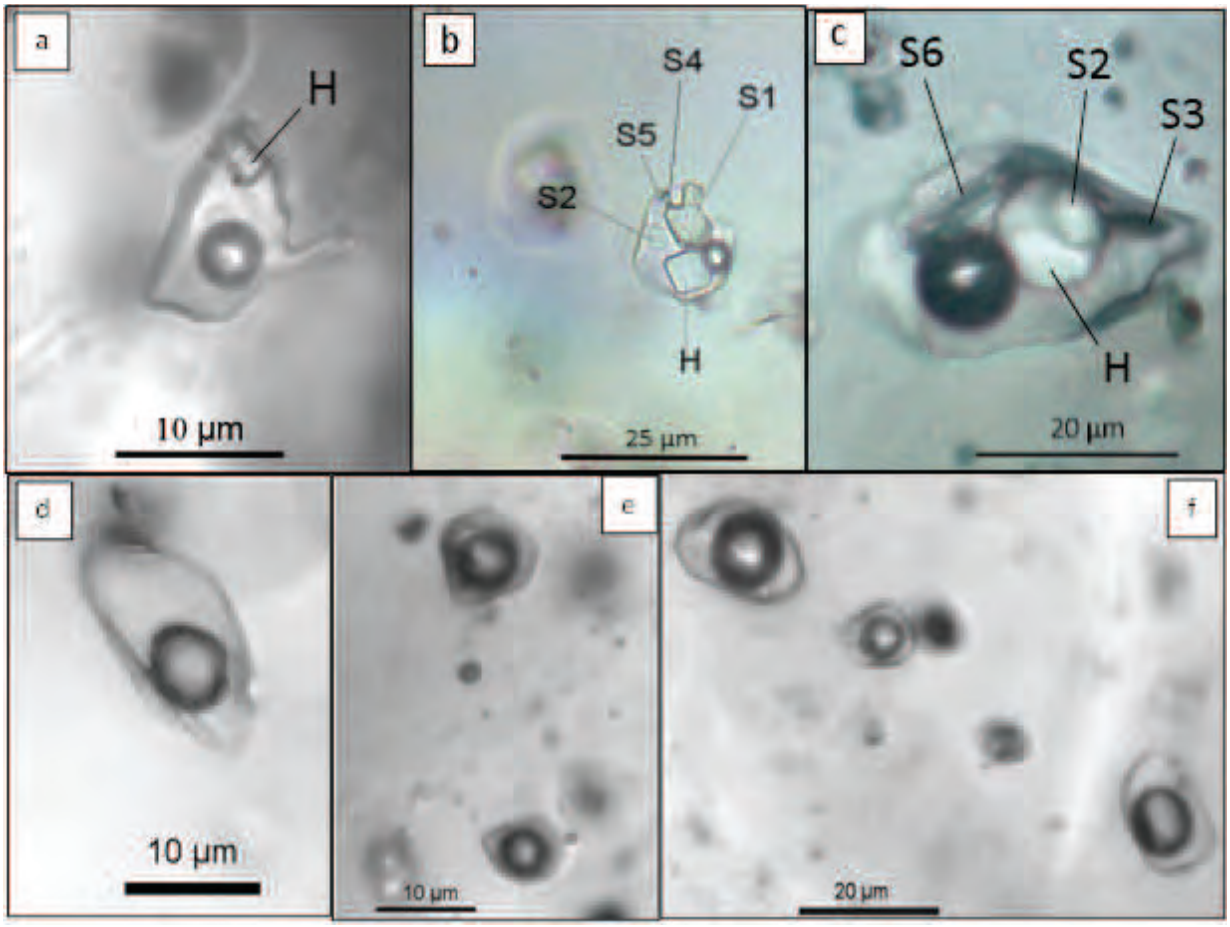

Fig. 2.3.11. Fluid inclusions type occurring at Stagnone: a,b,c) multiphase liquid rich fluid inclusions (L+V+S; S-type); d) L1 inclusions (L/V ~70%; e) L2 inclusions (L/V ~60%; f) V inclusion (L/V~40%). Letters refer to the mineral phases contained in S inclusions and recognized by optical examination, SEM-EDS and Raman spectroscopy: H stays for halite, S1 for pyrosmalite, S2 for an hydrated Fe-chloride species, S3 for hematite, S4 and S5 for unknown minerals, and S6 for a complex iron chloride.

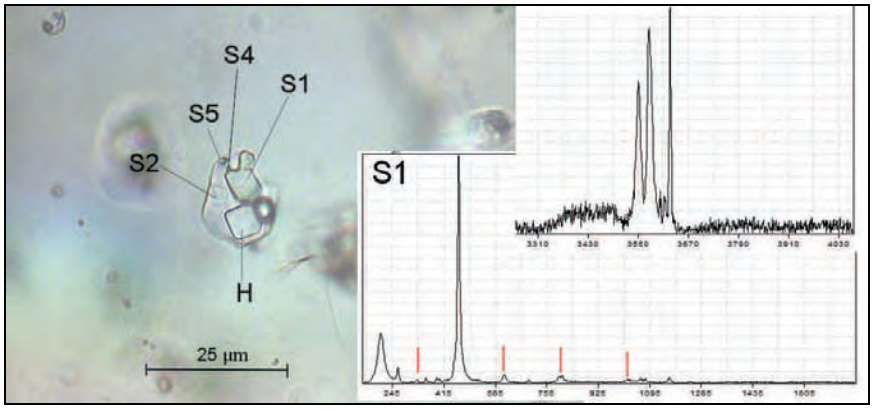

Fig. 2.3.12. Multi-phase fluid inclusion with pyrosmalite (S1) and the associated Raman spectrum, with the red marks indicating the diagnostic peaks for pyrosmalite (the others refer to the quartz matrix). The inset figure reports the triple peaks typical of pyrosmalite for the high frequency wave number range. Based on optical observation, Raman and SEM-EDS analysis, the other solid phases were identified as: halite (H), hydrated Fe-rich solid with Fe, Cl, Na, K, Al (S2), and an unidentified mineral phases (S4 and S5).

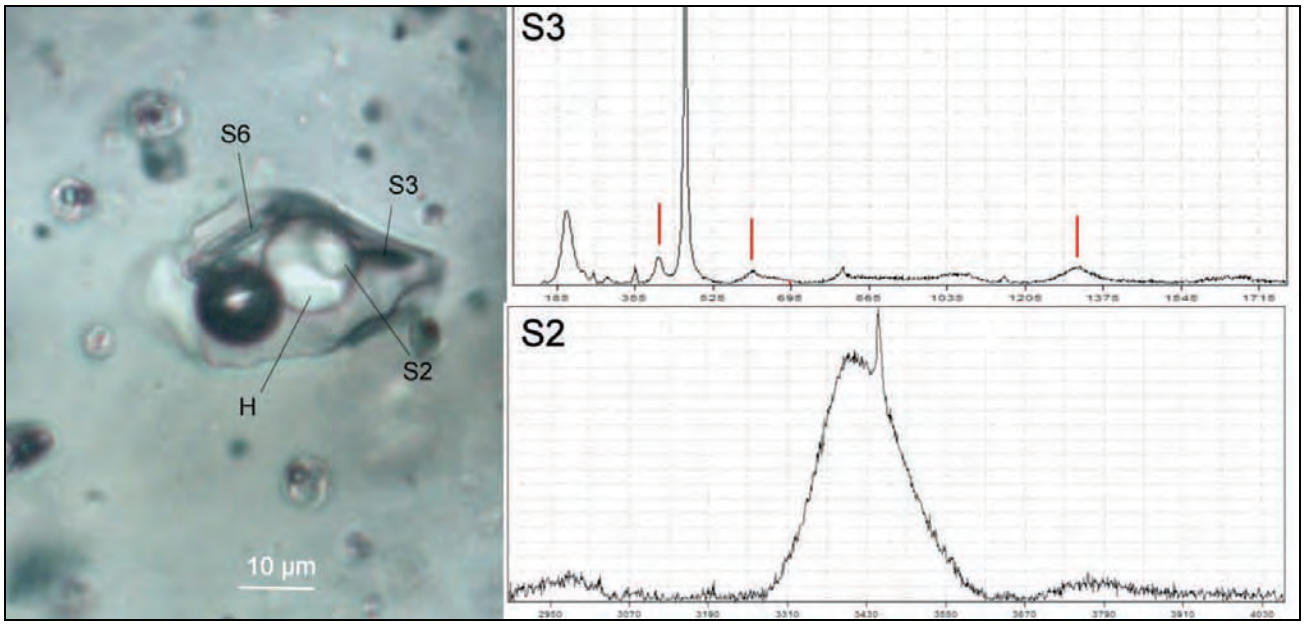

Fig. 2.3.13. Multi-phase fluid inclusion type with: 1) hematite (S3) and the associated Raman spectrum, with the red marks indicating the diagnostic peaks for hematite (the others refer to the quartz matrix); hydrated Fe(Mn)-chloride (S2) with the only identifiable peak corresponding to the OH stretching. Based on optical observation, Raman and SEM-EDS analysis, the other solid phases were identified as: halite (H), and Fe-rich solid with Cl, Na, K and minor Ca and Mn (S6).

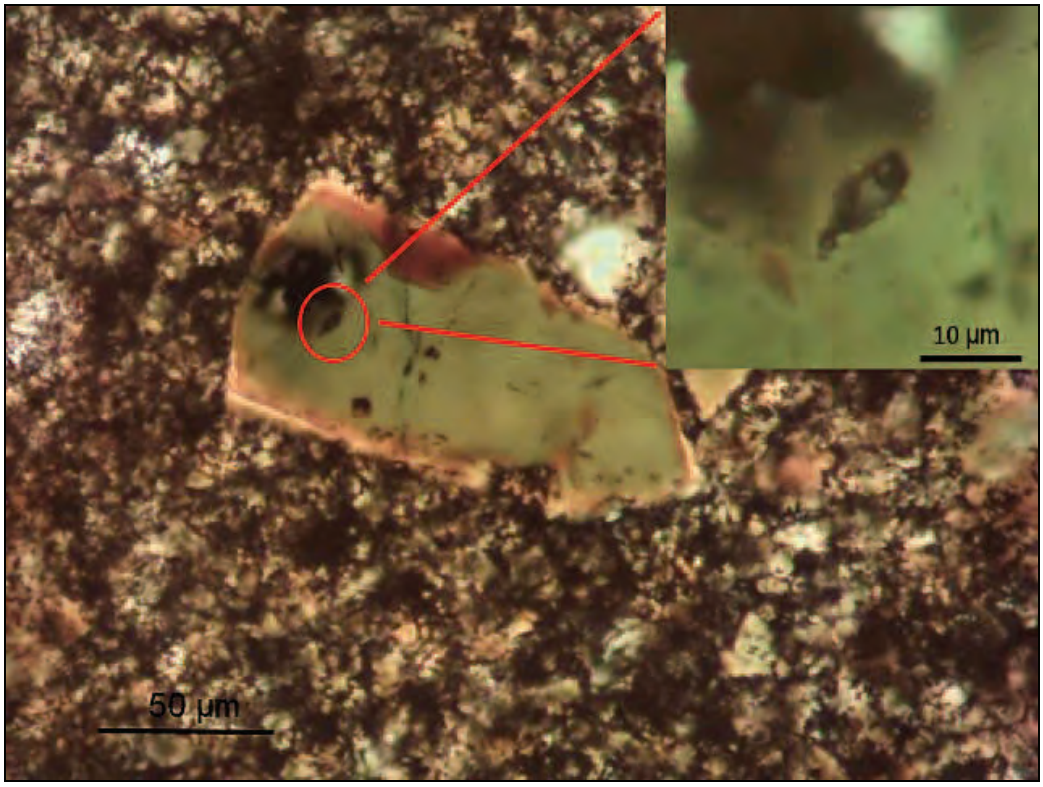

Fig. 2.3.14. Typical L-type fluid inclusions occurring in tourmaline of the Stagnone area.

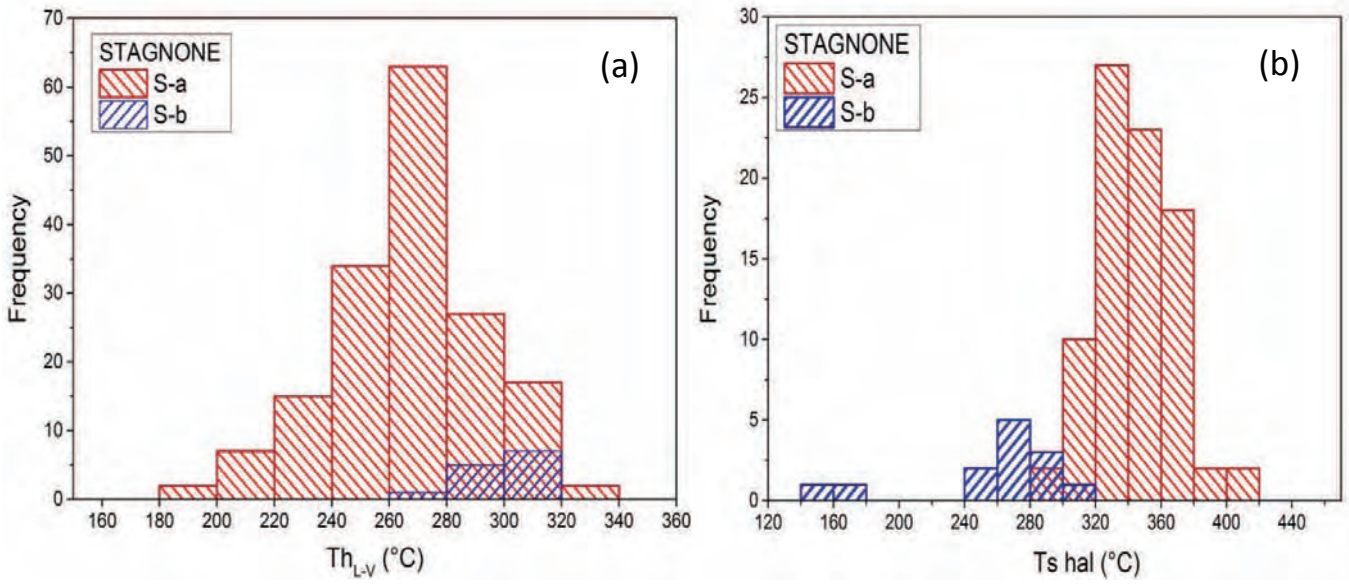

Fig. 2.3.15 . Microthermometric data for S-type (S-a and S-b) inclusions at Stagnone: a) Th_{L-V} and b) Ts hal.

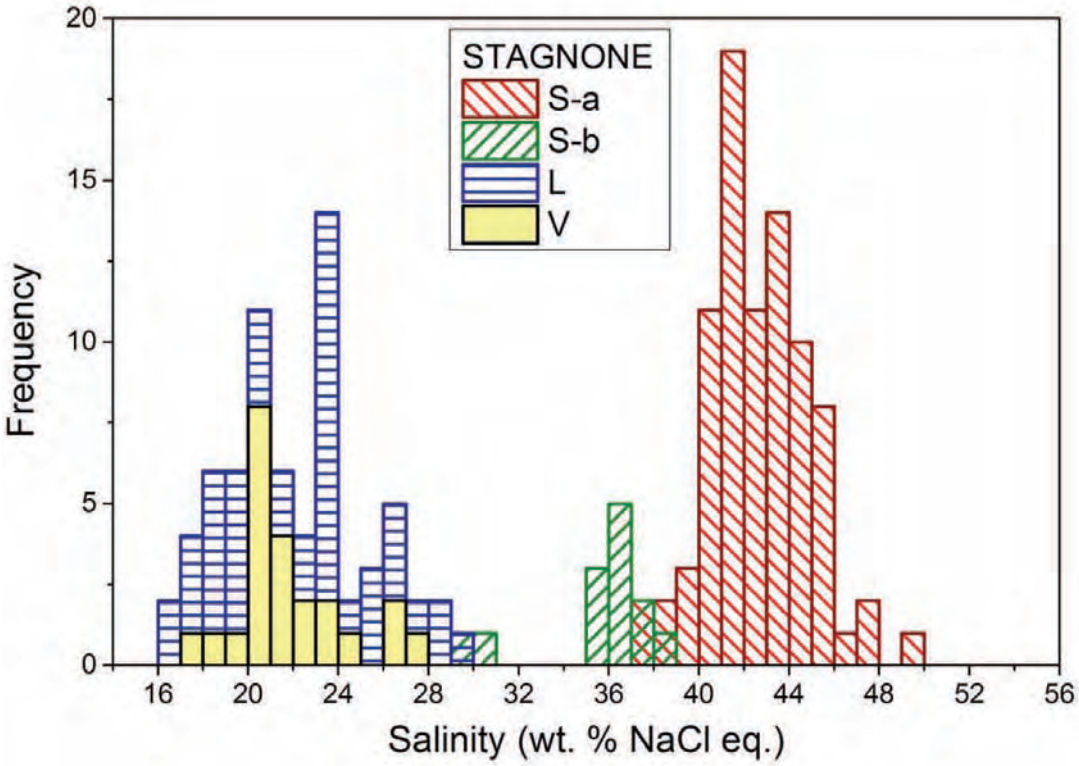

Fig. 2.3.16 . Calculated salinities for all type of fluid inclusions occurring at Stagnone.

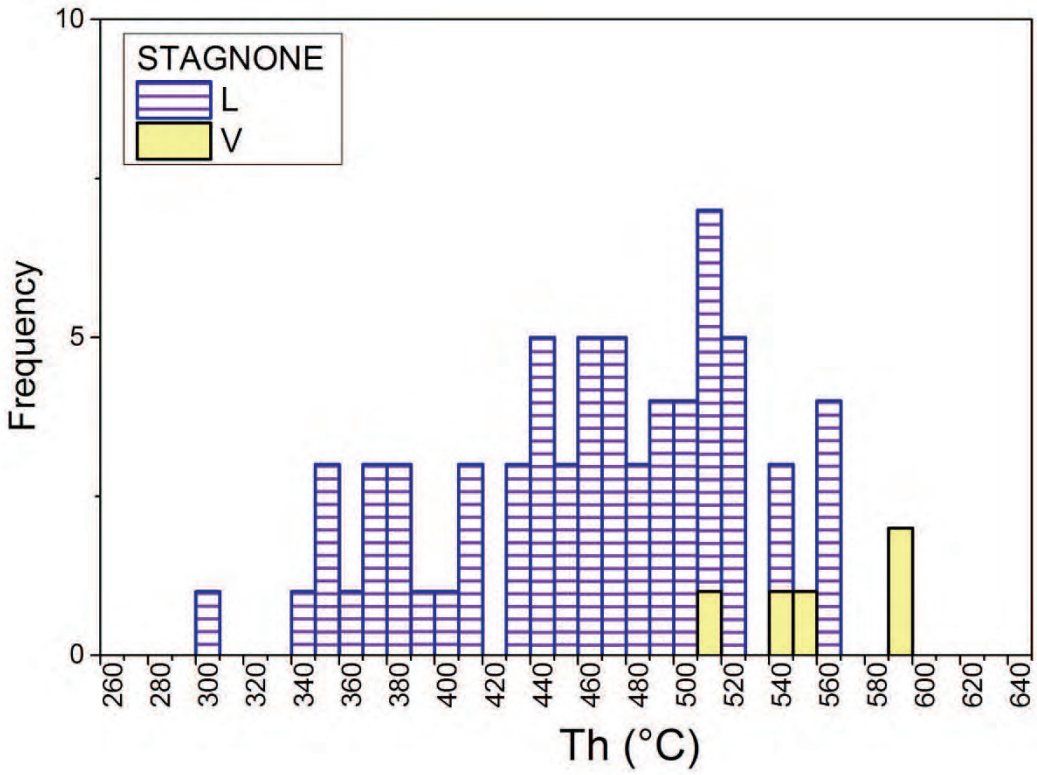

Fig. 2.3.17 . Th for L- and V- type fluid inclusions occurring at Stagnone.

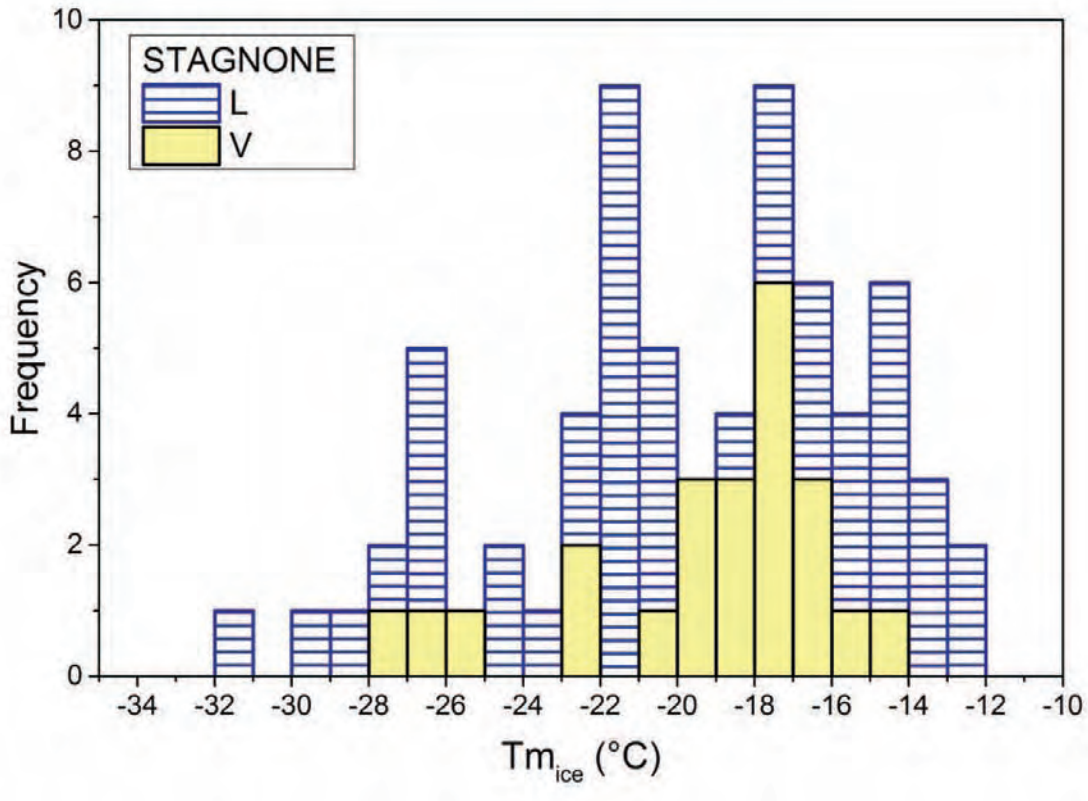

Fig. 2.3.18 . Tm_{ice} for L- and V- type fluid inclusions occurring at Stagnone.

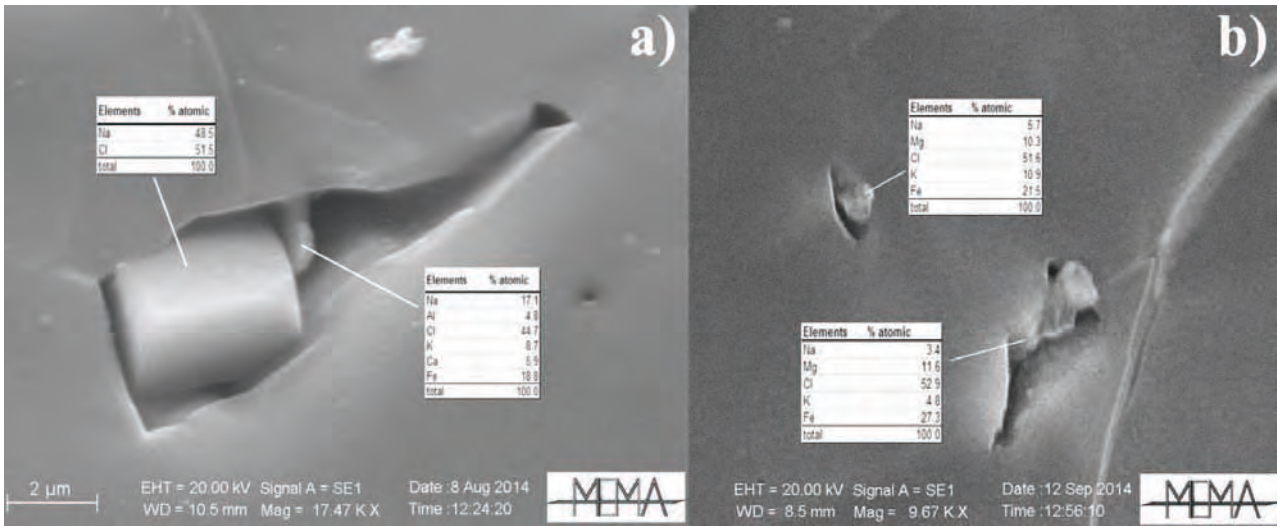

Fig. 2.3.19. Scanning electron microscope photographs (secondary electron) of fluid inclusions at Stagnone: a) S inclusions with halite and a iron (+Mn)-chloride corresponding to the minerak phase S2; b) L inclusions with mixed salts composed Cl, Fe, K, Mg and Na. The EDS analysis has been normalized to the quartz matrix.

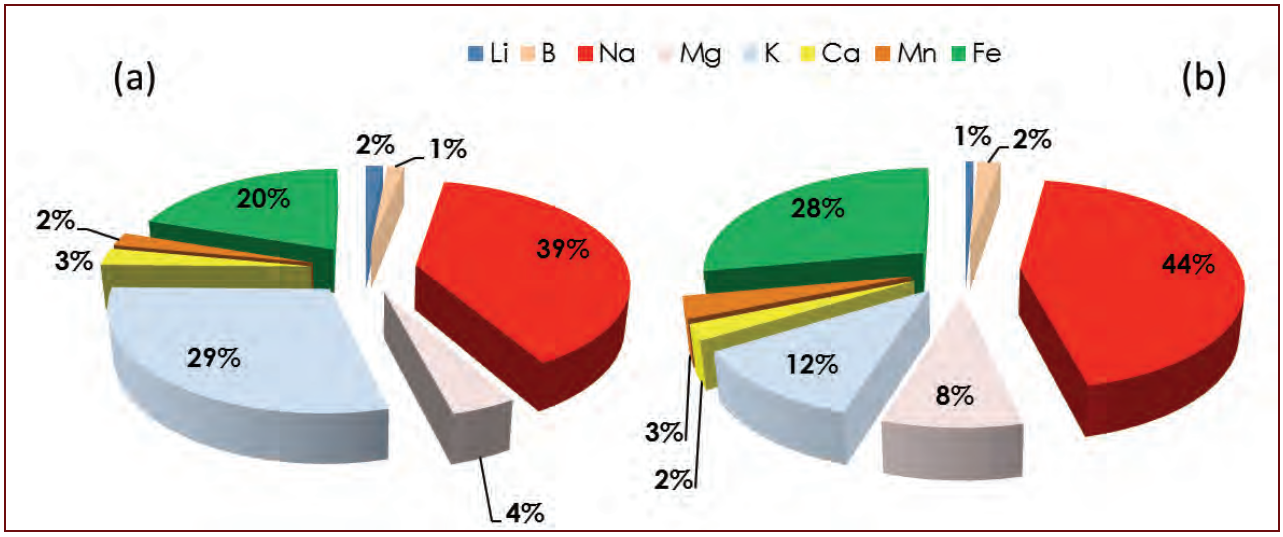

Fig. 2.3.20. Weight percent abundances of major and minor cations (mean composition in mg/kg) for fluid analyzed at Stagnone by LA-ICPMS in: a) L-type fluid inclusions; b) S-type fluid inclusions.

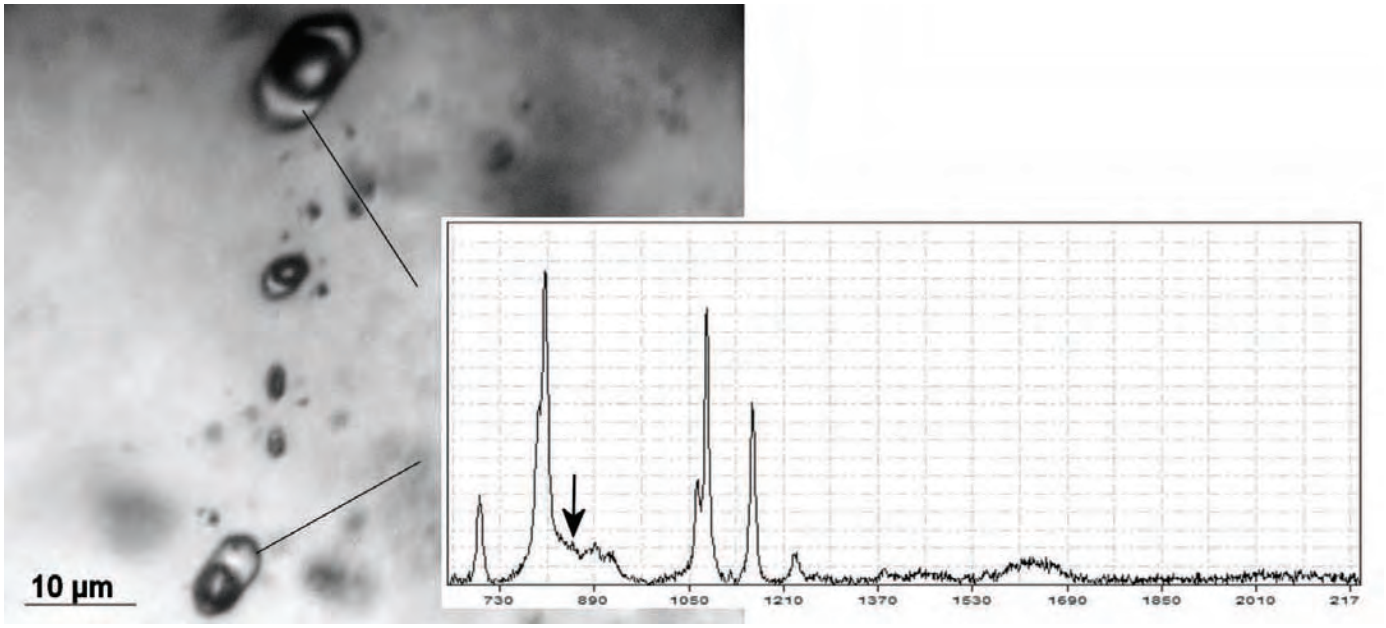

Fig. 2.3.21. Liquid-rich fluid inclusion, and associated Raman spectrum of the liquid phase; the diagnostic peak of borate is reported (black arrow).

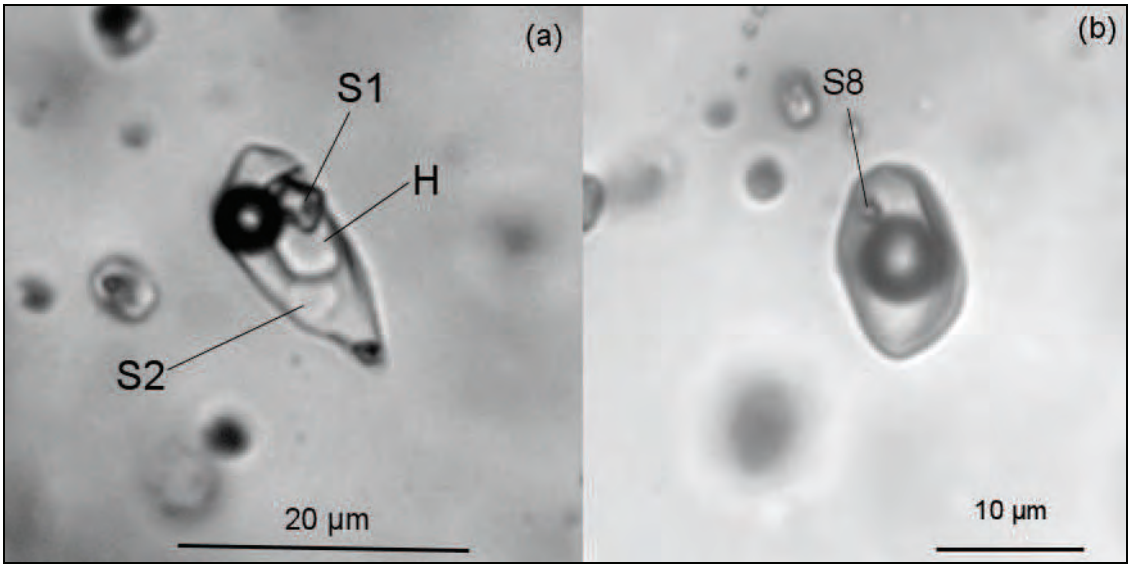

Fig. 2.3. 22. Fluid inclusions hosted in quartz at Ripalte: a) multiphase liquid-rich fluid inclusions (L+V+S; S-type); b) liquid rich (L+V±S; L1-type) fluid inclusions. Minerals occurring in fluid inclusions were identified as: halite (H), pyrosmalite (S1), hydrated complex Fe-chloride (S2), and S8 as an unidentified solid.

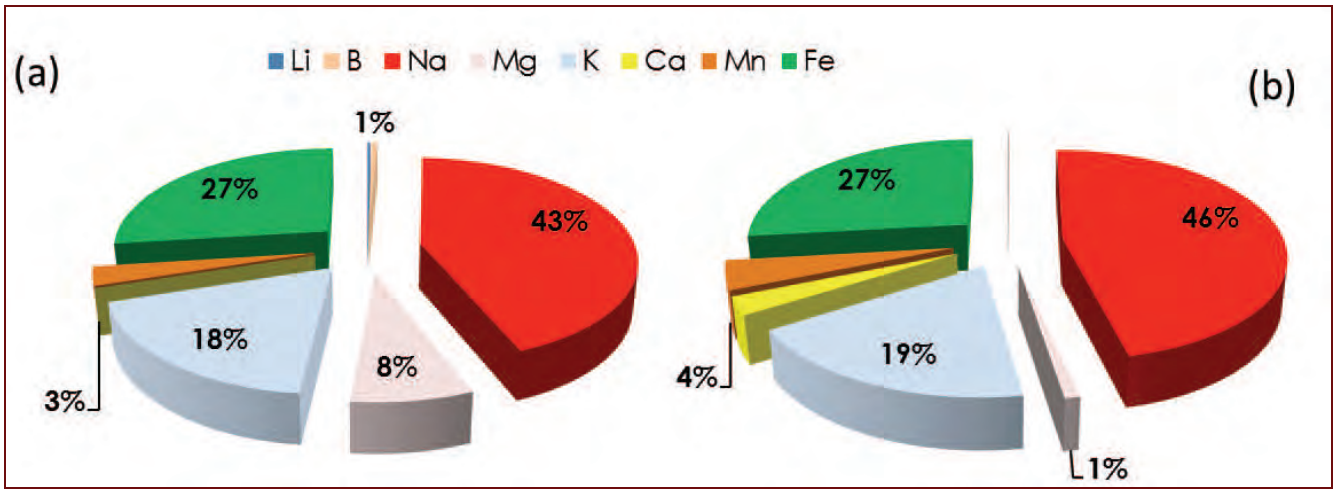

Fig. 2.3.23. Weight percent abundances of major and minor cations (mean composition in mg/kg) for fluid analyzed at Ripalte by LA-ICPMS in: a) L-type fluid inclusions; b) S-type fluid inclusions.

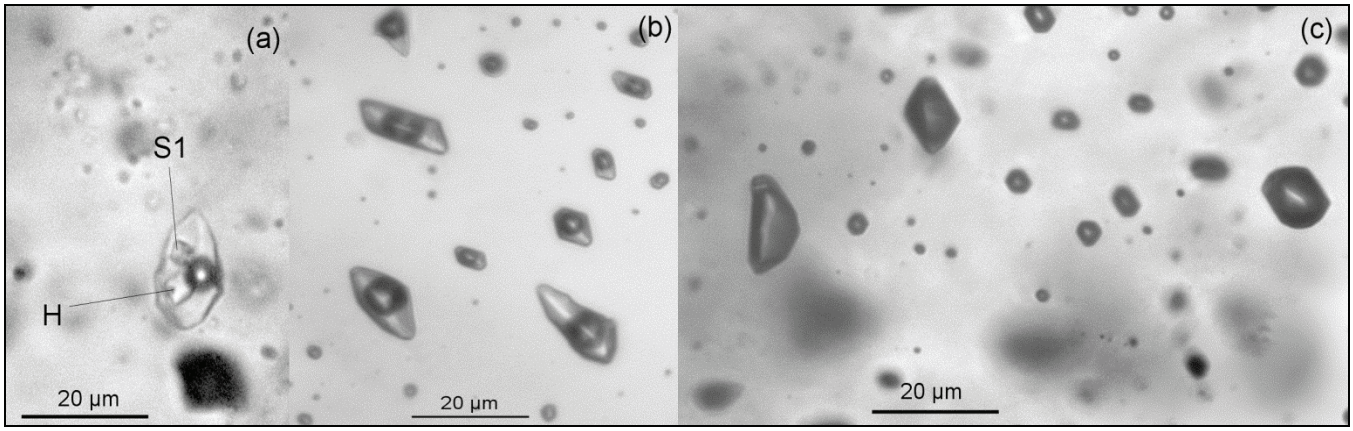

Fig. 2.3.24. Fluid inclusions hosted in quartz at Morocne: a) multiphase liquid-rich fluid inclusions (L+V+S; S-type); b) liquid-rich (L+V; Ltype); c) vapour (V±L+; V-type) fluid inclusions. Minerals occurring in fluid inclusions were identified as: halite (H), and pyrosmalite (S1).

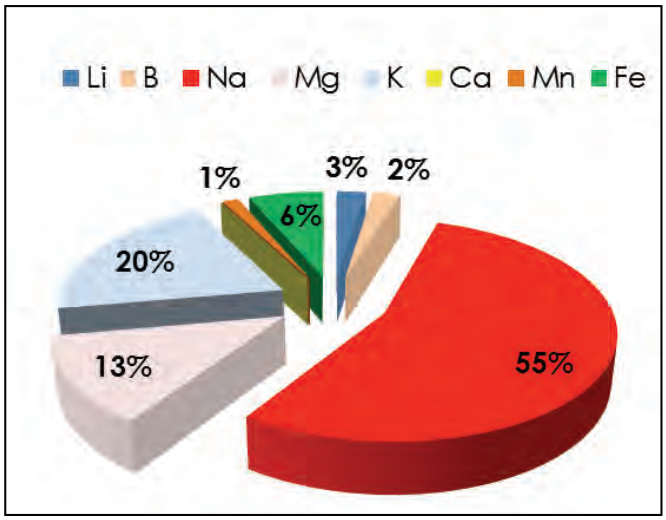

Fig. 2.3.25. Weight percent abundances of major and minor cations (mean composition in mg/kg) for fluid analyzed at Morcone by LA-ICPMS in L-type fluid inclusions.

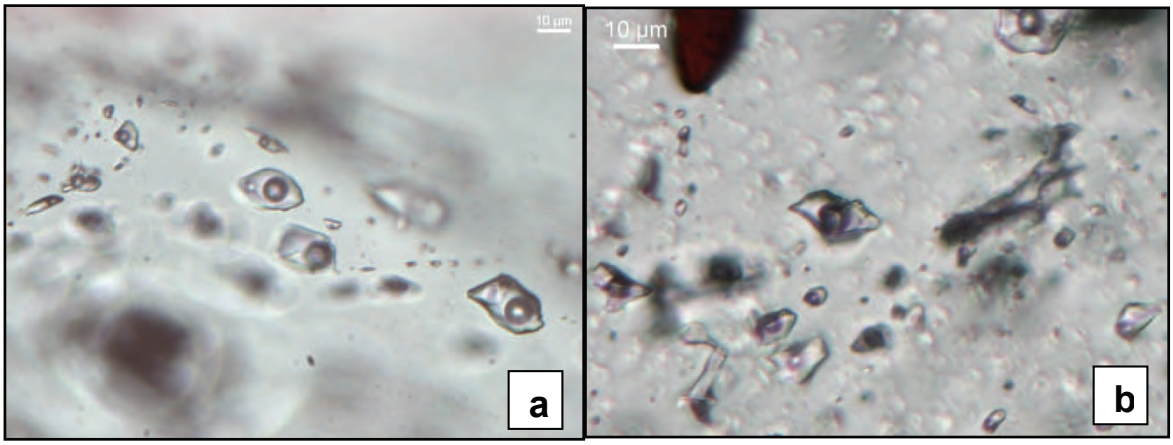

Fig. 2.3.26 a,b) Optical micrographs of L-type fluid inclusions characterized by a constant L/V ratio around 70% occurring in quartz at Terra Nera.

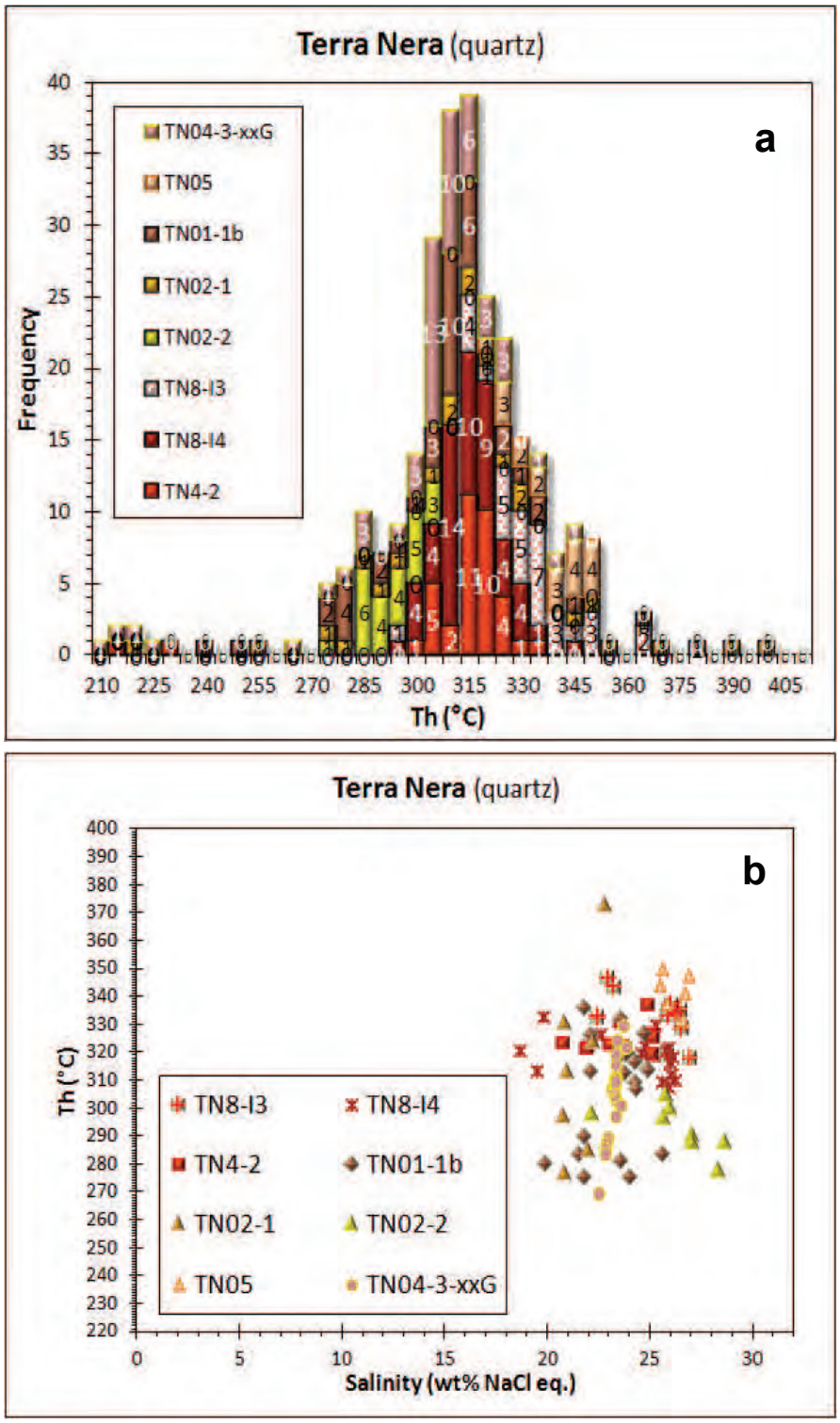

Fig. 2.3.27. Graphs of microthermometric results for samples from Terra Nera area: (a) Cumulative frequency histogram for homogenization temperatures, Th (°C); (b) salinity (wt% NaCl eq.) against homogenization temperatures, Th (°C), plot.

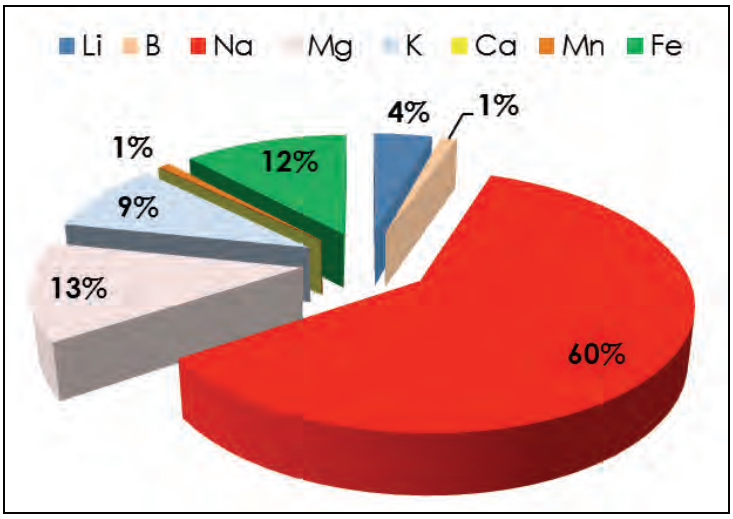

Fig. 2.3.28. Weight percent abundances of major and minor cations (mean composition in mg/kg) for fluid analyzed at Terra Nera by LA-ICPMS in L-type fluid inclusions.

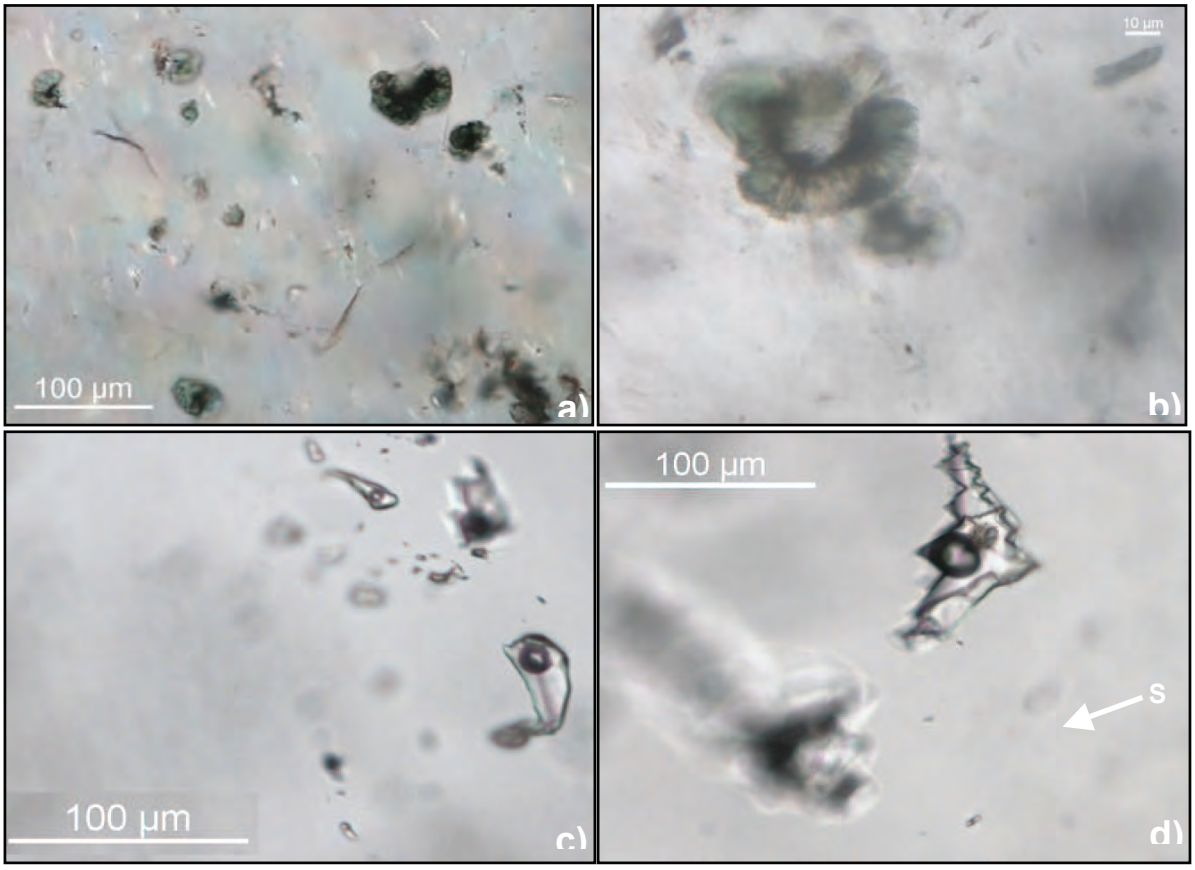

Fig. 2.3.29. Optical micrographs of Inclusions in quartz crystals from Bacino: (a), (b) chlorite solid inclusions; (c), (d) L-type fluid inclusions characterized by a constant L/V ratio, around 80%, sometimes containing solids (S) identified as captive minerals (possibly chlorite).

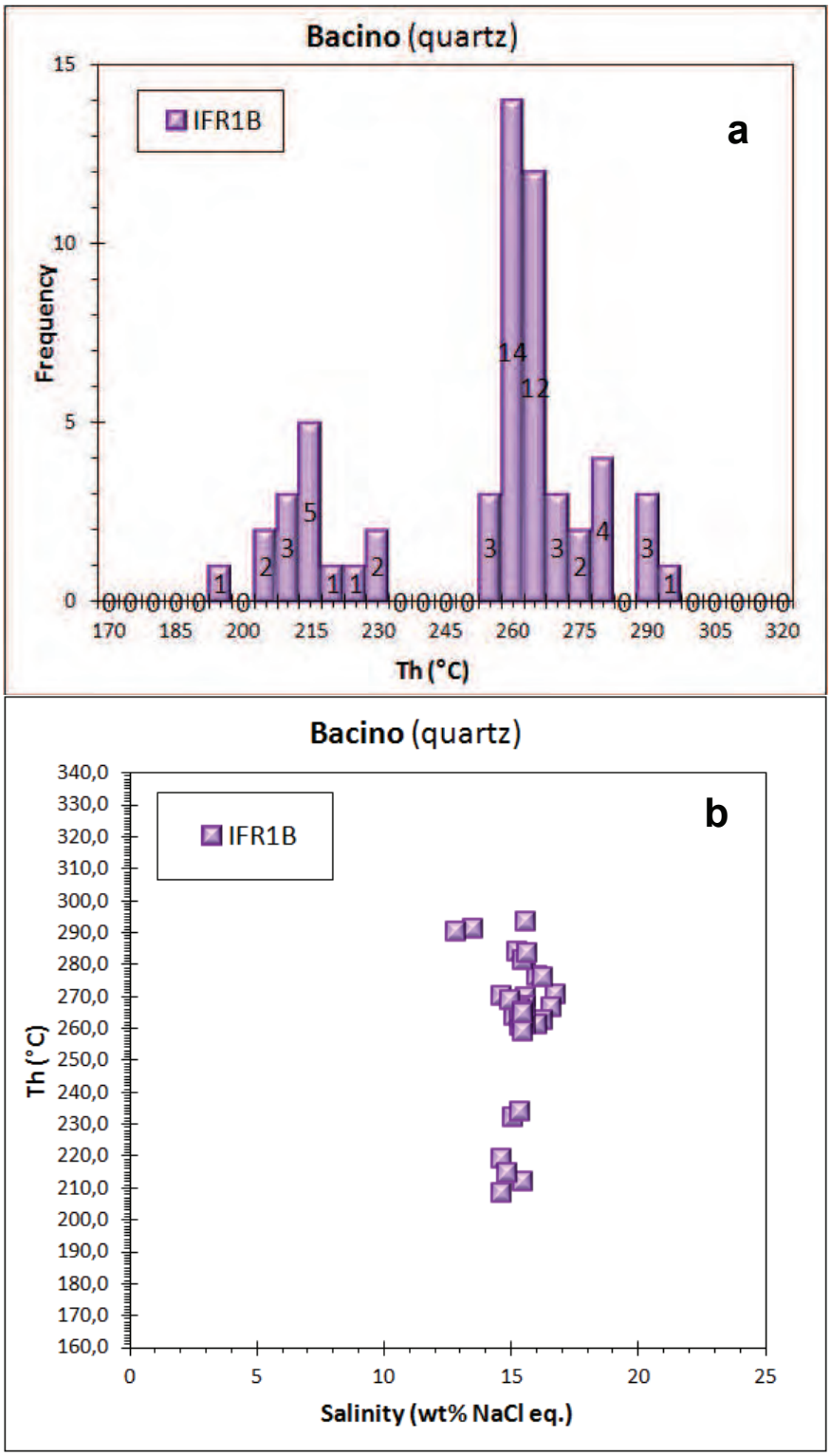

Fig. 2.3.30. Graphs of microthermometric results for samples from the Bacino area: (a) Cumulative frequency histogram for homogenization temperatures, Th (°C); (b) Salinity (wt% NaCl eq.) against homogenization temperatures, Th (°C), plot.

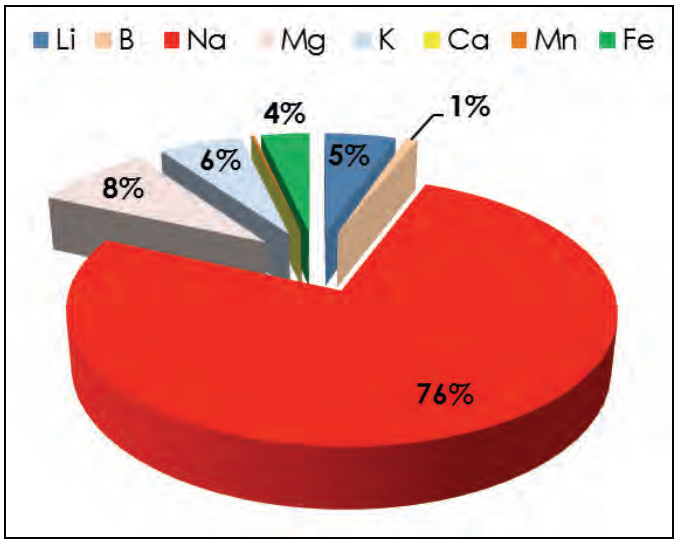

Fig. 2.3.31. Weight percent abundances of major and minor cations (mean composition in mg/kg) for fluid analyzed at Bacino by LA-ICPMS in L-type fluid inclusions.

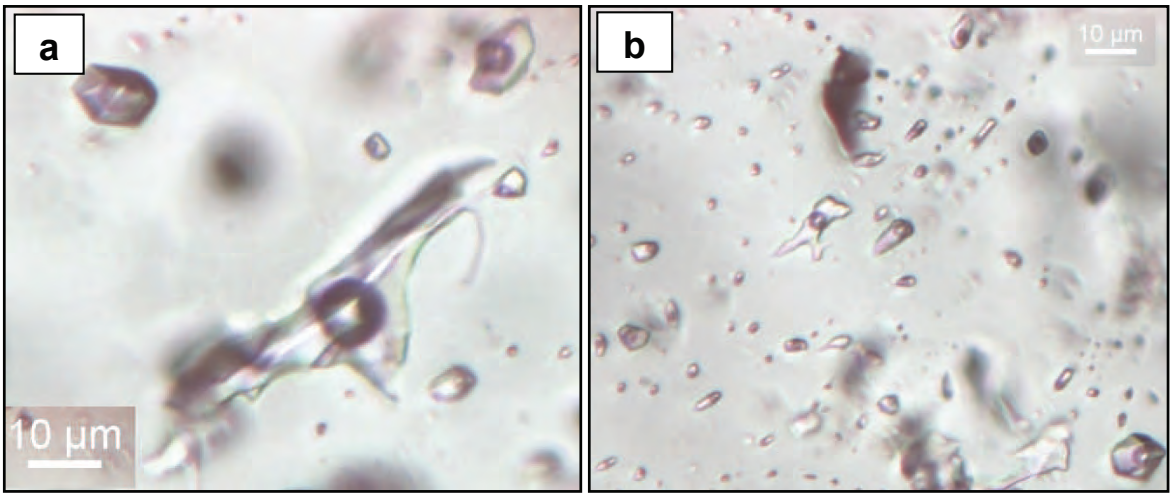

Fig. 2.3.32 (a), (b). Optical micrographs of L-type fluid inclusions occurring in quartz at Topinetti. Constant L/V ratios, around 70-80%, and mainly regular up to negative-crystal froms are observed. A few irregular forms for the biggest inclusions are also shown.

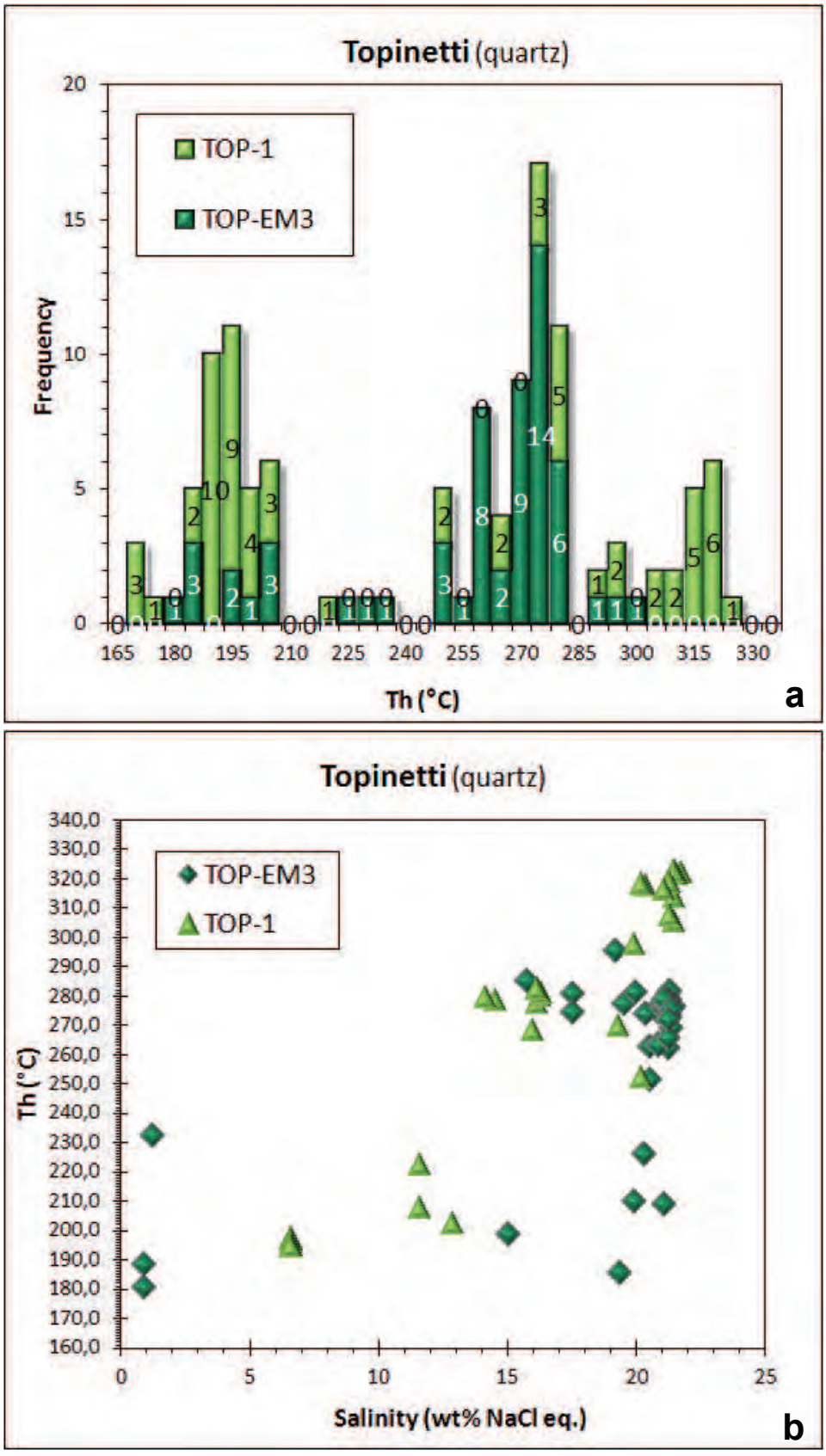

Fig. 2.3.33. Graphs of microthermometric results for samples from the Topinetti area: (a) Cumulative frequency histogram for homogenization temperatures, Th (°C); (b) Salinity (wt% NaCl eq.) against homogenization temperatures, Th (°C), plot.

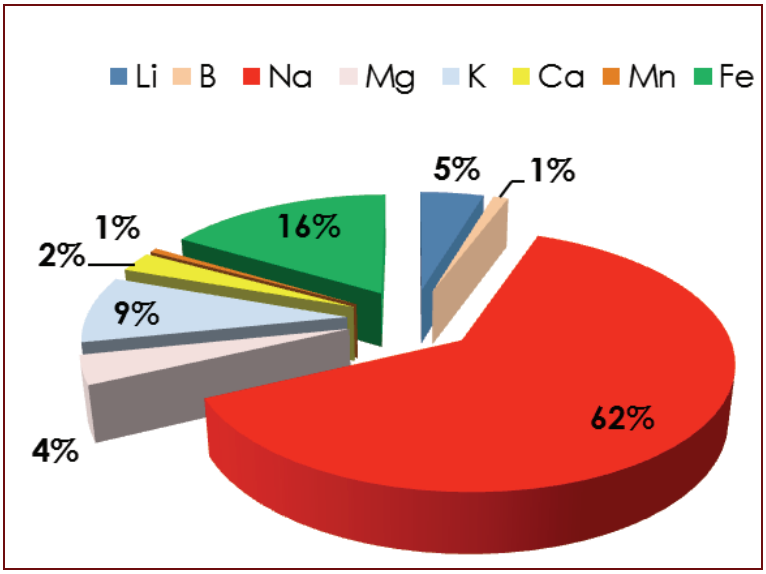

Fig. 2.3.34. Weight percent abundances of major and minor cations (mean composition in mg/kg) for fluid analyzed at Topinetti by LA-ICPMS in L-type fluid inclusions.

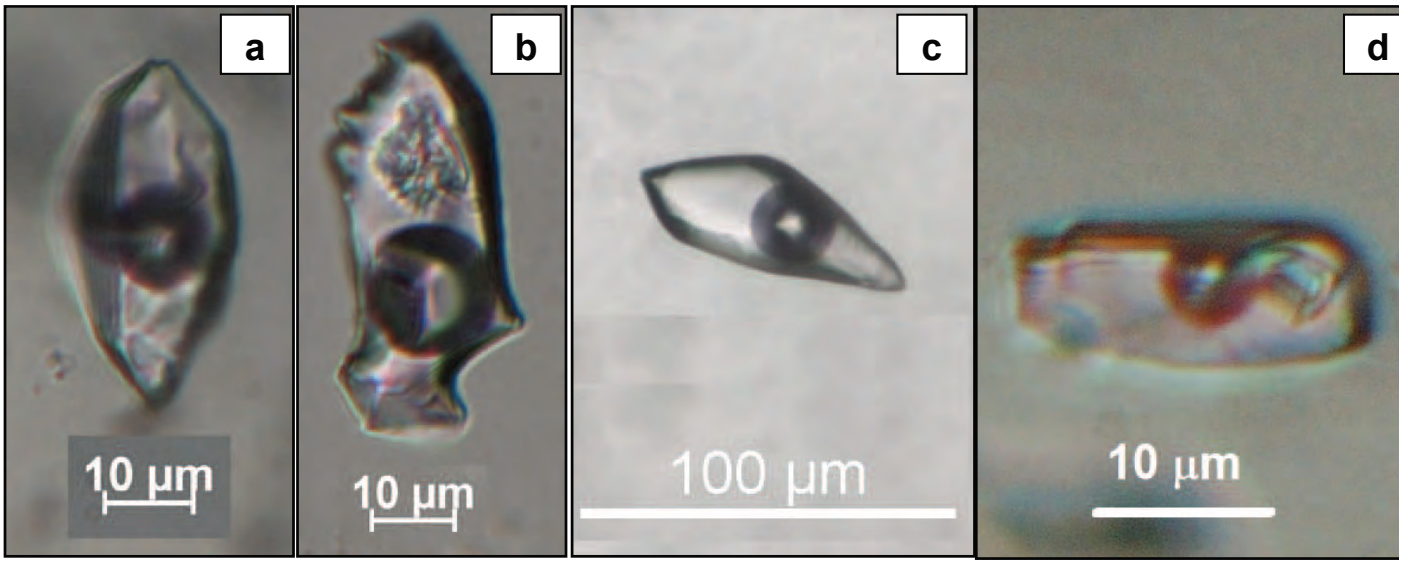

Fig. 2.3.35. Optical micrographs of fluid inclusions occurring at Valle Giove. **(a)** L-type FIs in quartz with constant L/V ratios, around 70%, with mainly regular up to negative-crystal froms; **(b)** entrapped captive minerals are sometimes observed in FIs within quartz ; **(c)** L-type FIs within calcite crystals; **(d)** S-type FIs in calcite crystals with S = halite.

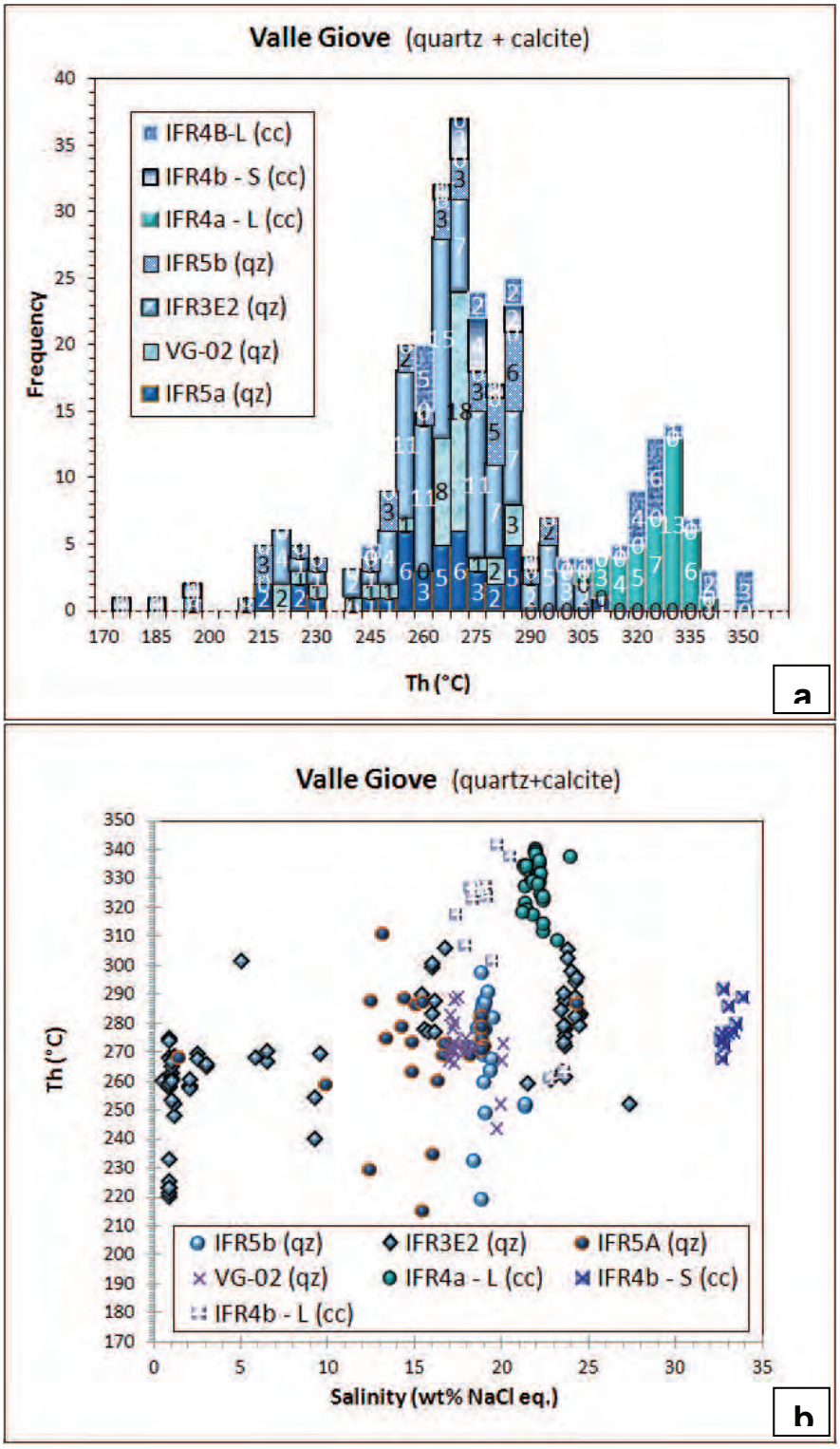

Fig. 2.3.36. Graphs of microthermometric results for samples from the Valle Giove area: (a) Cumulative frequency histogram for homogenization temperatures, Th (°C); (b) Salinity (wt% NaCl eq.) against homogenization temperatures, Th (°C), plot.

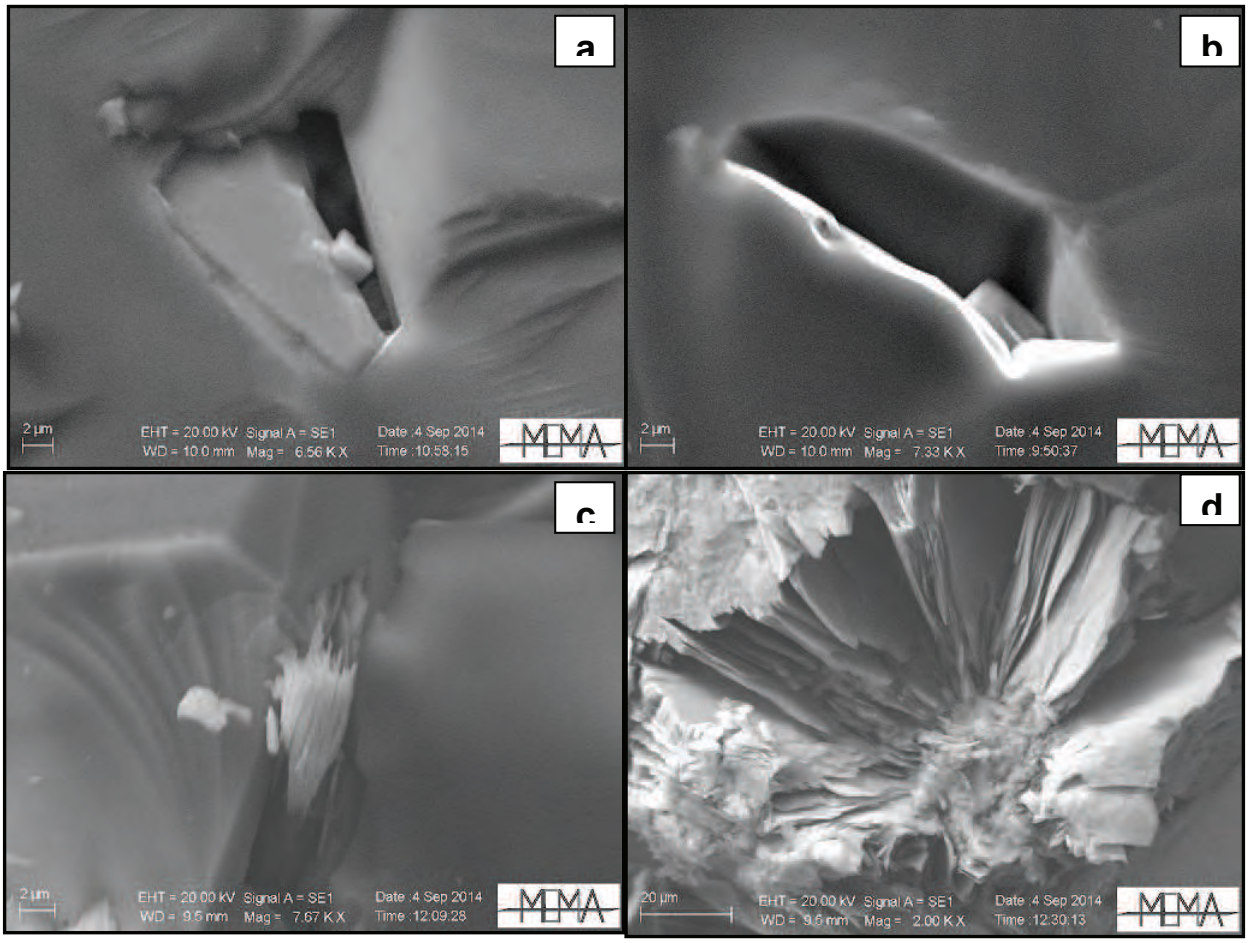

Fig. 2.3.37. SEM micrographs (secondary electron) of fluid inclusions entrapped within quartz crystals from Valle Giove: a) precipitated cubic crystal of halite, NaCl; b) precipitated crystal of (Na,K,Ca) -chloride; c) captive mineral of biotite; d) captive mineral of chlorite.

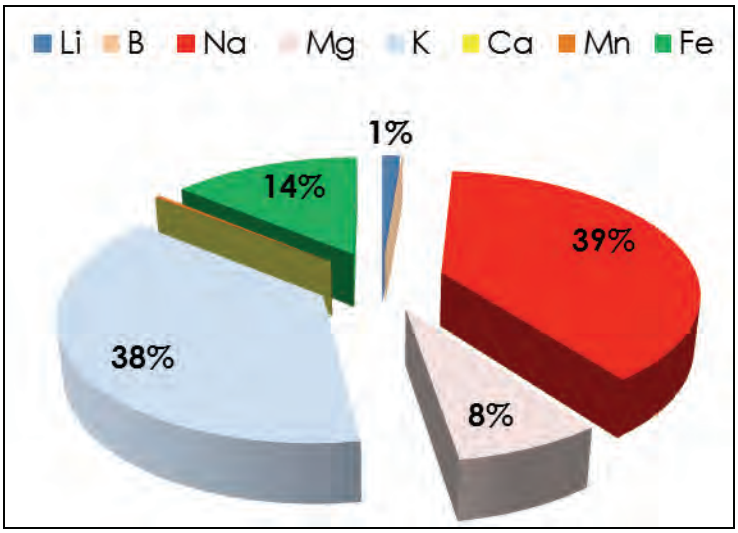

Fig. 2.3.38. Weight percent abundances of major and minor cations (mean composition in mg/kg) for fluid analyzed at Valle Giove by LA-ICPMS in quartz L-type fluid inclusions.

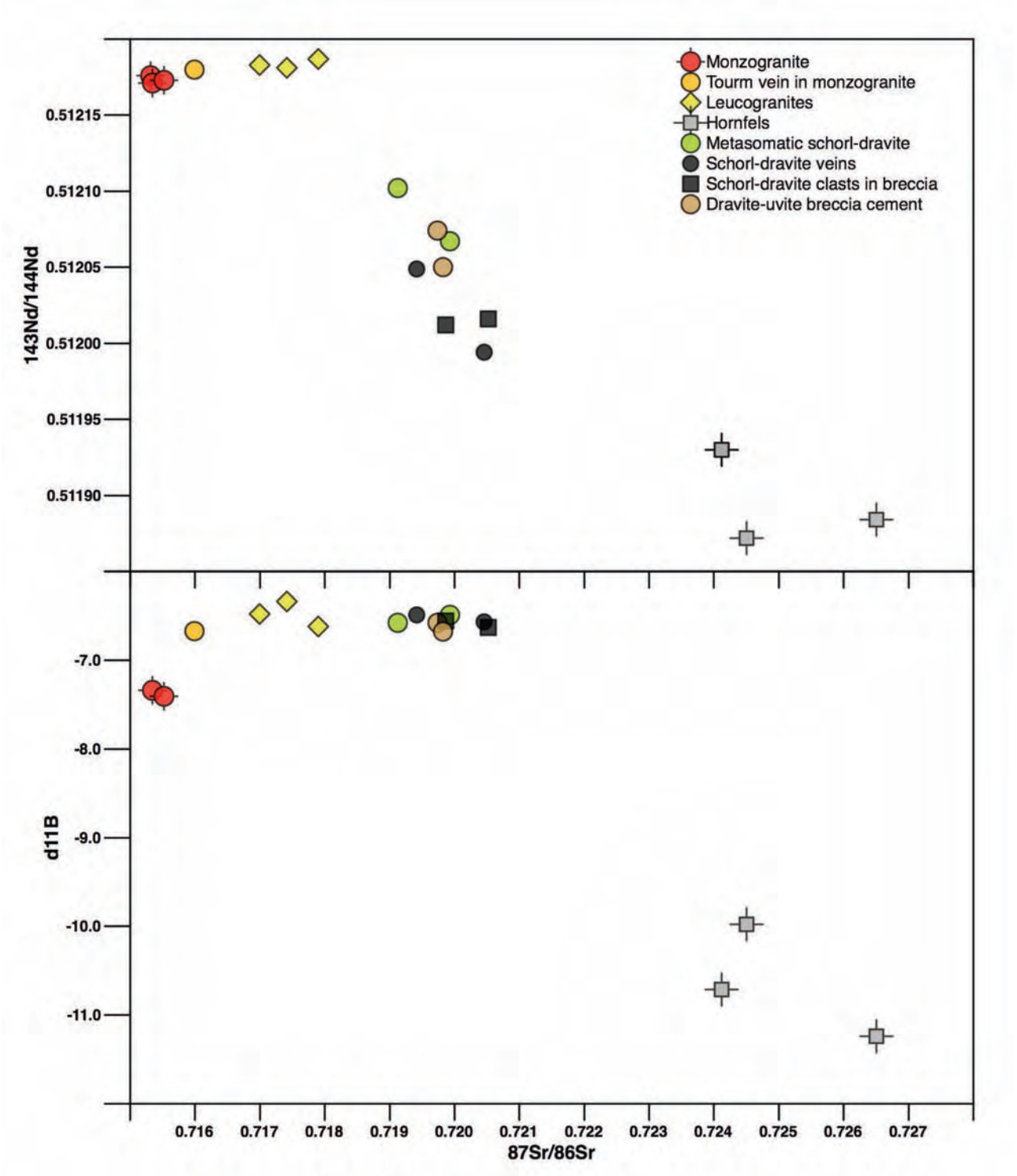

Fig. 2.3.38/1 and 2.3.38/2 – isotopic diagrams illustrating the results obtained for the indicated rock-samples

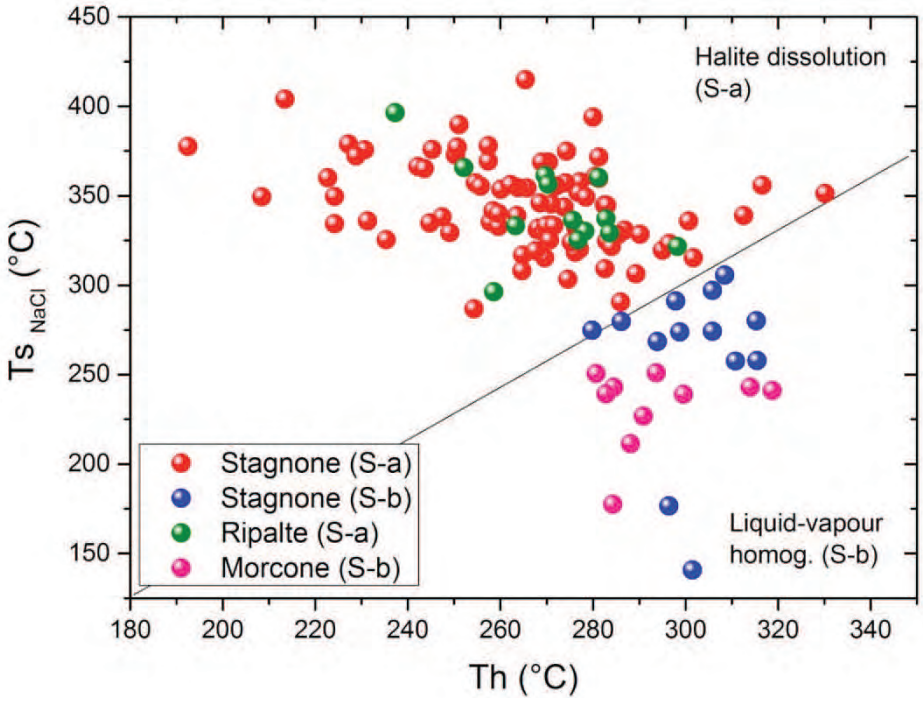

Fig. 2.3.39. Halite dissolution temperature (TsNaCl) as a function of liquid-vapour homogenization temperature (Th) for multiphase inclusions at Stagnone, Ripalte and Morcone. The diagonal line separates inclusions which undergo final homogenization by halite dissolution (S-a) from those that display homogenization by disappearance of the vapour phase (S-b).

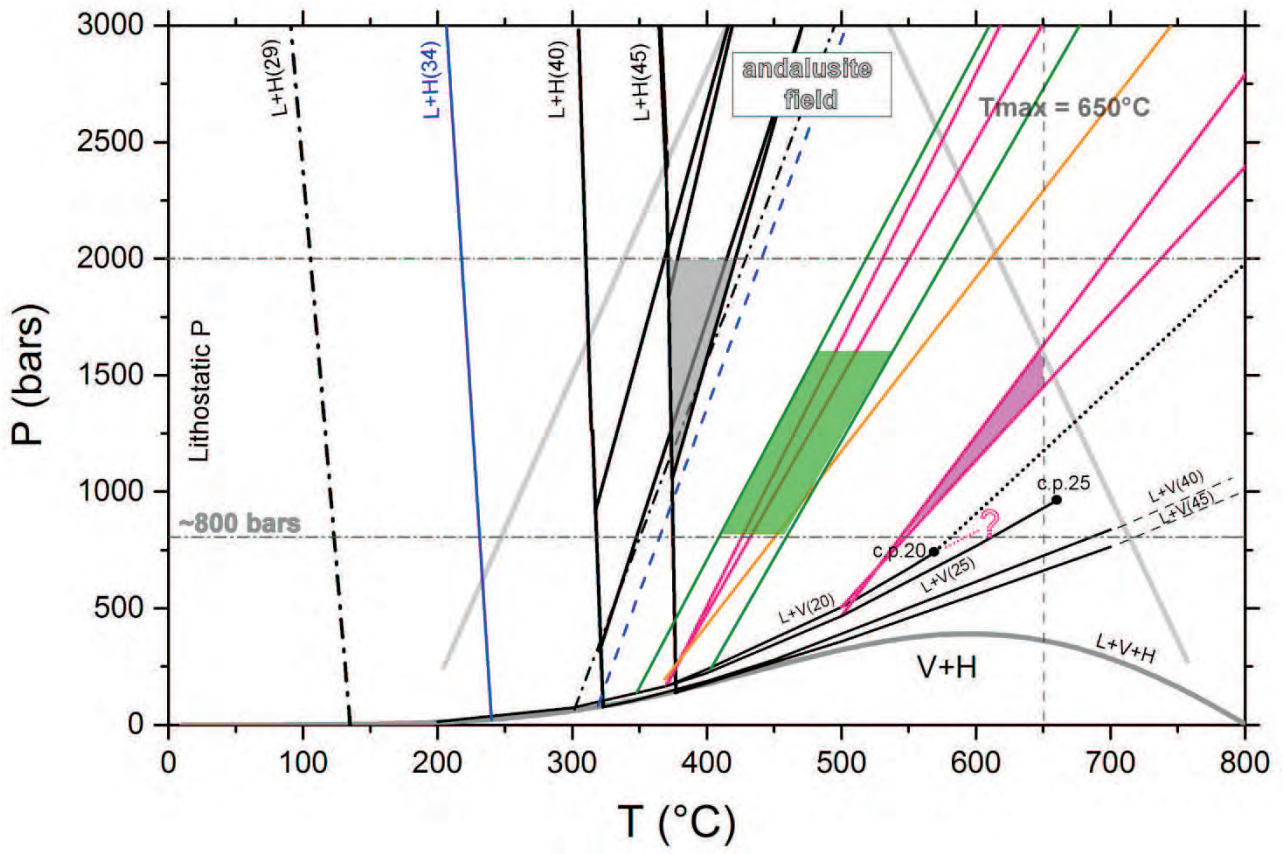

Fig. 2.3..40. Pressure-temperature diagram illustrating trapping conditions for all the inclusions types observed at Stagnone, Ripalte and Morcone. Isochores are depicted as black solid lines for S-a inclusions (Stagnone and Ripalte), point-dotted black line for S-b inclusions at Stagnone, point-dotted blue line for S-b inclusions at Morcone, pink solid lines for L inclusions at Stagnone, pink point-dotted line for V inclusions at Stagnone, green solid line for L inclusions at Ripalte, orange solid line for L inclusions at Morcone, black pointed line for the critical isochore at 20 wt. % NaCl eq. See the text for the details on how these isochores have been calculated. The three phase curve (L+V+H) separates the stability field of vapour+halite (V+H) and liquid+vapour (L+V) (data from Driesen and Heinrich, 2007); liquid-vapour curves (L+V) have been calculated at salinities of 20, 25, 40 and 45 wt.% NaCl eq. and separate the stability fields for liquid+vapour (L+V) and liquid (L) (data from Steele-MacInnis et al., 2012); critical point (c.p.) at 20 and 25 wt.% NaCl eq. are reported following the work of Knight and Bodnar (1989); liquidus (LIQ) separates the stability fields for liquid+halite (L+H) and liquid (L) (calculated from Bodnar 1994); the limit for the andalusite field is reported in gray color. Shaded area defines the P-T trapping conditions for S-a inclusions at Stagnone and Ripalte (black color), L2 inclusions at Stagnone (pink color), L1 inclusions at Ripalte and Stagnone (green color).
For V inclusions, the isochores are calculated using the program ISOC (Bakker, 1997, 2003) and the equation of state (Bowers & Helgeson, 1983) revised by Bakker (1999) for the system H_2O-CO_2-CH_4-N_2-NaCl, with P-T domain of validity, T : 350-600 °C and P : 50-200 MPa.

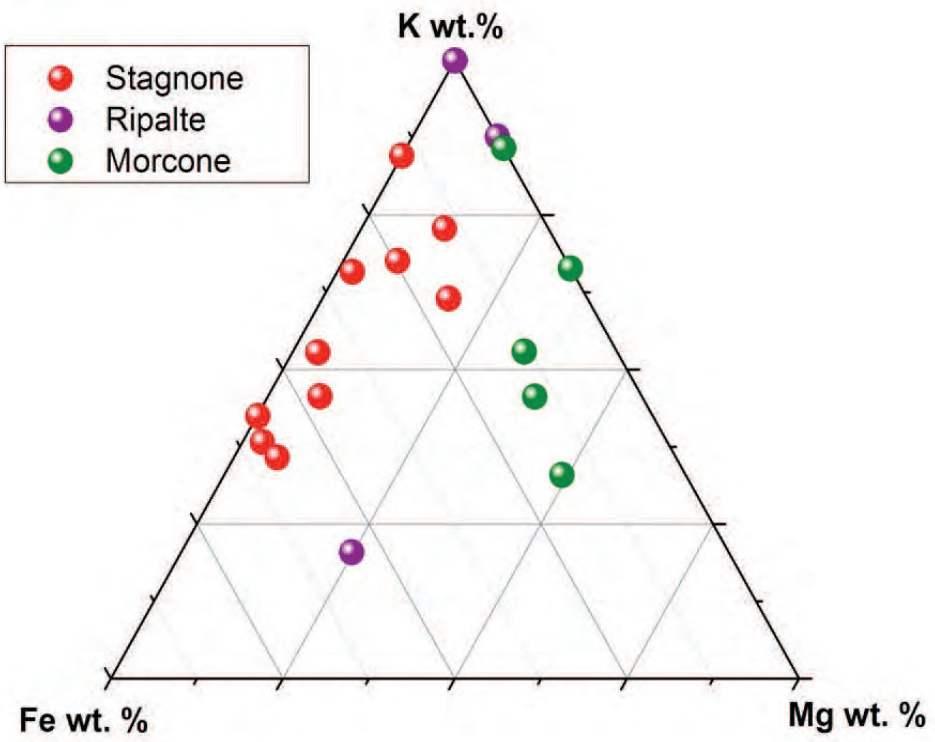

Fig. 2.3.41. Ternary diagram showing K, Fe, and Mg (wt. %) for fluids trapped in L inclusions at Stagnone, Ripalte and Morcone as quantified by LA-ICPMS.

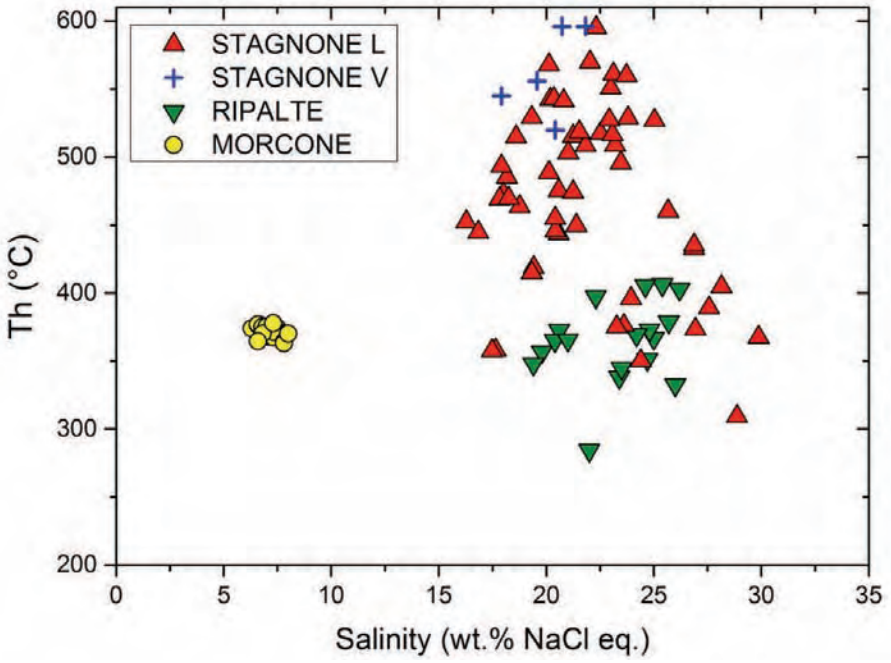

Fig. 2.3.42. Salinity of liquid-rich (L1+L2) and vapour-rich (V) inclusions at Stagnone, Ripalte and Morcone as a function of liquid-vapour homogenization temperature (Th).

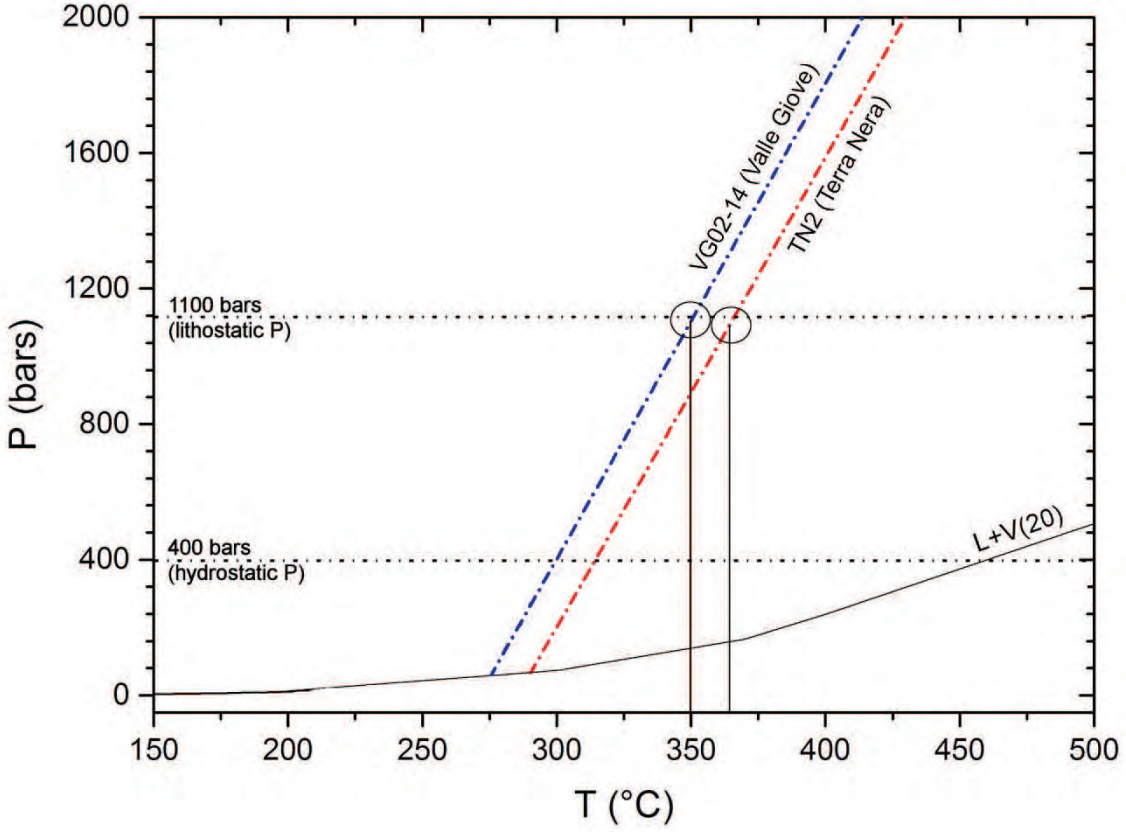

Fig. 2.3.43. Pressure-temperature diagram illustrating trapping conditions for TN2 and VG02-14 samples based on intersection between the quartz-hematite isotopic temperature of TN2 and VG02-14 samples and the mean isochores of fluid inclusions of these samples. In both cases the intersection occur at a pressure of about 1100 bars corresponding to a depth of about 4 km under lithostatic pressure regime. Hydrostatic pressure at 4 km is also shown.

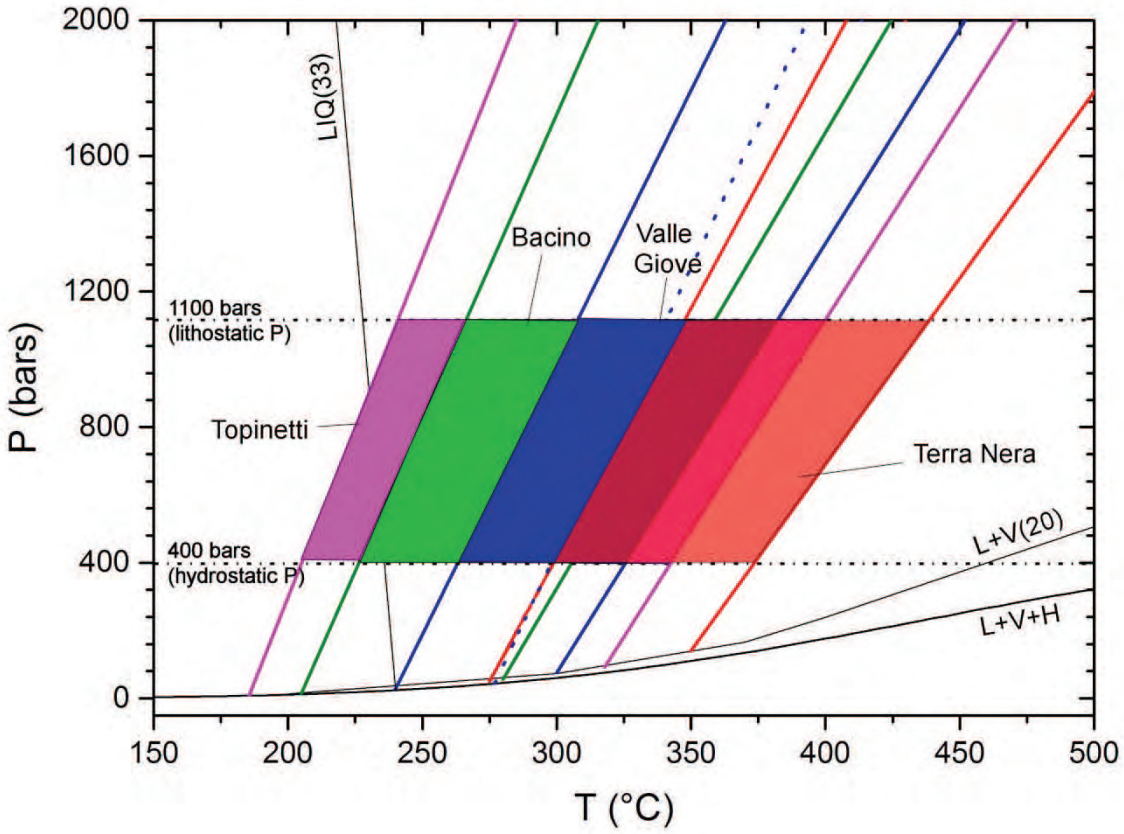

Fig. 2.3.44. Pressure-temperature diagram illustrating trapping conditions of all fluid inclusions observed at Terra Nera, Valle Giove, Topinetti and Bacino in quartz and calcite. Isochores are depicted as red lines for Terra Nera, blue lines for Valle Giove, pink solid lines for Topinetti, green lines for Bacino, blue pointed line indicates the isochore for halite-saturated inclusions occurring in calcite at Valle Giove. The three phase curve (L+V+H) separates the stability field of vapour+halite (V+H) and liquid+vapour (L+V) (data from Driesen and Heinrich, 2007); liquid-vapour curves (L+V) have been calculated at salinities of 20 wt.% NaCl eq. and separate the stability fields for liquid+vapour (L+V) and liquid (L) (data from Steele-MacInnis et al., 2012); LiQ(33) separates the stability fields for liquid+halite (L+H) and liquid (L) for a halite-saturated fluid with a salinity of 33 wt. % NaCl eq. (calculated from Bodnar 1994). Shaded area delimited the P-T trapping conditions for all areas considering a maximum and minimum pressure corresponding to the lithostatic and hydrostatic pressure at the depth of formation of Fe deposits (this depth was calculated from the FIs and isotopic data of TN2 and VG02-14 samples).

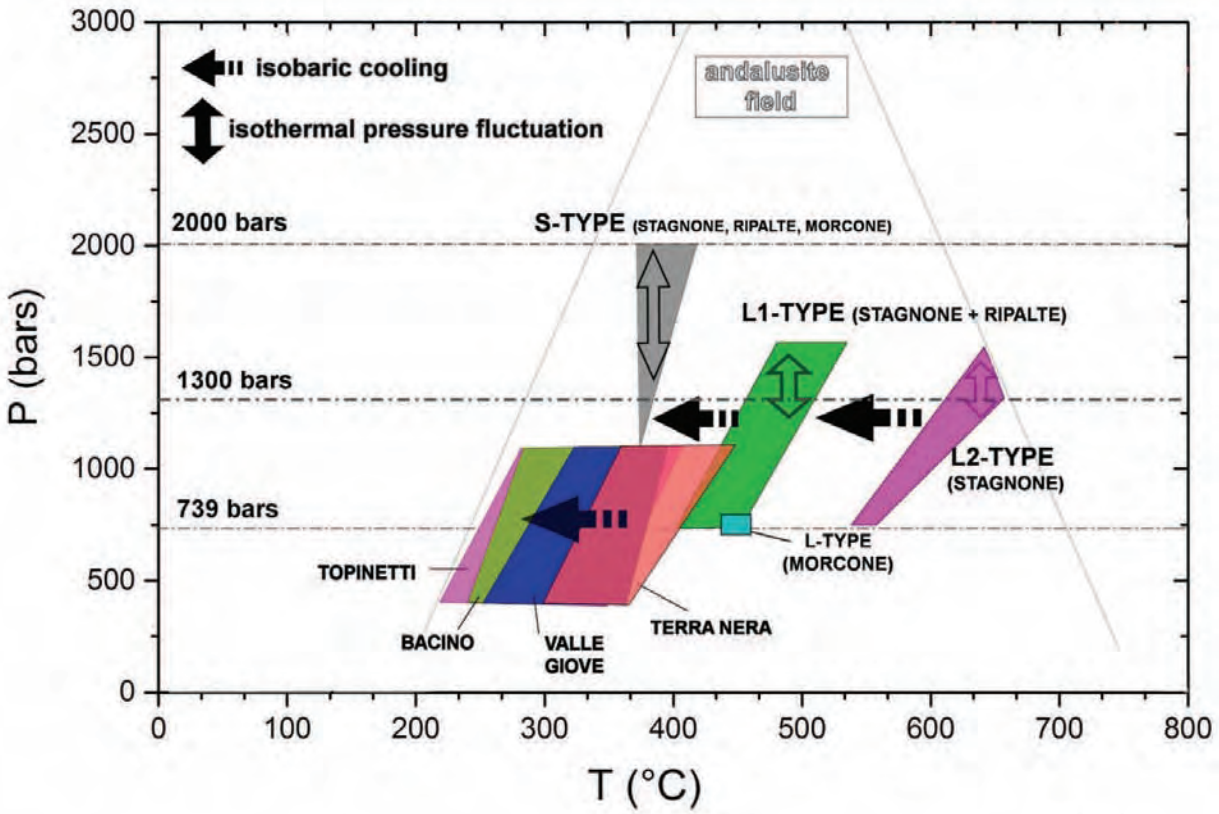

Fig. 2.3.45. P-T diagram showing the evolution of the trapping conditions for the fluids trapped in different systems on the base of the fluid inclusions analyzed in this study.

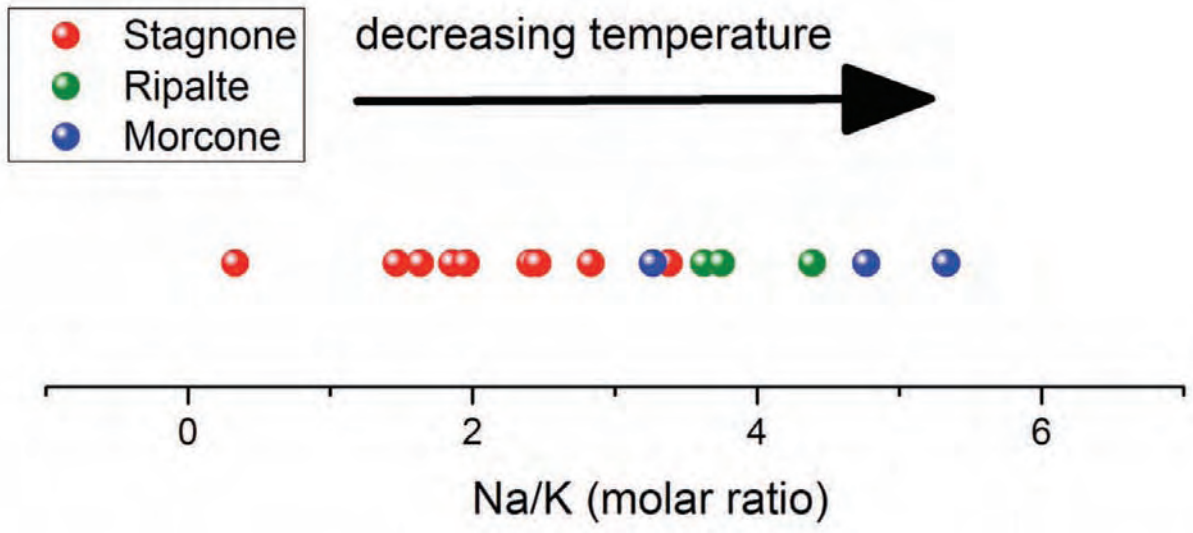

Fig. 2.3.46. Na/K molar ratios of the fluid inclusions for Calamita Peninsula as quantified by LA-ICPMS analysis.

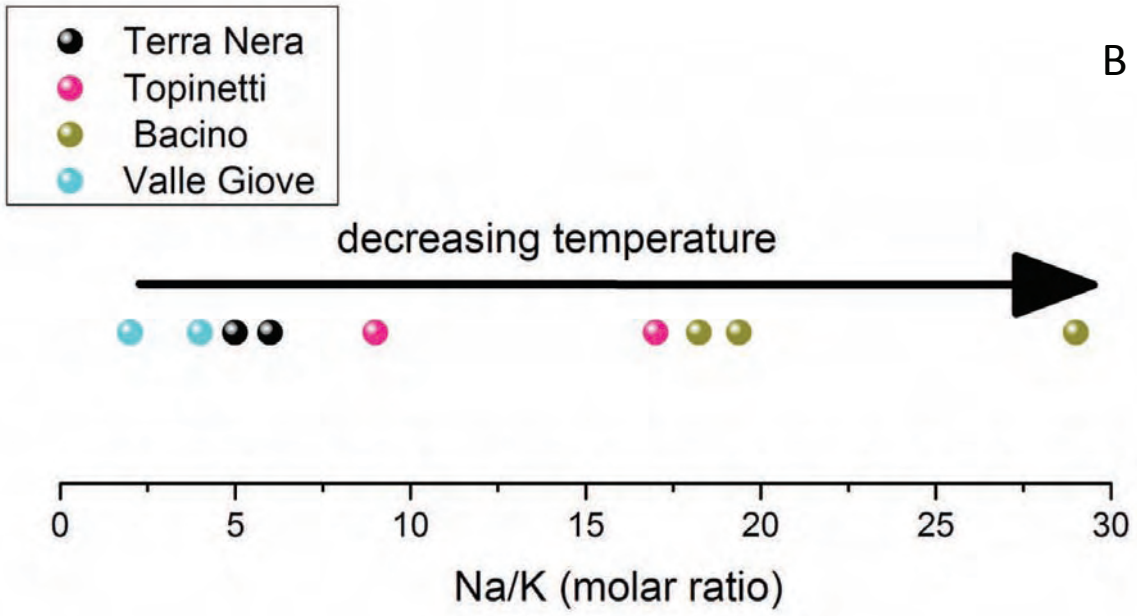

Fig. 2.3. 47. Na/K molar ratios of the fluid inclusions of Rio Marina and Terra Nera iron mineralized area as quantified by LA-ICPMS analysis.

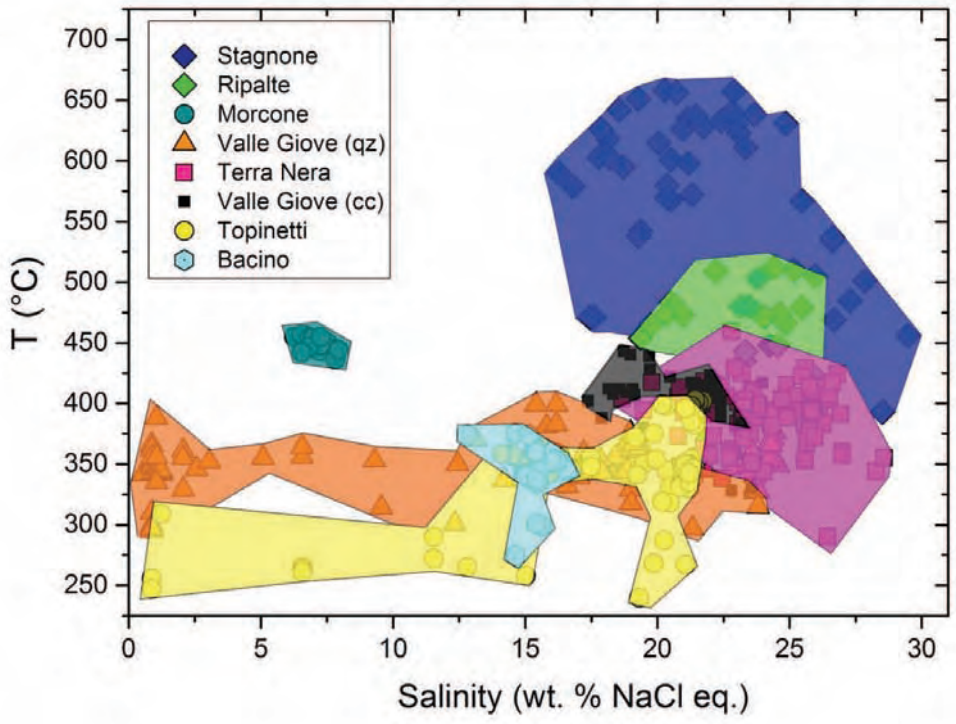

Fig. 2.3.48. Trapping temperature against salinity for L inclusions of Calamita Peninsula and Rio Marina and Terra Nera iron mineralized areas.

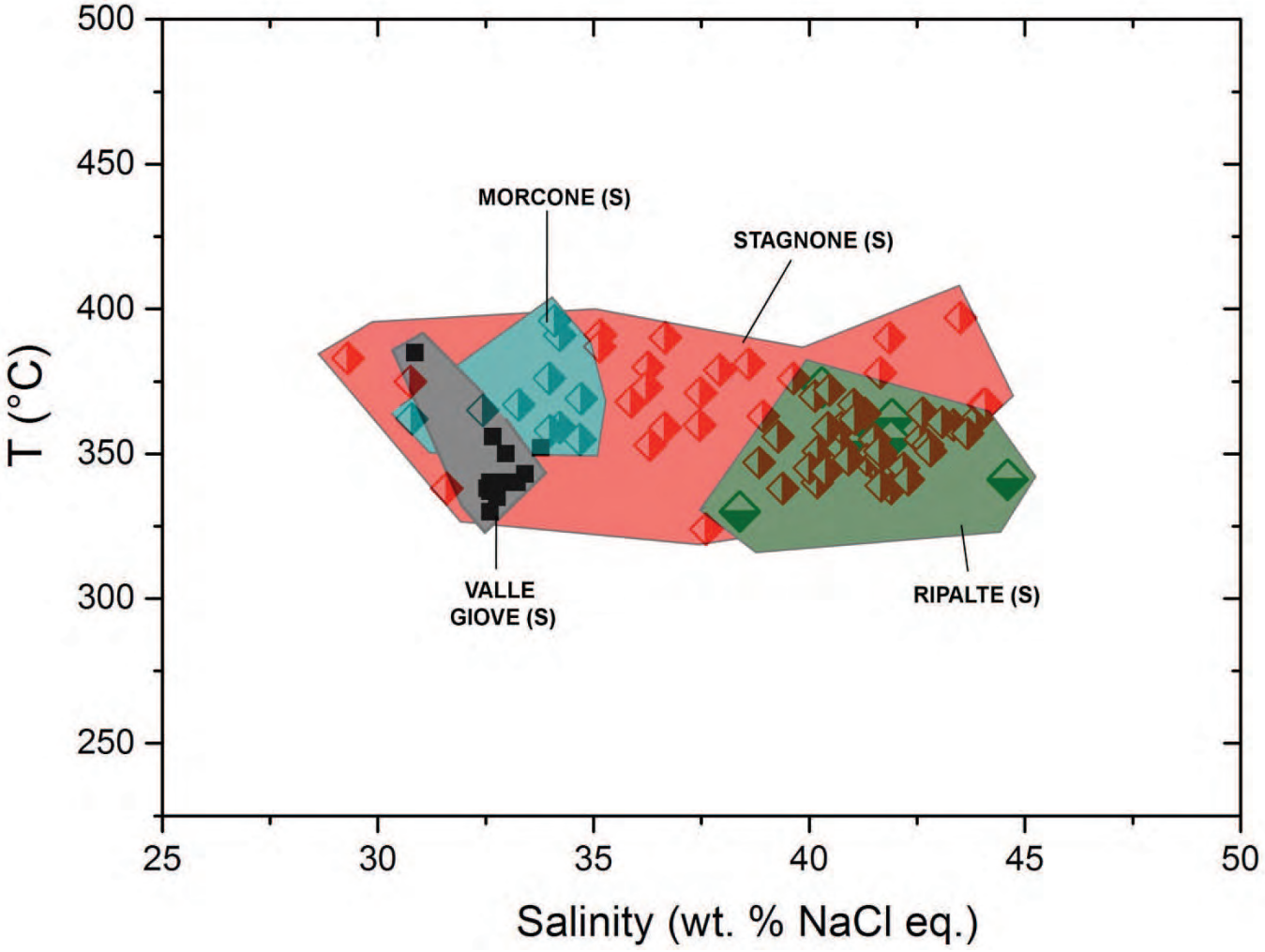

Fig. 2.3.49. Trapping temperature against salinity for S inclusions of Calamita Peninsula and Terra Nera iron mineralized areas.

SAMPLE ID	LOCATION	SAMPLE DESCRIPTION	HOST MINERAL	ANALYZING UNIT
14VG02	Valle Giove	Hematite-bearing hydrothermal vein hosted in rocks of the "Verrucano" group (Triassic) within the Monticiano-Roccastrada Unit. Mineralogical association: hematite (variety oligisto), pyrite, quartz, adularia	quartz	University of Bari
IFR3E2		Large quartz crystals (ca. 2.2 - 0.65 cm size range) from geode in extensional shear vein hosted in rocks of the Verrucano group (Triassic) within the Monticiano-Roccastrada Unit. Mineralogical association: quartz + adularia + pyrite + hematite.	quartz	
IFR5A		Light quartz + adularia + a few hematite (± pyrite) bearing sample from a shear vein within metasandstones from the Monticiano-Roccastrada Unit.	quartz	
IFR5B		Dark hematite + a few quartz (± adularia ± pyrite) bearing sample from a shear vein within phyllites from the Monticiano-Roccastrada Unit.	quartz	
IFR4A		Large single crystal of calcite (ca. 4.1 x 2.5 cm sized) from a shear vein within the Monticiano-Roccastrada Unit.	calcite	
IFR4B		Calcite+pyrite mineralization from a shear vein within the Monticiano-Roccastrada Unit.	calcite	
TN01 -14	Terra Nera	Hematite-bearing hydrothermal vein along high-angle second generation normal faults in the Rio Marina fm. (Permian-Carboniferous) within the Monticiano-Roccastrada Unit. Mineralogical association: hematite, quartz.	quartz	
TN02 -14		Hematite-bearing hydrothermal vein along high-angle second generation normal faults in the Rio Marina fm. (Permian-Carboniferous) within the Monticiano-Roccastrada Unit. Mineralogical association: hematite, quartz.	quartz	
TN04 -14		Hydrothermal quartz collected along low-angle angle second generation normal faults in the Rio Marina fm. (Permian-Carboniferous) within the Monticiano-Roccastrada Unit.	quartz	
TN05 -14		Mineralized vein (minor hematite) occurring along second generation normal faults in the Rio Marina fm. (Permian-Carboniferous) within the Monticiano-Roccastrada Unit. Mineralogical association: hematite, quartz, pyrite.	quartz	
TN4-2		Hematite-bearing hydrothermal shear-vein within phyllites of the Rio Marina fm. (Permian-Carboniferous) within the Monticiano-Roccastrada Unit. Mineralogical association: hematite, quartz.	quartz	
TN8-I3		Hematite-bearing hydrothermal extensional-vein within phyllites the Rio Marina fm. (Permian-Carboniferous) within the Monticiano-Roccastrada Unit. Hematite-bearing hydrothermal extensional-vein within phyllites of the Rio Marina fm. (Permian-Carboniferous) within the Monticiano-Roccastrada Unit.	quartz	
TN8-I4		Hematite-bearing hydrothermal extensional-vein within phyllites of the Rio Marina fm. (Permian-Carboniferous) within the Monticiano-Roccastrada Unit. Hematite-bearing hydrothermal extensional-vein within phyllites of the Rio Marina fm. (Permian-Carboniferous) within the Monticiano-Roccastrada Unit.	quartz	
TOP-PY	Topinetti	Large quartz crystal from a hydrothermal vein crossing the Rio Marina Fm. (Permian-Carboniferous) within the Monticiano-Roccastrada Unit.	quartz	
TOP-EM3		Hematite- bearing hydrothermal vein crossing the Rio Marina Fm. (Permian-Carboniferous) within the Monticiano-Roccastrada Unit. Mineralogical association: hematite, minor pyrite, quartz.		
IFR1B	Bacino	Quartz crystals (ca. 0.5 x 0.2 cm sized) from extensional hematite-bearing mineralized vein cutting rocks of the Verrucano group (Triassic) within the Monticiano-Roccastrada Unit. Mineralogical association: hematite + quartz (with chlorite inclusions).	quartz	
F1-ST6-14	Stagnone	Tourmaline-bearing hydrothermal vein cutting across biotite-rich hornfels (Calamita Schist Paleozoic); first generation, low-angle vein	quartz	CNR-IGG
F1-ST1-14			quartz	
F1ST5-14			tourmaline	
F1-ST3-14			quartz	
PA104		B vein of the of the tourmaline-quartz vein from the work of Dini et al. (2008)	quartz	
PA102			quartz	
F3ST1-14		Hydrothermal quartz-bearing vein cutting across the I and II tourmaline veins	quartz	
F2ST5-14		Tourmaline-bearing hydrothermal vein cutting across the Calamita Schist (biotite-rich hornfels, Paleozoic Calamita Unit); second-generation, high angle vein	quartz	
F2-MOR01-14	Morcone	Tourmaline-bearing hydrothermal vein cutting across the Calamita Schist; high-angle vein.	quartz	
F2-MOR02-14		Tourmaline-bearing hydrothermal vein cutting across the Calamita Schist; high-angle vein.	quartz	
RIP01-14	Ripalte	Tourmaline-bearing hydrothermal vein cutting across the Calamita Schist; low-angle vein.	quartz	

Table 2.3.1. Brief summary of the samples analyzed for fluid inclusions. For sample location refer to Fig. 2.3.2.

	tourmaline	tourmaline	tourmaline	tourmaline	tourmaline	tourmaline	tourmaline	tourmaline	tourmaline	tourmaline	tourmaline	tourmaline	tourmaline	tourmaline	tourm_core	tourm_core	tourmaline	tourmaline	tourmaline
Sample	F2ST3A	F2ST3A	F2ST3A	F2ST3A	F2ST3A	F2ST3A	F2ST1C	F2ST1C	F2ST1C	F2ST1C	F2ST1C	F2ST1C	F1ST1A	F1ST1A	F1ST1A	F1ST1A	F1ST1A	F1ST1A	F1ST1A
analysis	1	2	3	5	6	10	35	39	40	41	75	76	1	3	7	8	10	11	12
rock type	F2vein	F2vein	F2vein	F2vein	F2vein	F2vein	F2vein	F2vein	F2vein	F2vein	F2vein	F2vein	F1vein	F1vein	F1vein	F1vein	F1vein	F1vein	F1vein
SiO_2	36.01	36.55	35.04	36.15	36.20	35.28	34.68	34.55	34.62	37.60	38.31	35.86	36.68	37.00	36.32	36.04	35.87	36.64	36.55
TiO_2	0.26	0.14	0.98	0.45	0.36	0.33	1.12	0.91	1.17	0.06	0.26	0.31	1.07	0.69	1.52	1.90	1.46	0.63	0.57
Al_2O_3	31.28	31.88	32.18	31.37	33.57	33.96	32.99	33.25	33.55	32.31	32.34	33.82	30.75	31.08	29.21	28.73	28.24	30.23	31.57
Cr_2O_3	0.54	0.39	0.34	0.67	0.05	0.14	0.00	0.00	0.15	0.14	0.22	0.00	0.00	0.00	0.46	0.00	0.25	0.12	0.57
FeO	5.91	6.13	9.36	7.41	8.19	13.42	11.71	11.38	11.45	4.86	5.07	11.28	3.09	3.42	4.20	6.69	3.74	2.66	2.82
MnO	0.60	1.01	0.51	1.02	0.72	0.53	0.36	0.38	0.27	0.19	0.18	0.63	0.57	0.54	0.58	0.81	0.90	0.65	0.42
MgO	7.99	7.34	5.05	7.21	5.07	1.92	2.12	2.57	2.41	7.57	7.45	2.01	9.92	9.67	10.98	8.66	11.01	10.54	9.75
CaO	0.78	0.64	0.64	0.86	0.39	0.14	0.57	0.48	0.45	0.29	0.53	0.31	1.90	1.25	2.80	2.11	2.57	2.39	1.26
Na_2O	2.01	1.88	1.87	1.68	1.68	1.32	1.90	1.98	1.92	2.34	1.38	1.48	1.64	1.80	1.30	1.60	1.50	1.60	1.83
K_2O	0.07	0.01	0.00	0.14	0.00	0.00	0.05	0.00	0.00	0.31	0.09	0.00	0.08	0.22	0.10	0.12	0.37	0.00	0.00
H_2O*	3.64	3.66	3.60	3.66	3.66	3.60	3.55	3.56	3.58	3.69	3.72	3.59	3.69	3.69	3.72	3.64	3.64	3.68	3.69
B_2O_3*	10.54	10.61	10.44	10.62	10.60	10.44	10.29	10.31	10.37	10.70	10.78	10.41	10.70	10.71	10.77	10.56	10.56	10.67	10.70
Li_2O*	0.00	0.00	0.00	0.00	0.00	0.00	0.00	0.00	0.00	0.00	0.00	0.00	0.00	0.00	0.00	0.00	0.00	0.00	0.00
Total	99.63	100.24	100.00	101.24	100.49	101.08	99.35	99.37	99.94	100.06	100.31	99.70	100.10	100.06	101.94	100.86	100.13	99.82	99.73
Structural formula based on 31 anions (O, OH, F)																			
T: Si	5.94	5.99	5.83	5.92	5.94	5.87	5.855	5.824	5.800	6.106	6.179	5.989	5.96	6.01	5.86	5.93	5.90	5.97	5.94
Al	0.06	0.01	0.17	0.08	0.06	0.13	0.145	0.176	0.200	0.000	0.000	0.011	0.04	0.00	0.14	0.07	0.10	0.03	0.06
sum T	6.00	6.00	6.00	6.00	6.00	6.00	6.000	6.000	6.000	6.106	6.179	6.000	6.00	6.01	6.00	6.00	6.00	6.00	6.00
B	3.00	3.00	3.00	3.00	3.00	3.00	3.000	3.000	3.000	3.000	3.000	3.000	3.00	3.00	3.00	3.00	3.00	3.00	3.00
Z: Al	6.00	6.00	6.00	5.97	6.00	6.00	6.000	6.000	6.000	6.000	6.000	6.000	5.84	5.95	5.42	5.51	5.38	5.77	5.98
Mg	0.00	0.00	0.00	0.03	0.00	0.00	0.000	0.000	0.000	0.000	0.000	0.000	0.16	0.05	0.58	0.49	0.62	0.23	0.02
sum Z	6.00	6.00	6.00	6.00	6.00	6.00	6.000	6.000	6.000	6.000	6.000	6.000	6.00	6.00	6.00	6.00	6.00	6.00	6.00
Y: Al	0.02	0.14	0.15	0.00	0.42	0.53	0.420	0.429	0.425	0.184	0.148	0.646	0.00	0.00	0.00	0.00	0.00	0.00	0.00
Ti	0.03	0.02	0.12	0.05	0.04	0.04	0.143	0.115	0.147	0.008	0.031	0.039	0.13	0.08	0.18	0.24	0.18	0.08	0.07
Cr	0.07	0.05	0.04	0.09	0.01	0.02	0.000	0.000	0.020	0.018	0.028	0.000	0.00	0.00	0.06	0.00	0.03	0.02	0.07
Mg	1.96	1.79	1.25	1.73	1.24	0.48	0.533	0.647	0.603	1.832	1.791	0.501	2.24	2.29	2.06	1.63	2.08	2.33	2.34
Mn	0.08	0.14	0.07	0.14	0.10	0.07	0.051	0.054	0.038	0.027	0.025	0.089	0.08	0.07	0.08	0.11	0.13	0.09	0.06
Fe2+	0.81	0.84	1.30	1.01	1.12	1.87	1.653	1.604	1.605	0.661	0.683	1.575	0.42	0.46	0.57	0.92	0.51	0.36	0.38
sum Y	2.99	2.98	2.95	3.03	2.94	3.01	2.801	2.849	2.838	2.729	2.706	2.849	2.87	2.91	2.95	2.90	2.93	2.88	2.93
X: Ca	0.14	0.11	0.11	0.15	0.07	0.03	0.103	0.086	0.081	0.050	0.091	0.056	0.33	0.22	0.48	0.37	0.45	0.42	0.22
Na	0.64	0.60	0.60	0.53	0.53	0.43	0.622	0.647	0.624	0.735	0.430	0.478	0.52	0.57	0.41	0.51	0.48	0.51	0.58
K	0.01	0.00	0.00	0.03	0.00	0.00	0.011	0.000	0.000	0.065	0.018	0.000	0.02	0.05	0.02	0.03	0.08	0.00	0.00
vacancy	0.21	0.29	0.28	0.29	0.40	0.55	0.265	0.267	0.295	0.150	0.460	0.466	0.14	0.17	0.09	0.09	0.00	0.08	0.20
OH	4.00	4.00	4.00	4.00	4.00	4.00	4.000	4.000	4.000	4.000	4.000	4.000	4.00	4.00	4.00	4.00	4.00	4.00	4.00
Mineral Name	Dravite	Dravite	Schorl	Dravite	Dravite	Foitite	Schorl	Schorl	Schorl	Dravite	Mg-Foitite	Schorl	Dravite	Dravite	Uvite	Dravite	Dravite	Dravite	Dravite
Tourmaline Recalculation: Developed by Julie Selway & Jian Xiong																			
** B2O3, H2O and Li2O = calculated by stoichiometry; B = 3 apf u, OH+F = 4 apf u & Li = 15-total(T+Z+Y).*																			

Table 2.3.2. Electron microprobe analyses and calculated structural formulae (a.p.f.u.) of selected hydrothermal minerals found within quartz-tourmaline veins (cont.)

	tourmaline	tourmaline	tourmaline	tourmaline	tourmaline	tourmaline	tourmaline	tourmaline		tourmaline	tourmaline	tourmaline	tourmaline	tourmaline	tourmaline
Sample	F1ST4C	F1ST4C	F1ST4C	F1ST4C	F1ST4C	F1ST4C	F1ST4C	F1ST4C		F1ST3A	F1ST3A	F1ST3A	F1ST3A	F1ST3A	F1ST3A
analysis	1	2	3	4	5	6	10	18		91	96	97	102	103	104
rock type	F1vein	F1vein	F1vein	F1vein	F1vein	F1vein	F1vein	F1vein		F1vein	F1vein	F1vein	F1vein	F1vein	F1vein
SiO_2	35.73	36.00	36.56	36.15	35.47	36.66	35.65	35.68		36.50	35.88	37.04	36.78	37.37	35.74
TiO_2	1.24	1.81	1.41	0.85	1.17	1.16	0.68	0.63		1.58	1.37	1.38	1.49	0.41	1.83
Al_2O_3	28.80	28.28	28.06	30.71	31.16	29.77	31.02	32.29		28.19	30.14	29.60	28.14	30.95	29.03
Cr_2O_3	0.38	0.21	0.48	0.00	0.13	0.47	0.16	0.65		0.24	0.00	0.03	0.00	0.18	0.00
FeO	6.37	7.47	3.44	5.79	5.51	3.31	4.81	5.40		5.13	4.77	4.19	3.03	2.79	5.23
MnO	0.79	0.56	0.25	0.91	0.54	0.74	0.75	0.49		0.12	0.26	0.82	0.75	0.33	0.50
MgO	8.51	8.02	11.33	8.39	8.34	10.97	8.70	7.14		10.31	9.21	9.84	10.97	9.98	8.72
CaO	1.67	1.88	3.23	1.50	1.75	2.35	1.21	1.12		2.72	1.80	1.72	3.12	1.47	2.19
Na_2O	1.55	1.60	1.01	1.65	1.82	1.56	1.84	1.74		1.64	1.87	1.89	1.15	1.82	1.72
K_2O	0.09	0.00	0.04	0.12	0.00	0.00	0.22	0.29		0.07	0.07	0.07	0.00	0.19	0.06
H_2O*	3.59	3.60	3.67	3.65	3.65	3.72	3.63	3.64		3.67	3.64	3.70	3.66	3.70	3.61
B_2O_3*	10.41	10.44	10.63	10.59	10.57	10.78	10.51	10.56		10.63	10.56	10.72	10.61	10.73	10.46
Li_2O*	0.00	0.00	0.00	0.00	0.00	0.00	0.00	0.00		0.00	0.00	0.00	0.00	0.00	0.00
Total	99.14	99.87	100.12	100.32	100.10	101.49	99.17	99.63		100.79	99.57	100.98	99.70	99.92	99.09
Structural formula based on 31 anions (O, OH, F)															
T: Si	5.97	5.99	5.98	5.93	5.83	5.91	5.89	5.87		5.969	5.907	6.007	6.025	6.054	5.940
Al	0.03	0.01	0.02	0.07	0.17	0.09	0.11	0.13		0.031	0.093	0.000	0.000	0.000	0.060
sum T	6.00	6.00	6.00	6.00	6.00	6.00	6.00	6.00		6.000	6.000	6.007	6.025	6.054	6.000
B	3.00	3.00	3.00	3.00	3.00	3.00	3.00	3.00		3.000	3.000	3.000	3.000	3.000	3.000
Z: Al	5.63	5.54	5.38	5.87	5.87	5.56	5.94	6.00		5.402	5.755	5.656	5.435	5.908	5.627
Mg	0.37	0.46	0.62	0.13	0.13	0.44	0.06	0.00		0.598	0.245	0.344	0.565	0.092	0.373
sum Z	6.00	6.00	6.00	6.00	6.00	6.00	6.00	6.00		6.000	6.000	6.000	6.000	6.000	6.000
Y: Al	0.00	0.00	0.00	0.00	0.00	0.00	0.00	0.14		0.000	0.000	0.000	0.000	0.000	0.000
Ti	0.16	0.23	0.17	0.11	0.14	0.14	0.08	0.08		0.195	0.169	0.168	0.184	0.050	0.229
Cr	0.05	0.03	0.06	0.00	0.02	0.06	0.02	0.08		0.031	0.000	0.004	0.000	0.024	0.000
Mg	1.75	1.53	2.14	1.93	1.91	2.20	2.08	1.75		1.915	2.014	2.034	2.114	2.319	1.787
Mn	0.11	0.08	0.03	0.13	0.07	0.10	0.10	0.07		0.017	0.036	0.112	0.104	0.045	0.070
Fe2+	0.89	1.04	0.47	0.79	0.76	0.45	0.66	0.74		0.701	0.657	0.568	0.416	0.377	0.727
sum Y	2.96	2.90	2.88	2.95	2.90	2.95	2.96	2.87		2.859	2.876	2.886	2.817	2.815	2.813
X: Ca	0.30	0.34	0.57	0.26	0.31	0.41	0.21	0.20		0.477	0.318	0.298	0.547	0.256	0.390
Na	0.50	0.52	0.32	0.53	0.58	0.49	0.59	0.56		0.521	0.596	0.594	0.366	0.571	0.555
K	0.02	0.00	0.01	0.03	0.00	0.00	0.05	0.06		0.015	0.015	0.015	0.000	0.038	0.013
vacancy	0.18	0.15	0.10	0.18	0.11	0.11	0.15	0.19		0.000	0.071	0.093	0.086	0.135	0.042
OH	4.00	4.00	4.00	4.00	4.00	4.00	4.00	4.00		4.000	4.000	4.000	4.000	4.000	4.000
Mineral Nam	Dravite	Dravite	Uvite	Dravite	Dravite	Dravite	Dravite	Dravite		Dravite	Dravite	Dravite	Uvite	Dravite	Dravite
Tourmaline Recalculation: Developed by Julie Selway & Jian Xiong															
**B2O3, H2O and Li2O = calculated by stoichiometry; B = 3 apfu, OH+F = 4 apfu & Li = 15-total (T+Z+Y).*															

Table 2.3.2: Electron microprobe analyses and calculated structural formulae (a.p.f.u.) of selected hydrothermal minerals found within quartz-tourmaline veins (cont.).

	plagioclase	plagioclase		plagioclase	plagioclase	K-feldspar	K-feldspar	plagioclase	plagioclase	plagioclase		K-feldspar	K-feldspar	plagioclase		K-feldspar	K-feldspar	K-feldspar	K-feldspar			phlogopite
Sample	F2ST3A	F2ST3A		F2ST1C	F2ST1C	F2ST1C	F2ST1C	F2ST1C	F2ST1C	F2ST1C		F1ST4C	F1ST4C	F1ST4C		F1ST3A	F1ST3A	F1ST3A	F1ST3A		Sample	F2 21 mic
analysis	12	13		78	79	83	87	88	89	90		8	12	13		92	93	94	99		analysis	86
rock type	F2vein	F2vein		F2vein	F2vein	F2vein	F2vein	F2vein	F2vein	F2vein		F1vein	F1vein	F1vein		F1vein	F1vein	F1vein	F1vein		rock type	F2vein
SiO2	64.01	63.71		62.57	62.80	64.62	63.72	66.01	62.63	64.75		63.26	63.99	64.49		65.06	64.86	65.32	63.80		SiO2	35.57
Al2O3	21.27	21.60		23.00	23.07	17.53	17.53	21.12	22.28	21.09		17.70	17.94	21.15		17.95	18.05	17.71	17.80		TiO2	3.23
FeO	1.01	1.21		0.10	0.13	0.09	0.15	0.10	0.41	0.18		0.95	0.54	0.91		0.14	0.25	0.21	0.13		Al2O3	18.65
CaO	2.98	3.05		4.79	4.73	0.10	0.00	2.90	3.86	2.92		0.01	0.06	2.14		0.12	0.00	0.00	0.12		Cr2O3	0.06
Na2O	10.24	10.30		9.33	9.64	0.40	0.69	10.11	9.55	10.26		0.28	0.37	10.02		0.31	0.31	0.25	0.36		FeO	12.12
K2O	0.16	0.00		0.37	0.52	17.25	16.88	0.11	0.46	0.42		17.51	16.57	0.38		15.67	15.22	16.13	17.12		MnO	0.77
Sum	99.67	99.86		100.17	100.88	99.98	98.97	100.36	99.19	99.62		99.71	99.46	99.08		99.26	98.68	99.63	99.33		MgO	12.35
																					CaO	0.52
																					Na2O	0.14
																					K2O	9.28
Cations per 8 O																					Sum	92.69
Si	2.84	2.83		2.78	2.77	3.01	3.00	2.89	2.80	2.87		2.97	2.99	2.87		3.02	3.02	3.02	2.99		*Cations per 22 O:*	
Al	1.11	1.13		1.20	1.20	0.96	0.97	1.09	1.17	1.10		0.98	0.99	1.11		0.98	0.99	0.97	0.98		Si	5.402
Fe3+	0.04	0.05		0.00	0.01	0.00	0.01	0.00	0.02	0.01		0.04	0.02	0.04		0.01	0.01	0.01	0.01		Al IV	2.598
sum T	4.00	4.00		3.98	3.98	3.97	3.98	3.99	3.99	3.98		3.99	4.00	4.02		4.01	4.02	4.00	3.98		sum	8.000
Ca	0.14	0.14		0.23	0.22	0.01	0.00	0.14	0.19	0.14		0.00	0.00	0.10		0.01	0.00	0.00	0.01		Al VI	0.739
Na	0.88	0.89		0.80	0.82	0.04	0.06	0.86	0.83	0.88		0.03	0.03	0.86		0.03	0.03	0.02	0.03		Ti	0.369
K	0.01	0.00		0.02	0.03	1.02	1.01	0.01	0.03	0.02		1.05	0.99	0.02		0.93	0.90	0.95	1.02		Fe2+	1.541
sum Y	1.03	1.03		1.05	1.08	1.07	1.08	1.00	1.04	1.05		1.07	1.02	0.99		0.96	0.93	0.98	1.06		Mn	0.099
sum T+Y	5.03	5.04		5.03	5.05	5.04	5.05	4.99	5.03	5.03		5.06	5.02	5.00		4.97	4.95	4.98	5.04		Mg	2.796
																					Cr	0.007
An	13.71	14.05		21.66	20.75	0.49	0.00	13.62	17.80	13.27		0.03	0.29	10.31		0.62	0.00	0.00	0.58		sum	5.552
Ab	85.39	85.95		76.36	76.55	3.40	5.88	85.78	79.68	84.45		2.35	3.24	87.50		2.93	2.98	2.33	3.08			
Or	0.90	0.00		1.99	2.71	96.11	94.12	0.60	2.53	2.28		97.62	96.47	2.19		96.45	97.02	97.67	96.34		Ca	0.084
																					Na	0.043
																					K	1.798
																					sum	1.925
																					Tot.	15.477
																					Mg #	64.466
																					H2O calc	3.948
																					Sum calc	96.639
																					IVAl/2	1.299
																					XMg	0.645
																					XFe	0.355
																					2-IVAl	0.701
																					IVAl-1	0.299
																					annite (Fe3AlSi3)	0.249
																					siderophyllite (Fe2AlAl2S	0.106
																					phlog (Mg3AlSi3)	0.452
																					eastonite (Mg2AlAl2Di2	0.193
																						1.000

Table 2.3.2 Electron microprobe analyses and calculated structural formulae (a.p.f.u.) of selected hydrothermal minerals found within quartz-tourmaline veins

Sample	MOR 6	MOR 8	MOR 9	MOR 11	MOR 12		RIP 2	RIP 3	RIP 4	RIP 7	RIP 8	RIP 11
analysis	9	11	12	14	15		17	18	19	22	23	26
SiO_2	34.67	35.94	36.25	35.10	35.71		36.65	36.89	36.11	36.80	36.08	36.84
TiO_2	0.80	0.20	0.31	0.40	0.42		0.46	0.48	0.57	0.45	0.22	0.84
Al_2O_3	33.85	33.73	35.16	34.65	33.89		32.69	32.94	33.57	32.50	34.08	31.48
Cr_2O_3	0.02	0.00	0.21	0.18	0.10		0.03	0.18	0.00	0.00	0.08	0.17
FeO	6.65	6.64	6.16	7.20	7.05		6.91	6.30	7.01	7.96	7.63	6.28
MnO	0.26	0.34	0.38	0.28	0.36		0.41	0.64	0.32	0.38	0.59	0.15
MgO	5.79	5.21	4.72	4.34	5.28		5.38	5.14	4.99	4.76	4.44	6.49
CaO	0.88	0.69	0.30	0.67	0.62		0.24	0.58	0.55	0.20	0.46	0.43
Na_2O	1.59	1.68	1.05	1.55	1.62		1.88	1.60	1.57	1.84	1.87	2.44
K_2O	0.15	0.00	0.01	0.13	0.25		0.08	0.00	0.19	0.06	0.29	0.00
H_2O*	3.61	3.62	3.65	3.61	3.64		3.63	3.64	3.63	3.62	3.64	3.64
B_2O_3*	10.46	10.48	10.59	10.45	10.54		10.51	10.54	10.51	10.49	10.56	10.55
Li_2O*	0.00	0.00	0.00	0.00	0.00		0.00	0.00	0.00	0.00	0.00	0.00
Total	98.72	98.54	98.79	98.54	99.47		98.88	98.93	99.01	99.05	99.94	99.32
Structural formula based on 31 anions (O, OH, F)												
T: Si	5.762	5.958	5.952	5.839	5.890		6.062	6.082	5.969	6.099	5.940	6.070
Al	0.238	0.042	0.048	0.161	0.110		0.000	0.000	0.031	0.000	0.060	0.000
sum T	6.000	6.000	6.000	6.000	6.000		6.062	6.082	6.000	6.099	6.000	6.070
B	3.000	3.000	3.000	3.000	3.000		3.000	3.000	3.000	3.000	3.000	3.000
Z: Al	6.000	6.000	6.000	6.000	6.000		6.000	6.000	6.000	6.000	6.000	6.000
Mg	0.000	0.000	0.000	0.000	0.000		0.000	0.000	0.000	0.000	0.000	0.000
sum Z	6.000	6.000	6.000	6.000	6.000		6.000	6.000	6.000	6.000	6.000	6.000
Y: Al	0.394	0.547	0.754	0.630	0.477		0.374	0.401	0.509	0.348	0.552	0.113
Ti	0.100	0.025	0.038	0.050	0.052		0.057	0.060	0.070	0.056	0.027	0.104
Cr	0.003	0.001	0.027	0.023	0.013		0.004	0.024	0.000	0.000	0.010	0.023
Mg	1.434	1.288	1.155	1.077	1.299		1.328	1.263	1.229	1.177	1.090	1.595
Mn	0.037	0.048	0.053	0.039	0.050		0.058	0.090	0.044	0.053	0.083	0.021
Fe2+	0.924	0.920	0.845	1.001	0.972		0.956	0.869	0.970	1.103	1.051	0.866
sum Y	2.892	2.830	2.874	2.821	2.864		2.776	2.706	2.823	2.737	2.812	2.722
X: Ca	0.157	0.123	0.053	0.120	0.109		0.043	0.103	0.097	0.035	0.081	0.076
Na	0.511	0.539	0.334	0.499	0.519		0.604	0.512	0.502	0.590	0.597	0.779
K	0.032	0.000	0.001	0.027	0.052		0.017	0.000	0.040	0.012	0.061	0.000
vacancy	0.301	0.338	0.612	0.354	0.320		0.335	0.386	0.361	0.363	0.262	0.145
OH	4.000	4.000	4.000	4.000	4.000		4.000	4.000	4.000	4.000	4.000	4.000
Mineral Name	Dravite	Dravite	Mg-Foitite	Dravite	Dravite		Dravite	Dravite	Dravite	Dravite	Dravite	Dravite
Tourmaline Recalculation: Developed by Julie Selway & Jian Xiong												
**B2O3, H2O and Li2O = calculated by stoichiometry; B = 3 apfu, OH+F = 4 apfu & Li = 15-total (T+Z+Y).*												

Table 2.3.3: Electron microprobe analyses and calculated structural formulae (a.p.f.u.) of selected hydrothermal minerals found within quartz-tourmaline veins (cont.).

	K-feldspar	K-feldspar	K-feldspar	K-feldspar					phlogopite
Sample	RIP 12 K	RIP 13 K	RIP 16 K	RIP 17 K			Sample		RIP 14 mic
analysis	27	28	31	32			analysis		29
rock type							rock type		
SiO_2	63.94	64.02	63.80	63.72			SiO2		37.72
Al_2O_3	17.93	17.45	17.86	17.69			TiO2		0.23
FeO	0.07	0.00	0.05	0.14			Al2O3		20.13
CaO	0.16	0.04	0.14	0.00			Cr2O3		0.13
Na_2O	0.64	0.50	0.22	0.25			FeO		12.84
K_2O	16.80	17.53	17.44	16.74			MnO		0.32
Sum	99.54	99.55	99.51	98.54			MgO		9.58
							CaO		0.05
							Na2O		0.18
							K2O		10.25
							Sum		91.42
Cations per 8 O							***Cations por 22 O:***		
Si	2.988	3.002	2.989	3.002			Si		5.779
Al	0.987	0.964	0.986	0.982			Al IV		2.221
Fe3+	0.003	0.000	0.002	0.006			sum		8.000
sum T	3.979	3.966	3.978	3.990					
							Al VI		1.414
Ca	0.008	0.002	0.007	0.000			Ti		0.026
Na	0.058	0.046	0.020	0.023			Fe2+		1.647
K	1.002	1.049	1.043	1.007			Mn		0.042
sum Y	1.068	1.097	1.070	1.030			Mg		2.188
sum T+Y	5.047	5.063	5.048	5.020			Cr		0.016
							sum		5.333
An	0.747	0.188	0.675	0.000					
Ab	5.442	4.152	1.847	2.224			Ca		0.008
Or	93.811	95.660	97.478	97.776			Na		0.053
							K		2.004
							sum		1.925
							Tot.		15.477
							Mg #		64.466
							H2O calc		3.948
							Sum calc		96.639
							IVAl/2		1.299
							XMg		0.645
							XFe		0.355
							2-IVAl		0.701
							IVAl-1		0.299
							annite (Fe3AlSi3)		0.249
							siderophyllite (Fe2A		0.106
							phlog (Mg3AlSi3)		0.452
							eastonite (Mg2AlAl2		0.193
									1.000

Table 2.3.3: Electron microprobe analyses and calculated structural formulae (a.p.f.u.) of selected hydrothermal minerals found within quartz-tourmaline veins.

Area of study	Mineral host	Fluid inclusion type	Homogenization*	Th range (°C)	Ts S1	Ts S2/S6	Ts NaCl range (°C)	Tm_{ice} range (°C)	Tm_{hy} range (°C)
Stagnone	quartz (F1&F2 veins)	**Sa**	L+V+H → L+H → L	192/330 (167)	130/600 (8)	62/360 (5)	287/415 (84)	n.d.	n.d.
		Sb	L+V+H → L+V → L	279/315 (13)	/	n.d.	141/306 (13)	n.d.	n.d.
		L	L+V→ L	309/595 (72)	/	/	/	-12.3/-31.3 (72)	-23.2/-33.1 (37)
		V	V+L→ V	520/596 (5); >600 (19)	/ /	/	/	-14.1/-27.2 (23)	-23.8/-28.1 (14)
	tourmaline (F1&F2 veins)	**L**	L+V→ L	178/413 (5)	/	/	/	-31.5/-16.1 (4)	n.d.
	quartz (F3 veins)	**L**	L+V→ L	365/401 (2); >500 (2)	/	/	/	-14.0/-21.4 (4)	n.d.
Morcone	quartz	**L**	L+V→ L	323/378 (30)	/	/	/	-3.9/-5.1 (27)	n.d.
		Sb	L+V+H → L+V → L	289/319 (13)	/	/	177/251 (10)	n.d.	n.d.
Ripalte	quartz	**Sa**	L+V+H → L+H → L	196/298 (22)	359/390 (5)	/	296/396 (12)	n.d.	n.d.
		L	L+V→ L	284/406 (19)	/	/	/	-15.9/-25.6 (28)	-24.7/-25.8 (6)
Terra Nera	quartz	**L**	L+V→ L	211/403 (271)	/	/	/	-29.9/-15.0 (111)	-33.0/-14.1 (15)
Valle Giove	quartz	**L**	L+V→ L	210/311 (208)	/	/	/	-28.0/-0.3 (149)	-26.6/-21.0 (18)
	calcite	**Sb**	L+V+H→L+V→L	178/292 (15)	/	/	194/235 (14)	n.d.	n.d.
		L	L+V→ L	247/353 (71)	/	/	/	-22.4/-13.5 (67)	-28.0/-24.8 (12)
Topinetti	quartz	**L**	L+V→ L	172/326 (123)	/	/	/	-19.0/-0.5 (79)	-29.2/-22.1 (9)
Bacino	quartz	**L**	L+V→ L	199/297 (57)	/	/	/	-12.9/-9.0 (43	-24.1/-22.5 (8)

* Owing to the complex homogenization sequence characterizing multiphase inclusions (S), only halite (H) has been reported between all solid phases, whose behaviour during heating allows the distinction between Sa- and Sb-type inclusions.

numbers in brackets refer to the number of fluid inclusions analyzed.

Table 2.3.4: Summary of fluid inclusion microthermometric data.

Fluid inclusions type	Samples	Li	B	Na	Mg	K	Ca	Mn	Fe	Cu	Zn	Sr	Sn	Ba	W
STAGNONE			**Elements in mg/kg**												
	L-type														
F1 vein	F1B2_7-8	371	518	63140	3389	19321	4243	3714	32076	63	789	70	7777	333	45905
	F1B2_7-8 b	488	327	47861	88	33783	17296	3757	46839	<bdl	765	65	<bdl	307	14
	F1B2_7-8 t	645	3109	63136	<bdl	43696	<bdl	1961	8169	<bdl	352	134	<bdl	188	<bdl
	F1_B2_3	2624	7359	38050	7316	44067	<bdl	3609	46355	<bdl	1188	141	291	257	<bdl
	F1B_6	1843	2847	74249	4723	67955	<bdl	<bdl	5093	65352	251	1642	347	332	466
	F1B_18-1	2123	<bdl	62486	2171	64994	<bdl	4801	32413	<bdl	347	95	<bdl	242	<bdl
	F1B_18-2	<bdl	<bdl	63039	4160	54855	<bdl	7489	86466	6008	2179	<bdl	<bdl	7738	<bdl
F2 vein	F2_B_3B	2170	169	69886	5836	35147	<bdl	883	7460	342	392	493	45	<bdl	1553
	F2_B_3B bis	8994	2310	59210	10597	35565	<bdl	578	11987	123	261	312	97	<bdl	307
	PA102_A1	795	3813	21549	12740	109599	<bdl	440	40800	1156	184	46	71	71	3
	mean	*2407*	*2377*	*60118*	*6367*	*45477*	*4243*	*3349*	*30762*	*14378*	*725*	*369*	*1711*	*1343*	*9649*
	S-type														
F1 vein	F1_16	1850	2052	176620	31926	119941	<bdl	32257	268818	7357	11748	1210	615	3324	297
	F1_4	134	261	177690	1029	7558	7716	1310	11508	<bdl	700	36	46	67	63
F2 vein	PA104A_7	487	923	173000	10762	19371	11593	3626	46399	43	2180	203	109	324	32
	PA104A_3	4286	5399	170000	1224	43887	173566	12684	100361	590	4417	283	3098	1953	62
	PA104A_8	2167	10232	170000	15653	1182421	195930	22997	145256	131	14132	1162	1939	2024	17
	PA104_9	7075	29086	170000	139613	36817	<bdl	7127	89976	1249	5557	439	235	188	74
	mean	*2667*	*7992*	*172885*	*33368*	*45515*	*9655*	*13333*	*110386*	*1874*	*6456*	*556*	*1007*	*1313*	*91*
RIPALTE	**L-type**														
	RIPB_29	<bdl	<bdl	41660	23711	19528	<bdl	10220	53745	<bdl	3518	659	<bdl	1443	<bdl
	RIPB_7-8	358	707	100404	6403	45552	<bdl	5570	<bdl	<bdl	590	123	<bdl	<bdl	<bdl
	RIPB_7-8 bis	639	1430	115896	<bdl	44910	<bdl	1808	<bdl	<bdl	562	846	<bdl	444	<bdl
	mean	*499*	*1069*	*85987*	*15057*	*36664*	*<bdl*	*5866*	*53745*	*<bdl*	*1557*	*543*	*<bdl*	*944*	*<bdl*
	S-type														
	RIP_11	53	53	164831	2261	8286	10263	2343	12514	<bdl	2171	61	11	543	12
	RIP-10	334	430	185180	4795	132479	<bdl	30764	189843	<bdl	12468	1263	164	5328	89
	average	*193*	*242*	*175006*	*3528*	*70382*	*10263*	*16554*	*101179*	*<bdl*	*7319*	*662*	*87*	*2935*	*51*
MORCONE	**L-type**														
	MOR_1	125	683	11688	6203	4168	<bdl	460	2336	<bdl	435	12	<bdl	<bdl	<bdl
	MOR_4	<bdl	703	17073	3453	5444	<bdl	87	1424	67	<bdl	<bdl	124	<bdl	<bdl
	MOR_14	3037	516	15019	6650	7814	<bdl	299	2746	<bdl	539	48	74	<bdl	<bdl
	MOR_15	113	1363	26822	1414	8561	<bdl	921	<bdl	93500	210	<bdl	371	<bdl	<bdl
	MOR_24-25	124	763	22402	4179	8257	<bdl	569	<bdl	<bdl	206	<bdl	<bdl	<bdl	<bdl
	mean	*850*	*806*	*18601*	*4380*	*6849*	*<bdl*	*467*	*2169*	*67*	*347*	*30*	*190*	*<bdl*	*<bdl*
TERRA NERA	**L-type**														
	TN04-3_xxG-5	3038	149	116774	604	54	<bdl	<bdl	<bdl	<bdl	<bdl	<bdl	<bdl	<bdl	<bdl
	TN04_3 A	7258	2689	81965	11007	23969	<bdl	1669	2409	<bdl	322	1200	13	172	0
	TN04_3 B	5776	1608	31696	36415	10508	<bdl	417	27877	<bdl	<bdl	617	<bdl	283	53
	mean	*5358*	*1482*	*76812*	*16009*	*11510*	*<bdl*	*1043*	*15143*	*<bdl*	*322*	*909*	*13*	*228*	*26*
BACINO	**L-type**														
	1BXX1-20	2339	733	46811	6068	2723	<bdl	<bdl	<bdl	142	<bdl	148	<bdl	<bdl	<bdl
	1BXX1-21	7872	862	43179	7610	4028	<bdl	253	4002	254	<bdl	317	<bdl	79	11
	1BXX1-4	185	110	61622	3347	5409	<bdl	56	694	1390	643	103	<bdl	0	0
	mean	*3465*	*568*	*50537*	*5675*	*4053*	*<bdl*	*155*	*2348*	*595*	*643*	*189*	*<bdl*	*40*	*6*
TOPINETTI	**L-type**														
	TOP3_E_1	7148	1151	92384	3252	9055	<bdl	1035	<bdl	<bdl	74	570	<bdl	74	<bdl
	TOP3_E_3	5451	1847	77357	6903	14448	3543	614	22372	51	168	506	105	88	16
	mean	*6300*	*1499*	*84871*	*5077*	*11752*	*3543*	*825*	*22372*	*51*	*121*	*538*	*105*	*81*	*16*
VALLE GIOVE	**L-type**														
	4B_A	3	5	256	617	97	78369	1505	781	<bdl	<bdl	106	<bdl	<bdl	<bdl
	E2xx4_6	1280	89	38606	7712	38314	<bdl	356	13976	1176	115	112	233	<bdl	<bdl
	S-type														
	4Bxx4_8	1719	2546	130000	109580	36212	21301797	91873	37261	88	2014	26062	<bdl	818	9

Table 2.3.5: Resume of LA-ICPMS data for fluid inclusions at Stagnone, Morcone, Ripalte, Terra Nera, Bacino, Topinetti and Valle Giove areas. In red are reported anomalous values which can be related to solid phases contained in the fluid inclusions.

Location	Sample	Mineral	δD	δD_{H2O}	δO_{QTZ}	δO_{HM}	δO_{AD}	δO_{H2O}
Stagnone	F2ST3	tourmaline	-75	-64.2				
Stagnone	F2ST1	tourmaline	-60	-48.9				
Stagnone	F1ST3	tourmaline/quartz	-64	-53.1	13.90			11.3
Stagnone	F1ST5	tourmaline	-66	-55.0				
Morcone	F2MOR01	tourmaline/quartz	-49	-24.9	15.75			11.2
Stagnone	F0ST1	tourmaline	-56	-44.5				
Stagnone	GN1B	biotite	-83	-55.0				
Terra Nera	TN3 EP	epidote	-59	-17.1				
Ginevro	GINEVRO	epidote	-63	-21.2				
Torre di Rio	TR01A	ilvaite	-154	-60.3				
Valle Giove	14VG02	quartz			12.51	-1.14	10.65	6.9
Valle Giove	14VG03	quartz			10.49	-1.97	10.90	4.9
Valle Giove	14VG04	quartz			11.08	-2.67		5.4
Terra Nera	14TN1	quartz			15.90			10.6
Terra Nera	14TN2	quartz			13.39	0.2		8.1
Torre di Rio	TR02	quartz			6.13			3.6
Topinetti	TOP-QZ	quartz			12.17			5.1

Table 2.3.6 : Summary od isotope composition (‰) of D and O recalculed isotope composition of the fluid.

Sample	*Rock Type*	*Locality*	$^{87}Sr/^{86}Sr$	$^{143}Nd/^{144}Nd$	$\delta^{11}B$
PA04g	monzogranite	Barbarossa	0.715313	0.512176	
PA04s	tourmaline spot in monzogranite	Barbarossa	0.71534	0.51217	-7.34
PA04v	tourmaline venlet in monzogranite	Barbarossa	0.71599	0.51218	-6.67
PA11	Leucogranito	Barbarossa	0.71700	0.51218	-6.48
PA220	tourmaline spot in monzogranite	Carvisi	0.71552	0.51217	-7.41
PA115	Qtz in Micaschist	Stagnone	0.72412	0.51193	-10.71
PA212	Micaschist	Spiaggia Ginevro N	0.72651	0.51188	-11.24
PA221	Micaschist	Carvisi	0.72451	0.51187	-9.98
PA101	Leucogranite	Stagnone	0.71741	0.51218	-6.34
PA102	Metasomatic tourmaline	Stagnone	0.71993	0.51207	-6.49
PA104v	Vein of black tourmaline	Stagnone	0.71942	0.51205	-6.49
PA104br1	Black tourm clasts in breccia	Stagnone	0.72052	0.51202	-6.63
PA104br2	Brown tourm cement in breccia	Stagnone	0.71974	0.51207	-6.58
PA212	Leucogranite	Spiaggia Ginevro N	0.71790	0.51219	-6.62
PA203	Metasomatic tourmaline	Spiaggia Ginevro N	0.71912	0.51210	-6.58
PA204	Vein of black tourmaline	Spiaggia Ginevro N	0.72045	0.51199	-6.57
PA205br1	Black tourm clasts in breccia	Spiaggia Ginevro N	0.71987	0.51201	-6.56
PA205br2	Brown tourm cement in breccia	Spiaggia Ginevro N	0.71982	0.51205	-6.68

Sr and Nd isotope ratios were recalculated at 6 Ma

Table 2.3.7 – whole-rock isotopic composition